

# STUDIES ON DUCTILE PHASE TOUGHENING OF MOLYBDENUM DISILICIDE BASED COMPOSITES

## A THESIS

*Submitted in partial fulfilment of the  
requirements for the award of the degree*

*of*

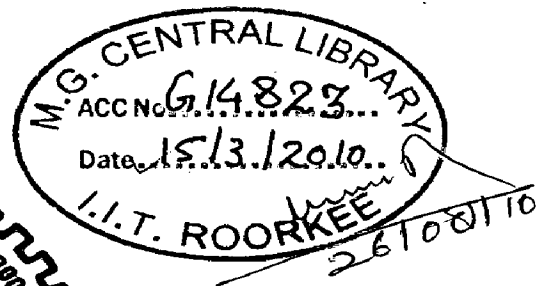
DOCTOR OF PHILOSOPHY

*in*

METALLURGICAL AND MATERIALS ENGINEERING

*by*

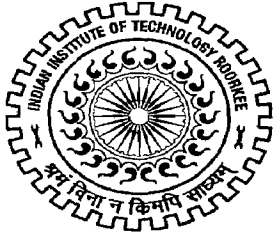
**MANOJ KUMAR JAIN**



DEPARTMENT OF METALLURGICAL AND MATERIALS ENGINEERING  
INDIAN INSTITUTE OF TECHNOLOGY ROORKEE  
ROORKEE - 247 667 (INDIA)

NOVEMBER, 2008

©INDIAN INSTITUTE OF TECHNOLOGY ROORKEE, ROORKEE, 2008  
ALL RIGHTS RESERVED



# INDIAN INSTITUTE OF TECHNOLOGY ROORKEE ROORKEE


## CANDIDATE'S DECLARATION

I hereby certify that the work which is being presented in the thesis entitled **“STUDIES ON DUCTILE PHASE TOUGHENING OF MOLYBDENUM DISILICIDE BASED COMPOSITES”** in partial fulfilment of the requirements for the award of the Degree of Doctor of Philosophy and submitted in the Department of Metallurgical and Materials Engineering of the Indian Institute of Technology Roorkee, Roorkee is an authentic record of my own work carried out during a period from July, 2002 to November, 2008 under the supervision of Dr. Subrata Ray, Professor, Department of Metallurgical and Materials Engineering, Indian Institute of Technology Roorkee, Roorkee and Dr. J Subrahmanyam, Scientist “G” & Division Head, Ceramics and Composites Group, Defence Metallurgical Research Laboratory, Hyderabad.

The matter presented in the thesis has not been submitted by me for the award of any other degree of this or any other Institute.

  
(MANOJ KUMAR JAIN)

This is to certify that the above statement made by the candidate is correct to the best of our knowledge.

  
(J Subrahmanyam)  
Supervisor  
Date: 27.11.2008

  
(Subrata Ray)  
Supervisor

---

The Ph.D. Viva-Voce Examination of **Mr. Manoj Kumar Jain**, Research Scholar has been held on .....

Signature of Supervisors

Signature of External Examiner

## ABSTRACT

Silicides are a new class of engineering materials, which offers the advantages of a ceramic as well as of a metal. Out of a large number of silicide compounds known,  $\text{MoSi}_2$  has been proposed as a model material for high temperature structural applications due to its unique physical and mechanical properties. It is brittle like ceramics at room temperature and undergoes plastic deformation and creep like metals at high temperatures. It has recently become a potential candidate material for several advanced high temperature aerospace applications. The current and potential applications of  $\text{MoSi}_2$  and its composites include heating elements, industrial gas burners, molten metal lances, components requiring contact with molten glasses, diesel engine glow plugs and components for aerospace gas turbine engine.

The most promising materials for high temperature structural applications include Ni base superalloys, the aluminides of nickel, titanium and iron, Si base ceramics like  $\text{SiC}$ ,  $\text{Si}_3\text{N}_4$ ,  $\text{SiC-SiC}$  composites and aluminides of refractory metals. However, Ni base superalloys have a relatively higher density. Nickel, titanium and iron aluminides have melting points in the range of 1400-1600 °C. This limits the use of these materials to temperatures less than 1200 °C, although density wise these aluminides look potentially attractive. In addition to their relatively lower melting points, aluminides have poor oxidation resistance above 650 °C. Si-base ceramics are brittle over the entire temperature range, while refractory metal aluminides are brittle at room temperature and have low strength and creep resistance at required high temperatures.

$\text{MoSi}_2$  has the potential of meeting structural and oxidation requirements up to a temperature of 1600 °C and therefore has been proposed as an alternative to structural ceramics. Efforts to develop  $\text{MoSi}_2$  have been hampered by its extreme brittleness at temperatures below 1000 °C, coupled with relatively low creep resistance. For its effective use as a high temperature structural material, it becomes necessary to toughen the material at lower temperatures (within the  $\text{MoSi}_2$  brittle regime) while simultaneously improving the strength at higher temperatures. It has

been recognized by most workers in the field that the best approach to solve these twin problems is to develop MoSi<sub>2</sub> matrix composites with a variety of reinforcements and its alloying with other elements.

MoSi<sub>2</sub> is a line (no off stoichiometry) compound and does not easily alloy with other elements. WSi<sub>2</sub> has been added due to its similarity in crystal structure and lattice parameters with MoSi<sub>2</sub>. WSi<sub>2</sub> alloying leads to considerable improvements in high temperature strength and creep resistance but its effects on room temperature ductility are found to be very limited (Flinn et al 1989, Petrovic and Honnell 1990, Frankwicz et al 1993). MoSi<sub>2</sub> can be engineered by addition of suitable reinforcements (brittle ceramics as well as ductile metals) to improve its mechanical properties. Ceramic reinforcements are aimed to improve its high temperature strength and creep resistance while the metallic reinforcements may be effective to improve its low temperature fracture toughness. Extensive studies have been carried out on MoSi<sub>2</sub> matrix composites reinforced with high strength ceramics such as SiC (Gac and Petrovic 1985, Petrovic and Honnell 1990, Gibbs et al 1987, Yang and Jeng 1990, Bhattacharya and Petrovic 1991), TiC (Yang et al, 1989), Si<sub>3</sub>N<sub>4</sub> (Petrovic and Honnell 1990, Hebsur 1994), Al<sub>2</sub>O<sub>3</sub> (Tuffe et al, 1993), and ZrO<sub>2</sub> (Petrovic and Honnell 1990, Bhattacharya and Petrovic 1991, Petrovic et al 1991). At high temperatures they improve creep resistance by inhibiting the excessive dislocation motion.

Although the ceramic reinforcements result in considerable improvements in mechanical properties of MoSi<sub>2</sub>, their effect on improving the room temperature fracture toughness of MoSi<sub>2</sub> is marginal. Only moderate room temperature toughening effects are derived with the addition of ceramic reinforcements. Almost all components used for high temperature structural applications are subjected to some degree of stresses at low temperatures, which could be catastrophic for materials having very poor toughness at lower temperatures. The room temperature fracture toughness ( $K_{IC}$ ) of MoSi<sub>2</sub> has been reported to be in the range of 3-4 MPa√m. Since a fracture toughness level of 12 to 15 MPa√m is desirable for possible structural applications, other types of reinforcements, e.g., ductile phases need to be explored. The ductile phase may provide toughness at room and intermediate temperatures while the matrix provides for oxidation resistance.

Ductile phase toughening of  $\text{MoSi}_2$  was proposed originally by V. D. Kristic (Kristic et al, 1981). It was first investigated by Fitzner and Remmele (1985). Other silicides, such as  $\text{Nb}_5\text{Si}_3$ , have exhibited dramatic increase in toughness when a pure Nb phase was incorporated in it. However, there are very limited fracture toughness data on the use of ductile reinforcements in  $\text{MoSi}_2$  matrix. The candidate ductile reinforcements are various refractory metals like Nb, Ta, Mo and W. Most of the work reported till date is on the use of Nb as a ductile reinforcement (Xiao 1991, Xiao and Abbaschian 1992, Alman and Stoloff 1995, Alman et al 1992, Venkateswara Rao et al 1992).

The success achieved in improving the room temperature fracture toughness of  $\text{MoSi}_2$  by incorporating Nb motivates further studies on understanding the effect of other ductile reinforcements on microstructure and mechanical properties of  $\text{MoSi}_2$ . The present study aims to explore and investigate the toughening of  $\text{MoSi}_2$  by different ductile phases. In the present investigation, an attempt has been made to understand the role of various ductile refractory metals like tungsten, molybdenum, tantalum and niobium, in toughening of  $\text{MoSi}_2$  matrix. A comparative study of their compatibility with  $\text{MoSi}_2$  and their effect on its room temperature mechanical behaviour has been carried out. The composites in the present investigation were made by Powder Metallurgy (PM) techniques using vacuum hot pressing (VHP). The ductile refractory metals were incorporated in  $\text{MoSi}_2$  matrix in particulate form (discontinuously reinforced) as well as in foil form (laminated approach). The observations and results obtained in this work have further added to the existing information base and thus results in enhanced understanding of the ductile phase toughening of  $\text{MoSi}_2$ .

*Chapter-1* contains an introduction to the present study in the context of technological importance of the material.

*Chapter-2* begins with the structure and properties of  $\text{MoSi}_2$  including its historical background, thermo-physical and mechanical properties, slip systems, oxidation resistance and its potential applications. A comprehensive survey of literature has been carried out to understand critically the existing knowledge about various approaches to improve the mechanical properties of  $\text{MoSi}_2$  for its use as a high temperature structural material. These include alloying with other elements and

reinforcing with ceramics to create composites. Literature survey has revealed that the idea of incorporating ductile phases in  $\text{MoSi}_2$  for improvement in its room temperature fracture toughness has found very limited attention. Therefore, the problem under present investigation i.e., ductile phase toughening of  $\text{MoSi}_2$  has been formulated. An exhaustive literature survey has been carried out on toughening mechanisms for brittle materials, which revealed that numerous concepts have been proposed for toughening of ceramic matrix composites often leading to confusion. Many of these concepts differ with each other only marginally and use different terminology to describe the similar toughening mechanisms. Therefore, an attempt has been made to regroup various toughening mechanisms for brittle materials bringing out the exclusive and salient features of each one of them and is presented in a brief and systematic manner.

*Chapter-3* presents the experimental procedure and techniques employed for characterization of raw materials, processing of various  $\text{MoSi}_2$  based particulate and laminated composites, microstructural characterization and evaluation of room temperature mechanical behaviour of all the composite systems prepared in the present study. Various combinations of matrix ( $\text{MoSi}_2$  based) and the reinforcements (different ductile refractory metals) were used to prepare a variety of composite systems. Pure  $\text{MoSi}_2$ ,  $\text{MoSi}_2 + 2 \text{ wt}\% \text{ Al}$  and  $\text{MoSi}_2 + 20 \text{ vol}\% \text{ SiC}_p$  were used as the matrix materials with W, Mo, Ta and Nb as reinforcements in particulate as well as in foil form to synthesize various particulate and laminated composites. Nb foil was used with and without application of an inert  $\text{Al}_2\text{O}_3$  coating. Nb foil was also used in embrittled condition after allowing it to undergo partial oxidation during the processing.

The various composite materials were processed by powder metallurgy route. The monolithic matrix materials were also produced by the same processing methods to provide a reference material against which the properties of the composites could be compared. Vacuum hot pressing was used as the main technique to consolidate the matrix and the reinforcement components together to make the different particulate and laminated composites. In the present investigation, the work was restricted to only model "tri-layer" laminates. The microstructural characterization was carried out using optical microscopy (with and without polarized light), x-ray diffraction analysis (XRD), electron probe micro-analysis (EPMA) and scanning electron microscopy (SEM).

The various mechanical properties evaluated included density, elastic modulus, hardness, indentation fracture toughness, flexural strength and fracture toughness. In case of laminated composites, the flexural strength and fracture toughness were measured in crack arrester as well as in crack divider modes by a three-point bend test (SENB test specimen). Apart from the stress intensity factor based fracture toughness, energy driven fracture toughness in terms of 'work of fracture' was also evaluated. Micro-hardness measurements were made at the interface regions between matrix and the reinforcement to understand the mechanical characteristics of the various interfacial reaction products. The metallic foils used as the reinforcements were characterized for their hardness and tensile properties. Cracks generated by the hardness indentations and the crack paths were observed using optical and scanning electron microscopes to have an understanding of the crack propagation and interactions with different reinforcing phases such as SiC particulates and refractory metal foils. This led to an enhanced understanding of the toughening micro mechanisms. The fracture surfaces of the tested specimens were studied using scanning electron microscope. The unbroken specimens were also observed in scanning electron microscope as well as under the stereomicroscope to study the macroscopic crack path behaviour.

Residual thermal stresses are very important in all composite materials. The high processing temperatures involved and a very low strain to fracture make the residual stress problems more severe in ceramic matrix composites. The subject of residual thermal stresses is an area, which has often been neglected in the development of new structural materials. In the present work, an attempt has been made to understand the nature and magnitude of residual thermal stresses in these composites by analytical methods as well as by FEM analysis. *Chapter-4* describes in detail the analysis of residual thermal stresses carried out for  $\text{MoSi}_2 + 20 \text{ vol\% SiC}_p$  particulate composite and various laminated composites prepared using  $\text{MoSi}_2 + 20 \text{ vol\% SiC}_p$  as the matrix layer. As the residual thermal stresses may significantly affect the mechanical behaviour of a composite material, a quantitative idea of residual stresses from the results obtained in the present study was found to be very useful to understand the ductile phase toughening behaviour of  $\text{MoSi}_2$  by different refractory metal foils. It was found that Nb foil reinforced composite has the lowest residual thermal stresses owing to its minimum thermal expansion mismatch with the matrix layer. The results obtained by FEM analysis were found quite similar to the values



obtained by analytical method thus validating the analytical models used in the present work.

*Chapter-5* describes the results of the studies on ductile phase toughening of MoSi<sub>2</sub> based composites by various refractory metal reinforcements. Addition of 20 vol% W, Mo and Nb particulates in MoSi<sub>2</sub> resulted in a considerable improvement in hardness and flexural strength while retaining the fracture toughness over the monolithic MoSi<sub>2</sub>. Only marginal improvement in fracture toughness might be attributed to the conversion of W, Mo and Nb particulates into their silicides due to extensive diffusion of Si from MoSi<sub>2</sub> during high temperature processing. The silicides formed were identified to be of R<sub>5</sub>Si<sub>3</sub> (R = refractory metal) type. Hardness and strength improvement could be attributed to the formation of hard, brittle silicide phases while the same silicides did not result in improved toughness by way of crack bridging. Therefore, the strategy was changed and the ductile refractory metals were used in continuous (foil) form rather than in discontinuous (particulate) form.

Model tri-layer laminated composites were made by sandwiching a single ductile refractory metal foil in between two layers of MoSi<sub>2</sub> powder by vacuum hot pressing. 2 wt% Al was added in MoSi<sub>2</sub> matrix. Al addition into MoSi<sub>2</sub> matrix was found to substantially decrease the amount of free SiO<sub>2</sub> in MoSi<sub>2</sub>. Al reacted with SiO<sub>2</sub> and formed Al<sub>2</sub>O<sub>3</sub> in-situ. This configuration resulted in a considerable improvement in fracture toughness of laminated composite with Ta foil but there was extensive interfacial debonding in the laminated composite with Mo foil due to the large thermal expansion mismatch between MoSi<sub>2</sub> and pure Mo foil. The coefficient of thermal expansion of MoSi<sub>2</sub> is higher than the coefficient of thermal expansion of all the refractory metal foils used in the present study resulting in large residual thermal stresses. To address the problem of thermal expansion mismatch between the layers of the laminated composites, the strategy adopted was to add a moderate amount of 20 vol% SiC particulates in MoSi<sub>2</sub> matrix. The coefficient of thermal expansion of SiC is much lower than the coefficient of thermal expansion of MoSi<sub>2</sub>. Addition of SiC<sub>p</sub> into MoSi<sub>2</sub> decreases the effective coefficient of thermal expansion of the matrix layer and thus results in lower residual thermal stresses in the composite.

These hybrid laminated composites (with brittle SiC particulates and ductile refractory metal foils) exhibited very significant improvement in room temperature fracture toughness over the monolithic  $\text{MoSi}_2 + 20 \text{ vol\% SiC}_p$ . The highest fracture toughness measured from the peak load obtained in a three-point bend test on notched (SENB) specimen was of the order of  $20 \text{ MPa}\sqrt{\text{m}}$  in case of laminated composite with Ta foil. Such improvements in fracture toughness could be attributed to the synergistic effect of brittle (SiC particulates) and ductile (refractory metal foils Mo, Ta and Nb) reinforcements together, as well as improved thermal compatibility between the layers of the laminated composites. However, interfacial reaction layers are formed due to diffusion of Si from  $\text{MoSi}_2$  towards the refractory metal foils at high processing temperatures. The thickness of the interfacial reaction layers was measured as  $40 \mu\text{m}$ ,  $20 \mu\text{m}$  and  $10 \mu\text{m}$  for Mo, Nb and Ta foil laminated composites, respectively. The various interfacial reaction products in different composites were identified as  $\text{Mo}_5\text{Si}_3$ ,  $\text{Mo}_3\text{Si}$ ,  $\text{Mo}_2\text{C}$ ,  $\text{Nb}_5\text{Si}_3$ ,  $\text{Ta}_5\text{Si}_3$ , and  $\text{Ta}_2\text{Si}$  by extensive use of EPMA studies. To suppress the chemical interactions between  $\text{MoSi}_2$  and refractory metal foils at high processing temperatures, application of an inert diffusion barrier coating on the metal foil was tried.

$\text{Al}_2\text{O}_3$  coating on Nb foil was applied by plasma spray method prior to consolidation into a tri-layer laminated composite by vacuum hot pressing. Microstructural and EPMA studies have revealed that  $\text{Al}_2\text{O}_3$  coating on Nb foil effectively inhibited the Si diffusion across the interface and suppressed the matrix-reinforcement chemical interactions during the high temperature processing. Only a very thin Si rich layer was found at the  $\text{Al}_2\text{O}_3$  coating / Nb foil interface due to limited diffusion of Si through the  $\text{Al}_2\text{O}_3$ . However, the  $\text{Al}_2\text{O}_3$  coated Nb foil laminated composite exhibited a relatively lower increase in stress intensity factor based fracture toughness than uncoated Nb foil laminated composite over the monolithic  $\text{MoSi}_2 + 20 \text{ vol\% SiC}_p$ . However, the energy derived fracture toughness measured in terms of work of fracture for  $\text{Al}_2\text{O}_3$  coated Nb foil composite was found to be higher than for the uncoated Nb foil composite. This is attributed to a weak interfacial bonding between  $\text{MoSi}_2$ - $\text{Al}_2\text{O}_3$  coated Nb system.

The formation of various interfacial reaction products in different laminated composites is analysed based on binary and ternary (if available) phase diagrams and

thermodynamic calculations (standard free energy change vs. temperature) for several possible chemical reactions between the constituents of the various composite systems. An attempt has also been made to analyse the interfacial debonding ahead of a propagating crack based on the theories proposed by Cook and Gordon (1964), He and Hutchinson (1989) and Evans and Marshall (1989). The criteria for interfacial debonding seems to be satisfied in all the laminated composites prepared in the present work. However, observations of indentation crack paths under optical and scanning electron microscopes revealed no debonding at the interface upon impingement of the crack on the metal foils. The indentation cracks were arrested by ductile refractory metal foils. It is believed that the impingement of the crack on the interface caused local dislocation slip in the reinforcement instead of interfacial failure, leading to the release of the stress concentration. The present results suggested that interfacial failure was not the only mechanism of blunting cracks in case of ductile reinforcements. The slip capability of ductile reinforcement can play an important role. The fracture toughness of laminated composites measured in crack arrester mode was found to be much higher than the fracture toughness measured in crack divider mode. The improvement in fracture toughness in crack divider mode was found to be moderate for all the laminated composites prepared in the present study. The fracture toughness measured as "*Work of fracture*" exhibited a trend opposite to the "damage tolerance" calculated from the peak load. The mechanisms of crack propagation in crack arrester and crack divider modes were analysed based on the typical load-displacement curves obtained, photographs of the specimens taken after the completion of the test under stereo and scanning electron microscopes and the typical fracture surface features revealed by the SEM.

*Chapter-6* outlines the conclusions of the present investigation. In summary, it has been successfully demonstrated that ductile phase toughening of MoSi<sub>2</sub> is a viable approach to improve fracture toughness of MoSi<sub>2</sub> based materials. The experiments and models establish the necessary basis for understanding and designing the MoSi<sub>2</sub> matrix composites with toughness levels larger than that of monolithic MoSi<sub>2</sub>. The principles and the methods of residual thermal stress analysis employed in the present work may hold equally good and useful for other ceramic matrix composite systems under development.

## ACKNOWLEDGEMENTS

I take this opportunity to express my deep sense of gratitude and profusely thank my guide Professor *Subrata Ray*, Department of Metallurgical and Materials Engineering, Indian Institute of Technology Roorkee, Roorkee for his excellent guidance and painstaking efforts in carrying out this work. His invaluable and prompt remarks at the time of preparation of the manuscript are especially appreciated. The thought provoking discussions I had with him and his valuable suggestions make my association with him memorable.

I have no words to express my indebtedness to my guide at DMRL, Hyderabad, *Dr. J Subrahmanyam*, Scientist "G" and Head, Ceramics and Composites Group for his unstinted support extended throughout the course of this work. His ideas and helpful attitude have contributed significantly in shaping up this thesis as well as my personal life. It is my pleasure to be associated with him.

I am immensely indebted to *Dr. G Malakondiah*, Director, DMRL, Hyderabad for his support and providing the facilities to carry out this work. It is my pleasure to thank *Professor S K Nath*, Head, Metallurgical and Materials Engineering Department, IIT Roorkee for extending the support at various stages of this work.

My sincere thanks to *Dr. D Banerjee*, presently Chief Controller (R&D), DRDO, New Delhi and *Dr. Rahul Mitra*, presently Associate Professor, IIT, Kharagpur, who inspired and encouraged me to undertake the present work during their tenure at DMRL, Hyderabad. I was very fortunate to be associated with them.

I am especially thankful to *Dr. Vikas Kumar* for helping in all possible ways to carry out the experimental work as well as in analyzing the results. I shall always remain grateful to him. I am also grateful to *Mr. Soumya Deb* for helping in carrying out the theoretical analysis work.

I convey my sincere appreciation of *Mr. M Srinivasa Rao*, for his contribution in carrying out the vacuum hot pressing and maintaining the Vacuum Hot Press.

When hurdles appeared insurmountable and targets unachievable, the encouragement and camaraderie of friends helped keep things in perspective. I am highly obliged and wish to express my sincere thanks to many friends and

colleagues who helped lighten the burden, especially *Dr. V V Bhanu Prasad* and *Dr. Amitava Chakraborty*, who stood by me on all occasions during this work. My association with them is memorable.

Thanks are due to all the officers and staff of Ceramics & Composites Group, especially *Dr. M Vijaya Kumar, Dr. T Rajasekharan, Dr. J J Reddy, Dr. R V Krishna Rao, Dr. A R James, Dr. Subir Kumar Roy, Mr. Kumar Saurabh, Mr. Manish Patel, Mr. K Soma Raju, Mr. A Chandrasekhar Rao, Mr. R D Sharma, Mr. R Mohan Rao, Mr N V Visweswara Rao, Mr. R Ravindar Naik, Mr. S Shafiyullah, Mr. A Manik Rao* and *Mr. K Padma Chary*. I am especially thankful to *Mr. P Ramulu* and *(Late) Mr. Ch. Anjaiah* without whose hard work this task could not have been completed successfully.

The help received from Microstructural (Metallography, XRD, EPMA, SEM), Mechanical Characterization and Surface Engineering Groups as well as from TIC, Photography and Design & Drawing sections is thankfully acknowledged. I express my sincere thanks to *Mr. B G Sastry, Mr. T Venugopal Rao, Mr. V Rama Krishna, Mr. V V Rama Rao, Mr. Sheo Muni Gupta, (Late) Mr. David* and *Ms. Sweety Kumari*.

I am grateful to my friends and colleagues *Dr. Dilshad Akhtar, Dr. Amol A Gokhale, Dr. S V Kamat, Dr. T K Nandy, Dr N Eswara Prasad, Dr. Deepak Das, Dr. G Madhusudan Reddy, Dr. Ashok Kumar Singh, Dr. K S Prasad, Dr. (Ms.) Archana Paradakar, Mr. A Balavardhana Rao* and *Mr. Satish Gupta* for their constant encouragement during the course of this work.

It is my pleasure to thank my friends from IIT, Roorkee, *Dr. Sandeep Bansal* and *Dr. Rajneesh Tyagi* whom I found always willing to help, even at the expense of their own work.

I would like to express my gratitude to my parents to whom I owe everything. I express my great admiration to my parents-in-law who have been a guiding force all my life and I have tried my best to measure up to their expectations. I am greatly indebted to my wife *Nupur* and daughter *Runjhun* who have shown great patience during the entire period of this work. Their support kept my spirits always high. I humbly dedicate this work to them.

MANOJ KUMAR JAIN

# CONTENTS

	<i>Page No.</i>
<b>Candidate's declaration</b>	i
<b>Abstract</b>	ii
<b>Acknowledgements</b>	x
<b>Contents</b>	xii
<b>List of Figures</b>	xv
<b>List of Tables</b>	xxxi
<b><i>CHAPTER 1 INTRODUCTION</i></b>	<b>1</b>
1.1 DUCTILE PHASE TOUGHENING OF MoSi <sub>2</sub>	6
1.2 OBJECTIVES AND SCOPE OF PRESENT WORK	7
<b><i>CHAPTER 2 LITERATURE REVIEW</i></b>	<b>12</b>
2.1 HISTORICAL BACKGROUND	12
2.2 STRUCTURE AND PROPERTIES OF MoSi <sub>2</sub>	13
2.2.1 Slip Systems in MoSi <sub>2</sub>	17
2.2.2 Oxidation Resistance of MoSi <sub>2</sub>	17
2.3 APPLICATIONS	22
2.4 MoSi <sub>2</sub> BASED HIGH TEMPERATURE STRUCTURAL MATERIALS	26
2.4.1 Alloying of MoSi <sub>2</sub> with Other Elements	26
2.4.2 MoSi <sub>2</sub> Based Composites with Ceramic Reinforcements	27
2.5 ROOM TEMPERATURE FRACTURE TOUGHNESS OF MoSi <sub>2</sub> MATRIX COMPOSITES	32
2.6 TOUGHENING MECHANISMS FOR BRITTLE MATERIALS	35
2.6.1 Process Zone Mechanisms	41
2.6.2 Bridging Zone Mechanisms	45
2.7 FORMULATION OF THE PROBLEM	57
<b><i>CHAPTER 3 EXPERIMENTAL PROCEDURE</i></b>	<b>60</b>
3.1 RAW MATERIALS	60
3.1.1 Characterization of Raw Materials	61
3.1.2 Tensile Properties of Refractory Metal Foils	63
3.2 PROCESSING	63
3.2.1 Consolidation by Vacuum Hot Pressing	64

3.2.2	Processing of Refractory Metal Particulates Reinforced MoSi <sub>2</sub> Matrix Composites	68
3.2.3	Processing of Laminated Composites with MoSi <sub>2</sub> + 2 wt% Al as Matrix	69
3.2.4	Processing of Laminated Composites with MoSi <sub>2</sub> + 20 vol% SiC <sub>p</sub> as Matrix	73
3.2.5	Application of Al <sub>2</sub> O <sub>3</sub> Coating on Nb Foil	79
3.2.6	Embrittlement of Nb Foil	83
3.3	CHARACTERIZATION	83
3.3.1	Microstructural Studies	83
3.3.2	Evaluation of Mechanical Properties	87
	<b>CHAPTER 4 ANALYSIS OF RESIDUAL THERMAL STRESSES</b>	<b>106</b>
4.1	INTRODUCTION	106
4.2	RESIDUAL THERMAL STRESSES IN PURE MoSi <sub>2</sub>	107
4.2.1	Effect of SiO <sub>2</sub>	
4.3	RESIDUAL THERMAL STRESSES IN MoSi <sub>2</sub> - SiC PARTICULATE COMPOSITES	109
4.3.1	Residual Stresses in SiC Particles	112
4.3.2	Residual Stresses in MoSi <sub>2</sub> Matrix	113
4.3.3	Analysis of Residual Thermal Stresses by Finite Element Methods (FEM)	115
4.4	ANALYSIS OF RESIDUAL THERMAL STRESSES IN MoSi <sub>2</sub> / REFRACTORY METAL FOIL LAMINATED COMPOSITES	118
4.4.1	Properties of MoSi <sub>2</sub> + 20 vol% SiC <sub>p</sub> Outer Layer	118
4.4.2	Residual Thermal Stresses in Laminated Composites	122
4.4.3	Analysis of Residual Thermal Stresses in Laminated Composites by FEM	126
4.5	LIMITATIONS	137
4.6	EFFECT OF INTERFACIAL REACTIONS	138
4.6.1	Effect of Thickness	140
4.6.2	Effect of Thermal Expansion Mismatch	140
4.7	SUMMARY OF RESULTS	141
	<b>CHAPTER 5 RESULTS AND DISCUSSION</b>	<b>142</b>
5.1	RAW MATERIALS	142

5.1.1	Chemical and X-ray Diffraction Analysis	142
5.1.2	Particle Size and Size Distribution	143
5.1.3	Particle Shape and Morphology	151
5.1.4	Characterization of As Received Refractory Metal Foils	151
5.2	DUCTILE REFRACTORY METAL PARTICLES REINFORCED MoSi <sub>2</sub> MATRIX COMPOSITES	161
5.2.1	Microstructural Studies	161
5.2.2	Evaluation of Mechanical Properties	176
5.3	LAMINATED COMPOSITES WITH (MoSi <sub>2</sub> + 2 wt% Al) AS MATRIX	184
5.3.1	Microstructural Studies	190
5.3.2	Mechanical Behaviour	199
5.4	LAMINATED COMPOSITES WITH (MoSi <sub>2</sub> + 20 vol% SiC <sub>p</sub> ) AS MATRIX	217
5.4.1	Microstructural Studies	217
5.4.2	Evaluation of Mechanical Properties	247
5.5	INTERFACE MODIFICATION BY APPLICATION OF INERT COATINGS	284
5.5.1	Microstructure	288
5.5.2	Mechanical Properties	294
5.6	EFFECT OF NB FOIL EMBRITTLEMENT	299
5.7	DISCUSSION	303
5.7.1	Particulate Composites with Pure MoSi <sub>2</sub> as Matrix	305
5.7.2	Laminated Composites with (MoSi <sub>2</sub> + 2 wt% Al) as Matrix	314
5.7.3	Laminated Composites with (MoSi <sub>2</sub> + 20 vol% SiC <sub>p</sub> ) as Matrix	321
5.7.4	(MoSi <sub>2</sub> + 20 vol% SiC <sub>p</sub> ) + Al <sub>2</sub> O <sub>3</sub> Coated Nb Foil Laminated Composite	358
5.8	SUMMARY OF RESULTS	362
	<b>CHAPTER 6 CONCLUSIONS</b>	<b>367</b>
	<b>REFERENCES</b>	<b>371</b>



## LIST OF FIGURES

<b>No.</b>	<b>Title</b>	<b>Page No.</b>
<b>Fig. 1.1</b>	A plot of melting point vs. density for intermetallics having $T_m \geq 1600$ °C	5
<b>Fig. 1.2</b>	Effect of addition of pure Nb on room temperature fracture toughness of Nb <sub>5</sub> Si <sub>3</sub> intermetallic	8
<b>Fig. 1.3</b>	Thermal expansion coefficients of various materials	11
<b>Fig. 2.1</b>	An abbreviated history of MoSi <sub>2</sub> depicting a number of important events and milestones.	14
<b>Fig. 2.2</b>	Crystal structure of MoSi <sub>2</sub> .	15
<b>Fig. 2.3</b>	Mo-Si binary phase diagram.	15
<b>Fig. 2.4</b>	Possible arrangements for the free energy vs. temperature curves for the liquid, C11 <sub>b</sub> and C40 phases for pure MoSi <sub>2</sub> .	18
<b>Fig. 2.5</b>	Schematic showing some of the slip systems in MoSi <sub>2</sub> .	21
<b>Fig. 2.6</b>	Binary phase diagrams (a) Mo-W (b) Mo-Ta and (c) Mo-Nb.	29
<b>Fig. 2.7</b>	Homogeneity range in mole fraction and two-phase fields for various combinations of disilicides at 1300 °C.	30
<b>Fig. 2.8</b>	Creep rate of SiC particulates reinforced MoSi <sub>2</sub> matrix composites with different volume fractions of SiC phase.	30
<b>Fig. 2.9</b>	Temperature dependence of (a) Vickers hardness and (b) fracture toughness for pure MoSi <sub>2</sub> and MoSi <sub>2</sub> containing 2 wt% carbon.	33
<b>Fig. 2.10</b>	Improvement in room temperature fracture toughness due to additions of SiC and ZrO <sub>2</sub> to MoSi <sub>2</sub> .	34
<b>Fig. 2.11</b>	Schematic representation of crack tilting by a second phase particle.	43

<b>Fig. 2.12</b>	(a) Schematic representation of crack deflection and (b) Normalized local stress intensity factor vs. normalized delamination (deflection) length for 90° crack deflection in laminated composites.	44
<b>Fig. 2.13</b>	Schematic representation of crack bowing by second phase particles.	47
<b>Fig. 2.14</b>	Schematic representation of crack bridging by whiskers.	47
<b>Fig. 2.15</b>	Crack bridging by ductile particles.	50
<b>Fig. 2.16</b>	Schematic load-displacement curves for a ductile wire reinforced brittle matrix composite (a) without debonding between ductile wire and brittle matrix (b) with debonding between ductile wire and brittle matrix.	55
<b>Fig. 2.17</b>	Schematic showing crack bridging by a ductile metal foil in a brittle matrix.	55
<b>Fig. 2.18</b>	(a) Schematic of a laminated composite made of SiC laminas with weak interlayers of graphite (b) Experimental load vs. displacement curves in a three-point bend test for notched monolithic SiC and for the laminated material.	56
<b>Fig. 3.1</b>	(a) Schematic drawing of flat tensile specimen (ASTM Standard E8M) used to make tensile specimens of metal foils (b) Tensile test specimens of refractory metal foils.	65
<b>Fig. 3.2</b>	Relationship of hot pressing to other forming and consolidation processes.	66
<b>Fig. 3.3</b>	GCA vacuum hot press used in the present study.	70
<b>Fig. 3.4</b>	Typical hot pressing set up used with GCA vacuum hot press.	70
<b>Fig. 3.5</b>	Schematic illustration of sequence of various steps in the processing of ductile refractory metal particulates reinforced MoSi <sub>2</sub> matrix composites.	71
<b>Fig. 3.6</b>	Flow chart illustrating the various steps schematically in dry blending of MoSi <sub>2</sub> and refractory metal powders.	72
<b>Fig. 3.7</b>	Rubber roller mill used for blending of matrix and reinforcement powders.	72

<b>Fig. 3.8</b>	Schematic illustration of stacking and bonding of different layers in making of a tri-layer laminated composite.	75
<b>Fig. 3.9</b>	Flow chart illustrating the various steps schematically in the processing of Mo and Ta foil reinforced MoSi <sub>2</sub> matrix laminated composites.	76
<b>Fig. 3.10</b>	Flow chart showing schematically various steps in the processing of the ductile refractory metal foils reinforced MoSi <sub>2</sub> based laminated composites.	77
<b>Fig. 3.11</b>	Flow charts illustrating the various steps schematically in the process of (a) de-agglomeration of SiC particles and (b) wet blending of MoSi <sub>2</sub> and SiC powders.	80
<b>Fig. 3.12</b>	A typical time-temperature-pressure cycle used in the vacuum hot pressing of composites investigated in the present study.	81
<b>Fig. 3.13</b>	Schematic of plasma spray deposition processing.	82
<b>Fig. 3.14</b>	Schematic illustration of indentation induced cracks in ceramics formed at different load levels (A) Median or half-penny (B) Palmqvist	91
<b>Fig. 3.15</b>	Schematic showing a hardness indentation and Indentation cracks as viewed from the top on the surface of the specimen.	91
<b>3.16</b>	The various steps adopted in the preparation of three-point bend test specimens from the vacuum hot pressed composite discs.	94
<b>Fig. 3.17</b>	Variation in stress in a three-point bend flexural test specimen (a) through the thickness and (b) along the specimen length.	95
<b>Fig. 3.18</b>	Schematic showing failure load vs. span length for a three-point bend test specimen and conditions for failure in flexure and shear modes.	98
<b>Fig. 3.19</b>	Schematic illustration of loading modes in a three-point bend test of a laminated composite (a) crack arrester mode (b) crack divider mode.	99

<b>Fig. 3.20</b>	Schematic diagrams of the SENB fracture toughness test specimens (a) crack arrester mode (b) crack divider mode.	102
<b>Fig. 4.1</b>	Thermal expansion coefficients in tetragonal MoSi <sub>2</sub> .	108
<b>Fig. 4.2</b>	Residual thermal stresses in a particle reinforced composite consisting of a SiC particle of radius, $a$ , embedded in a MoSi <sub>2</sub> matrix of radius, $b$ .	111
<b>Fig. 4.3</b>	The variation of radial stress, $\sigma_r$ , with distance $r$ in MoSi <sub>2</sub> matrix.	116
<b>Fig. 4.4</b>	Residual thermal stresses (radial, $\sigma_r$ and tangential, $\sigma_\theta$ components) in MoSi <sub>2</sub> matrix varying with distance.	116
<b>Fig. 4.5</b>	Cross-sectional view of the model of composite used for the FEM analysis.	117
<b>Fig. 4.6</b>	Variation of radial compressive stress with distance in MoSi <sub>2</sub> matrix.	117
<b>Fig. 4.7</b>	Variation of tangential tensile (hoop) stress with distance in MoSi <sub>2</sub> matrix.	120
<b>Fig. 4.8</b>	Tri-layer MoSi <sub>2</sub> / ductile metal foil laminated composite.	120
<b>Fig. 4.9</b>	Designation of different layers in laminated composite.	123
<b>Fig. 4.10</b>	Development of residual thermal stresses in a laminated composite after cooling from processing temperature.	124
<b>Fig. 4.11</b>	Stress contour plots of MoSi <sub>2</sub> + 20 vol% SiC <sub>p</sub> with (a) Mo foil (b) Ta foil and (c) Nb foil laminated composites in a two dimensional planar view (X-Y plane).	130
<b>Fig. 4.12</b>	Stress contour plots of MoSi <sub>2</sub> + 20 vol% SiC <sub>p</sub> with (a) Mo foil (b) Ta foil and (c) Nb foil laminated composites in a full isometric view of the composite.	131
<b>Fig. 4.13</b>	Stress variation plots across the thickness of (MoSi <sub>2</sub> + 20 vol% SiC <sub>p</sub> ) with Mo, Ta and Nb foil laminated composites.	132
<b>Fig. 4.14</b>	View of stress contour plots along the mid-plane section of the top MoSi <sub>2</sub> matrix layer (a) Mo foil (b) Ta foil and (c) Nb foil laminated composites.	133

<b>Fig. 4.15</b>	Stress variation plots along the mid-plane of MoSi <sub>2</sub> matrix layer of laminated composites with Mo, Ta and Nb foils (a) across the length and (b) across the width.	134
<b>Fig. 4.16</b>	View of stress contour plots along the mid-plane section of the metal foils (a) Mo foil (b) Ta foil and (c) Nb foil laminated composites.	135
<b>Fig. 4.17</b>	Stress variation plots along mid-plane of the foil of laminated composites with Mo, Ta and Nb foils (a) across the length and (b) across the width.	136
<b>Fig. 4.18</b>	Interfacial reaction layers in tri-layer laminated composite.	139
<b>Fig. 5.1</b>	X-ray diffraction patterns of (a) MoSi <sub>2</sub> and (b) SiC powders.	145
<b>Fig. 5.2</b>	X-ray diffraction patterns of (a) W (b) Mo and (c) Nb powders.	147
<b>Fig. 5.3</b>	Particle size analysis of (a) MoSi <sub>2</sub> and (b) SiC powders.	148
<b>Fig. 5.4</b>	Particle size analysis of (a) W (b) Mo and (c) Nb powders.	150
<b>Fig. 5.5</b>	SEM pictures showing shape and morphology of (a) MoSi <sub>2</sub> and (b) SiC powder particles.	153
<b>Fig. 5.6</b>	SEM pictures showing shape and morphology of (a) W (b) Mo and (c) Nb powder particles.	155
<b>Fig. 5.7</b>	Optical micrographs of as received pure Mo foil taken at different magnifications.	156
<b>Fig. 5.8</b>	Optical micrographs of as received pure Ta foil taken at different magnifications.	157
<b>Fig. 5.9</b>	Engineering stress – strain curves of as received refractory metal foils (a) Mo foil (b) Ta foil and (c) Nb foil.	159
<b>Fig. 5.10</b>	SEM fractograph of as received Mo foil after the uniaxial tensile test.	159
<b>Fig. 5.11</b>	Fracture surfaces of as received (a) Ta foil and (b) Nb foil after the uniaxial tensile test.	160
<b>Fig. 5.12</b>	Polarized light optical micrographs of (a) MoSi <sub>2</sub> + 20 vol% W (b) MoSi <sub>2</sub> + 20 vol% Mo and (c) MoSi <sub>2</sub> + 20 vol% Nb composites	163

<b>Fig. 5.13</b>	SEM back scattered electron (BSE) images of MoSi <sub>2</sub> + 20 vol% W composite taken at different magnification.	164
<b>Fig. 5.14</b>	X-ray diffraction pattern of MoSi <sub>2</sub> + 20 vol% W composite	165
<b>Fig. 5.15</b>	EPMA images of MoSi <sub>2</sub> + 20 vol% W composite (a) back scattered electron image (b) x-ray map of W (c) x-ray map of Mo and (d) x-ray map of Si	166
<b>Fig. 5.16</b>	SEM back scattered electron (BSE) images of MoSi <sub>2</sub> + 20 vol% Mo composite taken at different magnifications.	169
<b>Fig. 5.17</b>	X-ray diffraction pattern of MoSi <sub>2</sub> + 20 vol% Mo composite	170
<b>Fig. 5.18</b>	EPMA images of MoSi <sub>2</sub> + 20 vol% Mo composite (a) back scattered electron image and (b) x-ray map of Si	171
<b>Fig. 5.19</b>	SEM back scattered electron (BSE) images of MoSi <sub>2</sub> + 20 vol% Nb composite taken at different magnifications.	172
<b>Fig. 5.20</b>	X-ray diffraction pattern of MoSi <sub>2</sub> + 20 vol% Nb composite	173
<b>Fig. 5.21</b>	EPMA images of MoSi <sub>2</sub> + 20 vol% Nb composite (a) back scattered electron image (b) x-ray map of Nb (c) x-ray map of Si and (d) x-ray map of Mo	174
<b>Fig. 5.22</b>	EPMA images showing a silica particle present inside MoSi <sub>2</sub> (a) back scattered electron image (b) x-ray map of Si and (c) x-ray map of oxygen	175
<b>Fig. 5.23</b>	Optical micrographs showing typical hardness indentation marks and associated radial cracks in (a) MoSi <sub>2</sub> + 20 vol% W and (b) MoSi <sub>2</sub> + 20 vol% Mo composites.	179
<b>Fig. 5.24</b>	Indentation load ( $P$ ) vs. the crack length ( $c^{3/2}$ ) graph as obtained in the case of MoSi <sub>2</sub> + 20 vol% Nb composite.	180
<b>Fig. 5.25</b>	SEM fractographs of flexural strength (three point bend) test specimens of (a) MoSi <sub>2</sub> + 20 vol% W (b) MoSi <sub>2</sub> + 20 vol% Nb and (c) MoSi <sub>2</sub> + 20 vol% Mo composites.	182
<b>Fig. 5.26</b>	Typical load-displacement curves for K <sub>IC</sub> test specimens (notched three point bend) of (a) MoSi <sub>2</sub> + 20 vol% W (b) MoSi <sub>2</sub> + 20 vol% Mo and (c) MoSi <sub>2</sub> + 20 vol% Nb composites.	183

<b>Fig. 5.27</b>	Fracture surfaces of $K_{IC}$ (notched three point bend) test specimens of (a) $\text{MoSi}_2 + 20 \text{ vol\% W}$ (b) $\text{MoSi}_2 + 20 \text{ vol\% Mo}$ and (c) $\text{MoSi}_2 + 30 \text{ vol\% Nb}$ composites.	187
<b>Fig. 5.28</b>	SEM back scattered electron images showing indentation crack paths in (a) $\text{MoSi}_2 + 20 \text{ vol\% Mo}$ and (b) $\text{MoSi}_2 + 20 \text{ vol\% W}$ composites.	188
<b>Fig. 5.29</b>	Standard free energy change ( $\Delta G$ vs. <i>temperature</i> ) for reduction of $\text{SiO}_2$ and in-situ formation of $\text{Al}_2\text{O}_3$ by addition of Al in $\text{MoSi}_2$ .	189
<b>Fig. 5.30</b>	Polarized light optical microstructure of $\text{MoSi}_2 + 2 \text{ wt\% Al}$ alloy.	192
<b>Fig. 5.31</b>	Polarized light optical microstructure of ( $\text{MoSi}_2 + 2 \text{ wt\% Al}$ ) and Mo foil laminated composite taken at the interfacial region.	192
<b>Fig. 5.32</b>	Polarized light optical microstructures of ( $\text{MoSi}_2 + 2 \text{ wt\% Al}$ ) with Ta foil laminated composite showing (a) interfacial reaction layers on both sides of Ta foil and (b) interfacial region at a higher magnification.	193
<b>Fig. 5.33</b>	SEM back scattered electron images of (a) ( $\text{MoSi}_2 + 2 \text{ wt\% Al}$ ) + Mo foil and (b) ( $\text{MoSi}_2 + 2 \text{ wt\% Al}$ ) + Ta foil laminated composites showing interfacial reaction layers	194
<b>Fig. 5.34</b>	X-ray diffraction patterns of (a) $\text{MoSi}_2 + 2 \text{ wt\% Al} + \text{Mo}$ foil composite and (b) $\text{MoSi}_2 + 2 \text{ wt\% Al} + \text{Ta}$ foil composite	195
<b>Fig. 5.35</b>	EPMA images of ( $\text{MoSi}_2 + 2 \text{ wt\% Al}$ ) + Mo foil laminated composite (a) back scattered electron image (b) x-ray map of Mo (c) x-ray map of Si and (d) line scan of Si.	196
<b>Fig. 5.36</b>	EPMA images of ( $\text{MoSi}_2 + 2 \text{ wt\% Al}$ ) + Mo foil laminated composite (a) x-ray map of Al (b) line scan of Al (c) x-ray map of oxygen and (d) line scan of oxygen.	197
<b>Fig. 5.37</b>	EPMA images of ( $\text{MoSi}_2 + 2 \text{ wt\% Al}$ ) + Ta foil laminated composite (a) back scattered electron image (b) x-ray map of Mo (c) x-ray map of Ta (d) x-ray map of Si and (e) line scan of Si.	200

<b>Fig. 5.38</b>	EPMA images of (MoSi <sub>2</sub> + 2 wt% Al) + Ta foil laminated composite (a) x-ray map of Al (b) line scan of Al (c) x-ray map of oxygen and (d) line scan of oxygen.	201
<b>Fig. 5.39</b>	A typical indentation load ( $P$ ) vs. crack length ( $c^{3/2}$ ) graph as obtained in the case of MoSi <sub>2</sub> + 2 wt% Al matrix.	205
<b>Fig. 5.40</b>	Optical micrograph showing a typical hardness indentation mark taken inside the Mo foil.	205
<b>Fig. 5.41</b>	Polarized light optical micrograph showing a typical indentation crack originating from a corner of the hardness indentation mark taken inside the matrix layer of (MoSi <sub>2</sub> + 2 wt% Al) + Mo foil laminated composite.	206
<b>Fig. 5.42</b>	SEM back scattered electron image showing indentation crack paths in (MoSi <sub>2</sub> + 2 wt% Al) + Ta foil.	206
<b>Fig. 5.43</b>	Indentation crack paths in (MoSi <sub>2</sub> + 2 wt% Al) + Mo foil composite (a) polarized light optical micrograph (b) SEM back scattered electron image of the same area.	207
<b>Fig. 5.44</b>	SEM fractograph of a three point bend test specimen of MoSi <sub>2</sub> + 2 wt% Al alloy matrix.	210
<b>Fig. 5.45</b>	SEM secondary electron images (taken at different magnifications) of (MoSi <sub>2</sub> + 2 wt% Al) + Ta foil laminated composite being tested in crack arrester mode.	211
<b>Fig. 5.46</b>	SEM fractographs of fracture toughness, $K_{IC}$ (notched three point bend) test specimen of (MoSi <sub>2</sub> + 2 wt% Al) + Ta foil composite (a) taken inside the matrix layer and (b) taken inside the Ta foil.	214
<b>Fig. 5.47</b>	Stereo photomicrographs of a three-point bend test specimen of (MoSi <sub>2</sub> + 2 wt% Al) + Mo foil laminated composite.	215
<b>Fig. 5.48</b>	(a) The fracture surface of a three-point bend test specimen of (MoSi <sub>2</sub> + 2 wt% Al) + Mo foil laminated composite failed in the shear mode. (b) Optical microstructure of (MoSi <sub>2</sub> + 2 wt% Al) + Mo foil composite.	216



<b>Fig. 5.49</b>	Standard free energy change ( $\Delta G$ vs. <i>temperature</i> ) for a possible chemical reaction between $\text{MoSi}_2$ and $\text{SiC}$ .	219
<b>Fig. 5.50</b>	Microstructures of $\text{MoSi}_2$ reinforced with 20 vol% $\text{SiC}$ particulates. (a) and (b) are taken under ordinary light while (c) and (d) are taken under polarized light at different magnifications.	220
<b>Fig. 5.51</b>	X-ray diffraction pattern of $\text{MoSi}_2 + 20 \text{ vol}\% \text{ SiC}_p$ composite.	221
<b>Fig. 5.52</b>	SEM back scattered electron image of $\text{MoSi}_2 + 20 \text{ vol}\% \text{ SiC}_p$ composite.	221
<b>Fig. 5.53</b>	Image analysis for calculating volume fraction of $\text{SiC}$ particulates in $\text{SiC}_p$ reinforced $\text{MoSi}_2$ matrix after processing at high temperature.	222
<b>Fig. 5.54</b>	Ordinary light optical microstructures of ( $\text{MoSi}_2 + 20 \text{ vol}\% \text{ SiC}_p$ ) + Mo foil laminated composite exhibiting (a) interfacial reaction layers on both sides of Mo foil and (b) interfacial reaction zone at a higher magnification.	223
<b>Fig. 5.55</b>	Polarized light optical microstructures of ( $\text{MoSi}_2 + 20 \text{ vol}\% \text{ SiC}_p$ ) + Mo foil laminated composite showing interfacial reaction zone at different magnifications.	223
<b>Fig. 5.56</b>	SEM back scattered electron images of ( $\text{MoSi}_2 + 20 \text{ vol}\% \text{ SiC}_p$ ) + Mo foil laminated composite showing (a) interfacial reaction layers on both sides of the Mo foil and (b) interfacial reaction layer at a higher magnification	226
<b>Fig. 5.57</b>	X-ray diffraction pattern of ( $\text{MoSi}_2 + 20 \text{ vol}\% \text{ SiC}_p$ ) + Mo foil laminated composite.	227
<b>Fig. 5.58</b>	SEM secondary electron image of ( $\text{MoSi}_2 + 20 \text{ vol}\% \text{ SiC}_p$ ) + Mo foil laminated composite and EDS analysis.	228
<b>Fig. 5.59</b>	SEM back scattered electron image of ( $\text{MoSi}_2 + 20 \text{ vol}\% \text{ SiC}_p$ ) + Mo foil laminated composite with EDS analysis.	229
<b>Fig. 5.60</b>	EPMA images of ( $\text{MoSi}_2 + 20 \text{ vol}\% \text{ SiC}_p$ ) + Mo foil laminated composite (a) BSE image (b) x-ray map of Mo (c) x-ray map of Si and (d) line scan of Si.	231

<b>Fig. 5.61</b>	EPMA back scattered electron image of (MoSi <sub>2</sub> + 20 vol% SiC <sub>p</sub> ) + Mo foil composite.	234
<b>Fig. 5.62</b>	High magnification EPMA images of the area surrounded by a rectangle in Fig. 5.61 (a) back scattered electron image (b) x-ray map of Si and (c) x-ray map of carbon.	235
<b>Fig. 5.63</b>	Optical microstructures of (MoSi <sub>2</sub> + 20 vol% SiC <sub>p</sub> ) + Ta foil laminated composite (a) micrograph in as polished condition and (b) micrograph after optical etching.	236
<b>Fig. 5.64</b>	X-ray diffraction pattern of (MoSi <sub>2</sub> + 20 vol% SiC <sub>p</sub> ) + Ta foil laminated composite.	237
<b>Fig. 5.65</b>	SEM back scattered electron image of (MoSi <sub>2</sub> + 20 vol% SiC <sub>p</sub> ) + Ta foil laminated composite.	238
<b>Fig. 5.66</b>	EPMA images of (MoSi <sub>2</sub> + 20 vol% SiC <sub>p</sub> ) + Ta foil laminated composite (a) back scattered electron image (b) x-ray map of Mo (c) x-ray map of Ta (d) x-ray map of Si and (e) line scan of Si.	239
<b>Fig. 5.67</b>	EPMA images of (MoSi <sub>2</sub> + 20 vol% SiC <sub>p</sub> ) + Ta foil composite revealing the presence of SiO <sub>2</sub> particles (a) BSE image with matrix area shaded dark (b) x-ray map of oxygen and (c) x-ray map of Si.	240
<b>Fig. 5.68</b>	Optical microstructures of (MoSi <sub>2</sub> + 20 vol% SiC <sub>p</sub> ) + Nb foil laminated composite (a) micrograph in as polished condition using ordinary light and (b) micrograph using polarized light.	243
<b>Fig. 5.69</b>	SEM back scattered electron image of (MoSi <sub>2</sub> + 20 vol% SiC <sub>p</sub> ) + Nb foil laminated composite.	244
<b>Fig. 5.70</b>	X-ray diffraction pattern of (MoSi <sub>2</sub> + 20 vol% SiC <sub>p</sub> ) + Nb foil laminated composite.	244
<b>Fig. 5.71</b>	EPMA images of (MoSi <sub>2</sub> + 20 vol% SiC <sub>p</sub> ) + Nb foil laminated composite (a) back scattered electron image (b) x-ray map of Si (c) x-ray map of Mo and (d) x-ray map Nb.	245

<b>Fig. 5.72</b>	EPMA images of (MoSi <sub>2</sub> + 20 vol% SiC <sub>p</sub> ) + Nb foil composite (a) BSE image with matrix area shaded dark revealing the SiO <sub>2</sub> particles present at the interface (b) x-ray map of Mo and (c) x-ray map of Nb.	246
<b>Fig. 5.73</b>	Optical micrographs showing typical hardness indentation marks in (a) MoSi <sub>2</sub> + 20 vol% SiC <sub>p</sub> monolithic material and (b) (MoSi <sub>2</sub> + 20 vol% SiC <sub>p</sub> ) + Ta foil laminated composite.	251
<b>Fig. 5.74</b>	A typical indentation load ( $P$ ) vs. crack length ( $c^{3/2}$ ) graph as obtained in the case of MoSi <sub>2</sub> + 20 vol% SiC <sub>p</sub> matrix.	254
<b>Fig. 5.75</b>	SEM back scattered electron images of MoSi <sub>2</sub> + 20 vol% SiC <sub>p</sub> monolithic material showing the indentation crack interactions with SiC particles.	255
<b>Fig. 5.76</b>	Optical micrographs of (MoSi <sub>2</sub> + 20 vol% SiC <sub>p</sub> ) + Mo foil laminated composite showing (a) a typical hardness indentation mark in the matrix taken near the interface and (b) the same area as shown in (a) exhibiting crack path interactions with Mo foil, at a higher magnification.	256
<b>Fig. 5.77</b>	Optical micrographs showing typical hardness indentation mark and crack paths in (MoSi <sub>2</sub> + 20 vol% SiC <sub>p</sub> ) + Ta foil laminated composite (a) in MoSi <sub>2</sub> matrix taken close to the interface and (b) same area as in (a) taken at a higher magnification.	257
<b>Fig. 5.78</b>	(a) Optical micrograph showing a typical hardness indentation mark and radial indentation cracks in (MoSi <sub>2</sub> + 20 vol% SiC <sub>p</sub> ) + Nb foil laminated composite (b) SEM back scattered electron image of the area bounded by the rectangle in Fig. 5.78(a).	258
<b>Fig. 5.79</b>	A typical load-displacement curve obtained from fracture toughness testing of MoSi <sub>2</sub> + 20 vol% SiC <sub>p</sub> matrix (monolithic).	261

<b>Fig. 5.80</b>	SEM fractograph of fracture toughness (notched three point bend) test specimen of $\text{MoSi}_2 + 20 \text{ vol}\% \text{ SiC}_p$ matrix.	261
<b>Fig. 5.81</b>	Typical load-displacement curves obtained from fracture toughness testing of $(\text{MoSi}_2 + 20 \text{ vol}\% \text{ SiC}_p) + \text{Ta}$ foil laminated composite (a) crack arrester mode and (b) crack divider mode.	264
<b>Fig. 5.82</b>	SEM secondary electron images (taken at different magnifications) of a $K_{IC}$ specimen of $(\text{MoSi}_2 + 20 \text{ vol}\% \text{ SiC}_p) + \text{Ta}$ foil laminated composite tested in crack arrester mode.	269
<b>Fig. 5.83</b>	SEM secondary electron images (taken at different magnifications) of a $K_{IC}$ specimen tested in crack arrester mode showing plastic deformation and necking in Nb metal foil.	270
<b>Fig. 5.84</b>	SEM secondary electron images of a fracture toughness ( $K_{IC}$ ) specimen of $(\text{MoSi}_2 + 20 \text{ vol}\% \text{ SiC}_p) + \text{Ta}$ foil laminated composite tested in crack divider mode (a) the side along the loading axis (b) the same side at a higher magnification (c) the bottom (notch) side and (d) the top (loading side) view.	271
<b>Fig. 5.85</b>	SEM secondary electron images of a flexural strength specimen of $(\text{MoSi}_2 + 20 \text{ vol}\% \text{ SiC}_p) + \text{Ta}$ foil laminated composite tested in crack divider mode (a) the side along the loading axis (b) the bottom side and (c) the top view.	272
<b>Fig. 5.86</b>	SEM fractographs of fracture toughness ( $K_{IC}$ ) test specimen of $(\text{MoSi}_2 + 20 \text{ vol}\% \text{ SiC}_p) + \text{Mo}$ foil laminated composite tested in crack arrester mode (a) interfacial area (b) inside matrix layer and (c) Mo foil region.	274
<b>Fig. 5.87</b>	Fracture surfaces of Ta foil taken at different magnifications.	275

<b>Fig. 5.88</b>	(a) SEM fractograph of fracture toughness ( $K_{IC}$ ) test specimen of $(\text{MoSi}_2 + 20 \text{ vol}\% \text{ SiC}_p) + \text{Nb}$ foil laminated composite tested in crack arrester mode (b) Enclosed area in Fig. 5.88(a) viewed at a higher magnification.	276
<b>Fig. 5.89</b>	SEM fractographs of fracture toughness ( $K_{IC}$ ) test specimen of $(\text{MoSi}_2 + 20 \text{ vol}\% \text{ SiC}_p) + \text{Nb}$ foil laminated composite tested in crack arrester mode (a) fracture surface of the $\text{MoSi}_2\text{-SiC}_p$ matrix layer and (b) fracture surface of Nb foil.	277
<b>Fig. 5.90</b>	SEM fractographs of fracture toughness ( $K_{IC}$ ) test specimen of $(\text{MoSi}_2 + 20 \text{ vol}\% \text{ SiC}_p) + \text{Nb}$ foil laminated composite tested in crack divider mode taken at different locations showing predominantly the Nb foil area.	280
<b>Fig. 5.91</b>	Optical micrographs showing micro-hardness indentation mark inside the interfacial reaction layer in $(\text{MoSi}_2 + 20 \text{ vol}\% \text{ SiC}_p) + \text{Mo}$ foil laminated composite (a) ordinary light photomicrograph and (b) microstructure using polarized light.	282
<b>Fig. 5.92</b>	Optical micrographs showing micro-hardness indentation mark inside the interfacial reaction layer in $(\text{MoSi}_2 + 20 \text{ vol}\% \text{ SiC}_p) + \text{Ta}$ foil laminated composite taken at different magnifications.	285
<b>Fig. 5.93</b>	Optical micrographs showing micro-hardness indentation mark inside the interfacial reaction layer in $(\text{MoSi}_2 + 20 \text{ vol}\% \text{ SiC}_p) + \text{Nb}$ foil laminated composite taken at different magnifications.	286
<b>Fig. 5.94</b>	Standard free energy change (per mole of $\text{MoSi}_2$ ) for chemical reactions likely to take place between (a) $\text{Al}_2\text{O}_3$ and $\text{MoSi}_2$ and (b) between $\text{Al}_2\text{O}_3$ and Nb.	289
<b>Fig. 5.95</b>	Microstructures of $(\text{MoSi}_2 + 20 \text{ vol}\% \text{ SiC}_p) + \text{Al}_2\text{O}_3$ coated Nb foil laminated composite (a) ordinary light optical micrograph and (b) polarized light optical micrograph.	290

<b>Fig. 5.96</b>	X-ray diffraction pattern of $(\text{MoSi}_2 + 20 \text{ vol}\% \text{ SiC}_p) + \text{Al}_2\text{O}_3$ coated Nb foil laminated composite.	291
<b>Fig. 5.97</b>	EPMA images of $(\text{MoSi}_2 + 20 \text{ vol}\% \text{ SiC}_p) + \text{Al}_2\text{O}_3$ coated Nb foil laminated composite (a) back scattered electron image (b) x-ray map of Mo (c) x-ray map of Nb (d) x-ray map Al and (e) x-ray map of oxygen.	292
<b>Fig. 5.98</b>	EPMA images of $(\text{MoSi}_2 + 20 \text{ vol}\% \text{ SiC}_p) + \text{Al}_2\text{O}_3$ coated Nb foil laminated composite (a) back scattered electron image (b) BSE image shaded dark to reveal the Si rich interfacial layer between $\text{Al}_2\text{O}_3$ coating and Nb foil and (c) x-ray map of Si.	295
<b>Fig. 5.99</b>	Low magnification EPMA images of $(\text{MoSi}_2 + 20 \text{ vol}\% \text{ SiC}_p) + \text{Al}_2\text{O}_3$ coated Nb foil composite showing $\text{Al}_2\text{O}_3$ coating on both sides of the Nb foil (a) back scattered electron image (b) x-ray map of Si and (c).line scan of Si.	296
<b>Fig. 5.100</b>	(a) Optical micrograph showing a typical hardness indentation mark and radial indentation cracks in $(\text{MoSi}_2 + 20 \text{ vol}\% \text{ SiC}_p) + \text{Nb}$ foil ( $\text{Al}_2\text{O}_3$ coated) laminated composite (b) SEM back scattered electron image of the area bounded by the rectangle in Fig. 5.100(a).	300
<b>Fig. 5.101</b>	A typical load - displacement curve of $(\text{MoSi}_2 + 20 \text{ vol}\% \text{ SiC}_p) + \text{Nb}$ foil embrittled laminated composite tested for fracture toughness in crack arrester mode.	301
<b>Fig. 5.102</b>	Fracture surface of an embrittled Nb foil in $(\text{MoSi}_2 + 20 \text{ vol}\% \text{ SiC}_p) + \text{Nb}$ foil laminated composite tested in crack arrester mode.	304
<b>Fig. 5.103</b>	W-Si binary phase diagram	307
<b>Fig. 5.104</b>	Standard free energy change ( $\Delta G$ vs. <i>Temperature</i> ) for the possible chemical reactions between $\text{MoSi}_2$ and pure W resulting in the formation of various tungsten silicides.	307
<b>Fig. 5.105</b>	Standard free energy change ( $\Delta G$ vs. <i>Temperature</i> ) for possible chemical reactions between $\text{MoSi}_2$ and pure Mo resulting in the formation of other molybdenum silicides.	308

<b>Fig. 5.106</b>	Standard free energy change ( $\Delta G$ vs. <i>temperature</i> ) for oxidation of pure Mo.	311
<b>Fig. 5.107</b>	Mo-O binary phase diagram	311
<b>Fig. 5.108</b>	Nb-Si binary phase diagram	312
<b>Fig. 5.109</b>	Standard free energy change ( $\Delta G$ vs. <i>Temperature</i> ) for the possible chemical reactions between MoSi <sub>2</sub> and pure Nb resulting in the formation of niobium silicides.	312
<b>Fig. 5.110</b>	Ta-Si binary phase diagram	317
<b>Fig. 5.111</b>	Standard free energy change ( $\Delta G$ vs. <i>Temperature</i> ) for the possible chemical reactions between MoSi <sub>2</sub> and pure Ta resulting in the formation of tantalum silicides.	320
<b>Fig. 5.112</b>	Standard free energy change ( $\Delta G$ vs. <i>Temperature</i> ) for the possible chemical reactions between SiC and pure Mo resulting in the formation of Mo <sub>2</sub> C.	323
<b>Fig. 5.113</b>	An isothermal section of Mo-Si-C ternary phase diagram at 1600 °C.	326
<b>Fig. 5.114</b>	Mo-Si-Nb isothermal section at 800 °C (Savitskiy et al, 1965).	329
<b>Fig. 5.115</b>	Schematic diffusion path observed for the reaction between Nb and MoSi <sub>2</sub> at 1600 °C superimposed on the ternary triangle of Fig. 5.114 at 800 °C.	329
<b>Fig. 5.116</b>	Schematic of stress distribution at a crack tip.	340
<b>Fig. 5.117</b>	A chart of $G_i/G_f$ vs. $\alpha$	341
<b>Fig. 5.118</b>	A typical load-displacement curve obtained in fracture toughness ( $K_{IC}$ ) testing of (MoSi <sub>2</sub> + 20 vol% SiC <sub>p</sub> ) + Nb foil laminated composite in crack arrester mode.	349
<b>Fig. 5.119</b>	A typical stereo photomicrograph of a $K_{IC}$ specimen of MoSi <sub>2</sub> / ductile refractory metal foil laminated composite tested in crack arrester mode.	349

<b>Fig. 5.120</b>	Schematic representation of a $K_{IC}$ specimen of a tri-layer laminated composite tested in crack arrester mode showing necking and plastic deformation in ductile metal foil and crack advancement in the brittle matrix.	352
<b>Fig. 5.121</b>	A typical load-displacement curve obtained in fracture toughness ( $K_{IC}$ ) testing of $(MoSi_2 + 20 \text{ vol\% } SiC_p) + Nb$ foil laminated composite in crack divider mode.	352
<b>Fig. 5.122</b>	(a) Schematic representation of a $K_{IC}$ test specimen of a tri-layer laminated composite used for testing in crack divider mode. (b), (c) and (d) are the stereo photomicrographs of the three sides of the specimen as designated by ABCD, BQRC and PQRS in Fig. a, respectively after the completion of the test.	355
<b>Fig. 5.123</b>	Schematic representation of mechanism of crack propagation (crack front convolution) in alternate $MoSi_2 /$ ductile metal foil tri-layer laminated composites.	356
<b>Fig. 5.124</b>	SEM fractographs of $K_{IC}$ test specimen (crack divider mode) of Nb foil laminated composite (a) at low magnification showing notched as well as fractured area covering both matrix and the foil, while (b) and (c) are the foil areas designated as A and B in Fig. (a) taken at higher magnifications.	357
<b>Fig. 5.125</b>	Crystal structure of $\alpha-Al_2O_3$	360
<b>Fig. 5.126</b>	Improvement in room temperature fracture toughness (damage tolerance, $K_{max}$ ) of various laminated composites investigated in the present study.	363
<b>Fig. 5.127</b>	Improvement in room temperature fracture toughness (work of fracture) of various laminated composites investigated in the present study.	364



## LIST OF TABLES

<b>No.</b>	<b>Title</b>	<b>Page No.</b>
<b>Table 1.1</b>	Compositions of known silicides in the form of a periodic table	3
<b>Table 1.2</b>	List of candidate materials for high temperature structural applications	4
<b>Table 1.3</b>	Comparative properties of MoSi <sub>2</sub> and Si-based ceramics	4
<b>Table 2.1</b>	Thermo-physical & mechanical properties of pure MoSi <sub>2</sub> .	19
<b>Table 2.2</b>	Possible slip systems in MoSi <sub>2</sub> .	20
<b>Table 2.3</b>	Oxidation resistance of high melting point silicides.	20
<b>Table 2.4</b>	Potential applications of MoSi <sub>2</sub> based materials.	24
<b>Table 2.5</b>	Fracture toughness data for MoSi <sub>2</sub> based composites.	37
<b>Table 3.1</b>	Source and the average particle size of various powders used as matrix and the reinforcement materials.	62
<b>Table 3.2</b>	Source and the thickness of the refractory metal foils used in making MoSi <sub>2</sub> based laminated composites.	62
<b>Table 3.3</b>	Hot pressing process parameters to consolidate MoSi <sub>2</sub> based materials.	67
<b>Table 4.1</b>	No. of independent coefficients of thermal expansion in various crystal systems.	108
<b>Table 4.2</b>	Material properties and processing parameters for MoSi <sub>2</sub> / SiC particulate composite.	113
<b>Table 4.3</b>	Physical properties of MoSi <sub>2</sub> and SiC.	119
<b>Table 4.4</b>	Physical properties of different layers in the laminated composites.	127
<b>Table 4.5</b>	The calculated values of residual thermal stresses in various laminated composites.	127
<b>Table 4.6</b>	The values of residual thermal stresses in various laminated composites obtained by FEM analysis.	139
<b>Table 4.7</b>	Chemical nature and properties of interfacial reaction layers in various laminated composites.	140
<b>Table 5.1</b>	Chemical analysis of the MoSi <sub>2</sub> , SiC and Al powders.	144

<b>Table 5.2</b>	Chemical analysis of the W, Mo and Nb powders used as reinforcements.	144
<b>Table 5.3</b>	Chemical analysis of the as received Mo, Ta and Nb foils used for making MoSi <sub>2</sub> based laminated composites.	144
<b>Table 5.4</b>	Particle size distribution for MoSi <sub>2</sub> , W, Mo and Nb powders.	147
<b>Table 5.5</b>	Tensile properties of as received refractory metal foils used in preparing various laminated composites.	152
<b>Table 5.6</b>	Composition of the reaction products between MoSi <sub>2</sub> and W particulates as determined by EPMA in Fig. 5.15(a).	165
<b>Table 5.7</b>	Composition of the reaction products between MoSi <sub>2</sub> and Mo particulates as determined by EPMA in Fig. 5.18(a).	170
<b>Table 5.8</b>	Composition of the reaction products between MoSi <sub>2</sub> and Nb particulates as determined by EPMA in Fig. 5.21(a).	173
<b>Table 5.9</b>	Mechanical properties of refractory metal particulate reinforced MoSi <sub>2</sub> matrix composites.	178
<b>Table 5.10</b>	Electron probe micro analysis (EPMA) of the interfacial region between MoSi <sub>2</sub> matrix and Mo foil in (MoSi <sub>2</sub> + 2 wt% Al) + Mo foil laminated composite (Fig. 5.35(a)).	197
<b>Table 5.11</b>	Electron probe micro analysis (EPMA) of the interfacial region between MoSi <sub>2</sub> matrix and Ta foil in (MoSi <sub>2</sub> + 2 wt% Al) + Ta foil laminated composite (Fig. 5.37(a)).	201
<b>Table 5.12</b>	Mechanical properties of (MoSi <sub>2</sub> + 2 wt% Al) + Mo and Ta foil laminated composites.	202
<b>Table 5.13</b>	Mechanical properties of (MoSi <sub>2</sub> + 2 wt% Al) + Mo and Ta foil laminated composites.	202
<b>Table 5.14</b>	Estimation of volume fraction of phases in MoSi <sub>2</sub> + 20 vol% SiC <sub>p</sub> composite by image analysis software.	222
<b>Table 5.15</b>	Composition of the various phases identified in (MoSi <sub>2</sub> + 20 vol% SiC <sub>p</sub> ) + Mo foil laminated composite as determined by energy dispersive spectroscopy (EDS).	230

<b>Table 5.16</b>	Composition of the various phases identified in (MoSi <sub>2</sub> + 20 vol% SiC <sub>p</sub> ) + Ta foil laminated composite as determined by energy dispersive spectroscopy (EDS).	238
<b>Table 5.17</b>	Electron probe micro analysis (EPMA) of the interface between MoSi <sub>2</sub> + 20 vol% SiC <sub>p</sub> matrix and Nb foil laminated composite (Fig. 5.71(a)).	242
<b>Table 5.18</b>	Mechanical properties of (MoSi <sub>2</sub> + 20 vol% SiC <sub>p</sub> ) + Mo, Ta and Nb foil laminated composites.	249
<b>Table 5.19</b>	Mechanical properties of (MoSi <sub>2</sub> + 20 vol% SiC <sub>p</sub> ) + Mo, Ta and Nb foil laminated composites.	250
<b>Table 5.20</b>	Micro-hardness data for (MoSi <sub>2</sub> + 20 vol% SiC <sub>p</sub> ) + Mo, Ta and Nb foils laminated composites.	281
<b>Table 5.21</b>	Electron probe micro-analysis (EPMA) of the interface between MoSi <sub>2</sub> + 20 vol% SiC <sub>p</sub> matrix and Al <sub>2</sub> O <sub>3</sub> coated Nb foil laminated composite (Fig. 5.97(a)).	293
<b>Table 5.22</b>	Mechanical properties of (MoSi <sub>2</sub> + 20 vol% SiC <sub>p</sub> ) + Al <sub>2</sub> O <sub>3</sub> coated Nb foil laminated composite.	297
<b>Table 5.23</b>	Strength and toughness values of (MoSi <sub>2</sub> + 20 vol% SiC <sub>p</sub> ) + Al <sub>2</sub> O <sub>3</sub> coated Nb foil laminated composite.	297
<b>Table 5.24</b>	Properties of (MoSi <sub>2</sub> + 20 vol% SiC <sub>p</sub> ) + Nb foil embrittled laminated composite	30.1
<b>Table 5.25</b>	Melting points and atomic sizes of elements forming various phases present in the laminated composites.	328
<b>Table 5.26</b>	Residual thermal stresses and <i>R</i> values for different laminated composites.	336
<b>Table 5.27</b>	Elastic constants of different ductile refractory metals and the MoSi <sub>2</sub> based matrix layer.	344
<b>Table 5.28</b>	Elastic mismatch parameter, $\alpha$ for various laminated composites consisting of different refractory metal foils sandwiched between two layers of MoSi <sub>2</sub> - SiC <sub>p</sub> matrix.	344

### INTRODUCTION

---

Silicides are a new class of materials, which offers the advantages of a ceramic as well as of a metal. Aronsson et al (1965) have catalogued various compositions of well-characterized silicides in the form of a periodic table (Table 1.1). The table clearly shows quite a large number of silicide compounds but only a limited number of them have been considered for structural applications. Out of these,  $\text{MoSi}_2$  has been proposed as a model material for high temperature structural applications due to its unique physical and mechanical properties. It has recently become a potential candidate material for several advanced high temperature aerospace applications.

A generic definition of a ceramic is that, it is a solid, ionic-covalent, inorganic compound.  $\text{MoSi}_2$  deviates from this definition because its atomic bonding is a mixture of covalent and metallic (Alouani et al, 1991) bonding and so, It behaves like brittle ceramics at room temperature while it behaves like metals at high temperatures, undergoing plastic deformation and creep.  $\text{MoSi}_2$  has better ductility than competitive ceramics for use at and above 1200 °C (Badrinarayanan et al, 1996).

One can broadly classify high temperature structural materials into two application groups as shown in Table 1.2, on the basis of large body of data on applications of available in the literature.

Ni-base superalloys have relatively higher density. The density of  $\text{MoSi}_2$  is nearly 25% lower than that of Ni-base superalloys. The most promising intermetallics for high temperature structural applications include the aluminides of nickel, titanium and iron. However, nickel, titanium and iron aluminides have melting points in the range of 1400-1600 °C. This limits the use of these materials to temperatures less than 1200 °C, although density wise these aluminides look potentially attractive. In addition to their relatively lower melting points, aluminides have poor oxidation resistance above 650 °C. Si-base ceramics are brittle over the entire temperature range, while refractory metal aluminides are brittle at room temperature and have low strength and creep resistance at required high temperatures.

Many silicide intermetallics have the potential of meeting structural and oxidation requirements up to a temperature of 1600 °C. Therefore, silicides have been identified as a new class of structural materials, which provides an alternative to structural ceramics. Figure 1.1 shows a plot of melting point,  $T_m$ , versus density for several intermetallics having  $T_m \geq 1600$  °C (Meschter and Schwartz, 1989). Assuming that intermetallics retain strength up to 80 %  $T_m$  ( $T_m$  in K), there is, thus, a lower limit on  $T_m$  equal to 2067 °C for a service temperature of 1600 °C. If an upper limit on density is selected as density of nickel, only seven silicides plus  $\text{MoSi}_2$  are left in this window. Meschter and Schwartz (1989) surveyed these silicide intermetallics for high temperature applications. On the basis of criterion such as availability, phase changes in the temperature range of interest, and oxidation resistance,  $\text{Ti}_5\text{Si}_3$  and  $\text{MoSi}_2$  appear to be the most promising materials.  $\text{Ti}_5\text{Si}_3$  has the lowest density and  $\text{MoSi}_2$  has superior oxidation resistance. Table 1.3 lists some of the similarities, advantages and disadvantages of  $\text{MoSi}_2$  as compared to Si-base ceramics.

Table 1.1 Compositions of known silicides in the form of a periodic table.

Li <sub>4</sub> Si Li <sub>2</sub> Si	Composition of Known Silicides									
NaSi	Mg <sub>2</sub> Si									
KSi	Ca <sub>2</sub> Si	Sc <sub>5</sub> Si <sub>3</sub>	Ti <sub>3</sub> Si	V <sub>3</sub> Si	Cr <sub>3</sub> Si	Mn <sub>3</sub> Si	Fe <sub>3</sub> Si	Co <sub>2</sub> Si	Ni <sub>3</sub> Si	κ(CuSi) β(CuSi) γ-Cu <sub>5</sub> Si Cu <sub>31</sub> Si <sub>8</sub> Cu <sub>15</sub> Si <sub>4</sub>
	CaSi		Ti <sub>5</sub> Si <sub>3</sub>	V <sub>5</sub> Si <sub>3</sub>	Cr <sub>5</sub> Si <sub>3</sub>	Mn <sub>5</sub> Si <sub>3</sub>	Fe <sub>5</sub> Si <sub>3</sub>	CoSi	Ni <sub>5</sub> Si <sub>2</sub>	
	CaSi <sub>2</sub>		TiSi	VSi <sub>2</sub>	CrSi	MnSi	FeSi	CoSi <sub>2</sub>	Ni <sub>2</sub> Si*	
			TiSi <sub>2</sub>		CrSi <sub>2</sub>	MnSi <sub>1.7</sub>	FeSi <sub>2</sub> *		Ni <sub>3</sub> Si <sub>2</sub>	
									NiSi	
									NiSi <sub>2</sub>	
RbSi	Sr <sub>2</sub> Si	Y <sub>5</sub> Si <sub>3</sub>	Zr <sub>3</sub> Si	Nb <sub>3</sub> Si	Mo <sub>3</sub> Si		Ru <sub>2</sub> Si	Rh <sub>2</sub> Si	Pd <sub>3</sub> Si	
	SrSi	YSi	Zr <sub>2</sub> Si	Nb <sub>5</sub> Si <sub>3</sub> *	Mo <sub>5</sub> Si <sub>3</sub>		RuSi*	Rh <sub>5</sub> Si <sub>3</sub>	Pd <sub>2</sub> Si	
	SrSi <sub>2</sub>	YSi <sub>2</sub> *	Zr <sub>3</sub> Si <sub>2</sub>	NbSi <sub>2</sub>	MoSi <sub>2</sub>		Ru <sub>2</sub> Si <sub>3</sub>	Rh <sub>20</sub> Si <sub>13</sub>	PdSi	
			Zr <sub>6</sub> Si <sub>5</sub>					Rh <sub>3</sub> Si <sub>2</sub>		
			ZrSi					RhSi		
			ZrSi <sub>2</sub>							
CaSi	BaSi	LaSi <sub>2</sub>	Hf <sub>2</sub> Si	Ta <sub>3</sub> Si	W <sub>5</sub> Si <sub>3</sub>	Re <sub>5</sub> Si <sub>3</sub>	OsSi	Ir <sub>3</sub> Si	Pt <sub>3</sub> Si*	
	BaSi <sub>2</sub> *		Hf <sub>3</sub> Si <sub>2</sub>	Ta <sub>2</sub> Si <sub>3</sub>	WSi <sub>2</sub>	ReSi	Os <sub>2</sub> Si <sub>3</sub>	Ir <sub>2</sub> Si	Pt <sub>2</sub> Si*	
			HfSi	Ta <sub>5</sub> Si <sub>3</sub> *		ReSi <sub>2</sub>		Ir <sub>3</sub> Si <sub>2</sub>	Pt <sub>6</sub> Si <sub>5</sub>	
			HfSi <sub>2</sub>	TaSi <sub>2</sub>				IrSi	PtSi	
								IrSi <sub>3</sub>		

LaSi <sub>2</sub>	CeSi	PrSi <sub>2</sub> *	NdSi <sub>2</sub> *	SmSi <sub>2</sub> *	EuSi <sub>2</sub>	Gd <sub>2</sub> Si <sub>3</sub>	Tb <sub>2</sub> Si <sub>3</sub>	Dy <sub>2</sub> Si <sub>3</sub>	Ho <sub>2</sub> Si <sub>3</sub>	Er <sub>2</sub> Si <sub>3</sub>	Tm <sub>2</sub> Si <sub>3</sub>	Yb <sub>2</sub> Si <sub>3</sub>	Lu <sub>2</sub> Si <sub>3</sub>
	CeSi <sub>2</sub>					GdSi <sub>2</sub> *	TbSi <sub>2</sub>	DySi <sub>2</sub> *	HoSi <sub>2</sub>				

Th <sub>3</sub> Si <sub>2</sub>	U <sub>3</sub> Si	NpSi <sub>2</sub>	Pu <sub>5</sub> Si <sub>3</sub>	* There is more than one phase with or near this composition
ThSi	U <sub>3</sub> Si <sub>2</sub>		PuSi	
Th <sub>2</sub> Si <sub>3</sub>	USi*		Pu <sub>2</sub> Si	
ThSi <sub>2</sub> *	U <sub>3</sub> Si <sub>5</sub>		PuSi <sub>2</sub>	
	USi <sub>2</sub> *			

Table 1.2 List of candidate materials for high temperature structural applications.

Use Temperature < 1000 °C	Use Temperature > 1000 °C
Ni-base superalloys	Si-base ceramics (SiC, Si <sub>3</sub> N <sub>4</sub> , SiC-SiC composites)
Ni aluminides	Refractory metal aluminides (NbAl <sub>3</sub> , TaAl <sub>3</sub> )
Ti aluminides	Silicides (MoSi <sub>2</sub> , Ti <sub>5</sub> Si <sub>3</sub> )

Table 1.3 Comparative properties of MoSi<sub>2</sub> and Si-based ceramics.

MoSi <sub>2</sub>	Si-base Ceramics
High melting point ~ 2030 °C	Decomposition > 2100 °C
Excellent oxidation resistance	Excellent oxidation resistance
Thermodynamically stable with ceramic reinforcements	Thermodynamically stable with ceramic reinforcements
Good thermal conductivity	Good thermal conductivity
Poor fracture toughness at low temperatures	Poor fracture toughness at low temperatures
<b><u>Advantages</u></b>	
Ductile at high temperatures (BDTT ~ 1000 °C)	Brittle over the entire temperature range
Potential for alloying with other silicides	Difficult to alloy with other elements
Can be electro-discharge machined (EDM) due to adequate electrical conductivity	Difficult to machine (diamond grinding)
Relatively cheaper and non-toxic	Expensive
Good toughness at high temperatures	Poor toughness at high temperatures
Excellent thermal shock resistance	Poor thermal shock resistance
<b><u>Disadvantages</u></b>	
Relatively higher density	Lower density
Adequate creep resistance	Good creep resistance
Higher coefficient of thermal expansion	Lower coefficient of thermal expansion
Existence of PEST oxidation behaviour	No PEST phenomenon
Very good wear	Excellent wear

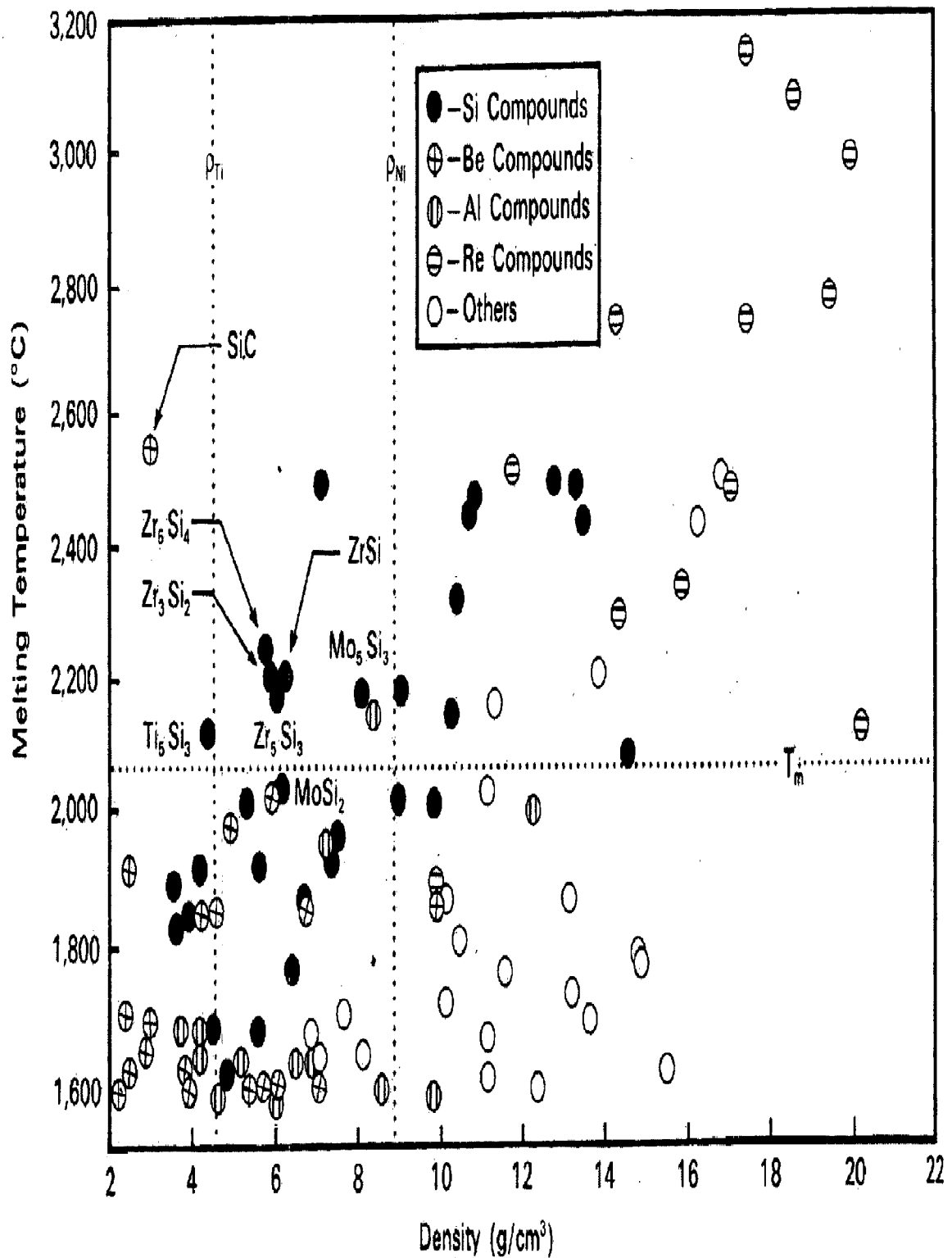


Fig. 1.1 A plot of melting point vs. density for intermetallics having  $T_m \geq 1600$  °C.



Efforts to develop MoSi<sub>2</sub> have been hampered by its extreme brittleness at temperatures below 1000 °C, coupled with relatively low creep resistance. For its effective use as a high temperature structural material, it becomes necessary to toughen the material at lower temperatures (within the MoSi<sub>2</sub> brittle regime) while simultaneously improving the strength at higher temperatures. It has been recognized by most workers in the field that the best chance to solve these twin problems is to develop MoSi<sub>2</sub> matrix composites with a variety of reinforcements and its alloying with other elements.

Although the ceramic reinforcements result in considerable improvements in mechanical properties of MoSi<sub>2</sub>, their effect on improving the room temperature fracture toughness of MoSi<sub>2</sub> is marginal. Only moderate room temperature toughening effects are derived with the addition of ceramic reinforcements. Toughening levels for these reinforcements are similar to those observed in ceramic matrix composites, and are associated with mechanisms such as crack deflection and crack bridging.

## **1.1 DUCTILE PHASE TOUGHENING OF MoSi<sub>2</sub>**

Interest in MoSi<sub>2</sub> and composites based on MoSi<sub>2</sub> for high temperature applications has been renewed in recent years. To develop MoSi<sub>2</sub> as a material for elevated temperature structural applications, it is necessary to improve both, its high temperature strength and creep resistance, and its low temperature fracture toughness. MoSi<sub>2</sub> can be engineered by addition of a variety of reinforcements to improve its mechanical properties. Ceramic reinforcements are used to improve the high temperature strength and creep resistance. However, their effect on improving the room temperature fracture toughness is very marginal. Only moderate room temperature toughening is obtained with the addition of ceramic reinforcements. Toughening levels achieved by these reinforcements are similar to those observed in ceramic matrix composites, and are associated with mechanisms such as crack deflection / crack branching.

Almost all components used for high temperature structural applications are subjected to some degree of stresses at low temperatures, which could be catastrophic for materials having very poor toughness at lower temperatures. The room temperature fracture toughness ( $K_{IC}$ ) of MoSi<sub>2</sub> has been reported to be in the range of 3-4 MPa√m.

Since a fracture toughness level of 12 to 15 MPa√m is desirable for possible structural applications, other types of reinforcements, e.g., ductile phases need to be explored. The ductile phase may provide toughness at room and intermediate temperatures while the matrix provides for oxidation resistance. Generally, the reinforcing material in a composite has a higher elastic modulus compared to the matrix material. Since the ductile reinforcements commonly have a lower elastic modulus than MoSi<sub>2</sub>, it has been termed as INVERSE COMPOSITE (Fitzer, 1988).

Ductile phase toughening of MoSi<sub>2</sub> was proposed originally by V. D. Kristic (Kristic et al, 1981 and Kristic, 1983). It was first investigated by Fitzer and Remmele (1985). Other silicides, such as Nb<sub>5</sub>Si<sub>3</sub>, have exhibited dramatic increase in toughness when a pure Nb phase was incorporated in it as depicted in Fig. 1.2 (Nekkanti and Dimiduk, 1990). Much effort has centered on enhancing the strength and creep resistance of MoSi<sub>2</sub> by incorporating brittle ceramic reinforcement phases. There are very limited fracture toughness data on the use of ductile reinforcements in MoSi<sub>2</sub> matrix. The candidate ductile reinforcements are various refractory metals like Nb, Ta, Mo and W. However, most of the work reported till date is only on the use of Nb as a ductile reinforcement (Xiao 1991<sup>a</sup>, 1991<sup>b</sup>, Xiao and Abbaschian 1992<sup>a</sup>, 1992<sup>b</sup>, Alman and Stoloff 1992, 1994, 1995, Alman et al 1992, 1994, 1998, Venkateswara Rao and Ritchie 1994, Venkateswara Rao et al 1992<sup>a</sup>, 1992<sup>b</sup>).

## **1.2 OBJECTIVES AND SCOPE OF PRESENT WORK**

The success achieved in improving the room temperature fracture toughness of MoSi<sub>2</sub> by incorporating Nb motivates further studies on understanding the effect of other ductile reinforcements on microstructure and properties of MoSi<sub>2</sub>. Only limited information is available on ductile phase toughening of MoSi<sub>2</sub>. The aim of the present work is to investigate further the toughening of MoSi<sub>2</sub> by different ductile phases. Therefore, in the present investigation, an attempt has been made to understand the role of various ductile refractory metals in toughening of MoSi<sub>2</sub> matrix. Different ductile refractory metals like tungsten, molybdenum, tantalum and niobium are selected as the reinforcements to carry out a comparative study of their compatibility with MoSi<sub>2</sub> and their effect on its room temperature mechanical behaviour.

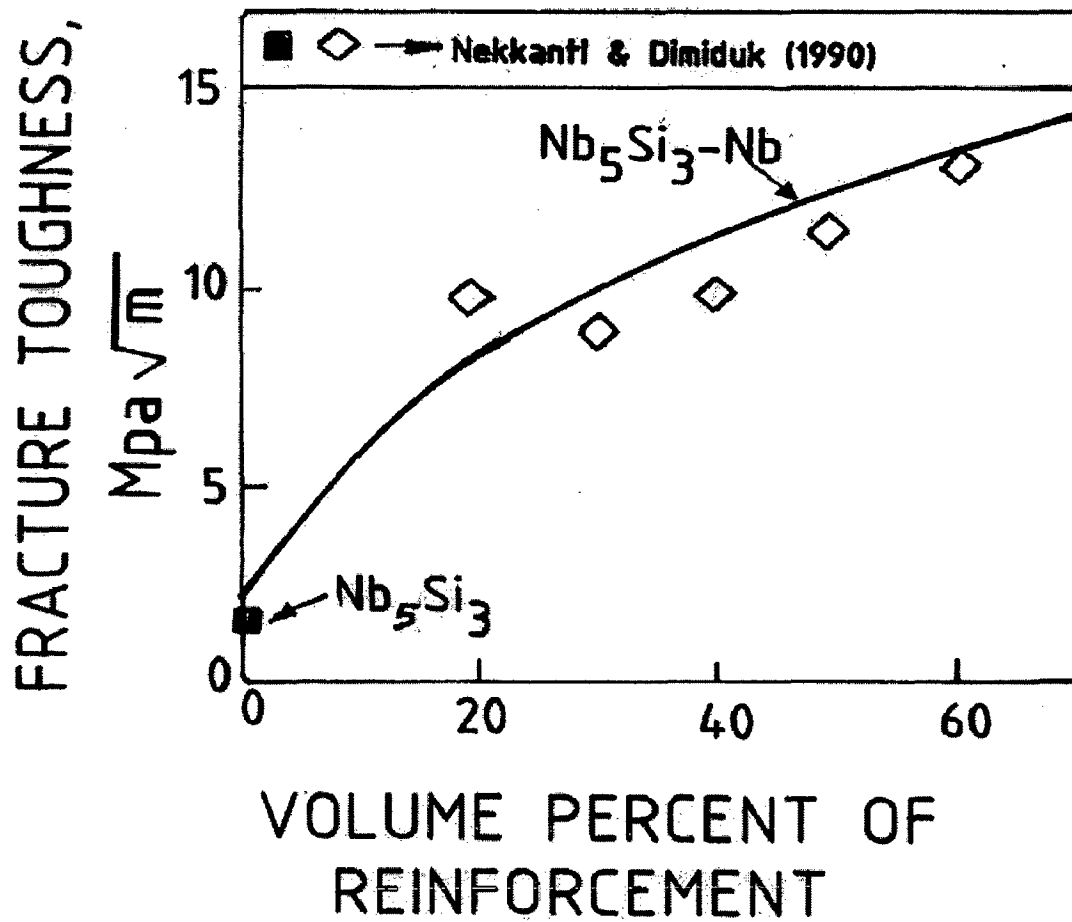


Fig. 1.2

Effect of addition of pure Nb on room temperature fracture toughness of  $\text{Nb}_5\text{Si}_3$  intermetallic.

The composites for the present investigation are made by Powder Metallurgy (PM) techniques using vacuum hot pressing (VHP). The ductile refractory metals are incorporated in  $\text{MoSi}_2$  matrix in particulate form (discontinuously reinforced) as well as in foil form (laminated approach). As most of these refractory metals are thermodynamically unstable with  $\text{MoSi}_2$ , Interfacial reactions are expected to occur between  $\text{MoSi}_2$  and different refractory metals. The use of  $\text{Al}_2\text{O}_3$  coating as a diffusion barrier has been tried to inhibit the chemical interactions between matrix and the reinforcement. Its effects on microstructure and mechanical properties of the composites have been studied.  $\text{MoSi}_2$  has a higher coefficient of thermal expansion than most of the refractory metals, as illustrated in Fig. 1.3 (Vasudevan and Petrovic, 1992). This may give rise to residual thermal stresses in the composites during cooling from processing temperatures to the room temperature. These residual stresses may affect the interfacial bonding and the resultant mechanical properties of the composites. To improve thermal compatibility between  $\text{MoSi}_2$  and the refractory metal foils, SiC particulates in suitable amount have been added in  $\text{MoSi}_2$  matrix. SiC which is thermodynamically stable with  $\text{MoSi}_2$  as well as has a lower coefficient of thermal expansion than  $\text{MoSi}_2$ , when added to  $\text{MoSi}_2$  matrix is expected to reduce the thermal expansion mismatch between  $\text{MoSi}_2$  and the refractory metals.

The various composites made have been characterized for their microstructure including identification and properties of various interfacial reaction products using techniques like optical microscopy, x-ray diffraction, scanning electron microscopy (SEM) and electron probe micro analyzer (EPMA). The mechanical properties evaluated includes elastic modulus, hardness, indentation fracture toughness, observations of crack path interactions with the reinforcements, micro-hardness (interfacial reaction layer products), flexural strength and fracture toughness ( $K_{IC}$ , as well as work of fracture). The toughness evaluation has been carried out in crack arrester as well as in crack divider modes. Extensive use of SEM has been made to evaluate the fracture modes in different composite systems made and investigated in the present work. The observations and results obtained in this work have further added to the existing information base and thus results in enhanced understanding of the ductile phase toughening of  $\text{MoSi}_2$ .

The subject of residual thermal stresses has often been neglected in the development of new structural materials. These stresses are very important in all composite materials and more so in MoSi<sub>2</sub> based composites due to high processing temperatures involved and a very low strain to fracture. A quantitative idea of the residual thermal stresses may be very useful and can give some important guidelines to obtain the enhanced mechanical properties. Therefore, in the present work, an attempt has been made to understand the nature and magnitude of residual thermal stresses in MoSi<sub>2</sub> based particulate and laminated composites by analytical methods as well as by FEM analysis. The principles and the methods of analysis employed in the present work may hold equally useful for other ceramic matrix composite systems under development.

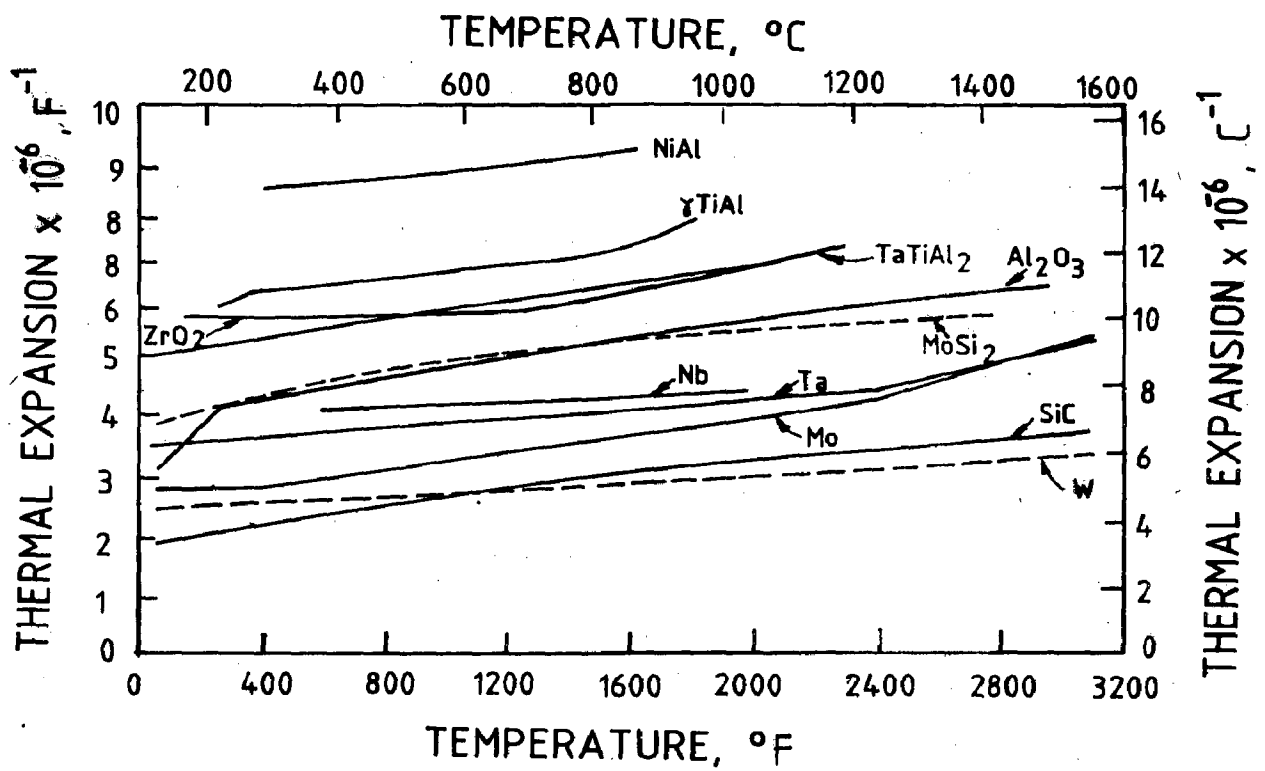


Fig. 1.3 Thermal expansion coefficients of various materials.

# LITERATURE REVIEW

---

## 2.1 HISTORICAL BACKGROUND

MoSi<sub>2</sub> is known since 1907. It was first considered as a high temperature protective coating material for ductile metals (Hoenigschmid, 1907). Beidler and Campbell (USA) were granted the patent on MoSi<sub>2</sub> composition in 1950 (Vasudevan and Petrovic, 1992). The first patent on MoSi<sub>2</sub> for its application as heat conductors made by powder metallurgy route was granted to Kieffer et al in 1951 (Kieffer et al, 1951). Kanthal patented the first commercial heating elements in 1956 (Kanthal, 1956).

Maxwell (1951) appears to have been the first person to seriously suggest the use of MoSi<sub>2</sub> as a structural material in the early 1950s. He determined some of its elevated temperature mechanical properties. Maxwell noted that the low temperature brittleness of MoSi<sub>2</sub> was its major drawback for structural applications.

Nowotny et al (1954) studied Mo-Si-C ternary phase diagram, in which various phases and their relations are identified. In 1973, Fitzer and co-workers (Fitzer et al, 1973) published work on the addition of Al<sub>2</sub>O<sub>3</sub>, SiC and niobium wires to MoSi<sub>2</sub>, which revealed an improvement in mechanical properties. These developments led Fitzer's colleague, Schlichting (Schlichting, 1978) to publish a detailed review article in 1978, suggesting that MoSi<sub>2</sub> was an important matrix material for high temperature structural composites.

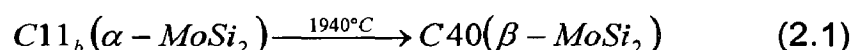
In 1985, two key articles were published. The first was by Fitzer and Remmele (1985), describing in detail their work on niobium wire-reinforced MoSi<sub>2</sub> matrix composites. In the second article, Gac and Petrovic (1985) established the feasibility of SiC whisker reinforced MoSi<sub>2</sub> matrix composites. After 1985, work continued at Los Alamos National Laboratory (LANL) and improvements were made in mechanical properties of SiC-MoSi<sub>2</sub> composites. This LANL work attracted the attention of researchers in the aerospace industry. In about 1986, researchers at Pratt and Whitney began examining SiC-MoSi<sub>2</sub> composites for aerospace applications.

First high temperature structural silicides conference was held at NIST in Gaithersburg, MD in November 1991, following that, many other research groups began initiating work on MoSi<sub>2</sub> composites for structural applications. Fig. 2.1 depicts a number of important events and milestones in the history of MoSi<sub>2</sub>.

## 2.2 STRUCTURE AND PROPERTIES OF MoSi<sub>2</sub>

MoSi<sub>2</sub> has a body-centered tetragonal (C11<sub>b</sub>) crystal structure as shown in Fig. 2.2. Its Pearson's symbol is tI6 with lattice parameters,  $a = 3.20 \text{ \AA}$ ,  $c = 7.85 \text{ \AA}$  and  $c/a = 2.45$  (Adler and Houska, 1978). MoSi<sub>2</sub> possesses a layered structure, consisting of double cross-packed silicon layers alternating with molybdenum layers in a body-centered tetragonal lattice. The tI6 type structure of MoSi<sub>2</sub> is a long range ordered crystal structure which can be viewed as the stacking of three body-centered sub-unit cells and compressing along the c-axis where Mo and Si atoms are placed at the body centres, alternately (Petrovic, 1995).

The Mo-Si binary phase diagram is shown in Fig. 2.3 (Gokhale and Abbaschian, 1991). At approximately 1900 °C, MoSi<sub>2</sub> undergoes a polymorphic transformation (Svechnikov et al, 1971) from tetragonal structure to a hexagonal (hp9 type) crystal structure as follows:





# HISTORY OF MoSi<sub>2</sub>

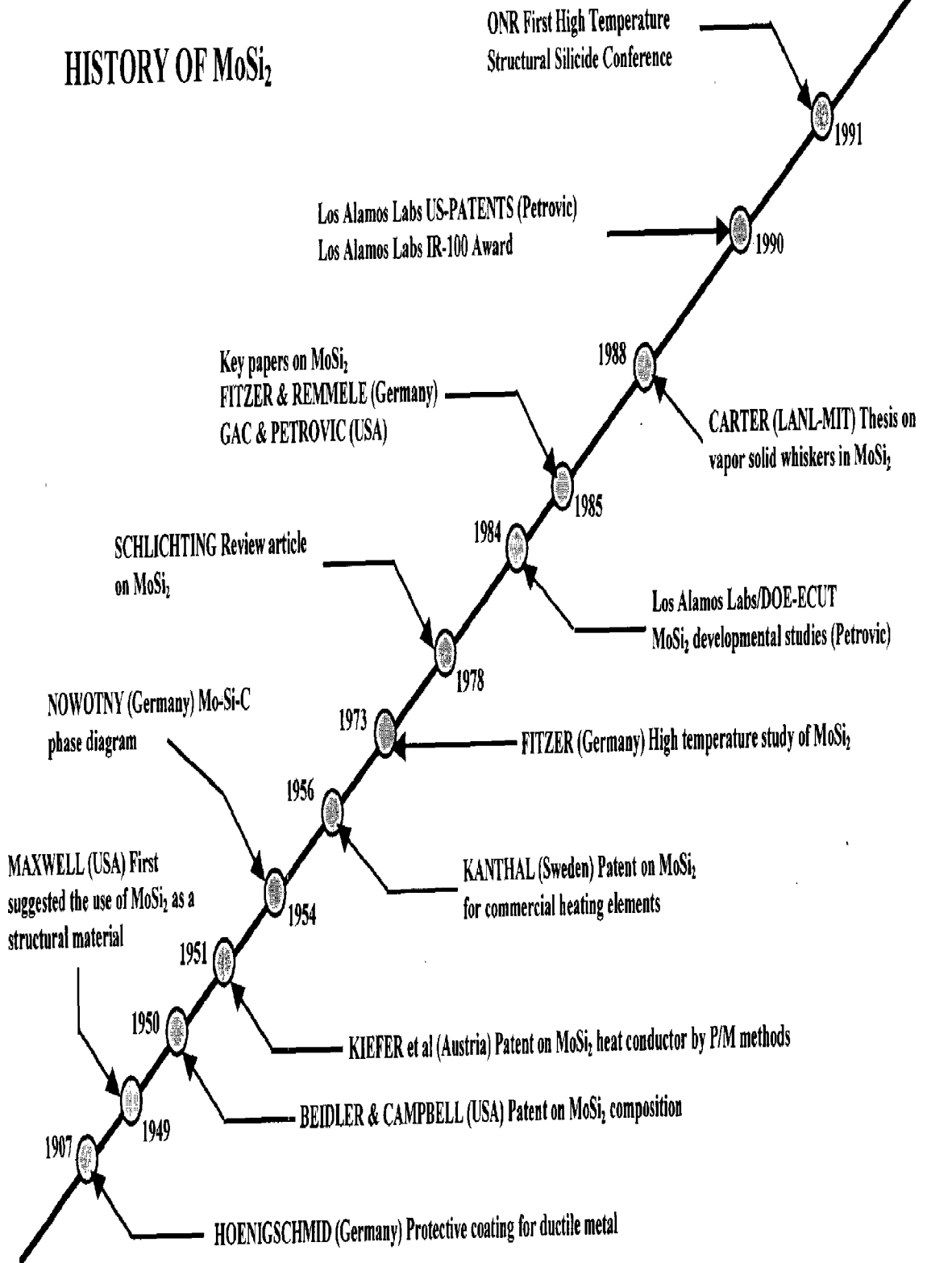


Fig. 2.1 An abbreviated history of MoSi<sub>2</sub> depicting a number of important events and milestones.

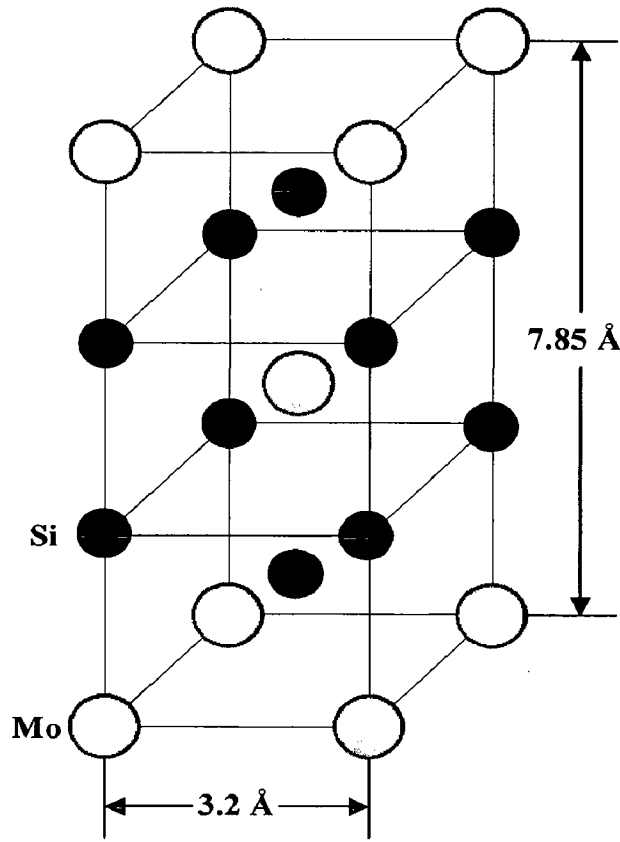


Fig. 2.2 Crystal structure of MoSi<sub>2</sub>.

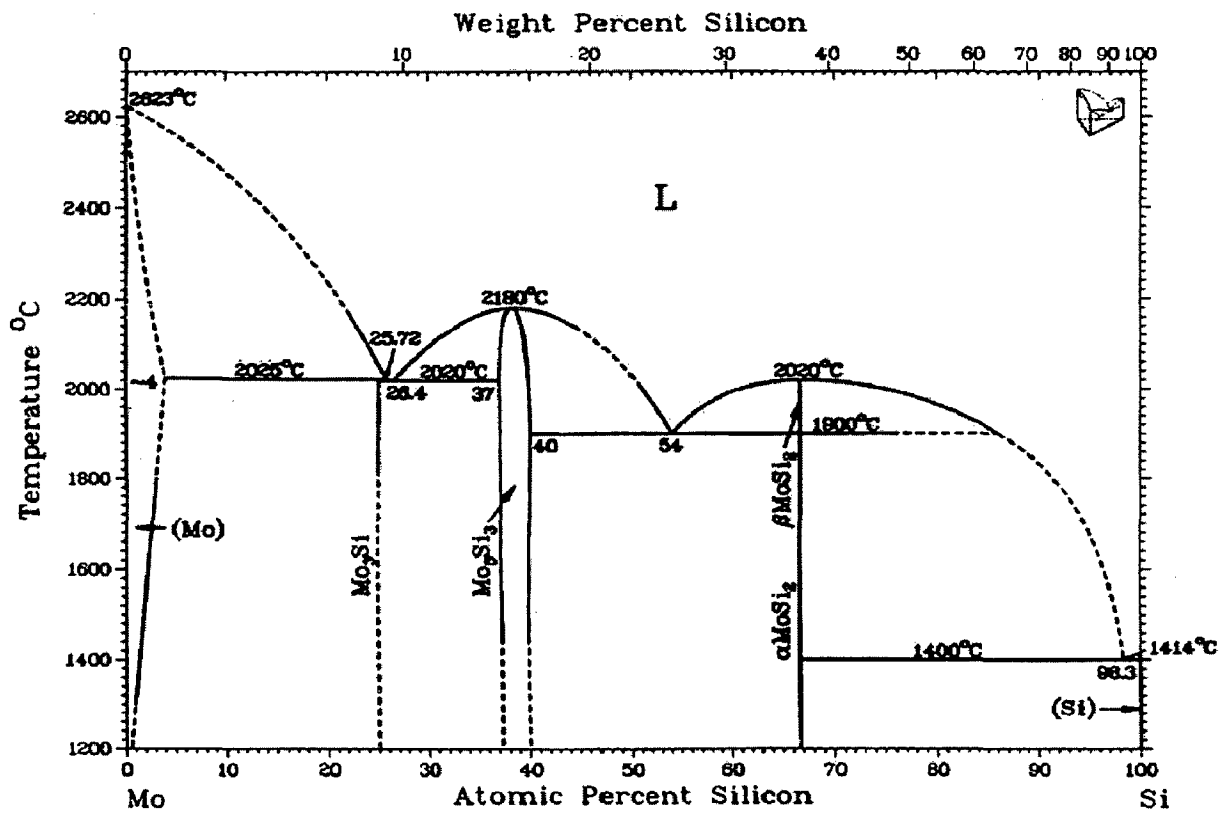


Fig. 2.3 Mo-Si binary phase diagram.

The Pearson's symbol for high temperature  $\beta$ -phase is hP9. The possible arrangements for the free energy vs. temperature behaviour for the liquid, C11<sub>b</sub> and C40 phases for pure MoSi<sub>2</sub> are shown schematically in Fig. 2.4. In this figure, the lowest curve at any temperature represents the stable equilibrium phase and the intersections of the free energy curves correspond to the transition temperatures (Boettinger et al, 1992).

MoSi<sub>2</sub> is an abundant, low cost material, which is non-toxic and environmentally benign (Petrovic et al, 1992). Its coefficient of thermal expansion matches very well with Al<sub>2</sub>O<sub>3</sub> (Vasudevan and Petrovic, 1992). Lower thermal expansion is beneficial for imparting lower thermal stresses and improving shock resistance. It has high thermal conductivity, which is very beneficial for increased cooling effectiveness of engine components. Thermal conductivity of MoSi<sub>2</sub> is comparable with Ni-base superalloys, SiC and Si<sub>3</sub>N<sub>4</sub>. In this respect, the cooling efficiency of a component would not be degraded by MoSi<sub>2</sub> replacement (Vasudevan and Petrovic, 1992). Due to its electrical resistivity, it is widely used as a heating element in industrial furnaces. It has adequate electrical conductivity which makes it amenable to electro-discharge machining (Petrovic, 1995).

Above ~ 1000 °C, MoSi<sub>2</sub> deforms plastically but strength levels are low (Gibbs et al, 1987). Wade and Petrovic (1992<sup>a</sup>) measured hardness and indentation fracture toughness of polycrystalline MoSi<sub>2</sub> hot pressed at 1600 °C. They found hardness as well as indentation fracture toughness,  $K_{IC}$  of MoSi<sub>2</sub> were independent of indentation load. The strength of polycrystalline MoSi<sub>2</sub> generally depends on the SiO<sub>2</sub> content and grain size of the material. The flexural stress-displacement curves resemble that of a brittle solid, as no resistance to fracture is observed. Once a crack becomes unstable, it is able to propagate through the specimen without any deflection or increase in resistance. The thermo-physical and mechanical properties of pure MoSi<sub>2</sub> collected from the literature are presented in Table 2.1. As there is a lot of scatter in property data of pure MoSi<sub>2</sub> in the literature, only the values, more often quoted in the literature, have been included in Table 2.1.

### 2.2.1 Slip Systems in $\text{MoSi}_2$

Unal et al (1990) and Maloy et al (1994) have analyzed the possible slip systems in  $\text{MoSi}_2$ . Potential slip systems are shown in Table 2.2. In general, the Peierls stress for a given slip system is expected to decrease with increasing ratio of slip plane spacing / Burgers vector,  $d / b$ . The slip systems with the highest value of  $d/b$  might be expected to be favoured in the deformation of  $\text{MoSi}_2$ . However, this is not necessarily the case always for  $\text{MoSi}_2$  (Petrovic, 1995).  $\text{MoSi}_2$  single crystals exhibit macroscopic compressive deformation in some orientations at temperatures as low as  $-100\text{ }^\circ\text{C}$ . The  $\{011\}\langle 100\rangle$  slip system is operative at these low temperatures (Ito et al, 1995). In general, the onset of plastic deformation in single crystal  $\text{MoSi}_2$  begins at temperature of approximately  $900\text{ }^\circ\text{C}$  (Umakoshi et al, 1990). Fig. 2.5 exhibits some of the slip systems in  $\text{MoSi}_2$  schematically.

### 2.2.2 Oxidation Resistance of $\text{MoSi}_2$

$\text{MoSi}_2$  exhibits excellent oxidation resistance up to temperatures as high as  $1600\text{ }^\circ\text{C}$ . Materials for high temperature applications generally obtain their oxidation resistance by the selective oxidation of Cr or Al to form protective surface films of chromium oxide and alumina. However,  $\text{MoSi}_2$  selectively forms a silica film. This film results in usable lifetimes in excess of 2000 hours at  $1650\text{ }^\circ\text{C}$  (Singh and Bose, 1992). Table 2.3 presents the data on the oxidation resistance of several silicide compounds (Vasudevan and Petrovic, 1992). Its oxidation resistance is best among the silicides (as evident from Table 2.3), nearly as good as SiC and better than  $\text{Si}_3\text{N}_4$ . It has the same oxidation protection mechanism as SiC and  $\text{Si}_3\text{N}_4$ . A thin vitreous  $\text{SiO}_2$  surface layer forms during initial oxidation, which is adherent and coherent, creating an effective barrier to further oxidation (Fitzer and Remmele, 1985). The oxidation rate is controlled by diffusion through the oxide layer.

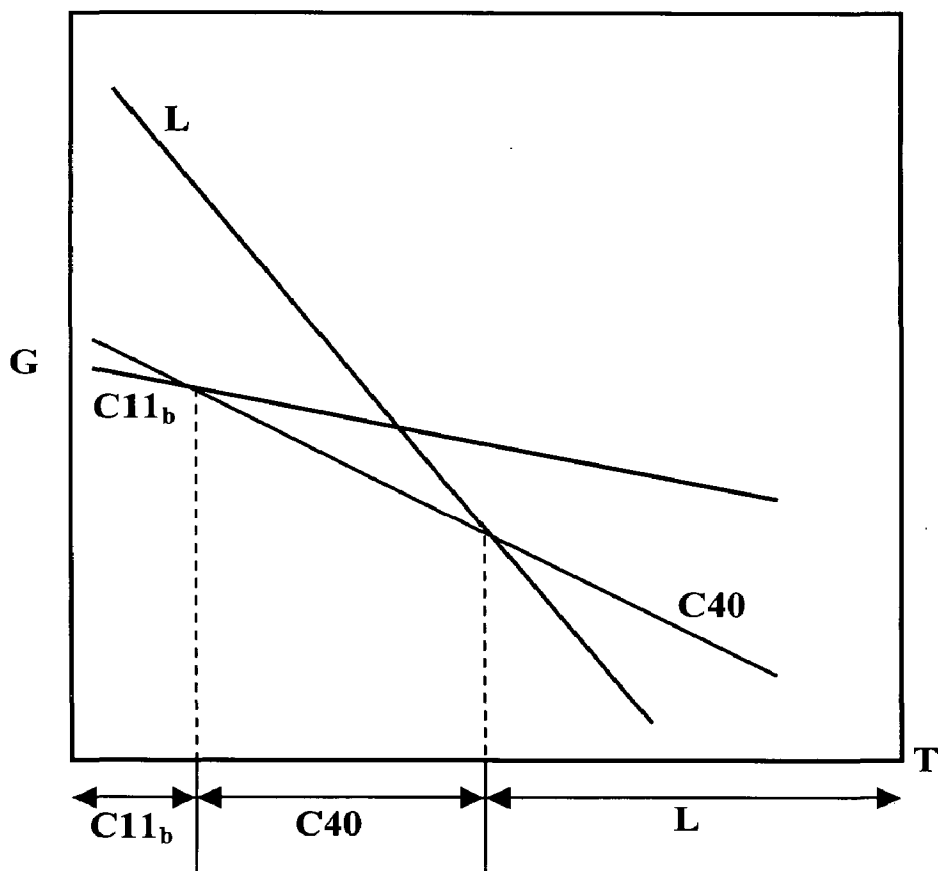


Fig. 2.4 Possible arrangements for the free energy vs. temperature curves for the liquid, C11<sub>b</sub> and C40 phases for pure MoSi<sub>2</sub>.

Table 2.1 Thermo-physical and mechanical properties of pure MoSi<sub>2</sub>.

S No.	Property	Value	References
1	Density	6.30 g/cm <sup>3</sup>	Vasudevan et al, 1991
2	Melting Point	2030 °C	Carter and Hurley, 1987 Xiao et al, 1990
3	Coefficient of Thermal Expansion	8.1-8.8x10 <sup>-6</sup> /°C 9.5x10 <sup>-6</sup> /°C at 1000 °C 10.0x10 <sup>-6</sup> /°C at 1800 °C	Lynch et al, 1966 Bhattacharya & Petrovic, 1991 Venkateswara Rao et al, 1992
4	Thermal Conductivity	65 W/mK at RT 30 W/mK at 1400 °C	Petrovic et al, 1992
5	Electrical Resistivity	10 µΩcm at RT	Petrovic et al, 1992
6	Elastic Modulus	440 GPa	Nakamura et al, 1990 Badrinarayanan et al, 1996
7	Poisson's Ratio	0.151	Nakamura et al, 1990
8	Brittle to Ductile Transition Temperature (BDTT)	~ 1000 °C	Gac and Petrovic, 1985
9	Hardness	9-10 GPa	Bhattacharya & Petrovic, 1991 Wade and Petrovic, 1992 <sup>a</sup> Wade and Petrovic, 1992 <sup>b</sup>
10	Indentation Fracture Toughness, K <sub>c</sub>	3.0-3.5 MPa√m	Wade and Petrovic, 1992 <sup>a</sup> Wade and Petrovic, 1992 <sup>b</sup>
11	Flexural Strength	150-200 MPa	Gac and Petrovic, 1985 Gibbs et al, 1987 Chen et al, 1994 <sup>a</sup>
12	Fracture Toughness, K <sub>IC</sub>	3-4 MPa√m  4.5 MPa√m at 1200 °C	Xiao et al, 1990 Xiao et al, 1991 Venkatesh Rao et al, 1992 Chen et al, 1994 <sup>b</sup> Badrinarayanan et al, 1996 Soboyejo et al, 1996 Badrinarayanan et al, 1996
13	Work of Fracture	690 ± 30 J/m <sup>2</sup>	Xiao & Abbaschian, 1992 <sup>a</sup>

Table 2.2 Possible slip systems in MoSi<sub>2</sub>.

Slip System	Slip Plane Spacing, d (Å)	Burgers Vector, b (Å)	d/b Ratio
{013}<100>	2.02	3.204	0.630
{010}<100>	1.60	3.204	0.499
{110}<110>	2.26	4.531	0.499
{110}1/2<111>	2.26	4.531	0.499
{001}<100>	1.31	3.204	0.409
{011}<100>	0.989	3.204	0.309
{110}1/2<331>	2.26	7.848	0.288
{013}1/2<331>	2.02	7.848	0.257
{011}1/2<111>	0.989	4.531	0.218

Table 2.3 Oxidation resistance of high melting point silicides.

Silicide	Oxidation Temperature (°C)	Oxidation Time (h)	Weight Change (mg/cm <sup>2</sup> )
MoSi <sub>2</sub>	1200	4	+0.3
	1500	4	+1.3
WSi <sub>2</sub>	1200	4	-17
	1500	4	-23
NbSi <sub>2</sub>	1200	6	+40
TaSi <sub>2</sub>	1200	4	+60
TiSi <sub>2</sub>	1200	4	+22
Mo <sub>5</sub> Si <sub>3</sub>	1500	4	-67
W <sub>5</sub> Si <sub>3</sub>	1500	4	-205
Ta <sub>5</sub> Si <sub>3</sub>	1500	1	+125
Ti <sub>5</sub> Si <sub>3</sub>	1500	2	+32

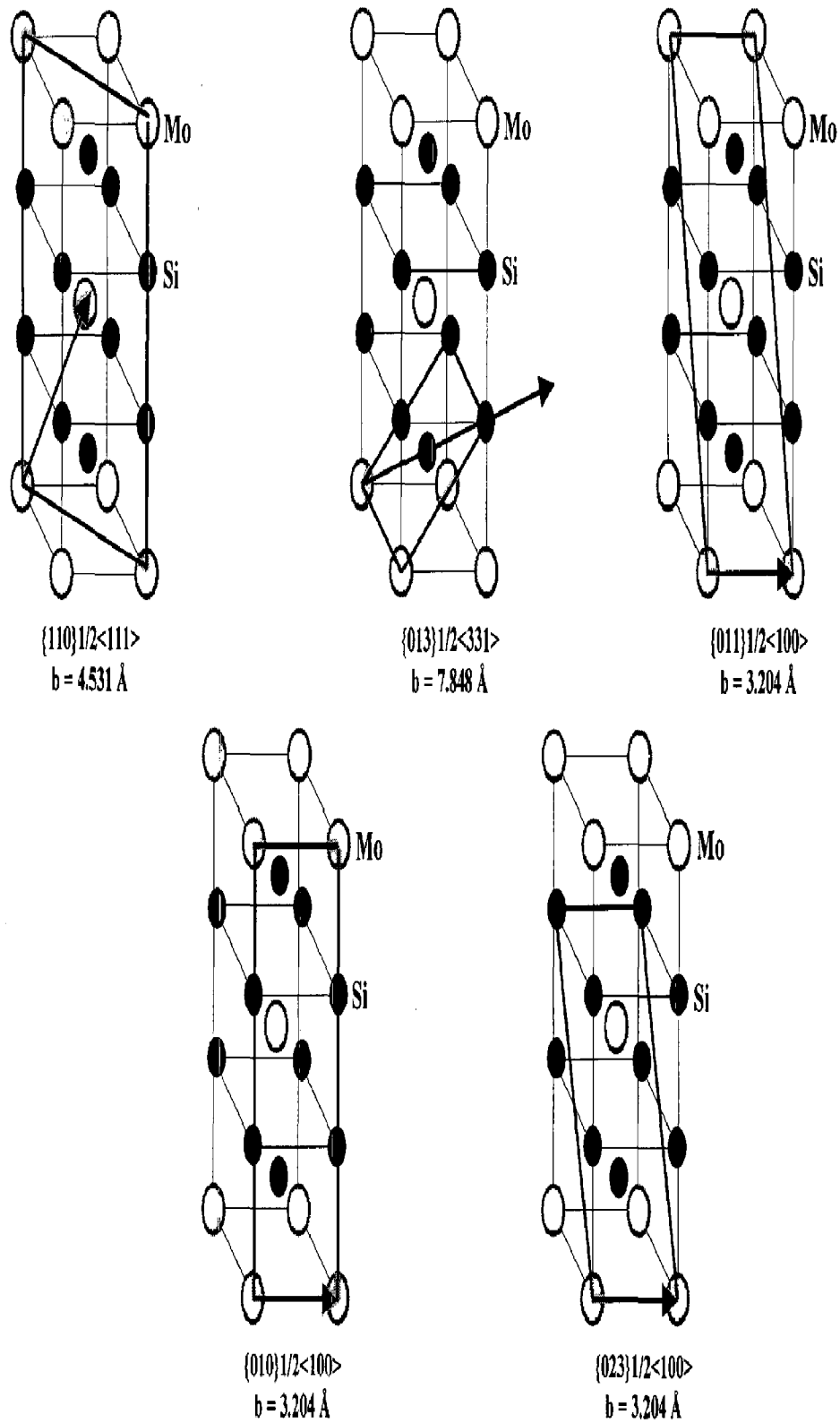


Fig. 2.5 Schematic showing some of the slip systems in  $\text{MoSi}_2$ .

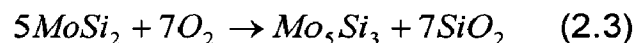


### 2.2.2.1 Pesting Phenomenon

However, MoSi<sub>2</sub> is prone to a low temperature intergranular oxidation problem known as Pesting (Berkowitz-Mattuck et al, 1970). Pesting phenomenon disintegrates the exposed material along grain boundaries rapidly (Meschter and Schwartz, 1989). It is associated with the formation of non-protective MoO<sub>3</sub> crystals at grain boundaries during oxidation at temperatures between 500 - 600 °C. The oxidation in MoSi<sub>2</sub> proceeds according to the following reaction:



The melting point of MoO<sub>3</sub> is 802 °C while its boiling point is 1155 °C. At T < 700 °C, MoO<sub>3</sub> does not volatilize and the SiO<sub>2</sub> layer is highly porous. Therefore, grain boundaries, pores and microcracks are readily attacked by oxygen. Above 800 °C, the surface reaction occurs as follows (Alman and Stoloff, 1994):



Pesting behaviour does not occur in materials of density greater than 98 %, crack or pore-free samples and stress free single crystals of MoSi<sub>2</sub>. Therefore, Pesting is not an 'intrinsic' characteristic of MoSi<sub>2</sub>. Pesting behaviour can also be eliminated with the addition of MoGe<sub>2</sub>. GeO<sub>2</sub> in SiO<sub>2</sub> increases the coefficient of thermal expansion of SiO<sub>2</sub> layer and decreases viscosity of the modified surface oxide (Fitzer and Remmele, 1985).

## 2.3 Applications

Silicides of refractory metals have been employed in a wide variety of industrial applications ranging from electronics to aerospace technology. Silicide films are employed extensively in the electronics industry as contacts and interconnect in integrated silicon devices. Petrovic (1995) has described the four general aspects of the structural use of MoSi<sub>2</sub>:

- (i) As matrix for MoSi<sub>2</sub> based composites.
- (ii) As reinforcement in structural ceramic matrix composites.
- (iii) As high temperature joining material for structural ceramics.

(iv) As oxidation resistant coatings for refractory metals and carbon based materials.

The current and potential applications of  $\text{MoSi}_2$  and its composites are listed in Table 2.4. Some of the important applications are briefly described below:

**(i) Heating elements**

Heating elements for furnaces operating in air at temperatures of about 1750 °C is the major commercial use of  $\text{MoSi}_2$  at present (Gac and Petrovic, 1985). It is based on its electrical resistivity. Kanthal Super 1900 is a solid solution alloy of  $\text{MoSi}_2$  and  $\text{WSi}_2$ , which can operate at 1900 °C in air and oxidizing environments (Petrovic, 1997).

**(ii) Industrial gas burners**

The gas burner industry is in the process of developing gas burners, which will burn oxygen-natural gas mixtures rather than air-natural gas mixtures in order to reduce  $\text{NO}_x$  environmental emissions. Because such oxygen-natural gas burners must operate at higher temperatures than air-natural gas burners, new burner materials are required.  $\text{MoSi}_2$  possesses significant resistance to oxygen-natural gas combustion at high temperatures. Prototype  $\text{MoSi}_2$  gas burners have been fabricated by plasma spray forming process (Castro et al, 1994).

**(iii) Molten metal lances**

A number of foundry operations require that gases be injected into molten metals. Microlaminate  $\text{MoSi}_2\text{-Al}_2\text{O}_3$  composite tubes have been fabricated by plasma spray forming which performs very well in molten aluminium at 725 °C and molten copper at 1200 °C (Barlett et al, 1996). Tubes made by alternative materials like graphite lasted only 15 minutes in molten copper.

**Table 2.4 Potential applications of MoSi<sub>2</sub> based materials.**

<b>Industrial Applications</b>	<b>Automotive Applications</b>	<b>Aerospace Applications</b>
Furnace heating elements	Turbocharger rotors	Aircraft engine hot-section components
Power generation components	Valves	Turbine blades
High temperature heat exchangers	Glow plugs	Vanes
Gas burners		Combustors
Lances for liquid metals and glasses		Nozzles
Igniters		Seals
High temperature filters		

#### **(iv) Glass processing**

Components requiring contact with molten glasses are presently made of refractory metal molybdenum or precious metal platinum. Molybdenum is highly resistant to corrosion but has poor oxidation resistance, while platinum is very expensive.  $\text{MoSi}_2$  is a material, which is quite resistant to corrosion by molten glasses. Kanthal Corporation is marketing a new  $\text{MoSi}_2$  immersion tube for injection of gases into molten glasses (Kanthal, 1995).

#### **(v) Diesel engine glow plugs**

Toyota Central R & D in Japan has recently developed  $\text{MoSi}_2\text{-Si}_3\text{N}_4$  composite diesel engine glow plugs (Petrovic, 1997). These glow plugs have two distinct advantages over metal glow plugs:

- (a) They are highly resistant to diesel fuel combustion environment and thus have a long lifetime of about 13 years.
- (b) They can be heated at higher heating rates with the result that the engine can be started faster by a factor of two.

The glow plug is a micro-structurally tailored  $\text{Si}_3\text{N}_4\text{-30 vol\% MoSi}_2$  composite. It is composed of two layers (a core and a sheath) both of which have same composition of  $\text{MoSi}_2$  and  $\text{Si}_3\text{N}_4$  phases but with different  $\text{MoSi}_2$  phase morphology. The core (inner layer) has  $\text{Si}_3\text{N}_4$  particles distributed in  $\text{MoSi}_2$  matrix phase and hence electrically conductive. The sheath (outer layer) is made of  $\text{MoSi}_2$  particles distributed in  $\text{Si}_3\text{N}_4$  matrix phase and is, therefore, electrically insulating. Since both core and sheath are essentially made of composite having the same composition except for the phase interconnectivity, there is therefore, a perfect match of coefficients of thermal expansion (Denso, 1992).

#### **(vi) Aerospace gas turbine engines**

In the engine, Blade Outer Air Seal (BOAS) is a stationary part, which is exposed to high turbine gas temperatures and significant thermal stresses. The hybrid composites consisting of reinforcement of SiC continuous fibers in a matrix of  $\text{MoSi}_2\text{-Si}_3\text{N}_4$  particulate composite are being developed by NASA-Lewis Centre (Petrovic, 1997). It possesses significant thermal shock resistance. The composite

has impact energy of 10 J, which is comparable to that of cast super alloys (Hebsur and Nathal, 1997).

**(vi) Wear resistant materials**

It is likely that MoSi<sub>2</sub> based materials will find applications that require wear resistance at elevated temperatures and in oxidizing environments.

## **2.4 MoSi<sub>2</sub> BASED HIGH TEMPERATURE STRUCTURAL MATERIALS**

Efforts to develop MoSi<sub>2</sub> have been hampered by its extreme brittleness at temperatures below 1000 °C, coupled with relatively low creep resistance. For its effective use as high temperature structural material, it becomes necessary to toughen the material at lower temperatures (where MoSi<sub>2</sub> is brittle) while improving the strength at higher temperatures simultaneously. It has been recognized by most workers in the field that the best chance to solve these twin problems is to develop MoSi<sub>2</sub> matrix composites with a variety of reinforcements and its alloying with other elements.

### **2.4.1 Alloying of MoSi<sub>2</sub> with Other Elements**

MoSi<sub>2</sub> does not easily alloy with other elements. It can be metallurgically alloyed with other silicides to improve its properties (Vasudevan and Petrovic, 1992). The possible silicide species alloying with MoSi<sub>2</sub> are WSi<sub>2</sub>, TaSi<sub>2</sub>, NbSi<sub>2</sub>, CoSi<sub>2</sub>, Mo<sub>5</sub>Si<sub>3</sub> and Ti<sub>5</sub>Si<sub>3</sub> (Petrovic, 1995). The refractory metals Mo, W, Ta and Nb all have a body-centered cubic (bcc) crystal structure (cI2). Pure Mo forms isomorphous phase diagrams with W, Ta and Nb with complete solid solubility over the entire composition range as shown in Fig. 2.6 (Massalski ed., 1986). Among the disilicides of these refractory metals MoSi<sub>2</sub> and WSi<sub>2</sub> have a tetragonal crystal structure (tI6), while TaSi<sub>2</sub> and NbSi<sub>2</sub> have a hexagonal crystal structure (hP9). The data in the literature on the relative solubilities and two-phase fields of various disilicides when combined with MoSi<sub>2</sub> are summarized in Fig. 2.7 (Boettinger et al, 1992). These alloys under consideration contain phases that maintain a constant Si level but may vary the refractory metal content for example between MoSi<sub>2</sub> and NbSi<sub>2</sub>. Most familiar is the alloying of MoSi<sub>2</sub> with WSi<sub>2</sub>, which are tetragonal (tI6) and form a

complete solid solution across the entire composition range. The Combinations of  $\text{MoSi}_2$  with disilicides that have the hexagonal (hP9) structure necessarily require the formation of a two-phase field between tI6 and hP9 phases with various ranges of solubility.

Alloying limited to solid solution of  $\text{MoSi}_2$  has been attempted in order to improve its high temperature mechanical properties and room temperature ductility. Specifically,  $\text{WSi}_2$  has been added due to its similarity in crystal structure and lattice parameters with  $\text{MoSi}_2$ .  $\text{WSi}_2$  alloying leads to considerable improvements in high temperature strength and creep resistance but its effects on room temperature ductility are found to be very limited (Flinn et al 1989, Petrovic and Honnell 1990<sup>a</sup>, 1990<sup>b</sup>, Frankwicz et al 1993).

#### **2.4.2 $\text{MoSi}_2$ Based Composites with Ceramic Reinforcements**

$\text{MoSi}_2$  can be engineered by addition of suitable reinforcements (brittle ceramics as well as ductile metals) to improve its mechanical properties. Ceramic reinforcements are used to improve its high temperature strength and creep resistance while the metallic reinforcements may be effective to improve its low temperature fracture toughness.

$\text{MoSi}_2$  is thermodynamically stable with a large number of carbides, nitrides, oxides and borides such as SiC, TiC,  $\text{Si}_3\text{N}_4$ ,  $\text{ZrO}_2$ ,  $\text{Al}_2\text{O}_3$ ,  $\text{Y}_2\text{O}_3$ ,  $\text{TiB}_2$ ,  $\text{ZrB}_2$  (Meschter and Schwartz, 1989) and with mullite, YAG (Petrovic, 1995). Addition of ceramic particulate reinforcements in the matrix of  $\text{MoSi}_2$  results in overall improvements in mechanical properties. At high temperatures, these reinforcements improve creep resistance by inhibiting excessive dislocation motion. Extensive studies have been carried out on  $\text{MoSi}_2$  matrix composites reinforced with high strength ceramics such as SiC (Gac and Petrovic 1985, Petrovic and Honnell 1990<sup>a</sup>, Gibbs et al 1987, Yang and Jeng 1990, Bhattacharya and Petrovic 1991), TiC (Yang et al, 1989),  $\text{Si}_3\text{N}_4$  (Petrovic and Honnell 1990<sup>a</sup>, 1990<sup>b</sup>, Hebsur 1994),  $\text{Al}_2\text{O}_3$  (Tuffe et al, 1993), and  $\text{ZrO}_2$  (Petrovic and Honnell 1990<sup>a</sup>, Bhattacharya and Petrovic 1991, Petrovic et al 1991). These ceramic reinforcements are observed to improve both high and low temperature properties depending upon their volume fraction, size, aspect ratio, and distribution.

SiC is the most widely used reinforcement in MoSi<sub>2</sub>, as it is not only thermodynamically stable with MoSi<sub>2</sub> but also exhibits excellent oxidation resistance. SiC reinforcements in all forms, i.e., fibre, whisker and Particle have been incorporated in MoSi<sub>2</sub> matrix resulting in considerable improvements in its mechanical properties including elastic modulus, hardness, strength, creep and wear resistance. The effect of SiC addition on creep rate of MoSi<sub>2</sub> is shown in Fig. 2.8 (Sadananda et al, 1991, 1993).

The grain size of MoSi<sub>2</sub> decreases with increasing addition of SiC and therefore, the creep rate increases with volume fraction of SiC added. Creep rates for 5, 10 and 20 vol% SiC particulate composites are higher than those of unreinforced MoSi<sub>2</sub> while the creep rates in composite containing 40 vol% SiC particles are substantially lower. This behaviour is related to the fact that, with increasing SiC addition below 30 vol% the reduction of grain size of MoSi<sub>2</sub> matrix dominates the creep behaviour. The reduced matrix grain size then promotes the operation of grain boundary sliding mechanism of creep. But above 30 vol%, SiC is able to counter creep deformation overcoming the effect of reduced grain size.

TiC and TiB<sub>2</sub> reinforcements in MoSi<sub>2</sub> matrix have also been investigated (Yang et al 1989, Yang and Jeng 1991). Although TiC is thermodynamically compatible with MoSi<sub>2</sub>, the resulting composite fails to exhibit attractive combinations of mechanical properties. TiC, despite its high strength, high elastic modulus and chemical inertness, does not appear to yield significant improvements in fracture toughness as well as other mechanical properties of MoSi<sub>2</sub>. TiC / MoSi<sub>2</sub> interfacial bond strength appears to be high due to the absence of crack deflection or interfacial debonding (Yang et al, 1989). Hence the fracture behaviour of TiC reinforced MoSi<sub>2</sub> is brittle, exhibiting a transgranular fracture morphology. The TiB<sub>2</sub> reinforcement is found to oxidize slowly after an initial period.

MoSi<sub>2</sub> and Si<sub>3</sub>N<sub>4</sub> are thermodynamically stable compounds (Heikinheimo et al, 1992). Additions of Si<sub>3</sub>N<sub>4</sub> to MoSi<sub>2</sub> matrix significantly improve the intermediate temperature oxidation resistance of MoSi<sub>2</sub> and its elevated temperature mechanical properties (Hebsur, 1994). Si<sub>3</sub>N<sub>4</sub> addition to MoSi<sub>2</sub> completely eliminates the MoSi<sub>2</sub> oxidation pest behaviour.

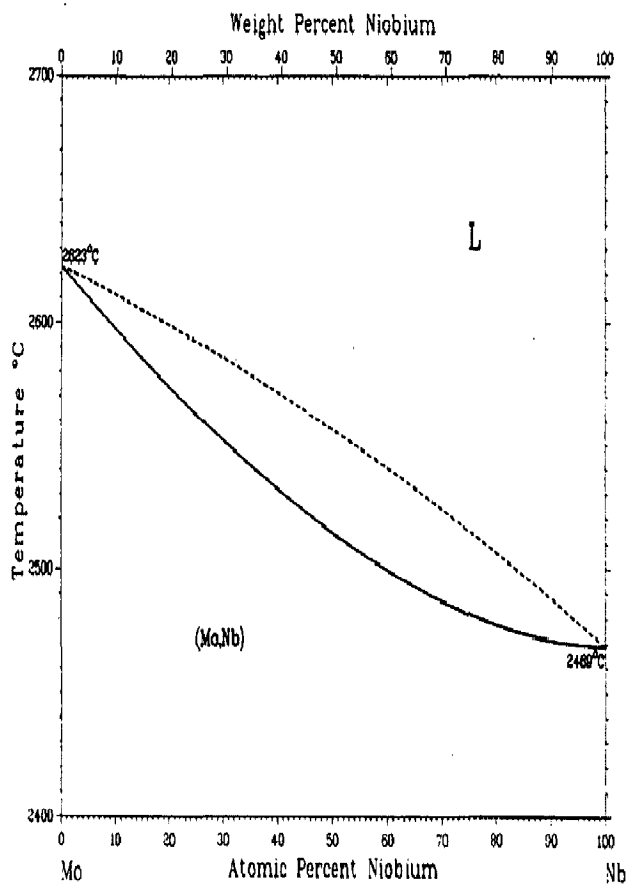
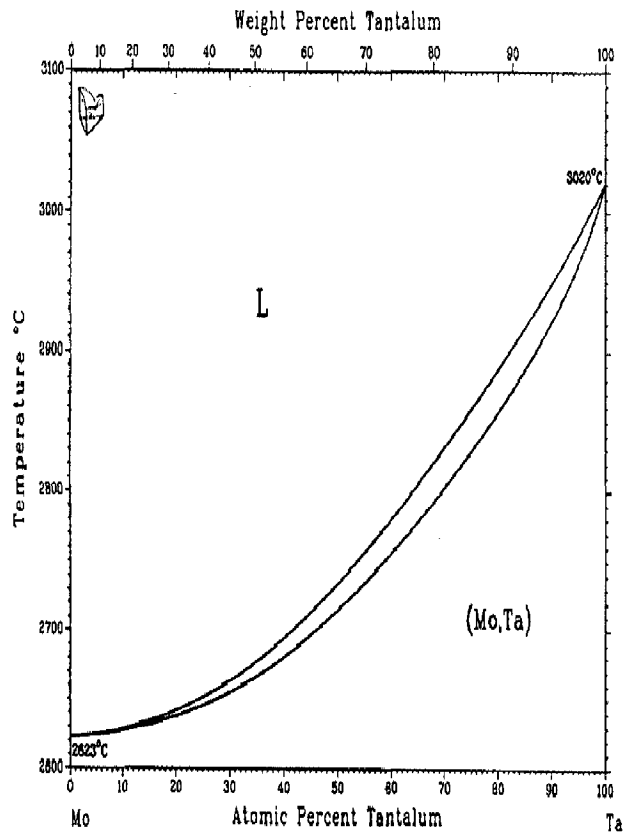
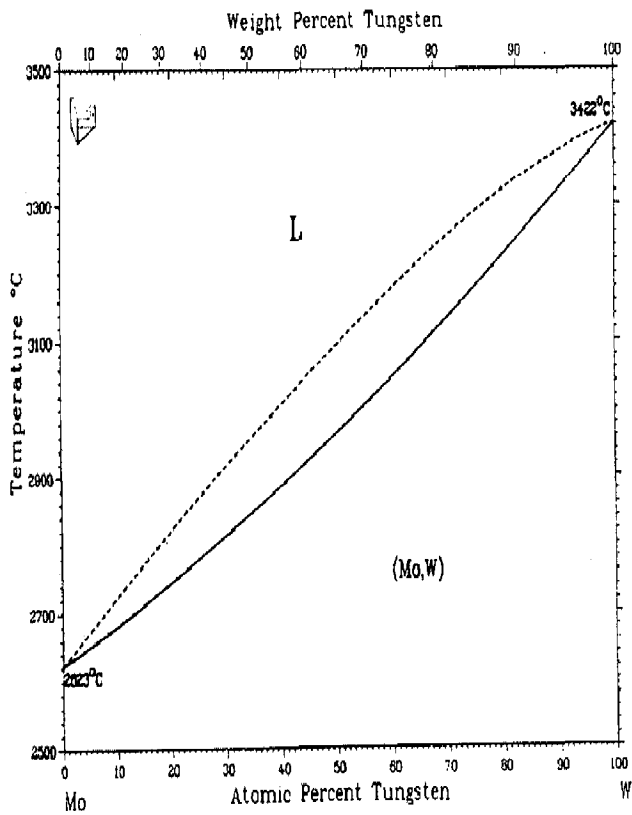


Fig. 2.6 Binary phase diagrams (a) Mo-W (b) Mo-Ta and (c) Mo-Nb.



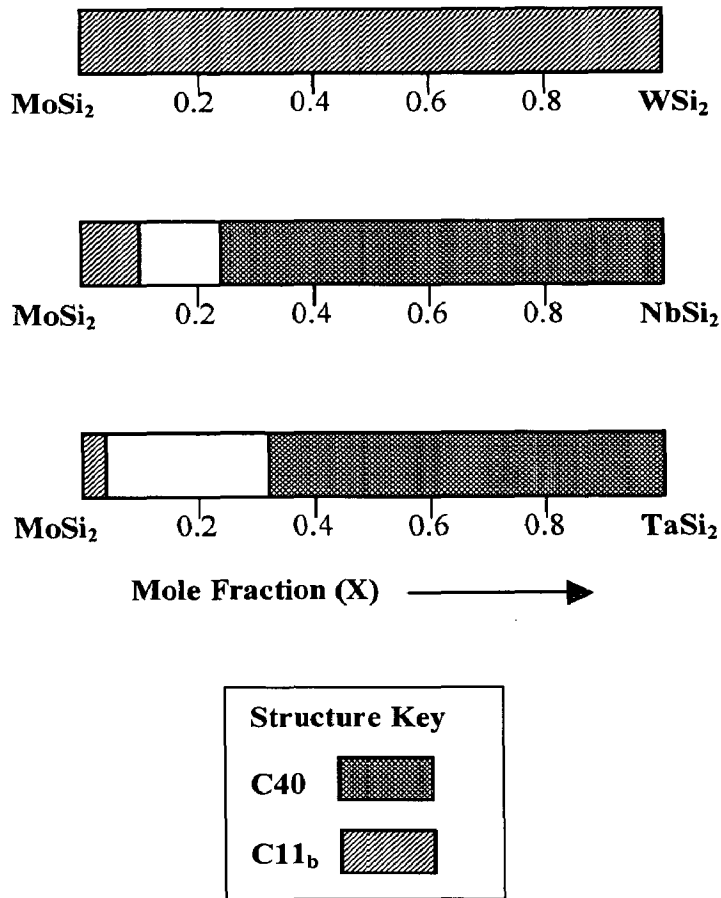


Fig. 2.7

Homogeneity range in mole fraction and two-phase fields for various combinations of disilicides at 1300 °C (800 °C for MoSi<sub>2</sub> – NbSi<sub>2</sub>).

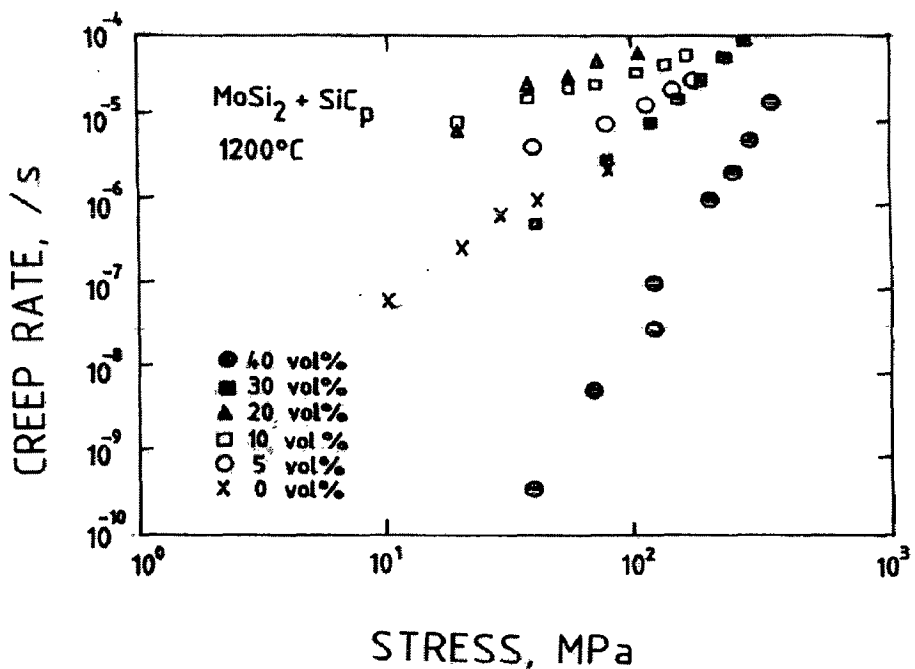
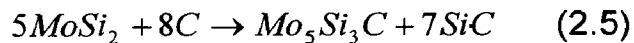
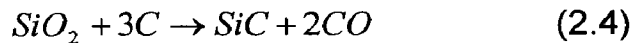


Fig. 2.8

Creep rate of SiC particulates reinforced MoSi<sub>2</sub> matrix composites with different volume fractions of SiC phase.

Maloy et al (1991) carried out extensive studies on the effect of carbon addition in MoSi<sub>2</sub>. Carbon addition in MoSi<sub>2</sub> results in the following chemical reactions:



Carbon in MoSi<sub>2</sub> essentially removes SiO<sub>2</sub> and forms SiC and the Nowotny phase Mo<sub>5</sub>Si<sub>3</sub>C.

It was observed that 2 wt% carbon addition to MoSi<sub>2</sub> acts as deoxidant, removing the grain boundary phase of SiO<sub>2</sub>, and thereby, causing an improvement in the Vickers hardness of the base material. In addition, carbon interacts with MoSi<sub>2</sub> to form SiC. The micro-hardness data at room temperature and at 1000 °C of MoSi<sub>2</sub> containing carbon revealed a marked improvement over that observed in carbon free MoSi<sub>2</sub> as shown in Fig. 2.9(a). At lower temperatures (below 1000 °C) the hardness increase can be due to the SiC formation, while at higher temperatures (above 1000 °C) there could be an added effect from the lack of grain boundary silica phase. Fig. 2.9(b) shows the temperature dependence of fracture toughness of MoSi<sub>2</sub> with and without carbon additions (Maloy et al, 1991).

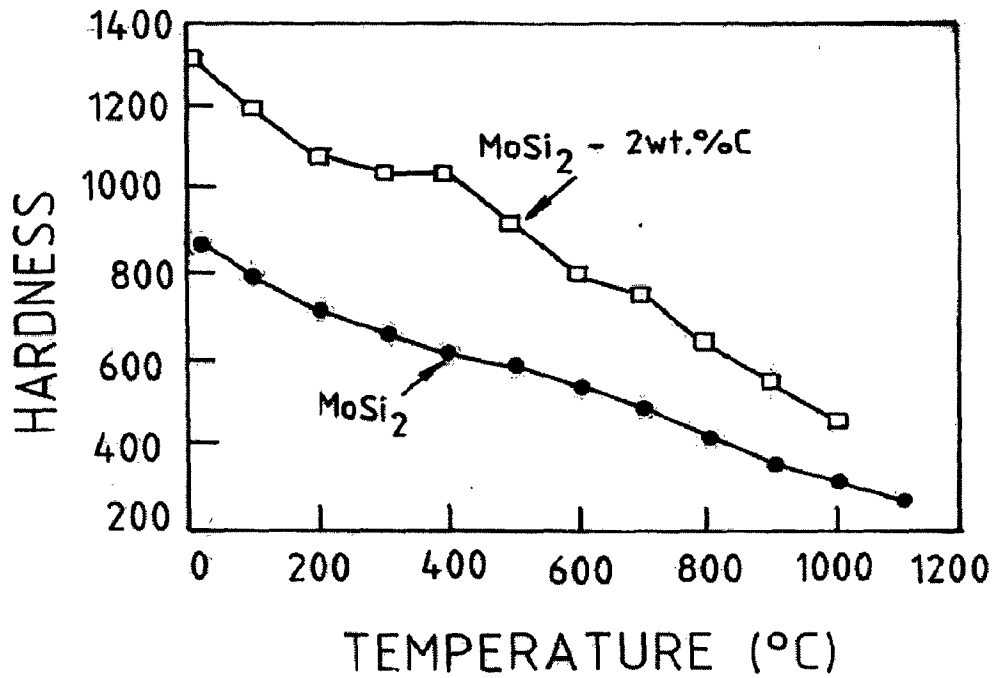
The fracture toughness of MoSi<sub>2</sub> containing SiO<sub>2</sub> decreases with increasing temperature from 800 to 1400 °C. However, the carbon additions improve it dramatically. The fracture mode also changed from intergranular (no carbon) to transgranular (with carbon), as a result of the removal of grain boundary phase of silica by reaction with carbon. In MoSi<sub>2</sub> containing SiO<sub>2</sub> (without carbon), the viscosity of the grain boundary silica decreases with increasing temperature, resulting in more grain boundary sliding with cavitations, thereby producing a decrease in toughness. On the contrary, the addition of 2 wt% carbon reduces the grain boundary silica, thereby minimizing grain boundary sliding and improving high temperature toughness as a result of dislocation plasticity. Therefore, absence of SiO<sub>2</sub> and presence of SiC and Mo<sub>5</sub>Si<sub>3</sub>C are clearly responsible for the improved mechanical behaviour of MoSi<sub>2</sub> containing carbon.

Among all the ceramic reinforcements, SiC has been found to be most effective reinforcement in MoSi<sub>2</sub>. It provides excellent improvements in high temperature strength and creep but its effect on improvement in room temperature fracture toughness is marginal.

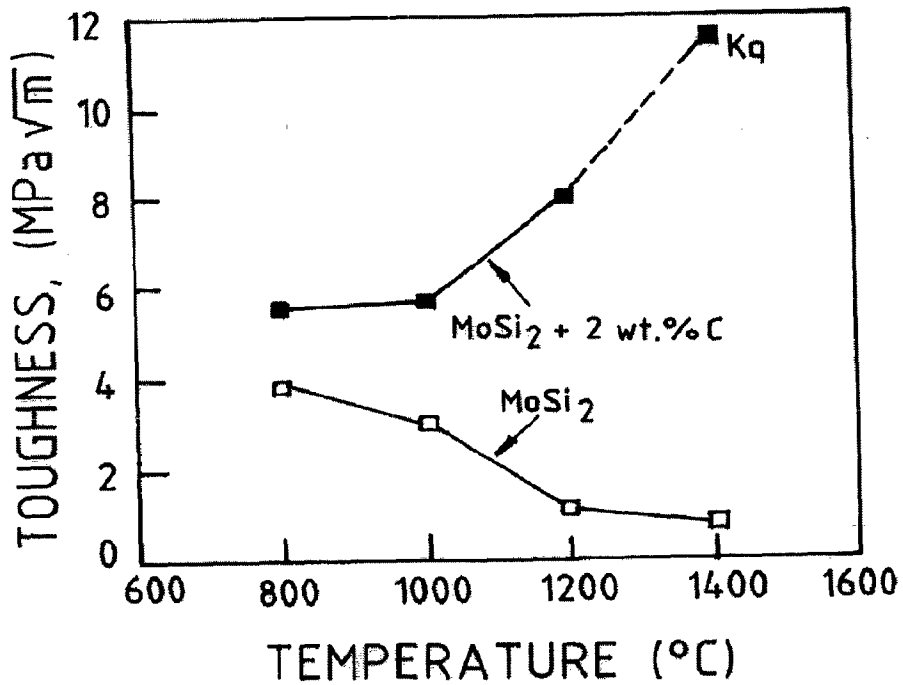
## **2.5 ROOM TEMPERATURE FRACTURE TOUGHNESS OF MoSi<sub>2</sub> MATRIX COMPOSITES**

Although the ceramic reinforcements result in considerable improvements in mechanical properties of MoSi<sub>2</sub>, their effect on improving the room temperature fracture toughness of MoSi<sub>2</sub> is marginal. Only moderate room temperature toughening effects are derived with the addition of ceramic reinforcements. Toughening levels for these reinforcements are similar to those observed in ceramic matrix composites, and are associated with mechanisms such as crack deflection and crack bridging. Fig. 2.10 shows the fracture toughness of MoSi<sub>2</sub> containing increasing levels of SiC and ZrO<sub>2</sub> (Vasudevan et al, 1991).

Petrovic and Honnell (1990<sup>a</sup>) and Petrovic et al (1991) reported a fracture toughness value of 7.8 MPa√m for MoSi<sub>2</sub> + 20 vol% ZrO<sub>2</sub> particle reinforced composites. These composites contain particles of partially stabilized ZrO<sub>2</sub>, which has a metastable tetragonal structure. In the vicinity of the crack tip stress field, the tetragonal particles transform to the monoclinic crystal structure, with an associated volume increase of about 4 %. This crack induced phase transformation, thus, produces compressive stresses, which shield the crack tip from the applied external tensile stresses, leading to increased toughening in the composite (Petrovic et al, 1991). This transformation initiates in the vicinity of 1175 °C > BDTT i.e., brittle-ductile transition temperature of MoSi<sub>2</sub>. So, dislocation “pumping” occurs as a result of the spontaneous ZrO<sub>2</sub> transformation strains. Unstabilized ZrO<sub>2</sub> is observed to produce maximum toughening effects in these composites. Dislocation “pumping” into MoSi<sub>2</sub> matrix will have beneficial effects on BDTT (Petrovic et al, 1992).



(a)



(b)

Fig. 2.9 Temperature dependence of (a) Vickers hardness and (b) fracture toughness for pure MoSi<sub>2</sub> and MoSi<sub>2</sub> containing 2 wt% carbon.

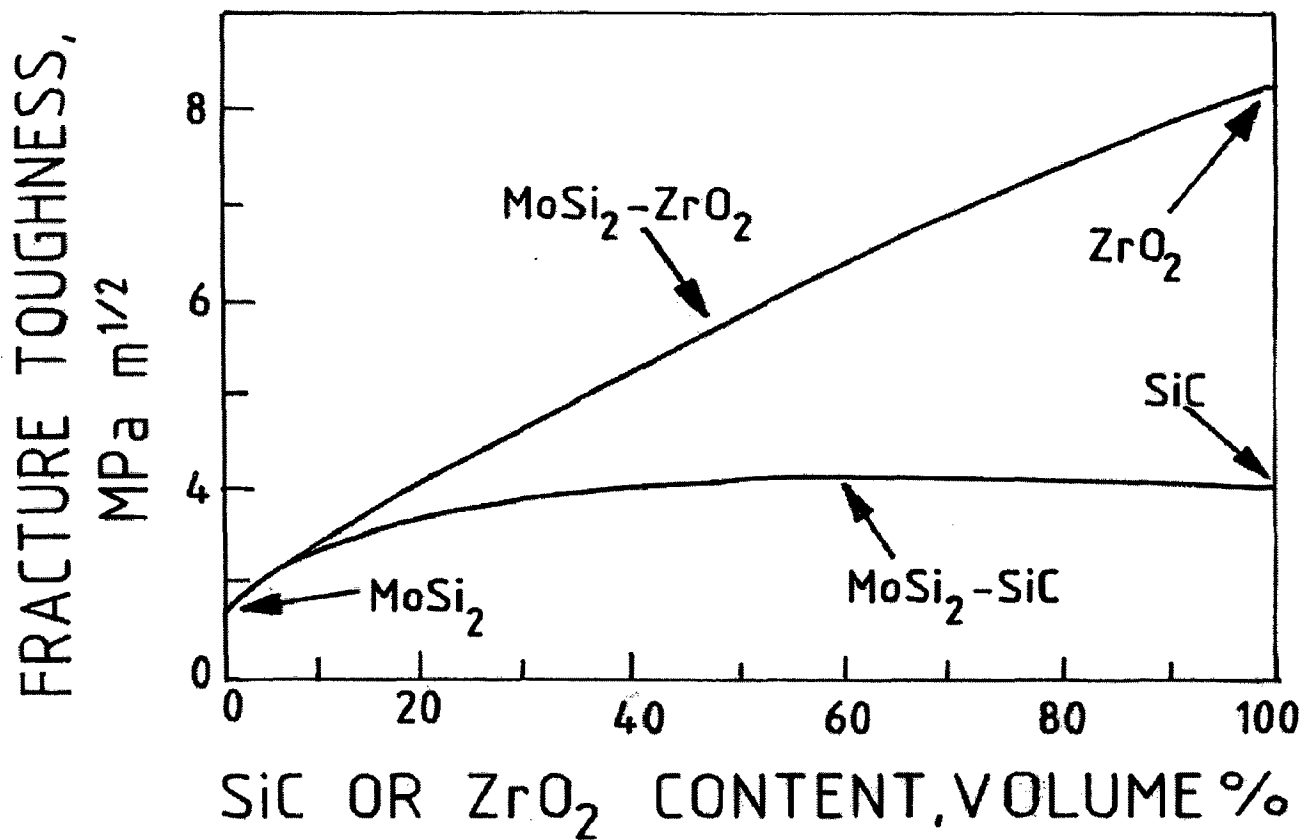


Fig. 2.10 Improvement in room temperature fracture toughness due to additions of SiC and ZrO<sub>2</sub> to MoSi<sub>2</sub>.

Pure  $\text{MoSi}_2$  has a fracture toughness that is less than  $3 \text{ MPa}\sqrt{\text{m}}$ . The addition of SiC increases the fracture toughness only moderately to a value slightly greater than  $4 \text{ MPa}\sqrt{\text{m}}$ . The mechanism for this improvement is believed to be crack deflection / crack branching phenomenon. The addition of  $\text{ZrO}_2$  is much more effective in improving the toughness and is the result of transformation toughening caused by the transformation of metastable tetragonal  $\text{ZrO}_2$  to monoclinic. The highest toughness level achieved in such composites is about  $8 \text{ MPa}\sqrt{\text{m}}$ . Table 2.5 summarizes the fracture toughness data available in the literature for various  $\text{MoSi}_2$  matrix composites reinforced with a variety of brittle ceramics.

The strength and toughness properties of  $\text{MoSi}_2$  can be controlled by plastic deformation through dislocation motion only at high temperatures as  $\text{MoSi}_2$  exhibits plasticity at temperatures above  $\sim 1000 \text{ }^\circ\text{C}$ . However,  $\text{MoSi}_2$  like most ceramics exhibits brittle behaviour at room temperature as dislocations are immobile and also due to lack of active independent slip systems. Neither strength nor toughness of ceramics is controlled by dislocation motion as with metals. Increase in toughness of  $\text{MoSi}_2$  at room temperature can be accomplished by modifying the microstructure and providing resistance to fracture via these microstructural modifications and not by the movement of dislocations. The purpose is to interrupt the path of the propagating crack by lowering the stress field around the crack tip and in front of the crack tip. Numerous concepts have been proposed for toughening of ceramic matrix composites often leading to confusion as many of these concepts differ with each other only marginally and use different terminology to describe the similar toughening mechanisms. Therefore, an attempt has been made to regroup various toughening mechanisms for brittle materials bringing out the exclusive and salient features of each one of them and is presented in a brief and systematic manner in the following section.

## **2.6 TOUGHENING MECHANISMS FOR BRITTLE MATERIALS**

Toughening in materials can result from two different types of mechanisms (i) Intrinsic and (ii) Extrinsic (Ritchie, 1988). The former mechanism of toughening results from the inherent resistance of the microstructure to crack growth and thus is influenced by grain size, particle size, particle spacing etc, while the latter results

from mechanisms that reduce the local stress intensity at the crack tip and thus reduce the local driving force for crack growth.

All the known toughening mechanisms can be conveniently divided into two broad groups:

## **1. Process zone mechanisms**

- (i) Transformation toughening
- (ii) Microcrack toughening
- (iii) Crack tip interactions
  - (a) Crack deflection
  - (b) Crack bowing
  - (c) Crack blunting

## **2. Bridging zone mechanisms**

- (i) Bridging by ceramic reinforcements (brittle phases)
  - (a) Ceramic Particles
  - (b) Ceramic whiskers / fibers
- (ii) Bridging by ductile phases (ductile phase toughening)
  - (a) Metal particles
  - (b) Metal wires
  - (c) Metal foils
- (iii) Grain bridging

The operation of multiple mechanisms is common. Interactions between multiple mechanisms must be considered. The interactions may be highly beneficial and produce synergism between mechanisms. Synergism is most likely when bridging zone and process zone mechanisms interact.

Table 2.5 Fracture toughness data for MoSi<sub>2</sub> based composites.

S No.	Composition	Processing Method	Fracture Toughness (MPa√m)	Reference
1	Monolithic MoSi <sub>2</sub>	Hot Press	2.5-3.0	Gac & Petrovic, 1985
		Hot Press	4.38	Gibbs et al, 1987
		Hot Press	5.32	Carter et al, 1989
		Hot Press	2.6	Petrovic & Honnell, 1990 <sup>a</sup>
		Hot Press	2.85 <sup>γ</sup>	Bhattacharya & Petrovic, 1991
		Hot Press	3.60 <sup>γ</sup>	Wade & Petrovic, 1992 <sup>a</sup> , 1992 <sup>b</sup>
2	Monolithic MoSi <sub>2</sub>	HIP (1400 °C, 207 MPa, 4 h)	4.2	Brooks et al, 1994
3	Monolithic MoSi <sub>2</sub>	Plasma Spray	5.7±0.2 <sup>α</sup> 2.7±0.1 <sup>β</sup>	Castro et al, 1992
		Plasma Spray + Anneal (1100 °C, 24 h)	3.6±0.2 <sup>α</sup> 2.2±0.2 <sup>β</sup>	Castro et al, 1992
		Plasma Spray	4.7	Tiwari et al, 1992
		Plasma Spray + HIP (1200 °C, 206 MPa, 1 h)	5.9	Tiwari et al, 1992
4	MoSi <sub>2</sub> + 2 wt % C	Hot Press (1830 °C in air)	5.5 (800 °C)	Maloy et al, 1991
			11.5 (1400 °C)	
5	MoSi <sub>2</sub> + 8.7 vol% SiC <sub>p</sub>	Plasma Spray	4.6 <sup>α</sup>	Jeng et al, 1993
			4.2 <sup>β</sup>	



6	MoSi <sub>2</sub> + 20 vol% SiC <sub>p</sub>	Hot Press (1700 °C, 35 MPa, inert atmosphere)	6.37	Yang & Jeng, 1990
		-	4.0	Bhattacharya & Petrovic, 1991
		HIP (1400 °C, 207 MPa, 4 h)	2.5	Brooks et al, 1994
7	MoSi <sub>2</sub> + 30 vol% SiC <sub>p</sub>	Hot Press & Solid State Reaction (at 1350 & 1700 °C)	8.7	Henager Jr. et al, 1992
8	MoSi <sub>2</sub> + 20 vol% VLS SiC <sub>w</sub>	Hot Press (1640 °C, 41 MPa, in CO-CO <sub>2</sub> air)	8.2	Gac & Petrovic, 1985
	MoSi <sub>2</sub> + 20 vol% VS SiC <sub>w</sub>	Hot Press (1800-1900 °C in Ar)	6.59	Gibbs et al, 1987
	MoSi <sub>2</sub> + 20 vol% SiC <sub>w</sub>	-	4.4	Petrovic & Honnell, 1991
9	MoSi <sub>2</sub> + 20 vol% TiC	Hot Press (1700 °C, 35 MPa, inert atmosphere)	5.0	Yang et al, 1989
10	MoSi <sub>2</sub> + 20 vol% TiB <sub>2</sub>	Plasma Spray	6.1	Tiwari et al, 1992
		HIP (1400 °C, 207 MPa, 4 h)	2.9	Brooks et al, 1994
11	MoSi <sub>2</sub> + 25 vol% Al <sub>2</sub> O <sub>3</sub>	Hot Press (1500-1600 °C, 46 MPa, in vacuum)	4.8 (RT) 6.5 (1100 °C)	Tuffe et al, 1993
12	MoSi <sub>2</sub> + 20 vol% ZrO <sub>2</sub>	Hot Press (1700 °C, 32 MPa)	7.8	Petrovic et al, 1991
13	MoSi <sub>2</sub> + 30 vol% PSZ	Hot Press (1700 °C, 30 MPa)	6.56	Petrovic & Honnell, 1990 <sup>b</sup>

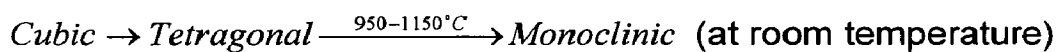
$\alpha$  along spray direction  
 $\beta$  perpendicular to spray direction  
 $\gamma$  by indentation method

## 2.6.1 Process Zone Mechanisms

### 2.6.1.1 Transformation Toughening

Transformation toughening can be regarded as a process dominated by an increase in volume. A residual compressive stress is created within the transformation zone. This stress inhibits crack opening, resulting in crack shielding (Evans, 1990).

ZrO<sub>2</sub> ceramics exist in three main crystallographic structures depending on temperature:



While cooling, tetragonal to monoclinic transformation takes place between 1150 °C – 950 °C. Tetragonal to monoclinic transformation, accompanied by a volume expansion of 3 – 5 %, is often suppressed to result in metastable tetragonal structure at room temperature. If a crack starts to propagate in such a system, high tensile stresses arise in the process zone in front of the crack tip. Under this stress, the metastable tetragonal grains of ZrO<sub>2</sub> in the vicinity of a crack are transformed from tetragonal to monoclinic. The volume expansion causes compressive stresses in the surrounding area and because this is taking place in front of a propagating crack, an additional energy is required for its further propagation (Claussen, 1975).

### 2.6.1.2 Microcrack Toughening

The basic factors in a material that allow microcracking are (i) Residual stresses and (ii) Low fracture energy paths or interfaces.

Microcracks occur within regions having local residual tensile stresses, caused by thermal expansion mismatch. The microcracks occur along the lowest fracture energy paths and locally relieve the residual tensile stresses. Consequently, a dilatation occurs governed by the volume displaced by the microcrack. Furthermore, the microcracks reduce the elastic modulus within the microcrack process zone. The volume change coupled with reduction in modulus results in crack shielding (Evans and Faber 1984, Hutchinson 1987, Evans 1990).

It is also likely that microcracks near the main crack tip region would serve to reduce the 'intrinsic toughness' because they provide easy paths for crack extension (Ortiz, 1988). Near tip microcracks will reduce the fracture energy appropriate to the area fraction of 'microcracks coalesced' with the propagating main crack. Therefore, there are two effects of microcracking on fracture toughness providing the competing processes for crack growth resistance (Ortiz, 1988).

- (i) One increases the crack growth resistance due to 'dilation', which is governed by the volume displaced and reduction in modulus.
- (ii) The other reduces the intrinsic fracture toughness.

### **2.6.1.3 Crack Tip Interactions**

Second phase particles near the tip of a propagating crack may result in (i) crack deflection and (ii) crack bowing causing a reduction in the stress intensity. It is essential to discriminate between the two as crack deflection produces a non-planar crack while crack bowing produces a non-linear crack (Lange, 1970).

#### **(a) Crack deflection**

Crack deflection occurs due to:

- (i) Residual thermal stresses present in the material as a result of thermal expansion mismatch between matrix and the second phase particles.
- (ii) Weak interfaces between matrix and the second phase particles.

A second phase with a greater coefficient of thermal expansion than the matrix produces tangential compressive stress in the matrix near the particle / matrix interface and diverts the crack around the particle. A second phase with a lower coefficient of thermal expansion than the matrix induces tangential tensile stress in the matrix causing the crack to deflect towards the particle.

When a crack approaches or intercepts a second phase particle, it will characteristically tilt at an angle,  $\theta$ , out of its original plane, as shown schematically in Fig. 2.11. Subsequent advance of the crack may result in crack front twist (Faber and Evans, 1983). The tilted and twisted cracks are subjected to mixed mode local loading, characterized by the corresponding local stress intensities. The tilted crack has Mode I (opening) and Mode II (sliding) contributions to the stress intensity.

Twisted crack incorporates both Mode I and Mode III (tearing) components. The increase in fracture toughness imparted by deflection of the crack is evaluated from the local stress intensities at the tilted and twisted portions of the crack front.

For a tilted crack, the local stress intensity factors are (Cottrell and Rice, 1980):

$$k_1 = \cos^3(\theta/2)K_I \quad (2.6)$$

$$k_2 = \sin(\theta/2)\cos^2(\theta/2)K_I \quad (2.7)$$

where,  $K_I$  is the applied stress intensity factor and  $\theta$  is the angle of deflection.

For a twisted crack, the local stress intensity factors,  $k_1^{\text{twist}}$  and  $k_3^{\text{twist}}$  depend on the twist angle,  $\phi$ , (with the undeflected crack) as well as on tilt angle,  $\theta$ . If the adjacent particles produce tilt angles of opposite sign, twist of the crack front will result. Alternately, tilt angles of like sign at adjacent particles cause the entire crack front to tilt.

The increase in toughness depends on particle shape and particle volume fraction. It does not depend on particle size (Faber and Evans, 1983). The effect of particle shape in toughening due to crack deflection increases in the following order:

- (i) Spherical particles
- (ii) Platelets (disc-shaped particles)
- (iii) Whiskers of high aspect ratio (rod-shaped particles)

The fracture toughness, regardless of morphology, is determined by 'twist' of the crack front, rather than the initial 'tilt' of the crack front. The amount of twisted crack is greatly influenced by the aspect ratio of the whiskers. Therefore, particles with high aspect ratios are more suitable for maximum toughening. Faber and Evans (1983) have argued that the second phase should be present in amounts of 10 – 20 vol%. Greater amounts may diminish the toughness increase due to overlapping particles.

In many laminate systems, layer delamination can occur ahead of an advancing crack or as the result of a crack encountering an interface. These local delaminations can result in crack deflection as shown schematically in Fig. 2.12(a). This can significantly reduce the Mode I component of the local stress intensity

because of the large deviations in crack path (up to 90° in crack arrester orientation) that are possible. The expression for the effective local stress intensity resulting from deflected cracks (assuming far field Mode I loading) that can be applied to laminated composites is given by (Suresh, 1983):

$$\frac{\bar{k}}{K_I} = \frac{\left(\frac{d}{L}\right) \cos^2 \frac{\theta}{2} + 1}{\left(\frac{d}{L}\right) + 1} \quad (2.8)$$

where  $\bar{k}$  is the effective local stress intensity factor,  $K_I$  is the far field Mode I stress intensity factor,  $d$  is the delamination length,  $L$  is the foil thickness and  $\theta$  is the angle of deflection of the crack.

Application of the above equation for the case of 90° crack deflection at the laminate interface produces the results as shown in Fig. 2.12(b). The curve shows that the crack deflection is an effective method of reducing the driving force for crack growth. For a delamination length equal to the foil thickness, the local stress intensity is about 75 % of the applied stress intensity.

### (b) Crack bowing

Crack bowing originates from second phase particles in the path of a propagating crack. The crack tends to bow between the particles causing the stress intensity,  $K$  along the bowed segment of the crack to decrease (while resulting in a corresponding increase in the stress intensity,  $K$ , at the particle). The degree of bowing increases until the fracture toughness of the particle is reached (Faber and Evans, 1983). The increase in toughness due to crack bowing depends on:

- (i) Fracture toughness of the second phase particles.
- (ii) Volume fraction and particle size of the second phase particles.

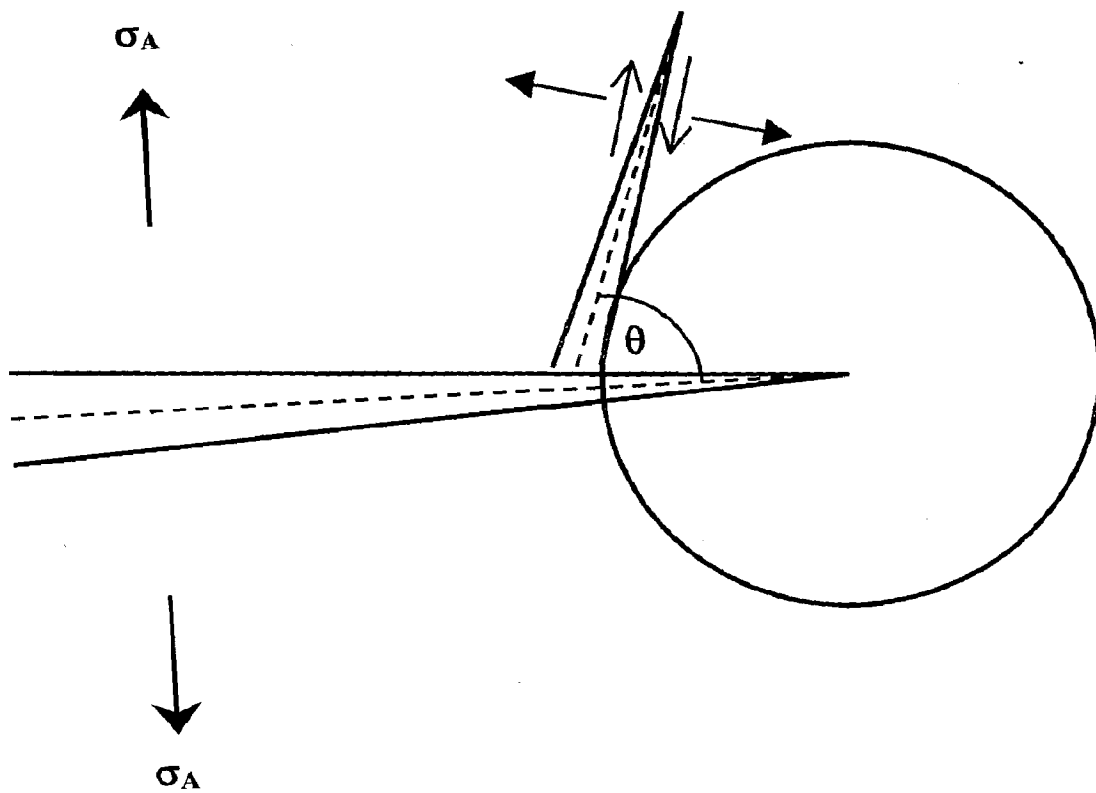
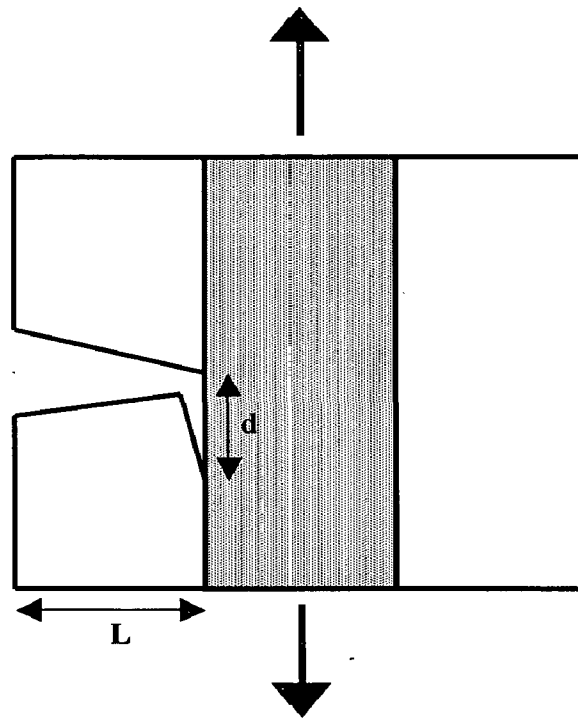
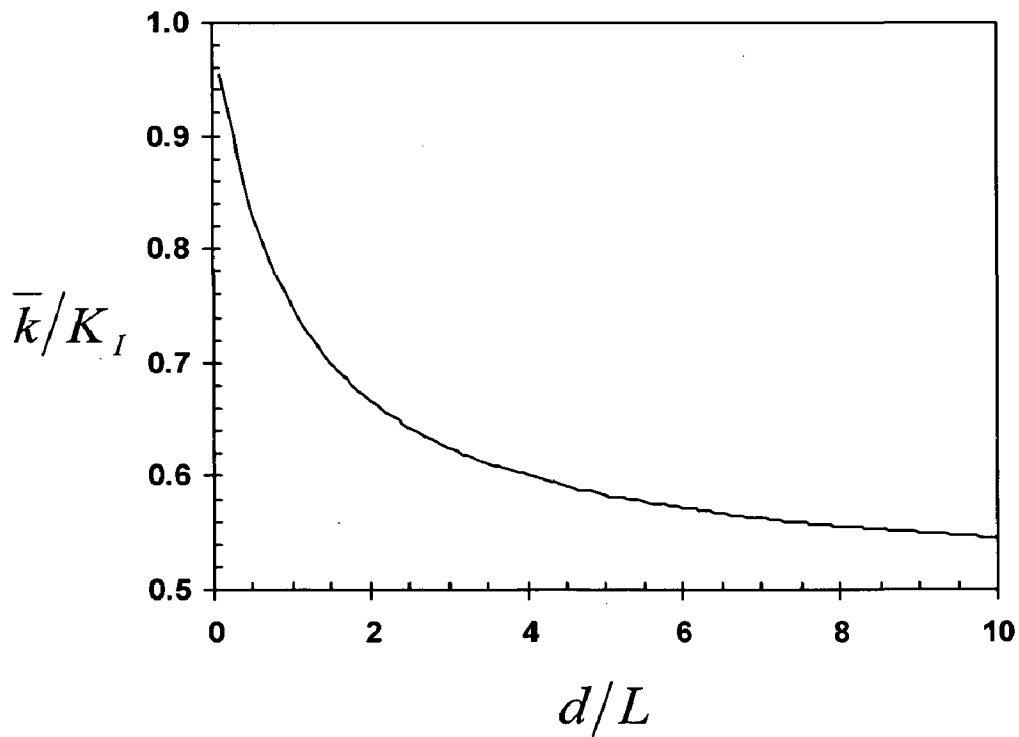


Fig. 2.11 Schematic representation of crack tilting by a second phase particle.



(a)



(b)

Fig. 2.12

(a) Schematic representation of crack deflection and (b) Normalized local stress intensity factor vs. normalized delamination (deflection) length for 90° crack deflection in laminated composites.

The 'crack bowing' concept is illustrated in Fig. 2.13 (Lange, 1970). Lange proposed a model that was based upon the hypothesis that a crack front possesses a 'line energy' similar to a dislocation. The toughness increases with increasing volume fraction of particles and hence, with decreasing interparticle spacing. The toughness will also increase with decreasing particle size at a given volume fraction as smaller particles will provide more crack-pinning sites per unit volume. However, he noted that significant toughening does not occur unless the particle spacing is significantly less.

**(c) Crack blunting**

Crack blunting can result when a propagating crack encounters a 'ruptured region'. For example, in a fiber reinforced composite in which fiber has already failed ahead of the propagating crack tip. The arresting and renucleation process results in a significant increase in the amount of energy required for the crack growth.

**2.6.2 Bridging Zone Mechanisms**

In crack bridging mechanism, contribution to toughness results from the bridging of crack surfaces by 'intact reinforcements' in a zone behind the crack tip. Fig. 2.14 exhibits schematically an intact ceramic whisker bridging the crack surfaces behind the crack tip. The important aspect of this mechanism is the ability of reinforcements to avert fracture at the crack tip and, thereby, to remain intact in the crack wake (Evans and McMeeking, 1986). These intact reinforcements can be both brittle ceramics (particles, whiskers, fibers) as well as ductile metals (particles, wires, foils). The residually compressed microstructural regions can also bridge the crack surfaces.

The increase in toughness,  $\Delta G$  (the change in strain energy release rate), caused by crack bridging (intact ligaments) is given by (Rice, 1968):

$$\Delta G = f \int_0^{u^*} \sigma(u) du \quad (2.9)$$

where  $f$  is the area fraction of the reinforcement on the crack plane ( $= V_r$ , volume fraction of the reinforcement),  $u$  is the crack opening,  $u^*$  is the crack opening at the



end of the bridging zone (critical crack opening at the time of ligament failure) and  $\sigma$  is the normal stress carried by the ligament, which is a function of  $u$ . It varies with increasing  $u$ .

In all the cases, the toughness due to crack bridging increases with increasing volume fraction, size and strength of the reinforcements.

### **2.6.2.1 Crack Bridging by Ceramic Reinforcements (Brittle Ligaments)**

When the bridging material is brittle, the toughness of the bridge (ligament) is similar to that of the non-bridging material (matrix). It requires either or both:

- (i) Microstructural residual stresses
- (ii) Weak interfaces

#### **(i) Microstructural residual stresses**

It may be appreciated by noting that large local residual stresses caused by thermal expansion mismatch are capable of suppressing local crack propagation and, thereby, may allow intact ligaments to exist behind the crack front. When these ligaments eventually fail in the crack wake, energy is dissipated as acoustic waves and causes toughening (Evans, 1990).

#### **(ii) Weak interfaces**

It may be understood by recognizing that low fracture energy interfaces can cause the crack to deflect along the interfaces, again permitting intact ligaments. As the crack extends, further debonding can occur. Eventually, the bridging material fails, either by debonding around the end or by fracture. Following failure, frictional sliding may occur along the debonded surface. The energy dissipation upon crack propagation thus includes terms to account for:

- (a) the energy of the debonded interfaces.
- (b) the acoustic energy dissipated upon reinforcement failure.
- (c) the frictional dissipation during pullout.

These contributions lead to a unified model of the fracture resistance of materials that exhibit bridging by brittle ligaments (Evans, 1990).

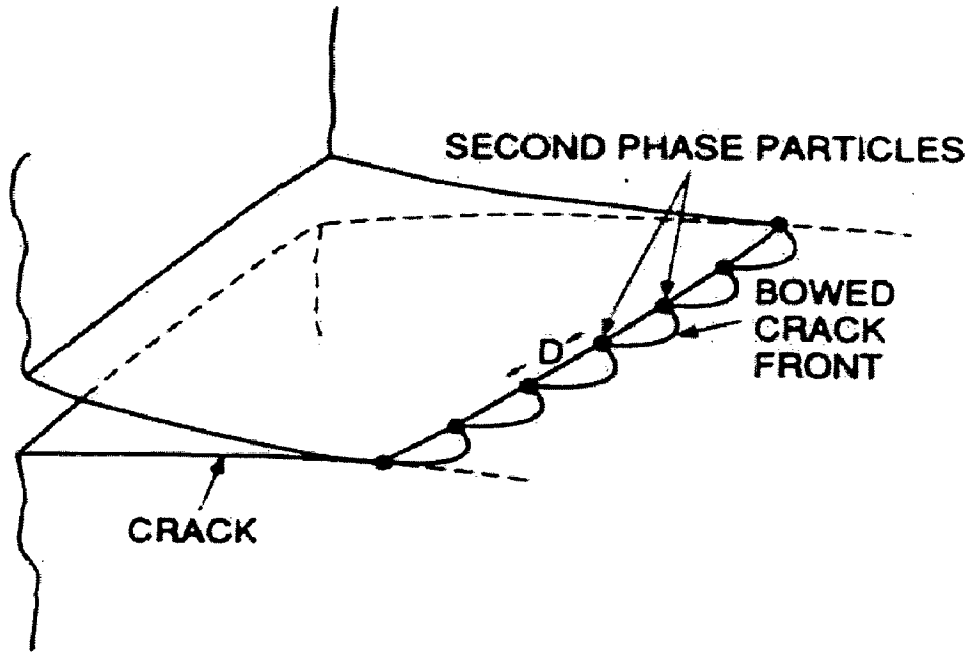


Fig. 2.13 Schematic representation of crack bowing by second phase particles.

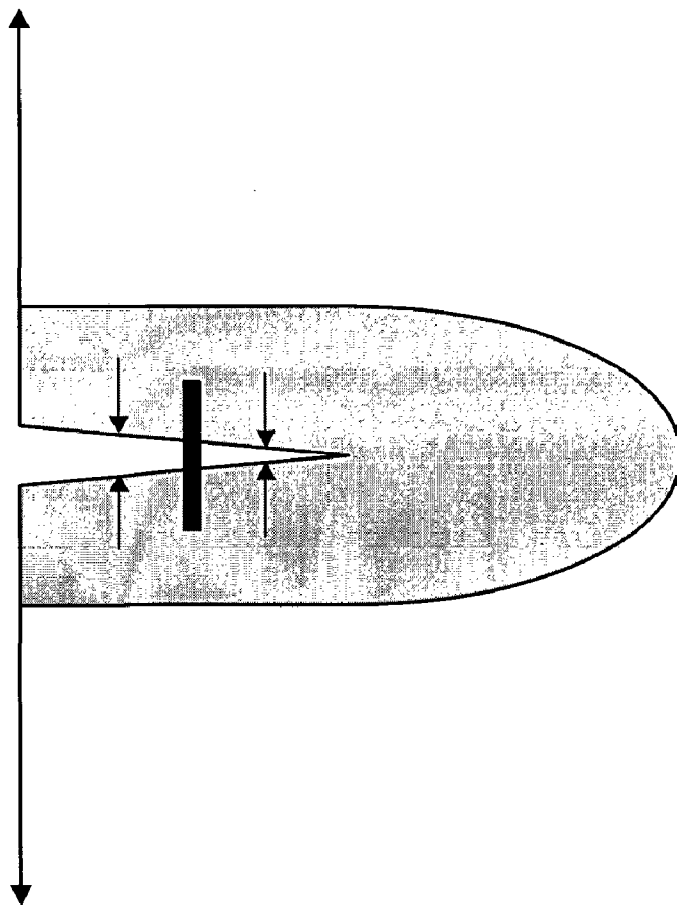


Fig. 2.14 Schematic representation of crack bridging by whiskers.

### **(a) Bridging by ceramic particles**

Various types of particles are capable of remaining intact at the crack front and have sufficient strength that they locally inhibit crack opening in the wake. Strong whiskers that partially debond at the crack tip have this attribute. In other words, it is crack surface pinning by the strong particles (Evans and McMeeking, 1986).

### **(b) Bridging by ceramic fibers**

The following events seem to take place in the same order as listed:

- (i) As the crack approaches the fiber, debonding at the fiber / matrix interface takes place (low fracture energy interfaces).
- (ii) Crack deflects at the debonded interface along these interfaces.
- (iii) As the crack extends, further debonding can occur.
- (iv) Eventually, the fiber fails by fracture. Fiber fracture involves the statistics of fiber failure (weakest link statistics).
- (v) Following the fiber failure, fiber pullout occurs with frictional sliding along the debonded surface.

Although debonding is a prerequisite for high toughness, the properties of the composite are dominated by the sliding resistance of the debonded interface, which dictates the major contribution to toughness caused by pullout (Evans, 1990). For a tough composite, a weak interface and a smaller coefficient of friction,  $\mu$  are desirable. C and BN coatings are applied on fibers to facilitate debonding and to decrease the sliding resistance, i.e., lower  $\mu$ .

### **2.6.2.2 Crack Bridging by Ductile Phases**

Brittle materials can also be toughened by ductile metallic reinforcements. The physical mechanism of toughening is straightforward enough. If the bridging of crack surfaces is by intact ductile reinforcements in a zone behind the crack tip, these intact ductile ligaments must stretch as the crack opens until they fracture. The work of stretching (Eq. 2.9) contributes to the overall toughness of the material (Ashby et al, 1989).

It was assumed earlier, that the 'flow strength' and 'fracture strain' of a ductile phase inside the brittle matrix was the same as that measured in a simple tensile test on the ductile phase alone. Ashby et al (1989) have shown that this assumption was false. If the ductile phase is strongly bonded, it is "constrained". Then its force displacement curve is very different from that of unconstrained ductile material as measured in an ordinary tensile test. This is an important difference because the energy absorbed in stretching the ductile phase is crucial in calculating the contribution to the toughness, which depends strongly on "degree of constraint".

The material systems that exhibit ductile phase toughening have three distinct microstructures:

- (i) Isolated ductile reinforcements (metal particles).
- (ii) Interpenetrating ductile phase networks, e.g., WC reinforced with Co (Sigl and Exner, 1987), Al<sub>2</sub>O<sub>3</sub> reinforced with Al (Sigl et al, 1988) and Al<sub>2</sub>O<sub>3</sub> reinforced with Al alloy produced by Lanxide process.
- (iii) Continuous ductile phase (metal wires and foils).

**(a) Bridging by ductile particles**

The addition of a dispersed ductile phase to a brittle material may lead to significant increase in fracture toughness. The primary mechanism responsible for the enhanced toughness appears to be bridging by intact ligaments of the ductile particles behind the advancing crack tip as shown schematically in Fig. 2.15 (Mataga, 1989). It is presumed that the faces of an advancing crack are pinned together by intact metal particles for some distance behind the crack tip, reducing the crack-tip stress intensity that would otherwise occur. The metal particles intercepted by the crack, when bonded to the matrix, exhibit extensive plastic stretching in the crack wake and contribute to the toughness by inhibiting crack opening (Evans and McMeeking, 1986). If the particle is so weakly bonded to the matrix that it easily pulls free as the crack approaches, then it is not stretched and there is almost no contribution to toughness (Ashby et al, 1989). However, Mataga (1989) has demonstrated that the ductile phase need not be completely bonded to the matrix during deformation to provide toughening. Limited debonding may well be beneficial in terms of toughness enhancement.

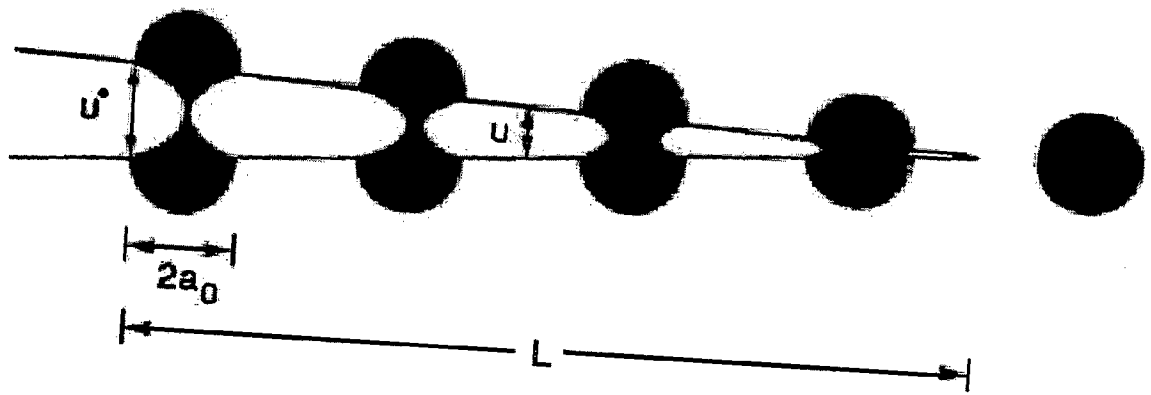
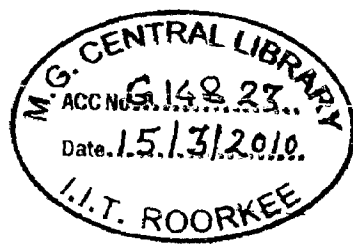


Fig. 2.15 Crack bridging by ductile particles.



The increase in toughness for a plastically deformable enclave within an elastic medium is given by Eq. 2.9 (Evans and Mcmeeking, 1986), which was modified by Budiansky et al (1988) as follows:

$$\Delta G = f \int_0^{u^*} \sigma(u) du - fG_m \quad (2.10)$$

where  $G_m$  is the matrix fracture energy. The term on the right hand side is introduced to account for the fact that the area of the matrix fracture is reduced by the presence of the ductile phase.

$\sigma$  ( the stress carried by the particle) vs.  $u$  (crack opening) plot is normalized and plotted as  $\sigma/\sigma_0$  vs.  $u/a_0$  ( $\sigma_0$  is unconstrained yield strength of the ductile particle and  $a_0$  is the particle radius). Ashby et al (1989) tried different methods of analyzing the above problem, i.e., to obtain  $\sigma/\sigma_0$  vs.  $u/a_0$  curves by theoretical analysis. They observed that:

- (i) There is a sharp rise in stress to a peak value of  $\sigma/\sigma_0 = 5$  to 6, reflecting the very large constraint imposed by the matrix on the particle. Qualitatively, the constraint conditions, which raise the hydrostatic stress levels in the bridging ligament in the initial stages, will increase the peak load.
- (ii) Sharp decline in stress from the peak, falling to near zero before the final fracture of the ductile particle (at  $u/a_0 \sim 0.5$ ).

By ignoring right hand side negative term, Eq. 2.10 can be written as:

$$\Delta G = f\sigma_0 a_0 \int_0^{u^*/a_0} \frac{\sigma}{\sigma_0} d\left(\frac{u}{a_0}\right) \quad (2.11)$$

$$\text{or, } \Delta G = f\sigma_0 a_0 W \quad (2.12)$$

$$\text{where, } W = \int_0^{u^*/a_0} \frac{\sigma}{\sigma_0} d\left(\frac{u}{a_0}\right) \quad (2.13)$$

$W$  is a dimensionless quantity, which is a measure of the toughening capacity of the constrained ductile particle. Therefore, fracture energy of the composite,  $G_c$ , can be estimated by (Mataga, 1989):

$$G_c = f\sigma_0 a_0 W + (1 - f)G_m \quad (2.14)$$

where  $G_m$  is fracture energy of the matrix as defined earlier.

The amount of toughening increases with increasing volume fraction, size and strength of the metal particles. The effectiveness of toughening of a ductile phase will, in general, be enhanced by its increasing elastic modulus, strain hardening exponent (Mataga, 1989) and plastic deformation before failure (Budiansky et al, 1988).

Some of the material systems studied that exhibit improved toughness due to bridging by ductile particles are:

- (i) TiAl reinforced with Nb (Elliot et al, 1988).
- (ii) Glass reinforced with Al particles (Krstic et al 1981, Krstic 1983).
- (iii) Glass reinforced with Pb, Nb and W particles (Ashby et al, 1989).

Ashby (1989) has demonstrated that using the same volume fraction and the same size of well-bonded particles of lead, niobium and tungsten increases the toughness of glass matrix in the same order. Large particles are found to be more effective than the smaller ones. It has also been found that if limited decohesion is allowed, the contributions more than double.

Apart from bridging, the ductile metal particles may also result in crack deflection and crack trapping.

### **(b) Crack bridging by ductile metal wires**

Ashby et al (1989) have studied the flow behaviour of highly constrained lead wires in glass matrix using a specimen consisting of a single lead wire embedded in a glass tube having a circumferential crack round the specimen in the glass matrix keeping the central lead core intact. Tensile test using a table-model Instron test machine has been conducted and the load-displacement curves are recorded. The curves are normalized and plotted as  $\sigma/\sigma_0$  vs.  $u/a_0$ . Where,  $\sigma_0$  is the yield strength of the lead wire tested in unconstrained condition,  $a_0$  is the radius of the

lead wire and  $u$  is the crack-opening displacement (axial displacement). The results are schematically reproduced in Fig. 2.16. It has been observed that:

- (i) When the interfacial bond between ductile metal wire and brittle matrix is strong, no decohesion (or debonding) takes place at the interface. The sample failed by nucleation of a single internal void, which grew until it occupied most of the section. Stress  $\sigma/\sigma_0$  rises rapidly to a peak value of  $\sim 6$ . It then falls rapidly. The displacement at failure is relatively small. The normalized areas under these curves are small.
- (ii) In samples with partial loss of adhesion between ductile metal wire and brittle matrix, i.e., limited debonding at the interface, the normalized stress  $\sigma/\sigma_0$  rises rapidly to a smaller peak value of  $\sim 4 - 5$  and then falls away as earlier. The areas under these curves are larger. When the ductile metal / brittle matrix bond is weak, the interface separates partially giving rise to a “gauge length”. The metal wire is less constrained at the “gauge length” region. It can draw down at a lower stress but with a greater elongation.

It has been observed that multiple cracking in brittle matrix with a strong interfacial bond also ‘frees a length of the ductile metal wire from the matrix’ giving rise again to a “gauge length”. The load-displacement curves are similar as with partial debonding.

Ashby et al (1989) based on their above work on a model “single Pb wire embedded in a glass tube” composite has concluded that as the constraint is lost, peak stress falls, maximum displacement increases in such a way that the total energy absorbed increases. If energy absorption is the goal, full constraint is not ideal. Some (limited) decohesion is desirable. As the length of decohesion increases, the peak in the curve falls and the curve broadens.

### **(c) Bridging by ductile metal foils**

The mechanism of bridging by foils is similar to crack bridging by ductile metal wires. Unbroken foil spans the wake of the crack as depicted schematically in Fig. 2.17. Growth of the crack requires stretching of the metal foil. The foil must have sufficient ductility to avoid fracture at or ahead of the advancing crack tip. Therefore,



crack bridging will occur, when ductility or toughness differences exist between the component layers of the composite. This has led to the concept of laminated composites, which consist of alternating layers of relatively brittle and ductile materials. The toughness enhancement is a function of foil thickness, yield and work hardening behaviour of the metal foil and delamination length at the matrix / foil interface.

The concept of laminates with weak interfaces for toughening brittle materials was first used by Clegg and co-workers (Clegg et al 1990, Clegg and Seddon 1992, Phillips et al 1992<sup>a</sup>, 1992<sup>b</sup>). Fig. 2.18(a) shows a schematic of such laminated composite consisting of SiC laminates with weak graphite interlayers. Fig. 2.18(b) exhibits an experimental load versus displacement curve in a three-point bend test for notched monolithic SiC and for the laminated material (Phillips et al, 1992<sup>b</sup>). The most characteristic feature of these laminates was the phenomenon of crack deflection at the interfaces between laminae. This resulted in a work of fracture of 6000 J/m<sup>2</sup> as compared to 28 J/m<sup>2</sup> of the bulk SiC produced by the same route. In Fig. 2.18(b), successive load drops represent the characteristic crack deflection at the interfaces between laminas.

### 2.6.2.3 Grain Bridging

If microstructural regions like grains remain residually compressed and intact as the crack front extends through the material, the intact regions would contribute to toughness (Evans and McMeeking, 1986). Grain bridging can be induced in two ways:

#### (i) Residual stress induced bridging

If some grains are residually compressed, they can bridge the crack. The crack circumvents local, highly stressed regions. Such a bridging process increases the steady state toughness in accordance with (Evans, 1990):

$$\Delta K_c = 2.5VE\Delta\alpha\Delta T\sqrt{R} \quad (2.15)$$

where  $V$  is the volume fraction of the compressed grains that result in bridging and  $2R$  is the grain diameter.

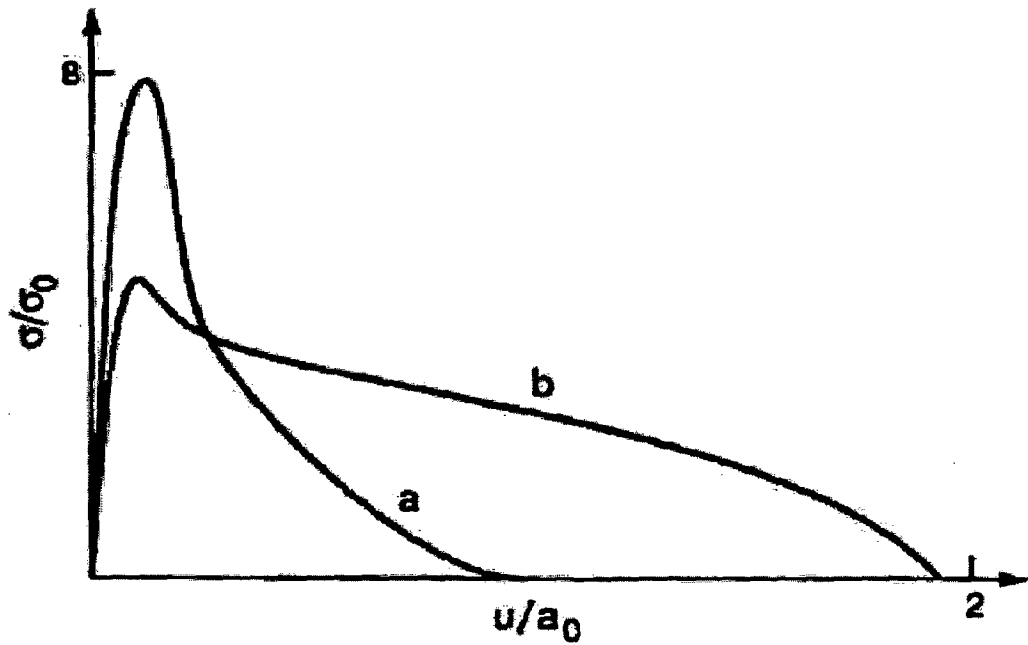


Fig. 2.16 Schematic load-displacement curves for a ductile wire reinforced brittle matrix composite (a) without debonding between ductile wire and brittle matrix (high degree of constraint) (b) with debonding between ductile wire and brittle matrix (lower constraint).

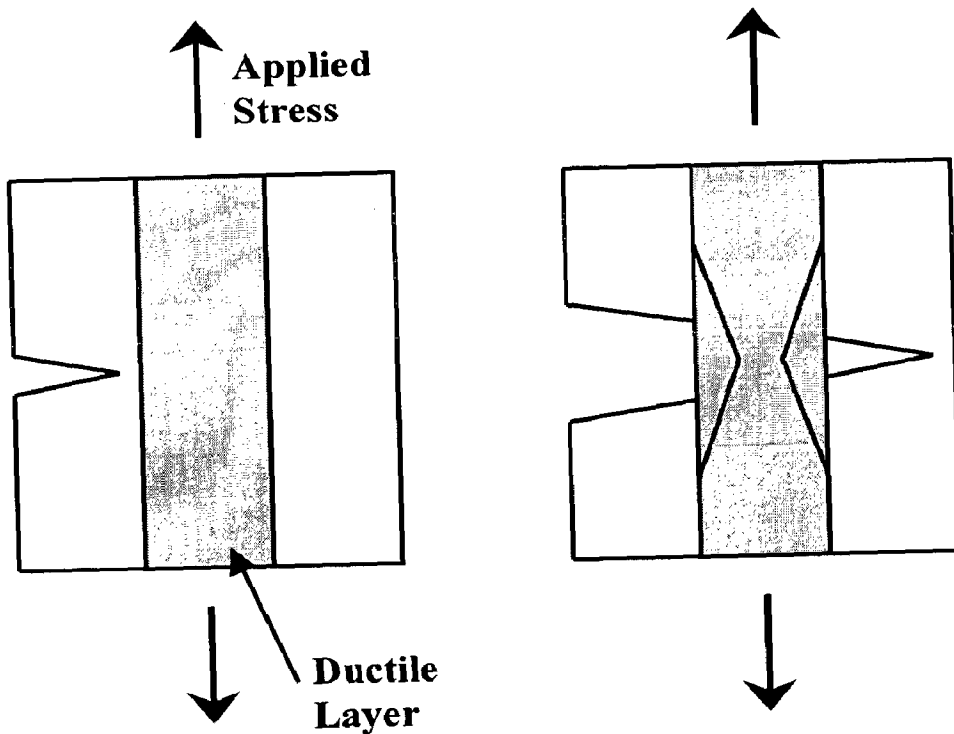
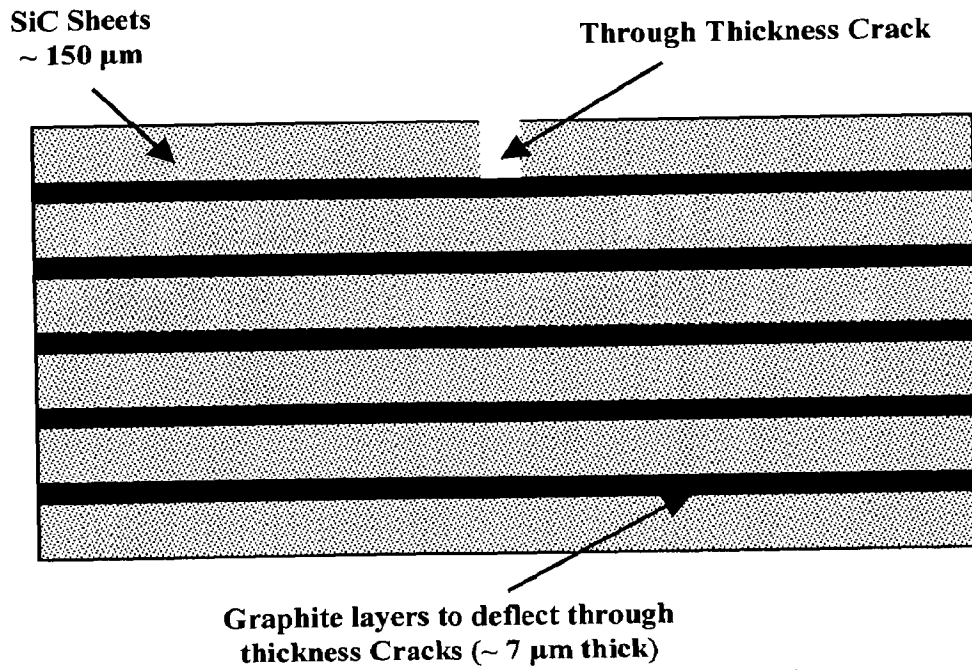
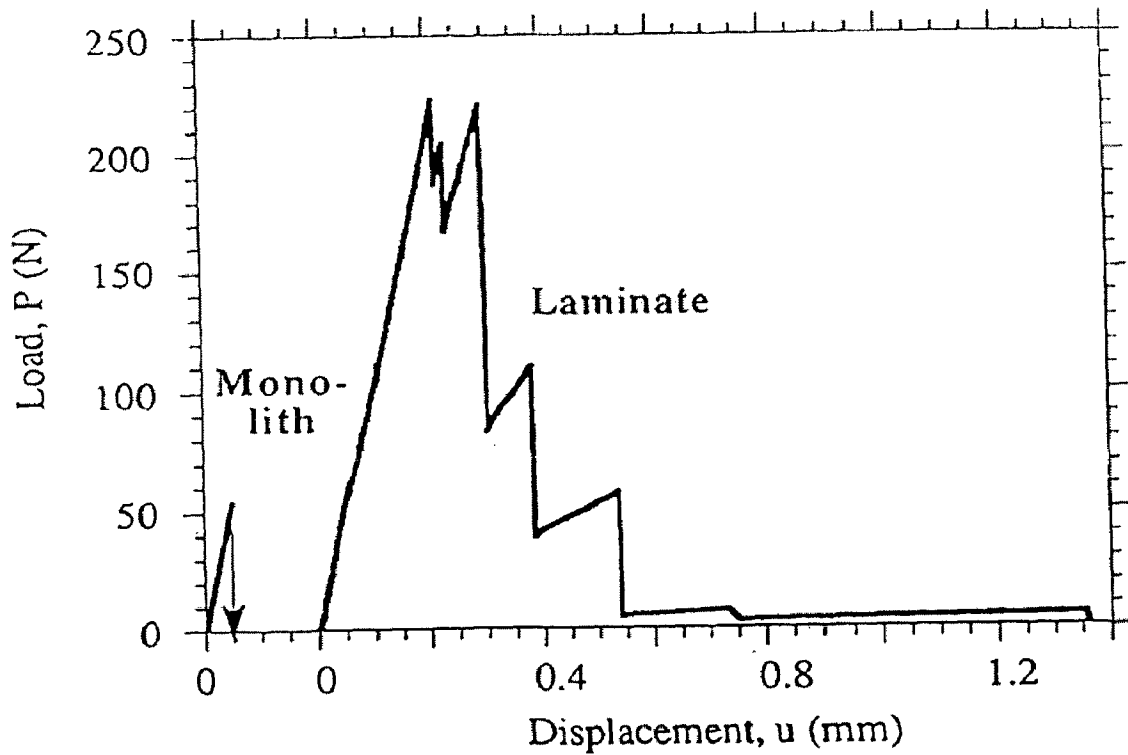


Fig. 2.17 Schematic showing crack bridging by a ductile metal foil in a brittle matrix.



(a)



(b)

Fig. 2.18

(a) Schematic of a laminated composite made of SiC laminas with weak interlayers of graphite (b) Experimental load vs. displacement curves in a three-point bend test for notched monolithic SiC and for the laminated material.

This increase in toughness arises because ligament failure occurs unstably and energy is dissipated in this process as acoustic waves.

## **(ii) Grain boundary debonding**

Low fracture energy grain boundaries can allow debonding, as in fiber reinforced materials. Elongated grains, which allow larger debond lengths, could lead to higher toughness (Lawn, 1983).

Evans (1990) has arranged different mechanisms of toughening of brittle materials in the following order of decreasing importance:

1. The toughest ceramics incorporate continuous fiber reinforcements.
2. The next toughest ceramics are those with a second phase dispersion of ductile metals.
3. This is followed by ceramic materials incorporating  $ZrO_2$  transformation toughening effects.
4. Second phase brittle particles / platelets / whiskers fall next in the hierarchy.
5. Finally, matrix microcracking constitutes the least effective although still significant, toughening approach.

## **2.7 FORMULATION OF THE PROBLEM**

The detailed literature survey as presented above clearly indicates that the interest in  $MoSi_2$  based materials for high temperature structural applications has gained momentum in recent years. The literature review revealed that to develop  $MoSi_2$  as a material for elevated temperature structural applications, it was necessary to improve both, its high temperature strength and creep resistance as well as its room temperature fracture toughness. A variety of reinforcements have been used to improve the mechanical properties of  $MoSi_2$ . Ceramic reinforcements have been successfully used to improve the high temperature strength and creep resistance of  $MoSi_2$ . However, the various studies on addition of ceramic reinforcements in  $MoSi_2$  matrix revealed that the brittle ceramic reinforcements did not result in significant improvement in room temperature fracture toughness of  $MoSi_2$ . Their effect on improving the room temperature fracture toughness was found to be very marginal. Only moderate room temperature toughening effects have been derived with the addition of brittle ceramic Particles and whiskers. Toughening levels achieved by these

reinforcements were similar to those observed in ceramic matrix composites, and are associated with mechanisms such as crack deflection / crack branching.

The room temperature fracture toughness ( $K_{IC}$ ) of  $MoSi_2$  has been reported to be in the range of 3-4  $MPa\sqrt{m}$ . Almost all components used for high temperature structural applications are subjected to some degree of stresses at low temperatures also. This could be catastrophic for  $MoSi_2$  based materials having very poor toughness at lower temperatures. Since a fracture toughness level of 12 to 15  $MPa\sqrt{m}$  is desirable for possible structural applications, other types of reinforcements, e.g., ductile phases have also been explored. However, the literature review revealed that there were very limited studies on the use of ductile reinforcements in  $MoSi_2$  matrix. Most of the work reported till date is only on the use of Nb as a ductile reinforcement in  $MoSi_2$ . The other candidate ductile reinforcements could be refractory metals like Ta, Mo and W. However, the data available in the literature on the use of ductile reinforcements other than Nb in  $MoSi_2$  was found to be limited. The success achieved in improving the room temperature fracture toughness of  $MoSi_2$  by incorporating Nb motivates further studies on understanding the effect of other ductile reinforcements on microstructure and properties of  $MoSi_2$ .

Due to the limited information available on ductile phase toughening of  $MoSi_2$ , it was decided to investigate further the toughening of  $MoSi_2$  by different ductile refractory metals. Therefore, in the present work, an attempt has been made to understand the role of various ductile refractory metals in toughening of  $MoSi_2$  matrix. Different ductile refractory metals like tungsten, molybdenum, tantalum and niobium are selected (in Particle as well as in foil form) as the reinforcements to carry out a comparative study of their compatibility with  $MoSi_2$  and their effect on its room temperature mechanical behaviour. The  $MoSi_2$  matrix was also modified by additions of pure Al and SiC Particles to obtain the synergistic effects with ductile reinforcements as well as to improve the thermal compatibility between  $MoSi_2$  and the various ductile phases. The literature also revealed that a comprehensive study of residual thermal stresses in  $MoSi_2$  based composites has not been carried out. These stresses are very important in all composite materials and more so in  $MoSi_2$  based composites due to high processing temperatures involved and a very low strain to fracture. Therefore, in the present work, an attempt has been made to

understand the nature and magnitude of residual thermal stresses in  $\text{MoSi}_2$  based particulate and laminated composites by analytical methods as well as by FEM analysis. A quantitative idea of the residual thermal stresses in  $\text{MoSi}_2$  based materials could be very useful and could provide some important guidelines to obtain the enhanced mechanical properties.

**EXPERIMENTAL PROCEDURE**

---

**3.1 RAW MATERIALS**

Composites and monolithic materials used in the present study were prepared from the powders of  $\text{MoSi}_2$ ,  $\text{SiC}$ ,  $\text{W}$ ,  $\text{Mo}$ ,  $\text{Nb}$ ,  $\text{Al}$  and  $\text{Al}_2\text{O}_3$  as well as foils of  $\text{Mo}$ ,  $\text{Ta}$  and  $\text{Nb}$  metals. Commercial purity  $\text{MoSi}_2$ ,  $\text{MoSi}_2$  with 2 wt%  $\text{Al}$  and  $\text{MoSi}_2$  with 20 vol%  $\text{SiC}$  particless ( $\text{SiC}_p$ ) were used as matrix materials.  $\text{W}$ ,  $\text{Mo}$  and  $\text{Nb}$  in the form of particless, and  $\text{Mo}$ ,  $\text{Ta}$ , and  $\text{Nb}$  in the form of foils had been used as reinforcements.  $\text{Al}_2\text{O}_3$  powder was used to apply a diffusion barrier coating on the refractory metal foils.

Commercial grade  $\text{MoSi}_2$  for this investigation was obtained from H.C. Starck, Germany. The average particle size was 5.5  $\mu\text{m}$ . The  $\text{SiC}$  powder was obtained from Superior Graphite Co., USA and had an average particle size of 2  $\mu\text{m}$ . The powders of refractory metals  $\text{Mo}$  and  $\text{Nb}$  were obtained from Mishra Dhatu Nigam Ltd. (MIDHANI), India and New Metals Co., UK, respectively. The  $\text{W}$  powder used was from Defence Metallurgical Research Laboratory (DMRL), Hyderabad. All refractory metal powders used were -325 # (below 45  $\mu\text{m}$  size). Commercial  $\text{Al}$  was obtained from National Aluminium Company (NALCO), India and atomised in inert gas by Metal Powder Company, Madurai, India. The average particle size of  $\text{Al}$  was about 45  $\mu\text{m}$ . The sources of various powders used as matrix and the reinforcement materials along with their average particle sizes are summarized in Table 3.1.

Table 3.2 gives the sources from which various refractory metal foils were procured for this investigation. The thickness of all the metal foils used was 0.50 mm.

### **3.1.1 Characterization of Raw Materials**

Characterization of raw materials included study of chemical composition, x-ray diffraction analysis, particle size distribution and morphology for both matrix and the reinforcement powders. The chemical composition of the refractory metal foils was also analyzed. The as received refractory metal foils were also evaluated for their microstructure and tensile properties.

The chemical composition of all the raw materials was determined by analytical chemistry methods. X-ray diffraction analysis of various powders was carried out using Cu K $\alpha$  radiation ( $\lambda = 1.5418 \text{ \AA}$ ).

Photo-extinction technique was used in Coulter's counter for analyzing the particle size and size distribution of various raw materials in the powder form. Stoke's law of sedimentation was applied for simulating particle size and size distribution with variation in light intensity as a measure of suspended particle concentration. A monochromatic light beam passes through the powder suspended in ethylene glycol and as the particles settle, the intensity of light changes depending on the scattering and absorption of light. A computer interfaced with photometer (Seshei Micron Photo Sizer Model 2000S) gives particle size distribution directly.



**Table 3.1** Source and the average particle size of various powders used as matrix and the reinforcement materials.

<b>S No.</b>	<b>Powder</b>	<b>Source</b>	<b>Average Particle Size, (<math>\mu\text{m}</math>)</b>
1	MoSi <sub>2</sub>	H. C. Starck, Germany	6
2	SiC	Superior Graphite Co., USA	2
3	W	DMRL, Hyderabad	11
4	Mo	Midhani, Hyderabad	4
5	Nb	New Metals Co., UK	10
6	Al	Metal Powder Co., Madurai	45

**Table 3.2** Source and the thickness of the refractory metal foils used in making MoSi<sub>2</sub> based laminated composites.

<b>S No.</b>	<b>Refractory Metal Foil</b>	<b>Source</b>	<b>Thickness, (mm)</b>
1	Mo	Midhani, Hyderabad	0.5
2	Ta	NFC, Hyderabad	0.5
3	Nb	NFC, Hyderabad	0.5

Shape and morphology of various powders were studied using scanning electron microscopy at an accelerating voltage of 15 kV. All the specimens were conductive except SiC. Nonconductive specimens were coated with a conductive thin film for SEM examination. Coating the specimen permitted use of higher voltages, which significantly enhanced image quality. Ultrasonically dispersed powders of different materials, in acetone, were spread on aluminium specimen studs and used for SEM study after drying of acetone. The SiC powder particles were sputter coated with Au-Pd alloy in Ar atmosphere using a Pelco SC-7 Auto Sputter Coater. The diode sputter coater consisted of the specimen stage (anode) and a small bell jar containing an Au-Pd metal target that functions as cathode. Under low vacuum conditions ( $\sim 10^{-2}$  torr), Ar was fed into the chamber, which formed a plasma. These energetic ions striking the metal target, transferred momentum to cause metal atoms to be ejected from the target. The metal atoms were attracted towards the specimen stage by the potential difference between the target and the stage.

### **3.1.2 Tensile Properties of Refractory Metal Foils**

As received refractory metal foils used in the present study were evaluated for their tensile properties. The tensile test was conducted on Instron Series IX Automated Materials Testing System 8.25.00 using a flat tensile specimen (ASTM Standard E8M). The tensile test specimens having a width of 4.0 mm and gauge length of 15 mm were cut by electro discharge machining from as received foils. The tensile test was performed using a crosshead speed of 1.0 mm/min with a full-scale load range of 5.0 kN. From stress – strain curves, 0.2 % offset yield strength, ultimate tensile strength (UTS) and % elongation were evaluated. Figs. 3.1(a) and 3.1(b) show a schematic drawing of the flat tensile specimen and the actual tensile test specimens of the refractory metal foils, respectively. All dimensions in Fig. 3.1(a) are in mm.

## **3.2 PROCESSING**

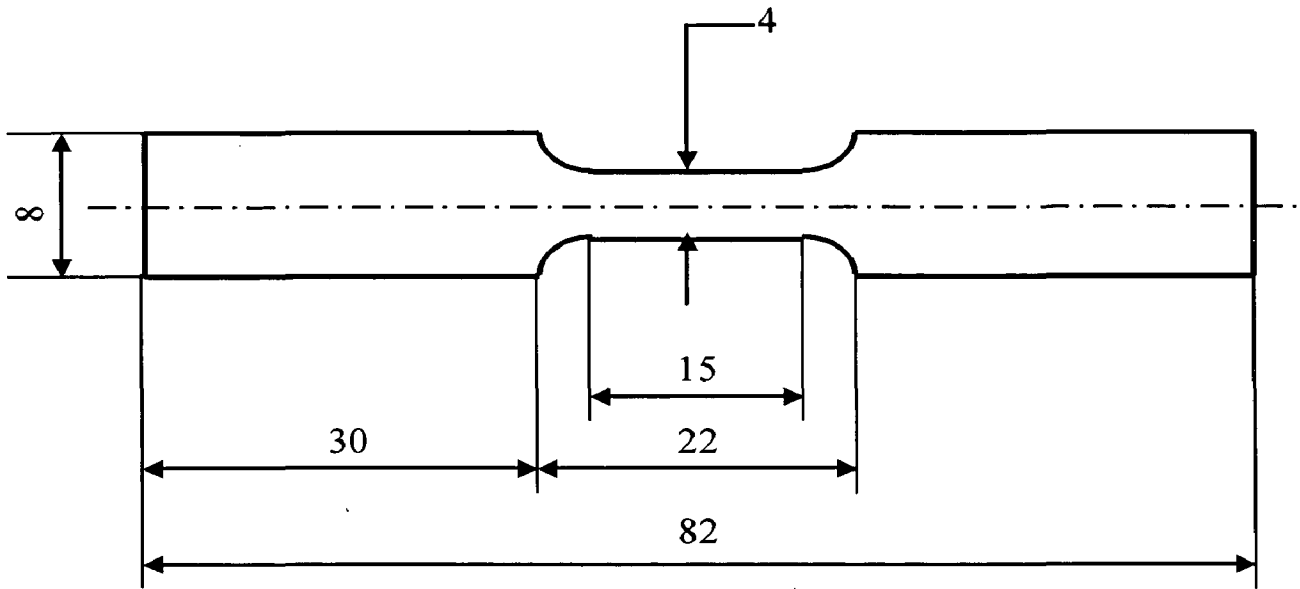
In the present work, the various composite materials were processed by powder metallurgy route. The monolithic matrix materials were also produced by the same processing methods to provide a reference against which the properties of the composites could be compared. Vacuum hot pressing was used as the main technique

to consolidate the matrix and the reinforcement components together to make the different particulate and laminated composites.

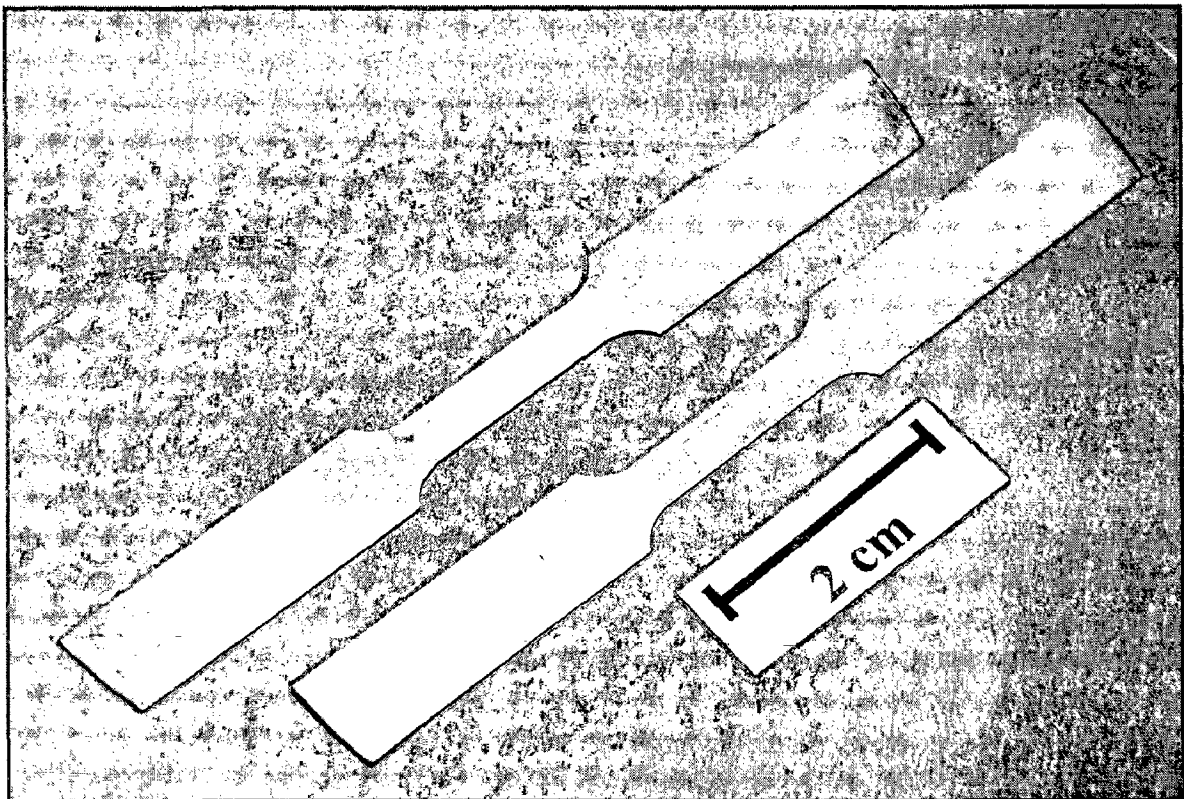
### **3.2.1 Consolidation by Vacuum Hot Pressing**

Vacuum hot pressing is the least complicated powder consolidation method. The unique feature of hot pressing is its ability to enhance the densification kinetics by application of external pressure during sintering at high temperature for a certain period of time. A fourth variable, the surrounding environment can also be controlled. Its relationship with other forming and consolidation processes is illustrated schematically in Fig. 3.2. With the presence of a superimposed pressure, mechanisms such as grain rotation, grain boundary sliding, fragmentation, plastic deformation and enhanced diffusion along grain boundaries all play a critical role in providing an enhanced densification rate.

The high melting point and brittleness of the silicides has necessitated using higher processing temperatures. To attain high densities in composites based on  $\text{MoSi}_2$ , high processing temperatures in the range of 1500 - 1800 °C are necessary. It is not difficult to fully densify the silicides by powder techniques. However, contamination by impurities such as oxygen has often been a problem (Stoloff, 1999). Vacuum hot pressing is the most widely used process to consolidate the  $\text{MoSi}_2$  based materials. A wide range of process parameters have been employed by different researchers during hot pressing of  $\text{MoSi}_2$  based materials. The  $\text{MoSi}_2$  based materials were hot pressed in the temperature range from 1400 - 1900 °C for durations ranging from 5 to 60 minutes. The applied pressure was in the range from 30 to 40 MPa. Hot pressing was conducted in vacuum as well as in inert gas atmosphere. Table 3.3 summarizes some of the hot pressing parameters used by different workers.



(a)



(b)

Fig. 3.1 (a) Schematic drawing of flat tensile specimen (ASTM Standard E8M) used to make tensile specimens of metal foils (b) Tensile test specimens of refractory metal foils.

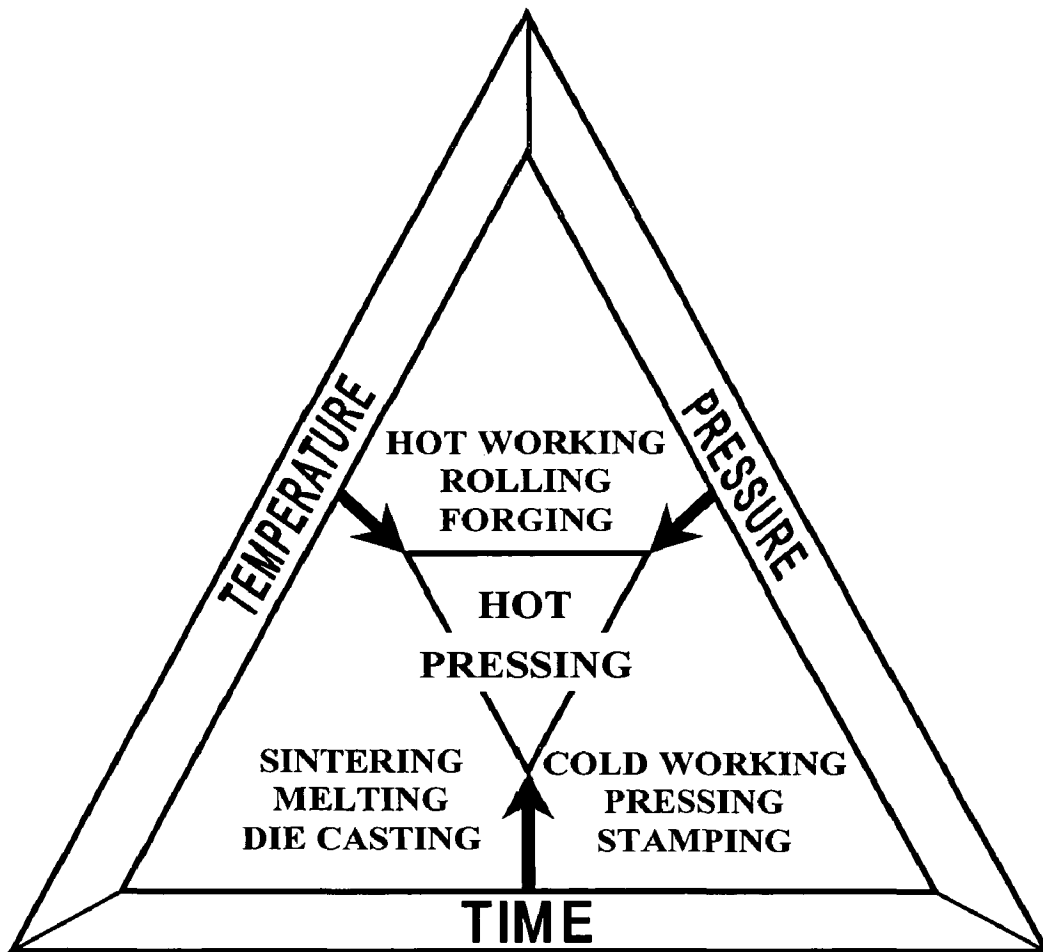


Fig. 3.2 Relationship of hot pressing to other forming and consolidation processes.

Table 3.3 Hot pressing process parameters to consolidate MoSi<sub>2</sub> based materials.

S No.	Process Parameters				Reference
	Temperature (°C)	Pressure (MPa)	Time (min)	Atmosphere	
1	1625 - 1640	41.4	-	CO - CO <sub>2</sub> rich air	Gac and Petrovic, 1985
2	1800 - 1900	-	5	Ar	Carter et al, 1989
3	1850	30	-	Ar	Bhattacharya and Petrovic, 1991
4	1830	-	50	Ar	Maloy et al, 1991
5	1820	32	15	Ar	Wade and Petrovic, 1992 <sup>a</sup>
6	1700	30	40	Vacuum	Xiao et al, 1990
7	1400	-	40	Vacuum	
8	1700	40	40	Vacuum	Xiao and Abbaschian, 1992 <sup>a</sup> , 1992 <sup>b</sup>
9	1400	40	60	Vacuum	Xiao and Abbaschian, 1992 <sup>a</sup>
10	1400	40	60	Vacuum	Xiao, 1991 <sup>a</sup>
					Xiao et al, 1992 Shaw et al, 1993, 1995
11	1470	-	-	-	Badrinarayanan et al, 1996

It has to be emphasised that the choice of optimised hot pressing parameters depend upon the types of reinforcements used in MoSi<sub>2</sub> matrix. The matrix and the particle size, shape and volume fraction of reinforcements as well as the impurities present also influence the choice of the most suitable process parameters. Higher temperatures are needed to press pre-alloyed powders to full density than would be required in pressing elemental powders. Hot isostatic pressing (HIP) has also been employed as an alternative to vacuum hot pressing to consolidate the composites based on MoSi<sub>2</sub> (Alman et al 1992, Alman and Stoloff 1992, Venkateshwara Rao et al 1992<sup>b</sup>, Chen et al 1994<sup>a</sup>, Soboyejo et al 1996).

Vacuum hot pressing involves heating of the blended powders placed in a die under vacuum to the required temperature and then pressing the porous mass into a fully dense compact. A GCA, USA vacuum hot press was used in the present work. The GCA hot press had the capacity to go up to 2000 °C temperature and to attain a vacuum of the order of 10<sup>-4</sup> torr. Its maximum load capacity was 100 T. The die, spacers and plungers were made of graphite. A vertical tubular graphite heating element was used. Furnace was fitted with a side door to load the dies. High density (1.8 g/cm<sup>3</sup>) graphite dies were used. Temperature was monitored by a chromel - alumel thermocouple. Fig. 3.3 exhibits the GCA vacuum hot press used in the present work. The schematic hot pressing set up is shown in Fig. 3.4.

### **3.2.2 Processing of Refractory Metal Particless Reinforced MoSi<sub>2</sub> Matrix Composites**

The processing of ductile refractory metal particless reinforced MoSi<sub>2</sub> matrix composites consisted of blending of the reinforcement powder with the matrix powder, vacuum degassing treatment of the blended powders followed by consolidation by vacuum hot pressing.

Figure 3.5 illustrates the sequence of processing steps, schematically. MoSi<sub>2</sub> and 20 vol% of W, 20 vol% of Mo and 20 vol% of Nb powders each were mixed and dry blended for 24 h in a ball mill. In dry blending practice, the refractory metal powders were added to the MoSi<sub>2</sub> powder and the mixture was milled in dry condition. The blending operation involved tumbling of the powder mixture with a few tungsten balls in cylindrical bottles using a horizontal rubber roller mill. A few intermediate sieving steps

were introduced to ensure the breaking of lumps formed during the dry blending, if any, and to facilitate the homogeneous distribution of reinforcement powder particles in MoSi<sub>2</sub> powder. Figure 3.6 shows a flow chart outlining the various steps in the dry blending practice adopted in the present work. The rubber roller mill used for blending of matrix and reinforcement powders is shown in Fig. 3.7.

The blended powders were vacuum degassed at 1100 °C for 1 h to remove any moisture and volatile matter before hot pressing at 1750°C for 1 h using a pressure of 27 MPa. The vacuum was maintained at around 10<sup>-4</sup> torr. Even though the press is of capacity of 100 T, maximum pressure that could be applied was limited to 27 MPa due to the limitation imposed by the graphite dies. Prior to hot pressing, the die is lined with a 0.2 mm thick graphite sheet coated with boron nitride to avoid any reaction between the powders and the die walls. The hot pressed product was a disc of 75 mm diameter with 5-6 mm thickness. The densities of the materials produced were above 99 % of the theoretical densities. Hot pressed MoSi<sub>2</sub>-W, MoSi<sub>2</sub>-Mo and MoSi<sub>2</sub>-Nb discs were sand blasted on both sides to remove the graphite layer. These were then polished using diamond impregnated discs and sectioned using electro discharge machining (EDM).

### **3.2.3 Processing of Laminated Composites with MoSi<sub>2</sub> + 2 wt% Al as Matrix**

To understand the effect of morphology of the reinforcements on ductile phase toughening of MoSi<sub>2</sub>, it was planned to carry out the further work on using these ductile refractory metals in the continuous form (foil) to prepare the laminated composite structures. Laminated composites represent a unique layered composite form.

The idea of laminating different metals and alloys to form a composite material (laminated metal composites) that exploits the good properties of the constituent materials has been known from antiquity. The internal 'interface' between layers limits crack propagation through several different mechanisms. The application of laminated metal composites (metal – metal) to gun barrels for through thickness toughness is not new (Hertzberg, 1983). However, the idea of making laminated structures with alternate brittle ceramics and ductile metal layers is relatively new.



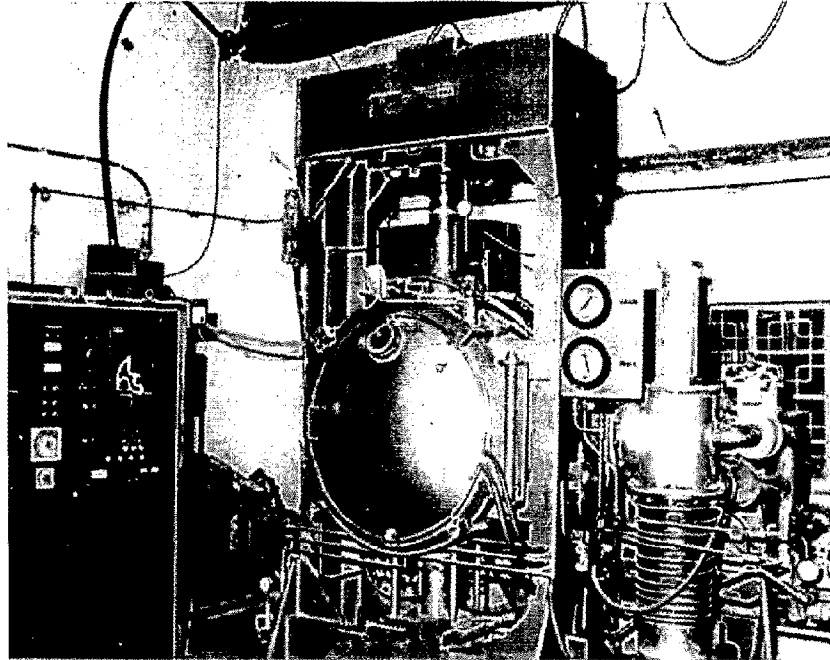


Fig. 3.3 GCA vacuum hot press used in the present study.

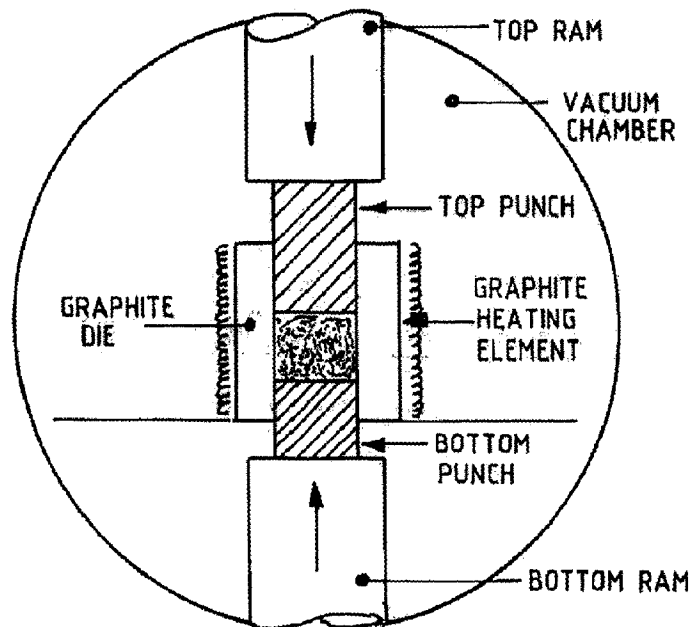


Fig. 3.4 Typical hot pressing set up used with GCA vacuum hot press.

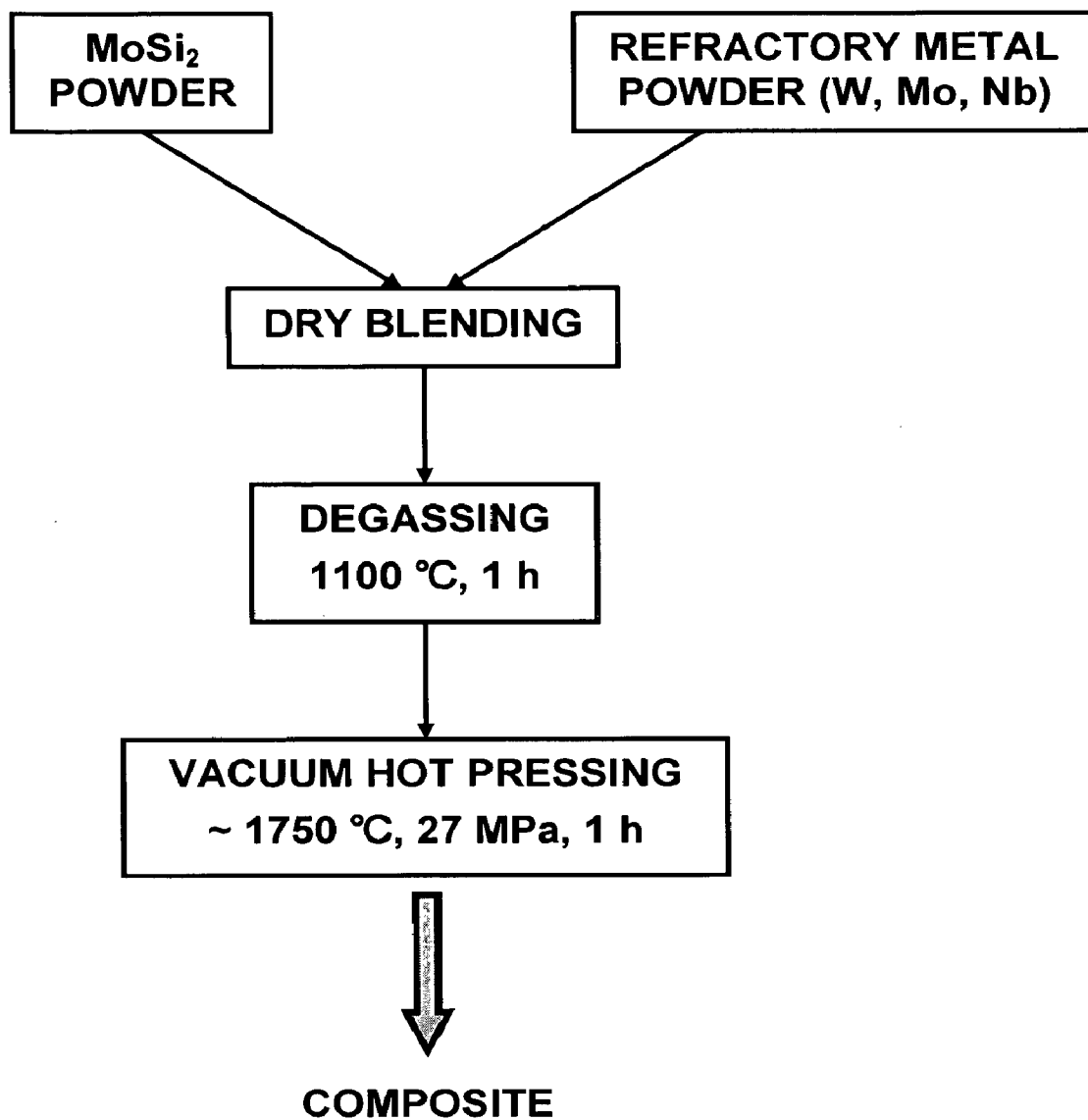


Fig. 3.5

Schematic illustration of sequence of various steps in the processing of ductile refractory metal particles reinforced MoSi<sub>2</sub> matrix composites.

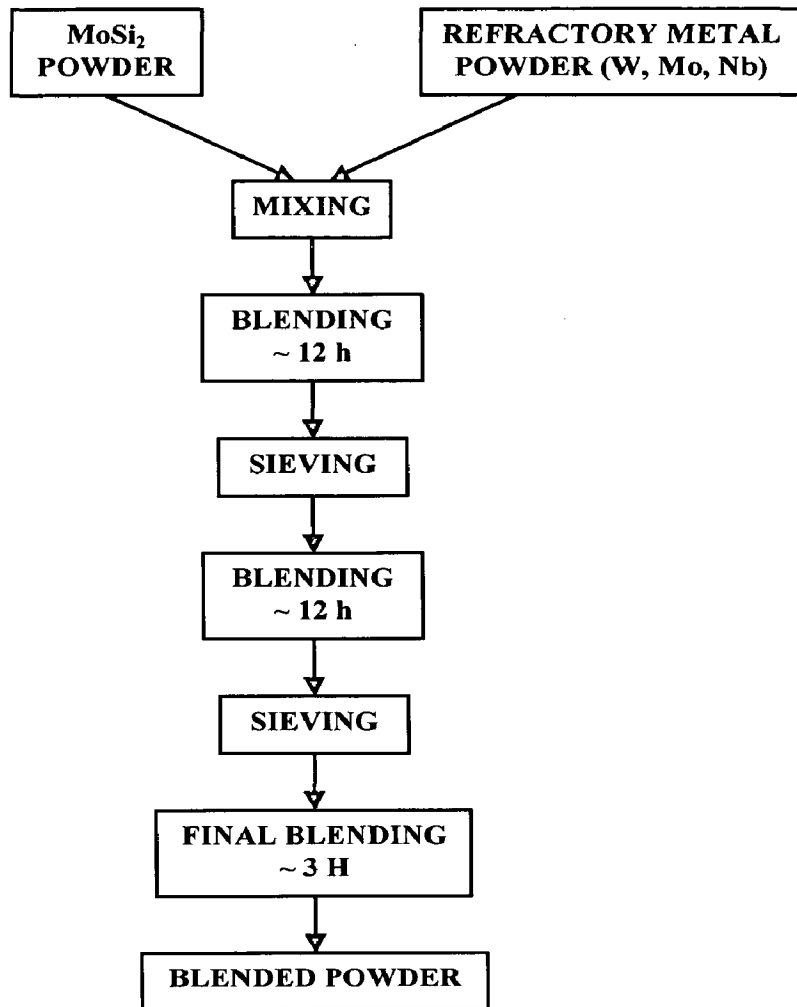


Fig. 3.6 Flow chart illustrating the various steps schematically in dry blending of MoSi<sub>2</sub> and refractory metal powders.

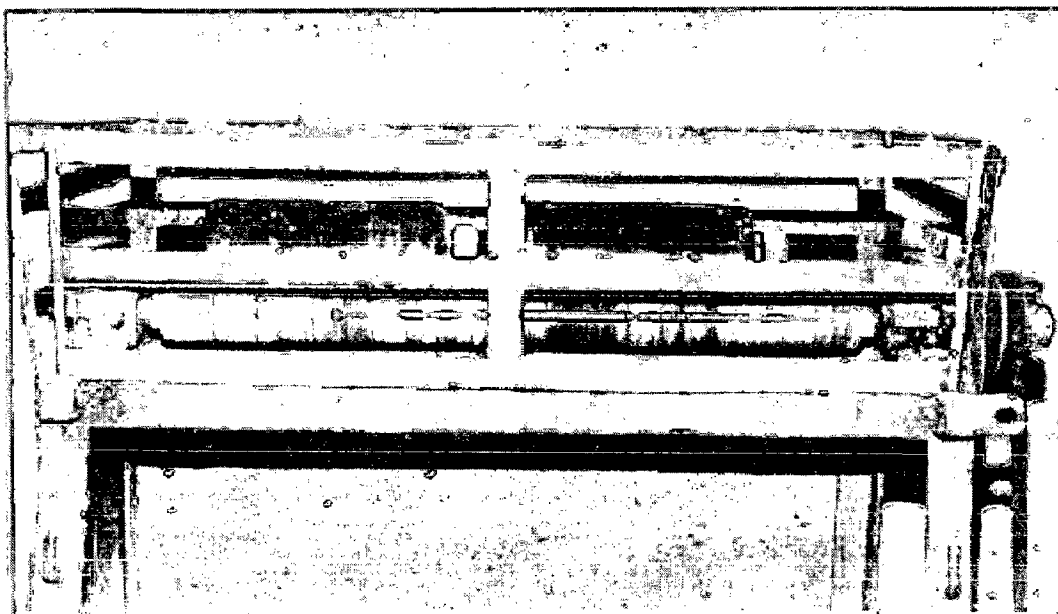
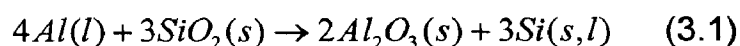


Fig. 3.7 Rubber roller mill used for blending of matrix and reinforcement powders.

Commercially pure MoSi<sub>2</sub> powders contain significant amounts of SiO<sub>2</sub> as impurity. The SiO<sub>2</sub> in MoSi<sub>2</sub>, which is present in the form of particles and films at the grain boundaries (Aikin Jr., 1992<sup>a</sup>), adversely affects high temperature strength and creep resistance of MoSi<sub>2</sub>. Even the fracture toughness has been found to decrease with increase in temperature above 1000 °C due to softening of SiO<sub>2</sub> phase and weakening of grain boundaries (Maloy et al, 1991, 1992). Therefore, eliminating or decreasing the SiO<sub>2</sub> content in MoSi<sub>2</sub> may result in higher strength at high temperatures. One of the ways of eliminating SiO<sub>2</sub> is by alloying of MoSi<sub>2</sub> with an element, whose oxide has a lower free energy of formation than that of SiO<sub>2</sub>. This is achieved by addition of 2 wt% Al to MoSi<sub>2</sub>, which leads to in-situ precipitation of α-Al<sub>2</sub>O<sub>3</sub>. The reaction taking place has been reported as (Costa de Silva and Kaufman, 1993, 1994):



The commercially pure MoSi<sub>2</sub> powder was intimately dry mixed with appropriate quantity of Al powder for 24 h in a ball mill. The laminated composites were made by stacking layers of MoSi<sub>2</sub> blended with 2 wt% Al alloy powder and a single refractory metal foil of either Mo or Ta in a predetermined sequence as shown schematically in Fig. 3.8. Further processing of vacuum degassing at 1100°C for 1 h and vacuum hot pressing at 1750°C for 1 h using a pressure of 26 MPa was carried out. The vacuum level achieved during the hot press was 10<sup>-4</sup>-10<sup>-3</sup> torr. The heating rate was kept in the range of 10 - 15 °C per minute to maintain the temperature uniformity. Fig. 3.9 shows various processing steps in the form of a flow chart.

As received refractory metal foils were used to prepare model “tri-layer” laminated composites.

### **3.2.4 Processing of Laminated Composites with MoSi<sub>2</sub> + 20 vol% SiC<sub>p</sub> as Matrix**

MoSi<sub>2</sub> has a higher coefficient of thermal expansion than most of the refractory metals, as illustrated in Fig. 1.21. This gives rise to high residual thermal stresses in the composites during cooling from processing temperatures to the room temperature. These residual stresses may adversely affect the interfacial bonding

and the resultant mechanical properties of the composites. To improve thermal compatibility between  $\text{MoSi}_2$  and the refractory metal foils, one way is to add ceramic particless in  $\text{MoSi}_2$  matrix. Ceramic particless having a lower coefficient of thermal expansion than  $\text{MoSi}_2$  when added in suitable amounts are expected to bring down the overall thermal expansion coefficient of  $\text{MoSi}_2$ . Therefore, it was decided to add 20 vol% of SiC particless in  $\text{MoSi}_2$  matrix layer in the development of laminated composites. SiC was chosen as it is not only thermodynamically stable with  $\text{MoSi}_2$  but reinforcement of  $\text{MoSi}_2$  with  $\text{SiC}_p$  also provides improved high temperature mechanical properties in comparison to pure  $\text{MoSi}_2$ . The size of SiC phase was kept small, so as to eliminate thermally induced cracking.

Processing of these hybrid composites (with brittle ceramic particless as well as ductile metal foils) is extremely challenging. The component material layers are stacked together in a vacuum hot press and heated to a high temperature with simultaneous application of pressure to facilitate diffusion bonding between the various layers. Surface preparation of the component materials, bonding temperature and pressure, inter-diffusion and chemical reactions between the component materials greatly influence the microstructure, chemistry, bond strength at the interfaces, and overall physical and mechanical properties of the resulting laminates.

The monolithic  $\text{MoSi}_2$  - 20 vol%  $\text{SiC}_p$  as well as the laminated composites with refractory metal foils were processed by hot pressing at 1600 °C in vacuum ( $10^{-4}$  torr) for 1 h using a pressure of 27 MPa. Three different refractory metal foils Mo, Ta and Nb were used to make different composites. A single refractory metal foil was sandwiched in between two layers of  $\text{MoSi}_2$  + 20 vol%  $\text{SiC}_p$  blended powder in an appropriate thickness ratio. The various processing steps followed are schematically presented in the form of a flow chart in Fig. 3.10.

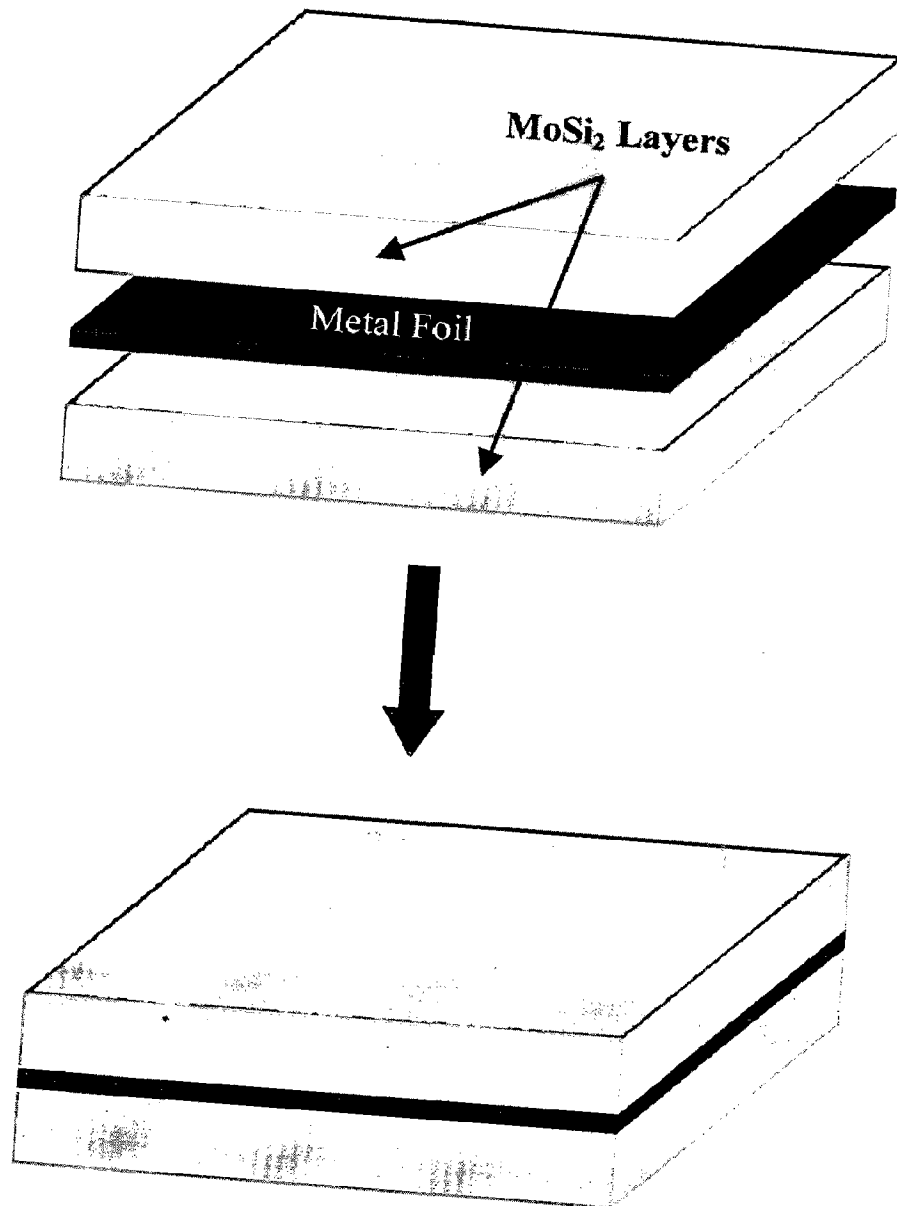


Fig. 3.8

Schematic illustration of stacking and bonding of different layers in making of a tri-layer laminated composite.

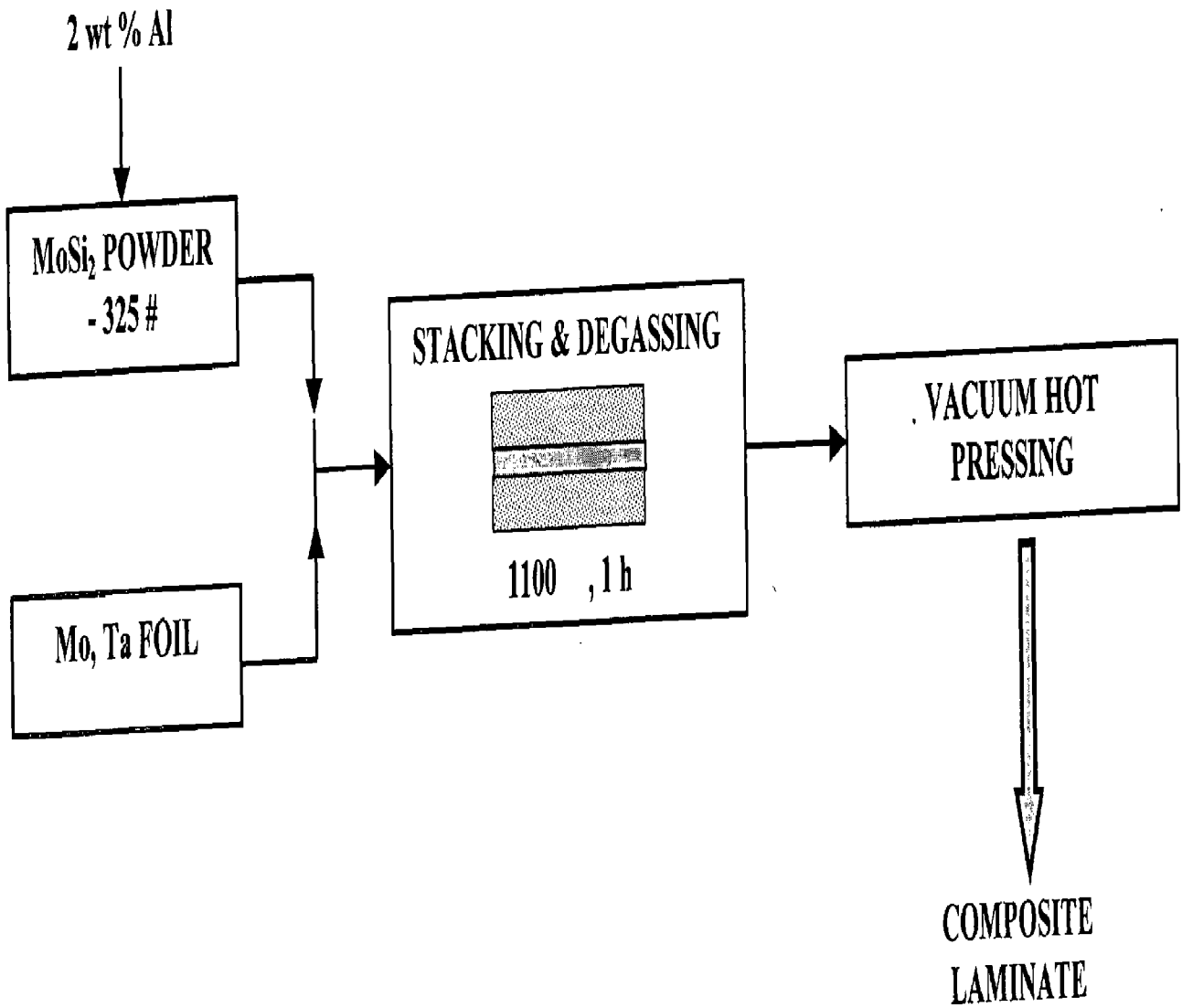


Fig. 3.9 Flow chart illustrating the various steps schematically in the processing of Mo and Ta foil reinforced MoSi<sub>2</sub> matrix laminated composites.

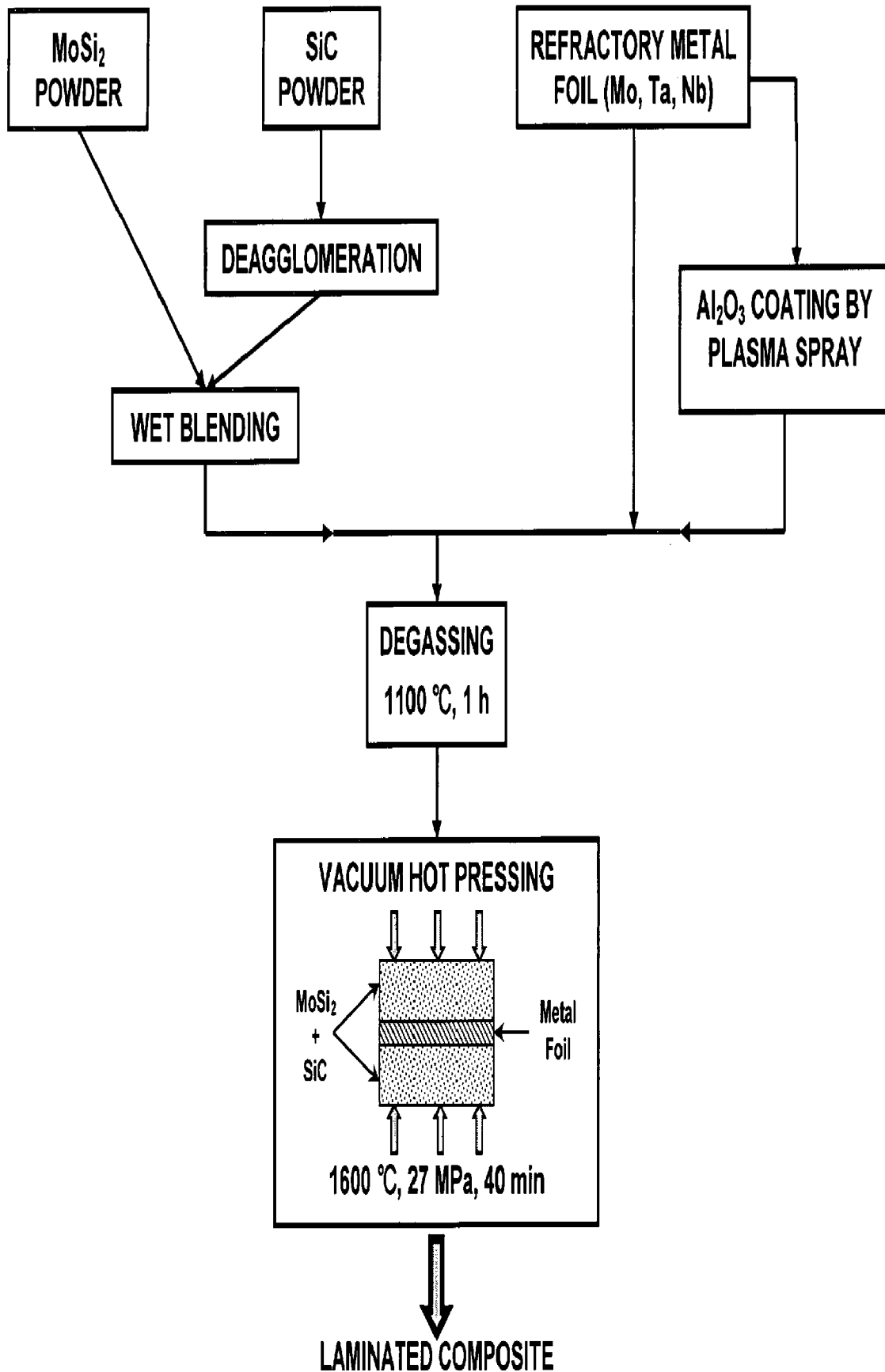


Fig. 3.10 Flow chart showing schematically various steps in the processing of the ductile refractory metal foils reinforced  $\text{MoSi}_2$  based laminated composites.



The SiC particless were given de-agglomeration treatment prior to blending with MoSi<sub>2</sub> powder. SiC particless have a tendency to agglomerate due to the static charge present on their surfaces. The tendency of agglomeration is more in finer SiC particless. Agglomerated particless result in inhomogeneous distribution of the reinforcing phase, which ultimately leads to inhomogeneous microstructure and density. The de-agglomeration of SiC powder particless is a preliminary requirement before blending with the matrix powders to get a uniform distribution in the matrix. De-agglomeration involves treating SiC powder with a polar solvent such as alcohol, which neutralizes the static charge present on the particle surfaces. The de-agglomeration process used in the present work is shown in Fig. 3.11(a). The process involved the milling of SiC<sub>p</sub> in a solvent with a couple of tungsten balls put together in plastic cylindrical containers for 3 h using a horizontal rubber roller mill. The polar solvent used was n-butanol.

Blending of the raw materials i.e., the matrix and the reinforcement powders is conceptually simple but a critical step in powder metallurgy processing techniques. Blending ultimately controls the distribution of the constituents and properties of the final product. MoSi<sub>2</sub> and SiC powders are blended using a wet blending process as depicted in Fig. 3.11(b). In wet blending method, de-agglomerated slurry of SiC with the solvent is added with MoSi<sub>2</sub> matrix powder. Additional quantity of solvent is added and milling is continued further for 8 h. After drying the wet slurry, the blended powder is ball milled for a period of 1 h in dry condition to break the lumps formed if any, during wet blending and drying operation. n-Butanol was used as the wet blending agent.

Degassing of the blended powders involves the removal of any moisture and other volatile species through the combined action of heat and vacuum. The moisture is associated with powder particles by Vander Wall forces. The degassing step is very crucial as any left over moisture or volatile matter can give rise to the evolution of gaseous products that are liberated during subsequent high temperature processing. The blended powders of MoSi<sub>2</sub> and SiC are vacuum degassed prior to consolidation under vacuum of 10<sup>-4</sup> torr for 1 h in the temperature range of 1000 – 1100 °C. The degassing temperature was kept lower than the sintering temperature (1300 °C) of MoSi<sub>2</sub>.

The refractory metal foils were finish-polished through 15  $\mu\text{m}$  diamond paste just before the vacuum hot pressing on both the bonding surfaces.

As before, the hot pressed product was a disc of 75 mm in diameter with 5 – 6 mm thickness. The densities of the composites produced were above 99 % of the theoretical densities. A typical time – temperature - pressure cycle used in the vacuum hot pressing of the composites investigated in the present study is shown in Fig. 3.12.

### 3.2.5 Application of $\text{Al}_2\text{O}_3$ Coating on Nb Foil

Coatings on the reinforcement prior to processing of the composites are applied to modify the matrix - reinforcement interface by minimizing the matrix - reinforcement chemical interactions during the processing. Coating should be chemically compatible with matrix and the reinforcement as well as it must act as a diffusion barrier. Studies were conducted to understand the effect of modifying the interface between  $\text{MoSi}_2$  matrix and the Nb foil on the microstructure and mechanical properties of the composite.  $\text{Al}_2\text{O}_3$  coating on Nb foil was applied by plasma spray method prior to vacuum hot pressing with  $\text{MoSi}_2 + 20 \text{ vol}\% \text{ SiC}_p$  matrix layer.

$\text{Al}_2\text{O}_3$  has been reported to be chemically compatible with  $\text{MoSi}_2$ . Xiao et al. (1990) have carried out tests on chemical compatibility and have shown that  $\text{Al}_2\text{O}_3$  is stable in contact with  $\text{MoSi}_2$  up to  $1400^\circ\text{C}$ . They found a sharp interface in hot pressed  $\text{Al}_2\text{O}_3$  particless reinforced  $\text{MoSi}_2$  matrix composite after annealing at  $1400^\circ\text{C}$  for 100 h. In the present investigation, thermodynamic calculations were performed in order to predict the chemical stability of  $\text{Al}_2\text{O}_3$  with  $\text{MoSi}_2$  and Nb.

The plasma spray processing involves the deposition of discrete droplets of  $\text{Al}_2\text{O}_3$  onto a Nb foil substrate. A schematic diagram showing plasma deposition is shown in Fig. 3.13 (Jackson et al, 1981). A stream of air plasma was used to accelerate the  $\text{Al}_2\text{O}_3$  powder particles as they are injected into the plasma gases.  $\text{Al}_2\text{O}_3$  is melted and strikes the substrate in the form of liquid droplets. Due to high speed of plasma gases, the time spent from injection to deposition is almost negligible.  $\alpha\text{-Al}_2\text{O}_3$  of relatively fine size was used. If the particles are coarse, they will not melt completely. However, an appropriate gun-to-substrate distance was selected to avoid vapourization of the fine  $\text{Al}_2\text{O}_3$  particles by plasma.

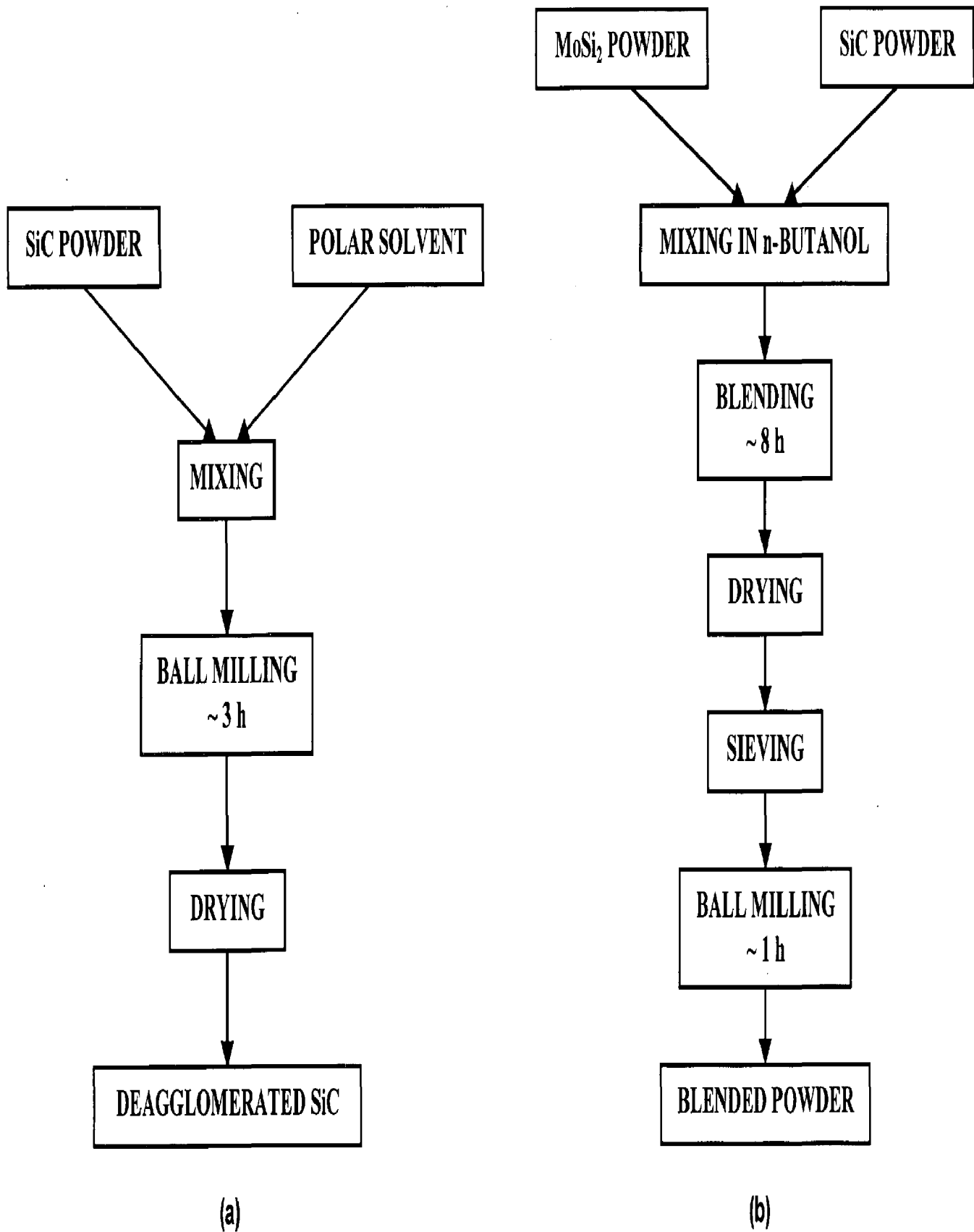


Fig. 3.11 Flow charts illustrating the various steps schematically in the process of (a) de-agglomeration of SiC particles and (b) wet blending of MoSi<sub>2</sub> and SiC powders.

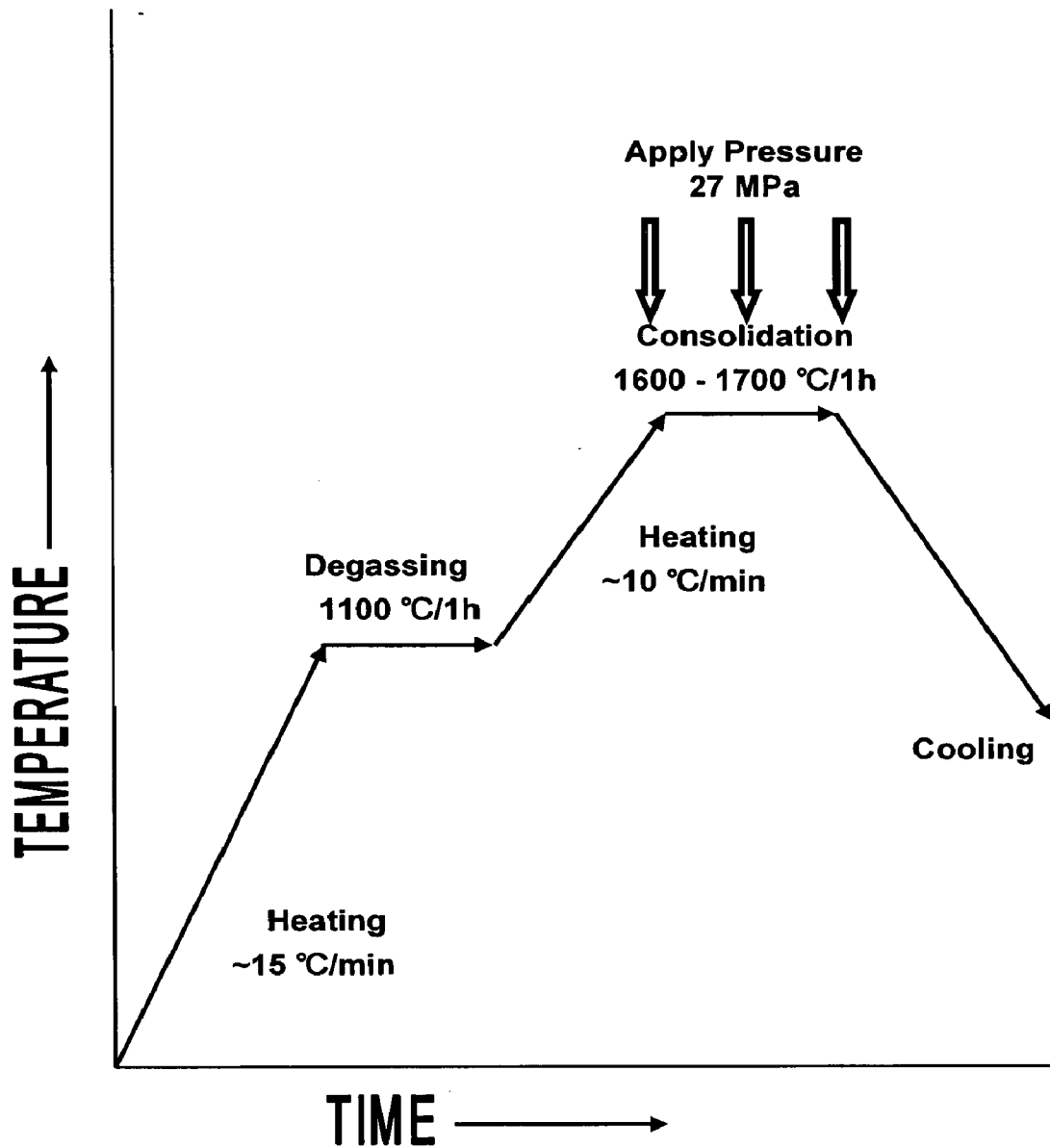


Fig. 3.12 A typical time-temperature-pressure cycle used in the vacuum hot pressing of composites investigated in the present study.

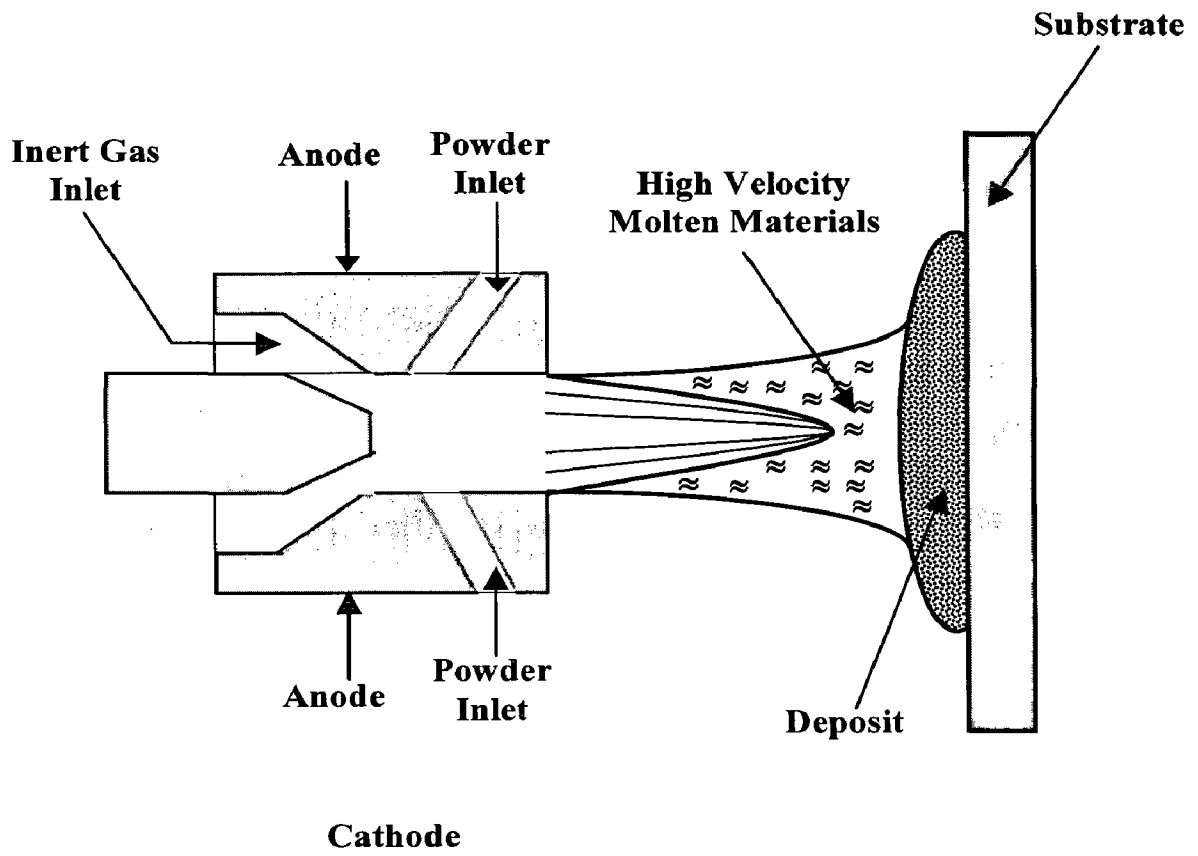


Fig. 3.13 Schematic of plasma spray deposition processing.

### **3.2.6 Embrittlement of Nb Foil**

To study the effect of embrittled refractory metal foil as reinforcement, a laminated composite consisting of alternate layers of MoSi<sub>2</sub> with 20 vol% SiC<sub>p</sub> and Nb foil was vacuum hot pressed at a lower vacuum level (10<sup>-2</sup> torr) to allow embrittlement of Nb foil due to oxygen pick up during the high temperature processing. All other processing parameters were kept the same as described in section 3.2.4.

## **3.3 CHARACTERIZATION**

Various MoSi<sub>2</sub> based monolithic and composite materials processed as a part of the present study were characterized for their microstructures and room temperature mechanical behaviour.

### **3.3.1 Microstructural Studies**

The microstructures of the metallographically polished specimens were studied using optical microscopy (with and without polarized light), x-ray diffraction analysis (XRD), electron probe micro-analysis (EPMA) and scanning electron microscopy (SEM).

#### **3.3.1.1 Optical Metallography**

Metallographic specimen preparation included sectioning, mounting, identification, grinding, polishing, cleaning, and etching. The specimens were cut using a precision diamond saw (ISOMET-4000). A thin, rapidly rotating, consumable low concentration (LC) diamond blade producing high-quality low-distortion cuts was used to cut the metallographic specimens. The specimens were then hot mounted in bakelite powder at 130 °C in a hydraulic mounting press. The mounted specimens were prepared for microstructural characterization by mechanical grinding and polishing methods. The specimens were coarse and fine ground on SiC papers of 320, 400, 600 and 800 grit sizes successively followed by polishing with diamond paste (down to 1 μm size) applied on a velvet cloth mounted on a rotating wheel. The samples were cleaned with acetone at the end of each step to avoid carryover of the coarse abrasive particles from the previous step. By polishing, the scratches as well as the deformed layer introduced by the previous grinding methods were

removed by the rolling action of loose, unsupported diamond abrasive particles on the cloth. All the polished specimens were subjected to ultrasonic cleaning to remove not only the surface contaminants, but also particulate matter held in crevices, cracks or pores, if any. After cleaning, the specimens were rapidly dried by placing under a hot-air drier for sufficient time to evaporate the liquids remaining in the cracks and pores.

The as-polished specimens were observed under an optical microscope to identify any cracks, pores, pits or inclusions. The conventional chemical etching which is the oldest and most commonly applied technique was found to be not suitable for the composite materials investigated in the present study. Several combinations of etchants were tried but none could successfully reveal the microstructure. Instead, the 'optical etching' was employed. Optical etching based on the application of certain illumination methods following the "Kohler" illumination principle, might include use of polarized light as one such method. The specimens when viewed under the optical microscope using a polarized light successfully produced the microstructural contrast revealing the grain size in most of the monolithic and composite specimens. Gibbs et al (1987) had also observed that with  $\text{MoSi}_2$ , it might not be necessary to chemically etch the material since the microstructure could be clearly viewed in polarized light due to anisotropy in its crystal structure.

However, the metallographic specimens of pure refractory metal foils were etched using conventional chemical etching techniques. The etching agent consisting of 20 vol% HF, 20 vol%  $\text{H}_2\text{SO}_4$  and 60 vol%  $\text{HNO}_3$  gave satisfactory results. The etchant reacted with the specimen surface and the etching proceeded by selective dissolution of the grain boundaries in case of the pure metals. Because of severe, localized crystal deformation, grain boundaries could have higher dissolution potential than grains themselves. Accumulation of impurities in grain boundaries also increased this effect.

Polarized light optical microscopy was used to study the grain size distribution and to estimate grain size by the linear intercept method (Vandervoort 1984) using a measuring eyepiece. Average of 10 readings measured at different places was taken to arrive at the grain size value. Image analysis was also done in a few specimens to

estimate the volume fraction of various phases formed during high temperature processing of the composites.

### **3.3.1.2 X-ray Diffraction & Electron Probe Micro Analysis**

The X-ray diffraction (XRD) analysis was carried out using the Cu K $\alpha$  ( $\lambda = 1.54056 \text{ \AA}$ ) radiation to analyse the nature of phases formed during processing in different composites.

In electron probe micro analysis (EPMA), the material under investigation is bombarded with a beam of electrons having energy sufficient enough to knock out electrons from the inner orbital of the atoms comprising the material. The electron from one of the outer orbital fills the vacancy thus created by emitting X-ray photon for the difference in energy between the outer shell and the core-shell. The energy of this X-ray photon is characteristic of the atom emitting it and the number of such photons emitted bears a relationship to the total number of atoms emitting them. The X-ray signal generated when the high-energy electron bombards the sample is analysed by energy / wavelength dispersive spectrometer. In other words, qualitative and quantitative chemical information about the material can be obtained by the analysis of energy / wave length and intensity of the X-ray emission from the material.

In the present investigation, CAMEBAX microprobe equipment, controlled by a CAMECA system was used. The samples were hot mounted in bakelite (25 mm diameter, 10 mm height) and analysed in un-etched condition. Elements were analysed using an accelerating voltage of 15 kV with a beam diameter of 1  $\mu\text{m}$ . The cosecant of the take-off angle was 1.556.

The qualitative analysis of the various elements present in the material was carried out using X-ray imaging as well as line scan recording. X-ray imaging revealed how various elements present in the material are distributed over an area. The electron beam was made to scan over an area in both X and Y directions. An image consisting of bright and dark areas was produced where bright areas indicated the enrichment and the dark areas the depletion or absence of a particular element for which the spectrometer was tuned. For each element a separate X-ray image was



obtained. The X-ray images so obtained were correlated with the corresponding back-scattered electron image taken at the same area and at the same magnification to develop an understanding how various elements were distributed among the various phases present in the material. Unlike in X-ray imaging, in line scan the electron beam was made to move along a linear path rather than scanning over an area. The X-ray intensity profiles so generated for various elements were plotted on a x-y plotter as intensity verses distance.

In quantitative analysis the aim was to precisely analyse the composition of various microstructural constituents. This was done by collecting the x-ray intensity from the respective standards of the elements and from the sample for the same elements for a predetermined time under identical physical conditions. The analysis was carried out using Energy Dispersive Spectroscopy (EDS). The oxygen content was determined as the balance.

### **3.3.1.3 Scanning Electron Microscopy**

In Scanning Electron Microscopy (SEM), a beam of electrons moves across a specimen. The specimen releases various data signals containing structural and compositional information. Use of electrons as the radiation source improves the resolution and depth of field and the images appear in 3-D. X-rays are released from the specimen that gives the elemental composition. A Leo 440i scanning electron microscope equipped with secondary and back scattered electron detectors as well as energy dispersive spectrometer (EDS) was used. An accelerating voltage of 20 kV was used. Back-scattered electrons arose from electron-nucleus collisions, retaining about 80 % of the incident beam energy. Back-scattered electrons could be used for atomic no. imaging since the number of back-scattered electrons reflected by a specimen increased with atomic weight. Secondary electrons arose from electron-electron collisions and were of low energy. Energy dispersive spectroscopy (EDS) in SEM was used for analysis of concentration from X-rays arising from electron transitions within the orbitals of an atom. The EDS system could quantitatively analyse the elements. All the fractography specimens were ultrasonically cleaned in acetone for a few minutes and dried before loading them into the specimen chamber of SEM.

### 3.3.2 Evaluation of Mechanical Properties

All the composite materials prepared in the present study were evaluated for their room temperature mechanical properties including density, elastic modulus, hardness, indentation fracture toughness, flexural strength and fracture toughness. In case of laminated composites, the flexural strength and fracture toughness were measured in crack arrester as well as in crack divider modes. Apart from the stress intensity factor based fracture toughness, energy driven fracture toughness in terms of 'work of fracture' was also evaluated. Micro-hardness measurements were made at the interface regions between matrix and the reinforcement to understand the mechanical nature of the various interfacial reaction products. The metallic foils used as the reinforcements were characterized for their hardness and tensile properties.

Cracks generated by the hardness indentations were observed using optical and scanning electron microscopes. The fracture surfaces of the tested specimens were studied using scanning electron microscope. The unbroken specimens were also observed under scanning electron microscope as well as under the stereomicroscope to study the macroscopic crack path behaviour.

#### 3.3.2.1 Elastic Modulus

Elastic constants were evaluated by the measurement of ultrasonic velocities. Measurement of the ultrasonic velocities was performed using pulse echo technique (Papadakis, 1967) with separate transducers to calculate velocities of longitudinal ( $V_L$ ) and shear ( $V_S$ ) waves. The specimen size used was 15 mm x 15 mm x 5mm. A pulse of approximately 1  $\mu$ s duration of variable pulse-repetition rate was generated and impressed on the transducer, acoustically bound to the specimen. The reflected echoes were received by the same transducer, amplified and displayed on the oscilloscope. Two of the displayed echoes were then chosen and exactly overlapped by critically adjusting the frequency of the CW oscillator. This frequency  $f$  was then employed to compute the ultrasonic velocity using the relation  $V = 2lf$ , where  $l$  was the thickness of the specimen. X and Y-cut Lithium Niobate transducers of 10 MHz were used for the generation of the shear and longitudinal waves, respectively.

The shear modulus ( $G$ ), Poisson's ratio ( $\nu$ ) and Young's modulus ( $E$ ) were calculated by the following relations:

$$G = \rho V_s^2 \quad (3.2)$$

where,  $\rho$  is the density of the material.

$$\nu = \frac{(R-2)}{2(R-1)} \quad (3.3)$$

where  $R = \left(\frac{V_L}{V_S}\right)^2$ , and

$$E = 2(1+\nu)G \quad (3.4)$$

In case of laminated composites, the elastic modulus was measured in a direction normal to the foil plane.

### 3.3.2.2 Hardness and Indentation Fracture Toughness

Hardness was measured using Vickers hardness test. The Vickers hardness test uses a square-base diamond pyramid as the indenter. The Vickers hardness test has received fairly wide acceptance for research work. The hardness was taken on metallographically polished specimens at three different loads of 10, 20 and 30 kg. A minimum of five readings at each load were taken and the average values were calculated. The Vickers Hardness is determined from the following equation (Dieter, 1987):

$$\text{Hardness} = \frac{2P \sin(\theta/2)}{d^2} = \frac{1.854P}{d^2} \quad (3.5)$$

where,  $P$  is the applied load,  $d$  is the average length of diagonals and  $\theta$  is the angle between opposite faces of diamond ( $136^\circ$ ). Individual indentations were separated sufficiently to prevent neighbouring indent - crack interactions.

Indentation techniques, used to measure hardness values, have more recently found widespread use to determine fracture toughness values,  $K_{IC}$ . Vickers indenters would produce a permanent indentation. At a high enough load, cracks would form at (or near) the ends of the diagonals of the indentations. The method required measurements of the size of cracks formed around the indentation

impression whenever the applied load surpassed a critical load. The method could be easily employed because of its relative ease of application, as no extensive machining or preparation of the test specimens was required, and only a small specimen was needed.

The formation of indentation cracks could be explained by the elastic and permanent deformation developed during indentation and unloading (Smith and Pletka 1983, Moussa et al 1982). At a critical indentation load, a crack was initiated below the contact point during loading due to the generation of a tensile stress component. The subsurface crack, which would form, is commonly referred to as a 'median crack' (Lawn, 1983). The median crack formed as two mutually perpendicular circular cracks lying in directions parallel to the indentation diagonals. When the load was relieved and the indenter was removed, the subsurface median cracks became unstable and expanded towards the indented surface since the elastic compressive stress at the surface became zero, while the tensile residual stress remained. This tensile stress arose from the mismatch between the elastic deformation of the bulk and the permanent deformation due to the indentation. The two perpendicular radial cracks appeared on the surface of the material as four cracks radiating outward from the indentation corners.

The dimensions of the indentation impression and the induced cracks could readily be controlled by the applied load. In certain brittle material systems with relatively higher toughness, shallow radial surface cracks known as Palmqvist cracks could form at relatively low indentation loads (Shetty et al, 1985).

The above-mentioned crack systems could be identified only in the cross section of the specimen as depicted schematically in Fig. 3.14. On the surface they had an identical shape as exhibited in Fig. 3.15.

There are a number of empirical toughness expressions that would be applicable to the specific indentation crack patterns. Most of these relations could be expressed into the simple form (Tanaka, 1987)

$$K_{IC} = A(E/H)^n P/c^{3/2} \quad (3.6)$$

where,  $E$  is the elastic modulus,  $H$  is the hardness,  $P$  is the applied load and  $c$  is the average crack length measured from the centre of the indentation mark.  $A$  is a constant.

For Palmqvist cracks, Palmqvist (1963) himself suggested first that the average length,  $l(= c - a)$ , of the cracks, measured from the corners of the indent to their end, should be a measure of the relative toughness. An equation relating Palmqvist cracks with  $K_{IC}$  was proposed by Niihara et al (1983)

$$K_{IC} = 0.0123E^{0.4}H^{0.1}(P/l)^{1/2} \quad (3.7)$$

This equation could be rewritten as

$$K_{IC} = 0.0057(E/H)^{2/5} P/a(c - a)^{1/2} \quad (3.8)$$

Palmqvist cracks could be considered predominant when  $\frac{c}{a} < 3$  at low loads.

In the present investigation, positions of the indentations were kept at sufficient distance from one another to avoid neighbouring indent-crack interactions. The thickness of the test specimen was kept a minimum of 10 times the crack length  $c$  to allow for the full development of the crack system. Indentation loads of 10 kg, 20 kg and 30 kg were applied to generate the indentation induced cracks in each specimen. All indents were made with a loading time of 10 s and a 5 s hold at full load. The crack length  $2c$  and the indentation diagonal length  $2a$  were measured on about 5 impressions at each load level with an optical microscope at 500X magnification. Only median cracks were formed in all the specimens tested at all the applied loads.

The following expression was used to determine the indentation fracture toughness of the monolithic and composite materials studied in the present investigation:

$$K_{IC} = 0.026(E/H)^{2/5} P/c^{3/2} \quad (3.9)$$

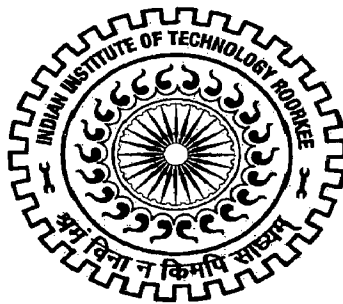
# STUDIES ON DUCTILE PHASE TOUGHENING OF MOLYBDENUM DISILICIDE BASED COMPOSITES

Ph.D. THESIS

by

MANOJ KUMAR JAIN

POINT-WISE REPLIES OF ALL QUESTIONS AND COMMENTS  
MADE BY THE EXAMINERS



DEPARTMENT OF METALLURGICAL AND MATERIALS ENGINEERING  
INDIAN INSTITUTE OF TECHNOLOGY ROORKEE  
ROORKEE – 247 667 (INDIA)  
JULY 2009

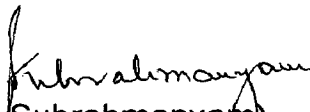
**Department of Metallurgical and Materials Engineering  
Indian Institute of Technology Roorkee**


**CERTIFICATE**

Sub : Revision of Ph.D. thesis of Mr. Manoj Kumar Jain

Ref : Letter No. PGS&R/3178/Ph.D./MKJ dated May 06, 2009

It is certified that all the revisions suggested by both the examiners have been incorporated in the revised thesis entitled **“STUDIES ON DUCTILE PHASE TOUGHENING OF MOLYBDENUM DISILICIDE BASED COMPOSITES”** by Shri Manoj Kumar Jain in partial fulfilment of the requirements for the award of the Degree of Doctor of Philosophy. The point-wise replies of all the questions and comments made by the examiners have also been prepared separately as per the samples provided. The supervisors are fully satisfied with the revisions and the replies. The revised thesis is now re-submitted in the Department of Metallurgical and Materials Engineering of the Indian Institute of Technology Roorkee, Roorkee.

  
(J. Subrahmanyam)  
Supervisor  
Scientist "G"  
DMRL  
Hyderabad

  
(Subrata Ray)  
Supervisor  
Professor  
Deptt of Met. & Mat. Engg.  
IIT, Roorkee

Date: 08-07-2009

## ANSWERS TO THE QUERIES OF REVIEWER 1

### Changes made throughout the text

SI No.	Comments & Reference	Answer to Comments	Present Reference
1	Change Å to nm	Å has been changed into nm.	Throughout the text
2	Change et al to et al., i.e., put a period (or full stop) after al because al. is the abbreviation of alii.	et al has been changed to et al.	Throughout the text
3	Give credit in the captions to source(s) from which the data in the tables are obtained and from where the figures were taken.	References have been added in the captions of tables and figures.	Throughout the text

## Chapter 1

No Queries



## Chapter 2

Sl No.	Comments & Reference	Answer to Comments	Present Reference
1	Page 22: Change Pesting to pesting, unless it is the first word of a sentence.	Pesting has been changed to pesting	Page 22
2	Page 25: Line 8 from top: Delete recently Line 2 from bottom: Change 'are being' to have been	The word "recently" has been deleted. "are being" changed to "have been"	Page 25: Line 8 from top Line 2 from bottom
3	Page 41: Cottrel-not right-spellings do not match with the ref.	The spelling has been corrected	Page 41
4	Page 41: Second Para from bottom: Regardless of morphology, .... not clear, morphology of what?	Morphology of <b>second phase particles</b> . The statement has been modified.	Page 41: Second Para from bottom
5	Page 52: Third Para from bottom: Change Ashby to Ashby et al. Change has to have	Changes incorporated as suggested. Ashby to Ashby et al. has to have	Page 52: Third Para from bottom
6	Page 53: Second Para from bottom: 2 <sup>nd</sup> line: Change has to have	Change incorporated as suggested has to have	Page 53: Second Para from bottom: 2 <sup>nd</sup> line
7	Page 57: Last line: Change Particles to particle	"Particles" changed to "particles"	Page 57: Last line

## Chapter 3

SI No.	Comments & Reference	Answer to Comments	Present Reference
8	Page 63: 2 <sup>nd</sup> Para: Change As to All	"As" has been changed to "All"	Page 63: 2 <sup>nd</sup> Para
9	Page 68: 1 <sup>st</sup> Para: 2 <sup>nd</sup> Line: Change depend to depends (the subject is singular "the choice")	"depend" has been changed to "depends"	Page 68: 1 <sup>st</sup> Para: 2 <sup>nd</sup> Line
10	Page 69: 2 <sup>nd</sup> Para: Line 5: Change "the die is" to "the die was"	"the die is" has been changed to "the die was"	Page 69: 2 <sup>nd</sup> Para: Line 5
11	Page 73: 2 <sup>nd</sup> Para: Line 7: Give vacuum pressure in Pa instead of torr	Vacuum pressure has been changed in Pa instead of torr throughout the document.	Page 73: 2 <sup>nd</sup> Para: Line 7
12	Page 74: Last Para: Line 2: Change torr to Pa	torr has been changed to Pa throughout the document	Page 74: Last Para: Line 2
13	Page 78: Last Para: Change Vander Wall to van der Waals	Vander Wall has been changed to van der Waals	Page 78: Last Para
14	Page 78: Last Para: Line 3 from bottom: Change torr to Pa (SI units)	torr has been changed to Pa throughout the document	Page 78: Last Para: Line 3 from bottom
15	Page 83: Line 4 from top: Change torr to Pa	torr has been changed to Pa throughout the document	Page 83: Line 4 from top

## Chapter 4

Sl No.	Comments & Reference	Answer to Comments	Present Reference
16	Page 108: Line 4 from bottom Delete the comma after where	Unable to make correction as suggested. No such entry exists on Page 108 as well as in the entire Chapter 4.	Page 108
17	Page 106: Page 107: Page 110: This introduction (Section 4.1) is taken word for word from the ref. Chawla, 1993. The fact that one gives a citation to the source does not mean one can copy the text from the source. One must use one's own words. I take it that this has been done inadvertently. However, it must be fixed.	There are no identical paragraphs and hardly any identical sentences (word for word) from Chawla, 1993 in Section 4.1 on Page No(s) 106, 107 and 110 in the thesis. The similar sentences on these pages are quoted side by side as Annexure-I (Table-1). However, all such sentences have been suitably modified.	Page 106 Page 107 Page 109 Page 110
18	Page 115: More information should be given for the NISA software package used for FEM analysis.	Information about NISA software package has been added.	Page 115 Page 117
19	Page 130: Fig. 4.11: Units must be provided for the stresses. Are these von Mises stresses? It should be so stated in the figure caption.	Units for stresses have been mentioned in the figure caption. These are $\sigma_{xx}$ stresses and the same has now been specified in the figure caption.	Page 131: Fig. 4.11
20	Page 131: Fig. 4.12: Same comments as for Fig. 4.11	Units for stresses have been mentioned in the figure caption. These are $\sigma_{xx}$ stresses and the same has now been specified in the figure caption.	Page 132: Fig. 4.12
21	Page 132: Fig. 4.13 Indicate in the figure the foil position	Foil position in the figure has been marked.	Page 133: Fig. 4.13
22	Page 133: Fig. 4.14: Same comments as for Fig. 4.11	Units for stresses have been mentioned in the figure caption. These are $\sigma_{xx}$ stresses and the same has now been specified in the figure caption.	Page 134: Fig. 4.14

23	Page 135: Fig. 4.16: Same comments as for Fig. 4.11	Units for stresses have been mentioned in the figure caption. These are $\sigma_{xx}$ stresses and the same has now been specified in the figure caption.	Page 136: Fig. 4.16
24	Page 141: Last Para: Line 2: Change reveals to reveal Line 6: Change decreases to decrease Line 10: Change owing to owing	"reveals" has been changed to "reveal" "decreases" has been changed to "decrease" "owing" has been changed to "owing"	Page 141: Last Para: Line 2 Line 6 Line 10

## Chapter 5

SI No.	Comments & Reference	Answer to Comments	Present Reference
25	Page 144: Tables 5.1, 5.2, 5.3: Indicate in the captions that the amount of elements are in wt %	The captions have been modified as suggested.	Page 144: Tables 5.1, 5.2, 5.3:
26	Page 152: Second Para: Second Line: Change show to shows	"show" has been changed to "shows"	Page 152: Second Para: Second Line:
27	Page 152: Third Para: Line 4: The grains slide over each other along the rolling direction. I don't think Mo foil, tested at room temperature, will show sliding of grains. Fig. 5.10 does not show sliding of grains. I suggest that this statement be deleted.	The statement "The grains slide over each other along the rolling direction" has been deleted.	Page 152: Third Para: Line 4:
28	Page 180: Fig. 5.26: The load should be in N	The load has been changed into N	Page 180: Fig. 5.26:
29	Page 199: Para 3: Line 3: Change MoSi2 to MoSi <sub>2</sub>	MoSi2 has been changed to MoSi <sub>2</sub> .	Page 199: Para 3: Line 3:
30	Page 205: Fig. 5.39: The load should be in N	The load has been changed into N	Page 205: Fig. 5.39:
31	Page 209: Line 7 from top: Change "a primary" to "the primary"	"a primary" has been changed to "the primary"	Page 209: Line 7 from top:
32	Page 212: 2 <sup>nd</sup> Para: Line 4: Use subscript 2	MoSi2 has been changed to MoSi <sub>2</sub>	Page 212: 2 <sup>nd</sup> Para: Line 4:
33	Page 217: 1 <sup>st</sup> Para: Line 2 from bottom: Insert spacing between 5.49 and 'and'	Spacing has been inserted between 5.49 and 'and'.	Page 217: 1 <sup>st</sup> Para: Line 2 from bottom:
34	Page 313: Line 2: Change Where, to where	Unable to change as no such entry exists	
35	Page 254: Fig. 5.74: The load should be in N	The load has been changed in N	Page 254: Fig. 5.74:
36	Page 289: Fig. 5.94: Change the units of Y-axis to kJ/mole	Units of Y-axis have been changed from KJ/mole to kJ/mole	Page 289: Fig. 5.94:
37	Page 339-342: The text is taken verbatim from Chawla, 1993, pp. 302-303. I repeat that the fact that one gives a citation to the source does not mean one can copy verbatim the text from the source. This is plagiarism. I give the benefit of the doubt to the author and ask the	The pages 339, 340, 341 and 342 of the thesis are not identical to the pages 302 and 303 of the book of Chawla, 1993. There are no identical paragraphs	Page 339-342

	text be fixed.	and hardly any identical sentences (verbatim) on Pages 339 to 342 in the thesis from the pages 302 and 303 of Chawla, 1993. The similar sentences are quoted as Annexure-II (Table-2) side by side. However, all these sentences have been suitably modified.	
38	Page 354: 2 <sup>nd</sup> Para: Line 2: Change into to in	into has been changed to in	Page 354: 2 <sup>nd</sup> Para: Line 2:

## Chapter 6

No Queries

Since the examiner has commented about 'plagiarism', the entire thesis, even beyond the comments of the examiner, has been re-looked for finding sentences to those in the book by Chawla, 1993. It may be kept in mind that it was the ideas in that book which was being communicated with legitimate reference to the book.

Comment No. 17

Table - 1

S No.	Thesis Sentence	Page No.	The Book of Chawla Sentence	Page No.
1	Thermal stresses arise when there is a "constraint" on free dimensional change of a body (Chawla, 1993).	Page 106 Para 1 Article 4.1	Thermal stresses are internal stresses that arise when there is a "constraint" on free dimensional change of a body [1].	Page 274 Para 2 Article 8.1
2	In the absence of this constraint, the body can experience free thermal strains without any accompanying thermal stresses.	Page 106 Para 1 Article 4.1	In the absence of this constraint, the body can experience free thermal strains without any accompanying thermal stresses.	Page 274 Para 2 Article 8.1
3	The constraint may result due to a temperature gradient, crystal structure anisotropy (for example, non-cubic structures), phase transformations resulting in a volume change and a composite material made of components having different coefficients of thermal expansion.	Page 106 Para 1 Article 4.1	The constraint can have its origin in: 1. a temperature gradient 2. crystal structure anisotropy (non-cubic structure, for example) 3. phase transformations resulting in a volume change, and 4. a composite material made of dissimilar materials (i.e. materials having different $\alpha_s$ ).	Page 274 Para 2 Article 8.1
4	Thermal stresses are very important in all composite materials, but particularly so in ceramic matrix composites because a ceramic matrix will generally have a very low strain to fracture.	Page 106 Para 2 Article 4.1	Thermal stresses are very important in all composite materials, but particularly so in ceramic matrix composites because a ceramic matrix will generally have a very low strain to fracture.	Page 274 Para 2 Article 8.1
5	Thermal strain is given by $\Delta\alpha\Delta T$ .	Page 106 Para 2 Article 4.1	Thermal strain, in the absence of any temperature gradients, is given by $\Delta\alpha\Delta T$ .	Page 276 Para 1 Article 8.1

6	During cooling from the high processing temperatures, a high magnitude of shrinkage stresses may result because of the thermal mismatch between the reinforcement and the matrix.	Page 106 Para 2 Article 4.1	During cooling from the <b>generally</b> high processing temperatures, a high magnitude of shrinkage stresses can result because of the thermal mismatch between the reinforcement ( <b>particle, short fiber or long fiber</b> ) and the matrix.	Page 276 Para 1 Article 8.1
7	Thermal stresses generated depend on the <b>reinforcement geometry, reinforcement volume fraction</b> , thermal mismatch ( $\Delta\alpha = \alpha_r - \alpha_m$ ), the temperature interval ( $T_{final} - T_{initial}$ ), and modulus ratio, $E_r/E_m$ , where the subscripts r and m denote the reinforcement and the matrix, respectively.	Page 106 Para 2 Article 4.1 & Page 107 Lines 1-2.	<b>Specifically</b> , thermal stresses generated depend on the <b>reinforcement volume fraction, reinforcement geometry</b> , thermal mismatch ( $\Delta\alpha = \alpha_r - \alpha_m$ ), the temperature interval ( $T_{final} - T_{initial}$ ), and modulus ratio, $E_r/E_m$ , where the subscript r denotes the reinforcement which can be a particle, a whisker or a long fiber.	Page 276 Para 1 Article 8.1
	<p><b>There is no other sentence on Page 107 from the book of Chawla.</b></p> <p>It contains Section 4.2 and describes the literature data on "Residual Thermal Stresses in Pure MoSi<sub>2</sub>" which is from other sources like Wade and Petrovic (1992), Berkowitz (1966) and Berkowitz et al. (1970) as mentioned at appropriate places in the text.</p>	107		
8	Thermal stresses are internal stresses that arise when there <b>exists</b> a "constraint" on "free contraction" of a body upon cooling from high processing temperatures.	Page 109 Para 2 Article 4.3	Thermal stresses are internal stresses that arise when there is a "constraint" on free <b>dimensional change</b> of a body [1].	Page 274 Para 2 Article 8.1
9	In the case of a particulate composite, an interfacial pressure can develop during cooling that is similar to that obtained on embedding a spherical ball of radius, $r + \Delta r$ , in a spherical hole of radius, $r$ .	Page 109 Para 2 Article 4.3	In the case of a particulate <b>or fibrous</b> composite, an interfacial pressure can develop during cooling that is similar to that obtained on embedding a spherical ball of radius, $r + \Delta r$ , in a spherical hole of radius, $r$ , <b>or a cylinder of radius, <math>r + \Delta r</math>, in a cylindrical hole of radius, <math>r</math>.</b>	Page 276 Para 1 Article 8.1



10	Consider a particulate composite consisting of small ceramic particles distributed in a ceramic matrix.	Page 110 Para 2 Article 4.3	Consider a particulate composite consisting of small ceramic particles distributed in a ceramic matrix.	Page 277 Para 2 Article 8.2
11	If we regard this composite as an assembly of elastic spheres of uniform size embedded in an infinite elastic continuum, then it can be shown from the theory of elasticity (Timoshenko and Goodier, 1951) that an axially symmetrical stress distribution will result around each particle.	Page 110 Para 2 Article 4.3	If we regard this composite as an assembly of elastic spheres of uniform size embedded in an infinite elastic continuum, then it can be shown from the theory of elasticity [2, 3] that an axially symmetrical stress distribution will result around each particle.	Page 277 Para 2 Article 8.2
12	Fig. 4.2 shows a schematic of such a particle reinforced composite in which a central SiC particle of radius, $a$ , is surrounded by its associated spherical shell of MoSi <sub>2</sub> matrix of radius, $b$ .	Page 110 Para 2 Article 4.3	Figure 8.2 shows a schematic of such a particle reinforced composite. Let us say that each particle has a radius $a$ while the surrounding matrix sphere has a radius $b$ .	Page 277 Para 2 Article 8.2
13	The SiC particle will be under a uniform radial pressure, $P$ , while the MoSi <sub>2</sub> matrix will have two unequal stress components: (i) The radial stress in the matrix will be 'compressive'. (ii) The tangential (hoop) stress in the matrix will be tensile.	Page 110 Para 2 Article 4.3	The particle is under a uniform pressure, $P$ , while the matrix has unequal radial and tangential stress components.	Page 279 Last Para of Article 8.2
14	Chawla (1993) obtained the analytical expressions for residual thermal stresses by applying the following boundary conditions: (i) The radial stress at the interface ( $r = a$ ) is the interfacial pressure, $P$ . (ii) The radial stress vanishes at the free surface (i.e., at $r = b$ ).	Page 110 Para 3 Article 4.3	We can now apply the following boundary conditions: (i) stress vanishes at the free surface (i.e. at $r = b$ ). (ii) the radial stress at the interface ( $r = a$ ) is the interfacial pressure, $P$ , i.e. $\sigma_r(a) = -p$	Page 279 1 <sup>st</sup> 4 lines Article 8.2

S No.	Thesis Sentence	Page No.	The Book of Chawla Sentence	Page No.
1	A crack in the matrix layer can lead to debonding at the interface of laminated composite, followed by crack deflection, crack bridging etc.	Page 338 Para 3	For a weak interfacial bond, a crack in the matrix can lead to debonding at the interface, followed by crack deflection, crack bridging, fiber fracture, and finally fiber pullout.	Page 169 Article 5.5 Para 1
2	All these additional energy-absorbing phenomena lead to enhanced fracture toughness and a non-catastrophic failure mode.	Page 338 Para 3	All these additional energy-absorbing phenomena lead to an enhanced fracture toughness and a non-catastrophic failure mode.	Page 169 Article 5.5 Para 1
3	At the tip of any crack, a tri-axial state of stress is present.	Page 338 Para 4	At the tip of any crack, a tri-axial state of stress (plane strain) or a biaxial stress (plane stress) is present.	Page 170 Para 2
4	The stress distribution at the crack tip is shown schematically in Fig. 5.116 (Cook and Gordon, 1964).	Page 338 Para 4	Figure 5.7 shows schematically the stress distribution at the crack tip.	Page 171 Para 1
5	The main applied stress component, $\sigma_y$ , has a very high value at the crack tip, and decreases sharply with distance from the crack tip.	Page 338 Para 4	The main applied stress component, $\sigma_y$ , has a very high value at the crack tip, and decreases sharply with distance from the crack tip.	Page 171 Para 1
6	The stress component acting normal to the interface, $\sigma_x$ , is zero at the crack tip. It rises to a maximum value at a small distance from the crack tip and then falls off in a manner similar to $\sigma_y$ .	Page 338 Para 4	The stress component acting normal to the interface, $\sigma_x$ , is zero at the crack tip; it rises to a maximum value at a small distance from the crack tip and then falls off in a manner similar to $\sigma_y$ .	Page 171 Para 1
7	Now, it is easy to visualize that if the interface tensile strength is less than the maximum value of $\sigma_x$ , then the interface will fail in front of the crack tip.	Page 338 Para 4	Now, it is easy to visualize that if the interface tensile strength is less than the maximum value of $\sigma_x$ , then the interface will fail in front of the crack tip.	Page 171 Para 1
8	According to the estimates of Cook and Gordon, if interfacial tensile strength $\leq 1/5 \sigma_y$ i.e., the main	Page 338 Para 4	According to the estimates of Cook and Gordon, an interfacial strength of 1/5 or less than that of the	Page 171 Para 1

	stress component, will cause the opening of interface in front of the crack tip.		main stress component, $\sigma_y$ , will cause the opening of interface in front of the crack tip.	
9	Cook and Gordon analyzed the crack deflection at an interface between materials of identical elastic constants, i.e., the same material joined at an interface.	Page 338 Para 5	Cook and Gordon [20] analyzed the crack deflection at an interface between materials of identical elastic constants, i.e., the same material joined at an interface.	Page 300 Article 9.2.1 Para 1
10	<b>However</b> , two materials that meet at an interface are likely to have different elastic constants <b>as in the case of laminated composites prepared in the present investigation.</b>	Page 338 Para 5	Two materials that meet at an interface are <b>more than</b> likely to have different elastic constants.	Page 300 Article 9.2.1 Para 2
11	The modulus mismatch causes shearing of the crack surfaces (He and Hutchinson, 1989 <sup>a</sup> , 1989 <sup>b</sup> ) <b>resulting</b> in a mixed mode stress state in the vicinity of an interface crack tip involving both the tensile and shear components.	Page 338 Para 5	The modulus mismatch causes shearing of the crack surfaces. <b>This results</b> in a mixed mode stress state in the vicinity of an interface crack tip involving both the tensile and shear components.	Page 300 Article 9.2.1 Para 2
12	This, in turn, results in a mixed-mode fracture at the crack tip or in the wake of the crack.	Page 339 Para 1	This, in turn, results in a mixed-mode fracture <b>which can occur</b> at the crack tip or in the wake of the crack.	Page 300 Article 9.2.1 Para 2
13	This means that instead of a simple, one parameter description by the critical stress intensity factor $K_{IC}$ , a more complex formalism of fracture mechanics is needed to describe the situation.	Page 339 Para 1	<b>What this means in practical terms is</b> that instead of a simple, one parameter description by the critical stress intensity factor $K_{IC}$ , a more complex formalism of fracture mechanics is needed to describe the situation.	Page 300 Article 9.2.1 Para 2
14	The parameter K under such a situation becomes scale sensitive, but the critical strain energy release rate, $G_{IC}$ , is not a scale sensitive parameter.	Page 339 Para 1	The parameter K under such a situation becomes scale sensitive, but the critical strain energy release rate, $G_{IC}$ , is not a scale sensitive parameter.	Page 301 Para 1
15	These expressions have been used by He and Hutchinson (1989 <sup>a</sup> , 1989 <sup>b</sup> ), Evans and Marshall (1989), Ruhle and Evans (1988) and Gupta et al. (1993) to analyze the conditions for fiber / matrix debonding in terms of the energy requirements.	Page 339 Last Para	These expressions have been used by He and Hutchinson <b>as well as others [21-24]</b> to analyze the conditions for fiber / matrix debonding in terms of the energy requirements.	Page 302 Para 2
16	<b>The results are shown in Fig. 5.117 (Evans and</b>	Page 339	<b>Their results are shown in Fig. 9.7</b> in terms of a	Page 302

	Marshall, 1989) in terms of a chart of $G_i/G_f$ versus $\alpha$ , where $G_i$ is the mixed-mode interfacial fracture energy of the interface, $G_f$ is the mode I fracture energy of the fiber, and $\alpha$ is the measure of elastic anisotropy as defined above.	Last Para	chart of $G_i/G_f$ versus $\alpha$ , where $G_i$ is the mixed-mode interfacial fracture energy of the interface, $G_f$ is the mode I fracture energy of the fiber, and $\alpha$ is the measure of elastic anisotropy as defined above.	Para 2
17	Page 340 contains only a Figure i.e., Fig. 5.116 "Schematic of stress distribution at a crack tip" for which reference has been quoted.	Page 340 Fig. 5.116	Fig. 5.7 Schematic of stress distribution at a crack tip (after [2]).	Page 171 Fig. 5.7
18	Page 341 contains only a Figure i.e., Fig. 5.117 "A chart of $G_i/G_f$ vs. $\alpha$ " for which reference has been quoted.	Page 341 Fig. 5.117	Fig. 9.7 A chart of $G_i/G_f$ vs. $\alpha$ (after [22]).	Page 302 Fig. 9.7
19	The above plot shows the conditions under which the crack will deflect along the interface (resulting in debonding at the interface) or propagate through the interface into the fiber.	Page 342 Para 1	The plot in Fig. 9.7 shows the conditions under which the crack will deflect along the interface or propagate through the interface into the fiber as well as the variation of $\psi$ as a function of elastic anisotropy, $\alpha$ .	Page 302 Para 2
20	For the special case of zero elastic mismatch, i.e., for $\alpha = 0$ (as in the case of Cook and Gordon theory), the fiber / matrix interface will debond for $G_i/G_f$ less than about 0.25.	Page 342 Para 1	For the special case of zero elastic mismatch, i.e., for $\alpha = 0$ , the fiber / matrix interface will debond for $G_i/G_f$ less than about 0.25.	Page 303 Para 1
21	Conversely, for $G_i/G_f$ greater than 0.25, the crack will propagate across the fiber.	Page 342 Para 1	Conversely, for $G_i/G_f$ greater than 0.25, the crack will propagate across the fiber.	Page 303 Para 1
22	In general, for the elastic mismatch, $\alpha$ greater than zero, the maximum interfacial toughness required for interface debonding increases.	Page 342 Para 1	In general, for the elastic mismatch, $\alpha$ greater than zero, the minimum interfacial toughness required for interface debonding increases, i.e. high modulus fibers tend to favor debonding.	Page 303 Para 1

Substantial amount of work in the thesis is in topics covered by the book and so, it has been referred time and again. The ideas in the book are to be properly communicated and in this effort only 10 sentences from different parts of the thesis could be considered

identical as evident from Tables 1 and 2 ( sentences 2, 4, 10 in Table-1 and the sentences 2, 5, 6, 7, 9, 14, 21 in Table-2). In oxford dictionary, 'plagiarize' means 'publish borrowed thoughts as original, steal thoughts from (work, author)' and so when references are given the question of plagiarism does not arise. However, all the sentences have been modified in view of the objection of the examiner 1 to their similarity.

# ANSWERS TO THE QUERIES OF REVIEWER 2

## Chapter 1

No Queries

## Chapter 2

**Query (1):** Page 17, section 2.2.1, last but one sentence:

"In general, the onset of plastic deformation in single crystal  $\text{MoSi}_2$  .....approximately 900 °C (Umakoshi et al. 1990). This statement is misleading and contradicts the statement couple of lines earlier, which says that plastic deformation is observed in crystals for specific orientations at temperatures as low as -100 °C. In fact, onset of slip occurs for certain orientations at temperatures much higher than 900 °C. Ito et al. [K. Ito, H. Inui, Y. Shirai and M. Yamaguchi, "Plastic deformation of  $\text{MoSi}_2$  single crystals," *Philos. Mag.*, 72(4), 1075-1097 (1995)] have studied the deformation behaviour of  $\text{MoSi}_2$  single crystals between -196 °C and 1500 °C, and reported that [001]-oriented crystals involving the activation of  $\{0\bar{1}3\}\langle 331\rangle$  slip system deform only above 1300 °C, while deformation could be observed at room temperatures in the crystals with other orientations. In polycrystalline  $\text{MoSi}_2$ , only 4 independent slip systems are found up to 1000 °C [S.A. Maloy, A.H. Heuer, J.J. Lewandowski and T.E. Mitchell, "On the slip systems in  $\text{MoSi}_2$ ," *Acta Metall. Mater.* 40(11) 3159-(1992).]

**Answer (1):** Page 17, section 2.2.1:

*The statements "MoSi<sub>2</sub> single crystals exhibit macroscopic compressive deformation in some orientations at temperatures as low as -100 ° C. The {011}<100> slip system is operative at these low temperatures (Ito et al., 1995)" and "In general, the onset of plastic deformation in single crystal MoSi<sub>2</sub> begins at temperature of approximately 900 ° C (Umakoshi et al., 1990) have been deleted. The paragraph has been suitably modified incorporating the results from the references [K. Ito, H. Inui, Y. Shirai and M. Yamaguchi, "Plastic deformation of MoSi<sub>2</sub> single crystals", *Philosophical Magazine A*, 72(4), 1075-1097 (1995)] and [S.A. Maloy, A.H. Heuer, J.J. Lewandowski and T.E. Mitchell, "On the slip systems in MoSi<sub>2</sub>," *Acta Metall. Mater.* 40(11) 3159-(1992)] as suggested by the reviewer. Accordingly, the list of references has also been modified.*

**Query (2):** Fig. 2.4:

The upper limiting temperatures for stability of C11<sub>b</sub> and C40 phases of pure  $\text{MoSi}_2$  may be mentioned.

**Answer (2):** Fig. 2.4:

*The upper limiting temperatures for stability of C11<sub>b</sub> and C40 phases of pure MoSi<sub>2</sub> have been incorporated in Fig. 2.4.*

**Query (3):** Page 22, section 2.2.2.1:

At  $T < 700$  °C,  $\text{MoO}_3$  does not volatilize .....In fact,  $\text{MoO}_3$  volatilizes even at temperatures less than 700 °C, because of its high vapour pressure. It is reported [M.S. Samant, A.S. Kerkar, S.R. Bharadwaj, S.R. Dharwadkar, J. Alloys Compd. 187 (1992) 373-379] that the vapour pressure of  $\text{MoO}_3$  increases sharply from  $10^{-2}$  Pa to  $10^2$  Pa, as the temperature rises from 500 to 700 °C. The rate of volatilization of  $\text{MoO}_3$  is expected to be low below 600 °C, although its vapourization has been reported at and above 500 °C [N. Floquet, O. Bertrand, J.J. Heizmann, Oxid. Met. 37 (1992) 253-280].

**Answer (3):** Page 22, section 2.2.2.1:

*The statement "At  $T < 700$  °C,  $\text{MoO}_3$  does not volatilize" has been deleted and the paragraph has been suitably modified incorporating the results from the references [N. Floquet, O. Bertrand, J.J. Heizmann, Oxid. Met. 37 (1992) 253-280] and [M.S. Samant, A.S. Kerkar, S.R. Bharadwaj, S.R. Dharwadkar, J. Alloys Compd. 187 (1992) 373-379] as suggested by the reviewer. Accordingly, the list of references has also been modified.*

**Query (4):** Fig. 2.9(a):

The y-axis title, HARDNESS does not have its unit.

**Answer (4):** Fig. 2.9(a):

*In the y-axis title, the unit of HARDNESS has been added.*

**Query (5):** Fig. 2.5 and Fig. 2.18:

Figure caption should be: "Schematic illustration of ..." instead of "Schematic of ..."

**Answer (5):** Fig. 2.5 and Fig. 2.18

*Changes in Figure captions of Fig. 2.5 and Fig. 2.18 have been made as suggested.*



## Chapter 3

**Query (6):** Page 60, section 3.1, 4<sup>th</sup> line from top:

Spelling written as “Particless” needs to be corrected at many places.

**Answer (6)** Page 60, section 3.1, 4<sup>th</sup> line from top::

*Spelling written as “Particless” has been corrected in the entire document.*

**Query (7):** Page 60, section 3.1, 5<sup>th</sup> line from top:

Scientific reason(s) should be provided for the choice of Al<sub>2</sub>O<sub>3</sub> for the purpose of coating.

**Answer (7):** Page 60, section 3.1, 5<sup>th</sup> line from top:

*Scientific reason for the choice of Al<sub>2</sub>O<sub>3</sub> for the purpose of coating has been added. The text has been modified (Page 60, section 3.1, 5<sup>th</sup> line from top) as follows:*

*“Al<sub>2</sub>O<sub>3</sub> powder was used to apply a diffusion barrier coating on Nb foil. Al<sub>2</sub>O<sub>3</sub> was chosen as a coating material due to its chemical and thermal compatibility with both MoSi<sub>2</sub> as well as Nb”.*

**Query (8):** Page 86, section 3.3.1.3:

Any abbreviation should be introduced first with expanded version, even if it is common (3-D). The SEM image is a two dimension projection of a three dimensional object. Those are not 3-D images.

**Answer (8):** Page 86, section 3.3.1.3

*The phrase “the images appear in 3-D” has been deleted.*

**Query (9):** Page 86, section 3.3.1.3, 7<sup>th</sup> line from bottom:

The use of “atomic number imaging” does not make sense. The backscattered electron images show contrast, which is sensitive to differences in atomic number. Present tense should be used instead of “increased with ....” It is a permanent reality. Again, fraction of backscattered electrons emitted from the specimen increases with its atomic number (that is, positive charge of nucleus of atoms) and there is no direct relationship with atomic weight.

**Answer (9):** Page 86, section 3.3.1.3, 7<sup>th</sup> line from bottom:

*The statement “Back-scattered electrons could be used for atomic no. imaging since the number of back-scattered electrons reflected by a specimen increased with atomic weight” has been replaced by “The images produced by back-scattered electrons*

*show contrast, which is sensitive to differences in atomic number since the fraction of back-scattered electrons emitted from the specimen increases with its atomic number”.*

**Query (10):** Page 93, 2<sup>nd</sup> line:

“In a few specimens, the .....15  $\mu\text{m}$  and 19  $\mu\text{m}$  diamond paste, respectively.” The word, “respectively” is not required here.

**Answer (10):** Page 93, 2<sup>nd</sup> line:

*The word “respectively” has been deleted.*

**Query (11):** Page 93, last paragraph:

Description of stress distribution in the 3-point bend sample should be in the present tense, as it is always like this for similar experimental conditions.

**Answer (11):** Page 93, last paragraph:

*Description of stress distribution in the 3-point bend sample has been modified using the present tense.*

**Query (12):** Page 96, 1<sup>st</sup> line:

Present tense should be used.

**Answer (12):** Page 96, 1<sup>st</sup> line:

*The statement “There were no standard specimen types or test methods .....” has been replaced by “There are no standard specimen types or test methods .....”*

**Query (13):** Page 97:

(c) Measurement of fracture toughness – Present tense should be used, because the matter being discussed is still true.

**Answer (13):** Page 97:

*The paragraph has been re-written using the present tense.*

**Query (14):** Page 101:

The position of notch tip with respect to that of the refractory metal foil should be mentioned. The  $P_{\text{max}}$  is expected to be a function of the position of notch tip with respect to the metallic foil.

**Answer (14):** Page 101, 2<sup>nd</sup> Para from bottom, 8<sup>th</sup> Line:

*The statement “The distance between the notch tip and the refractory metal foil was kept  $\sim 200 \mu\text{m}$ ” has been added.*

## Chapter 4

**Query (15):** Page 125, 9<sup>th</sup> line from bottom:

“The above analysis of residual stresses.....” The main reason for lower residual stress is difference in coefficients of thermal expansion, rather than lower Young's modulus. That is the reason, why the residual stress in the matrix is also lower.

**Answer (15):** Page 127, 4<sup>th</sup> line from top:

*The main reason for lower residual thermal strain is the difference in coefficients of thermal expansion. However, the residual stress depends on the residual thermal strain as well as the Young's modulus.*

**Query (16):** Page 128, 12<sup>th</sup> line from top:

“This localized high stresses ..... to the edge effect.” The “edge effect” should be explained.

**Answer (16):** Page 128, 12<sup>th</sup> line from bottom:

*The explanation for the “edge effect” has been included as per the following:*

*This localized high stress can be attributed to the edge effect. The edge effect results due to the material missing from the other side of the edge. Ho et al. (1995) have reported that the stresses at the free surface of a layered material are different from those within the body of the material. Although, the residual thermal stresses in the layers are bi-axial far away from the free surface, the stress distribution near the free surface is tri-axial. A stress perpendicular to the layer plane exists near the free surface. The component of the tri-axial stress acting perpendicular to the plane of the layer is a highly localized stress, which diminishes rapidly in magnitude with distance from the surface to the interior.*

*Accordingly, the reference Ho et al. (1995) has been added to the list of references.*

**Query (17):** Fig. 4.11:

Why is the nature of stress contour plot shown in Fig. 4.11(a) different from that in Fig. 4.11(b) and (c).

**Answer (17):** Fig. 4.11:

*The nature of stress contour plots obtained for Mo, Ta and Nb foil laminated composites as shown in Figs. 4.11(a), 4.11(b) and 4.11(c), respectively are essentially the same. Only certain regions (e.g., as depicted by pink colour) in Figs. 4.11(b) and 4.11(c) could not develop as the stresses are lower as compared to the stresses in Mo foil laminated composite (Fig. 4.11(a)).*

## Chapter 5

**Query (18):** Page 151, section 5.1.4.1:

“The microstructure as exhibited in .....developed texture through banding of planar orientation.” The message is not clear, the sentence needs to be re-written for more clarity.

**Answer (18):** Page 151, section 5.1.4.1:

*The statement “The microstructure as exhibited in Fig. 5.8(a) appears to have developed texture through banding of planar orientation” has been re-written as “The microstructure as exhibited in Fig. 5.8(a) shows a banded structure as typically observed in rolled products”.*

**Query (19):** Page 151, section 5.1.4.2, 4<sup>th</sup> line – 2<sup>nd</sup> from bottom:

“Mo foil has ..... as received Mo foil (Fig. 5.7). It is not clear how the as rolled microstructure is related to hardness of Mo foil. Moreover, it should be noted that the brittle-to-ductile transition temperature of Mo is just above or slightly more than room temperature, while that of Nb is sub-zero.

**Answer (19):** Page 151, section 5.1.4.2, 4<sup>th</sup> line from bottom:

*The statements “Mo foil has a high hardness and a much lower strain to failure as compared to Ta and Nb foils, which is consistent with rolled microstructure of as received Mo foil (Fig. 5.7). In contrast to Mo foil, as received Ta and Nb foils are in annealed condition showing more or less an equi-axed grain structure (Fig. 5.8(b))” have been deleted and the following has been added.*

*“All the foils were tested at room temperature in as received condition. The Mo foil under as received condition exhibits a highly rolled microstructure (Fig. 5.7). The Mo foil shows high hardness and low fracture strain, which may be attributed to work-hardening condition and/or brittle condition resulting from ductile-brittle transition. But Nb and Ta are likely to be ductile at room temperature since these are annealed as evident from equi-axed grain structure and their ductile-to-brittle transition temperatures are -126 °C and -248 °C, respectively”.*

**Query (20):** Page 152, 2<sup>nd</sup> paragraph:

The reason for lower work hardening rate of Mo than that of Nb and Ta should be explained. At least some rational explanation should be proposed.

**Answer (20):** Page 152, 2<sup>nd</sup> paragraph:

*The 2<sup>nd</sup> paragraph “Figures 5.9(a), 5.9(b) and 5.9(c) exhibit engineering stress–strain curves of as received Mo, Ta and Nb foils, respectively. The stress-strain curve of Mo foil shows very little further work hardening of the rolled material before fracture.*

However, the stress strain curves of Ta and Nb foils revealed very sharp yield points with well-defined work hardening behaviour. Both these stress strain curves show significant uniform deformation. Ta foil seems to have a higher work hardening rate than Nb foil" has been rewritten as:

*"Figures 5.9(a), 5.9(b) and 5.9(c) exhibit engineering stress–strain curves of as received Mo, Ta and Nb foils, respectively. The stress-strain curve of Mo foil shows early necking and lower strain hardening as the working of the foil has exhausted its ductility. The extent of necking is also less as it requires breaking some of the fiber like strands between bands, which does not take place early. The cracks appear to initiate between the strands but could not propagate without breaking the strands till fracture. This is substantiated by the observation of fractured surface in Fig. 5.10. However, the stress strain curves of Ta and Nb foils show extensive work hardening and very high uniform elongation as compared to Mo foil. This observation could be attributed to difference in their ductile-to-brittle characteristics as discussed previously. Ta foil seems to have a higher work hardening rate than Nb foil."*

**Query (21):** Page 152, 3<sup>rd</sup> paragraph:

"The grains slide over each other along the rolling direction. The deformation predominantly along grain boundaries....." This statement makes no sense, as there is no grain boundary sliding during rolling. It is conceptually wrong to say that grains slide against each other in a relatively coarse-grained material during rolling. Either the sentence should be modified or it should be deleted. Also it is not possible to prove deformation along grain boundaries using the SEM fractograph of Fig. 5.10. Moreover, why should the deformation be localized at grain boundaries in Mo at room temperature? Without support of TEM images, it is not possible to say anything like that.

**Answer (21):** Page 152, 3<sup>rd</sup> paragraph:

*The statements "The fracture surface of Mo foil revealed the deformation along grain (rolled) boundaries as depicted in Fig. 5.10. The grains slide over each other along the rolling direction. The deformation predominantly along the grain boundaries resulted in almost no strain hardening in Mo foil" have been deleted. The entire paragraph has been rewritten as:*

*Figure 5.10 shows the fractograph of the as received Mo foil while the fracture surfaces of the as received Ta and Nb foils are shown in Figs. 5.11(a) and 5.11(b), respectively. The fractograph of Mo foil (Fig. 5.10) shows cracking predominantly between the strands in a banded structure. In contrast, extensive plasticity was seen to result in dimpled fracture and shear zones in the Ta foil as exhibited in Fig. 5.11(a). Tearing ridges as well as micro-voids are seen in Fig. 5.11(a). Figure 5.11(b) shows dimpled fracture of the Nb foil. Fracture seems to have taken place by micro-void formation and coalescence.*

**Query (22):** Page 162, 3<sup>rd</sup> line from top:

What is meant by "free" SiO<sub>2</sub>? Either the use of "free" should be explained, or it should be dropped.

**Answer (22):** Page 162, 3<sup>rd</sup> line from top:

*The word "free" has been deleted.*

**Query (23):**Page 162, 2<sup>nd</sup> paragraph:

"WSi<sub>2</sub> and MoSi<sub>2</sub> ..... identical atom radius." How can two compounds have identical atom radius? The sentence needs to be modified. Their lattice constants are very close to one another, and the atomic radii of Mo and W atoms are almost identical.

**Answer (23):** Page 162, 2<sup>nd</sup> paragraph:

*The sentences have been modified as follows:*

*WSi<sub>2</sub> and MoSi<sub>2</sub> have similar crystal structures (t16, prototype MoSi<sub>2</sub>) and their lattice constants are very close to one another. The atomic radii of Mo and W atoms are almost identical (13.6 nm and 13.7 nm, respectively).*

**Query (24):** Page 167, 1<sup>st</sup> paragraph:

It must be noted that the formation of MoO<sub>2</sub> is preferred in oxygen deficient situations, and is usually found beneath the top layer of MoO<sub>3</sub>. Here, MoO<sub>2</sub> is found in place of MoO<sub>3</sub>, as it vapourizes with increase in temperature beyond 700 °C during high temperature processing.

**Answer (24):** Page 167, 1<sup>st</sup> paragraph:

*The statement "However, some oxidation of Mo could have occurred during high temperature processing due to its high affinity with oxygen. This could result in the formation of MoO<sub>2</sub>" has been replaced by:*

*"However, some oxidation of Mo could have occurred during processing under oxygen deficient situation when formation of MoO<sub>2</sub> is more likely. Since, the processing of the composite was carried out in vacuum using graphite dies and tooling, this could indeed result in the formation of MoO<sub>2</sub> as the formation of MoO<sub>2</sub> is preferred in oxygen deficient situations".*

**Query (25):** Page 176, 2<sup>nd</sup> paragraph, last sentence:

"Silicide solid solution may also have weakened the composite". The message is not clear. In the last sentence of third paragraph, solid solution strengthening has been mentioned as mechanism for increase in hardness.

**Answer (25):** Page 176, 2<sup>nd</sup> paragraph, last sentence:

*The statement "Silicide solid solution may also have weakened the composite" has been replaced by "As a result, the composites show a lower elastic modulus than MoSi<sub>2</sub> matrix".*

**Query (26):** Page 190, last line:

“Figure 4.32(b) should be replaced by “Figure 5.32(b).

**Answer (26):** Page 190, last line:

*“Figure 4.32(b) has been replaced by “Figure 5.32(b).*

**Query (27):** Page 198, 2<sup>nd</sup> paragraph:

It is assumed that there was no surplus Al, which entered into solid solution ....” This assumption is not correct. Quantitative EDS or WDS analysis will show the concentration of Al in MoSi<sub>2</sub>. 0.5 at.% Al was found in solid solution in MoSi<sub>2</sub> in MoSi<sub>2</sub>-1.5 wt.% (2.8 at.%) Al alloy (R. Mitra et al., Intermetallics, 7 (1999) 213-232.

**Answer (27):** Page 198, 2<sup>nd</sup> paragraph:

*The statements “It is assumed that there was no surplus Al, which entered into solid solution with MoSi<sub>2</sub> and the entire amount of Al, added to MoSi<sub>2</sub> was consumed in reduction of SiO<sub>2</sub> and MoO<sub>2</sub> phases. Pure Al was not detected as segregated or forming precipitates in elemental form anywhere” have been modified as below:*

*“Most of the Al added to MoSi<sub>2</sub> was consumed in reduction of SiO<sub>2</sub> and MoO<sub>2</sub> phases. It is likely that some Al was alloyed with MoSi<sub>2</sub> forming a substitutional solid solution, although it was not detected in the present investigation. Mitra et al. (1999) have reported 0.5 at% Al in solid solution in MoSi<sub>2</sub> in MoSi<sub>2</sub>-1.5 wt% (2.8 at%) Al alloy. It is possible that there is no excess Al after reduction of SiO<sub>2</sub> to be alloyed with MoSi<sub>2</sub>”.*

**Query (28):** Page 212, 4<sup>th</sup> line from top:

“The grains were retained with no change in the cleavage planes.” The message from this sentence is not clear. The sentence needs to be re-written for improvement in clarity.

**Answer (28):** Page 212, 4<sup>th</sup> line from top:

*The sentence “The grains were retained with no change in the cleavage planes” has been deleted.*

**Query (29):** Page 212, 2<sup>nd</sup> paragraph:

It has been claimed that the specimens failed in shear because of high thermal residual stresses. It is probably more appropriate to attribute this to interfacial embrittlement by formation of reaction layer. Moreover, actual thermal residual stress may be very different because of the interfacial reaction layer. Furthermore, similar thermal residual stress was also present in MoSi<sub>2</sub>-20 vol.% SiC – Mo laminated composite. Why the type of failure was not similar there (discussed in page 262-263)?

**Answer (29):** Page 212, 2<sup>nd</sup> paragraph:

The residual thermal stresses were not similar in (MoSi<sub>2</sub> + 2 wt% Al) + Mo foil and (MoSi<sub>2</sub> + 20 vol% SiC<sub>p</sub>) + Mo foil laminated composites because of the following reasons:

- (i) MoSi<sub>2</sub>-Al + Mo foil laminated composite was vacuum hot pressed at 1750 °C (as mentioned in section 3.2.3, page 73, para 2, 6<sup>th</sup> line from top) while MoSi<sub>2</sub>-SiC<sub>p</sub> + Mo foil laminated composite was processed at 1600 °C (as mentioned in section 3.2.4 (page 74, para 3, 2<sup>nd</sup> line from top).
- (ii) Addition of 2 wt% Al in MoSi<sub>2</sub> does not significantly alter the coefficient of thermal expansion of the MoSi<sub>2</sub> based matrix as the coefficient of thermal expansion of Al<sub>2</sub>O<sub>3</sub> is  $7.4 \times 10^{-6}/K$ , which is only marginally lower than that of MoSi<sub>2</sub> ( $8.52 \times 10^{-6}/K$ ). However, addition of 20 vol% SiC<sub>p</sub> ( $\alpha = 4.78 \times 10^{-6}/K$ ) results in a much lower coefficient of thermal expansion of the MoSi<sub>2</sub> based matrix.

Therefore, a higher  $\Delta T$  and a higher  $\Delta CTE$  will result much higher residual thermal stresses in MoSi<sub>2</sub>-Al + Mo foil laminated composite as compared to MoSi<sub>2</sub>-SiC<sub>p</sub> + Mo foil laminated composite.

Shear failure of MoSi<sub>2</sub>-Al + Mo foil laminated composite cannot be attributed to interfacial embrittlement by formation of reaction layer alone as interfacial reaction layer was formed in both the laminated composites. However, the thickness of the interfacial reaction layer in MoSi<sub>2</sub>-Al + Mo foil laminated composite was much higher (70-80  $\mu m$ , as mentioned in section 5.3.1, page 190, para 2, 2<sup>nd</sup> line from the bottom) as compared to a layer thickness of 50  $\mu m$  (section 5.4.1.2, page 224, para 1, 5<sup>th</sup> line from the top) in MoSi<sub>2</sub>-SiC<sub>p</sub> + Mo foil laminated composite. This of course may also contribute to the shear failure of MoSi<sub>2</sub>-Al + Mo foil laminated composite, in addition to the existence of higher residual thermal stresses.

**The statement “The specimens failed in shear possibly because of the existence of high residual thermal stresses at MoSi<sub>2</sub> based matrix / Mo foil interface” (page 212, para 2, 3<sup>rd</sup> line from top) has been rewritten as “After reaching the interface the crack propagated along MoSi<sub>2</sub> based matrix / Mo foil interface possibly because of the existence of high shear stress due to thermal mismatch across it and the interface weakening by a thick layer of brittle interfacial reaction products”.**

**Note:** The same has also been explained in subsequent sections (Section 5.7 Discussion, Sub-section 5.7.3 Laminated Composites with (MoSi<sub>2</sub> + 20 vol% SiC<sub>p</sub>) as Matrix). The relevant para on page 346 is reproduced here:

In notched three-point bend test of (MoSi<sub>2</sub> + 2 wt% Al) + Mo foil laminated composite, extensive debonding occurred at the interface (Fig. 5.47) resulting in the shear failure of the test specimens. However, in case of (MoSi<sub>2</sub> + 20 vol% SiC<sub>p</sub>) + Mo foil laminated composite, the test specimens failed in pure flexure (no shear failure



was observed). This can probably be attributed to a lower value of  $G_i/G_{Mo}$  in Mo foil / MoSi<sub>2</sub> laminated composite with Al in MoSi<sub>2</sub> matrix as compared to the Mo foil / MoSi<sub>2</sub> laminated composite with SiC<sub>p</sub> in MoSi<sub>2</sub> matrix. The SiC<sub>p</sub> addition in MoSi<sub>2</sub> matrix reduces the thermal expansion mismatch between the layers of MoSi<sub>2</sub> based matrix and the Mo foil resulting in relatively lower residual tensile stresses in the composite and hence a relatively stronger interface. A low value of  $G_i/G_{Mo}$  will lead to more chances of interfacial debonding as depicted in Fig. 5.117. In addition to a lower value of  $G_i/G_{Mo}$ , a higher thickness of the interfacial reaction zone in (MoSi<sub>2</sub> + 2 wt% Al) + Mo foil laminated composite as compared to the reaction zone thickness in (MoSi<sub>2</sub> + 20 vol% SiC<sub>p</sub>) + Mo foil composite may also play an important role in enhancing the interfacial debonding and shear failure.

**Query (30):** Page 232, section 5.4.1.3, 3<sup>rd</sup> sentence:

“The microstructure in as polished condition....” It is known that observation of microstructure by optical or scanning electron microscopy of samples require polishing of its surface. Hence, the use of “As-polished” is superfluous.

**Answer (30):** Page 232, section 5.4.1.3, 3<sup>rd</sup> sentence:

“As polished” has been deleted from all the places.

**Query (31):** Page 248, 2<sup>nd</sup> paragraph:

The decrease in hardness of Mo foil has been attributed to grain growth. If that is a valid reason, more grain growth is expected in case of Nb, which has a lower melting point. Proper modification may be carried out.

**Answer (31):** Page 248, 2<sup>nd</sup> paragraph:

The statements “As the Mo foil used was in work-hardened condition, the effect of annealing and grain growth during the high temperature processing was probably more pronounced than solid solution hardening. Apart from Si diffusion from MoSi<sub>2</sub>, oxygen pick-up and contamination from interstitial impurities such as carbon, H<sub>2</sub> and N<sub>2</sub> during processing could well influence the hardness and ductility of the refractory metal foils. The change in hardness of the processed refractory metal foils could also be due to the compressive residual stresses developed in the metal foils after cooling from the high processing temperatures” have been modified as follows:

“The Mo foil under as received condition exhibited a highly rolled unrecrystallized microstructure and therefore is expected to undergo annealing and grain growth during high temperature processing. However, the as received Ta and Nb foils were in annealed condition. Therefore, the recovery and recrystallization taking place in Mo foil during high temperature processing was responsible for significant reduction in hardness. But in the case of Ta and Nb foils, which were already annealed, solid solution strengthening due to Si diffusion from MoSi<sub>2</sub> appears to dominate to increase the hardness of these foils. Oxygen pick-up and contamination from interstitial impurities such as carbon, H<sub>2</sub> and N<sub>2</sub> during processing could also increase the hardness of all the refractory metal foils, and affect their ductility adversely. Further,

*there could be some contribution of the compressive residual stresses developed in the metal foils after cooling from the high processing temperatures”.*

**Query (32):** Page 262, 5<sup>th</sup> – 9<sup>th</sup> line from top:

“The degree of constraint on Nb foil.....laminated composite.” The reasoning is very weak. The constraint is expected to be higher for larger the thermal expansion mismatch. A more valid reason for greater constraint in case of Nb could be the formation of thicker interfacial reaction layer, which is brittle in nature.

**Answer (32):**

*The entire Para 1 on Page 262 has been modified as below:*

*As described earlier, the strength and toughness of the laminated composites have been calculated from the peak load obtained in three point bend tests. The peak load of a bending test carried out on a laminated composite specimen is governed by the yield strength of the refractory metal foil, residual thermal stresses and interfacial strength. The residual thermal stresses in various laminated composites have been calculated in section 4.4.2 and presented in Table 4.5. The residual thermal stress is lower for Nb foil reinforced laminated composite and so, it could have gone to higher peak load if interfacial strength would have permitted the same. But it is observed that the peak load is lower than that in case of Ta foil reinforced laminated composite, which has higher residual thermal stresses. The only inescapable conclusion is the interfacial strength is higher in Ta foil reinforced laminated composite and so, permitted higher peak load in spite of higher thermal stresses. Also, the yield strength of the as received Ta foil was found to be much higher than yield strength of the Nb foil (Table 5.5) and so, permitted application of increasing load. Osman et al. (1995) have also observed that as the yield strength of ductile metal foil increases, fracture toughness of the composite, which is a function of peak load, also increases. A higher strength ductile layer gives higher fracture toughness than that laminated with a lower strength ductile layer.*

**Query (33):** Page 281, Table 5.2:

Is the intrinsic hardness of Ta-silicide (when measured independently or based on literature data) higher? The intrinsic hardness of reaction products (from literature) could either be included in Table or in the text.

**Answer (33):** Page 281, Table 5.2:

*The intrinsic hardness of reaction products i.e.,  $Mo_5Si_3$ ,  $Ta_5Si_3$  and  $Nb_5Si_3$ , I could not found from the literature.*

**Query (34):** Page 293, 2<sup>nd</sup> paragraph, last sentence:

“However, it is assumed to be  $Nb_5Si_3$ .” What is the justification for such an assumption? Why can't it be  $Nb_3Si$ ?

**Answer (34):** Page 293, 2<sup>nd</sup> paragraph, last sentence:

*Nb<sub>3</sub>Si is a high temperature phase. It is stable only at 1770 – 1980 °C (Barin, 1989). The Nb-Si binary phase diagram as presented in Fig. 5.108 on page 312 also suggests the same (as mentioned on page 309, 2<sup>nd</sup> para, 3<sup>rd</sup> line). Therefore, it is more logical to assume this Si rich layer at Al<sub>2</sub>O<sub>3</sub> / Nb interface to be of Nb<sub>5</sub>Si<sub>3</sub>.*

*The literature data presented as a part of the discussion on page 358, 2<sup>nd</sup> para, 4<sup>th</sup> to 9<sup>th</sup> line also supports the above assumption. The following is reproduced here from page 358, 2<sup>nd</sup> para, 4<sup>th</sup> to 9<sup>th</sup> line:*

*Xiao et al. (1990) have measured the thickness of the reaction layer in MoSi<sub>2</sub> reinforced with Nb wires as 30 μm after vacuum hot pressing at 1700 °C. They found that the thickness of the reaction layer was reduced to 4 – 6 μm after applying ZrO<sub>2</sub> coating on Nb wires. They identified the reaction product to be Nb<sub>5</sub>Si<sub>3</sub> on the Nb side of the coating (at ZrO<sub>2</sub>-Nb interface).*

**Query (35):** Page 306, equation 5.16 and page 311, Fig. 5.106:

The conclusion based on Fig. 5.106 is wrong. The equation should be written as:  $2/3\text{Mo} + \text{O}_2 \rightarrow 2/3\text{MoO}_3$  for comparison of free energy change (kJ/mol) of oxygen with that for equation 5.17. Please refer to chapter 10 of Introduction to Thermodynamics by D.R. Gaskell, where Ellingham diagram has been discussed. One can compare the free energies of two different reactions and decide on their feasibility, only when partial pressure of oxygen is same for both. Even if an experiment is carried out, Mo will be subjected to one unique partial pressure, under which either of the reactions may be preferred.

**Answer (35):** Page 306, equation 5.16 and page 311, Fig. 5.106:

*The ΔG values plotted in Fig. 5.106 are calculated per mole of oxygen only for both the reactions represented by equations 5.16 and 5.17 as mentioned on page 309 (1<sup>st</sup> line). The purpose of comparing the free energies of these two reactions is only to determine their relative feasibility under all other conditions to be identical (like partial pressure of oxygen). However, in the present work the processing of the composite was carried out in vacuum using graphite dies and tooling which resulted in the formation of MoO<sub>2</sub> as the formation of MoO<sub>2</sub> is preferred in oxygen deficient situations.*

**Query (36):** Page 305, equations 5.12 & 5.13; Page 306, equations 5.14 & 5.15; Page 309, equations 5.18-5.21; Page 316, equations 5.23-5.25; Page 322, equations 5.26-5.29:

It is necessary that equations are re-written to maintain either one or same number of mole(s) of W, Mo, Nb or Ta without which such comparison is illogical. The argument is similar to that for Ellingham diagram or as shown in comment 35. See a related reference: M.E. Fine and J.G. Conley, "Discussion of on the free-energy of formation of TiC and Al<sub>4</sub>C<sub>3</sub>," Metallurgical Transactions A, Vol. 21(9), 2609-2610 (1990).

**Answer (36):** Page 305, equations 5.12 & 5.13; Page 306, equations 5.14 & 5.15; Page 309, equations 5.18-5.21; Page 316, equations 5.23-5.25; Page 322, equations 5.26-5.29:

*While plotting  $\Delta G$  vs. temperature, care has been taken to plot  $\Delta G$  values calculated per mole of  $\text{MoSi}_2$  for different chemical reactions considered. This has been mentioned throughout the text while discussing the various figures showing  $\Delta G$  vs. temperature plots.*

*On Page 305, Last para, 1<sup>st</sup> line for equations 5.12 & 5.13, on Page 306, 2<sup>nd</sup> para, 1<sup>st</sup> line for equations 5.14 & 5.15, on Page 309, 3<sup>rd</sup> para, 2<sup>nd</sup> line for equations 5.18-5.20, on Page 318, 1<sup>st</sup> line for equations 5.23-5.25, on Page 324, 1<sup>st</sup> line for equations 5.26-5.29 ( $\Delta G$  calculated per mole of SiC).*

**Query (37):** Page 345, last two lines & Page 346, 1<sup>st</sup> line:

*"....., multiple cracking in the matrix in the vicinity of the main propagating crack resulted in limited debonding at the interface". This mechanism is doubtful. Debonding of the interface requires different energy or stress level than that for matrix microcracking. Hence interfacial debonding and matrix microcracking are independent of one another.*

**Answer (37):** Page 345, last two lines & Page 346, 1<sup>st</sup> three lines:

*It is true that interfacial debonding and matrix microcracking are independent of one another as processes. But the energy input to the system has to be divided in these two modes and thus, they are related. Multiple cracking of the matrix may release so much strain energy that crack could not propagate through and across the interface. Only areas of the interface between matrix cracks could debond with the strain energy remaining.*

*Ashby et al. (1989) based on their work on a model "single Pb wire embedded in a glass tube" composite with a strong interfacial bond have shown that with increasing applied load, multiple cracking in brittle matrix may occur before interfacial failure (debonding). They observed that multiple cracks in brittle matrix also 'free a length of the ductile metal wire from the matrix' giving rise to a "gauge length" (partial or limited debonding). This has been described in detail in Chapter 2 Literature Review (page 53). Xiao et al. (1991) have also reported similar observations in  $\text{MoSi}_2 + \text{Nb}$  foil (uncoated) laminated composite. They found that as the load level is increased, the Nb foil at the opening of the primary crack becomes stretched and secondary cracks start to nucleate. On further increase in load, additional secondary cracks continue to form and propagate throughout the matrix, creating a region at the interface, which may be termed as "virtual debonding". In this area, the matrix-imposed constraints are relaxed and the foil can now deform freely until it fails in a ductile manner.*

*The statements "However, with increasing applied load (and therefore, with increasing stress intensity at the crack tip), multiple cracking in the matrix in the vicinity of the main propagating crack resulted in limited debonding at the interface.*

*This limited debonding at the interface decreased the constraint imposed by the brittle matrix on the ductile Nb foil and allowed the Nb foil to undergo plastic deformation resulting in necking as depicted in SEM images of the tested  $K_{IC}$  specimens (Figs. 5.82 and 5.83)” have been modified to as below:*

*“However, with increasing applied load (and therefore, with increasing stress intensity at the crack tip), multiple cracking in the matrix in the vicinity of the main propagating crack resulted in dissipation of energy by release of strain and thereby, limiting debonding at the interface. The debonding at the interface, although limited, decreased the constraint imposed by the brittle matrix on the ductile Nb foil and allowed the Nb foil to undergo plastic deformation resulting in necking as depicted in SEM images of the tested  $K_{IC}$  specimens (Figs. 5.82 and 5.83)”.*

**Query (38):** Page 364, Fig. 5.127:

It is necessary to explain in the text why the MoSi<sub>2</sub>-Ta (uncoated) laminated composite has shown higher work of fracture than MoSi<sub>2</sub>-Nb (Al<sub>2</sub>O<sub>3</sub> coated) composite, in spite of the fact that the former material has shown an interfacial reaction.

**Answer (38):** Page 362, Last Para:

*Necessary explanation has been added in the text on page 362 (last para) by replacing the statements “However, the weak interfacial bonding in Al<sub>2</sub>O<sub>3</sub> coated Nb foil reinforced laminated composite results in greater work of fracture as compared to the uncoated Nb foil reinforced laminated composite. Lower interfacial fracture energy results in lower constraint imposed by the matrix on the Nb foil. Therefore, more Nb participates in deformation resulting in higher work of fracture” by the following:*

*“The work of fracture in these laminated composites has two components – (i) energy spent on interfacial debonding and (ii) energy of plastic deformation of ductile foil. The weak interfacial bonding in Al<sub>2</sub>O<sub>3</sub> coated Nb foil laminated composite results in greater work of fracture as compared to the uncoated Nb foil reinforced laminated composite, which has a relatively stronger interfacial bonding. The energy of debonding in the former is lower but the debonding results in larger volume of Nb foil under plastic deformation due to removal of the constraint imposed by the matrix on the Nb foil in the bonded state. Therefore, one observes higher work of fracture in Al<sub>2</sub>O<sub>3</sub> coated Nb foil laminated composite in spite of a lower peak load. However, in Ta foil laminated composite, the interfacial bonding is quite strong as indicated by higher peak load and also, Ta-foil has higher contribution from plastic deformation. Thus, Ta foil laminated composite has still higher work of fracture compared to that observed in Al<sub>2</sub>O<sub>3</sub> coated Nb foil laminated composite”.*

## **Chapter 6**

**No Queries**

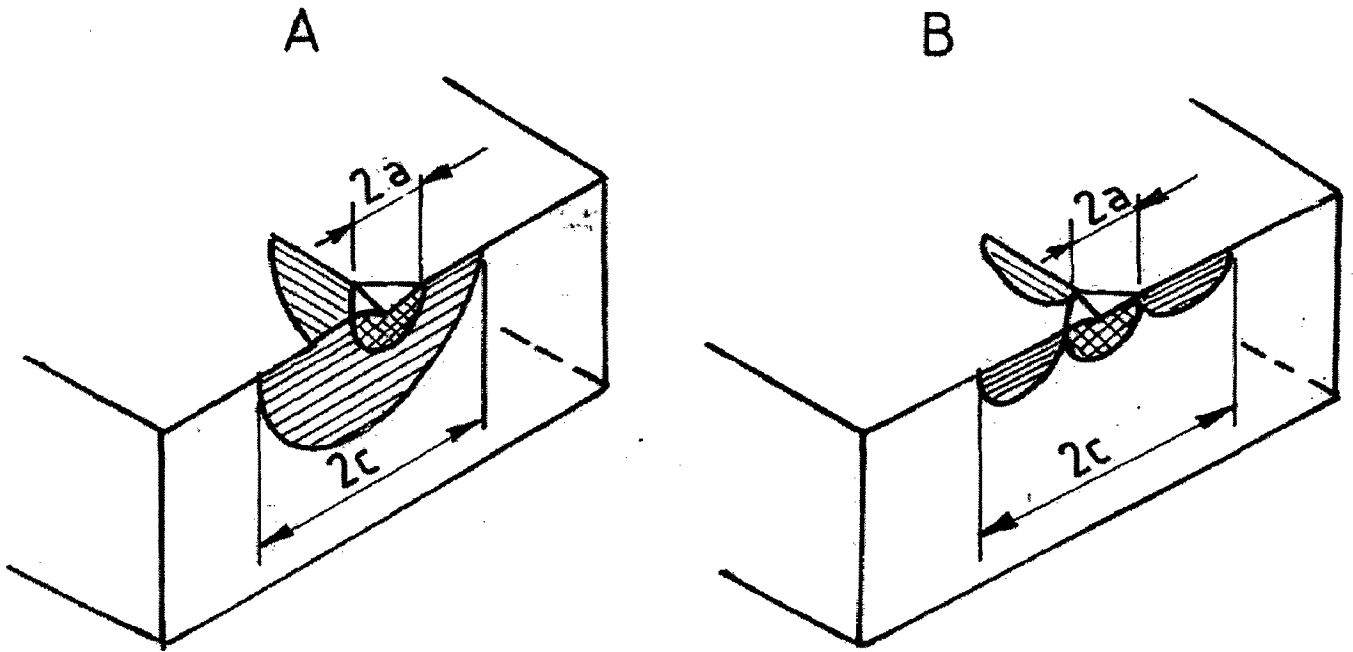


Fig. 3.14 Schematic illustration of indentation induced cracks in ceramics formed at different load levels (A) Median or half-penny (B) Palmqvist

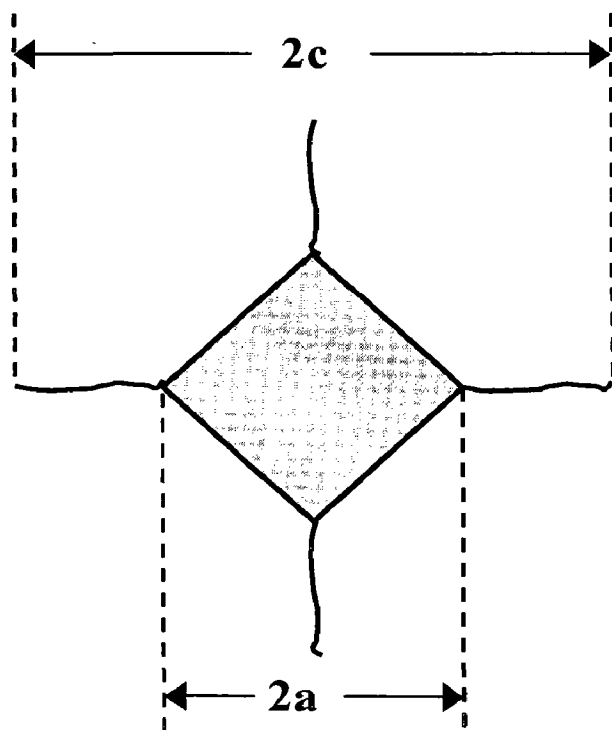


Fig. 3.15 Schematic showing a hardness indentation and Indentation cracks as viewed from the top on the surface of the specimen.

The above expression was first proposed by Evans and Charles (1976) and later modified by Marshall and Evans (1981). This is one of the most widely used relations to calculate  $K_{IC}$  from median cracks at Vickers indentation.

A graph was plotted between the load ( $P$ ) and the measured average crack length ( $c^{3/2}$ ), which revealed a straight line passing through the origin, satisfying the criterion  $P/c^{3/2} = \text{constant} \left[ = K_{IC}/0.026(E/H)^{2/5} \right]$ . The fracture toughness was estimated from the slope of the linear plot of  $P$  versus  $c^{3/2}$ . The measured values of Young's modulus and hardness were used to calculate the indentation fracture toughness.

### **Observations of crack interactions with reinforcing phases**

The indentation crack paths were observed using scanning electron microscope to have an understanding of the crack propagation and interactions with different reinforcing phases such as SiC particless and refractory metal foils. This led to an enhanced understanding of the toughening micro mechanisms. Imaging with polarized light optical microscopy allowed recording of the locations of the crack paths with respect to the grains and grain boundaries.

#### **3.3.2.3 Flexural Strength and Fracture Toughness**

In the present investigation, room temperature flexural strength and fracture toughness of various monolithic and composite materials were evaluated by a three-point bend test.

##### **(a) Preparation of bend test specimens**

The vacuum hot pressed  $\text{MoSi}_2$  based composite discs were sand blasted on both sides to remove the graphite layer. The discs were ground using different grades of diamond impregnated rotating discs up to a grit size of 200/230. The composite discs were then sectioned into rectangular bars to be used as specimens for three-point bend tests. The sectioning was performed by electro-discharge machining (EDM) using Supercut 734 Series 2000 Electra equipment except in case of laminated composite having a Nb foil coated with  $\text{Al}_2\text{O}_3$ . The laminated composite with  $\text{Al}_2\text{O}_3$  coated Nb foil was sectioned by using a high-speed precision diamond saw (ISOMET-

4000). In a few specimens, the specimen surfaces were metallographically polished using 15  $\mu\text{m}$  and 9  $\mu\text{m}$  diamond paste, respectively. The four long edges of the specimens were rounded off with a radius of  $0.15 \pm 0.05$  mm. The flexural strength is quite sensitive to surface finish and edge quality of the specimens. Fig. 3.16 is a schematic showing the various steps in the preparation of three-point bend test specimens for the measurement of flexural strength and fracture toughness of the composites.

### **(b) Measurement of flexural strength**

Flexural strength could be defined as a measure of the ultimate strength of a specified beam in bending. For brittle materials, tensile strength tests at room temperature are very rarely used. It would be more usual to employ tests in which one part of the specimen is subjected to tension during loading, and other to compression. The three-point (or four-point) bending tests data are the most frequently quoted strength data in case of non-ductile materials. Tensile strength testing methods are rare and could be carried out only in a few laboratories (Dusza and Sajgalik, 1995) known worldwide. The problems encountered in tensile strength testing of ceramics included large specimen sizes, expensive machining, expensive fixturing, elaborate instrumentation, slow generation of data and requirement of dedicated test frames and operators with high levels of skills in mechanics and electro-mechanical instrumentation. Grips and test methodology are not yet developed fully (Larsen and Stuchly, 1990).

Figure 3.17 exhibits a typical stress variation curve through the thickness and along the length of a three-point bend test specimen. The stress distribution, arising within the material, varied linearly from tensile (at the convex face) to compressive (at the concave face) stress. The stress value was zero at the neutral axis of the beam. Furthermore, the stress depended on the position along the length of the beam. Between the lower support points the stress increased linearly, reaching maximum under the upper support (Dusza and Sajgalik, 1995).



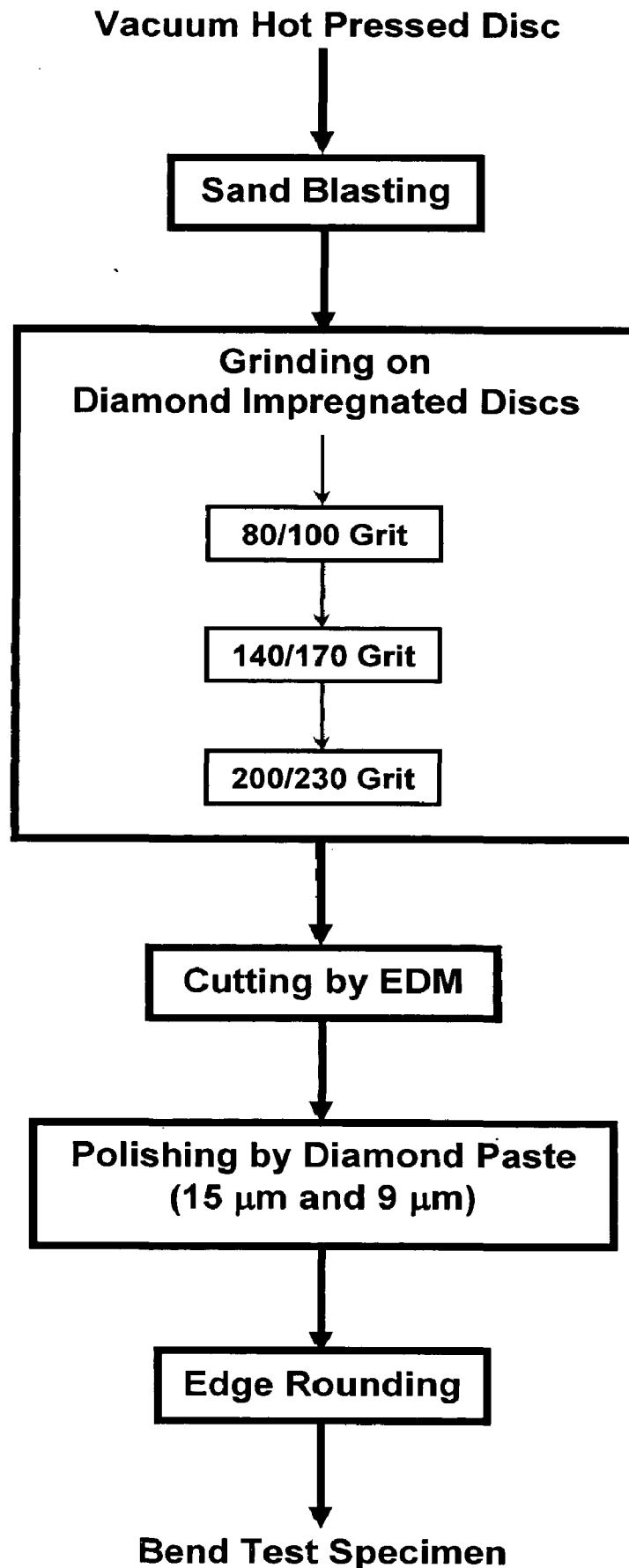


Fig. 3.16 The various steps adopted in the preparation of three-point bend test specimens from the vacuum hot pressed composite discs.

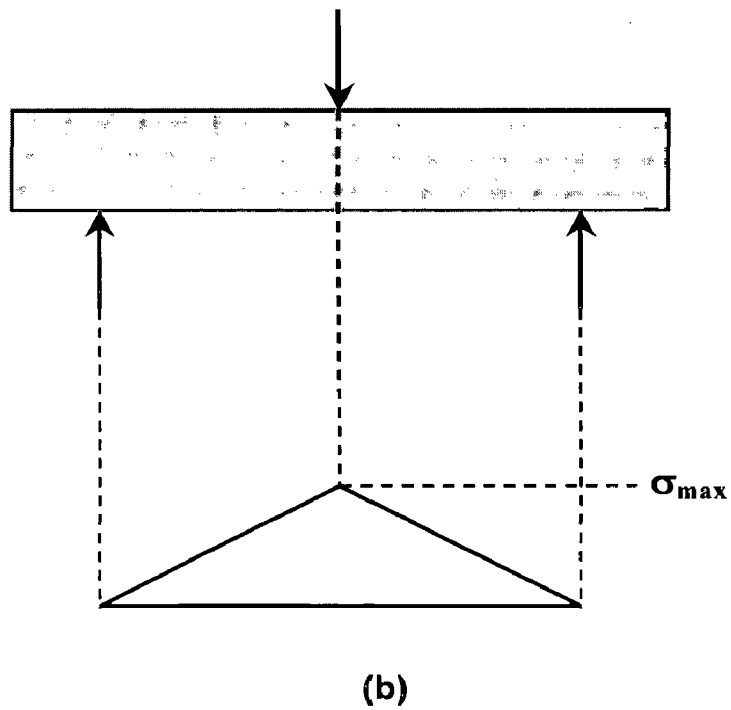
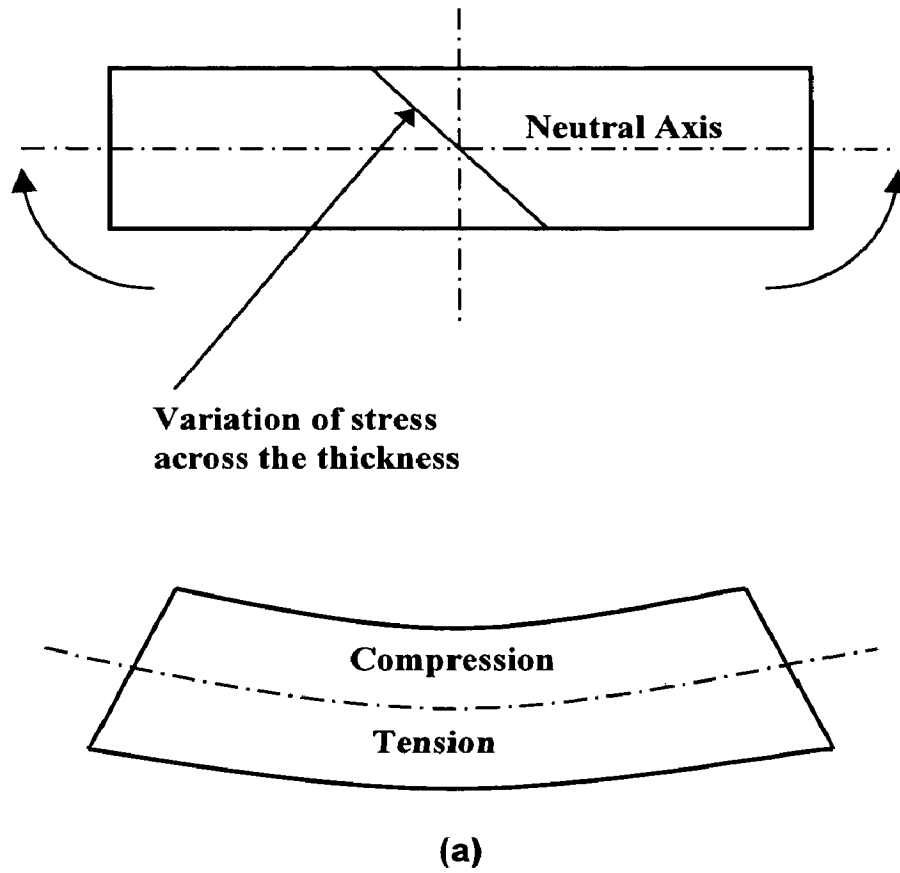


Fig. 3.17

Variation in stress in a three-point bend flexural test specimen (a) through the thickness and (b) along the specimen length.

There were no standard specimen types or test methods to evaluate the flexural strength of the advanced ceramic matrix composites except ASTM Standard C1161-94 (Re-approved 1996) and ASTM Standard C1341-97. The former could be applied for an isotropic and homogeneous as well as linearly elastic material; while the latter could be used only for continuous fiber reinforced ceramic matrix composites (1-D, 2-D, 3-D). The most important parameter in designing the geometry of a three-point (or four-point) bend test specimen was its span-to-depth ( $L/d$ ) ratio. A high  $L/d$  ratio was preferred to suppress the chances of test specimen failing in shear. Figure 3.18 exhibits schematically, the relationship between failure load vs. span length for a three-point bend specimen failing in flexure mode as well as in shear mode. It shows that the span length should be greater than the critical span length,  $L_c$  for a given material to ensure the specimen to fail in tension (to suppress the shear failure). In other words,  $L/d$  ratio of the specimen should be large enough. Typically, ceramic materials fail in shear when  $L/d < 5$  (Chawla, 1993).

Different researchers employed a variety of non-standardized specimen sizes and geometries. Gac and Petrovic (1985) and Gibbs et al (1987) used  $L/d$  ratio of 5.25, while Carter and Hurley (1987) used  $L/d$  ratio of 8 in carrying out the flexural strength testing of MoSi<sub>2</sub> based composites. Alman et al (1992), Alman and Stoloff (1992, 1994) used a cylindrical bar with a  $L/d$  ratio of 4 ( $d$  is the diameter of the specimen) in carrying out the three-point bend test to evaluate the flexural properties of Nb particless and Nb wire reinforced MoSi<sub>2</sub> matrix composites.

In the present investigation, the flexural strength of the composites was measured using a three-point bend test specimen of the dimensions as span ( $L$ ) = 40 mm, depth ( $d$ ) = 5 mm and width ( $b$ ) = 5 mm. The  $L/d$  ratio was kept as 8 and the minimum length of the specimen was kept as 45 mm. The flexural strength of the laminated composites was measured in crack arrester as well as crack divider modes as shown schematically in Fig. 3.19.

A minimum of 5 specimens were tested for each type of composite to develop an indication of material properties. The tests were carried out on a screw driven

Instron 1185 machine. The crosshead speed was kept 0.5 mm/min. The crosshead speed was so chosen that the strain rate upon the specimen was of the order of  $1 \times 10^{-4}$ /s.

$$\dot{\varepsilon} = \frac{6ds}{L^2} \quad (3.10)$$

where,  $d$  is the depth of the specimen,  $s$  is the crosshead speed and  $L$  is the span.

The flexural strength,  $S$  for a specimen tested in three-point bend would be given by:

$$S = \frac{3}{2} \frac{PL}{bd^2} \quad (\text{ASTM Standard C1161-94}) \quad (3.11)$$

where,  $P$  is the peak or breaking load.  $P$  is the load at which fracture occurs. Fracture was identified by the breakage of the test bar into two or more pieces or the load drop by at least 20 % from the maximum load without the sample clearly separating.

### **(c) Measurement of fracture toughness**

There were no standard specimen types or testing procedures for determining the fracture toughness of laminated composite materials consisting of alternate layers of brittle ceramics and ductile metals. Although numerous testing methods were available for structural monolithic ceramics (Dusza and Sajgalik, 1995), most of the test methods remain non-standardized, yet.

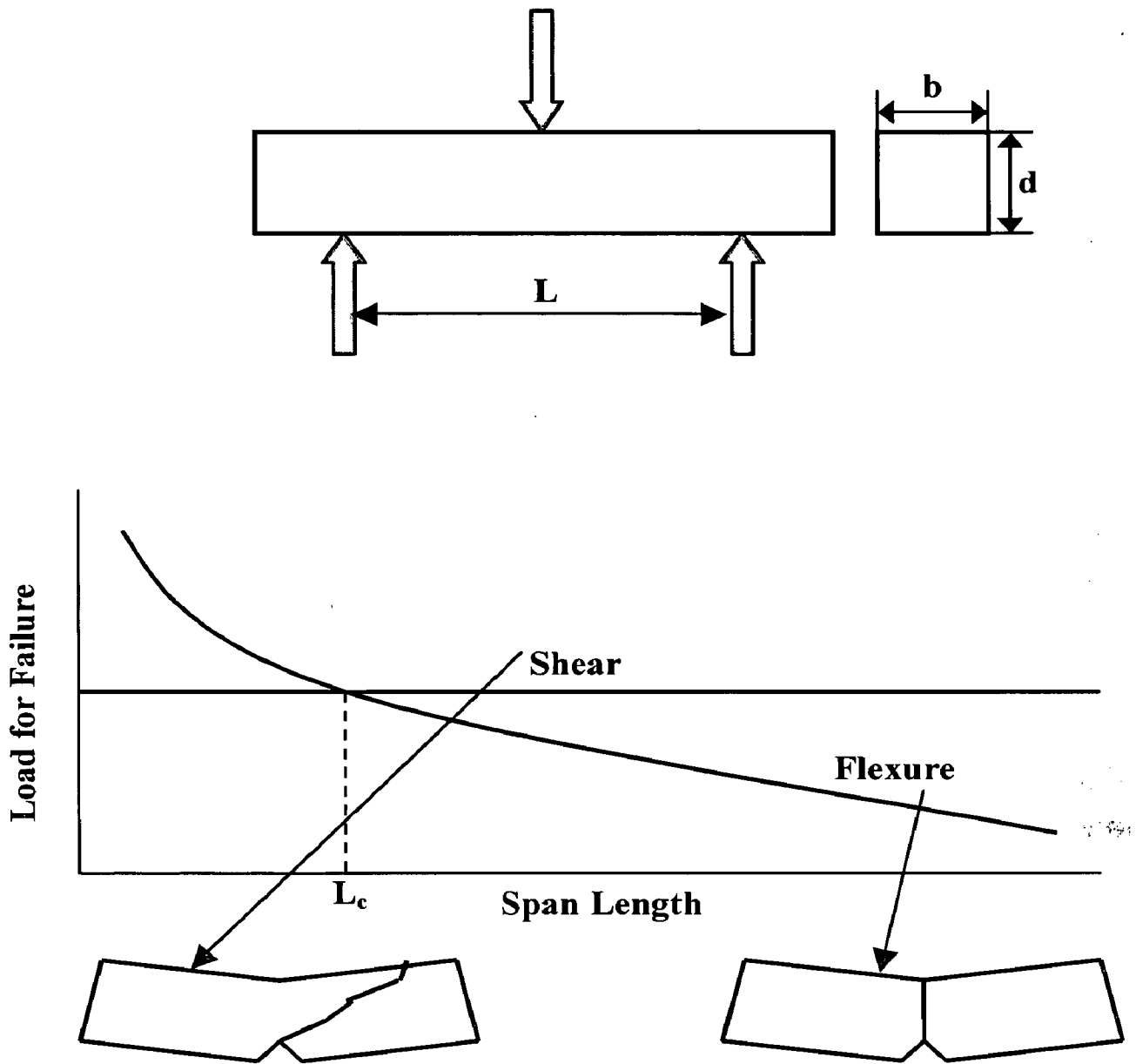


Fig. 3.18 Schematic showing failure load vs. span length for a three-point bend test specimen and conditions for failure in flexure and shear modes.

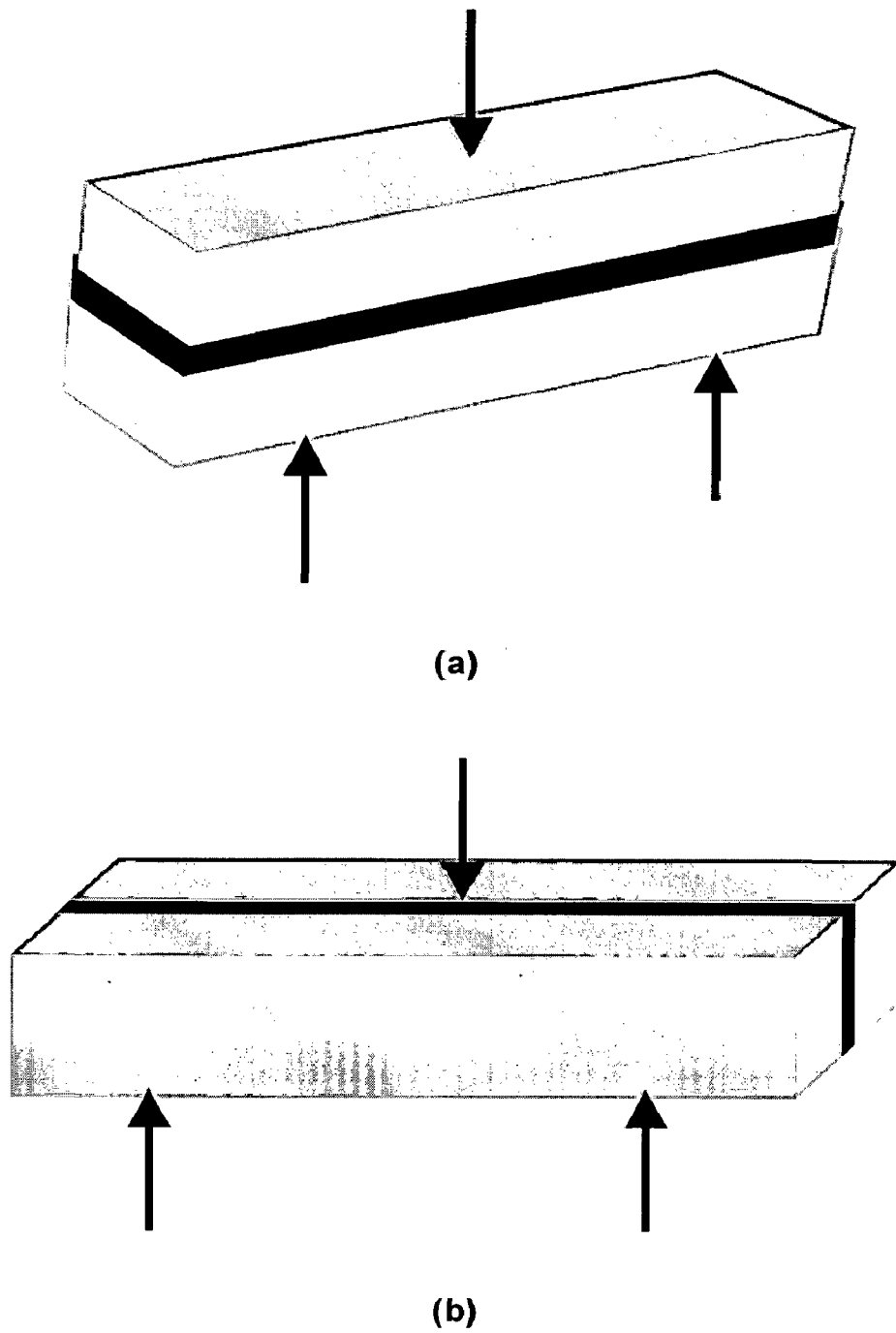


Fig. 3.19

Schematic illustration of loading modes in a three-point bend test of a laminated composite (a) crack arrester mode (b) crack divider mode.

Different workers used both bend specimens as well as the compact tension specimens to measure the fracture toughness of MoSi<sub>2</sub> based materials. Gac and Petrovic (1985), Gibbs et al (1987), Xiao et al (1990, 1991), Xiao and Abbaschian (1992<sup>a</sup>, 1992<sup>b</sup>), Chen et al (1994<sup>a</sup>), Shaw and Abbaschian (1994) and Soboyejo et al (1996) used bend specimens with a variety of notch configurations like single edge, double edge and chevron notches. The  $L/d$  ratio was kept as 4 in most of the cases. Fatigue pre-cracking was seldom employed. Venkateshwar Rao et al (1992<sup>a</sup>, 1992<sup>b</sup>) and Badrinarayanan et al (1996) used disc shaped compact tension DC(T) specimens to measure the fracture toughness of MoSi<sub>2</sub> matrix composites reinforced with ductile and brittle particless.

However, bend tests are most convenient with macro-notch for ease of machining. In the present investigation, the fracture toughness of the composites was evaluated by single edge notched beam (SENB) test method using a three-point bend test specimen of the following dimensions: span ( $S$ ) = 40 mm, width ( $W$ ) = 5 mm and thickness ( $B$ ) = 5 mm.

The minimum length of the specimen was kept as 45 mm. The toughness was measured in crack arrester as well as crack divider modes. The schematic diagrams of the test specimens notched in crack arrester and crack divider modes are shown in Fig. 3.20(a) and 3.20(b) respectively.

The fracture toughness,  $K_{IC}$  is given by:

$$K_{IC} = \frac{P_c S}{BW^{\frac{3}{2}}} f(\alpha) \quad (3.12)$$

where,  $\alpha = \frac{a}{W}$ . In the present case,  $P_c = P_{max}$ . Therefore,

$$K_{IC} = \frac{P_{max} S}{BW^{\frac{3}{2}}} f(\alpha) \quad (3.13)$$

The above can also be written as:

$$K_{IC} = \frac{P_{\max}}{BW^{\frac{1}{2}}} \frac{S}{W} f(\alpha) = \frac{P_{\max}}{BW^{\frac{1}{2}}} Y(\alpha) \quad (3.14)$$

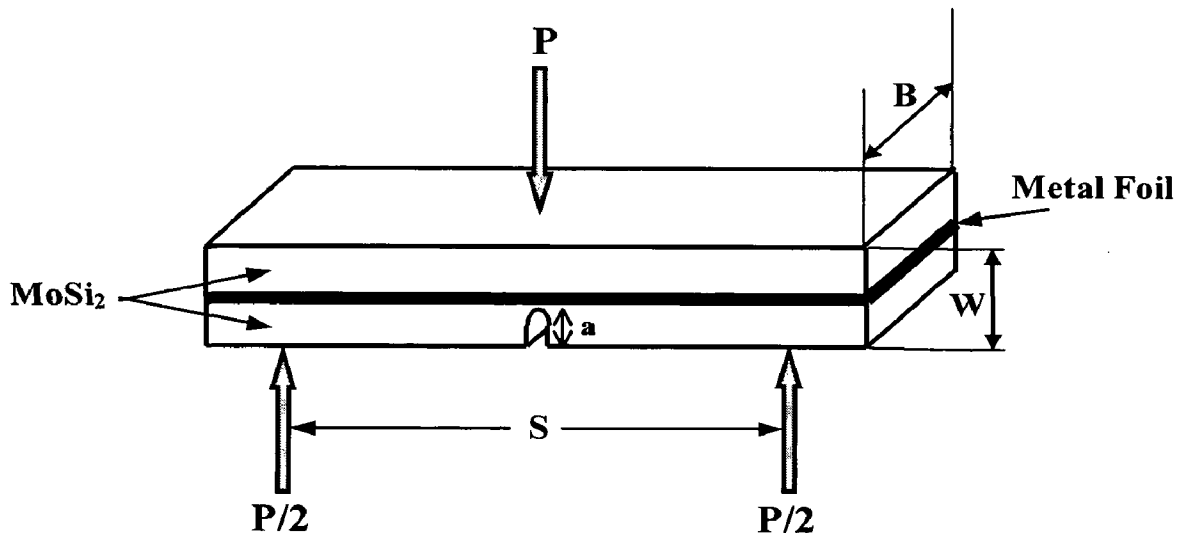
where,  $Y(\alpha) = \frac{S}{W} f(\alpha)$  is known as a shape factor.  $f(\alpha)$  depends upon the span / width ratio, i.e.,  $\frac{S}{W}$  ratio of the test specimen. In the present case,  $\frac{S}{W} = 8$  for which  $f(\alpha)$  is given by (Murakami et al, 1987):

$$f(\alpha) = \frac{3(\pi\alpha)^{\frac{1}{2}}}{2} (1.107 - 1.552\alpha + 7.71\alpha^2 - 13.55\alpha^3 + 14.25\alpha^4) \quad (3.15)$$

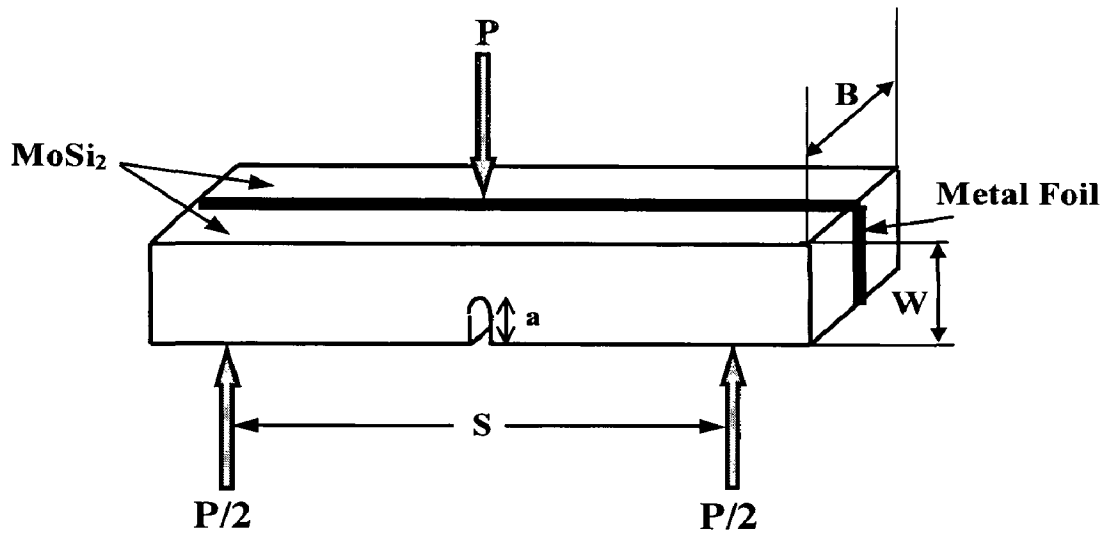
In principle, any notch or crack geometry could be used for fracture toughness measurements, provided that the shape factor  $f(\alpha)$  is known (Sakai and Ichikawa 1992, Sakai and Bradt 1993). Sakai and Ichikawa (1992) and Sakai and Bradt (1993) also observed that,  $\alpha$  should be less than 0.6 for all SENB specimens, because of the steep increase in  $f(\alpha)$  when  $\alpha > 0.6$ , resulting in appreciable errors in calculating  $f(\alpha)$  from the observed crack length. In the present case, notch depth,  $a$  was maintained between  $0.4W$  and  $0.45W$ , and was machined using a linear precision diamond saw. Fatigue pre-cracking was not performed.

Because natural cracks, such as fatigue cracks, are considered to be the sharpest cracks that could be produced in the laboratory, cyclic fatigue cracking ahead of a sawed or machined notch was conventionally applied to metals. However, because of the very limited extent of plastic deformation at the notch tip in brittle materials, metallurgical cyclic fatigue technique was considered inconvenient for ceramics (Sakai and Bradt, 1993). It was desirable to avoid pre-cracking procedures for straight through notches for ceramic materials. Schwartz (1992) also reported earlier that fracture toughness of fatigue pre-cracked and non pre-cracked specimens of  $\text{MoSi}_2$  materials did not show any significant difference.





(a)



(b)

Fig. 3.20 Schematic diagrams of the SENB fracture toughness test specimens (a) crack arrester mode (b) crack divider mode.

Because of very limited plasticity of most ceramics, a specimen thickness as low as 2 mm might be sufficient for the usual engineering ceramic materials. Thickness ( $B$ ) and width ( $W$ ) should be much larger than the grain size of the material. According to Sakai and Bradt (1993),  $B \geq 50 \times$  grain size. Dusza and Sajgalik (1995) also reported that thickness ( $B$ ) of the specimen would have only a negligible effect on the measured  $K_{IC}$  values.

The fracture toughness was calculated from the peak load,  $P_{max}$  of the load-displacement curve and reported in terms of  $K_{max}$ .

**(d) Measurement of work of fracture**

Various processes for toughening brittle ceramics resulted in extremely complex fracture processes and mechanisms. As a consequence, differences in the conventional fracture mechanics test methods (stress intensity factor based) might yield significant differences in the experimentally determined fracture toughness values,  $K_{IC}$ .

The researchers used different measures of energy derived fracture toughness for advanced ceramic matrix composites. One convenient term is the “work of fracture”. The work of fracture,  $\gamma_{WOF}$  (Sakai and Ichikawa, 1992) is defined as “the total energy consumed to produce a unit area of fracture surface”. It is one of the most useful non-linear toughness characterization parameters (Nakayama 1965, Tattersall and Tappin, 1966). It was widely applied to characterize the crack growth resistance for extremely complicated non-linear fracture processes (Sakai and Bradt, 1993). The work of fracture could be expressed by:

$$\gamma_{WOF} = \frac{W_{WOF}}{2S} \quad (3.16)$$

where,  $W_{WOF}$  is the total work done on the test specimen to break it into two pieces and  $2S$  is the resultant total fracture surface area (Nakayama 1965, Tattersall and Tappin 1966).

The key advantages in this equation are:

- (i) None of the assumptions of linearity for the test specimen are made for the fracture processes.
- (ii) It is possible to calculate  $\gamma_{WOF}$  in absence of any information on the (a) stress intensity factor,  $K_I$  (b) notch tip sharpness and (c) notch front geometry.

It is very useful in the analysis of very complicated fractures. Tattersall and Tappin (1966) analyzed the work of fracture and observed that, for a wide variety of materials, the work of fracture increases as the toughness increases.

In the present investigation, the work of fracture of the composites was calculated from the area measured under the load-displacement curves.

#### **3.3.2.4 Measurement of Micro-hardness**

Micro-hardness tests were conducted to determine the hardness over very small areas. In the present investigation, micro-hardness was measured for interfacial reaction products formed during the processing of different laminated composites. A MMT-3 MATSUZWA micro-hardness testing equipment having a load capacity of 5 kg was used for this purpose. Micro-hardness measurements were made on metallographically polished specimens with a Vickers diamond indenter using a load in the range of 50 g to 300 g for 15 s. The variation in applied load for different laminated composites was necessitated depending upon the thickness of the interfacial reaction layer. The applied load was selected to ensure that the size of the indentation mark generated falls within the interfacial reaction zone and would not overlap with either  $MoSi_2$  matrix or the refractory metal foil.

#### **3.3.2.5 Fractography**

The fracture surfaces of all the specimens tested for flexural strength, fracture toughness and tensile properties were examined using the scanning electron microscope to study the mode of failure. The samples were placed in a beaker containing acetone and ultrasonically cleaned for a few minutes before studying the fracture surfaces.

Some of the three-point bend specimens were unloaded at different load levels before completion of the test to avoid complete separation in two pieces. Such unbroken specimens were observed under the stereomicroscope. Stereomicroscope provided

depth perception. Samples were viewed under stereomicroscope up to a maximum magnification of 50x. The unbroken specimens were also viewed in scanning electron microscope to clearly establish the macroscopic crack path behaviour.

---

## ANALYSIS OF RESIDUAL THERMAL STRESSES

---

### 4.1 INTRODUCTION

Residual stresses are elastic stresses that remain in a body after all external loads have been removed. The most important source of residual stresses in ceramic matrix composites is the thermal mismatch between the components. Thermal stresses arise when there is a “constraint” on free dimensional change of a body (Chawla, 1987). In the absence of this constraint, the body can experience free thermal strains without any accompanying thermal stresses. The constraint may result due to a temperature gradient, crystal structure anisotropy (for example, non-cubic structures), phase transformations resulting in a volume change and a composite material made of components having different coefficients of thermal expansion.

Thermal stresses are very important in all composite materials, but particularly so in ceramic matrix composites because a ceramic matrix will generally have a very low strain to fracture. Thermal strain is given by  $\Delta\alpha\Delta T$ . In ceramic matrix composites, the high processing temperatures involved make the problem of residual stress particularly severe. During cooling from the high processing temperatures, a high magnitude of shrinkage stresses may result because of the thermal mismatch between the reinforcement and the matrix. Thermal stresses generated depend on the reinforcement geometry, reinforcement volume fraction, thermal mismatch ( $\Delta\alpha = \alpha_r - \alpha_m$ ), the temperature interval ( $T_{final} - T_{initial}$ ), and modulus ratio,

$E_r/E_m$ , where the subscripts r and m denote the reinforcement and the matrix, respectively.

## 4.2 RESIDUAL THERMAL STRESSES IN PURE MoSi<sub>2</sub>

The crystal structure of MoSi<sub>2</sub> is body-centered tetragonal (C11<sub>b</sub>) as shown in Fig. 1.1. The large axial ratio ( $c/a = 2.45$ ) is expected to generate anisotropic stresses within individual grains after cooling from the processing temperature (Wade and Petrovic, 1992<sup>a</sup>). Moreover, anisotropy in coefficient of thermal expansion values along a-axis and c-axis is also expected to result in residual thermal stresses in individual grains.

The maximum possible number of independent coefficients of thermal expansion (CTEs) in any crystal system is six. In different crystal systems, depending upon the symmetry, the number of independent CTEs is further reduced as shown in Table 4.1 (Chawla, 1993).

The independent coefficients of thermal expansion of MoSi<sub>2</sub> are depicted schematically in Fig. 4.1.

In MoSi<sub>2</sub> (Berkowitz, 1966):

$$\alpha_1 = \alpha_2 = \alpha_{\perp} = 8.25 \times 10^{-6}/\text{K}$$

$$\alpha_3 = \alpha_{\parallel} = 9.05 \times 10^{-6}/\text{K} \text{ (parallel to c-axis)}$$

The large difference in coefficient of thermal expansion values along a-axis and c-axis is expected to generate residual thermal stresses in individual grains upon cooling from processing temperature. With increasing grain size, MoSi<sub>2</sub> internal stresses are believed to increase. Berkowitz et al (1970) estimated a residual stress at room temperature as 84 MPa in a polycrystalline MoSi<sub>2</sub> having a grain size of 80  $\mu\text{m}$ .

Table 4.1 No. of independent coefficients of thermal expansion in various crystal systems.

Crystal Structure	Number of Components	Components
Triclinic	6	$\alpha_1, \alpha_2, \alpha_3, \alpha_4, \alpha_5, \alpha_6$
Tetragonal	2	$\alpha_1 = \alpha_2 = \alpha_{\perp}$ $\alpha_3 = \alpha_{\parallel}$
Cubic	1	$\alpha_1 = \alpha_2 = \alpha_3 = \alpha$

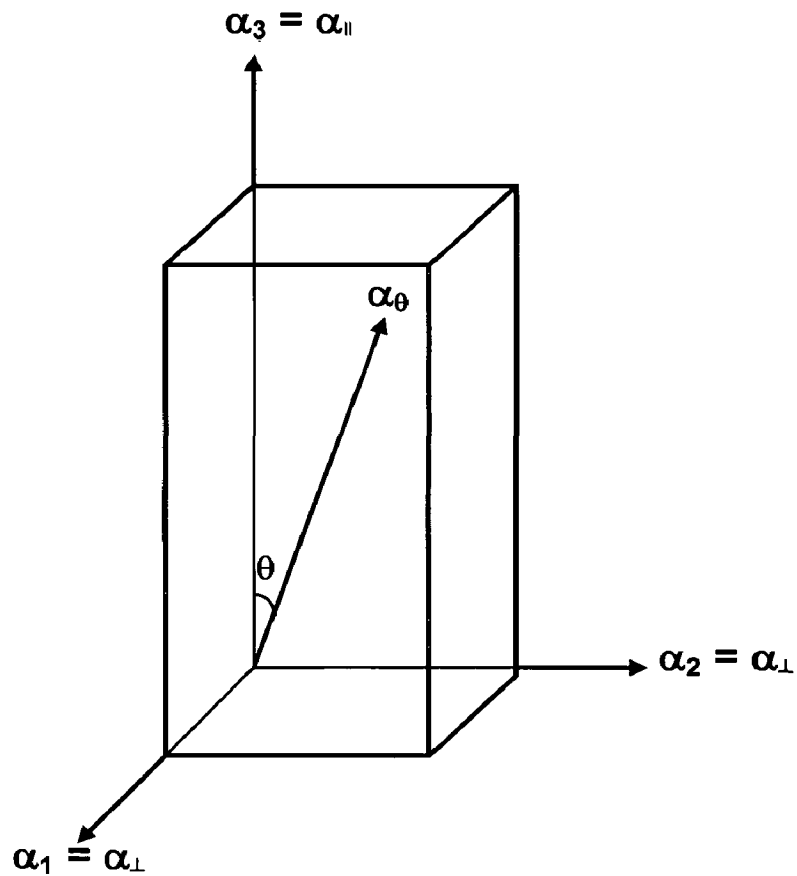


Fig. 4.1 Thermal expansion coefficients in tetragonal  $\text{MoSi}_2$ .

### 4.2.1 Effect of SiO<sub>2</sub>

The powders of MoSi<sub>2</sub> that are commercially available carry with them significant amounts of SiO<sub>2</sub> (Hardwick et al, 1992). SiO<sub>2</sub> phase is found mainly at grain boundaries but it is present inside MoSi<sub>2</sub> grains also. Apart from SiO<sub>2</sub> in starting MoSi<sub>2</sub> powders, the additional oxygen is picked up during hot pressing of MoSi<sub>2</sub> powders. Maloy et al (1991) reported the oxygen content in their hot pressed MoSi<sub>2</sub> as 2.8 wt% (~ 14 Vol% SiO<sub>2</sub>), while their starting MoSi<sub>2</sub> powder contained only 0.2 wt% SiO<sub>2</sub>. MoSi<sub>2</sub> reacts with oxygen during processing, forming vitreous SiO<sub>2</sub> on the surface of MoSi<sub>2</sub> powders. It forms on the surface of almost all powder particles. The SiO<sub>2</sub> on the surface of the powder particles ends up at grain boundaries in the microstructure after consolidation. The presence of vitreous SiO<sub>2</sub> within MoSi<sub>2</sub> grains and at grain boundaries is likely to increase further the internal stresses in MoSi<sub>2</sub> due to a very low coefficient of thermal expansion of SiO<sub>2</sub>, placing MoSi<sub>2</sub> grains in nonuniform tension after cooling (Wade and Petrovic, 1992<sup>a</sup>).

### 4.3 RESIDUAL THERMAL STRESSES IN MoSi<sub>2</sub> - SiC PARTICULATE COMPOSITES

Thermal stresses are internal stresses that arise when there exists a “constraint” on “free contraction” of a body upon cooling from high processing temperatures. In the case of a particulate composite, an interfacial pressure can develop during cooling that is similar to that obtained on embedding a spherical ball of radius,  $r + \Delta r$ , in a spherical hole of radius,  $r$ . The constraint results from thermal expansion mismatch  $\Delta\text{CTE}$  (or  $\Delta\alpha$ ) between matrix and the reinforcement (Chawla, 1987).

$$\text{Thermal strain} = \Delta\alpha \times \Delta T$$

$$\Delta\alpha = \alpha_r - \alpha_m$$

$\alpha_r$  = coefficient of thermal expansion of reinforcement particles

$\alpha_m$  = coefficient of thermal expansion of matrix

$$\Delta T = T_f - T_i \text{ during cooling}$$

$T_f$  = room temperature

$T_i$  = processing temperature

$\Delta T$  is always negative.



In the present case of SiC particles reinforced MoSi<sub>2</sub> matrix composite,  $\alpha_m > \alpha_r$ , i.e., on cooling, matrix would tend to contract more than the reinforcement, putting the reinforcement in compression.

Consider a particulate composite consisting of small ceramic particles distributed in a ceramic matrix. If we regard this composite as an assembly of elastic spheres of uniform size embedded in an infinite elastic continuum, then it can be shown from the theory of elasticity (Timoshenko and Goodier, 1951) that an axially symmetrical stress distribution will result around each particle. Fig. 4.2 shows a schematic of such a particle reinforced composite in which a central SiC particle of radius,  $a$ , is surrounded by its associated spherical shell of MoSi<sub>2</sub> matrix of radius,  $b$ . The SiC particle will be under a uniform radial pressure,  $P$ , while the MoSi<sub>2</sub> matrix will have two unequal stress components:

- (i) The radial stress in the matrix will be 'compressive'.
- (ii) The tangential (hoop) stress in the matrix will be tensile.

Chawla (1993) obtained the analytical expressions for residual thermal stresses by applying the following boundary conditions:

- (i) The radial stress at the interface ( $r = a$ ) is the interfacial pressure,  $P$ .
- (ii) The radial stress vanishes at the free surface (i.e., at  $r = b$ ).

The analytical expression for radial pressure,  $P$  is given by

$$P = \frac{(\alpha_m - \alpha_r)\Delta T}{\left[ \frac{0.5(1 + \nu_m) + (1 - 2\nu_m)V_r}{E_m(1 - V_r)} + \frac{1 - 2\nu_r}{E_r} \right]} \quad (4.1)$$

where  $E$  is the elastic modulus,  $\nu$  is the Poisson's ratio and  $V_r$  is the volume fraction of the reinforcement particles. Suffixes  $r$  and  $m$  stand for reinforcement and the matrix, respectively.

The expressions for the radial stress,  $\sigma_r$ , and the tangential stress,  $\sigma_\theta$  in the matrix as obtained by Chawla (1993) are given by

$$\sigma_r = \frac{P}{(1 - V_r)} \left[ \frac{a^3}{r^3} - V_r \right] \quad (4.2)$$

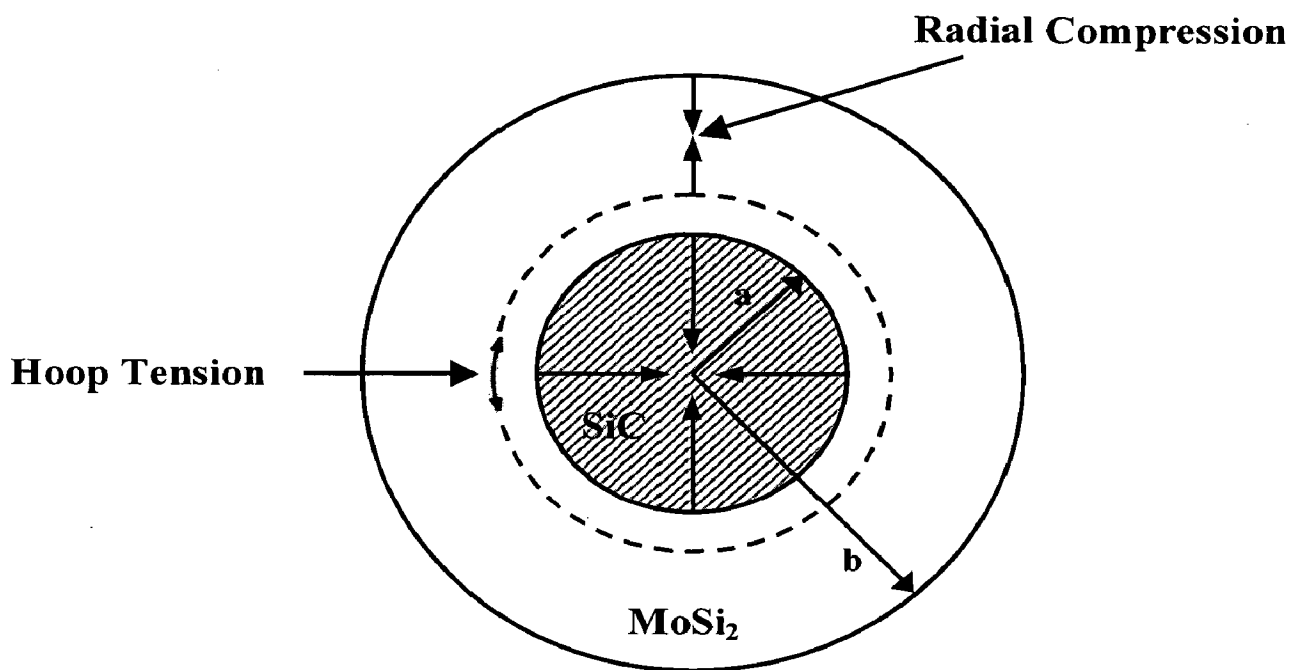


Fig. 4.2 Residual thermal stresses in a particle reinforced composite consisting of a SiC particle of radius,  $a$ , embedded in a MoSi<sub>2</sub> matrix of radius,  $b$ .

$$\sigma_{\theta} = -\frac{P}{(1-V_r)} \left[ \frac{a^3}{2r^3} + V_r \right] \quad (4.3)$$

where  $r$  is the distance from the center of the SiC particle and  $V_r = \left(\frac{a}{b}\right)^3$ .

### 4.3.1 Residual Stresses in SiC Particles

MoSi<sub>2</sub> due to its tetragonal crystal structure has two independent coefficients of thermal expansion,  $\alpha_1 = \alpha_2 = \alpha_{\perp}$  and  $\alpha_3 = \alpha_{\parallel}$  (parallel to c-axis). Referring to Fig. 4.1, in any arbitrary direction [hkl], if its direction cosines are  $n_1$ ,  $n_2$  and  $n_3$ , the  $\alpha_{hkl}$  in that direction can be written as (Chawla 1993)

$$\alpha_{hkl} = n_1^2 \alpha_1 + n_2^2 \alpha_2 + n_3^2 \alpha_3$$

where  $n_1^2 + n_2^2 + n_3^2 = 1$ . In MoSi<sub>2</sub>,

$$\alpha_{hkl} = (n_1^2 + n_2^2) \alpha_{\perp} + n_3^2 \alpha_{\parallel} = (1 - n_3^2) \alpha_{\perp} + n_3^2 \alpha_{\parallel} = \alpha_{\perp} + (\alpha_{\parallel} - \alpha_{\perp}) n_3^2$$

$n_3 = \cos \theta$ , where  $\theta$  is the angle between the direction [hkl] and c-axis. Therefore,

$$\alpha_{hkl} = \alpha_{\perp} + (\alpha_{\parallel} - \alpha_{\perp}) \cos^2 \theta$$

At  $\theta = 90^\circ$   $\alpha = \alpha_{\perp} = 8.25 \times 10^{-6}/K$  (minimum value of  $\alpha$  along a-axis)

$\theta = 0^\circ$   $\alpha = \alpha_{\parallel} = 9.05 \times 10^{-6}/K$  (maximum value of  $\alpha$  along c-axis)

$\theta = 45^\circ$   $\alpha = \alpha_{45} = 8.65 \times 10^{-6}/K$

In all other directions ( $0 < \theta < 90$ ),  $\alpha$  will vary from  $8.25 \times 10^{-6}/K$  to  $9.05 \times 10^{-6}/K$ . Assuming that grains are oriented randomly in a polycrystalline MoSi<sub>2</sub>, it is probably most appropriate to take an average of the values along three axial directions as the coefficient of thermal expansion of polycrystalline MoSi<sub>2</sub>. Therefore,

$$\alpha_{MoSi_2} = (\alpha_{\perp} + \alpha_{\perp} + \alpha_{\parallel}) / 3 = 8.52 \times 10^{-6}/K$$

SiC used in the present study was of  $\beta$ -type having a cubic crystal structure. In cubic structures,  $\alpha_1 = \alpha_2 = \alpha_3 = \alpha$ . Therefore, coefficient of thermal expansion (CTE) of polycrystalline  $\beta$ -SiC,  $\alpha_{SiC} = 4.78 \times 10^{-6}/K$ .

The values of other properties for the materials and processing parameters used in the present composite system are given in Table 4.2.

Table 4.2 Material properties and processing parameters for MoSi<sub>2</sub> / SiC particulate composite.

Material	$\alpha$ ( $\times 10^{-6}/K$ )	$E$ (GPa)	$\nu$	$V_r$	$\Delta T$ (K)
MoSi <sub>2</sub>	8.52	440	0.15	0.2	-1570
SiC	4.78	420	0.14		

Substituting the above values in equation (4.1) yields a residual thermal stress in SiC particle,  $P = 1568$  MPa (compressive). SiC particle will be under a uniform compressive stress,  $P$ .  $P$  is constant and does not vary from  $r = 0$  to  $r = a$ .

(Note: In literature, researchers have used different expressions to estimate the radial stress in the particle. Some of them are:

1. For a 2-dimensional problem in plane strain consisting of a circular reinforcement particle embedded in an infinite matrix, the particle experiences a radial stress,  $P$ , which is given by (Corten, 1967):

$$P = \frac{(\alpha_r - \alpha_m)\Delta T}{\frac{(1+\nu_r)}{E_r} + \frac{(1+\nu_m)}{E_m}}$$

2. Timoshenko and Goodier (1959), Selsing (1961) and Venkateswara Rao et al (1992<sup>b</sup>) have used the following expression to calculate the radial stress:

$$P = \frac{\Delta\alpha\Delta T}{\frac{(1-2\nu_r)}{E_r} + \frac{(1+\nu_m)}{2E_m}}$$

However, the above expressions seem to be less vigorous as these do not include the term,  $V_r$ , i.e., the effect of volume fraction of the reinforcement particles.)

## 4.3.2 Residual Stresses in MoSi<sub>2</sub> Matrix

### 4.3.2.1 The Radial Stress, $\sigma_r$

The radial stress in MoSi<sub>2</sub> matrix is compressive and vary with distance,  $r$ . At particle / matrix interface ( $r = a$ ),  $\sigma_r = P$  and at free surface located at  $r = b$ ,  $\sigma_r = 0$  (as per the boundary conditions).

$V_r = \left(\frac{a}{b}\right)^3$ . Therefore,

$$b = \frac{a}{(V_r)^{1/3}} \quad (4.4)$$

In the present study, the average particle size of SiC used was  $2 \mu\text{m}$  ( $a = 1 \mu\text{m}$ ) and  $V_r = 0.2$ . Substituting these values in equation 4.4 yields  $\sigma_r = 0$  at  $r = 1.7 \mu\text{m}$ . The variation of  $\sigma_r$  with distance  $r$  is schematically presented in Fig. 4.3. In Fig. 4.3,  $ab = 0.7 \mu\text{m}$ .

The radial compressive stress in  $\text{MoSi}_2$  matrix is maximum at particle / matrix interface. The stress decreases with increasing distance from the interface and falls off to zero at a distance of  $0.7 \mu\text{m}$  away from the particle / matrix interface.

#### 4.3.2.2 The Tangential (Hoop) Stress, $\sigma_\theta$

The tangential stress in the matrix also varies with distance,  $r$ . At  $r = a$  (particle / matrix interface), from equation 4.3

$$\sigma_\theta = -\frac{P}{(1-V_r)} \left[ \frac{1}{2} + V_r \right] = 0.875P = 1372 \text{ MPa (tensile)}.$$

At  $r = b$  (free surface), from equation 4.3

$$\sigma_\theta = -\frac{P}{(1-V_r)} \left[ \frac{1}{2} \frac{a^3}{b^3} + V_r \right] = -\frac{P}{(1-V_r)} \left[ \frac{1}{2} V_r + V_r \right] = -\frac{3}{2} \frac{PV_r}{(1-V_r)} = 0.375 P = 588 \text{ MPa (tensile)}$$

The above results reveal the following:

- (i) The tangential hoop stress,  $\sigma_\theta$  in  $\text{MoSi}_2$  matrix is tensile in nature.
- (ii)  $\sigma_\theta$  is maximum at particle / matrix interface.
- (iii)  $\sigma_\theta$  decreases with increasing  $r$ , but never reaches to a zero value inside  $\text{MoSi}_2$  matrix.

The graphical representation of the above results is shown schematically in Fig. 4.4. The tangential hoop stress in  $\text{MoSi}_2$  matrix has a non-zero value at the free surface.

### 4.3.5 Analysis of Residual Thermal Stresses by Finite Element Methods (FEM)

To check the validity of the analytical results, the problem was solved by finite element analysis using the NISA software package. The model considered for the analytical case assumes a spherical SiC particle of 1  $\mu\text{m}$  radius, embedded in a spherical MoSi<sub>2</sub> matrix with a volume fraction of the reinforcement particles as 0.2.

For the purpose of numerical analysis also, a spherical SiC particle of the same radius within a spherical matrix with the same volume fraction of the reinforcement particles was considered. However, due to a shortcoming of the FEM package used, it was not possible to model the shape of these two concentric spheres exactly as spherical. A certain degree of approximation was used in the model, which is shown in Fig. 4.5.

Essentially, instead of perfect geometrical spheres, the two entities (reinforcement and the matrix) of the model were constructed of small cubical elements as shown in the cross-sectional view in Fig. 4.5. In Fig. 4.5, the red elements represent the MoSi<sub>2</sub> matrix and the green elements represent the SiC particle. Due to this the surface of the model was not totally smooth and consisted of a number of small steps and sharp corners. The interface between the particle and matrix was assumed to be perfectly strong.

The variation of radial compressive stress with distance in the matrix as obtained by FEM analysis is graphically represented in Fig. 4.6. The stress distribution in the matrix is found to be similar with the analytical results as described in section 4.3.2.1, which says that the radial stress in the matrix is compressive and varies with the distance as per equation 4.2. The calculated stress values from equation 4.2 are also plotted in Fig. 4.6 for comparison with FEM results. These two plots are found to be in good agreement except that the stress values obtained from FEM analysis are slightly lower than the stress values calculated by analytical method.

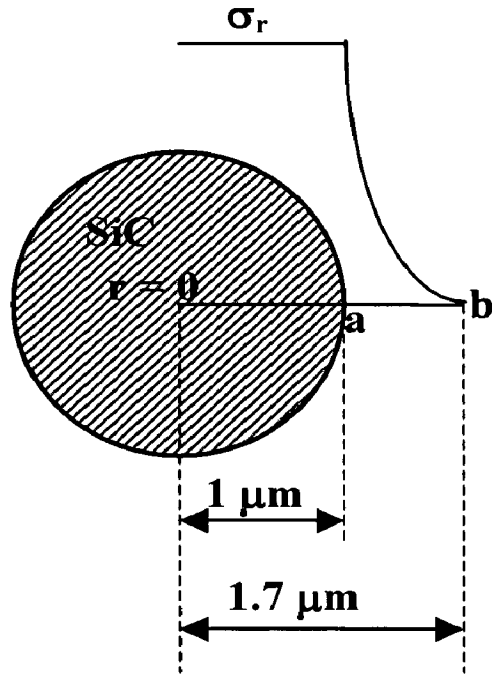


Fig. 4.3 The variation of radial stress,  $\sigma_r$ , with distance  $r$  in  $\text{MoSi}_2$  matrix.

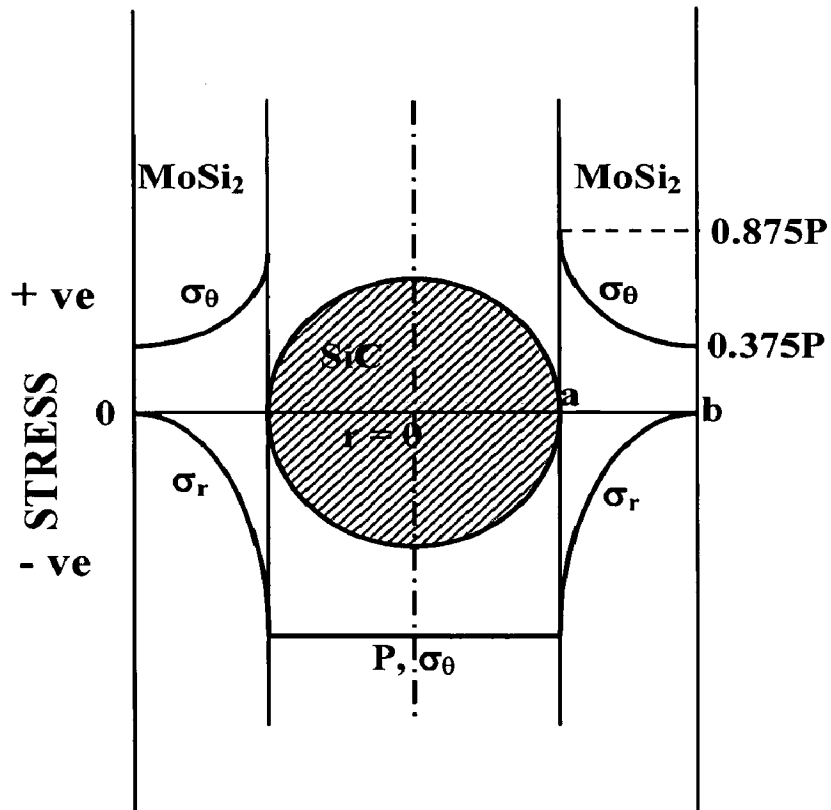


Fig. 4.4 Residual thermal stresses (radial,  $\sigma_r$  and tangential,  $\sigma_\theta$  components) in  $\text{MoSi}_2$  matrix varying with distance.

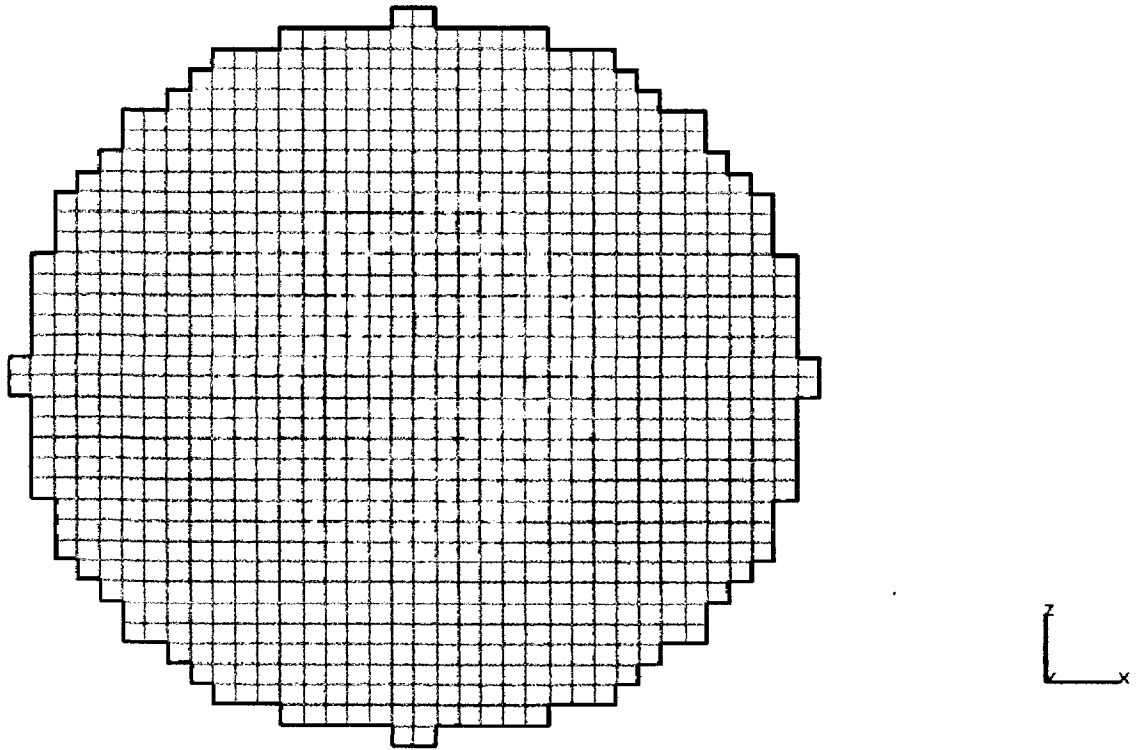


Fig. 4.5 Cross-sectional view of the model of composite used for the FEM analysis (Green – SiC particle and Red – MoSi<sub>2</sub> matrix).

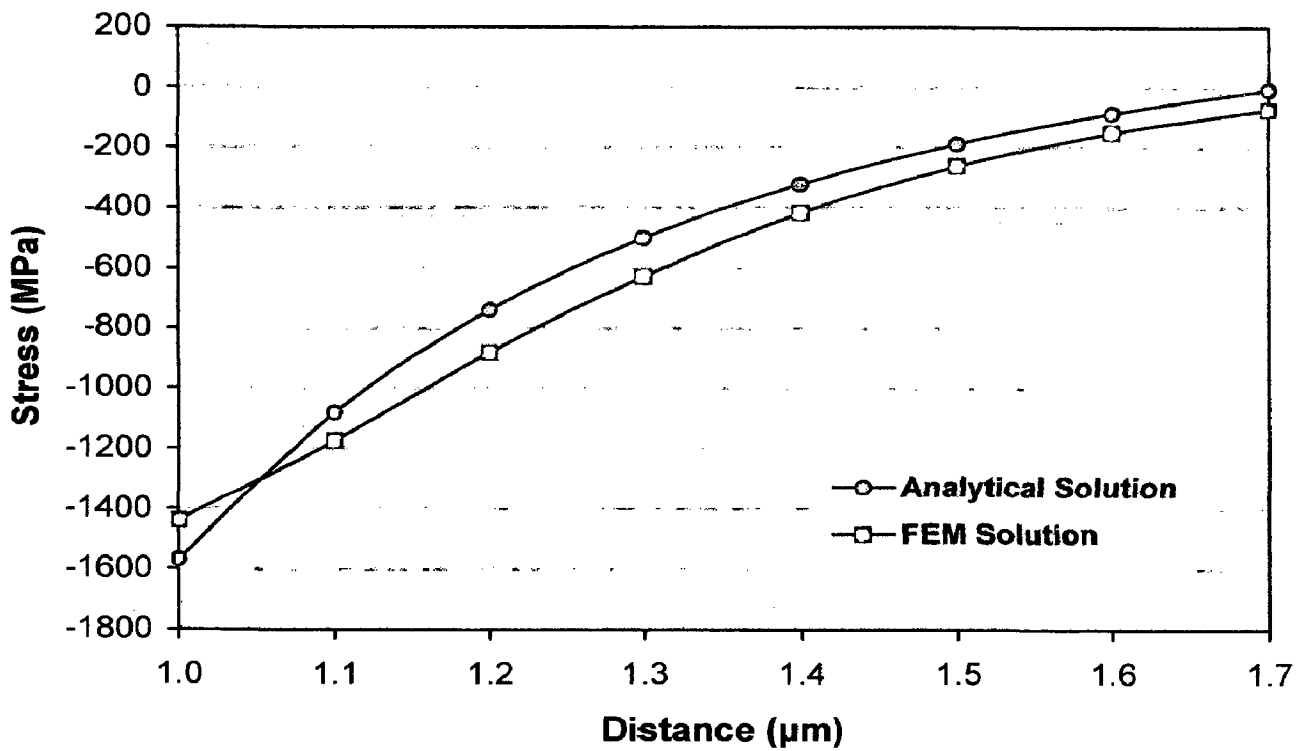


Fig. 4.6 Variation of radial compressive stress with distance in MoSi<sub>2</sub> matrix.



The magnitude of tensile hoop stress at the particle / matrix interface was found to be 1037 MPa by FEM analysis, which is lower than the analytically calculated value of 1372 MPa. In numerical solution the magnitude of this stress reduces with increasing distance from the interface as graphically represented in Fig. 4.7. The stress values calculated from equation 4.3 are also plotted in Fig. 4.7 for comparison with FEM results. The stress values obtained from FEM analysis are slightly lower than the calculated stress values by analytical method. However, the same trend is predicted by the results obtained from both the methods. The variation present in between the two plots may be attributed to a slightly different volume fraction of reinforcement particles as a result of roughness of the interface in the numerical model.

In case of stress in SiC particle, it was found that inside bulk of the particle the stress was almost uniform and compressive in nature. The magnitude of this compressive stress is estimated to be 1680 MPa, which is matching closely with the analytically calculated value of 1568 MPa.

#### **4.4 ANALYSIS OF RESIDUAL THERMAL STRESSES IN MoSi<sub>2</sub> / REFRACTORY METAL FOIL LAMINATED COMPOSITES**

In the present investigation, tri-layer laminated composites consisting of a single ductile metal foil sandwiched in between two outer layers of MoSi<sub>2</sub> + 20 vol% SiC<sub>p</sub>, as shown schematically in Fig. 4.8, were made by vacuum hot pressing.

The outer layers, i.e., the matrix itself is a particulate composite of MoSi<sub>2</sub> + 20 vol% SiC<sub>p</sub>. The inner layer, i.e., the reinforcement is a 0.5 mm thick single foil of pure metal. Three different refractory metals molybdenum, tantalum and niobium were used in the foil form to make these laminated composites.

##### **4.4.1 Properties of MoSi<sub>2</sub> + 20 vol% SiC<sub>p</sub> Outer Layer**

Let us first calculate the physical properties of the outer layer consisting of MoSi<sub>2</sub> and SiC. The various properties of MoSi<sub>2</sub> and SiC are given in Table 4.3.

Table 4.3 Physical properties of MoSi<sub>2</sub> and SiC.

Material	$\alpha$ (CTE) ( $\times 10^{-6}/K$ )	$E$ (GPa)	$\nu$	$G = \frac{E}{2(1+\nu)}$ (GPa)	$K = \frac{E}{3(1-2\nu)}$ (GPa)
MoSi <sub>2</sub>	8.52	440	0.15	191	210
SiC	4.78	420	0.14	184	194

#### 4.4.1.1 Elastic Modulus

The elastic modulus of the particulate composite is calculated using a model proposed by Hashin and Shtrikman (1963) rather than a simple rule of mixture. For an isotropic particulate composite, bounds for shear modulus,  $G$  of the composite are given as:

$$G_c = G_r + \frac{(1-V_r)}{\frac{1}{(G_m - G_r)} + \frac{6(K_r + 2G_r)V_r}{5G_r(3K_r + 4G_r)}} \quad \text{and}$$

$$G_c = G_m + \frac{V_r}{\frac{1}{(G_r - G_m)} + \frac{6(K_m + 2G_m)(1-V_r)}{5G_m(3K_m + 4G_m)}}$$

where  $G$  is the shear modulus,  $K$  is the bulk modulus and  $V_r$  is the volume fraction of the reinforcement. Suffixes  $c$ ,  $m$  and  $r$  represent composite, matrix and the reinforcement, respectively.

Using the values for MoSi<sub>2</sub> and SiC from Table 4.3 and substituting in the above equations results in shear modulus of the composite,  $G_c = 189.6$  GPa (lower and upper bounds for  $G$  were found to be same).

Bounds for Bulk Modulus,  $K$  of the composite are given as:

$$K_c = K_r + \frac{(1-V_r)}{\frac{1}{(K_m - K_r)} + \frac{3V_r}{(3K_r + 4G_r)}} \quad \text{and}$$

$$K_c = K_m + \frac{V_r}{\frac{1}{(K_r - K_m)} + \frac{3(1-V_r)}{(3K_m + 4G_m)}}$$

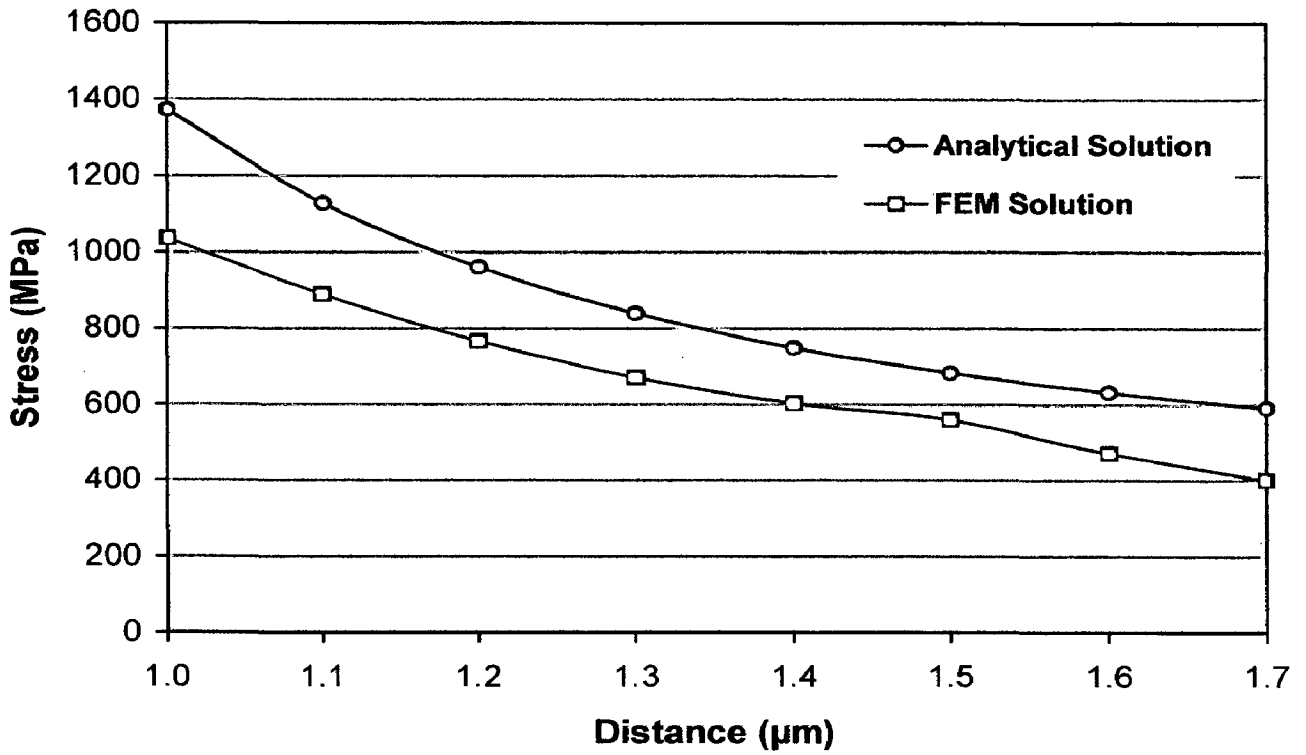


Fig. 4.7 Variation of tangential tensile (hoop) stress with distance in MoSi<sub>2</sub> matrix.

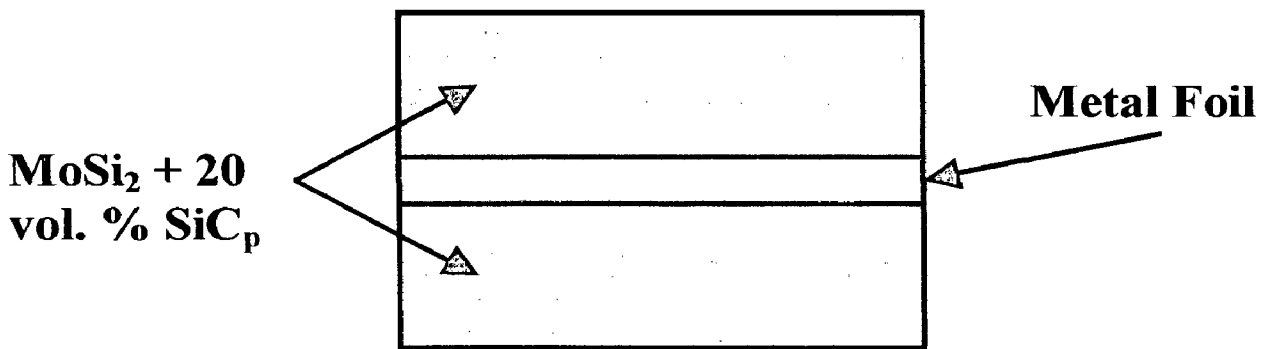


Fig. 4.8 Tri-layer MoSi<sub>2</sub> / ductile metal foil laminated composite.

Again, the lower and upper bounds of bulk modulus were found to be the same. The bulk modulus of the composite,  $K_c$  was estimated to be as 206.7 GPa.

Chawla (1993) has observed that the lower and upper bounds are close enough to give a value within ~ 10 % of the true modulus of the composite if

$$0.5 < \frac{E_r}{E_m} < 3$$

where  $E_r$  and  $E_m$  are the elastic moduli of the reinforcement and the matrix, respectively.

In the present case,

$$\frac{E_r}{E_m} = \frac{420}{440} = 0.95 \approx 1$$

Now, we can calculate the elastic modulus of the composite (MoSi<sub>2</sub> + 20 vol% SiC<sub>p</sub>) outer layer as:

$$E_c = \frac{9KG}{(3K + G)} = 436 \text{ GPa}$$

#### 4.4.1.2 Poisson's Ratio

$$\nu_c = \frac{E}{2G} - 1 = 0.15$$

It is same as of pure MoSi<sub>2</sub>, because Poisson's ratios of MoSi<sub>2</sub> and SiC are almost same.

#### 4.4.1.3 Coefficient of Thermal Expansion ( $\alpha$ )

Coefficient of thermal expansion of an isotropic particulate composite is estimated by a model proposed by Turner (1946).

$$\alpha_c = \frac{V_r \alpha_r K_r + V_m \alpha_m K_m}{V_r K_r + V_m K_m}$$

where  $\alpha$  is the coefficient of thermal expansion,  $K$  is the bulk modulus and  $V_r$  is the volume fraction of the reinforcement. Suffixes  $c$ ,  $m$  and  $r$  represent composite, matrix and the reinforcement, respectively.

Substituting the values of these properties from Table 4.3 in the above equation, gives the coefficient of thermal expansion of the composite outer layer as  $\alpha_c = 7.82 \times 10^{-6}/K$ .

Therefore, the estimated values of the various properties of the composite (MoSi<sub>2</sub> + 20 vol% SiC<sub>p</sub>) outer layer can be summarized as:

$$E = 436 \text{ MPa}, \nu = 0.15 \text{ and } \alpha_c = 7.82 \times 10^{-6}/K$$

#### 4.4.2 Residual Thermal Stresses in Laminated Composites

Let us designate the inner layer of refractory metal foil as layer 1 and the outer layer of MoSi<sub>2</sub> + 20 vol% SiC<sub>p</sub> as layer 2 as shown schematically in Fig. 4.9.

After cooling from the processing temperature to room temperature, the layer 1 with a lower coefficient of thermal expansion value develops residual compressive stress, while the layer 2 with a higher coefficient of thermal expansion value develops a residual tensile stress as shown schematically in Fig. 4.10.

The residual compressive stress in layer 1,  $\sigma_{R_1}$  is given by (Oeschner et al, 1996)

$$\sigma_{R_1} = \frac{\varepsilon_r E'_1}{1 + \frac{t_1 E'_1}{t_2 E'_2}} \quad (4.5)$$

$$\varepsilon_r = \Delta\alpha\Delta T = (\alpha_1 - \alpha_2)\Delta T$$

$$E'_1 = \frac{E_1}{(1 - \nu_1)} \quad \text{and} \quad E'_2 = \frac{E_2}{(1 - \nu_2)}$$

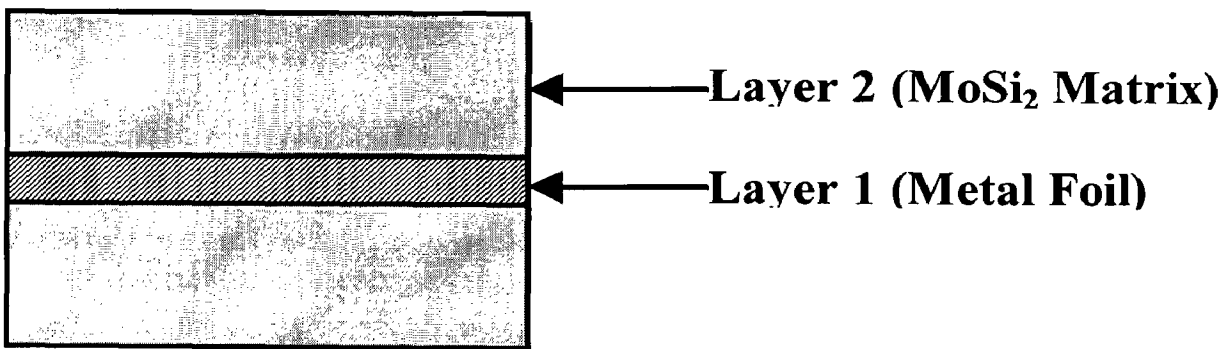


Fig. 4.9 Designation of different layers in laminated composite.

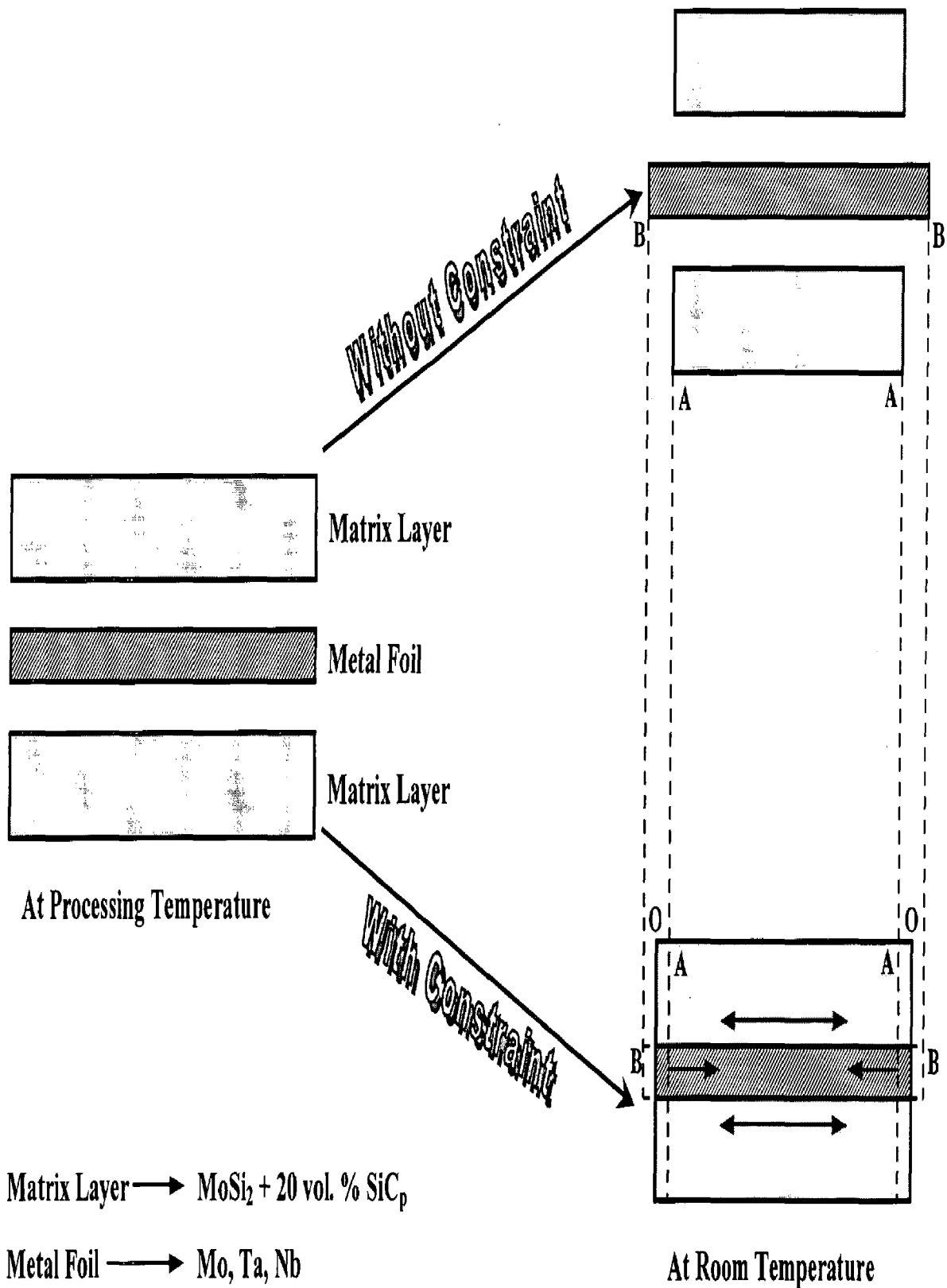


Fig. 4.10 Development of residual thermal stresses in a laminated composite after cooling from processing temperature.

Substituting the above in equation 4.5 and rearranging the terms,

$$\sigma_{R_1} = \frac{(\alpha_1 - \alpha_2)\Delta T}{\frac{(1 - \nu_1)}{E_1} + \frac{t_1(1 - \nu_2)}{t_2 E_2}} \quad (4.6)$$

where  $\alpha$  is the coefficient of thermal expansion,  $\Delta T$  is the temperature interval during cooling,  $\nu$  is the Poisson's ratio,  $E$  is the elastic modulus and  $t$  is the thickness of the layer. Suffixes 1 and 2 represent layer 1 and layer 2, respectively.

The residual tensile stress in layer 2,  $\sigma_{R_2}$  is given by (Oeschner et al, 1996)

$$\sigma_{R_2} = -\frac{n_1 t_1}{n_2 t_2} \sigma_{R_1} \quad (4.7)$$

where  $n_1$  and  $n_2$  are the number of layers of materials 1 and 2, respectively in the composite.

These residual stresses are uniform and bi-axial in both the layers. There is no residual stress in the direction of stacking, as no constraint for thermal contraction is present during cooling from the processing temperature. The values of various parameters of different layers in the composites are summarized in Table 4.4.

In the present case,  $t_1 = 0.5$  mm,  $t_2 = 2.25$  mm,  $n_1 = 1$ ,  $n_2 = 2$  and  $\Delta T = 1570$  °C. Substituting these values in equations 4.10 and 4.11, the residual thermal stresses in different composites are estimated and presented in Table 4.5.

The above analysis of residual thermal stresses in the laminated composites used in the present study clearly reveals that niobium foil reinforced composite has the lowest residual thermal stresses due to its minimum thermal expansion mismatch with the outer matrix layer. A lower value of elastic modulus of niobium as compared to other refractory metals used may also contribute to the lower residual thermal stresses in this composite.

Soaking the composite at an intermediate temperature while cooling from the processing temperature may be an effective method to lower the residual thermal stresses in these composites. Xiao (1991<sup>b</sup>) has estimated the residual stresses as 19



MPa and 79 MPa in MoSi<sub>2</sub> and niobium layers, respectively after holding the hot pressed discs at 800 °C for 1 h in hot pressing chamber before cooling.

#### **4.4.3 Analysis of Residual Thermal Stresses in Laminated Composites by FEM**

In case of layered composites, the analytical equations do not provide any information about the stress distribution within a layer and also whether the stress is uniform throughout the layer or not. To overcome these drawbacks and to get a deeper understanding of the state of residual stress within the laminated composites, the same numerical approach, NISA finite element package was used to carry out the finite element analysis of the residual thermal stresses in the laminated composites used in the present study. For carrying out the analysis a representative model of half of the length of laminated composite consisting of two layers of MoSi<sub>2</sub> with 20 vol% SiC<sub>p</sub> having a thickness of 2.25 mm each and a 0.5 mm thick refractory metal foil sandwiched between the two MoSi<sub>2</sub>-SiC<sub>p</sub> matrix layers was considered. The size of the analyzed half length is 10 mm in length and 5 mm in width. The entire model was meshed with standard rectangular block type elements. The model was allowed to cool down to room temperature from an initial stress free temperature of 1600 °C.

Using the various material properties from Table 4.4,  $\sigma_{xx}$  stress contour plots were obtained by FEM analysis for the various material configurations. The stress distribution curves along the length and the width in the middle plane of the foil as well as in the middle plane of the matrix layer were also plotted from the FEM results. The following assumptions were made for the FEM analysis:

1. At the temperature of processing, the composite was totally stress free and the residual stresses developed during cooling to room temperature, i.e., the entire residual stress is thermal in nature and no phase transformations were considered.
2. The material properties are assumed to be isotropic and are temperature independent.
3. Linear elastic material behaviour is assumed.
4. All interfaces are assumed to be ideally smooth and with perfect adhesion.

Table 4.4 Physical properties of different layers in the laminated composites.

	Material	$\alpha$ (CTE) ( $\times 10^{-6}/K$ )	$E$ (GPa)	$\nu$
Layer 1	Mo	4.9	324	0.32
	Ta	6.5	186	0.35
	Nb	7.3	103	0.38
Layer 2	MoSi <sub>2</sub> + 20 vol% SiC <sub>p</sub>	7.82	436	0.15

Table 4.5 The calculated values of residual thermal stresses in various laminated composites.

Composite	Residual Stress, $\sigma_{R_1}$ in Metal Foil (MPa)	Residual Stress, $\sigma_{R_2}$ in MoSi <sub>2</sub> Layer (MPa)
(MoSi <sub>2</sub> + 20 vol% SiC <sub>p</sub> ) + Mo Foil	1811	201
(MoSi <sub>2</sub> + 20 vol% SiC <sub>p</sub> ) + Ta Foil	528	59
(MoSi <sub>2</sub> + 20 vol% SiC <sub>p</sub> ) + Nb Foil	127	14

The  $\sigma_{xx}$  (effective stress in x direction) stress contour plots for the laminated composites with molybdenum foil, tantalum foil and niobium foil are shown in Fig. 4.11 in a two dimensional planar view (x-y plane). It can be seen from Fig. 4.11(a) that the maximum tensile stress in the composite with molybdenum foil is 563.1 MPa and the maximum compressive stress is 2133 MPa as against the analytically arrived values of 201 MPa tensile and 1811 MPa compressive. Though the maximum tensile stress value of 563 MPa obtained from the FEM analysis appears to be significantly higher than the analytical solution of 201 MPa, but a closer look at the FEM contour plot revealed that this stress value is a highly localized one and concentrated in an area close to the matrix-foil interface near the right edge of the composite. This area can be seen as a small red patch in Fig. 4.11(a). This localized high stress can be attributed to the edge effect. Except for this small area it is observed that the magnitude of the tensile stress in the bulk of the matrix layers varies in between 213 MPa and 221 MPa, which is matching closely with the calculated value of 201 MPa.

The stress contour plot obtained for tantalum foil composite as shown in Fig. 4.11(b) is slightly different than the stress contour plot of the laminated composite with molybdenum foil. However, It is observed that the stress contour plots of the laminated composite with niobium foil and the laminated composite with tantalum foil resemble with each other considerably. As the origin of the residual thermal stresses in these composites is thermal expansion mismatch between the matrix layer and the ductile refractory metal foil, this similarity between the stress contour patterns of these two composites may be attributed to the fact that the difference between the coefficients of thermal expansion of niobium and tantalum is marginal ( $0.8 \times 10^{-6}/K$  only).

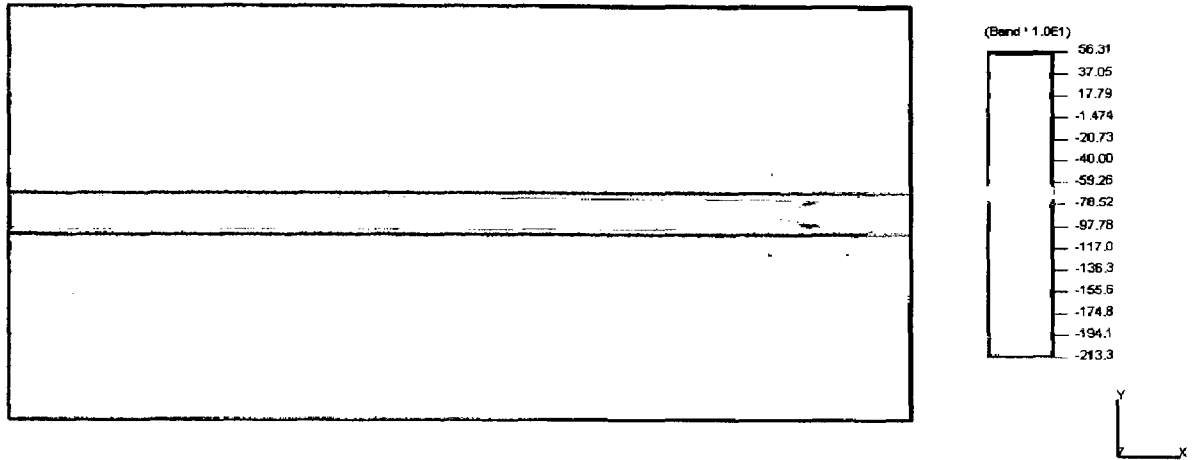
The stress contours of all the three composites in a full isometric view are presented in Fig. 4.12. Fig. 4.13 exhibits the stress variation plots across the thickness of the composites, along the line A-A in Figs. 4.12(a), 4.12(b) and 4.12(c), respectively. In case of molybdenum foil composite, It reveals a tensile stress of 220 MPa in two  $MoSi_2$  layers at the top and the bottom surfaces, which rapidly switches over across the interface to a compressive stress of 2132 MPa in the molybdenum foil. Similar trends are observed in tantalum foil and niobium foil laminated

composites although the magnitudes of the stresses are much lower. The tensile stresses in top and bottom MoSi<sub>2</sub> layers of tantalum foil and niobium foil composites are 65 MPa and 17 MPa, respectively while the compressive stresses in tantalum and niobium foils are found to be 636 MPa and 168 MPa, respectively.

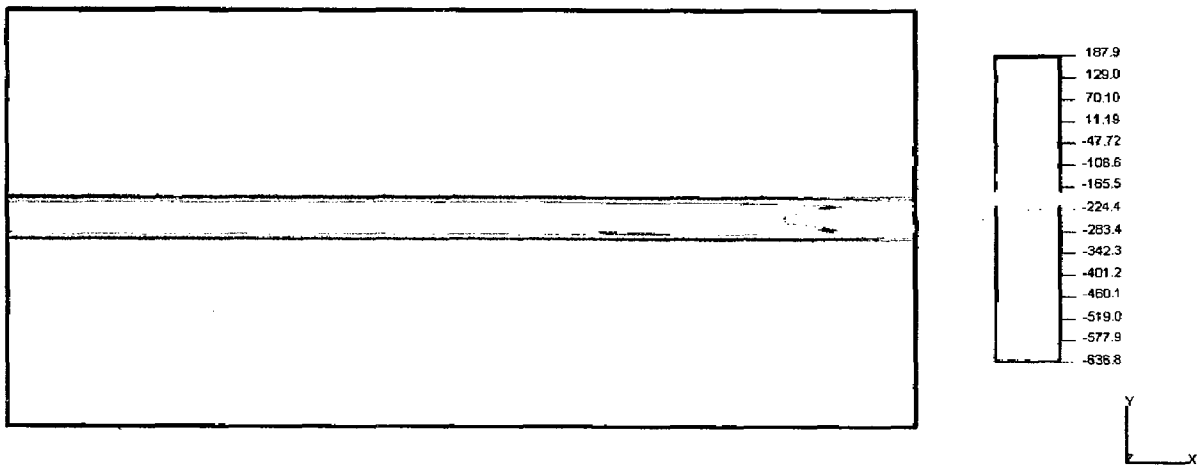
Figs. 4.14(a), (b) and (c) exhibit the stress contour views along the mid-plane section of the top MoSi<sub>2</sub> matrix layer of the laminated composites with molybdenum, tantalum and niobium foils, respectively. The stress distribution across the length in the mid-plane of the top MoSi<sub>2</sub> layer (along the line C-C in Fig. 4.14) is graphically represented in Fig. 4.15(a), while Fig. 4.15(b) shows the stress distribution curves across the width (along the line B-B in Fig. 4.14) for all the three composites.

In case of laminated composite with molybdenum foil, it is seen that in the bulk of the matrix the stress across the length is 220 MPa rising to a value of 244 MPa near the edge and then rapidly decaying off at the free surface on the right edge of the composite. The stress distribution curves for laminated composites with tantalum and niobium foils also show the similar trend differing only in the magnitudes of the stresses. The stress in the bulk of the matrix is 65 MPa in case of tantalum foil composite while, it is only 17 MPa in niobium foil composite. The stress distribution curves across the width of the top MoSi<sub>2</sub> matrix layer as depicted in Fig. 4.15(b), reveal similar trends for all the three composites as stress distribution curves across the length. These curves show almost uniform stresses in the bulk of the matrix. The stresses gradually decay to lower levels at the free surfaces on the front and the back of the composites. The asymmetry in the stress pattern across the length of the matrix layer, occurs due to the imposition of the boundary conditions on the free surface of the composite.

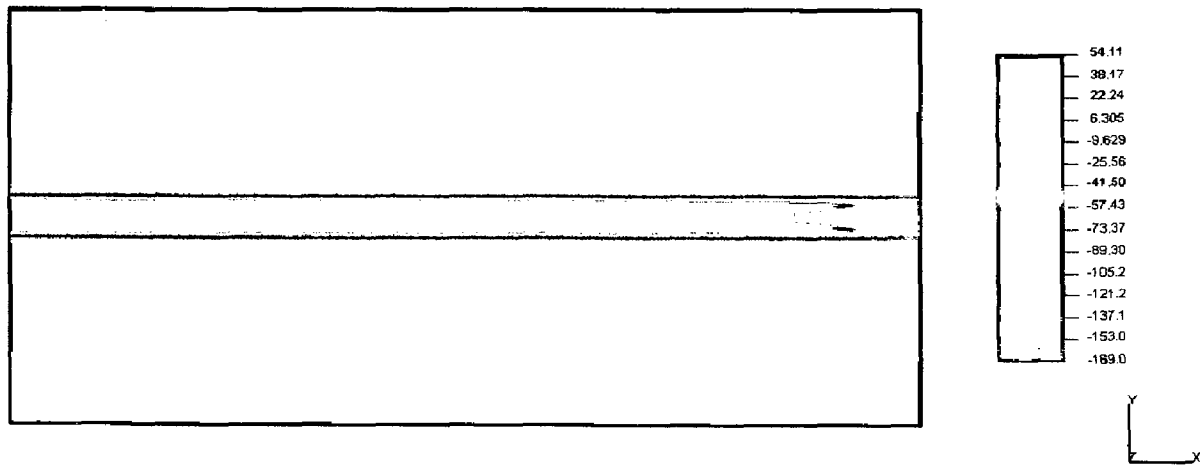
The stress contour views along the mid-plane section of the molybdenum foil, tantalum foil and niobium foil resemble with each other considerably as shown in Fig. 4.16(a), 4.16(b) and 4.16(c), respectively. In all the composites the foils are under compressive stresses. Figs. 4.17(a) and 4.17(b) exhibit the stress distribution plots in the mid-plane of the metal foils across the length (along the lines C-C in Fig. 4.16) and across the width (along the lines B-B in Fig. 4.16), respectively.



(a)



(b)



(c)

Fig. 4.11 Stress contour plots of MoSi<sub>2</sub> + 20 vol% SiC<sub>p</sub> with (a) Mo foil (b) Ta foil and (c) Nb foil laminated composites in a two dimensional planar view (X-Y plane).

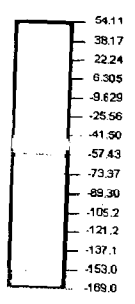
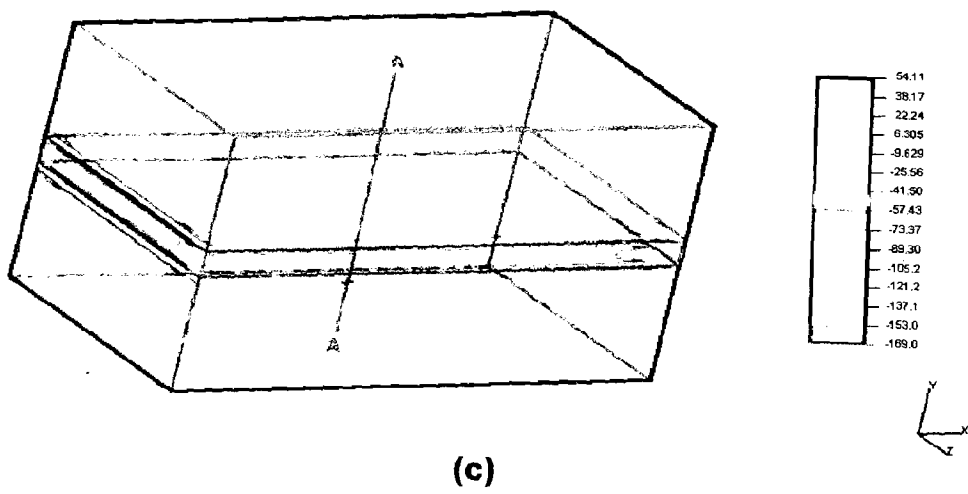
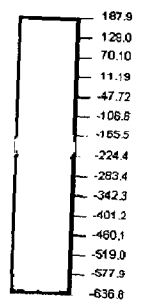
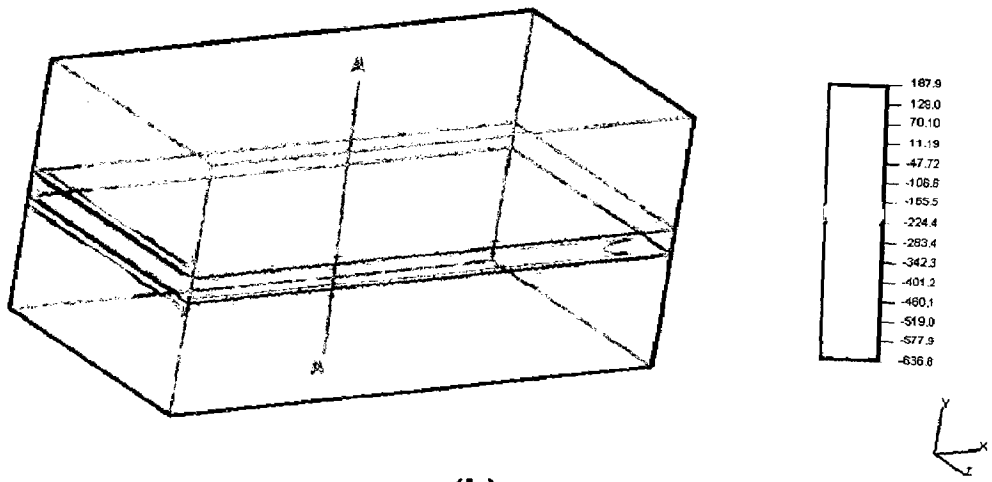
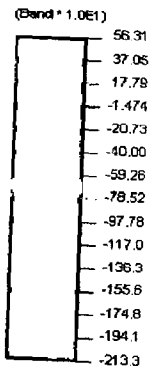
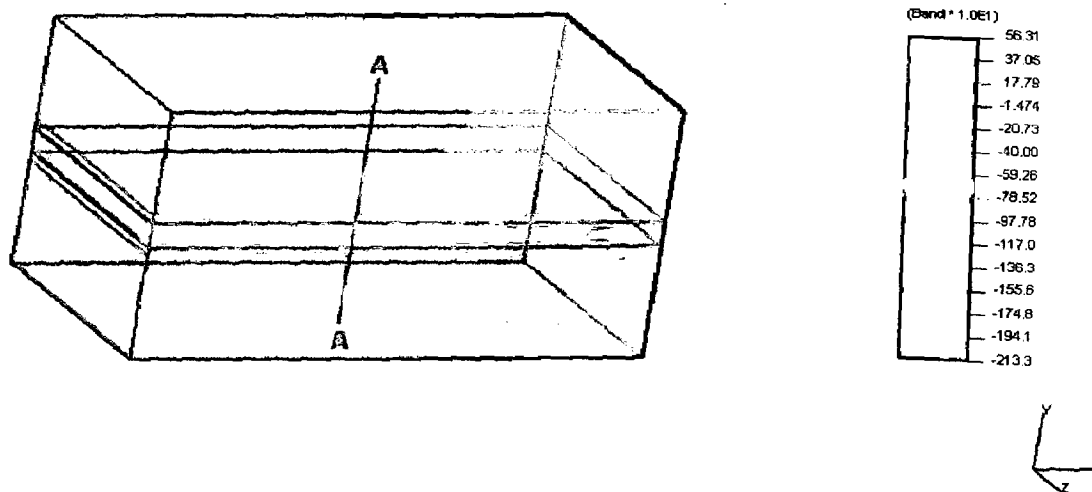


Fig. 4.12 Stress contour plots of  $\text{MoSi}_2 + 20 \text{ vol}\% \text{ SiC}_p$  with (a) Mo foil (b) Ta foil and (c) Nb foil laminated composites in a full isometric view of the composite.

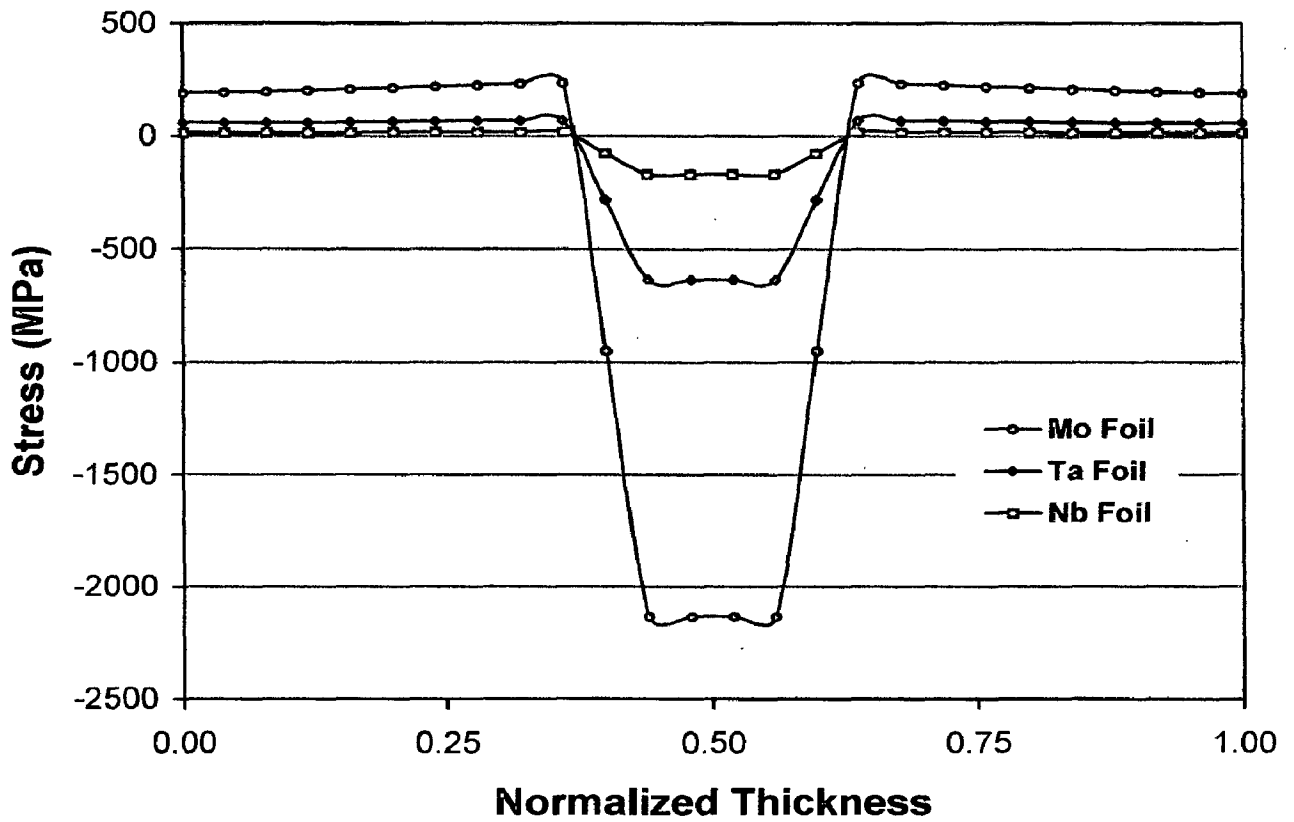


Fig. 4.13 Stress variation plots across the thickness of  $(\text{MoSi}_2 + 20 \text{ vol}\% \text{ SiC}_p)$  with Mo, Ta and Nb foil laminated composites (along the line A-A in Fig. 4.12).

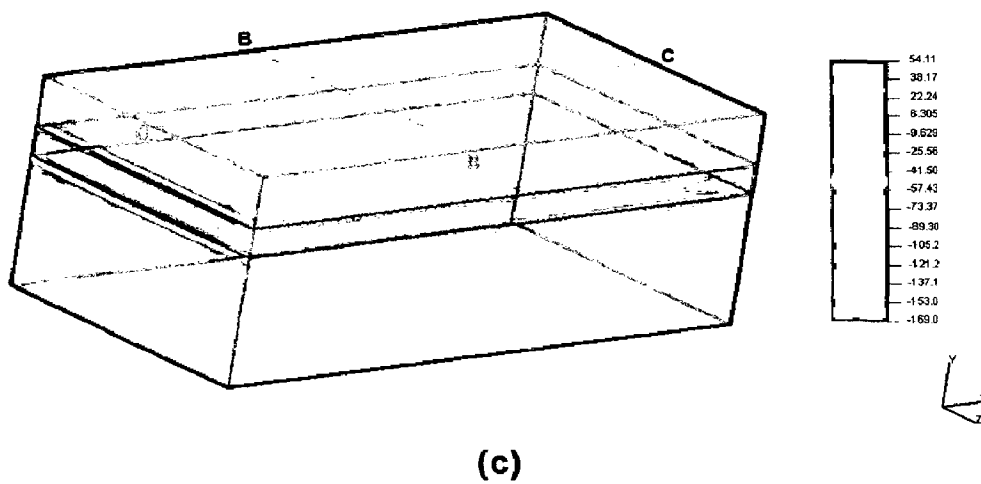
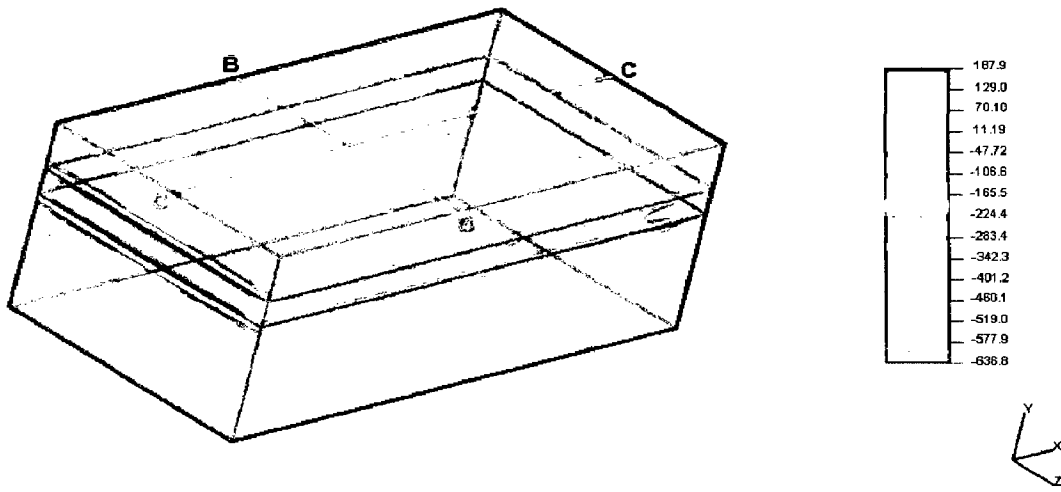
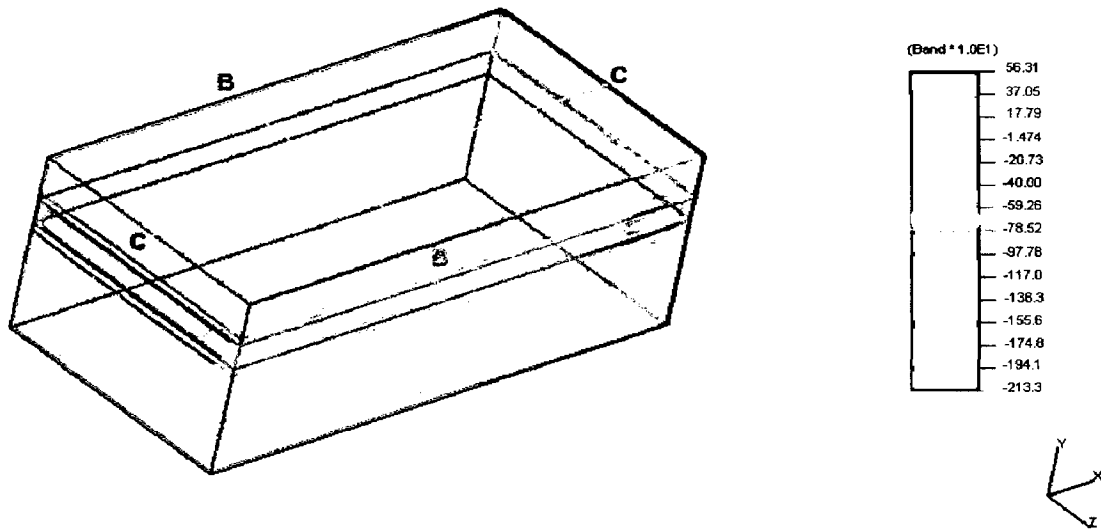
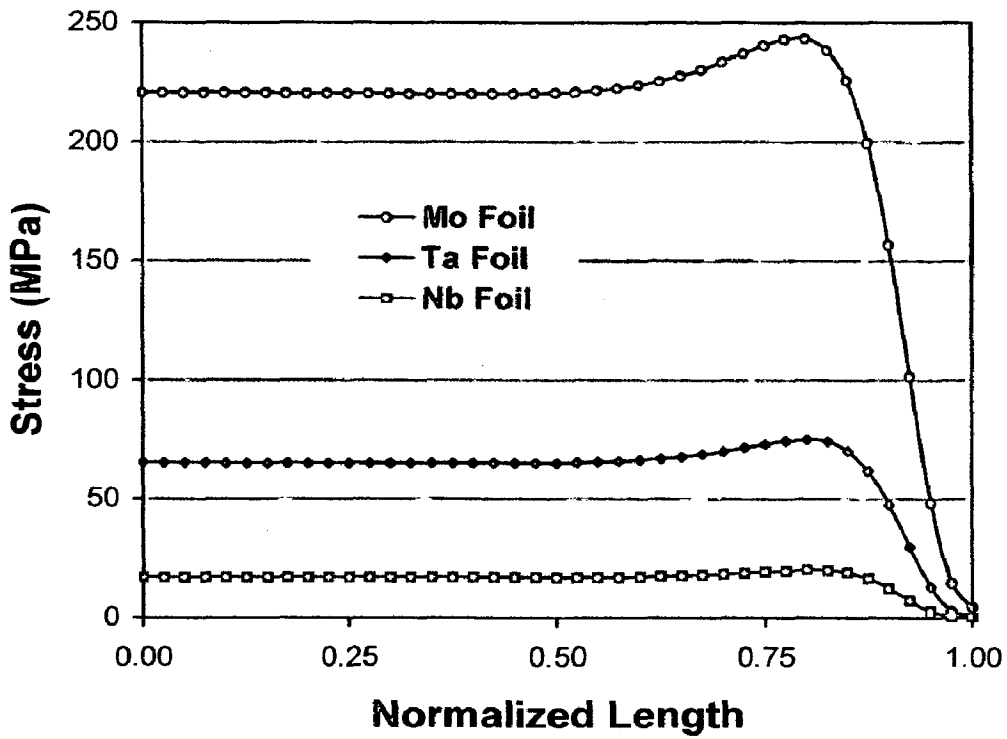


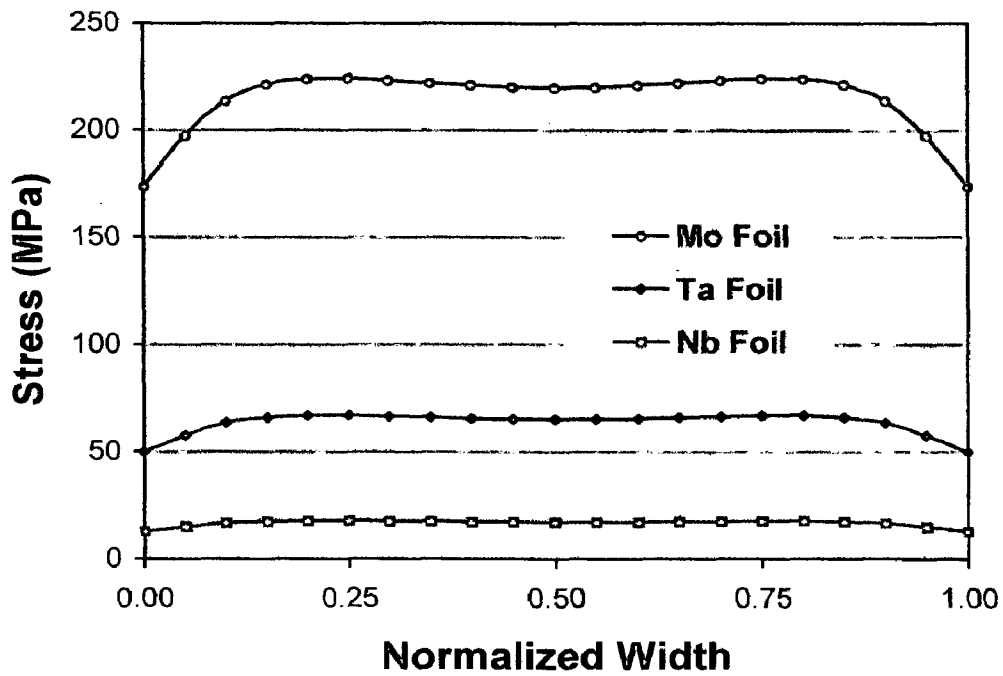
Fig. 4.14

View of stress contour plots along the mid-plane section of the top  $\text{MoSi}_2$  matrix layer (a) Mo foil (b) Ta foil and (c) Nb foil laminated composites.





(a)



(b)

Fig. 4.15

Stress variation plots along the mid-plane of  $\text{MoSi}_2$  matrix layer of laminated composites with Mo, Ta and Nb foils (a) across the length (line C-C in Fig. 4.14) and (b) across the width (line B-B in Fig. 4.14).

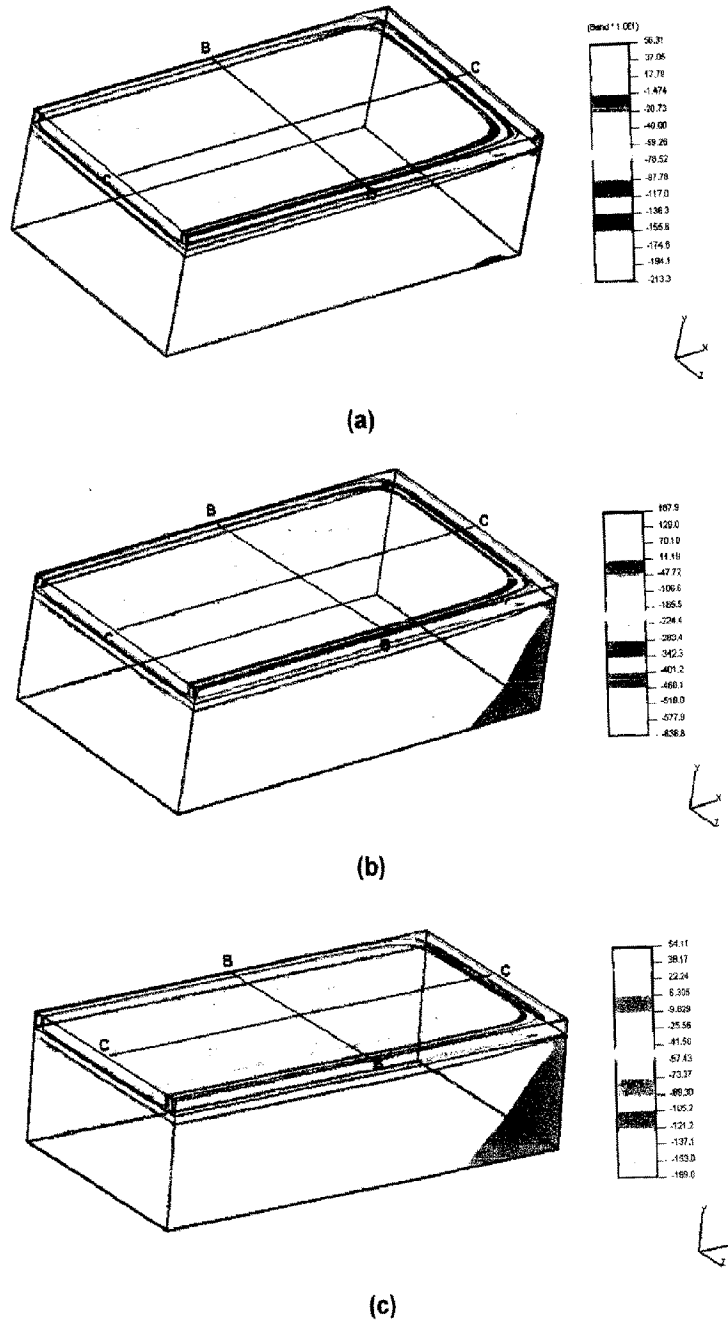
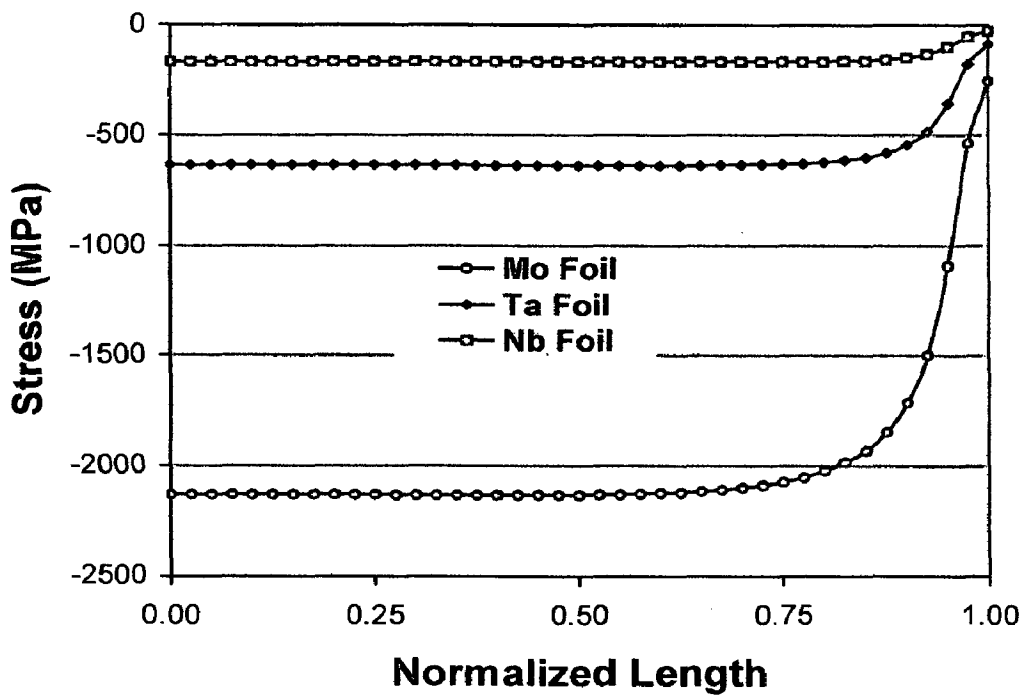
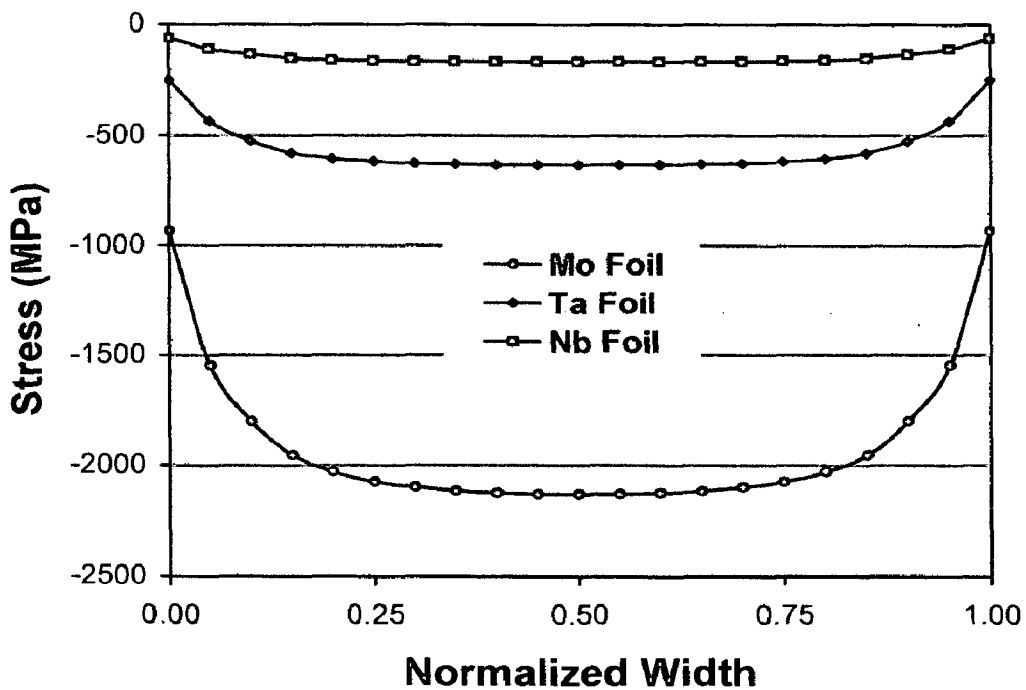


Fig. 4.16 View of stress contour plots along the mid-plane section of the metal foils (a) Mo foil (b) Ta foil and (c) Nb foil laminated composites.



(a)



(b)

Fig. 4.17

Stress variation plots along mid-plane of the foil of laminated composites with Mo, Ta and Nb foils (a) across the length (line C-C in Fig. 4.16) and (b) across the width (line B-B in Fig. 4.16).

The stress distribution curves for molybdenum foil laminated composite reveal that in the bulk of the foil the stress has almost a uniform value of 2133 MPa compressive, which decreases near the edges across the length as well as across the width. The asymmetry in the stress pattern across the length of the foil is again due to the imposition of the boundary conditions on the free surface of the composite. Similar trends are observed in stress distribution curves of tantalum and niobium foils across the length and the width in the mid-plane section of the foils. The maximum compressive stress in the metal foil occurs at regions within the bulk of the foil, away from the free edges. It is also revealed that the magnitude of the compressive stress across the length and across the width in a plane of the metal foils remains almost the same.

The FEM analysis carried out in the present study brings out the fact that the residual stress distribution in laminated composites with different refractory metal foils is almost similar. The stresses are tensile in MoSi<sub>2</sub> matrix layer and compressive in the metal foils showing the gradual transition from tensile to compressive at the interface. The stresses are uniform in the bulk of a layer and do not vary across the length or width of the layer. The values of residual thermal stresses obtained by FEM analysis in the bulk of the composites are presented in Table 4.6. It is significant to note that the nature and the magnitudes of residual stresses obtained by FEM analysis are in good agreement with the results arrived at by analytical methods as presented in Table 4.5.

## **4.5 LIMITATIONS**

The various limitations of the analysis to estimate the residual thermal stresses in MoSi<sub>2</sub> based particulate and laminated composites carried out in the present work by analytical as well as FEM methods are summarized below:

- (i) Coefficients of thermal expansion (CTEs) of MoSi<sub>2</sub>, SiC and refractory metals have been assumed to be constant with temperature.
- (ii) The elastic modulus values of MoSi<sub>2</sub> and SiC used in the present analysis are taken from the literature. However, as in the case of most of the ceramic materials, there is a lot of scatter in elastic modulus values of MoSi<sub>2</sub> and SiC reported in the literature. The elastic modulus of ceramic materials is highly sensitive to manufacturing process employed and the defects present in them.

- (iii) The effect of free SiO<sub>2</sub> in MoSi<sub>2</sub> has not been taken into account. The commercial MoSi<sub>2</sub> powders contain significant amounts of free SiO<sub>2</sub>. The coefficient of thermal expansion of SiO<sub>2</sub> is very low ( $\alpha = 0.55 \times 10^{-6}/K$ ). This may result in a net value of coefficient of thermal expansion of the MoSi<sub>2</sub> matrix considerably lower leading to a lower thermal expansion mismatch between matrix and the various reinforcements. Therefore, the values of residual thermal stresses arrived at in the present analysis may be an over-estimation.
- (iv) SiC particles are assumed to be perfectly spherical, to be of the same size and having a perfect uniform distribution. However, in the present study, SiC particles used were of irregular shape and of different sizes (having a large size distribution).
- (iv) No stress relaxation was assumed during cooling from the processing temperature. In case of ceramic matrix composites (CMCs), cracking may occur in the matrix to relieve the high level of thermal stresses. In metal matrix composites (MMCs), matrix is likely to deform plastically instead of cracking. However, in MoSi<sub>2</sub> based composites some stress relaxation during cooling will occur as MoSi<sub>2</sub> shows ductility at elevated temperatures.
- (v) The existence of an interfacial reaction layer between (MoSi<sub>2</sub> + 20 vol% SiC<sub>p</sub>) matrix layer and the refractory metal foils has been ignored in the present analysis. However, the interfacial reaction layer present in these composites may alter the nature and magnitude of the residual thermal stresses in these composites. The possible effects of interfacial reaction products on the residual thermal stresses in laminated composites studied in the present work are briefly described in the following section.

## 4.6 EFFECT OF INTERFACIAL REACTIONS

In these composite systems, there exists an interfacial reaction layer between MoSi<sub>2</sub> matrix and the metal foils. After cooling to room temperature, the tri-layer composite laminate will have two additional layers of interfacial reaction products as exhibited schematically in Fig. 4.18.

Table 4.6 The values of residual thermal stresses in various laminated composites obtained by FEM analysis.

Composite	Residual Stress in Metal Foil (MPa)	Residual Stress in MoSi <sub>2</sub> Layer (MPa)
(MoSi <sub>2</sub> + 20 vol% SiC <sub>p</sub> ) + Mo Foil	2132	220
(MoSi <sub>2</sub> + 20 vol% SiC <sub>p</sub> ) + Ta Foil	636	65
(MoSi <sub>2</sub> + 20 vol% SiC <sub>p</sub> ) + Nb Foil	168	17

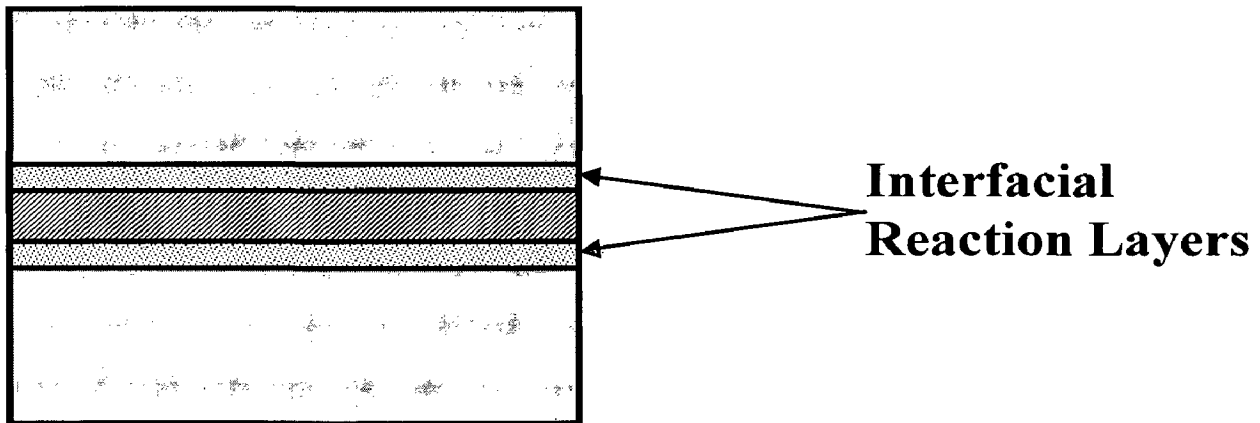


Fig. 4.18 Interfacial reaction layers in tri-layer laminated composite.

A third layer (layer 3) is introduced in between metal foil (layer 1) and MoSi<sub>2</sub> + 20 vol% SiC<sub>p</sub> (layer 2). The layer 3 consists of mainly M<sub>5</sub>Si<sub>3</sub> type of silicide (M = refractory metal) as discussed in subsequent. The properties of interfacial reaction products (layer 3) present in all the composites studied are summarized in Table 4.7.

Table 4.7 Chemical nature and properties of interfacial reaction layers in various laminated composites.

Composite	Chemical Nature of Layer 3	Thickness (μm)	$\alpha$ (x10 <sup>-6</sup> /K)	$\Delta\alpha_{13}$ (x10 <sup>-6</sup> /K)	$\Delta\alpha_{32}$ (x10 <sup>-6</sup> /K)
MoSi <sub>2</sub> + 20 vol% SiC <sub>p</sub> + Mo Foil	Mo <sub>5</sub> Si <sub>3</sub>	40	6.7	-1.80	-1.12
MoSi <sub>2</sub> + 20 vol% SiC <sub>p</sub> + Ta Foil	Ta <sub>5</sub> Si <sub>3</sub>	10	6.3	+0.2	-1.52
MoSi <sub>2</sub> + 20 vol% SiC <sub>p</sub> + Nb Foil	Nb <sub>5</sub> Si <sub>3</sub>	20	7.3	0	-0.52

where  $\Delta\alpha_{13} = \alpha_{layer1} - \alpha_{layer3}$  and  $\Delta\alpha_{32} = \alpha_{layer3} - \alpha_{layer2}$

#### 4.6.1 Effect of Thickness

The original thickness of the metal foils (layer 1) used is 500 μm in all the composites. The interfacial reaction product (layer 3) grows at the expense of both the layer 1 and the layer 2. However, it mostly consumes the metal foil and thus reduces the effective thickness of the layer 1.

#### 4.6.2 Effect of Thermal Expansion Mismatch

The coefficients of thermal expansion of all the interfacial reaction products (layer 3) are lower than the coefficient of thermal expansion of the outer layer 2 ( $\alpha = 7.82 \times 10^{-6}/K$ ). Therefore, the nature of the residual thermal stress in outer layer is likely to remain unchanged, i.e., tensile. However, its magnitude may get affected. The exact change cannot be calculated as, elastic constants of these interfacial reaction products ( $E$  and  $\nu$ ) are not known.

It has to be further noted that as Si diffuses out of MoSi<sub>2</sub> towards metal foils to form M<sub>5</sub>Si<sub>3</sub> type silicides, another layer of Mo<sub>5</sub>Si<sub>3</sub> is likely to form between matrix layer and the main reaction layer of M<sub>5</sub>Si<sub>3</sub> type silicide, due to Si depletion in MoSi<sub>2</sub> side.

A more rigorous analysis is required to estimate the residual thermal stresses in these composite systems incorporating all the above effects. Nevertheless, the analysis done in the present work gives a fairly good idea of the nature and magnitude of residual thermal stresses in these composites. A quantitative idea of the residual stresses in a body can be very useful. Some important guidelines to obtain enhanced fracture toughness in these materials can be derived from the results obtained in the present analysis. The thickness of the interfacial reaction layer is relatively small and can probably be neglected.

It has also to be noted that the residual stresses in the composites may be due to several factors other than thermal expansion mismatch, e.g., particle roughness. A more rigorous analysis should include the effect of particle surface roughness induced strain and the corresponding residual stress.

#### **4.7 SUMMARY OF RESULTS**

The results of theoretical analysis of residual thermal stresses in MoSi<sub>2</sub>-20 vol% SiC particulate composite reveals that SiC particle is under a compressive stress which is constant and does not vary within the particle from the center of the particle to the particle / matrix interface. The MoSi<sub>2</sub> matrix has two stress components, the radial compressive stress and the tangential tensile stress. These stresses are found to be maximum at particle / matrix interface and decreases with increasing distance from the interface. In case of MoSi<sub>2</sub>-SiC<sub>p</sub> + refractory metal foil laminated composites, the refractory metal foils are found to possess compressive stresses, while the MoSi<sub>2</sub>-SiC<sub>p</sub> matrix layer is under tensile stresses. The Nb foil reinforced laminated composite is found to possess the lowest residual stresses owing to a lower thermal expansion mismatch between MoSi<sub>2</sub>-SiC<sub>p</sub> matrix and the Nb foil as compared to the Mo and Ta foils. The residual thermal stresses estimated by finite element methods (FEM) are found to be similar to the as calculated by analytical approach, thus validating the analytical expressions used in the present study.



## **RESULTS AND DISCUSSION**

---

The various ductile refractory metal reinforced MoSi<sub>2</sub> based particulate and laminated composites prepared in the present study have been characterized for their microstructures and room temperature mechanical properties.

### **5.1 RAW MATERIALS**

The characterization of raw materials used to prepare various composites investigated in the present study, includes chemical composition, x-ray diffraction analysis, particle size distribution, particle shape and microstructure as well as mechanical properties of as received refractory metal foils. These results are important in understanding the properties of the composites made from these constituents.

#### **5.1.1 Chemical and X-ray Diffraction Analysis**

The chemical analysis of MoSi<sub>2</sub>, SiC and Al powders is presented in Table 5.1 while x-ray diffraction analysis of as received MoSi<sub>2</sub> and SiC powders is shown in Fig. 5.1. The oxygen content of MoSi<sub>2</sub> powder has been found to be about 1.3 wt%. The other principal impurities in MoSi<sub>2</sub> are Fe (0.11 wt%), Mn (0.036 wt%), C (0.08 wt%) and N (0.032 wt%). The oxygen content has been detected by an inert gas carrier technique. The oxygen in MoSi<sub>2</sub> is known to be present in the form of amorphous silica (SiO<sub>2</sub>) particles in free form and as thin films on the surface of MoSi<sub>2</sub> powder particles. Therefore, x-ray diffraction analysis as shown in Fig. 5.1(a) has not revealed any SiO<sub>2</sub>

peaks. The main impurities in SiC powder are C (0.8 wt%), O (0.25 wt%) and N (0.18 wt%). The x-ray diffraction analysis of SiC powder in Fig. 5.1(b) has revealed SiC of  $\beta$ -type, which has a cubic structure as no peaks were found from (100) and (101) planes which are characteristic of  $\alpha$ -SiC having a hexagonal structure. The impurity elements in Al include Si (0.05 wt%), Fe (0.051 wt%), O (0.29 wt%) and traces of Cu, Zn, Mg (<0.002 wt%) and N (35 ppm).

The chemical analysis of refractory metal powders is presented in Table 5.2, while Figs. 5.2(a-c) exhibit the x-ray diffraction analysis of W, Mo and Nb powders, respectively. The main impurities are O, C and Fe in all the three powders. The oxygen content of Mo powder is significantly higher (6.45 wt%). Mo is highly oxidising in nature and is known to pick up oxygen even at room temperature. The x-ray diffraction analysis has revealed that oxygen in Mo powder is present in the form of  $\text{MoO}_3$ , as depicted in Fig. 5.2(b). No oxide phases are detected in as received W and Nb powders, as given in Figs. 5.2(a) and 5.2(c). The other phases if present, are below the volume fraction detectable by XRD.

The chemical analysis of refractory metal foils is presented in Table 5.3. The main impurities are O and C in all the metal foils.

### **5.1.2 Particle Size and Size Distribution**

The particle size distribution curves for  $\text{MoSi}_2$  and SiC powders are shown in Figs. 5.3(a) and 5.3(b), respectively. Figs. 5.4(a-c) present the particle size distribution curves for W, Mo and Nb powders. The particle size distribution curves are generated directly by a computer interfaced with photometer (Seshei Micron Photo Sizer Model 2000S). The average particle sizes of various powders are given in Table 3.1, while a detailed particle size analysis is presented in Table 5.4 in terms of vol%.

Table 5.1 Chemical analysis of the MoSi<sub>2</sub>, SiC and Al powders.

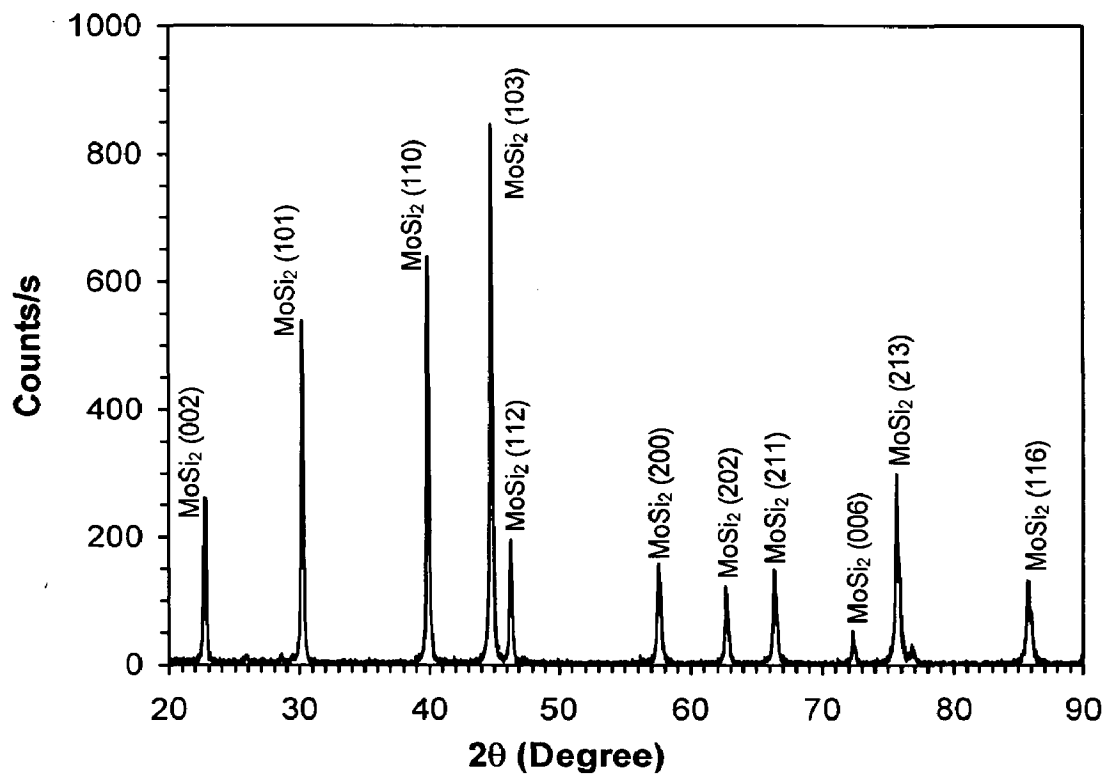
S No.	Powder	O	C	Si	Fe	N	Al	W	Mn	Mg	S
1	MoSi <sub>2</sub>	1.3	0.08		0.11	0.032	<0.02	<0.005	0.036	<0.005	<0.001
2	SiC	0.25	0.8	0.03		0.18					
3	Al	0.29		0.05	0.051	35 ppm	Balance			<0.002	

Table 5.2 Chemical analysis of the W, Mo and Nb powders used as reinforcements.

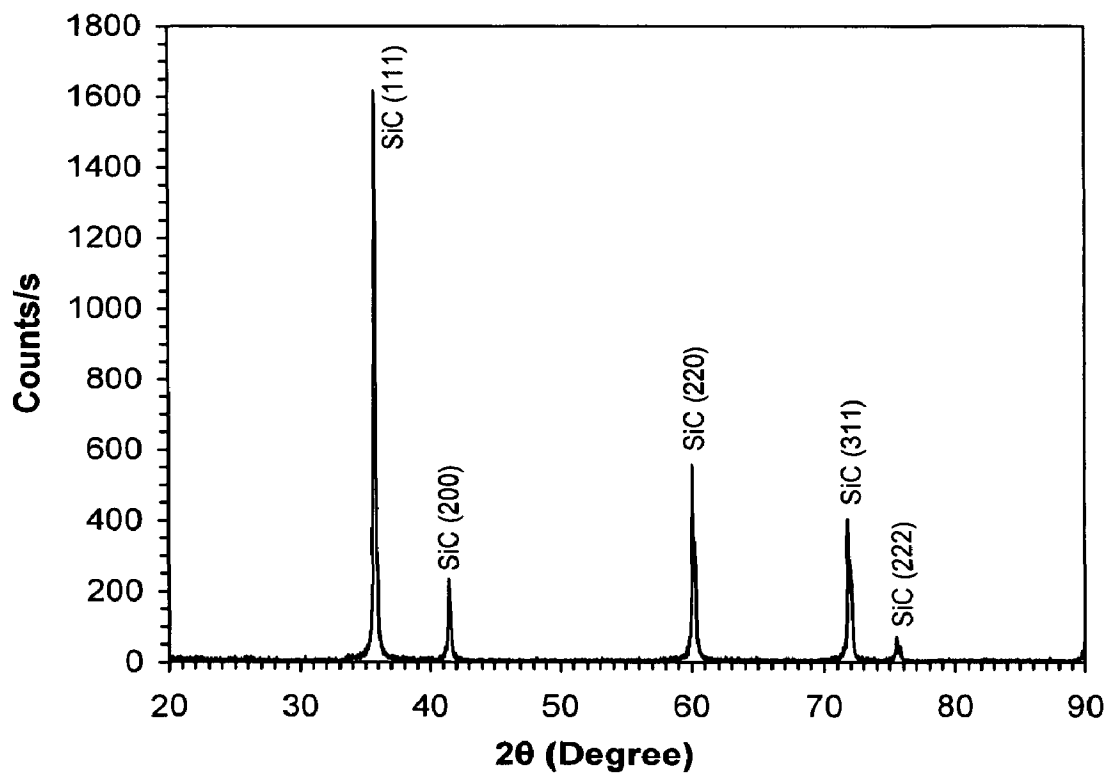
S No.	Powder	O	C	Fe	W	Ta	Mn	Mg	S
1	W	0.07	0.005	<0.01	Balance		<0.005	<0.005	<0.001
2	Mo	6.45	0.02	0.055	<0.005		<0.005	<0.005	<0.001
3	Nb	0.2	0.005	0.025	<0.005	0.1	<0.005	<0.005	<0.001

Table 5.3 Chemical analysis of the as received Mo, Ta and Nb foils used for making MoSi<sub>2</sub> based laminated composites.

S No.	Foil	O	C	Fe	Cr	Al	Ta	Nb	Ni	Si	Zr
1	Mo	0.03		0.004	0.002				0.001		
2	Ta	0.0127	0.003	<0.002	<0.001	<0.0025	Balance	<0.006		0.034	<0.01
3	Nb	0.0213	0.005	0.01	<0.02	<0.0025	<0.1	Balance	<0.001		

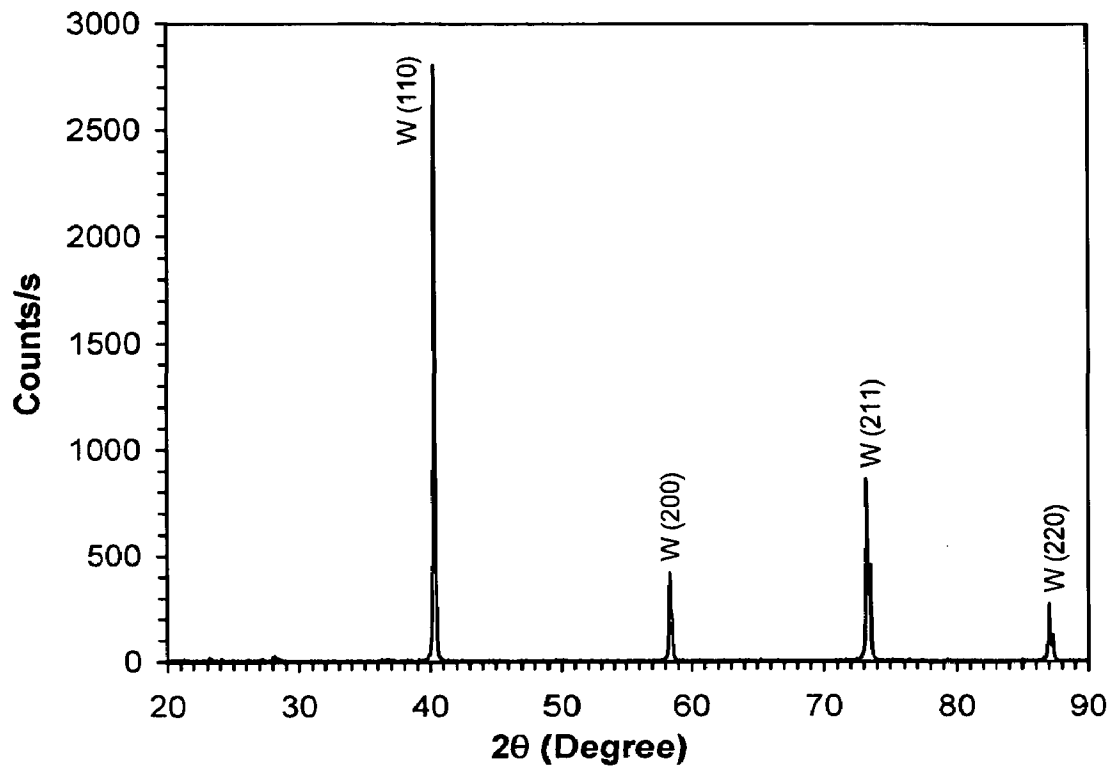


(a)

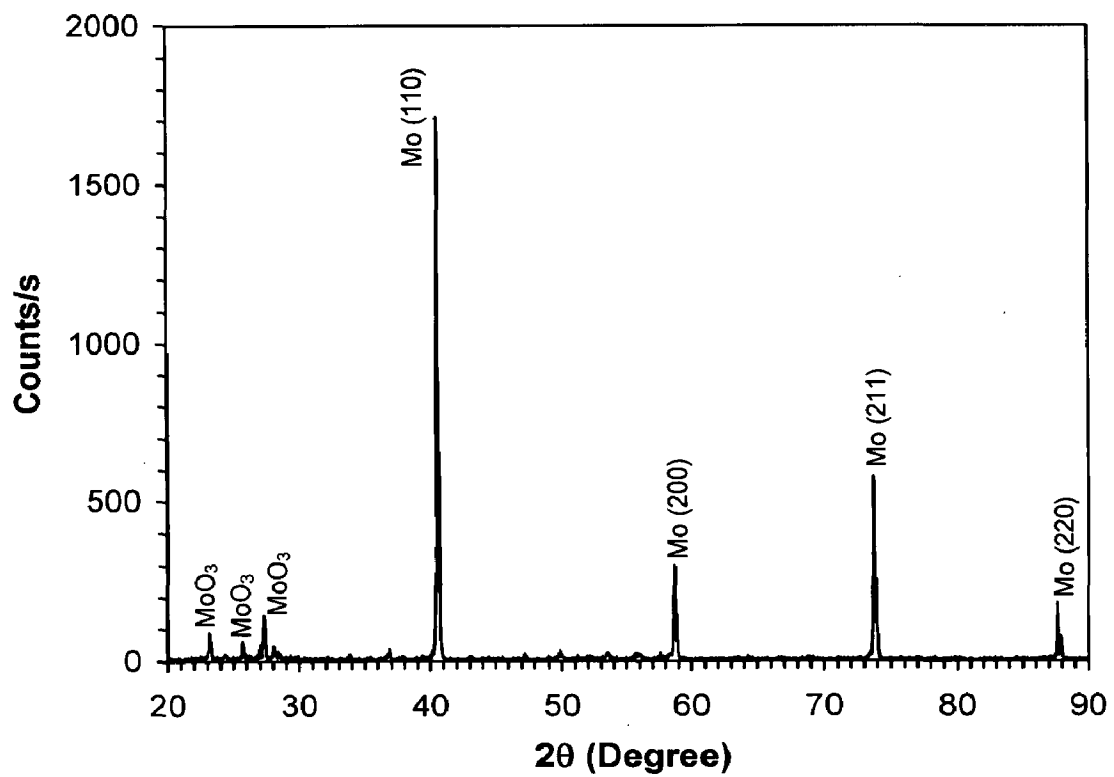


(b)

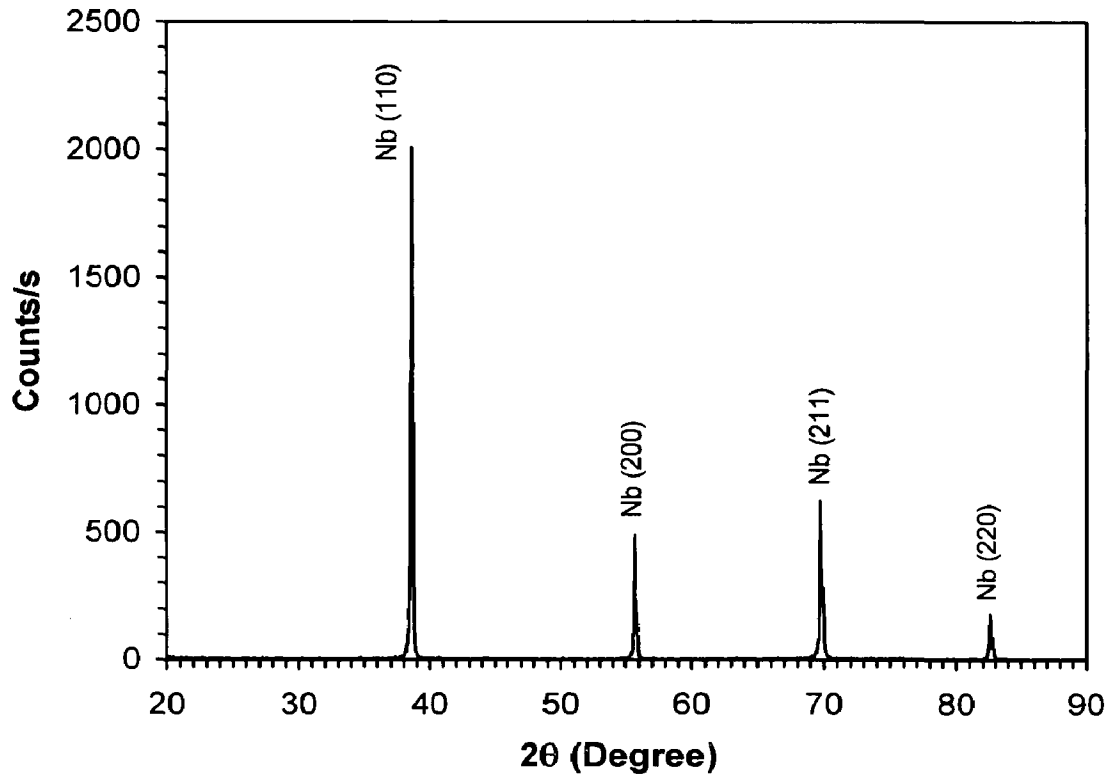
Fig. 5.1 X-ray diffraction patterns of (a) MoSi<sub>2</sub> and (b) SiC powders.



(a)



(b)

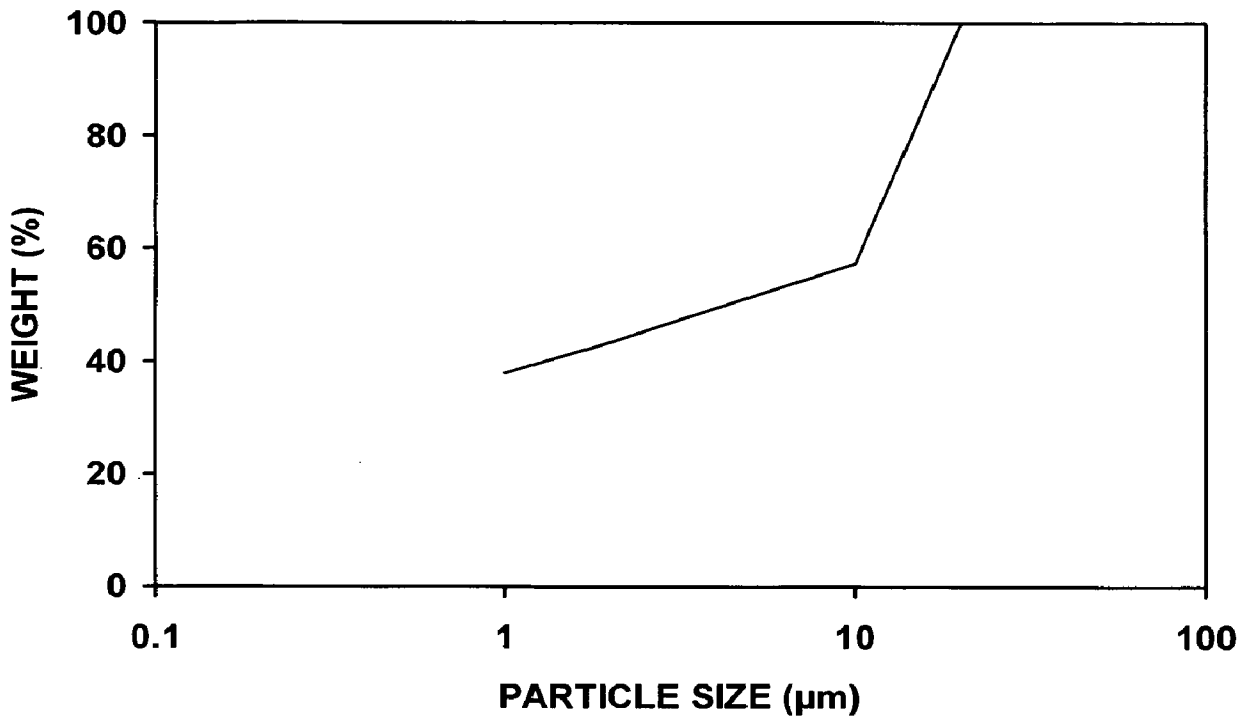


(c)

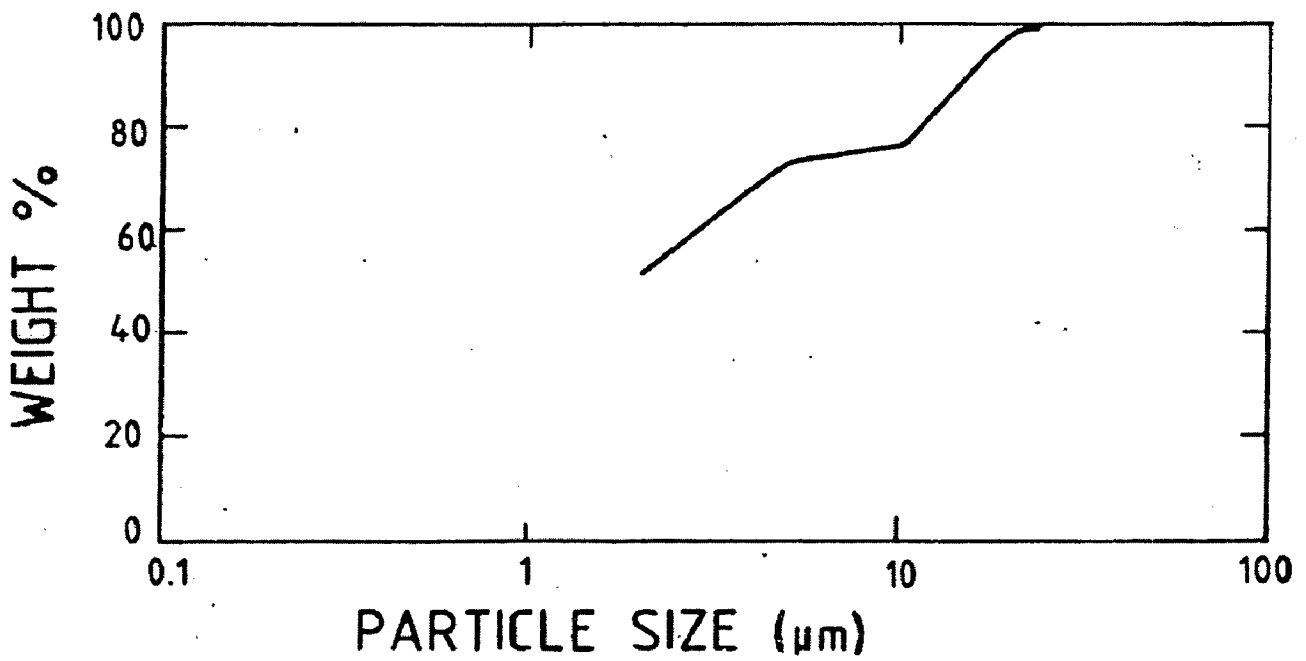
Fig. 5.2 X-ray diffraction patterns of (a) W (b) Mo and (c) Nb powders.

Table 5.4 Particle size distribution for MoSi<sub>2</sub>, W, Mo and Nb powders.

Range ( $\mu\text{m}$ )	Volume %			
	MoSi <sub>2</sub>	W	Mo	Nb
0.00 – 1.00	37.87	9.46	41.02	16.55
1.00 – 2.00	5.4			
2.00 – 5.00	13.98	28.86	13.83	12.64
5.00 – 10.00		9.63	19.25	20.74
10.00 – 20.00	42.75	54.05	25.90	50.07

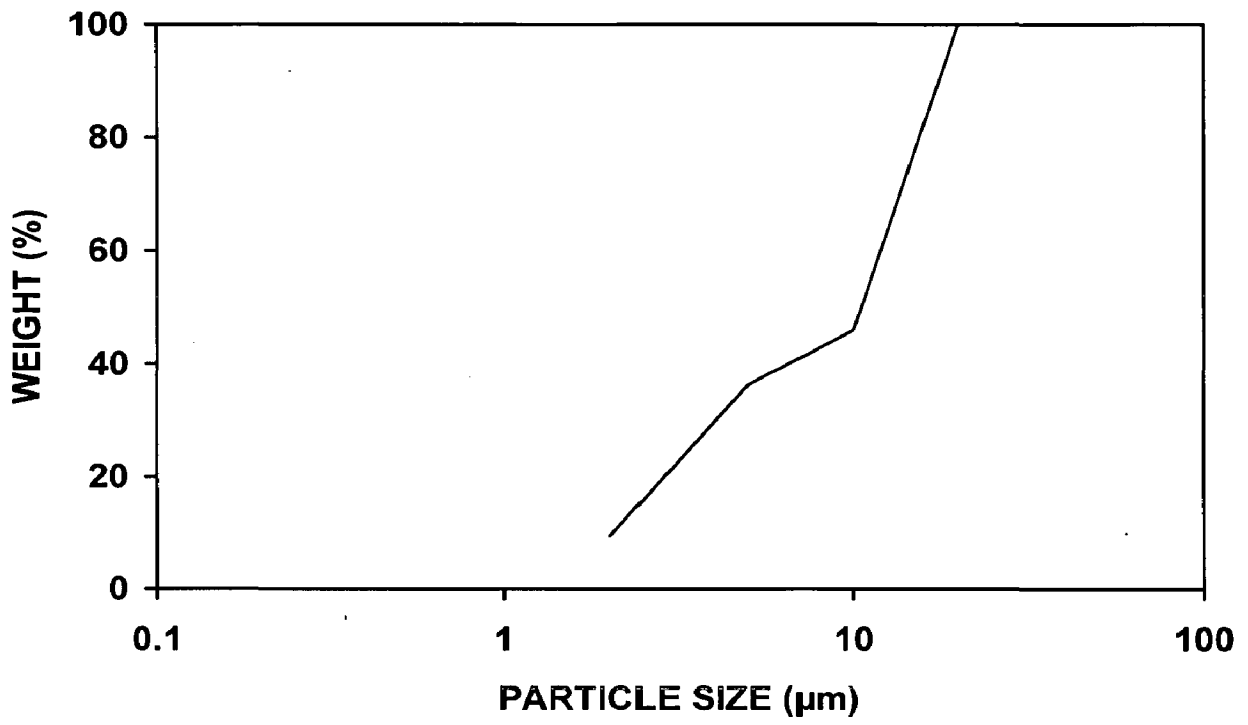


(a)

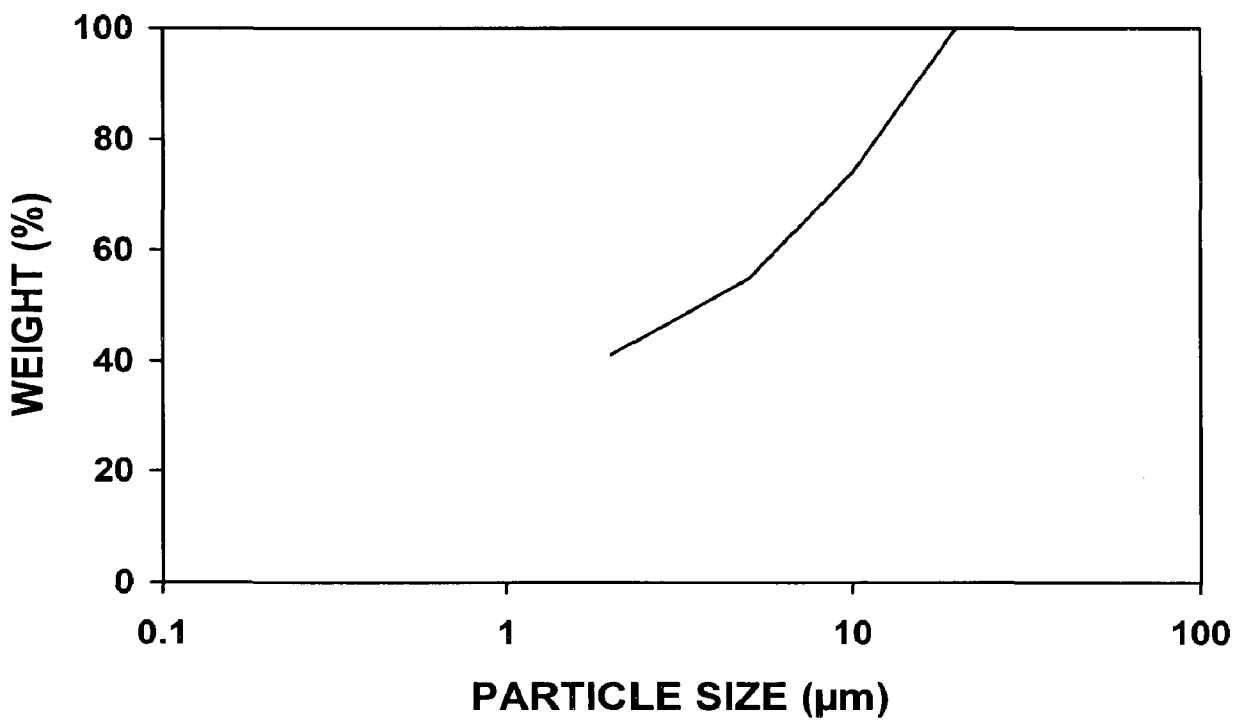


(b)

Fig. 5.3 Particle size analysis of (a) MoSi<sub>2</sub> and (b) SiC powders.

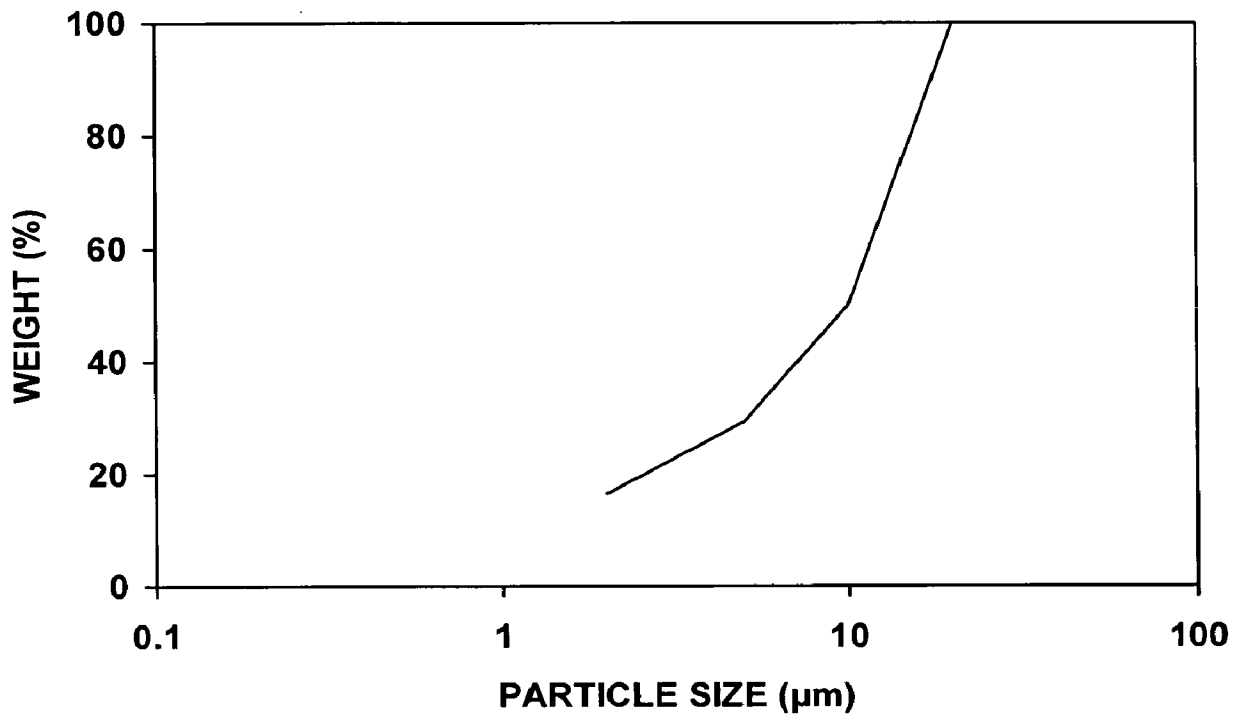


(a)



(b)





(c)

Fig. 5.4 Particle size analysis of (a) W (b) Mo and (c) Nb powders.

### **5.1.3 Particle Shape and Morphology**

Figs. 5.5(a) and 5.5(b) are secondary electron (SE) images of MoSi<sub>2</sub> and SiC powders, respectively, as observed under scanning electron microscope (SEM). The morphology of W, Mo and Nb powders is exhibited in Figs. 5.6(a-c). The shapes of MoSi<sub>2</sub> and SiC particles appear to be irregular and crystalline. The overall geometry of MoSi<sub>2</sub> and SiC particles may be described as angular. This irregularity helps in consolidation due to particle interlocking. The W and Mo powder particles are equiaxed and nearly spherical in shape but are somewhat agglomerated. The W particles appear to be more spherical (rounded) than Mo particles. However, the surface morphology of Nb powder particles consists of flat surfaces and sharp edges. In all the cases, no porosity or cracks are observed on the surface of the powder particles.

### **5.1.4 Characterization of as Received Refractory Metal Foils**

#### **5.1.4.1 Microstructure**

Figure 5.7 shows the optical micrographs of as received pure Mo foil taken at different magnifications. The micrographs reveal a rolled microstructure suggesting that as received Mo foil has been in work-hardened condition. In contrast to Mo foil, as received Ta and Nb foils are obtained in annealed condition. A typical microstructure of as received Ta foil is shown in Fig. 5.8. The microstructure as exhibited in Fig. 5.8(a) appears to have developed texture through banding of planar orientation. The same microstructure taken at a higher magnification in Fig. 5.8(b) reveals more or less an equiaxed grain structure. The contrast between the grains appears to be due to the difference in the etching response of the differently oriented grains.

#### **5.1.4.2 Mechanical Properties**

The as received refractory metal foils used to synthesize the various laminated composites are characterized for their hardness and tensile properties which are presented in Table 5.5. The as received Ta and Nb foils exhibit good ductility while Mo foil is found to be relatively brittle. Mo foil has a high hardness and a much lower strain to failure as compared to Ta and Nb foils, which is consistent with rolled microstructure of as received Mo foil (Fig. 5.7). In contrast to Mo foil, as received Ta and Nb foils are in annealed condition showing more or less an equi-

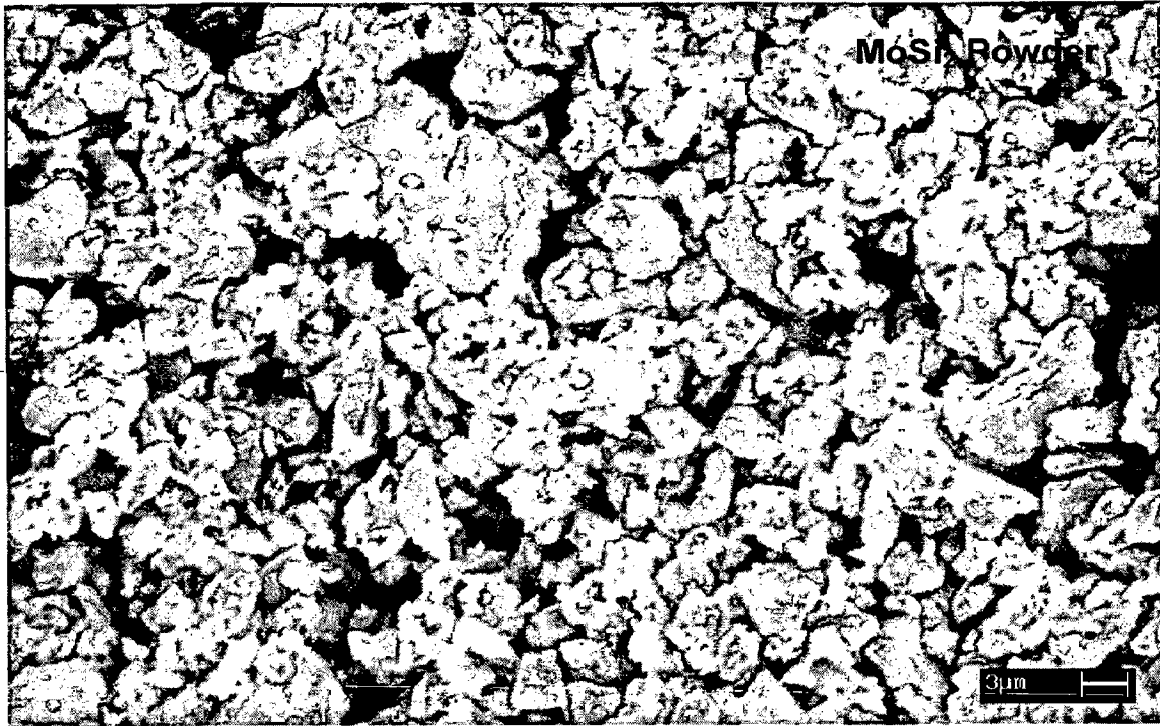
axed grain structure (Fig. 5.8(b)). Mataga (1989) has found the yield strength of as received Nb foil as 300 MPa while Chen et al (1994<sup>a</sup>, 1994<sup>b</sup>) have reported the tensile strength of Nb foil as 400 – 500 MPa. Similar value of yield strength has been obtained for Nb foil used in the present investigation.

Figures 5.9(a), 5.9(b) and 5.9(c) exhibit engineering stress–strain curves of as received Mo, Ta and Nb foils, respectively. The stress-strain curve of Mo foil show very little further work hardening of the rolled material before fracture. However, the stress strain curves of Ta and Nb foils revealed very sharp yield points with well-defined work hardening behaviour. Both these stress strain curves show significant uniform deformation. Ta foil seems to have a higher work hardening rate than Nb foil.

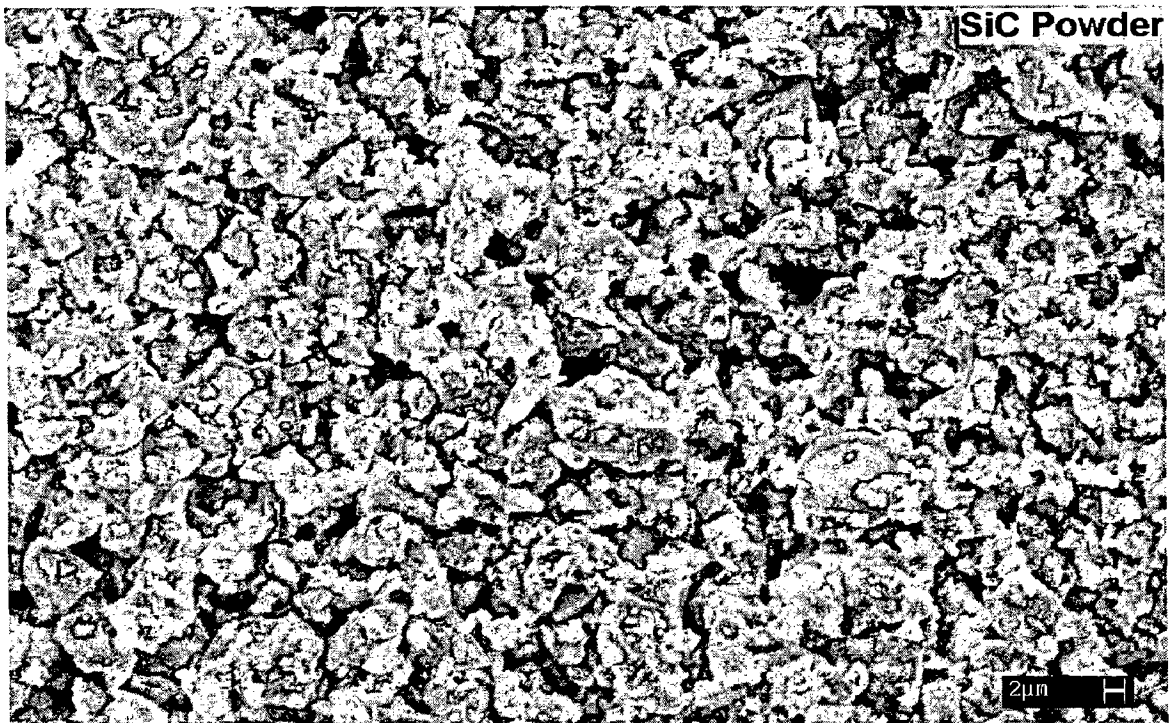
Figure 5.10 shows the fractograph of the as received Mo foil while the fracture surfaces of the as received Ta and Nb foils are shown in Figs. 5.11(a) and 5.11(b), respectively. The fracture surface of Mo foil revealed the deformation along grain (rolled) boundaries as depicted in Fig, 5.10. The grains slide over each other along the rolling direction. The deformation predominantly along the grain boundaries resulted in almost no strain hardening in Mo foil. In contrast, extensive plasticity was seen on fracture surface of the Ta foil as exhibited in Fig. 5.11(a). Tearing ridges as well as microvoids are seen in Fig. 5.11(a). Figure 5.11(b) shows the fracture surface of the Nb foil. Fracture seems to have taken place by micro-void formation and coalescence.

Table 5.5 Tensile properties of as received refractory metal foils used in preparing various laminated composites.

<b>Metal Foil</b>	<b>Hardness (VHN)</b>	<b>Yield Strength (MPa)</b>	<b>Ultimate Tensile Strength (MPa)</b>	<b>Plastic Strain (%)</b>
Mo	287	832	1033	3.2
Ta	161	426	548	17.3
Nb	118	319	401	22.8

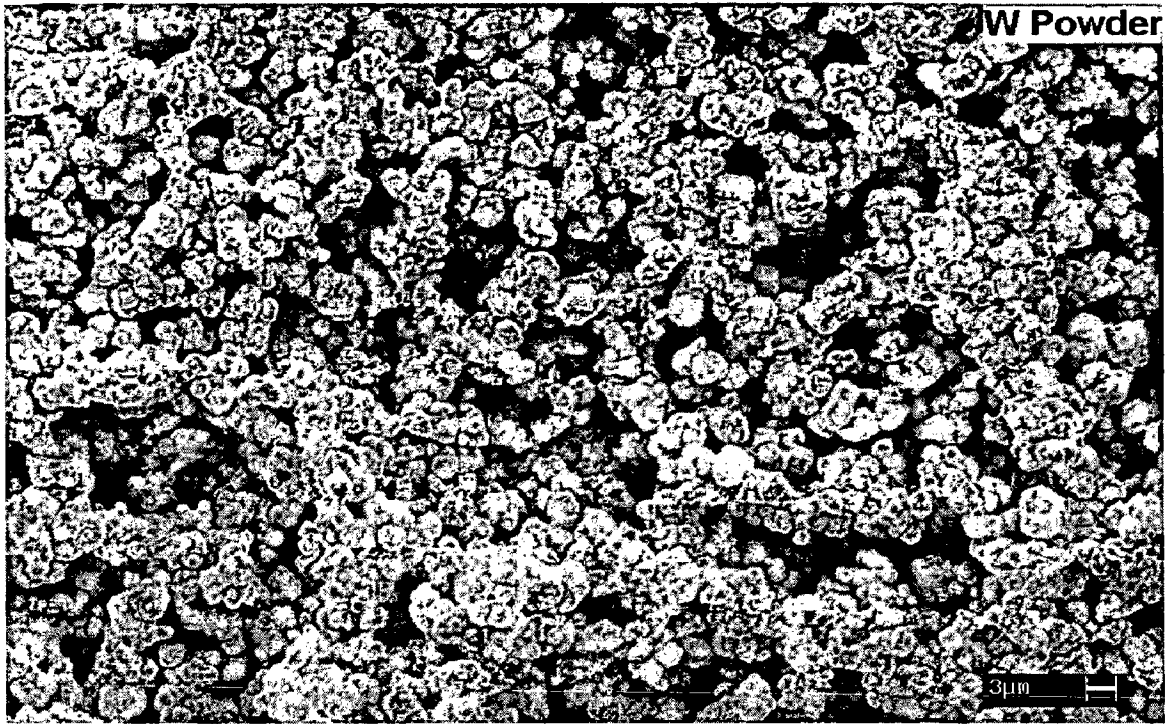


(a)

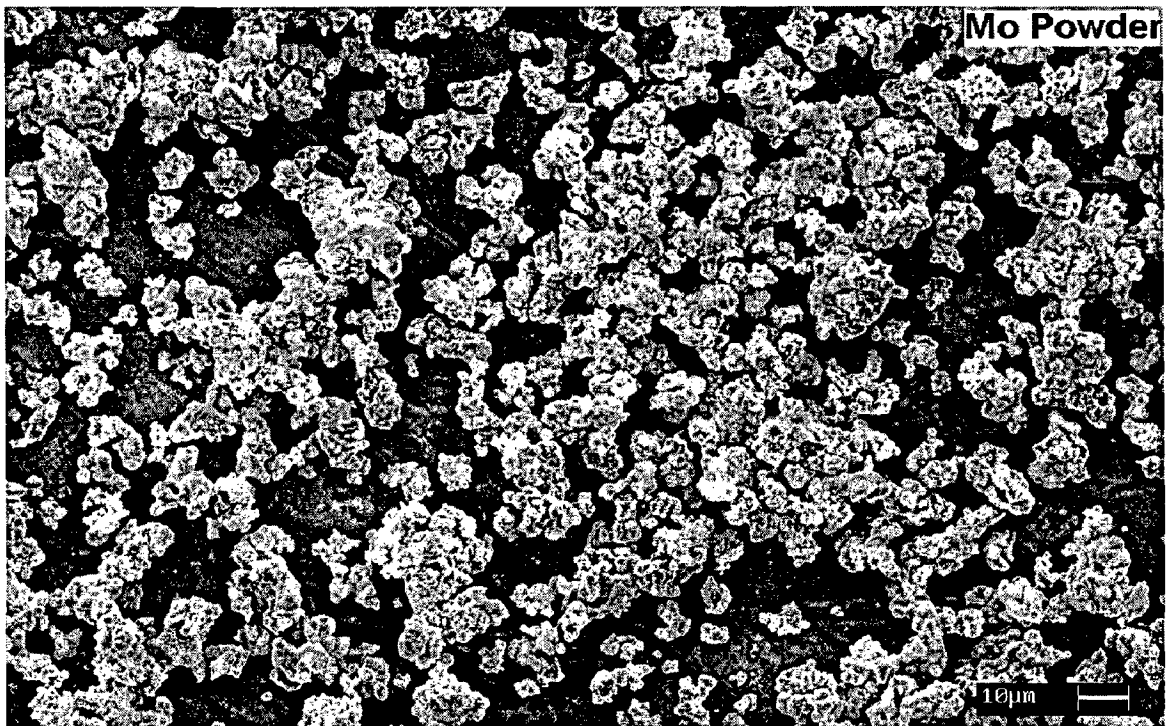


(b)

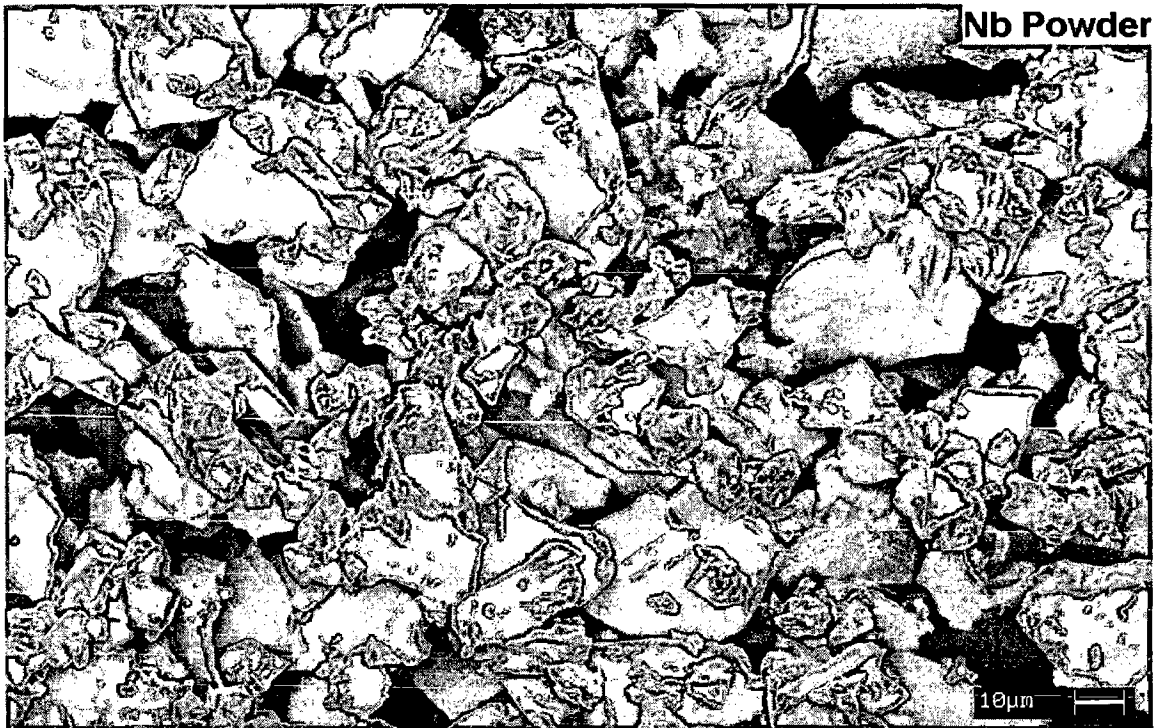
Fig. 5.5 SEM pictures showing shape and morphology of (a) MoSi<sub>2</sub> and (b) SiC powder particles.



(a)

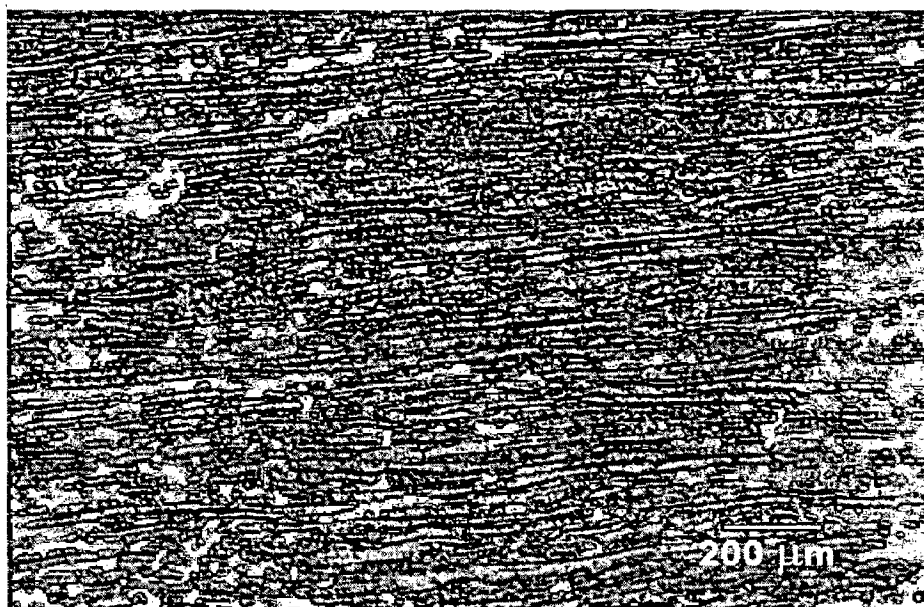


(b)

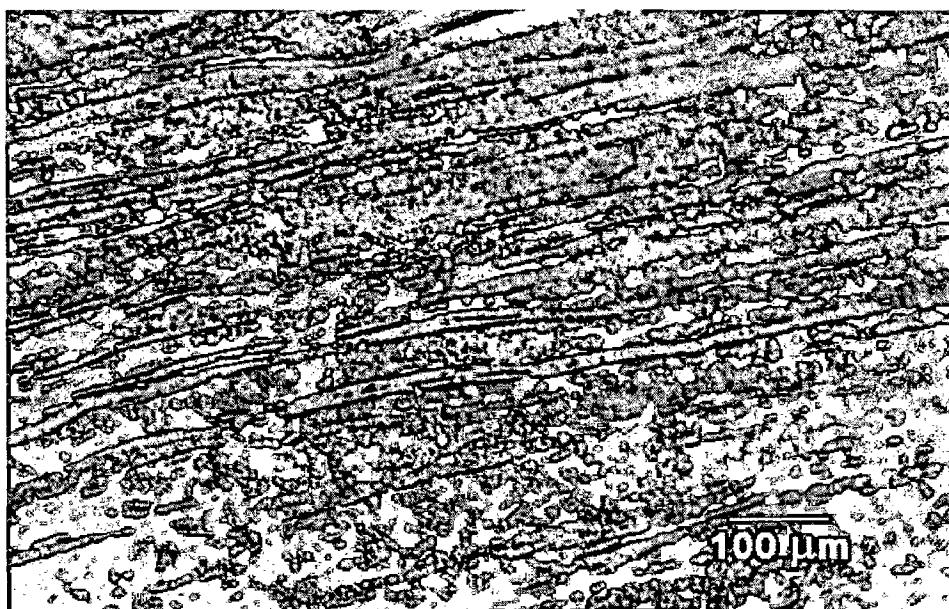


(c)

Fig. 5.6 SEM pictures showing shape and morphology of (a) W (b) Mo and (c) Nb powder particles.

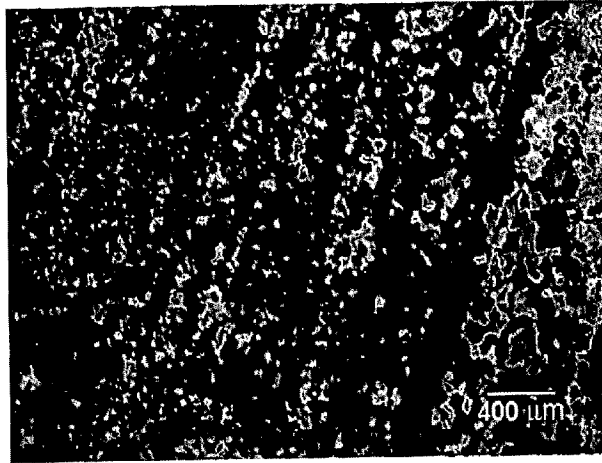


(a)

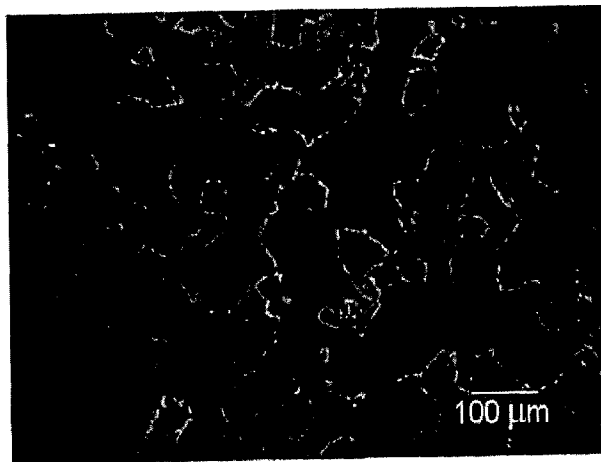


(b)

Fig. 5.7 Optical micrographs of as received pure Mo foil taken at different magnifications.



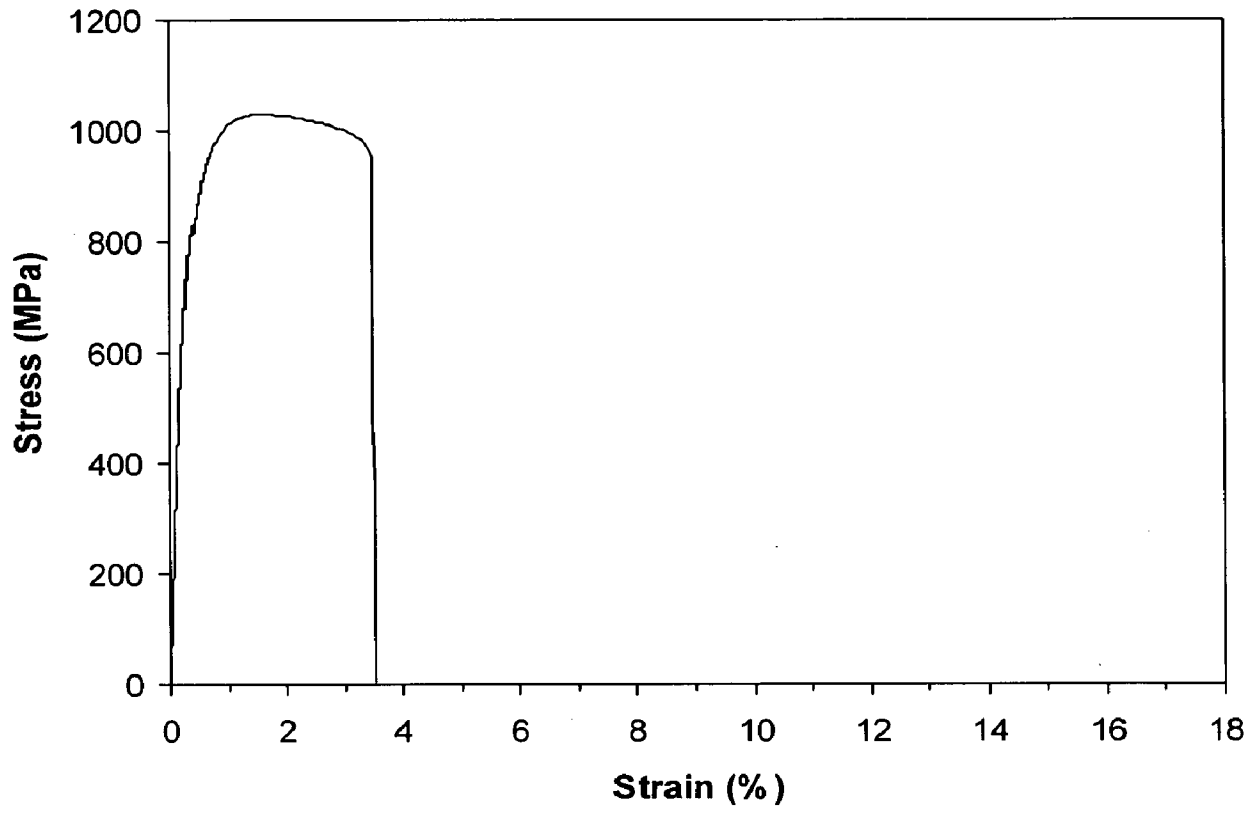
(a)



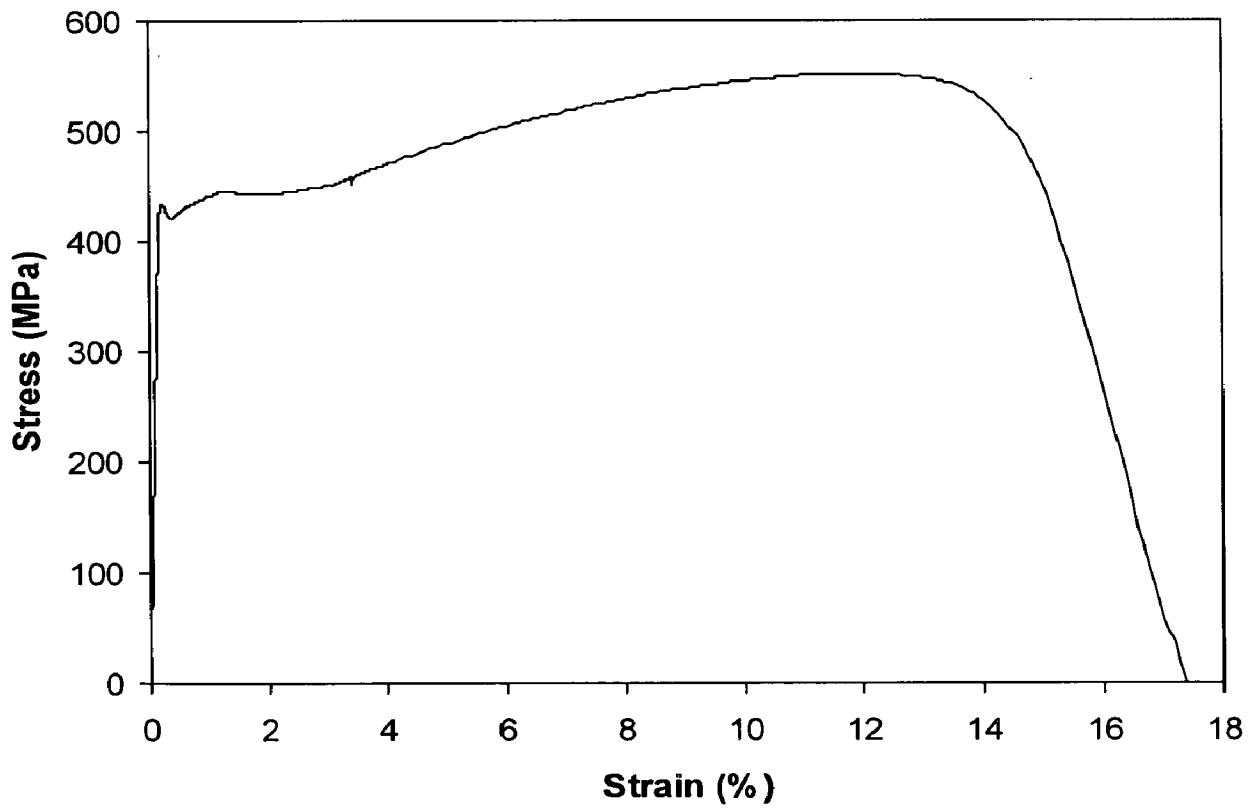
(b)

Fig. 5.8 Optical micrographs of as received pure Ta foil taken at different magnifications.

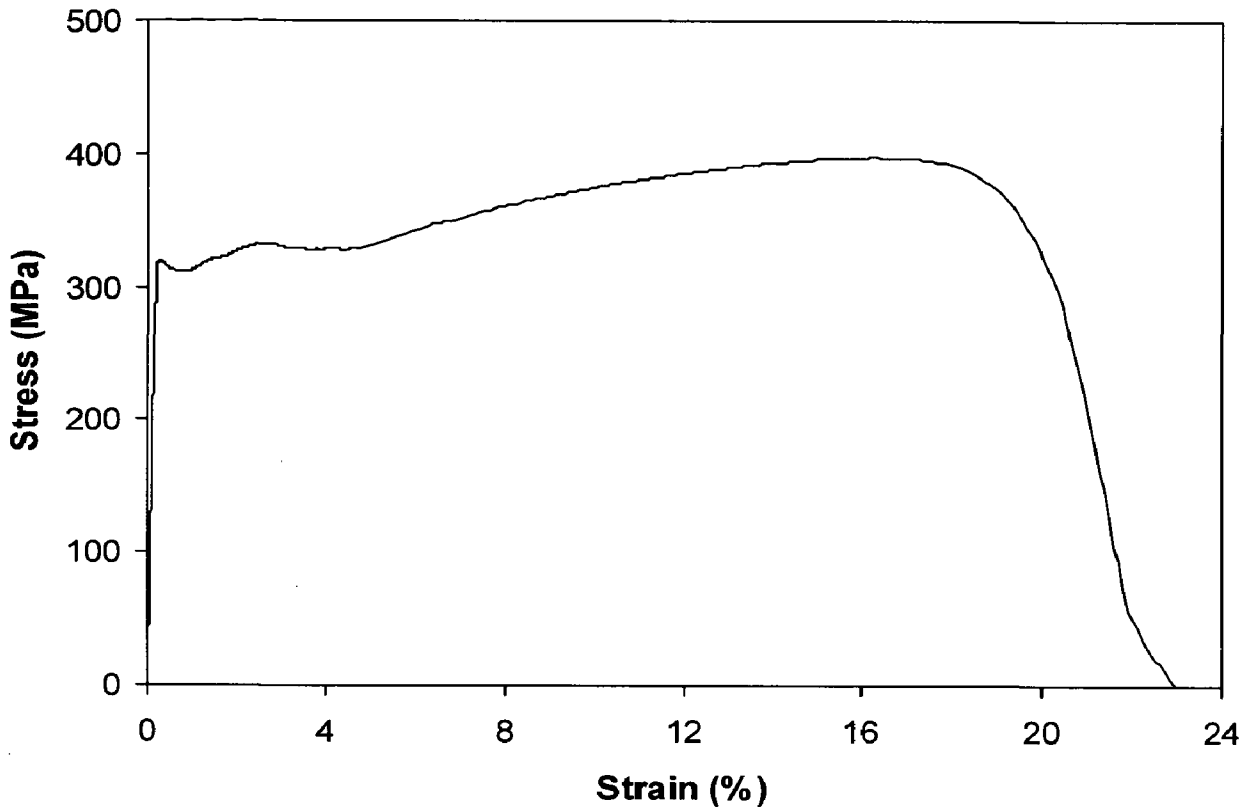




(a)



(b)



(c)

Fig. 5.9 Engineering stress – strain curves of as received refractory metal foils (a) Mo foil (b) Ta foil and (c) Nb foil.

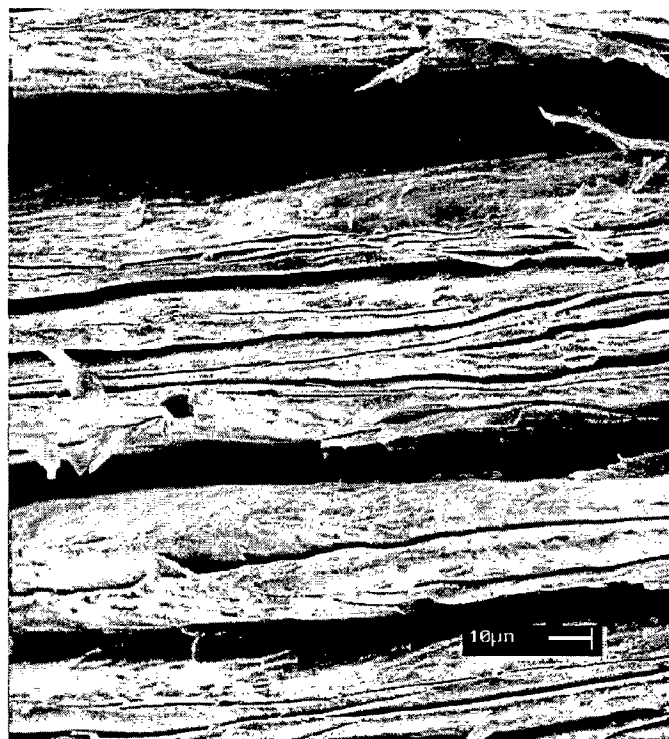


Fig. 5.10 SEM fractograph of as received Mo foil after the uniaxial tensile test.

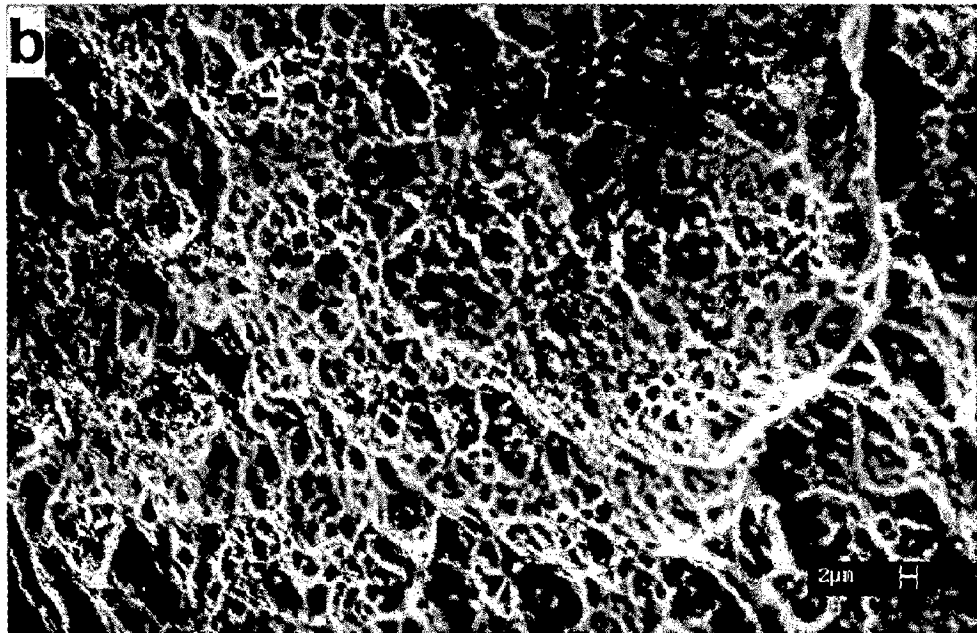
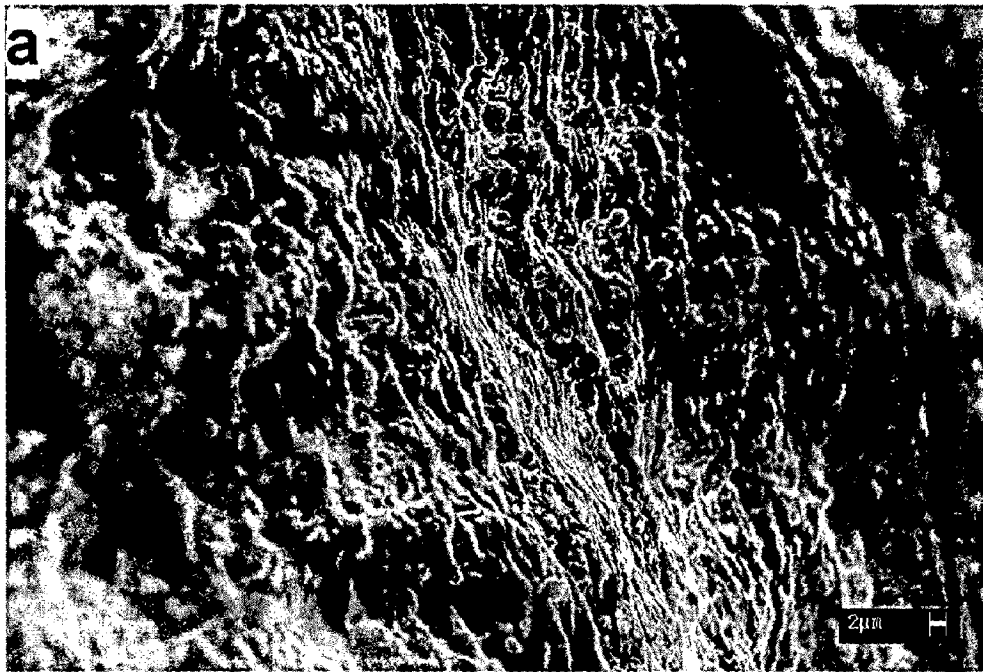


Fig. 5.11 Fracture surfaces of as received (a) Ta foil and (b) Nb foil after the uniaxial tensile test.

It should be noted that the mechanical properties of pure metal foils could be quite different than the properties of bulk materials. Moreover, the hardness and tensile properties of pure metal foils are thickness dependent. Xiao (1991<sup>a</sup>, 1991<sup>b</sup>) has observed that as thickness of the Nb foil increases or decreases, the intrinsic properties of Nb change. Shaw and Abbaschian (1993, 1994, 1995) have measured the hardness and yield strength of Nb foils having different thickness and concluded that thinner the Nb lamina, the less ductile it is. However, Xiao (1991<sup>b</sup>) has found that the ratio between the tensile strength (in MPa) and Vickers Hardness Number (VHN) remains more or less the same for Nb foils having different thicknesses and proposed the following empirical relations for the as received Nb foils:

$$\sigma_{YS}/VHN = 1.52 \quad (5.1)$$

$$\sigma_{UTS}/VHN = 2.48 \pm 0.04 \quad (5.2)$$

Thus, it has been claimed that it is reasonable to infer the strength of the Nb foil from the hardness measured. In the present investigation, the foils of three different materials having the same thickness have been used. Interestingly, the  $\sigma_{UTS}/VHN$  is found to be the same as 3.40 for Ta and Nb foils while it is 3.60 for Mo foil, which has a different microstructure than Ta and Nb foils. The  $\sigma_{YS}/VHN$  ratio is 2.90 for Mo foil, which is also higher than  $2.67 \pm 0.03$ , obtained for Ta and Nb foils. Based on the above findings, it can probably be assumed that the strength / hardness ratio for different refractory metal foils remains more or less the same provided the foils are in similar state having similar microstructures.

## 5.2 DUCTILE REFRACTORY METAL PARTICLES REINFORCED MoSi<sub>2</sub> BASED COMPOSITES

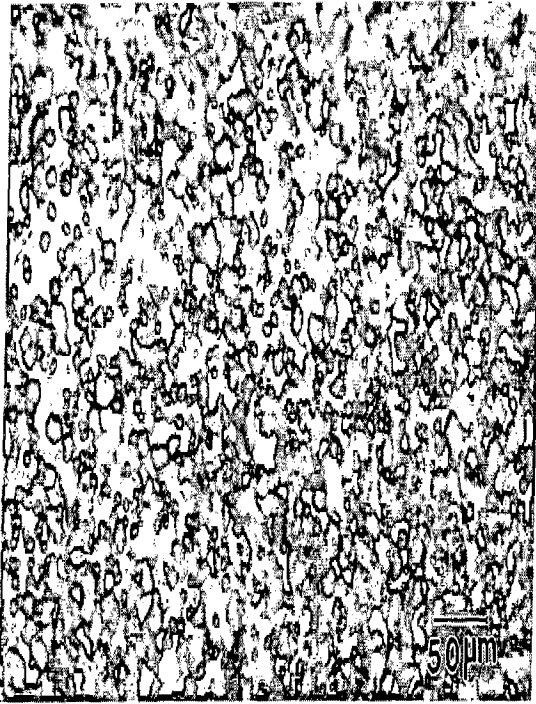
### 5.2.1 Microstructural Studies

The microstructures of MoSi<sub>2</sub> + 20 vol% W, MoSi<sub>2</sub> + 20 vol% Mo and MoSi<sub>2</sub> + 20 vol% Nb particulate composites using polarized light optical microscopy are shown in Fig. 5.12. In general, the MoSi<sub>2</sub> matrix grains are regular and equi-axed. The grain size of MoSi<sub>2</sub> is in the range of 10 - 15 μm in all the three composites which is significantly higher than the average particle size of MoSi<sub>2</sub> (6 μm) powder prior to hot pressing (Table 2.1). This could be attributed to the effect of grain growth in MoSi<sub>2</sub> at high processing temperatures.

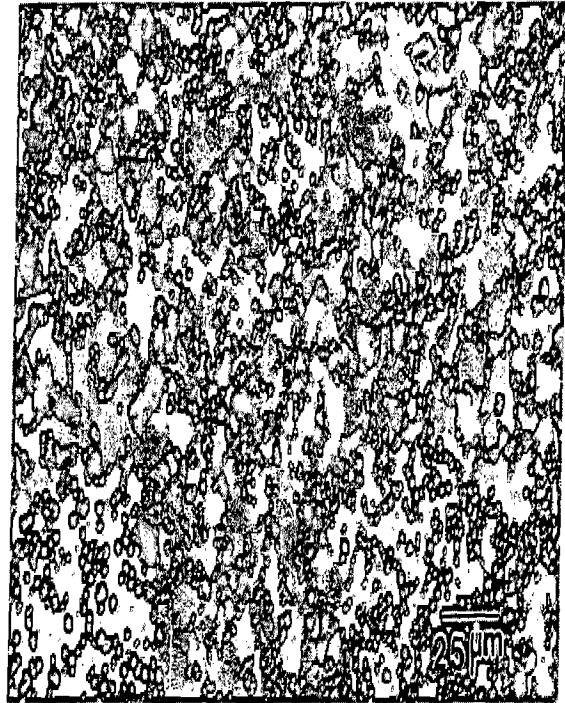
Figure 5.13 exhibits the SEM back scattered electron images of  $\text{MoSi}_2 + 20$  vol% W composite taken at different magnifications. The dark, small and rounded particles in the microstructure are of free  $\text{SiO}_2$ .  $\text{MoSi}_2$  has reacted with W and formed bright  $\text{W}_5\text{Si}_3$ . Different particles in microstructure were identified by EPMA studies. This is also evident from x-ray diffraction pattern of  $\text{MoSi}_2 - \text{W}$  composite as shown in Fig. 5.14. The x-ray diffraction data reveal the presence of  $\text{W}_5\text{Si}_3$  peaks while pure W peaks are missing. Si has diffused from  $\text{MoSi}_2$  towards W converting it into  $\text{W}_5\text{Si}_3$ . The entire W has been converted into  $\text{W}_5\text{Si}_3$ . The contrast in BSE image of Fig. 5.13(b) suggests that Si has diffused primarily through the  $\text{MoSi}_2$  grain boundaries. This results in depletion of Si in  $\text{MoSi}_2$ . As  $\text{MoSi}_2$  is a line compound and does not show non-stoichiometry, a part of it gets converted into  $\text{Mo}_5\text{Si}_3$ . The formation of  $\text{Mo}_5\text{Si}_3$  is more likely to occur in the regions close to the interface. Further studies by EPMA have revealed the presence of  $\text{Mo}_5\text{Si}_3$  and  $\text{WSi}_2$  phases. The x-ray diffraction pattern (Fig. 5.14) also shows the peaks of  $\text{Mo}_5\text{Si}_3$  and  $\text{WSi}_2$  in addition to  $\text{MoSi}_2$  and  $\text{W}_5\text{Si}_3$  peaks.

The EPMA images (BSE and elemental x-ray maps) of  $\text{MoSi}_2 - \text{W}$  composite are shown in Fig. 5.15. Si and Mo have diffused extensively in W as revealed by x-ray map of Si, Fig. 5.15(d) and x-ray map of Mo, Fig. 5.15(c). Figure 5.15(b) shows a significant amount of W diffusion in  $\text{MoSi}_2$  as W readily dissolves in  $\text{MoSi}_2$  as compared to other refractory metals.  $\text{WSi}_2$  and  $\text{MoSi}_2$  have similar crystal structures (tI6, prototype  $\text{MoSi}_2$ ) and almost identical atom radius. The atom radii of Mo and W are 1.36 Å and 1.37 Å, respectively. This results in similar lattice parameters and interatomic spacings in  $\text{WSi}_2$  and  $\text{MoSi}_2$ . They form a complete solid solution across the entire composition range as depicted schematically in Fig. 1.8.

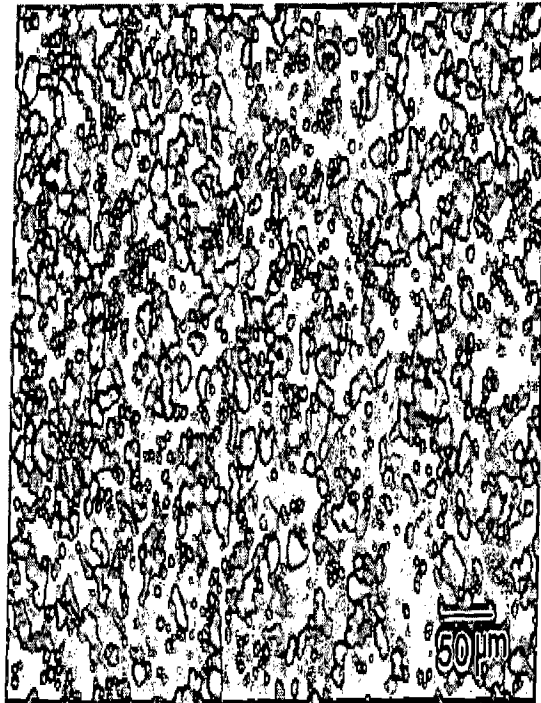
The composition of the reaction products between  $\text{MoSi}_2$  and W as determined by electron probe micro-analysis (EPMA) is presented in Table 5.6. The typical microprobe data obtained at two different locations (as indicated by A and B in the BSE image) correspond to  $(\text{Mo}_{0.73}, \text{W}_{0.27})\text{Si}_2$  and  $(\text{W}_{0.56}, \text{Mo}_{0.44})_5\text{Si}_3$  phases, respectively. Microprobe data has revealed a concentration gradient of Mo within the  $(\text{W}, \text{Mo})_5\text{Si}_3$  phase. Similarly, there was a concentration gradient of W inside  $(\text{Mo}, \text{W})\text{Si}_2$  phase.



(a)

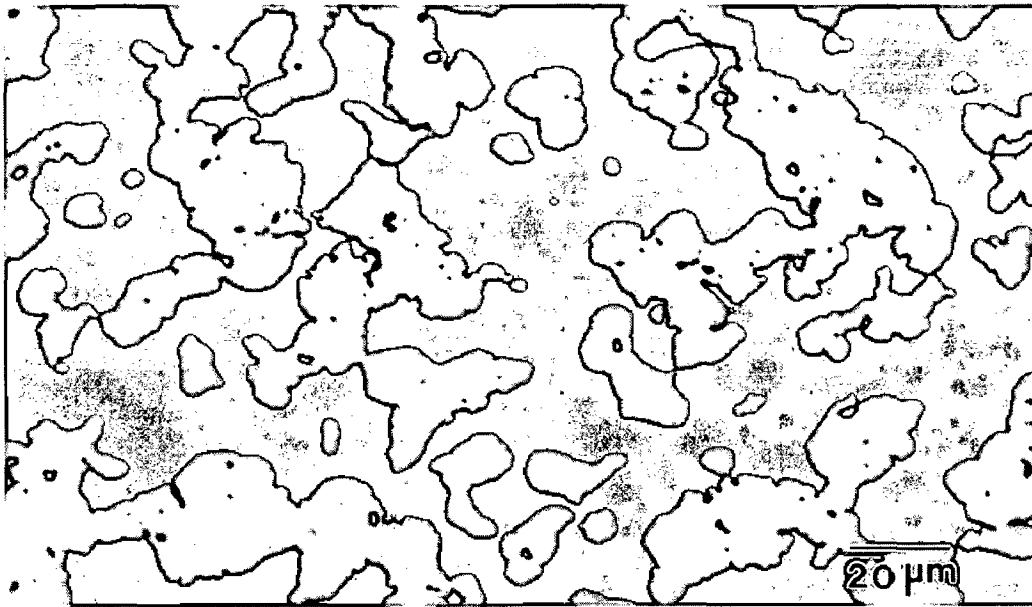


(b)

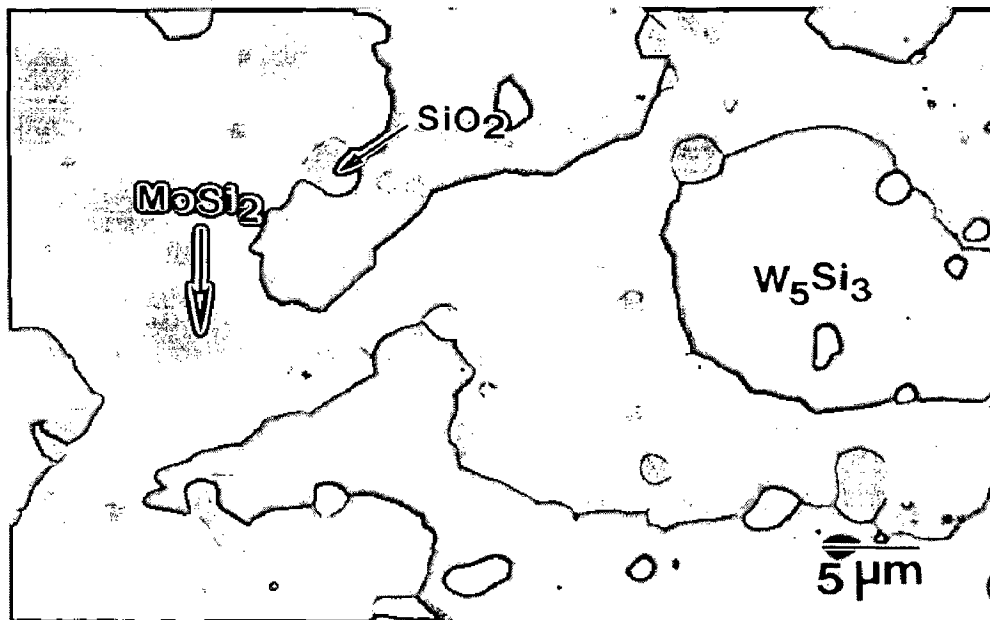


(c)

Fig. 5.12 Polarized light optical micrographs of (a)  $\text{MoSi}_2 + 20 \text{ vol\% W}$  (b)  $\text{MoSi}_2 + 20 \text{ vol\% Mo}$  and (c)  $\text{MoSi}_2 + 20 \text{ vol\% Nb}$  composites



(a)



(b)

Fig. 5.13 SEM back scattered electron (BSE) images of  $MoSi_2$  + 20 vol% W composite taken at different magnification.

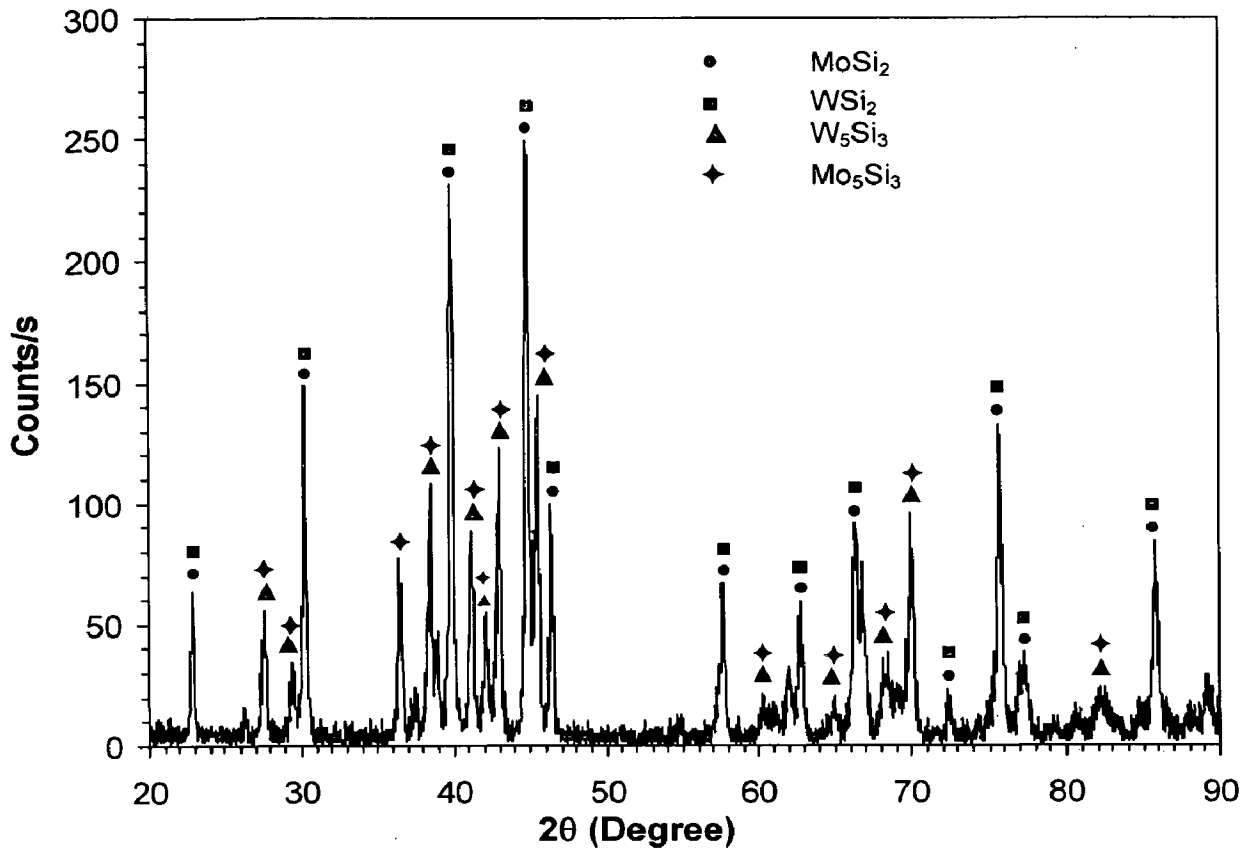


Fig. 5.14 X-ray diffraction pattern of  $\text{MoSi}_2 + 20 \text{ vol\% W}$  composite

Table 5.6 Composition of the reaction products between  $\text{MoSi}_2$  matrix and W particles as determined by electron probe micro-analysis (EPMA) in Fig. 5.15(a). All compositions are given in atom percent.

Region	Mo	Si	W	Phase
A	23.388	68.113	8.499	$\sim (\text{Mo, W})\text{Si}_2$
B	26.900	39.042	34.058	$\sim (\text{W, Mo})_5\text{Si}_3$



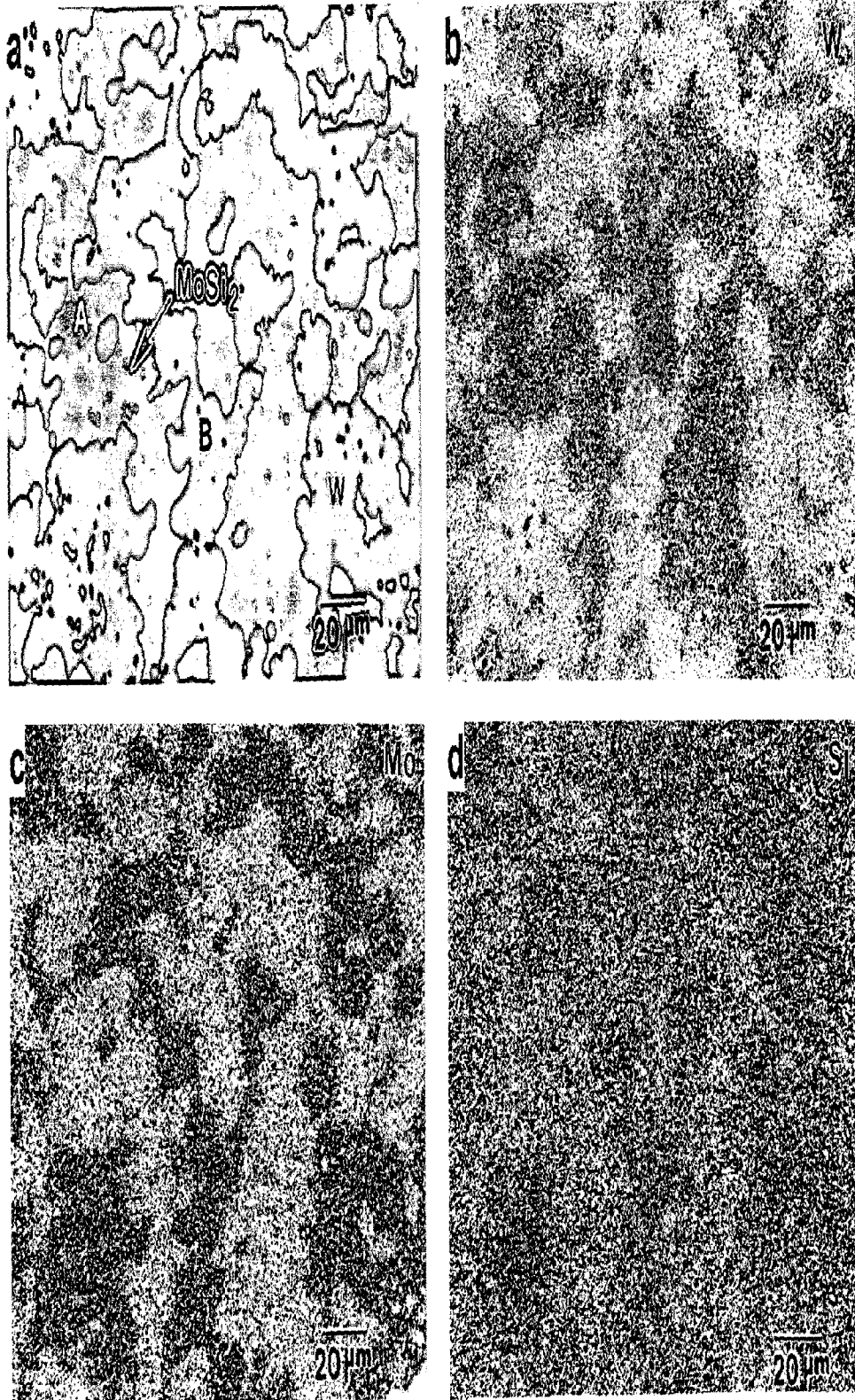


Fig. 5.15 EPMA images of MoSi<sub>2</sub> + 20 vol% W composite (a) back scattered electron image (b) x-ray map of W (c) x-ray map of Mo and (d) x-ray map of Si

The SEM back scattered electron images of  $\text{MoSi}_2 + 20 \text{ vol\% Mo}$  composite taken at different magnifications are shown in Fig. 5.16. A relatively large amount of dark particles seen in the microstructure are probably due to high oxygen content of the initial Mo powder. The dark particles in the microstructure are of free  $\text{SiO}_2$  and  $\text{MoO}_2$ . The pure Mo particles are converted into  $\text{Mo}_5\text{Si}_3$  due to Si diffusion from  $\text{MoSi}_2$ . The x-ray diffraction pattern of  $\text{MoSi}_2 - \text{Mo}$  composite is presented in Fig. 5.17. It exhibits peaks of  $\text{MoO}_2$  (melting point  $2327 \text{ }^\circ\text{C}$ ) apart from the  $\text{MoSi}_2$  and  $\text{Mo}_5\text{Si}_3$  peaks. This is in contrast to the x-ray diffraction pattern of as received Mo powder (Fig. 5.2(b)), which exhibited the peaks of  $\text{MoO}_3$ . The absence of  $\text{MoO}_3$  in the composite could be attributed to the fact that  $\text{MoO}_3$  is likely to get vaporized during the processing at high temperature owing to its low melting point ( $800 \text{ }^\circ\text{C}$ ). However, some oxidation of Mo could have occurred during high temperature processing due to its high affinity with oxygen. This could result in the formation of  $\text{MoO}_2$ .

The EPMA back scattered electron image of  $\text{MoSi}_2 - \text{Mo}$  composite and x-ray map of Si are shown in Figs. 5.18(a) and 5.18(b), respectively. Si has diffused into Mo converting it completely into  $\text{Mo}_5\text{Si}_3$ . Microprobe data (Table 5.7) taken inside the reinforcing phase also reveal the conversion of pure Mo into  $\text{Mo}_5\text{Si}_3$  phase. But no significant presence of  $\text{Mo}_3\text{Si}$  has been observed. The x-ray diffraction pattern (Fig. 5.17) also does not reveal any pure Mo peaks.

Figures 5.19(a) and 5.19(b) are the SEM back scattered electron images of  $\text{MoSi}_2 + 20 \text{ vol\% Nb}$  composite. The microstructure shows predominantly  $\text{MoSi}_2$  and  $\text{Nb}_5\text{Si}_3$  phases with small particles of free  $\text{SiO}_2$  (dark and rounded). The x-ray diffraction pattern as depicted in Fig. 5.20 does not reveal any pure Nb peak suggesting that the entire amount of Nb was converted into  $\text{Nb}_5\text{Si}_3$  due to Si diffusion from  $\text{MoSi}_2$ . The BSE image taken at a higher magnification (Fig. 5.19(b)) reveals an interfacial layer between  $\text{MoSi}_2$  and  $\text{Nb}_5\text{Si}_3$ . The development of this interfacial layer could be due to Si depletion in  $\text{MoSi}_2$  in the regions close to the interface and resulting in the formation of  $\text{Mo}_5\text{Si}_3$  phase. The x-ray diffraction pattern reveals the presence of  $\text{Mo}_5\text{Si}_3$  peaks in addition to the peaks of  $\text{MoSi}_2$  and  $\text{Nb}_5\text{Si}_3$ .

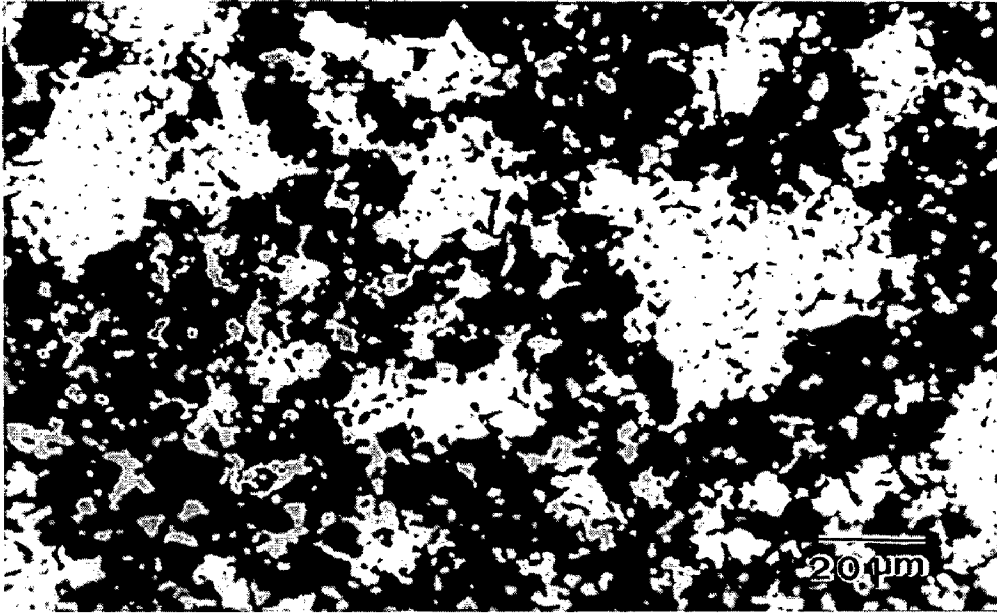
Figure 5.21(a) shows the EPMA back scattered electron image of  $\text{MoSi}_2 - \text{Nb}$  composite. The x-ray maps of Nb, Si and Mo are shown in Figs. 5.21(b), 5.21(c) and

5.21(d), respectively. It is evident from Fig. 5.21(c) and 5.21(d) that extensive diffusion of Si and Mo has taken place into pure Nb. Si seems to have diffused more rapidly and uniformly than Mo.

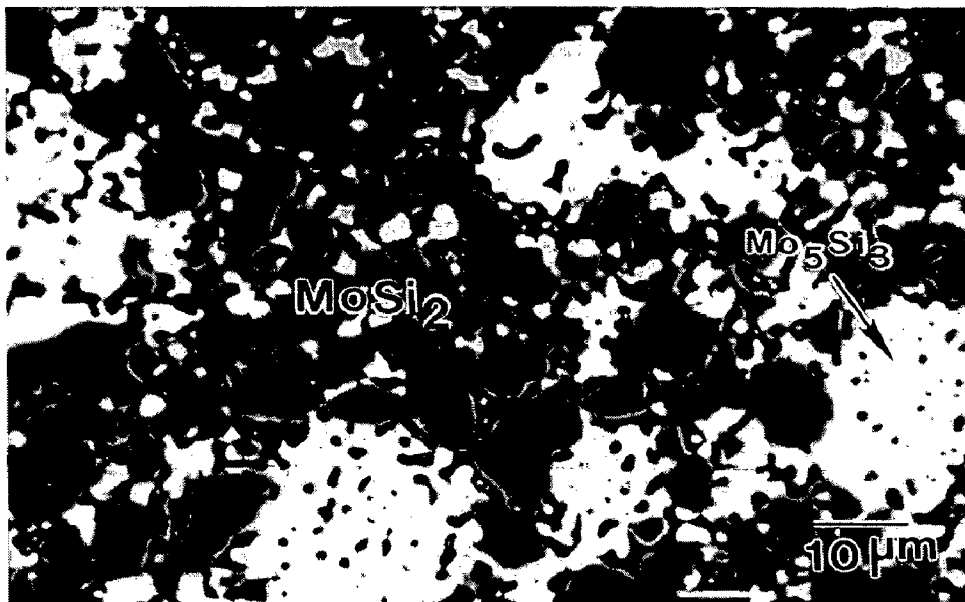
It is interesting to observe that there is little diffusion of Nb in MoSi<sub>2</sub> (Fig. 5.21(b)). Only traces of Nb are revealed inside MoSi<sub>2</sub> by microprobe data. This is in contrast with the MoSi<sub>2</sub> – W composite which exhibited extensive diffusion of W in MoSi<sub>2</sub>. This could be attributed to the limited solubility of NbSi<sub>2</sub> in MoSi<sub>2</sub> as depicted schematically in Fig. 1.8. NbSi<sub>2</sub> has a hexagonal crystal structure (hP9) while MoSi<sub>2</sub> and WSi<sub>2</sub> have similar tetragonal crystal structures (tI6).

The chemical composition of the reaction products between MoSi<sub>2</sub> and Nb as determined by electron probe micro-analysis (EPMA) is presented in Table 5.8. The typical microprobe data obtained at locations marked by A, B and C in the BSE image correspond to MoSi<sub>2</sub>, (Nb<sub>0.76</sub>, Mo<sub>0.24</sub>)<sub>5</sub>Si<sub>3</sub> and Nb<sub>5</sub>Si<sub>3</sub> phases, respectively. Microprobe data has revealed a concentration gradient of Mo within the (Nb, Mo)<sub>5</sub>Si<sub>3</sub> phase.

The powders of MoSi<sub>2</sub> that are commercially available carry with them significant amounts of free SiO<sub>2</sub>. Therefore, microstructures (polarized light optical micrographs as well as SEM back scattered electron images) of all the ductile refractory metal particle reinforced MoSi<sub>2</sub> matrix composites exhibit plenty of free SiO<sub>2</sub> particles. SiO<sub>2</sub> particles possess high reflectivity and hence appear bright in polarized light, and dark in ordinary bright field optical microscopy. The SiO<sub>2</sub> particles were distributed randomly all throughout the microstructures including grain boundaries, interfaces and inside the matrix and reinforcement phases. The SiO<sub>2</sub> particles present inside the reinforcing phases may be due to the diffusion of silicon from the adjacent MoSi<sub>2</sub> phase and its oxidation during the processing at high temperatures. Figure 5.22(a) shows a high magnification EPMA back scattered electron image of MoSi<sub>2</sub> + 20 vol% W composite exhibiting one such SiO<sub>2</sub> particle present within the MoSi<sub>2</sub> matrix. Elemental x-ray maps of Si and oxygen are shown in Figs. 5.22(b) and 5.22(c), respectively confirming that the particle indeed is rich in Si and oxygen. Cotton et al (1991) have carried out the TEM analysis of vacuum hot pressed MoSi<sub>2</sub> samples fabricated from the commercial MoSi<sub>2</sub> powders and indicated that these particles are of amorphous SiO<sub>2</sub> and so, does not show presence of any peak in XRD.



(a)



(b)

Fig. 5.16 SEM back scattered electron (BSE) images of  $\text{MoSi}_2 + 20 \text{ vol\% Mo}$  composite taken at different magnifications.

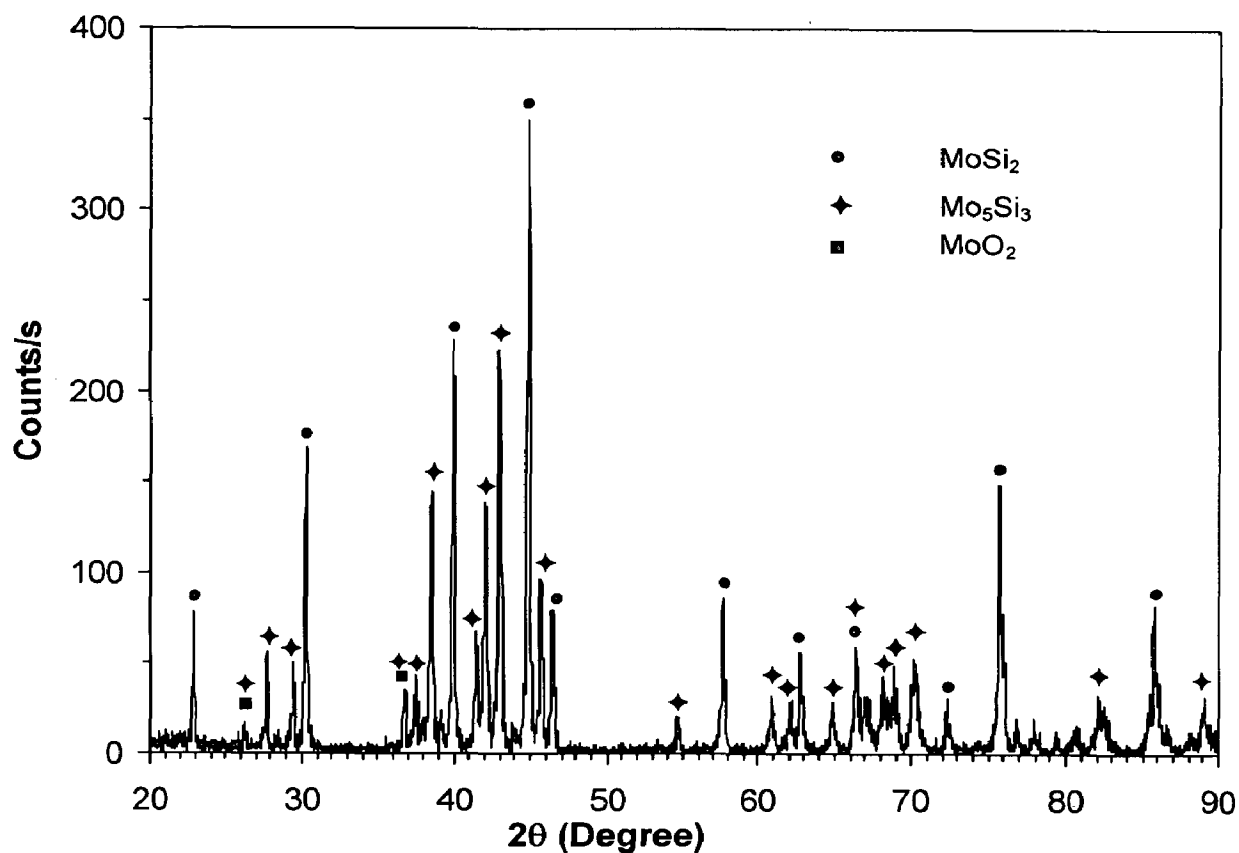


Fig. 5.17 X-ray diffraction pattern of  $\text{MoSi}_2 + 20 \text{ vol\% Mo}$  composite

Table 5.7 Composition of the reaction products between  $\text{MoSi}_2$  matrix and Mo particles as determined by electron probe micro-analysis (EPMA) in Fig. 5.18(a). All compositions are given in atom percent.

Region	Mo	Si	Phase
A	32.500	67.500	~ $\text{MoSi}_2$
B	60.804	39.196	~ $\text{Mo}_5\text{Si}_3$

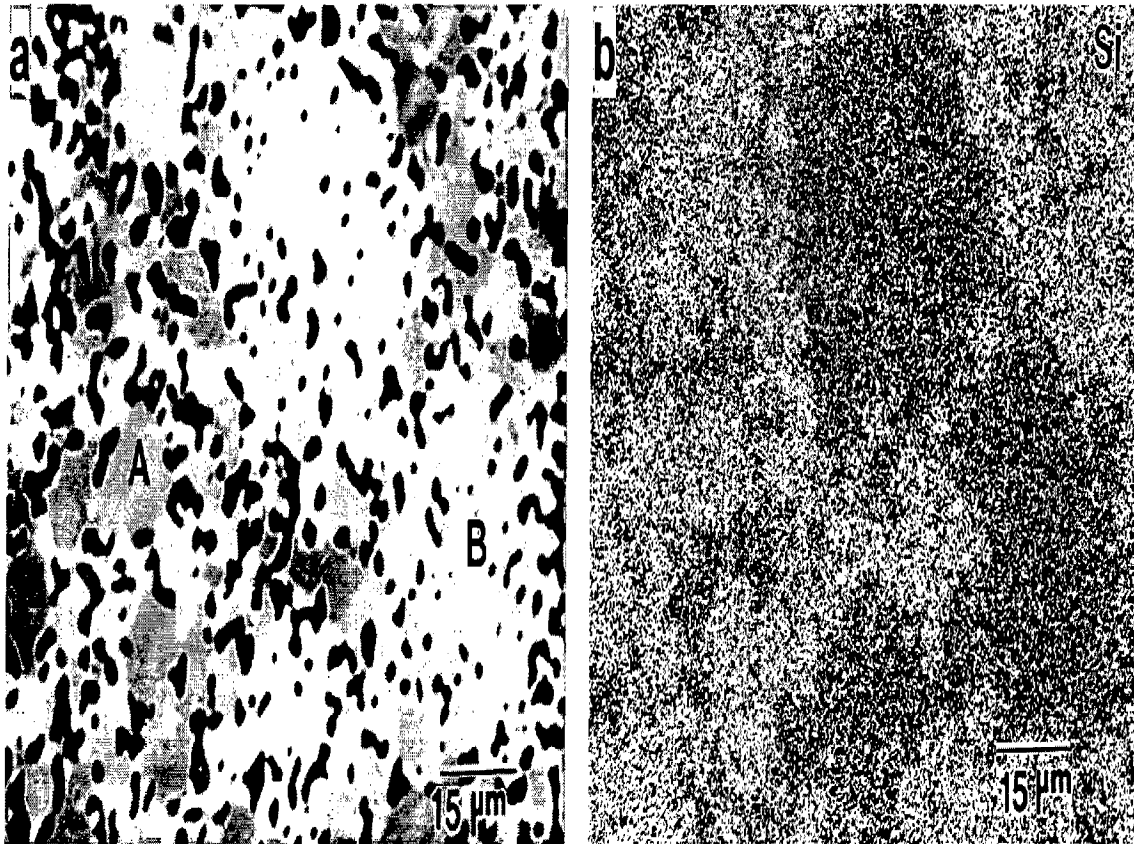
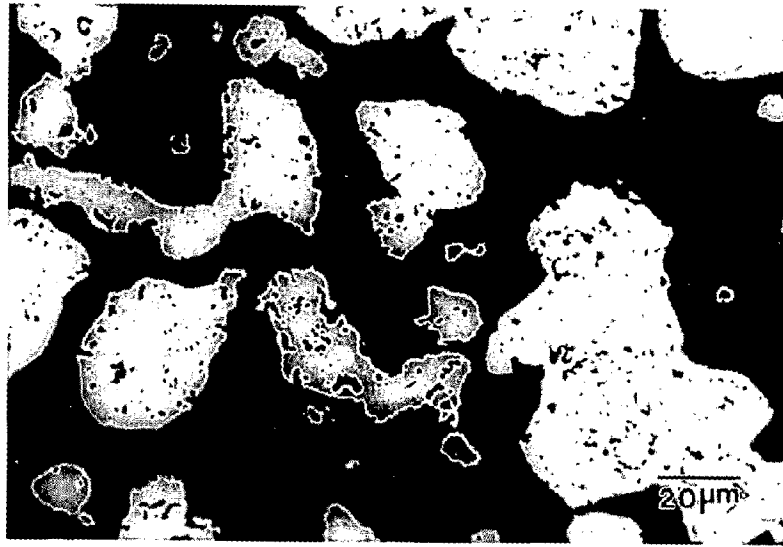
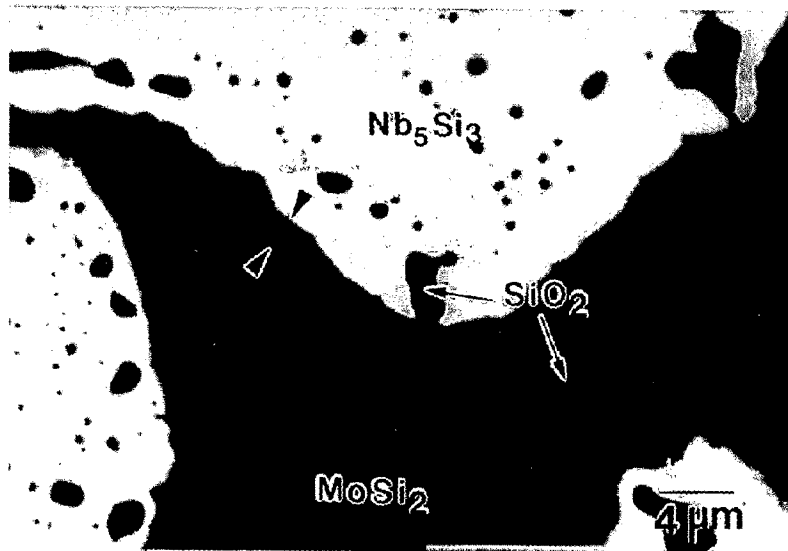


Fig. 5.18 EPMA images of  $\text{MoSi}_2 + 20 \text{ vol\% Mo}$  composite (a) back scattered electron image and (b) x-ray map of Si



(a)



(b)

Fig. 5.19 SEM back scattered electron (BSE) images of  $MoSi_2 + 20 \text{ vol\% Nb}$  composite taken at different magnifications.

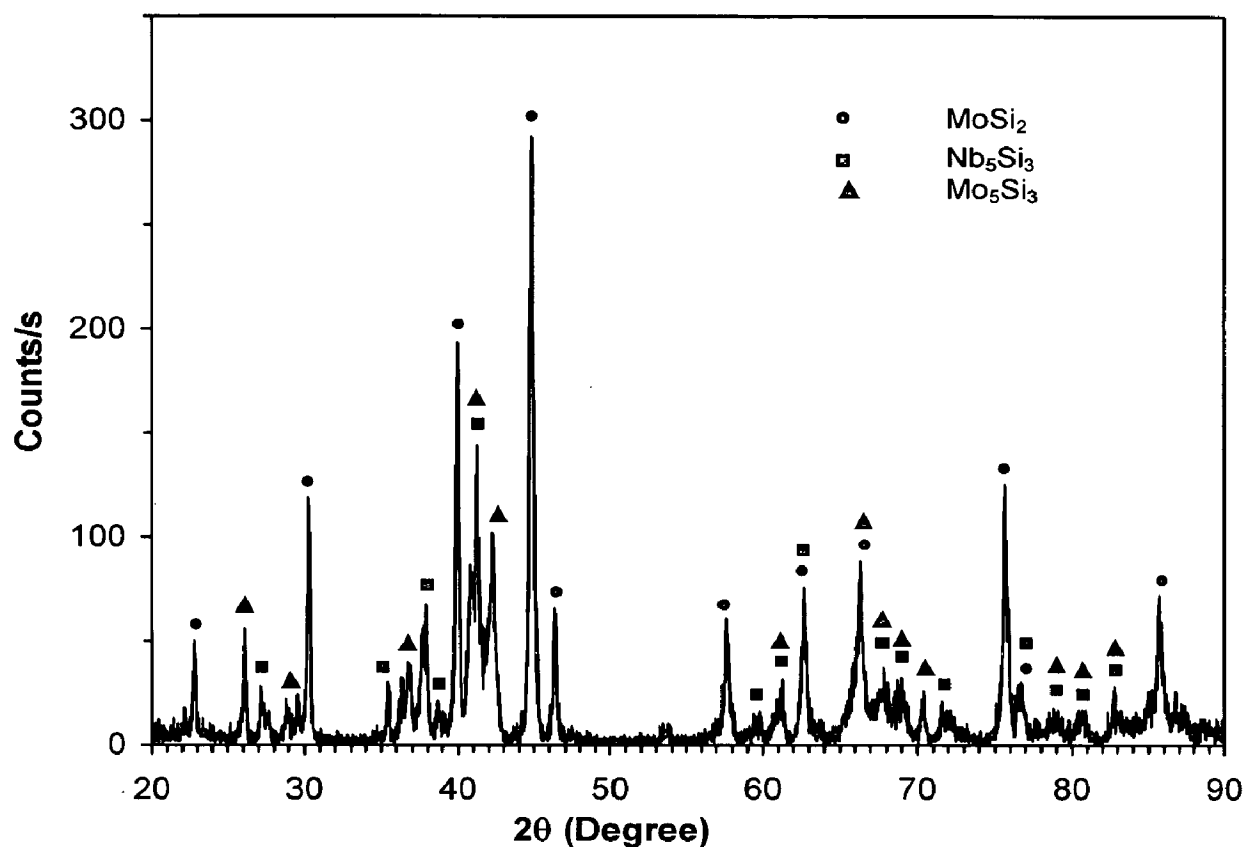


Fig. 5.20 X-ray diffraction pattern of  $\text{MoSi}_2 + 20 \text{ vol\% Nb}$  composite

Table 5.8 Composition of the reaction products between  $\text{MoSi}_2$  matrix and Nb particles as determined by electron probe micro-analysis (EPMA) in Fig. 5.21(a). All compositions are given in atom percent.

Region	Mo	Si	Nb	Phase
A	31.826	67.651	0.523	$\sim \text{MoSi}_2$
B	14.879	39.249	45.872	$\sim (\text{Nb, Mo})_5\text{Si}_3$
C	2.708	38.329	58.963	$\sim \text{Nb}_5\text{Si}_3$



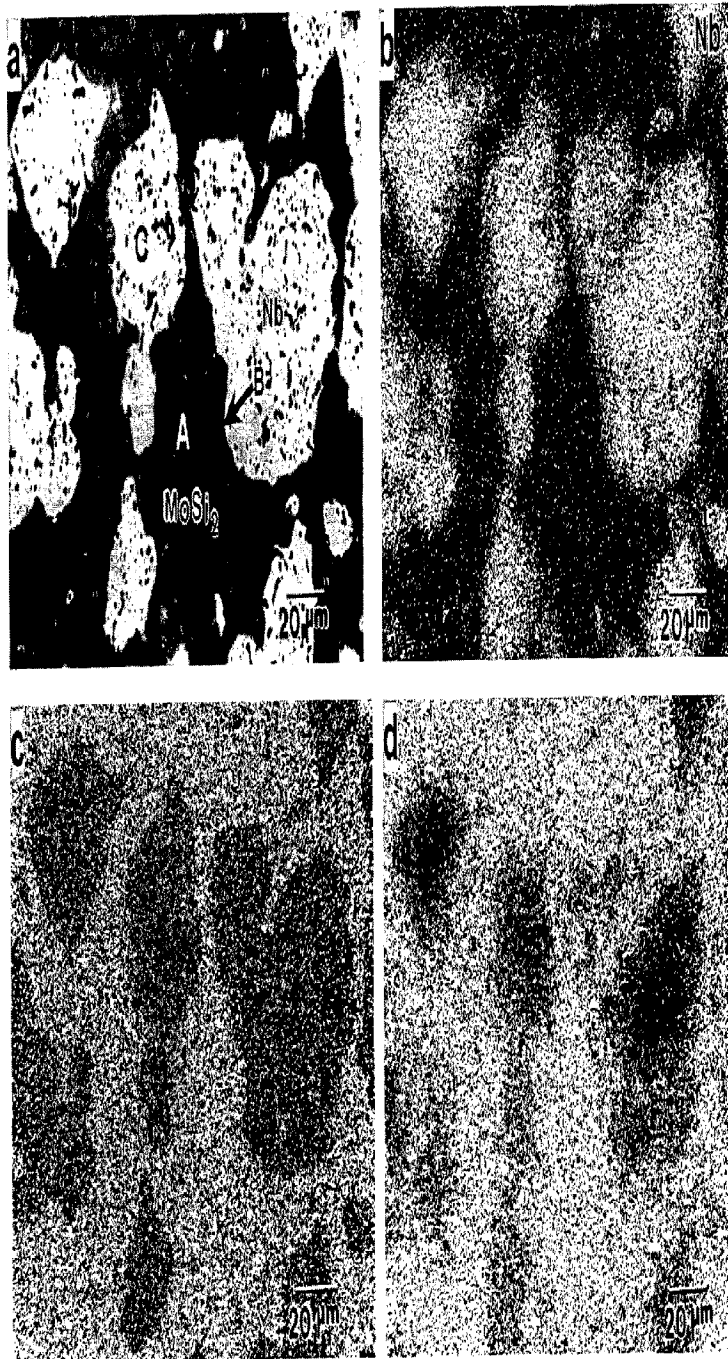


Fig. 5.21 EPMA images of MoSi<sub>2</sub> + 20 vol% Nb composite (a) back scattered electron image (b) x-ray map of Nb (c) x-ray map of Si and (d) x-ray map of Mo

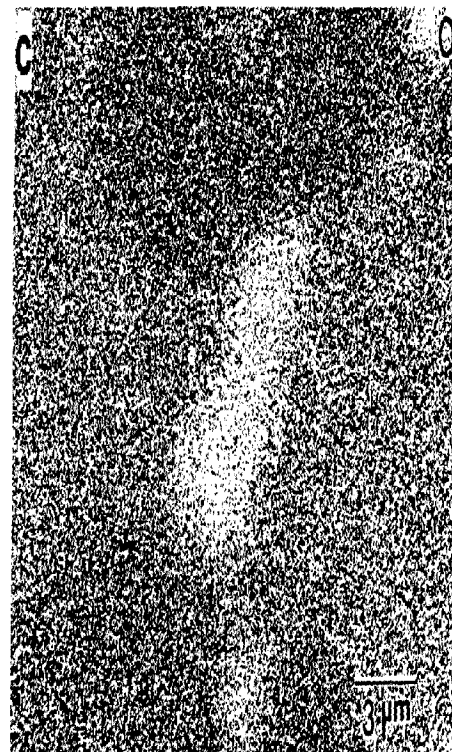
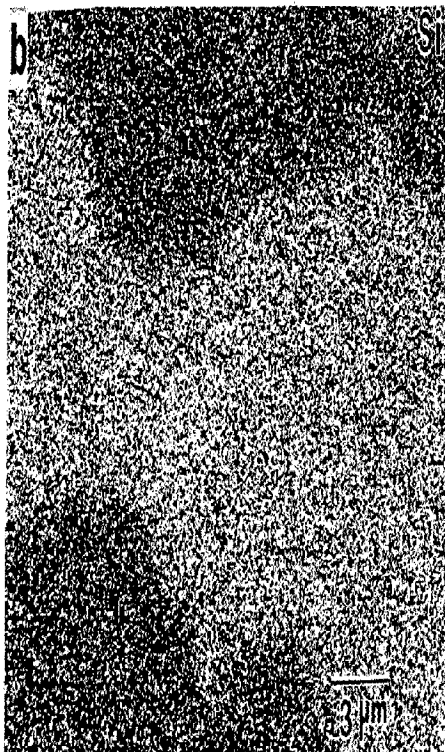


Fig. 5.22 EPMA images showing a silica particle present inside MoSi<sub>2</sub> (a) back scattered electron image (b) x-ray map of Si and (c) x-ray map of oxygen.

## 5.2.2 Evaluation of Mechanical Properties

The room temperature mechanical properties of  $\text{MoSi}_2 + 20 \text{ vol\% W}$ ,  $\text{MoSi}_2 + 20 \text{ vol\% Mo}$  and  $\text{MoSi}_2 + 20 \text{ vol\% Nb}$  composites are presented in Table 5.9. Each data point in Table 5.9 is an average of at least 4 or more tests.

The elastic modulus values measured for all the three composites were lower than the reported value of pure  $\text{MoSi}_2$  (440 GPa). There is no data available for the elastic moduli of the various silicide phases formed as a result of the chemical interactions between  $\text{MoSi}_2$  and the refractory metals used as the reinforcement. However, the experimental modulus values obtained for these  $\text{MoSi}_2$  based particulate composites which consisted of  $\text{MoSi}_2$  and 5 - 3 type of silicides of refractory metals ( $\text{R}_5\text{Si}_3$  where  $\text{R} = \text{W, Mo, Nb}$ ) suggest that the 5 - 3 type of refractory metal silicides have lower elastic moduli as compared to the elastic modulus of  $\text{MoSi}_2$ . Silicide solid solution may also have weakened the composite.

The hardness was measured at three different loads of 10 kg, 20 kg and 30 kg. The hardness values obtained for all the three composites were found to be independent of applied load and only the average values are reported in Table 5.9. The hardness values for all the three  $\text{MoSi}_2$  based particulate composites were much higher than the reported value for pure  $\text{MoSi}_2$  (9 – 10 GPa). The increase in hardness could be attributed to the grain refinement and solid solution strengthening of  $\text{MoSi}_2$  as well as formation of the new silicide phases which are assumed to be hard and brittle.

Figures 5.23(a) and 5.23(b) exhibit optical micrographs showing hardness indentation marks and the radial cracks originating from the indentation corners in  $\text{MoSi}_2 + 20 \text{ vol\% W}$  and  $\text{MoSi}_2 + 20 \text{ vol\% Mo}$  composites, respectively. The indentation cracks formed in all the three composites were of median type. Crack lengths were measured using ordinary light optical microscopy and the indentation toughness was calculated using the model proposed by Marshall and Evans (1981). A graph was plotted between the applied load ( $P$ ) and the measured average crack length ( $c^{3/2}$ ) for all the three composites. A typical indentation load ( $P$ ) vs. the crack length ( $c^{3/2}$ ) graph as obtained in the case of  $\text{MoSi}_2 + 20 \text{ vol\% Nb}$  composite is depicted in Fig. 5.24. The indentation fracture toughness was estimated from the slope of the linear plots, which passed through the origin in all the three cases. The

indentation toughness values calculated for all the three composite systems were in the range of 4.5 to 5.0  $\text{MPa}\sqrt{\text{m}}$  which were marginally higher than the reported value of 4.2  $\text{MPa}\sqrt{\text{m}}$  for the monolithic  $\text{MoSi}_2$ .

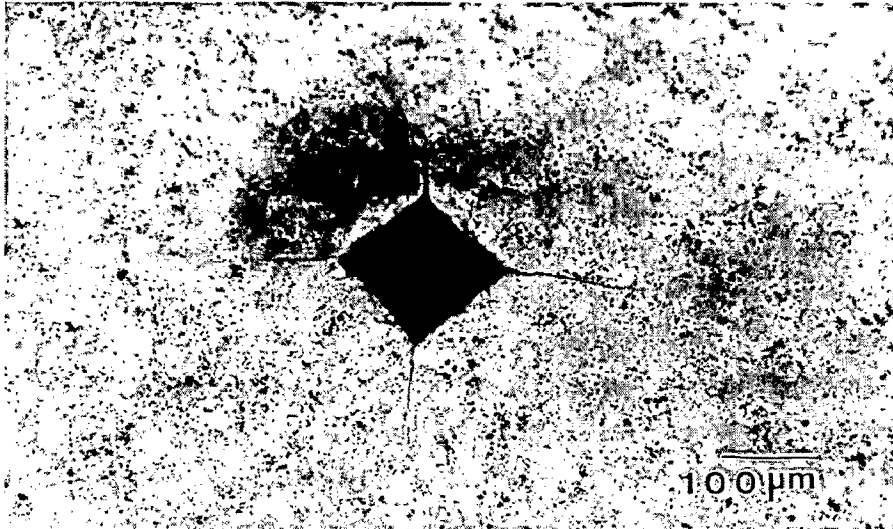
The flexural strength values for all the three composites show a considerable increase over monolithic  $\text{MoSi}_2$  as reported by Mitra et al (1997<sup>a</sup>). Mitra et al (1997<sup>a</sup>) have measured the flexural strength of monolithic  $\text{MoSi}_2$  as 150 MPa using the same grade of commercial purity  $\text{MoSi}_2$  powder consolidated by vacuum hot pressing. The most remarkable increase of 117 % was observed in case of  $\text{MoSi}_2$ -Mo composite. The increase in flexural strength may presumably be due to one or both of the following - formation of  $\text{R}_5\text{Si}_3$  type refractory metal silicides and grain refinement of  $\text{MoSi}_2$  matrix.

The fracture surfaces as presented in Fig. 5.25 exhibit predominantly transgranular cleavage fracture for all the three composites. Secondary cracking was observed in  $\text{MoSi}_2$ -Nb composite as indicated by arrow mark in Fig. 5.25(b). The small arrowheads in Figs. 5.25(a) and 5.25(c) indicate the presence of free  $\text{SiO}_2$  particles on the fracture surfaces.

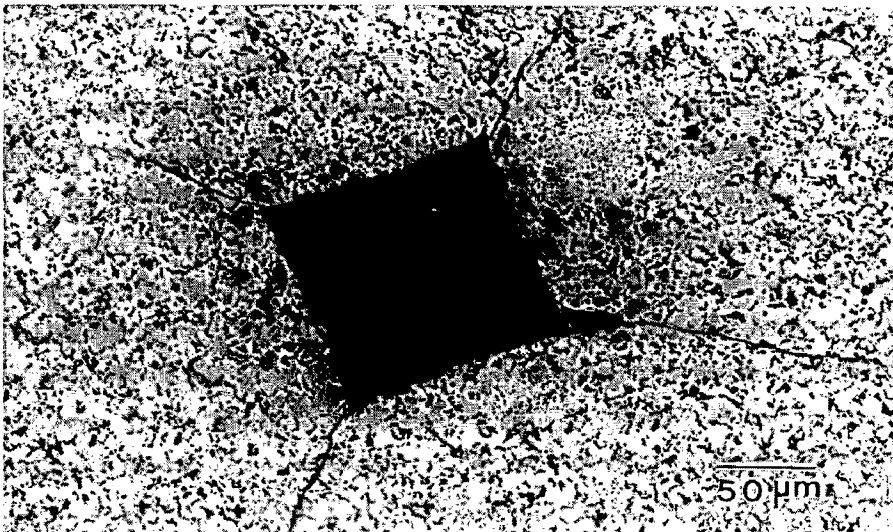
The fracture toughness ( $K_{\text{IC}}$ ) values as measured from the notched three-point bend tests are presented in Table 5.9. There was only a marginal improvement in fracture toughness of all the three composites as compared to the reported value of 4.2  $\text{MPa}\sqrt{\text{m}}$  of pure  $\text{MoSi}_2$  by Mitra et al (1997<sup>a</sup>). This is understandable as no benefit of ductile phase toughening could be obtained due to the extensive reactions between  $\text{MoSi}_2$  and the ductile refractory metal particles resulting in hard and brittle reaction products. The highest improvement in the toughness was observed in  $\text{MoSi}_2$ -Mo composite. However, the fracture toughness values were slightly higher than the toughness values calculated from the indentation cracks. The discrepancy in the data obtained by the two different methods could be attributed to the human errors involved in the measurement of the indentation crack lengths. Figure 5.26 exhibits the load vs. displacement curves for all the three composites. These curves are linear in nature and exhibit only elastic behaviour. The curves are typical of a brittle solid with no evidence of resistance to catastrophic failure.

Table 5.9 Mechanical properties of refractory metal particle reinforced MoSi<sub>2</sub> based composites.

Composite	Elastic Modulus (GPa)	Hardness (GPa)	Indentation Fracture Toughness, K <sub>IC</sub> (MPa√m)	Flexural Strength (MPa)	Fracture Toughness, K <sub>IC</sub> (MPa√m)
MoSi <sub>2</sub> + 20 vol% W	393	15.3	4.71	266	5.2
MoSi <sub>2</sub> + 20 vol% Mo	354	13.8	4.91	326	5.6
MoSi <sub>2</sub> + 20 vol% Nb	383	13.5	4.57	204	5.0



(a)



(b)

Fig. 5.23 Optical micrographs showing typical hardness indentation marks and associated radial cracks in (a)  $\text{MoSi}_2 + 20 \text{ vol\% W}$  and (b)  $\text{MoSi}_2 + 20 \text{ vol\% Mo}$  composites.

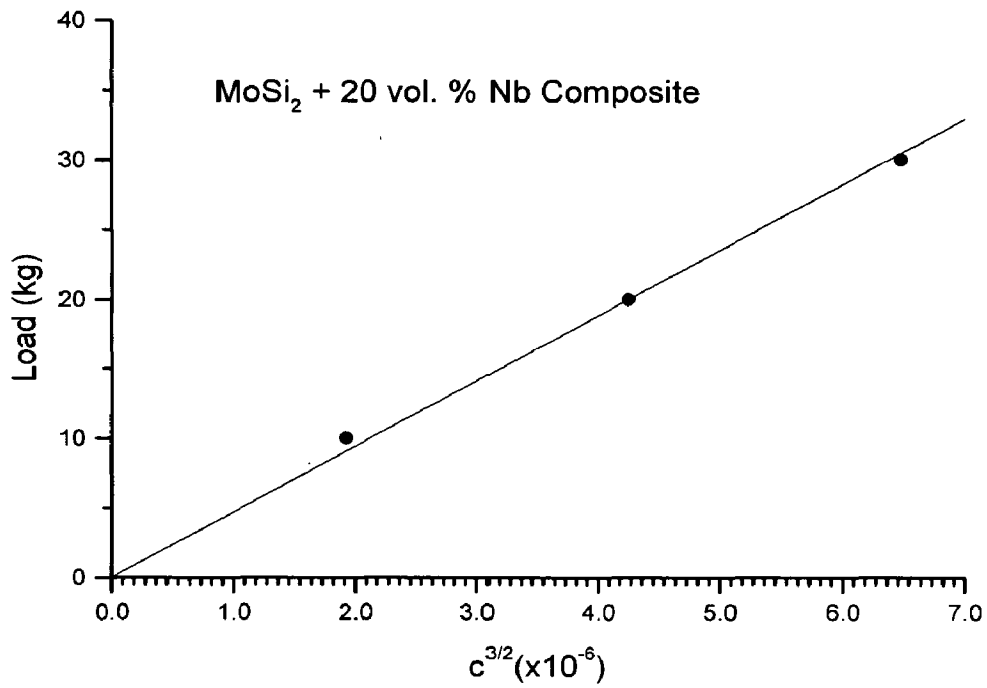
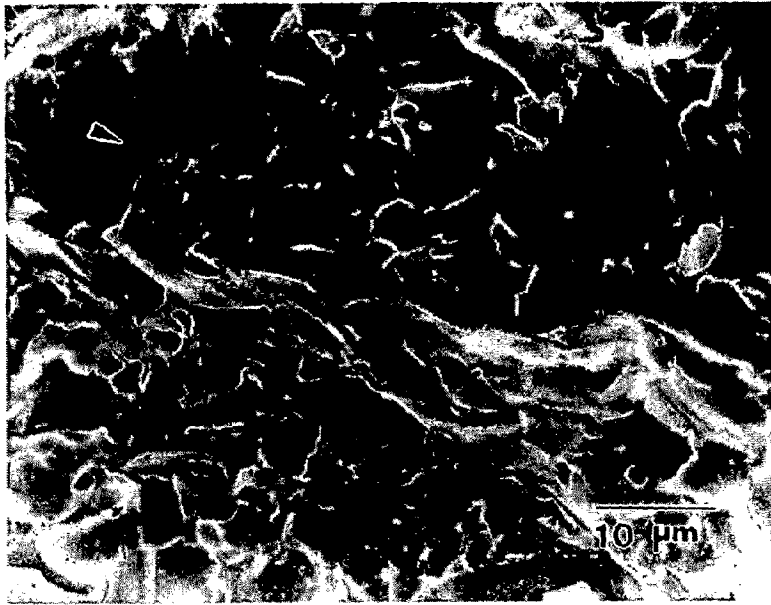
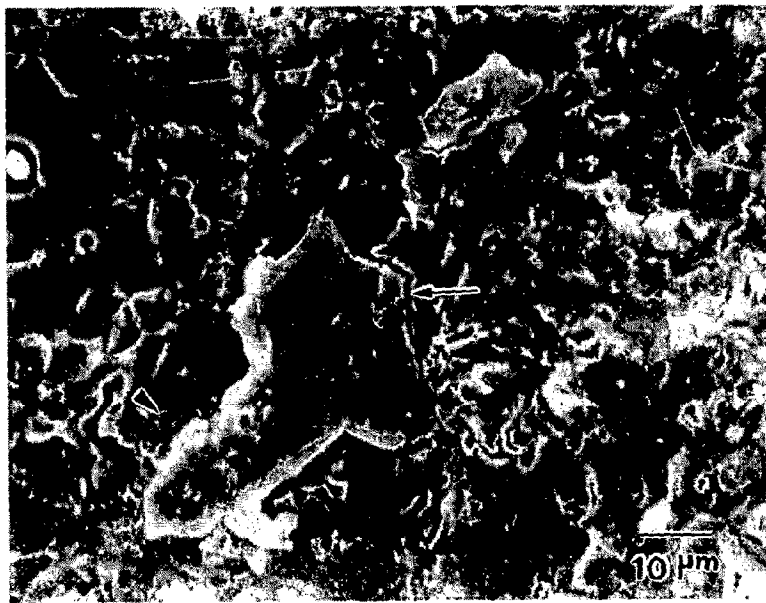


Fig. 5.24 Indentation load ( $P$ ) vs. the crack length ( $c^{3/2}$ ) graph as obtained in the case of MoSi<sub>2</sub> + 20 vol% Nb composite. The fracture toughness was estimated from the slope of the linear plot of  $P$  vs.  $c^{3/2}$ .

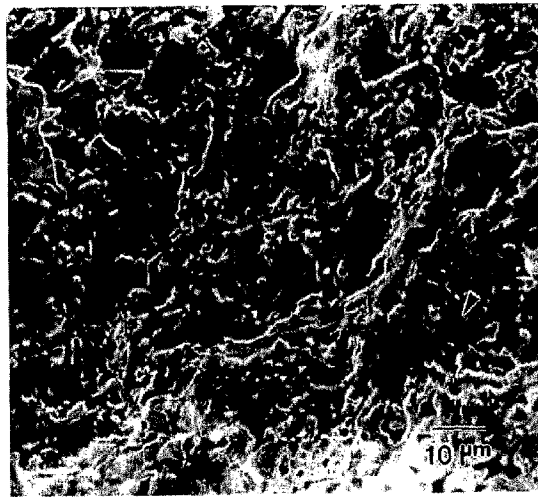


(a)



(b)





(c)

Fig. 5.25 SEM fractographs of flexural strength (three point bend) test specimens of (a)  $\text{MoSi}_2 + 20 \text{ vol\% W}$  (b)  $\text{MoSi}_2 + 20 \text{ vol\% Nb}$  and (c)  $\text{MoSi}_2 + 20 \text{ vol\% Mo}$  composites.

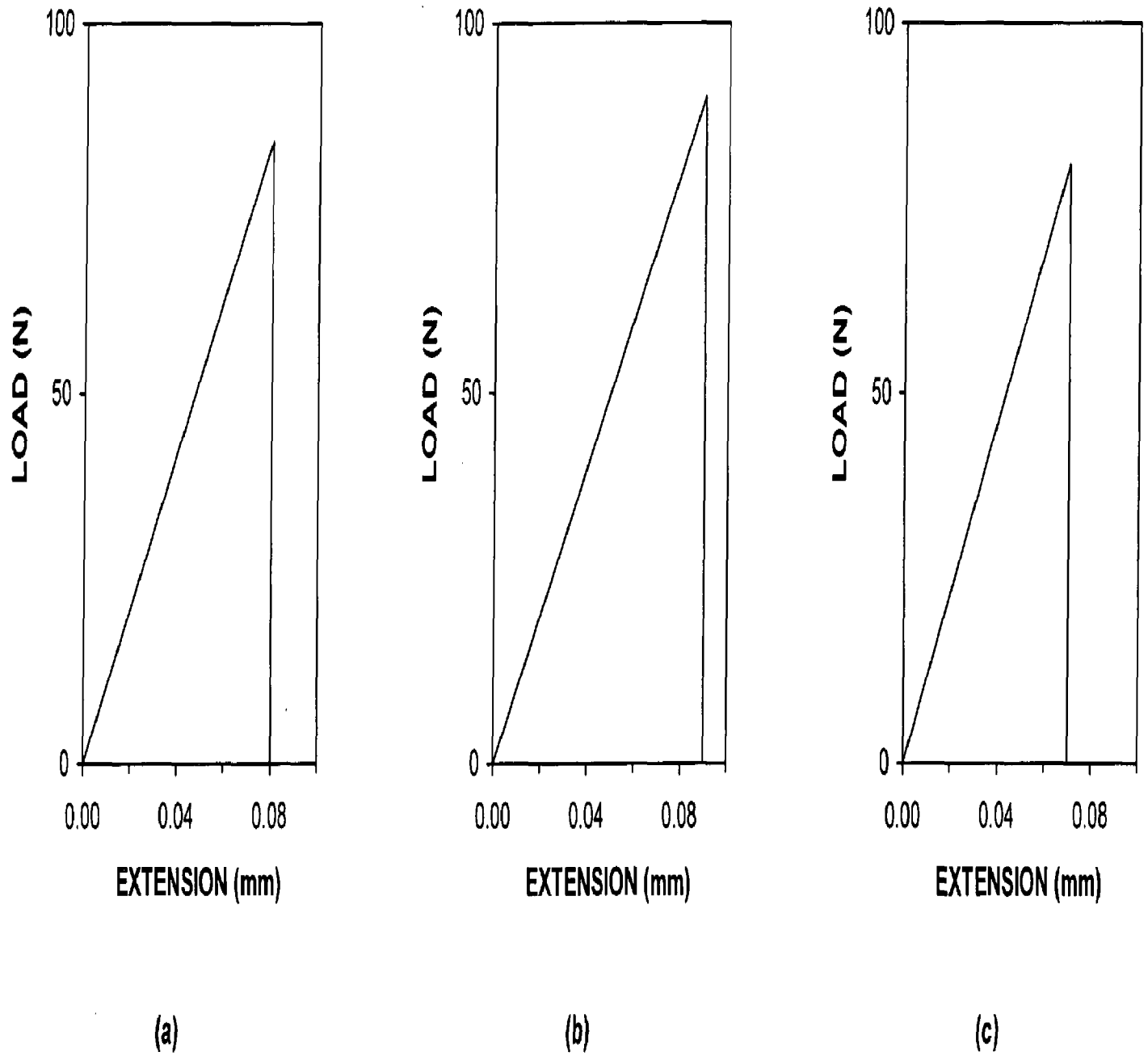


Fig. 5.26 Typical load-displacement curves for  $K_{IC}$  test specimens (notched three point bend) of (a) MoSi<sub>2</sub> + 20 vol% W (b) MoSi<sub>2</sub> + 20 vol% Mo and (c) MoSi<sub>2</sub> + 20 vol% Nb composites.

The fracture surfaces of  $K_{IC}$  specimens of all the three materials are shown in Fig. 5.27. The fracture process was mostly transgranular cleavage with the evidence of secondary cracking as shown by arrow marks in Figs. 5.27(b) and 5.27(c).

The physical concept for ductile phase toughening of brittle materials is based on the crack bridging and plastic deformation of the ductile particles. However, in the present case, the  $R_5Si_3$  types of silicide particles that are intercepted by the crack suffer brittle cleavage fracture, with no evidence of plastic deformation, and do not contribute to toughening. Only a few isolated incidents of crack bridging and crack arrest were observed as shown in Fig. 5.28. Figures 5.28(a) and 5.28(b) exhibit the SEM back scattered electron images of the indentation crack paths in  $MoSi_2$ -Mo and  $MoSi_2$ -W composites, respectively. Some evidence of crack bridging was found in case of  $MoSi_2$ -Mo composite as shown by an arrow mark in Fig. 5.28(a). This could possibly be attributed to some left over unreacted Mo particles. Gibala et al (1992) have observed that  $Mo_5Si_3$ , an elastically hard, strong and brittle second phase, apart from strengthening  $MoSi_2$  at high temperatures can also potentially impart low temperature toughness by crack deflection processes. Some evidence of crack bridging (marked as A) and crack arresting (marked by an arrowhead) was also observed in  $MoSi_2$ -W composite (Fig. 5.28(b)). In general, additional cracking and crack branching in the brittle silicide phases accompanied the propagation of the main indentation crack. Additional toughening may result from secondary cracking and crack branching. The crack has passed through the various phases present in the microstructure instead of propagating along the interface suggesting a strong interfacial bond between  $MoSi_2$  matrix and the silicide phases formed as reaction products.

The ductile reinforcements in the particle form appear to have only a marginal effect on the fracture toughness of  $MoSi_2$ . Therefore, further work was carried out by using the ductile refractory metals in the foil form (laminated approach).

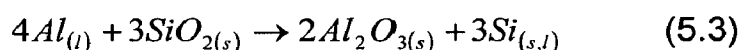
### **5.3 Laminated Composites with ( $MoSi_2$ + 2 wt% Al) as Matrix**

Laminated composites represent a unique layered composite form. The idea of laminating different metals and alloys to form a metal - metal composite material that exploits the good properties of the constituent materials has been well known. The application of laminated metal – metal composites to gun barrels for through

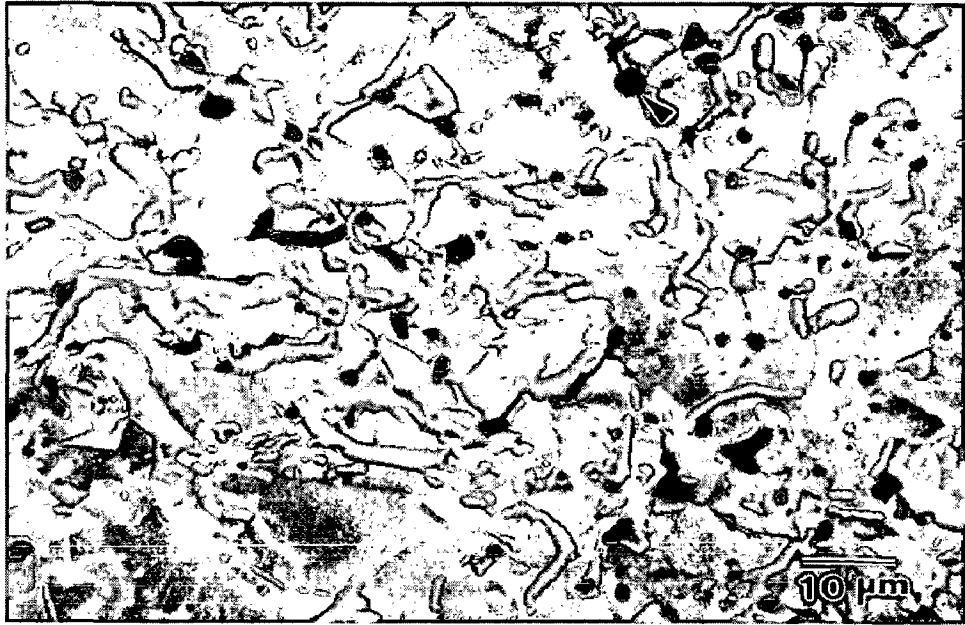
thickness toughness is not new (Hertzberg, 1983). The internal interfaces between layers limit crack propagation through several different mechanisms. The same approach has been adopted in the present work for preparing the laminated composites having alternate layers of brittle ( $\text{MoSi}_2 + 2 \text{ wt\% Al}$ ) and ductile Mo and Ta metals. Model tri-layer laminated composites have been made by sandwiching a single refractory metal foil in between two layers of  $\text{MoSi}_2$  based matrix.

Pure Al (2 wt%) was added to  $\text{MoSi}_2$  powder prior to hot pressing into laminated structures. Al was added primarily to reduce the amount of free  $\text{SiO}_2$  present in  $\text{MoSi}_2$  powder. The powders of  $\text{MoSi}_2$  that are commercially available carry with them significant amounts of  $\text{SiO}_2$ . The  $\text{MoSi}_2$  powder used in the present study has been procured from H. C. Stark, Germany and was found to contain about 1.3 wt% oxygen (Table 5.1). Apart from  $\text{SiO}_2$  in starting  $\text{MoSi}_2$  powders, the additional oxygen may also be picked up during hot pressing of  $\text{MoSi}_2$  powders.  $\text{SiO}_2$  is present in  $\text{MoSi}_2$  as amorphous glassy phase, which degrades the mechanical properties of  $\text{MoSi}_2$  at room as well as at elevated temperatures. Reducing or eliminating the  $\text{SiO}_2$  content could result in improved mechanical properties of  $\text{MoSi}_2$ . Removal of  $\text{SiO}_2$  is a way to improve the retention of strength in  $\text{MoSi}_2$  at high temperatures.

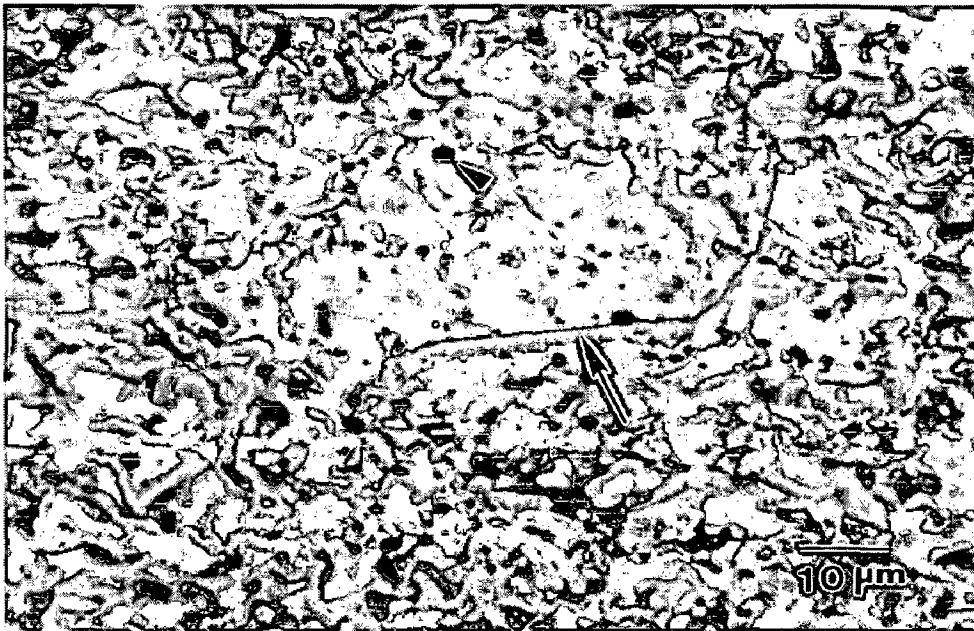
One promising approach is to react  $\text{SiO}_2$  with elemental Al powder in  $\text{MoSi}_2$  to result in  $\text{Al}_2\text{O}_3$ . Al has higher affinity towards oxygen as compared to Si. It is thermodynamically more stable than  $\text{SiO}_2$ . Al reacts with  $\text{SiO}_2$  forming  $\text{Al}_2\text{O}_3$  as per the following displacement reaction (Costa e Silva and Kaufman, 1994):



The variation of free energy change with temperature for the above reaction,  $\Delta G$  (per mole of  $\text{Al}_2\text{O}_3$ ) is plotted with thermodynamic data taken from Barin (1989) as depicted in Fig. 5.29 and was found to be negative for the entire temperature range. The formation of  $\text{Al}_2\text{O}_3$  by this method is believed to result in eliminating the detrimental effects of  $\text{SiO}_2$  as well as in in-situ composite of  $\text{MoSi}_2$  with  $\text{Al}_2\text{O}_3$ .



(a)

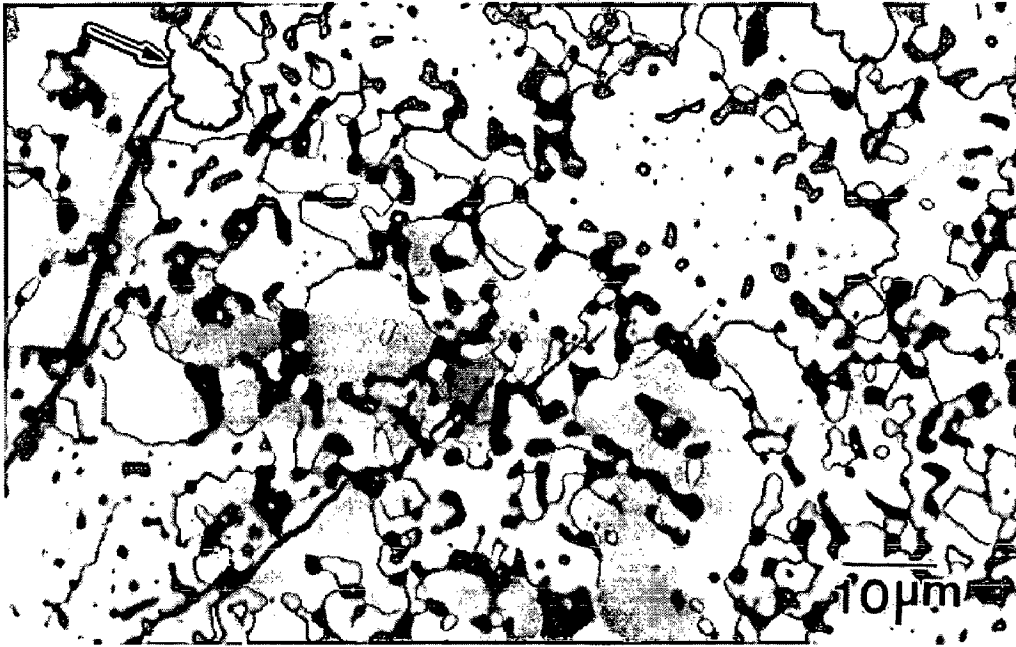


(b)



(c)

Fig. 5.27 Fracture surfaces of  $K_{IC}$  (notched three point bend) test specimens of (a)  $\text{MoSi}_2 + 20 \text{ vol\% W}$  (b)  $\text{MoSi}_2 + 20 \text{ vol\% Mo}$  and (c)  $\text{MoSi}_2 + 30 \text{ vol\% Nb}$  composites.



(a)



(b)

Fig. 5.28 SEM back scattered electron images showing indentation crack paths in (a)  $\text{MoSi}_2 + 20 \text{ vol\% Mo}$  and (b)  $\text{MoSi}_2 + 20 \text{ vol\% W}$  composites.

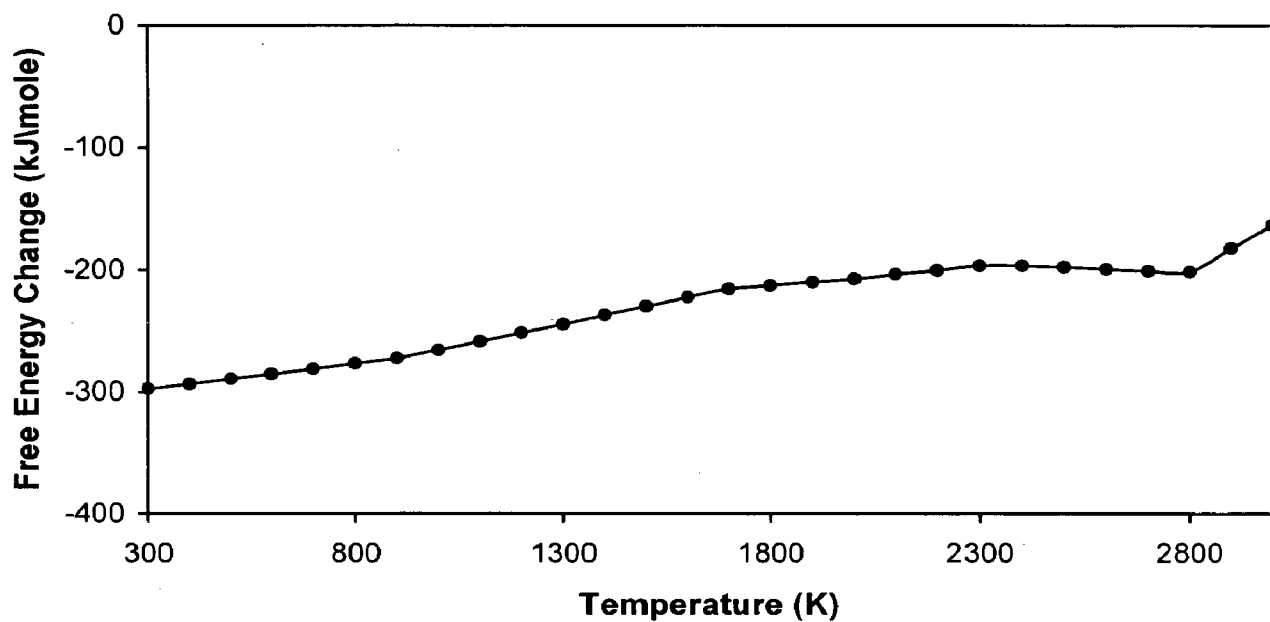


Fig. 5.29 Standard free energy change ( $\Delta G$  vs. *temperature*) for reduction of  $\text{SiO}_2$  and in-situ formation of  $\text{Al}_2\text{O}_3$  by addition of Al in  $\text{MoSi}_2$ .



### 5.3.1 Microstructural Studies

Figure 5.30 is a polarized light optical micrograph of  $\text{MoSi}_2 + 2 \text{ wt\% Al}$  monolithic alloy. Figures 5.31 and 5.32 exhibit microstructures of  $(\text{MoSi}_2 + 2 \text{ wt\% Al}) + \text{Mo}$  foil and  $(\text{MoSi}_2 + 2 \text{ wt\% Al}) + \text{Ta}$  foil laminated composites, respectively taken at the interfacial regions. The SEM back scattered electron images of both the laminated composites are shown in Fig. 5.33.

In general, the  $\text{MoSi}_2$  grains were regular and equi-axed with a relatively large variation in grain size. The grains appeared polygonal in shape and the grain size varied between 20 - 40  $\mu\text{m}$  in  $\text{MoSi}_2$  monolithic as well as  $\text{MoSi}_2$  with Mo and Ta foil laminated composites. A significantly large grain size could be the result of grain growth at high processing temperature of 1750 °C. The  $\text{Al}_2\text{O}_3$  particles formed in-situ seems to be not so effective in restricting the grain growth in  $\text{MoSi}_2$  during high temperature processing. No definite trend could be seen in the grain size refinement by  $\text{Al}_2\text{O}_3$  particles. This could be attributed to possibly poor pinning power of  $\alpha\text{-Al}_2\text{O}_3$  particles or to somewhat non-uniform distribution of  $\text{Al}_2\text{O}_3$  particles (Mitra et al, 1999). Thick interfacial reaction layers have formed in between  $\text{MoSi}_2$  and Mo foil as well as between  $\text{MoSi}_2$  and Ta foil as depicted in Figs. 5.31, 5.32 and 5.33. The thickness of the interfacial reaction zone was measured to be in the range of 70 - 80  $\mu\text{m}$  in both the laminated composites.

In case of  $(\text{MoSi}_2 + 2 \text{ wt\% Al}) + \text{Mo}$  foil composite, the interfacial reaction zone consisted of two distinct layers as revealed in optical microstructure (Fig. 5.31) and in SEM back scattered electron image (Fig. 5.33(a)). The reaction products in the interfacial reaction zone were identified as  $\text{Mo}_5\text{Si}_3$  adjacent to  $\text{MoSi}_2$  based matrix and  $\text{Mo}_3\text{Si}$  adjacent to the pure Mo foil by EPMA studies. The optical microstructure under polarized light revealed the grains of  $\text{Mo}_5\text{Si}_3$ , which could be attributed to its crystal structure.  $\text{Mo}_5\text{Si}_3$  has a tetragonal (tI32) crystal structure, which is more anisotropic as compared to the cubic (cP8) structure of  $\text{Mo}_3\text{Si}$ .

Figure 5.32(a) is a low magnification optical micrograph revealing the interfacial reaction layers on both sides of the metal foil in case of  $(\text{MoSi}_2 + 2 \text{ wt\% Al}) + \text{Ta}$  foil laminated composite. Figure 4.32(b) shows the same interfacial region at a

higher magnification. Observations of both optical microstructure (Fig. 5.32(b)) as well as SEM back scattered electron image (Fig. 5.33(b)) suggest that the interfacial reaction zone consisted of only one reaction layer in contrast to the interfacial reaction zone having two distinct layers in (MoSi<sub>2</sub> + 2 wt% Al) + Mo foil laminated composite. However, further studies by EPMA have confirmed the presence of two distinct reaction layers in case of laminated composite with Ta foil also. The reaction products present were identified to be Ta<sub>5</sub>Si<sub>3</sub> adjacent to MoSi<sub>2</sub> based matrix and Ta<sub>2</sub>Si adjacent to pure Ta foil.

Figures 5.34(a) and 5.34(b) present the x-ray diffraction patterns of laminated composites with Mo foil and Ta foil, respectively. The x-ray diffraction patterns reveal the presence of mainly the peaks of MoSi<sub>2</sub>, pure Mo and pure Ta. Some peaks of Mo<sub>5</sub>Si<sub>3</sub>, Mo<sub>3</sub>Si, Ta<sub>5</sub>Si<sub>3</sub> and Al<sub>2</sub>O<sub>3</sub> are also identified. However, most of these peaks are too small and also overlapp with each other and / or with the peaks of MoSi<sub>2</sub> and Mo / Ta.

The EPMA images of (MoSi<sub>2</sub> + 2 wt% Al) + Mo foil laminated composite are shown in Fig. 5.35 and Fig. 5.36. The back scattered electron image and x-ray maps of Mo and Si clearly reveal two distinct interfacial reaction layers. The quantitative analysis of chemical composition of the reaction products by EPMA is presented in Table 5.10. The typical microprobe data obtained at locations indicated by A, B, C and D in Fig. 5.35(a) correspond to MoSi<sub>2</sub>, Mo<sub>5</sub>Si<sub>3</sub>, Mo<sub>3</sub>Si and pure Mo phases, respectively. Mo / Mo<sub>3</sub>Si and Mo<sub>3</sub>Si / Mo<sub>5</sub>Si<sub>3</sub> interfaces are more or less planar. Microcracks running parallel to each other, are observed in tetragonal Mo<sub>5</sub>Si<sub>3</sub> (tI32) phase. Their propagation seems to get arrested in the adjacent cubic Mo<sub>3</sub>Si (cP8) phase. The microcracking could be a result of anisotropy in the coefficient of thermal expansion of tetragonal Mo<sub>5</sub>Si<sub>3</sub> phase.

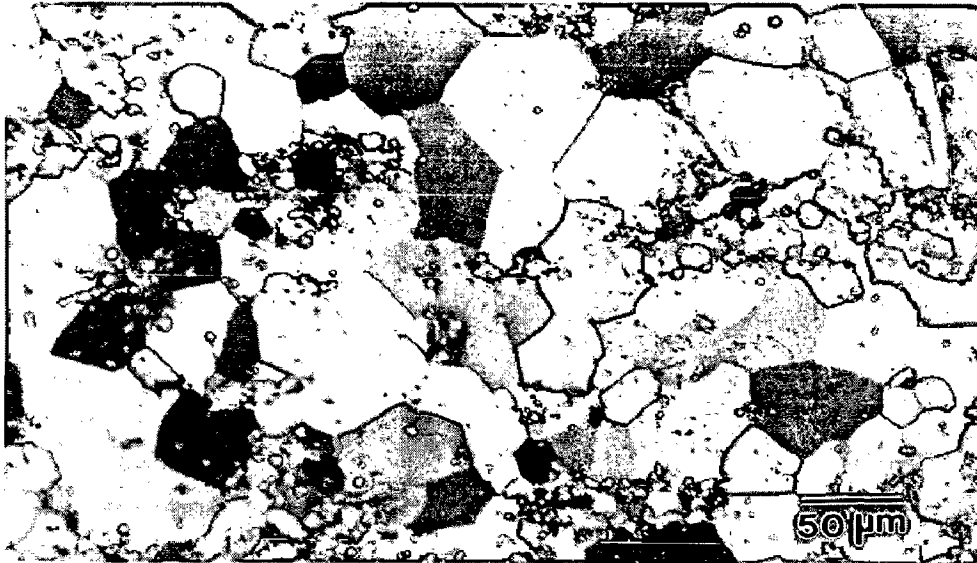


Fig. 5.30 Polarized light optical microstructure of  $\text{MoSi}_2 + 2 \text{ wt\% Al}$  alloy.

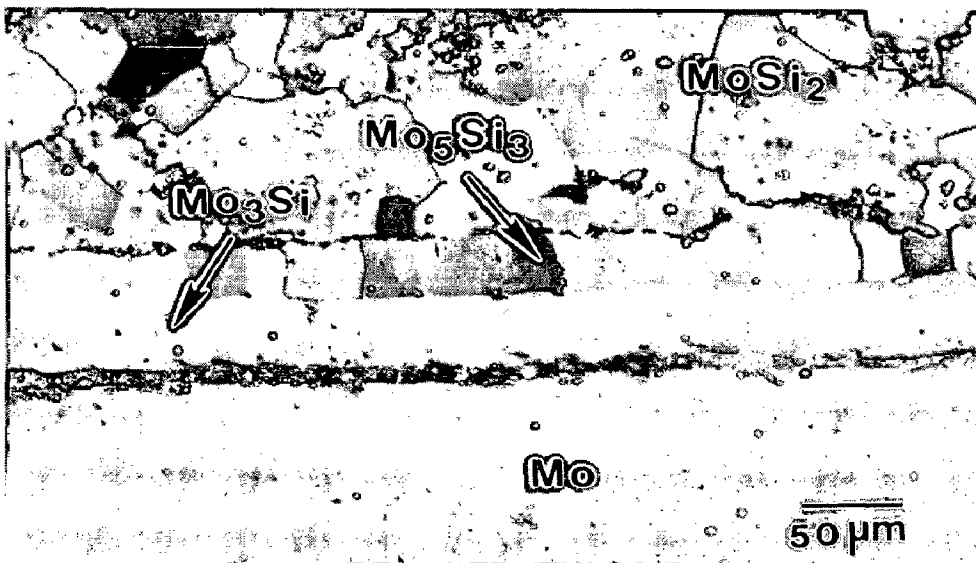
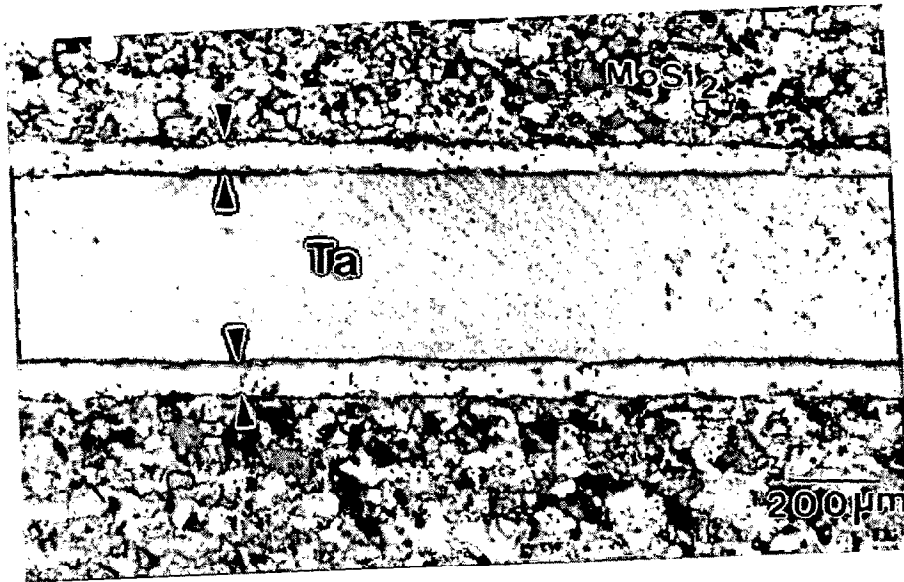
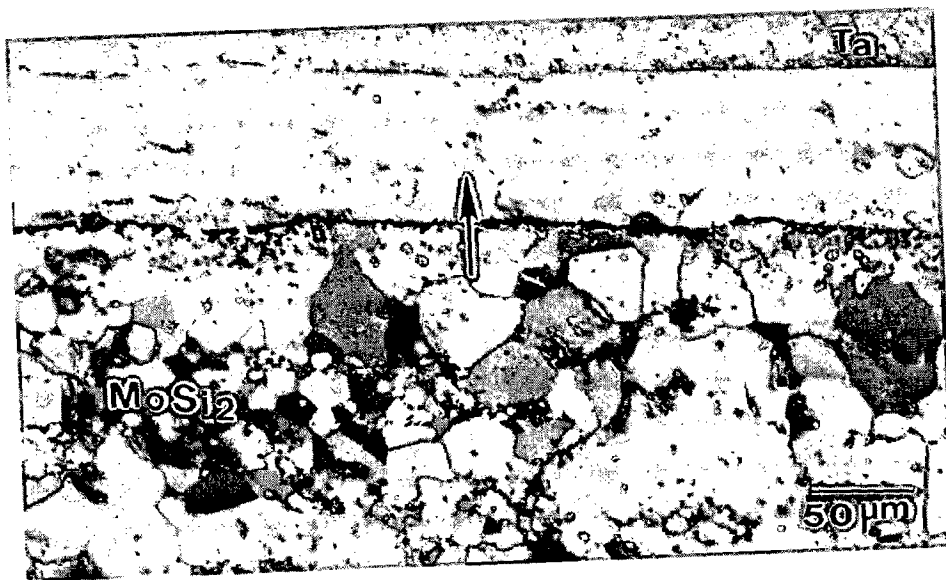


Fig. 5.31 Polarized light optical microstructure of  $(\text{MoSi}_2 + 2 \text{ wt\% Al})$  and Mo foil laminated composite taken at the interfacial region.

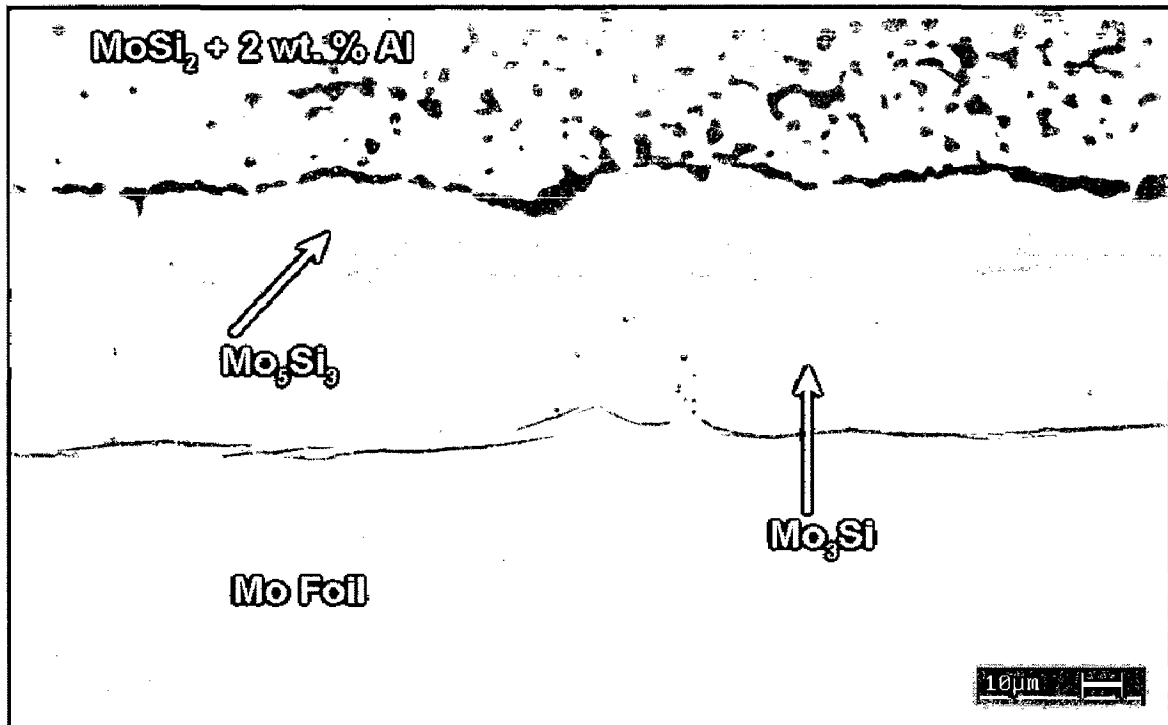


(a)

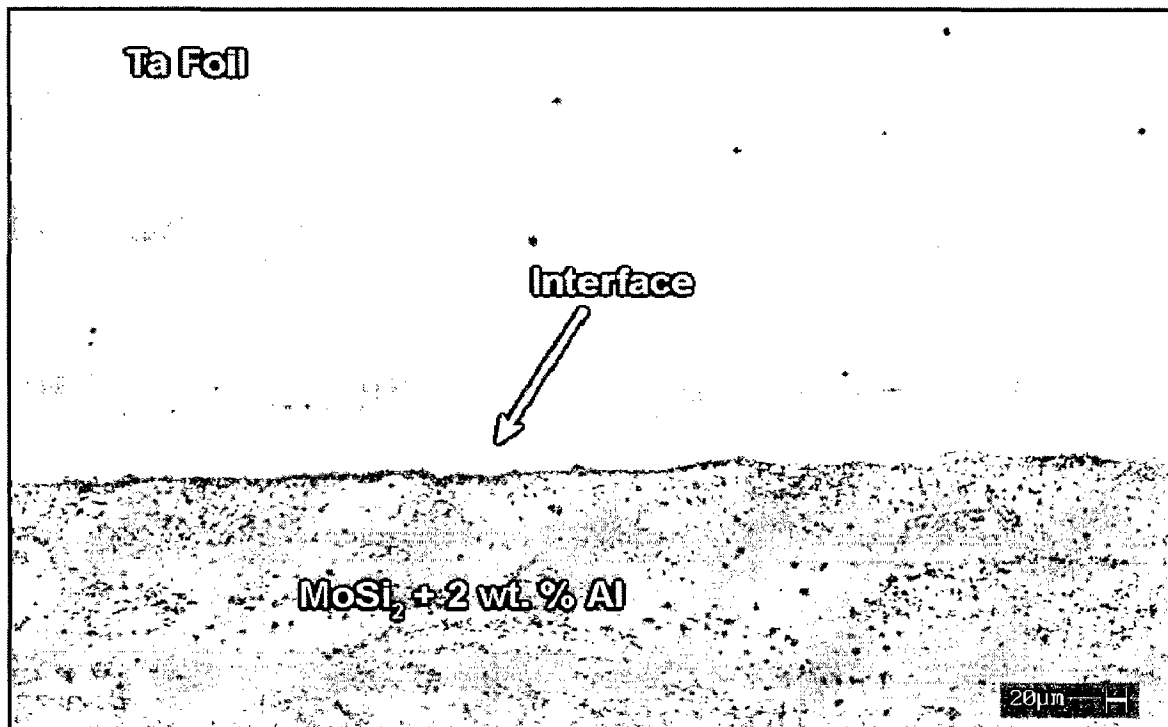


(b)

Fig. 5.32 Polarized light optical microstructures of ( $\text{MoSi}_2 + 2 \text{ wt}\% \text{ Al}$ ) with Ta foil laminated composite showing (a) interfacial reaction layers on both sides of Ta foil and (b) interfacial region at a higher magnification.

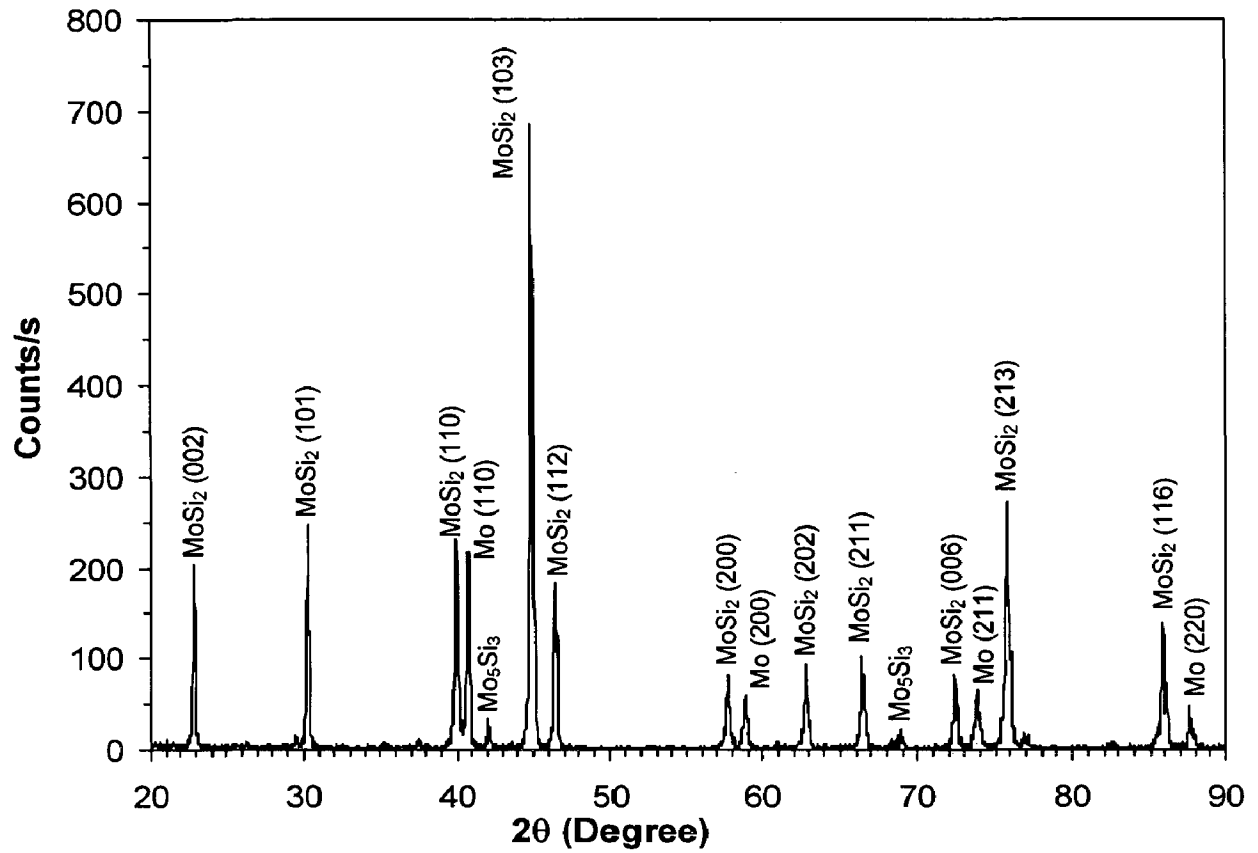


(a)

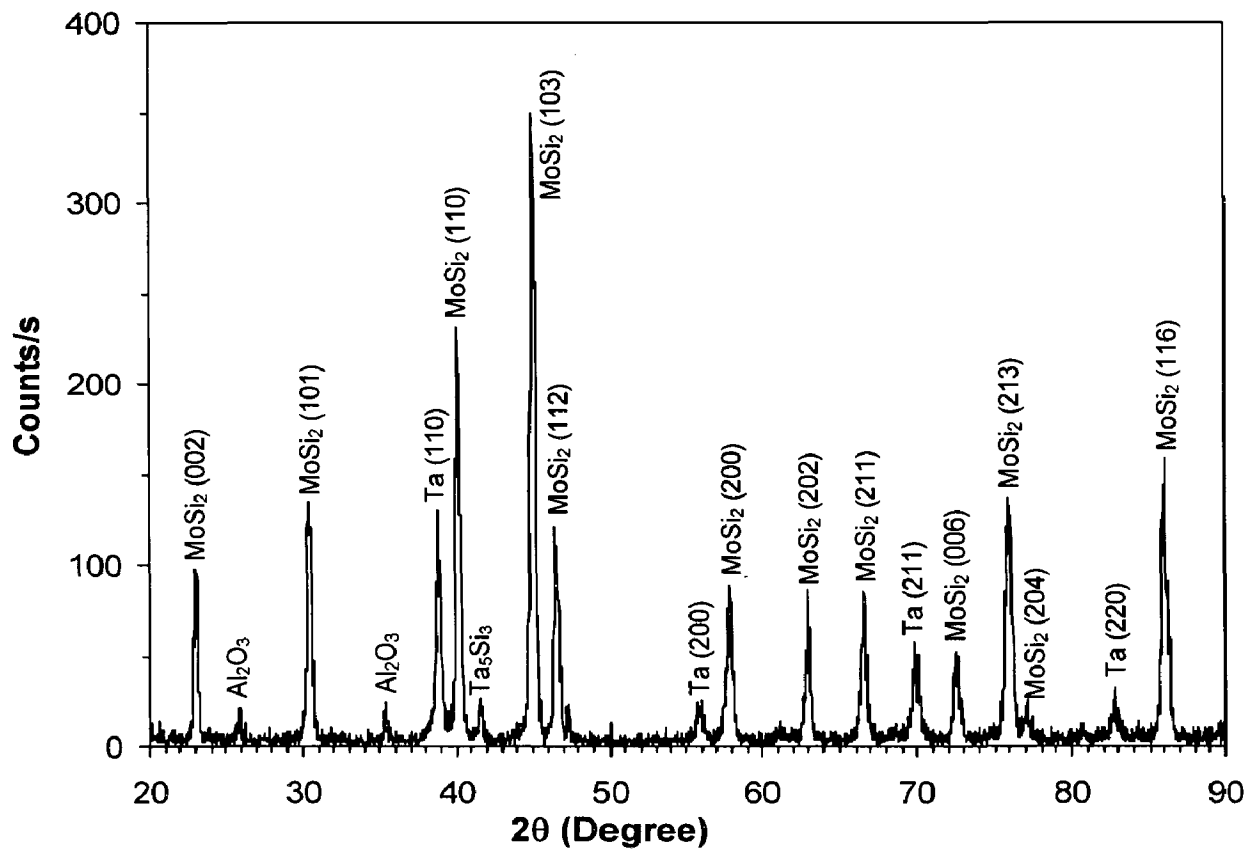


(b)

Fig. 5.33 SEM back scattered electron images of (a) (MoSi<sub>2</sub> + 2 wt% Al) + Mo foil and (b) (MoSi<sub>2</sub> + 2 wt% Al) + Ta foil laminated composites showing interfacial reaction layers



(a)



(b)

Fig. 5.34 X-ray diffraction patterns of (a) MoSi<sub>2</sub> + 2 wt% Al + Mo foil composite and (b) MoSi<sub>2</sub> + 2 wt% Al + Ta foil composite

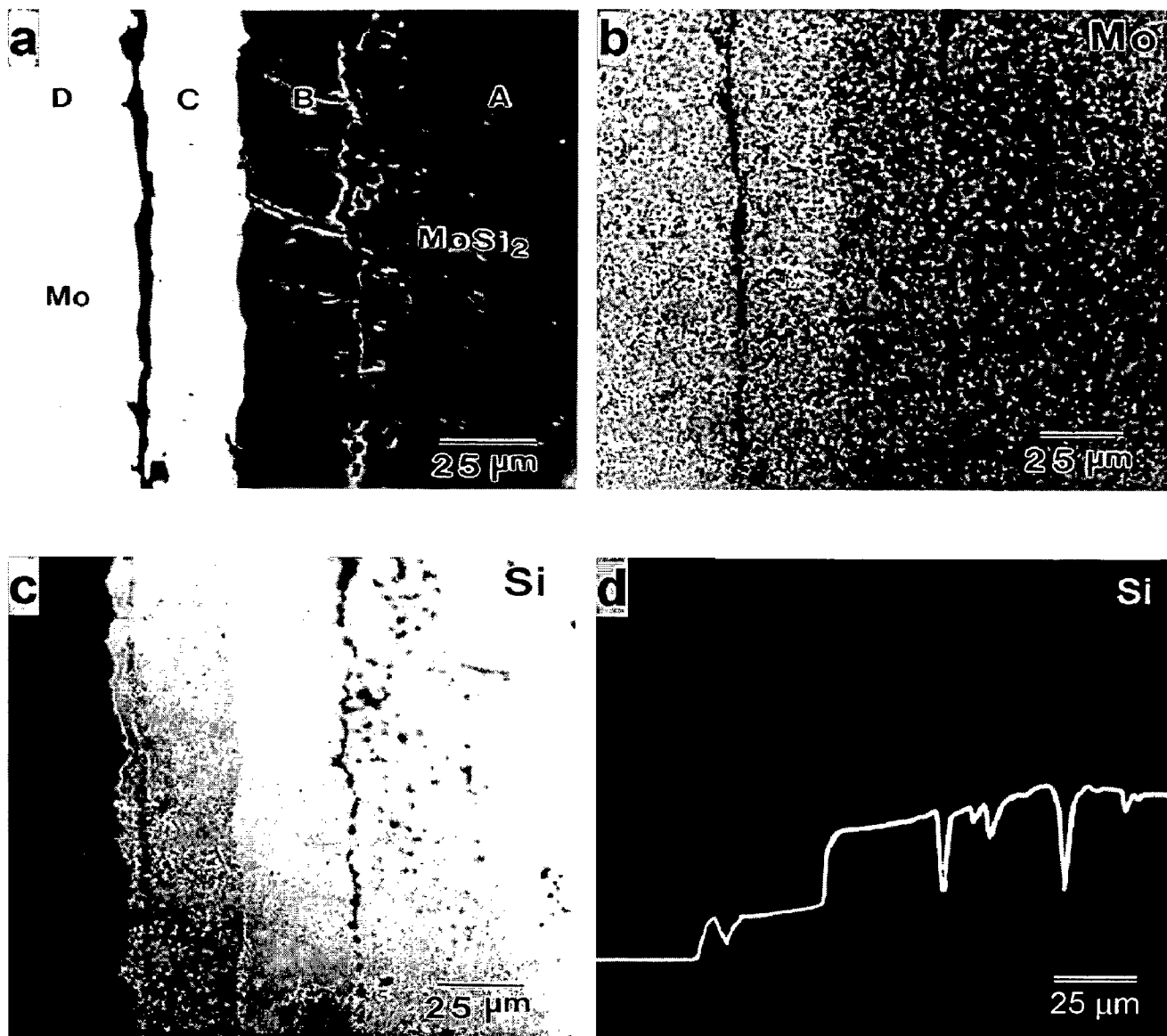


Fig. 5.35 EPMA images of (MoSi<sub>2</sub> + 2 wt% Al) + Mo foil laminated composite (a) back scattered electron image (b) x-ray map of Mo (c) x-ray map of Si and (d) line scan of Si.

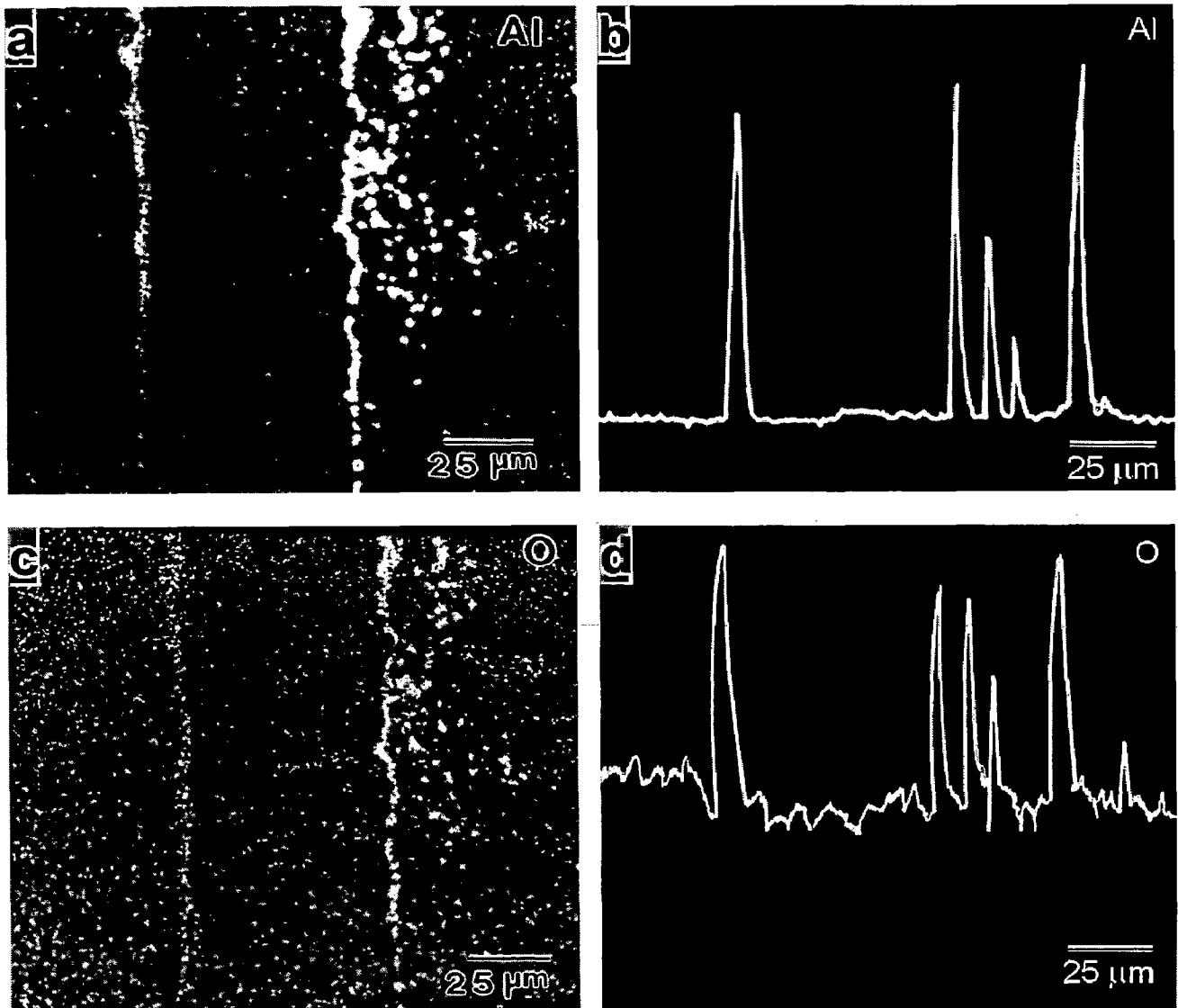


Fig. 5.36 EPMA images of  $(\text{MoSi}_2 + 2 \text{ wt}\% \text{ Al}) + \text{Mo}$  foil laminated composite (a) x-ray map of Al (b) line scan of Al (c) x-ray map of oxygen and (d) line scan of oxygen.

Table 5.10 Electron probe micro analysis (EPMA) of the interfacial region between  $\text{MoSi}_2$  based matrix and Mo foil in  $(\text{MoSi}_2 + 2 \text{ wt}\% \text{ Al}) + \text{Mo}$  foil laminated composite (Fig. 5.35(a)). All compositions are given in atom percent.

Region	Mo	Si	Phase
A	34.062	65.938	~ $\text{MoSi}_2$
B	61.539	38.461	~ $\text{Mo}_5\text{Si}_3$
C	74.327	25.673	~ $\text{Mo}_3\text{Si}$
D	99.452	0.548	~ Mo



The  $\text{SiO}_2$  is generally present in  $\text{MoSi}_2$  based matrix in the form of small and rounded particles and appear dark in BSE image. The x-ray map of Si (Fig. 5.35(c)) reveals these small and rounded particles inside  $\text{MoSi}_2$  based matrix are indeed depleted in Si. The x-ray maps and line scans for Al and oxygen as shown in Fig. 5.36, clearly establish that the small particles inside  $\text{MoSi}_2$  based matrix are rich in Al and oxygen suggesting that most of the  $\text{SiO}_2$  particles have reacted to form  $\text{Al}_2\text{O}_3$  particles. The x-ray mapped positions of Al and oxygen coincide, indicating formation of  $\text{Al}_2\text{O}_3$ . The troughs present in Si line scan (Fig. 5.35(d)) are indicative of the line scan passing through the  $\text{Al}_2\text{O}_3$  particles inside the  $\text{MoSi}_2$  based matrix region. The extent of  $\text{Al}_2\text{O}_3$  particles in  $\text{MoSi}_2$  based matrix was estimated to be approximately 6 vol%, using point counting method. Al addition to  $\text{MoSi}_2$  thus resulted in in-situ formation of  $\text{MoSi}_2$ -6 vol%  $\text{Al}_2\text{O}_3$  composite. Some  $\text{Al}_2\text{O}_3$  in the microstructure may also result from the commercial grade Al powder used. Al particles in commercial grade powder have an oxide coating. The SEM back-scattered electron images in Fig. 5.33 show that the  $\text{Al}_2\text{O}_3$  particles are distributed throughout the matrix.

It is assumed that there was no surplus Al, which entered into solid solution with  $\text{MoSi}_2$  and the entire amount of Al, added to  $\text{MoSi}_2$  was consumed in reduction of  $\text{SiO}_2$  and  $\text{MoO}_2$  phases. Pure Al was not detected as segregated or forming precipitates in elemental form anywhere. Similarly, elemental Si formed as a result of reaction between Al and  $\text{SiO}_2$  was not detected in the microstructure, indicating that it went into solution or reacted with  $\text{Mo}_5\text{Si}_3$  phase forming  $\text{MoSi}_2$ .  $\text{Mo}_5\text{Si}_3$  forms due to Si depletion of  $\text{MoSi}_2$  as a result of Si diffusion towards refractory metal foil as described earlier.  $\text{Mo}_5\text{Si}_3$  is unstable in excess Si, as  $\text{Mo}_5\text{Si}_3$  and Si do not co-exist in equilibrium in the binary Mo - Si system (Massalski, 1986). Hence,  $\text{Mo}_5\text{Si}_3$  would be converted to  $\text{MoSi}_2$  in presence of Si.

The EPMA images of ( $\text{MoSi}_2 + 2 \text{ wt}\% \text{ Al}$ ) + Ta foil laminated composite are shown in Fig. 5.37 and Fig. 5.38. The arrow marks in back scattered electron image (Fig. 5.37(a)) indicate the interface between pure Ta and the reaction layer as a good contrast between pure Ta and interfacial reaction layer could not be obtained in BSE image. There is almost no diffusion of Mo into Ta foil (Fig. 5.37(b)) while some Ta seems to have diffused inside  $\text{MoSi}_2$  across the interfacial reaction layer (Fig. 5.37(c)). However, the x-ray map of Si and Si line scan as shown in Figs. 5.37(d)

and 5.37(e), respectively, clearly revealed that the interfacial reaction zone consisted of two distinct layers. The quantitative analysis of chemical composition of the reaction products by EPMA is presented in Table 5.11. The typical microprobe data obtained at locations indicated by A, B, C and D in Fig. 5.37(a) correspond to  $\text{MoSi}_2$ ,  $\text{Ta}_5\text{Si}_3$ ,  $\text{Ta}_2\text{Si}$  and pure Ta phases, respectively.

The x-ray map of Si suggests that  $\text{Ta}_2\text{Si}$  layer was of much smaller thickness as compared to the  $\text{Ta}_5\text{Si}_3$  layer.  $\text{Ta}_2\text{Si}$  with negligible Mo content corresponds to the  $\text{Ta}_2\text{Si}$  phase on the binary Ta – Si phase diagram. The average atomic numbers of  $\text{Ta}_2\text{Si}$  and  $\text{Ta}_5\text{Si}_3$  phases are 68.75 and 67.97, respectively. A very small difference in the average atomic numbers could be the reason for these two phases not getting resolved in back scattered electron image under SEM, which revealed only one interfacial reaction layer as depicted in Fig. 5.33(b). However, the x-ray map of Si as well the Si line scan obtained in EPMA studies clearly establish qualitatively, the presence of two reaction layers differing in Si concentration. The quantitative microprobe data has further confirmed the presence of two different phases in the reaction zone.

As in the case of  $(\text{MoSi}_2 + 2 \text{ wt}\% \text{ Al}) + \text{Mo}$  foil composite, the x-ray maps and line scans of Al and oxygen as depicted in Fig. 5.38 once again establish that the small particles inside  $\text{MoSi}_2$  based matrix were of  $\text{Al}_2\text{O}_3$ . The x-ray mapped positions of Al and oxygen coincide, indicating formation of  $\text{Al}_2\text{O}_3$ .  $\text{SiO}_2$  particles originally present in  $\text{MoSi}_2$  were converted into  $\text{Al}_2\text{O}_3$ . The troughs present in Si line scan (Fig. 5.37(e)) are indicative of the line scan passing through the  $\text{Al}_2\text{O}_3$  particles inside the  $\text{MoSi}_2$  region.

### 5.3.2 Mechanical Behaviour

The room temperature mechanical properties of  $\text{MoSi}_2 + 2 \text{ wt}\% \text{ Al}$  monolithic,  $(\text{MoSi}_2 + 2 \text{ wt}\% \text{ Al}) + \text{Mo}$  foil and  $(\text{MoSi}_2 + 2 \text{ wt}\% \text{ Al}) + \text{Ta}$  foil laminated composites are presented in Tables 5.12 and 5.13. Each data point in Tables 5.12 and 5.13 is an average of 3 to 5 tests.

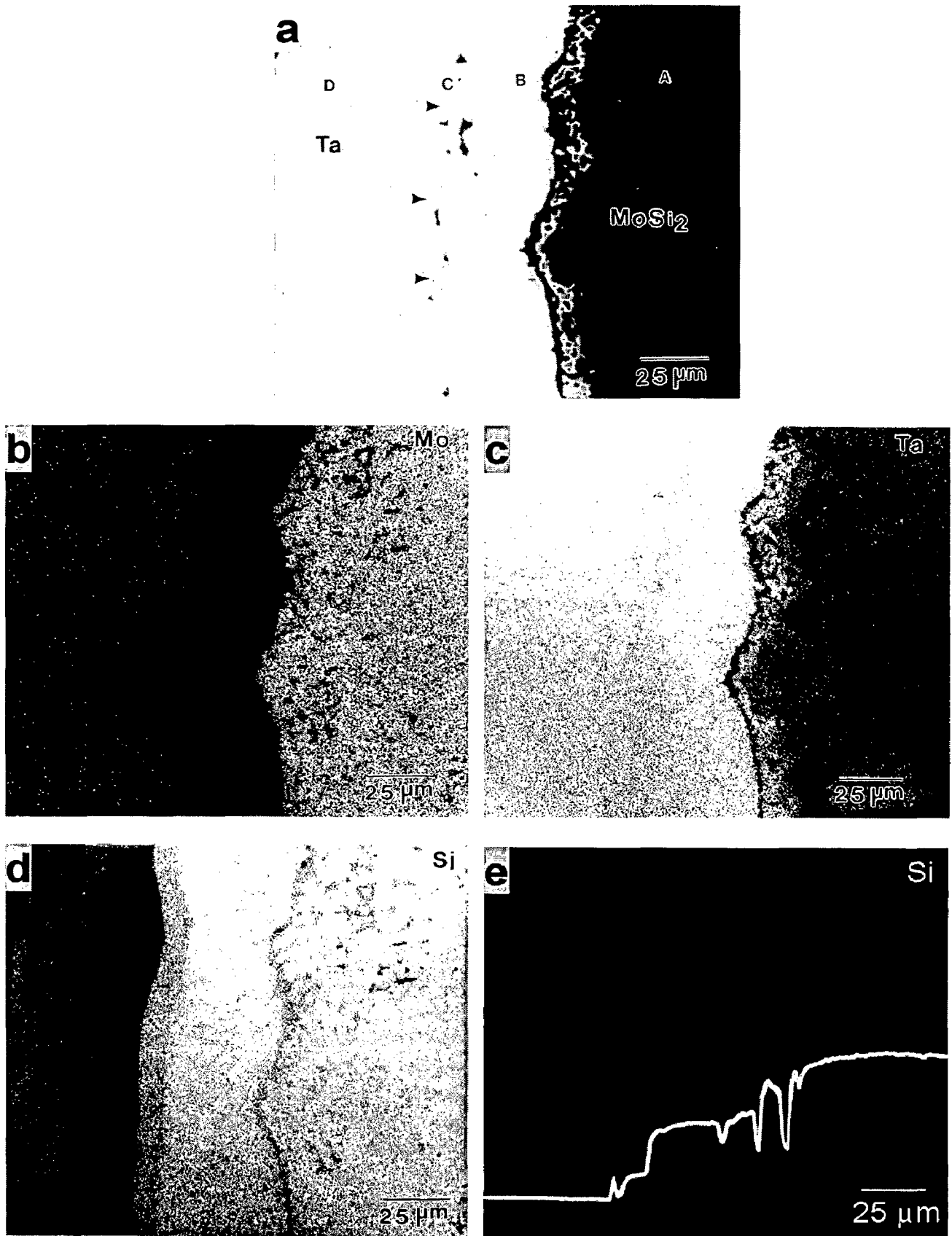


Fig. 5.37 EPMA images of (MoSi<sub>2</sub> + 2 wt% Al) + Ta foil laminated composite (a) back scattered electron image (b) x-ray map of Mo (c) x-ray map of Ta (d) x-ray map of Si and (e) line scan of Si.

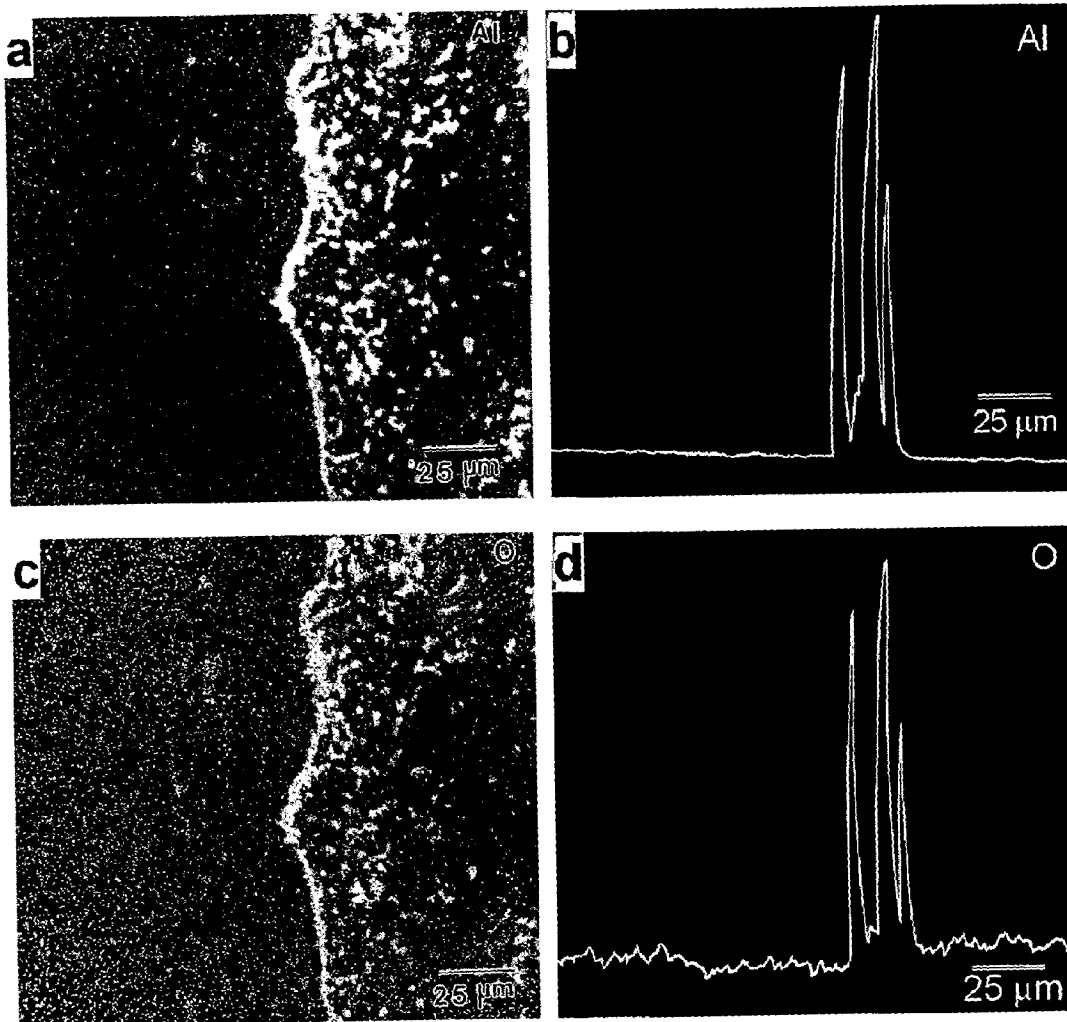


Fig. 5.38 EPMA images of  $(\text{MoSi}_2 + 2 \text{ wt\% Al}) + \text{Ta}$  foil laminated composite (a) x-ray map of Al (b) line scan of Al (c) x-ray map of oxygen and (d) line scan of oxygen.

Table 5.11 Electron probe micro analysis (EPMA) of the interfacial region between  $\text{MoSi}_2$  based matrix and Ta foil in  $(\text{MoSi}_2 + 2 \text{ wt\% Al}) + \text{Ta}$  foil laminated composite (Fig. 5.37(a)). All compositions are given in atom percent.

Region	Mo	Si	Ta	Phase
A	34.763	65.237	0.000	~ $\text{MoSi}_2$
B	0.204	37.900	61.896	~ $\text{Ta}_5\text{Si}_3$
C	0.151	32.437	67.412	~ $\text{Ta}_2\text{Si}$
D	0.000	0.234	99.766	~ Ta

Table 5.12 Mechanical properties of (MoSi<sub>2</sub> + 2 wt% Al) + Mo and Ta foil laminated composites.

Composite	Elastic Modulus (GPa)	Matrix Hardness (GPa)	Matrix Indentation Fracture Toughness, K <sub>IC</sub> (MPa√m)
MoSi <sub>2</sub> + 2 wt% Al	432	11.7	4.8
(MoSi <sub>2</sub> + 2 wt% Al) + Mo Foil	365	11.0	4.5
(MoSi <sub>2</sub> + 2 wt% Al) + Ta Foil	331	11.3	4.7
Pure MoSi <sub>2</sub>	440	10.2	4.2

Table 5.13 Mechanical properties of (MoSi<sub>2</sub> + 2 wt% Al) + Mo and Ta foil laminated composites.

Composite	Flexural Strength (MPa)		Fracture Toughness, K <sub>max</sub> (MPa√m)		Work of Fracture (J/m <sup>2</sup> )	
	Crack Arrestor	Crack Divider	Crack Arrestor	Crack Divider	Crack Arrestor	Crack Divider
	Mode	Mode	Mode	Mode	Mode	Mode
MoSi <sub>2</sub> + 2 wt% Al	220		4.6		-	
MoSi <sub>2</sub> + 2 wt% Al + Ta Foil	307	278	13.3	6.4	29,808	3,339
Pure MoSi <sub>2</sub>	150		4.2		-	

The elastic modulus of laminated composites was measured at right angles to the lamination direction. The modulus values of both the laminated composites were found to be lower than the  $\text{MoSi}_2 + 2 \text{ wt}\% \text{ Al}$  monolithic alloy. The modulus of Ta foil laminated composite was lower than the Mo foil laminated composite. This is understandable as pure Ta metal has a lower elastic modulus as compared to the pure Mo. The elastic modulus of  $\text{MoSi}_2 + 2 \text{ wt}\% \text{ Al}$  monolithic was also marginally lower than that of pure  $\text{MoSi}_2$ .

The hardness of  $\text{MoSi}_2$ -2 wt% Al alloy was slightly higher than that of pure  $\text{MoSi}_2$  as reported by Mitra et al (1999). Increase in hardness may be attributed to the formation of  $\text{Al}_2\text{O}_3$  in-situ.

The indentation fracture toughness of  $\text{MoSi}_2$ -2 wt% Al monolithic alloy was measured from the slope of the linear plot between indentation load and crack length ( $P$  vs.  $c^{3/2}$ ) as exhibited in Fig. 5.39. The fracture toughness underwent only a moderate improvement in  $\text{MoSi}_2$ -2 wt% Al alloy as compared to the pure  $\text{MoSi}_2$ . The indentation toughness was also measured in the matrix layers of both the laminated composites. The toughness measurement by indentation techniques cannot be done in the bulk-laminated composites as no radial cracks are generated by hardness indentations taken inside the ductile phases. Figure 5.40 is an optical micrograph showing a typical hardness indentation mark taken inside the Mo foil. The toughness of  $\text{MoSi}_2$ -2 wt% Al remained more or less same whether measured in the monolithic form or inside the laminated composites.

Figure 5.41 shows a typical indentation crack originating from a corner of the hardness indentation mark taken inside the matrix layer of the ( $\text{MoSi}_2 + 2 \text{ wt}\% \text{ Al}$ ) + Mo foil laminated composite. Observation of indentation crack paths using polarized light optical microscopy indicated that the crack paths were mostly transgranular and only partly intergranular. This is in agreement with the observations of Wade and Petrovic (1992<sup>a</sup>), who have reported 75 - 80% transgranular failure in pure  $\text{MoSi}_2$ . The grains with finer size in  $\text{MoSi}_2$  were responsible for a tendency towards a more intergranular mode of failure. The coarser grains in  $\text{MoSi}_2$  failed by transgranular mode in the present study.  $\text{SiO}_2$  particles did not have any effect on deflection of the crack paths, as has been reported earlier by Wade and Petrovic (1992<sup>a</sup>) in unalloyed  $\text{MoSi}_2$ .

The arrow mark in Fig. 5.41 exhibits the presence of micro-elastic bridging by a  $\text{MoSi}_2$  grain.  $\text{MoSi}_2$  has a tetragonal crystal structure with a large  $c/a$  ratio. Anisotropy in coefficient of thermal expansion values along  $a$ -axis and  $c$ -axis is expected to result in residual thermal stresses in individual grains after cooling from the processing temperature. This could result in tensile and compressive residual stresses in the  $\text{MoSi}_2$  grains depending upon their crystallographic orientations. If some grains are residually compressed, they can bridge the crack as described in section 2.6.2.3. With increasing grain size, internal stresses in  $\text{MoSi}_2$  are believed to increase. Earlier studies by Mitra et al (1997<sup>a</sup>) have also reported the micro-elastic bridging in  $\text{MoSi}_2$ .

Figure 5.42 is a SEM back scattered electron image of  $(\text{MoSi}_2 + 2 \text{ wt\% Al}) + \text{Ta}$  foil laminated composite showing the crack interactions with Ta foil. The indentation crack passed through the interfacial reaction layers of  $\text{Ta}_5\text{Si}_3$  and  $\text{Ta}_2\text{Si}$  before it was arrested by the ductile Ta foil. The crack gets arrested at  $\text{Ta}_2\text{Si} / \text{Ta}$  interface. This clearly demonstrates that the ductile Ta foil could effectively blunt a crack propagating inside the  $\text{MoSi}_2$  based matrix upon its impingement with the metal foil. The reaction zone was brittle. The brittle nature of the reaction zone is evidenced by the ease with which the crack propagated from the hardness indentation in the reaction zone.

Figure 5.43(a) is a polarized light optical micrograph showing the indentation crack paths in Mo foil laminated composite while the Fig. 5.43(b) is a SEM back scattered electron image taken at a higher magnification of the same area as shown in Fig. 5.43(a). The crack propagated inside the  $\text{MoSi}_2$  based matrix and the  $\text{Mo}_5\text{Si}_3$  reaction layer but was arrested at  $\text{Mo}_5\text{Si}_3 / \text{Mo}_3\text{Si}$  interface as depicted by an arrowhead in Fig. 5.43(a). It did not propagate further through the  $\text{Mo}_3\text{Si}$  layer suggesting that the  $\text{Mo}_3\text{Si}$  phase was not as brittle as  $\text{MoSi}_2$  and  $\text{Mo}_5\text{Si}_3$ . An examination of indentation cracking areas have shown that crack branching also took place, as the crack approached the metal foil. The SEM image in Fig. 5.43(b) reveals the clear evidence of crack branching.

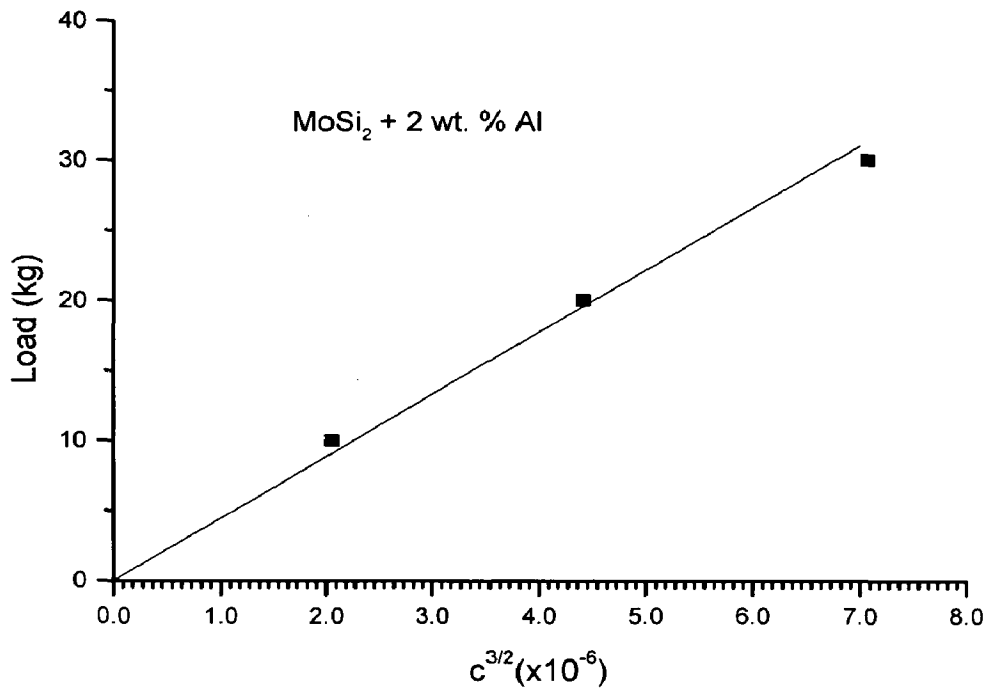


Fig. 5.39 A typical indentation load ( $P$ ) vs. crack length ( $c^{3/2}$ ) graph as obtained in the case of  $\text{MoSi}_2 + 2 \text{ wt}\% \text{ Al}$  matrix. The indentation fracture toughness was estimated from the slope of the linear plot of  $P$  vs.  $c^{3/2}$ .

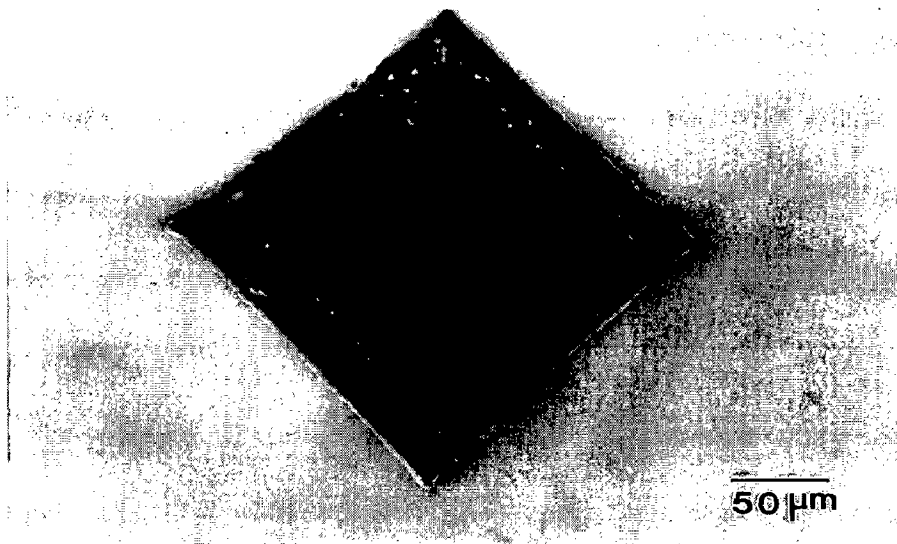


Fig. 5.40 Optical micrograph showing a typical hardness indentation mark taken inside the Mo foil. No radial cracks are generated by hardness indentations taken inside the ductile phases.



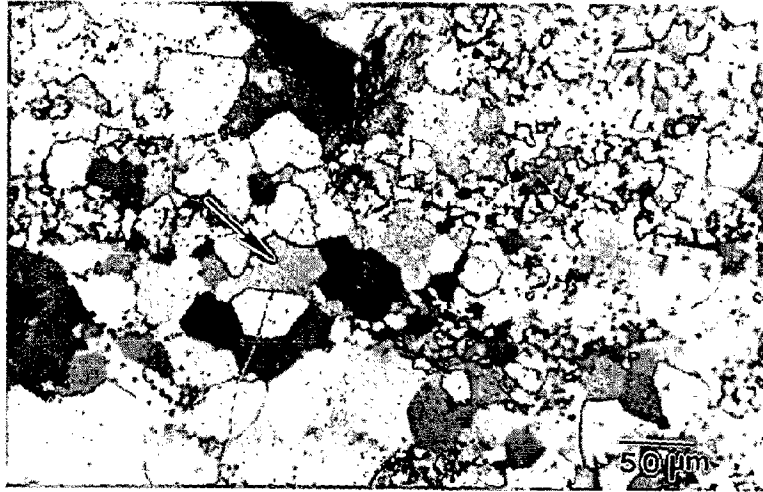


Fig. 5.41 Polarized light optical micrograph showing a typical indentation crack originating from a corner of the hardness indentation mark taken inside the matrix layer of  $(\text{MoSi}_2 + 2 \text{ wt\% Al}) + \text{Mo}$  foil laminated composite. The arrow exhibits the presence of micro bridging by a  $\text{MoSi}_2$  grain.

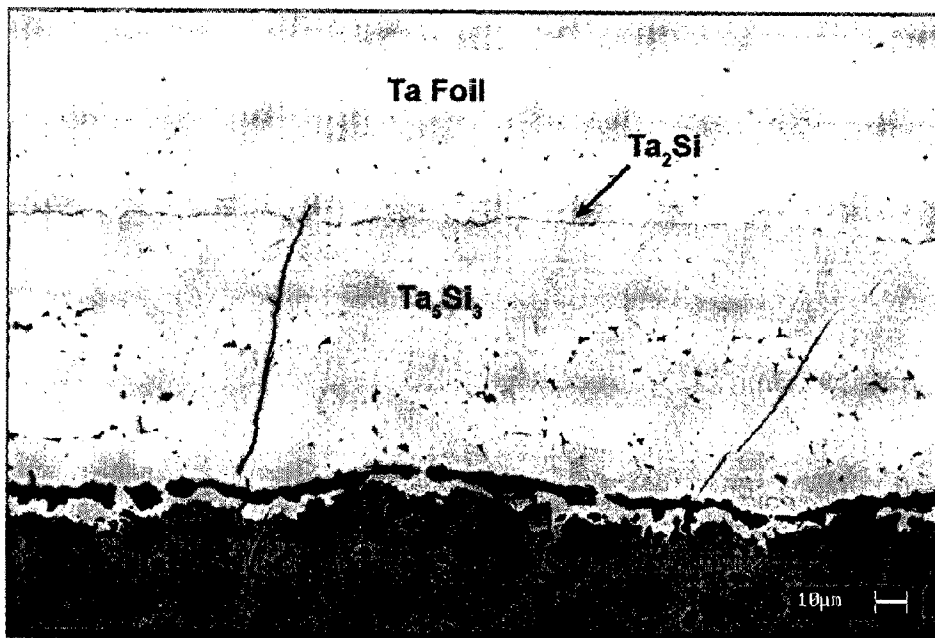
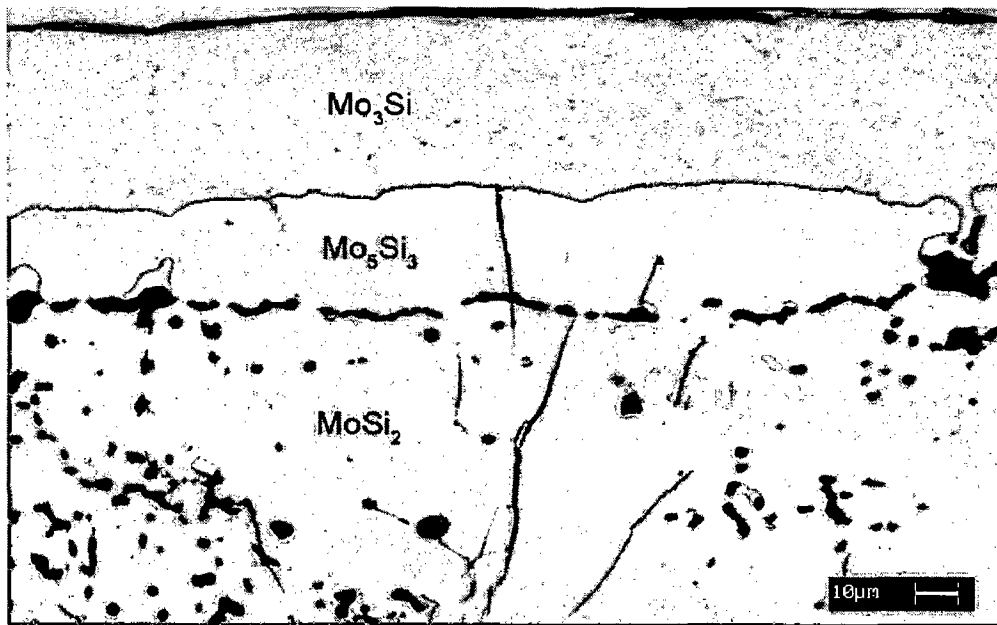


Fig. 5.42 SEM back scattered electron image showing indentation crack paths in  $(\text{MoSi}_2 + 2 \text{ wt\% Al}) + \text{Ta}$  foil composite. The crack gets arrested at  $\text{Ta}_2\text{Si} / \text{Ta}$  interface.



(a)



(b)

Fig. 5.43

Indentation crack paths in  $(\text{MoSi}_2 + 2 \text{ wt\% Al}) + \text{Mo}$  foil composite (a) polarized light optical micrograph (b) SEM back scattered electron image of the same area. The crack gets arrested at  $\text{Mo}_5\text{Si}_3 / \text{Mo}_3\text{Si}$  interface.

The average flexural strength of MoSi<sub>2</sub>-2 wt% Al monolithic material was found to be 220 MPa, in contrast to 150 MPa of pure (unalloyed) MoSi<sub>2</sub>. This accounts for a remarkable increase of 47% in flexural strength due to Al addition. Room temperature flexural strength improved significantly due to strengthening effect of Al<sub>2</sub>O<sub>3</sub> reinforcements, as observed in other MoSi<sub>2</sub> matrix composites reinforced with ceramic particles. The fracture toughness value of MoSi<sub>2</sub>-2 wt% Al obtained from testing SENB specimens was 4.6 MPa√m with respect to 4.2 MPa√m of pure MoSi<sub>2</sub>. The value of fracture toughness shows only a moderate increase by addition of Al in MoSi<sub>2</sub> matrix. Removal of vitreous SiO<sub>2</sub> also aids in improving strength and fracture toughness.

Figure 5.44 shows a SEM fractograph of MoSi<sub>2</sub> + 2 wt% Al monolithic alloy tested in a notched three point bend test. The fracture was predominantly transgranular cleavage with some evidence of intergranular failure similar to what has been revealed by the indentation crack paths. At the hot pressing temperature of 1750 °C, Al would be present in liquid state with high mobility. It appears that some Al has diffused to grain boundaries revealing the grain boundaries on the fracture surfaces.

There was a very significant improvement in both flexural strength as well as fracture toughness of (MoSi<sub>2</sub> + 2 wt% Al) + Ta foil laminated composite. The increase in flexural strength was 28 % while the toughness improved by almost a factor of 3 measured in crack arrester mode as compared to the monolithic (MoSi<sub>2</sub> + 2 wt% Al). However, the improvements in crack divider mode were moderate. Such remarkable improvements in room temperature mechanical properties are due to a unique layered structure employed in designing the MoSi<sub>2</sub> based composites. Ductile metallic phases were incorporated in MoSi<sub>2</sub> matrix in continuous (foil) form rather than in particle form distributed discontinuously in the matrix. A single 0.5 mm thick foil of ductile Ta metal separated the two layers of brittle MoSi<sub>2</sub> based matrix. The ductile metal foil acts as a barrier to unstable crack growth once initiated in the MoSi<sub>2</sub> based matrix resulting in ductile phase toughening of MoSi<sub>2</sub>.

The SENB fracture toughness test specimen used to evaluate the fracture toughness of laminated composites is depicted schematically in Fig. 3.20. During the initial stages of loading, on the notch side the stress concentration was on the notch tip and therefore, a crack initiates at the notch tip, which propagates further inside

the MoSi<sub>2</sub> based matrix until it meets the barrier in the form of a ductile metal foil capable of undergoing plastic stretching. This relaxes the high stresses associated with the crack tip. No interfacial debonding takes place at this stage. As the crack ends on one side of the Ta foil, with further increase in load it renucleates on the other side of the foil and propagates further. Because of a statistical distribution of crack nucleation sites on the other side of the foil, it is not necessary that the renucleation be coplanar with the original crack. As a primary crack opens, the load is transferred on the Ta foil and the foil starts stretching. However, as the metal foil is constrained by the brittle matrix it continues to take further load. A relatively large lateral deformation of the Ta foil as compared to the matrix results in secondary cracking and multiple fracture of the matrix. A test specimen, which was interrupted and unloaded during the test before its final fracture, was viewed under SEM. Its secondary electron images taken at different magnifications are shown in Fig. 5.45. The multiple cracks appear in bell shape and have a tendency to propagate towards one point (the point of loading). These secondary cracks create a debonded region at the interface as shown in Fig. 5.45(b). In this area, the matrix-imposed constraints are relaxed and the foil can now deform freely until it fails in a ductile manner.

However, only moderate improvement in toughness was achieved in crack divider mode. In crack divider mode, the primary crack propagates in the direction of foil lamination as depicted schematically in Fig. 3.20(b). The crack has a continuous path to propagate within the brittle matrix without encountering a ductile phase barrier and the need for renucleation. Only a small segment of the crack front, which propagates through the ductile foil in the middle, tries to hold back the crack front propagating through the MoSi<sub>2</sub> based matrix. Only a limited load transfer from matrix to the foil occurs.

The work of fracture was measured from the area under the load – displacement curve by a method as described in section 3.3.2.3(d). The high work of fracture obtained in (MoSi<sub>2</sub> + 2 wt% Al) + Ta foil laminated composite comes mainly from the plastic deformation of the ductile Ta foil before the separation of the specimen into two pieces.

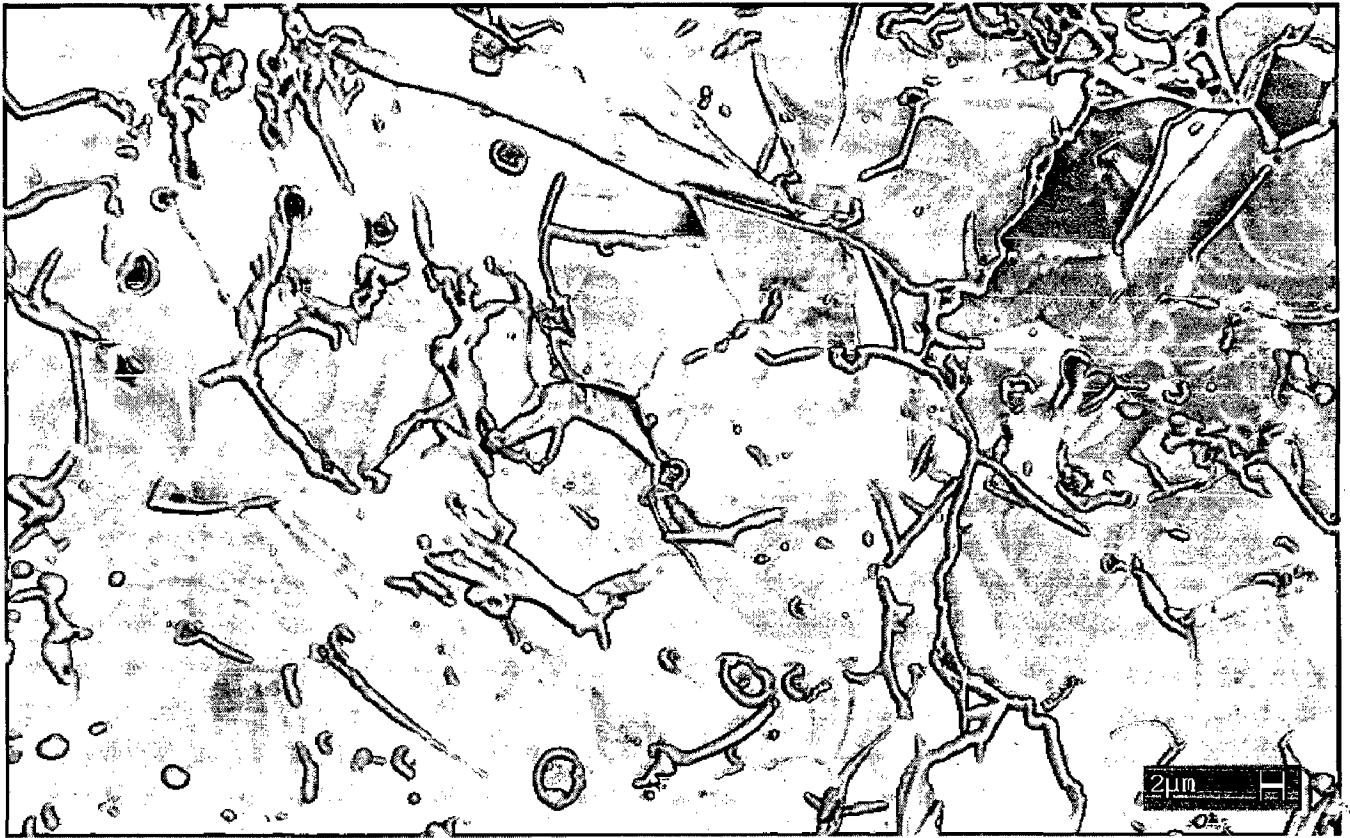
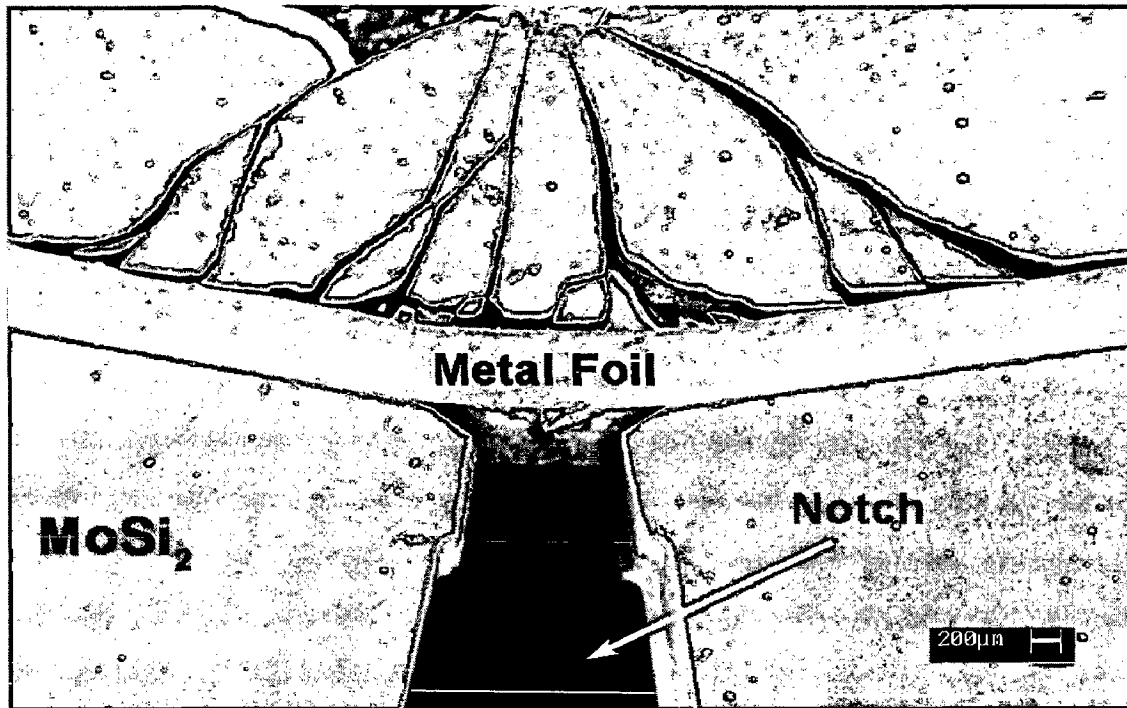
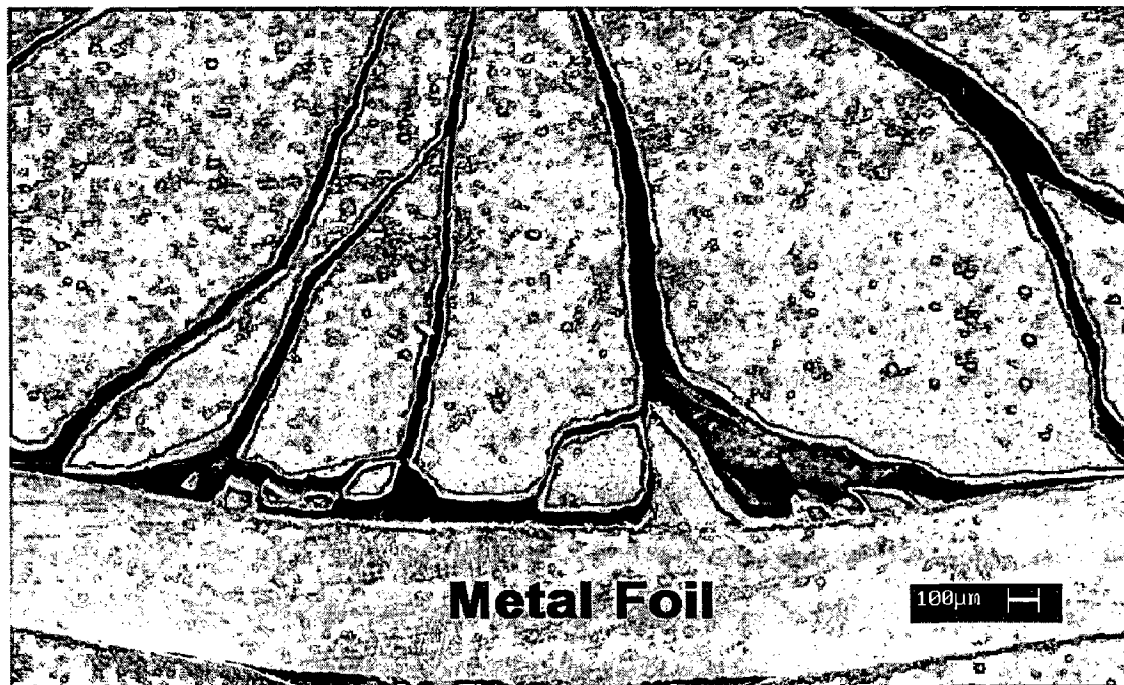


Fig. 5.44 SEM fractograph of a three point bend test specimen of MoSi<sub>2</sub> + 2 wt% Al alloy matrix.



(a)



(b)

Fig. 5.45 SEM secondary electron images (taken at different magnifications) of (MoSi<sub>2</sub> + 2 wt% Al) + Ta foil laminated composite being tested in crack arrester mode. The test was interrupted and the specimen was unloaded during the test before its final fracture.

Figure 5.46 exhibits the typical fracture surfaces of (MoSi<sub>2</sub> + 2 wt% Al) + Ta foil laminated composite taken inside the MoSi<sub>2</sub> based matrix layer and inside the Ta foil. As in earlier case, the fracture in MoSi<sub>2</sub> based matrix was predominantly transgranular. The grains were retained with no change in the cleavage planes. The fracture surface of the Ta foil exhibits a typical ductile fibrous fracture.

In case of (MoSi<sub>2</sub> + 2 wt % Al) + Mo foil laminated composite, a valid flexural strength or fracture toughness value could not be obtained due to shear failure of the three-point bend test specimens. The specimens failed in shear possibly because of the existence of high residual thermal stresses at MoSi<sub>2</sub> based matrix / Mo foil interface. The coefficient of thermal expansion of pure Mo is  $4.9 \times 10^{-6}/K$  as compared to the coefficient of thermal expansion of polycrystalline MoSi<sub>2</sub> which was calculated as  $8.52 \times 10^{-6}/K$  (section 4.3.1). Such a large thermal expansion mismatch between MoSi<sub>2</sub> and the Mo foil would result in high residual thermal stresses during cooling from the processing temperatures, which are expected to adversely affect the interfacial shear strength in the laminated composite. Therefore, the laminated structure failed in shear before the applied load could reach to a level of its flexural strength. The presence of a small amount of Al<sub>2</sub>O<sub>3</sub> in MoSi<sub>2</sub> matrix does not significantly contribute in reducing the thermal expansion mismatch between matrix and the foil. The coefficient of thermal expansion of Al<sub>2</sub>O<sub>3</sub> is  $7.4 \times 10^{-6}/K$ , which is only marginally lower than that of MoSi<sub>2</sub>.

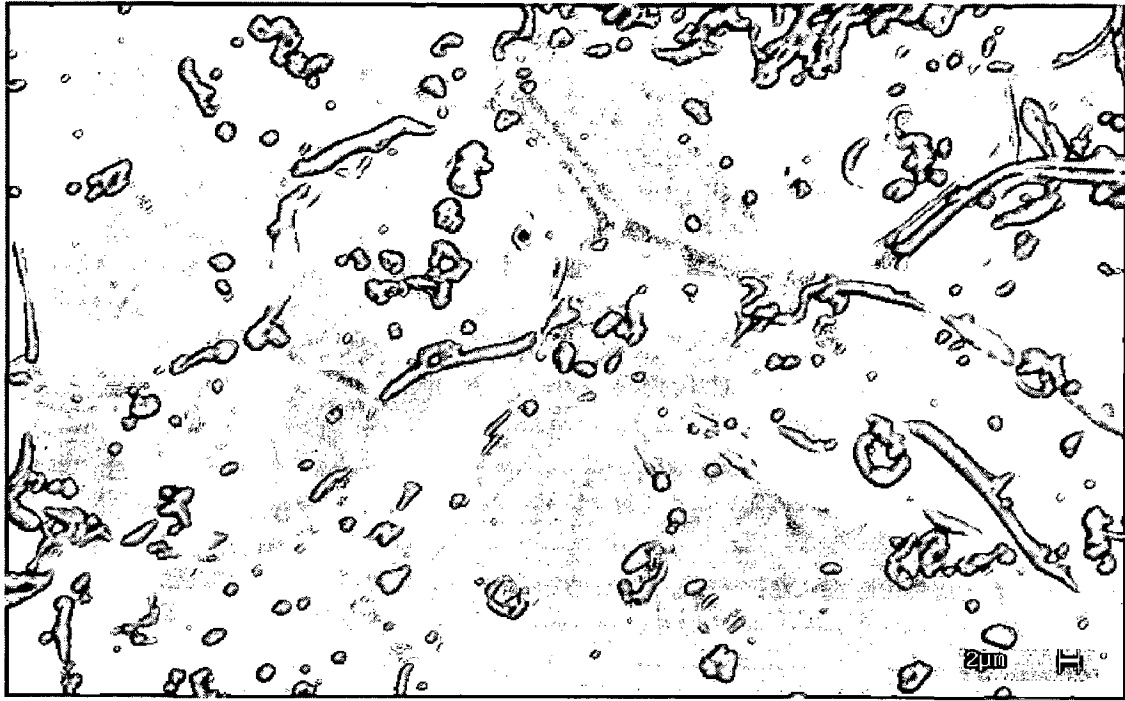
Figure 5.47 exhibits stereo photomicrographs (taken at different magnifications) of a three-point bend specimen of (MoSi<sub>2</sub> + 2 wt% Al) + Mo foil laminated composite, which failed in shear. Extensive delamination has taken place along the MoSi<sub>2</sub> / Mo interface. In a few specimens, delamination occurred up to the outer span loading point. The propagating crack was arrested by the metal foil, renucleated on the other side and propagated further through the entire thickness of the MoSi<sub>2</sub> layers. At this moment, the load is transferred to the metal foil through the interface resulting in the interfacial failure.

An examination of the fracture surface reveals that delamination has taken place along the MoSi<sub>2</sub> / Mo<sub>5</sub>Si<sub>3</sub> interface as shown in Fig. 5.48(a). This is clear if the fractograph in Fig. 5.48(a) is viewed in combination with the optical polarized light microstructure of Fig. 5.31 which has been reproduced here as Fig. 5.48(b). This

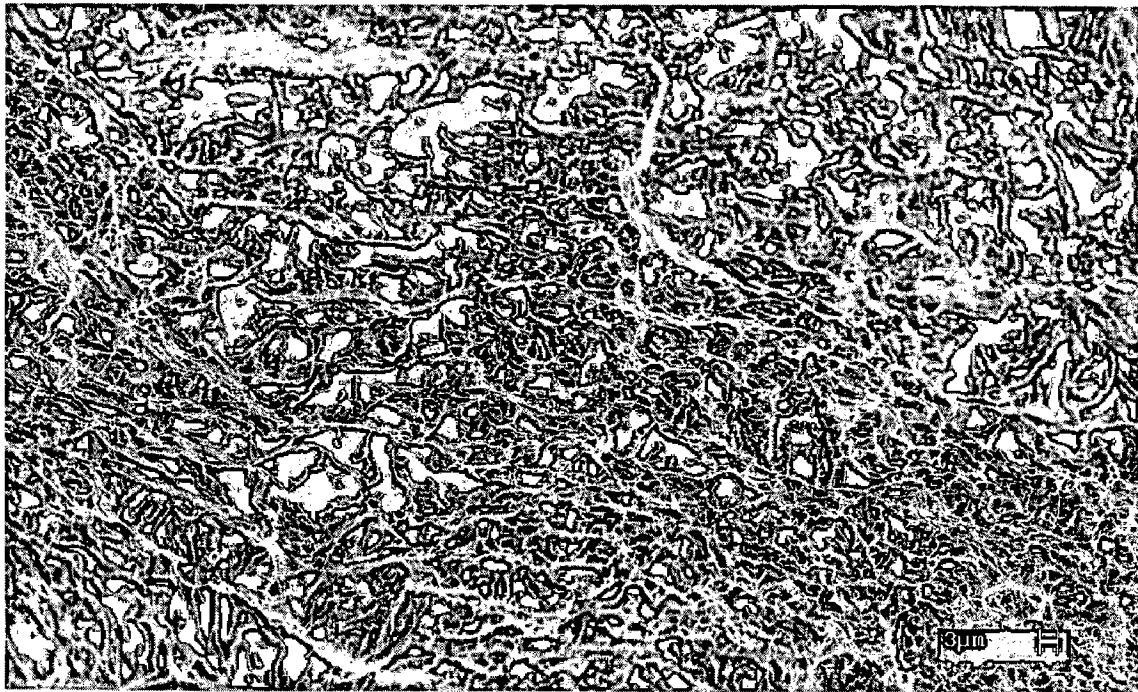
suggests that the interfacial bonding between  $\text{Mo}_5\text{Si}_3$  /  $\text{Mo}_3\text{Si}$  and between  $\text{Mo}_3\text{Si}$  / pure Mo was stronger as compared to the interfacial bonding between  $\text{MoSi}_2$  /  $\text{Mo}_5\text{Si}_3$ .

As described in section 3.3.2.3(b), a high span-to-depth ( $L/d$ ) ratio is preferred to suppress the chances of test specimen failing in shear. The relationship between failure loads vs. span length for a three-point bend specimen failing in flexure as well as in shear modes is schematically presented in Fig. 3.18. It shows that the span length should be greater than the critical span length,  $L_c$ , for a given material to ensure the specimen to fail in tension (to suppress the shear failure). The  $L/d$  ratio was kept as 8 for all the laminated composite systems studied in the present work. In case of  $(\text{MoSi}_2 + 2 \text{ wt } \% \text{ Al}) + \text{Mo}$  foil composite, a higher  $L/d$  ratio may be required for the specimens to fail in flexure. However, with the limitations of the existing hot pressing equipment, a higher  $L/d$  ratio could not be achieved in the as hot pressed laminated materials. Further work was carried out by adding 20 vol% SiC particles in  $\text{MoSi}_2$  matrix which resulted in a lower thermal expansion mismatch between  $\text{MoSi}_2$  based matrix and the ductile refractory metal foils.





(a)



(b)

Fig. 5.46 SEM fractographs of fracture toughness,  $K_{IC}$  (notched three point bend) test specimen of  $(\text{MoSi}_2 + 2 \text{ wt\% Al}) + \text{Ta}$  foil composite (a) taken inside the matrix layer and (b) taken inside the Ta foil.

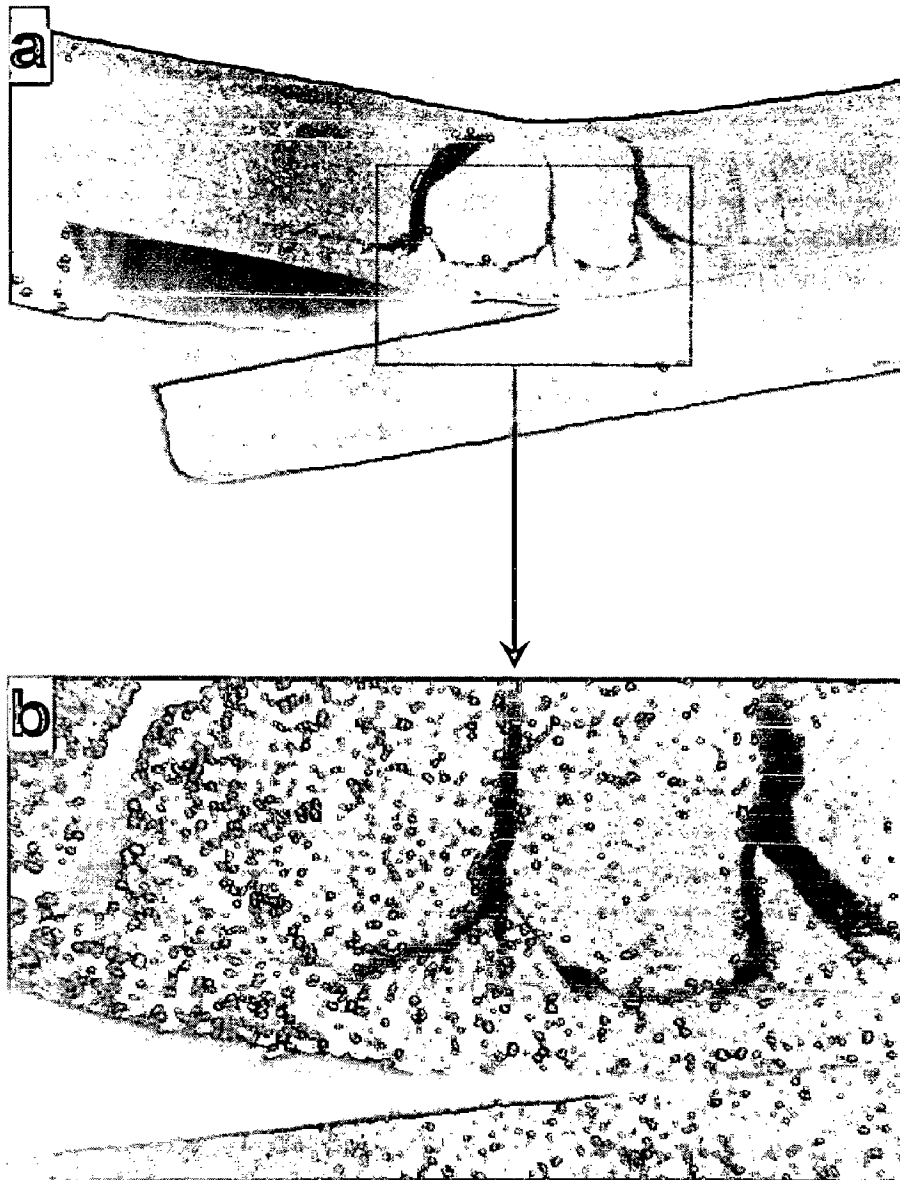
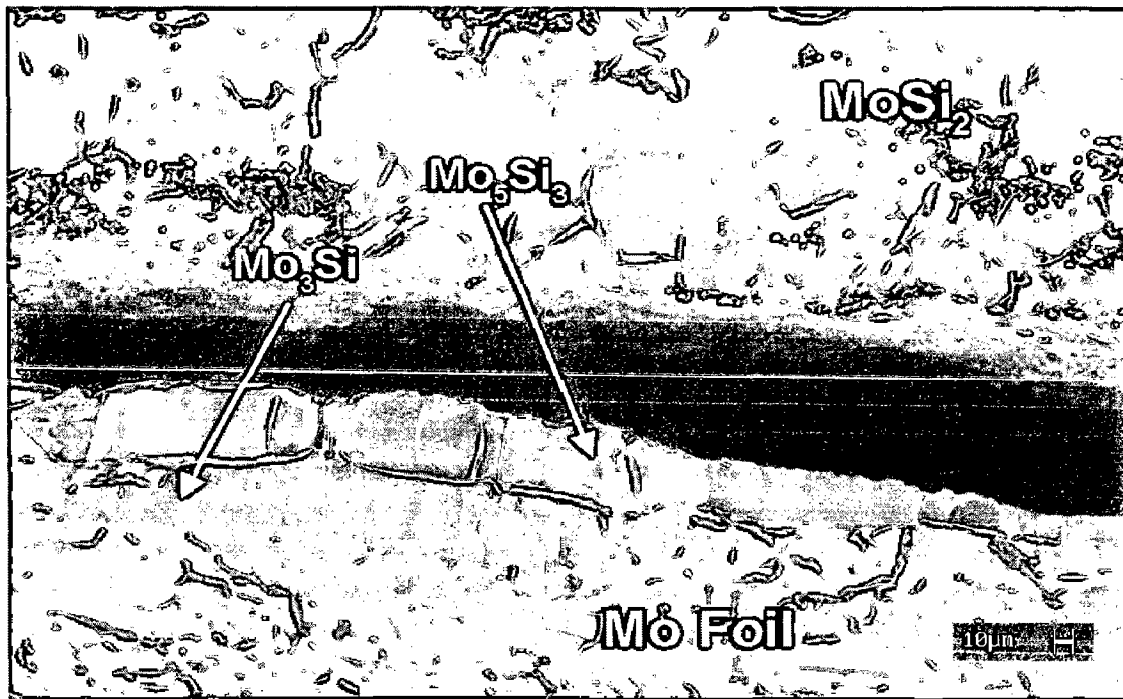
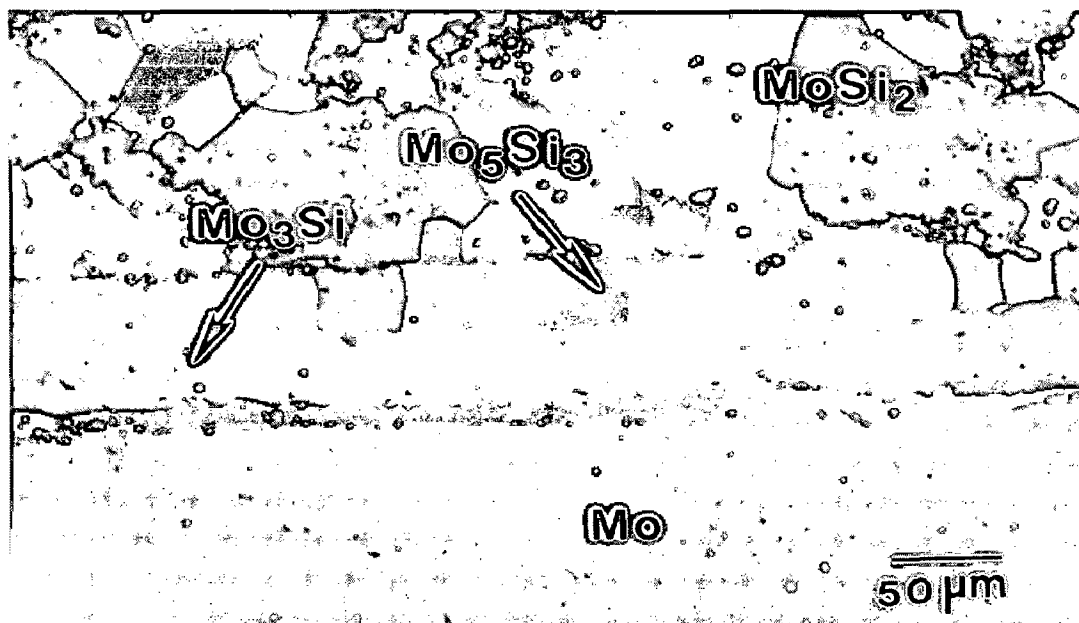


Fig. 5.47 Stereo photomicrographs of a three-point bend test specimen of ( $\text{MoSi}_2$  + 2 wt% Al) + Mo foil laminated composite. The specimen failed in shear mode.



(a)

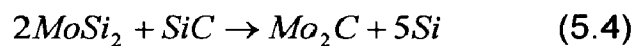


(b)

Fig. 5.48 (a) The fracture surface of a three-point bend test specimen of  $(\text{MoSi}_2 + 2 \text{ wt}\% \text{ Al}) + \text{Mo}$  foil laminated composite failed in the shear mode. The crack propagated along the  $\text{MoSi}_2 / \text{Mo}_5\text{Si}_3$  interface (b) Optical microstructure of  $(\text{MoSi}_2 + 2 \text{ wt}\% \text{ Al}) + \text{Mo}$  foil composite (same as shown in Fig. 5. 31).

## 5.4 LAMINATED COMPOSITES WITH (MoSi<sub>2</sub> + 20 vol% SiC<sub>p</sub>) AS MATRIX

MoSi<sub>2</sub> has a higher coefficient of thermal expansion than most of the refractory metals. In laminated composites, large thermal expansion mismatch between the layers of pure MoSi<sub>2</sub> and refractory metal foils may give rise to residual thermal stresses in the composites during cooling from processing temperature to the room temperature. These residual stresses may affect the bonding between the MoSi<sub>2</sub> layer and the refractory metal foils affecting the resultant mechanical properties of the laminated composites. SiC has a lower coefficient of thermal expansion than MoSi<sub>2</sub> and therefore, when added to MoSi<sub>2</sub> matrix, is expected to reduce the thermal expansion mismatch between MoSi<sub>2</sub> and the refractory metal foils resulting in the lower residual thermal stresses in the composites. SiC is thermodynamically stable with MoSi<sub>2</sub>. A possible reaction between MoSi<sub>2</sub> and SiC resulting in the formation of Mo<sub>2</sub>C can be described as follows:



The variation of free energy change with temperature for the above reaction,  $\Delta G$  (per mole of SiC) is plotted in Fig. 5.49 and found to be positive for the entire temperature range.

Therefore, to improve the thermal compatibility between MoSi<sub>2</sub> and the refractory metal foils, 20 vol% SiC particles (SiC<sub>p</sub>) were added in MoSi<sub>2</sub> matrix. SiC particles were dry blended with MoSi<sub>2</sub> powder prior to hot pressing into laminated structures. The size of SiC particles was kept small, so as to eliminate the thermally induced cracking.

### 5.4.1 Microstructural Studies

#### 5.4.1.1 (MoSi<sub>2</sub> + 20 vol% SiC<sub>p</sub>) Monolithic

The microstructures of MoSi<sub>2</sub> + 20 vol% SiC<sub>p</sub> monolithic material taken at different magnifications under ordinary as well as polarized light are shown in Fig. 5.50. The x-ray diffraction pattern and the SEM back scattered electron image of the same composite are presented in Figs. 5.51 and 5.52, respectively.

The ordinary light optical microstructures as well as SEM back scattered electron image reveal that SiC particles were uniformly distributed in MoSi<sub>2</sub> matrix. A uniform distribution of SiC particles results in better mechanical properties in the composite. The microstructures also reveal the presence of small and rounded particles distributed randomly throughout the matrix. These were identified as SiO<sub>2</sub> particles by EPMA studies as described earlier. The x-ray diffraction data (Fig. 5.51) does not exhibit the presence of any other crystalline phase formed due to any possible reaction between MoSi<sub>2</sub> and SiC during processing at high temperature and reveals the peaks of only MoSi<sub>2</sub> and SiC phases. The average grain size of MoSi<sub>2</sub> was found to be in the range of 5 – 8 μm as measured from the optical micrographs taken with polarized light. The grain structure of MoSi<sub>2</sub> is revealed only by polarized light optical microscopy due to anisotropy in its tetragonal crystal structure. In general, the MoSi<sub>2</sub> grains were regular and equi-axed.

Figure 5.53 exhibits an optical micrograph of MoSi<sub>2</sub> reinforced with SiC<sub>p</sub> used to estimate volume fraction of SiC particles by image analysis after vacuum hot processing at high temperature. The results of the estimated volume fraction of the two phases are presented in Table 5.14. The volume fraction of SiC in the microstructure was found to be the same as originally added to MoSi<sub>2</sub> powder prior to vacuum hot pressing indicating that there was no depletion of SiC during processing at high temperature. MoSi<sub>2</sub> and SiC form a highly stable composite system.

#### **5.4.1.2 (MoSi<sub>2</sub> + 20 vol% SiC<sub>p</sub>) / Mo Foil Laminated Composite**

The microstructures of (MoSi<sub>2</sub> + 20 vol% SiC<sub>p</sub>) + Mo foil laminated composite using ordinary light as well as polarized light are shown in Figs. 5.54 and 5.55, respectively. Figure 5.54(a) reveals the interfacial reaction layer on both sides of the Mo foil as indicated by arrow marks. Figure 5.54(b) exhibits the interfacial reaction zone between MoSi<sub>2</sub> based matrix and Mo at a higher magnification. SiC particles are uniformly distributed in MoSi<sub>2</sub> matrix. SiO<sub>2</sub> particles are also present distributed throughout the microstructure. The optical microstructures under polarized light as shown in Fig. 5.55 reveals the MoSi<sub>2</sub> grains with a grain size in the range of 5 – 8 μm. The interfacial reaction layer is indicated by the arrow marks.

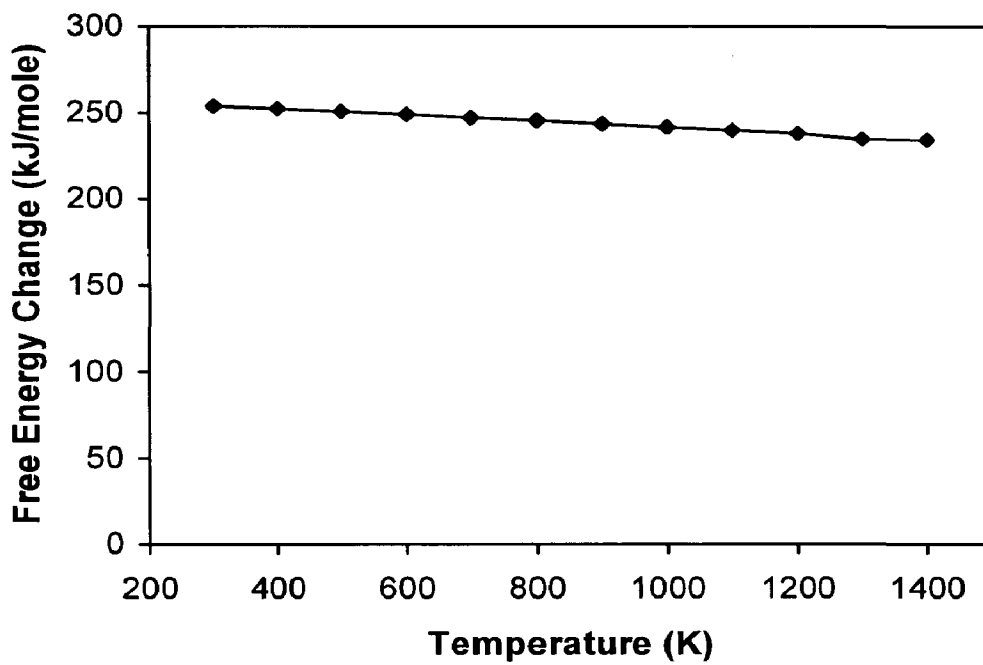


Fig. 5.49 Standard free energy change ( $\Delta G$  vs. *temperature*) for a possible chemical reaction between  $\text{MoSi}_2$  and  $\text{SiC}$ .

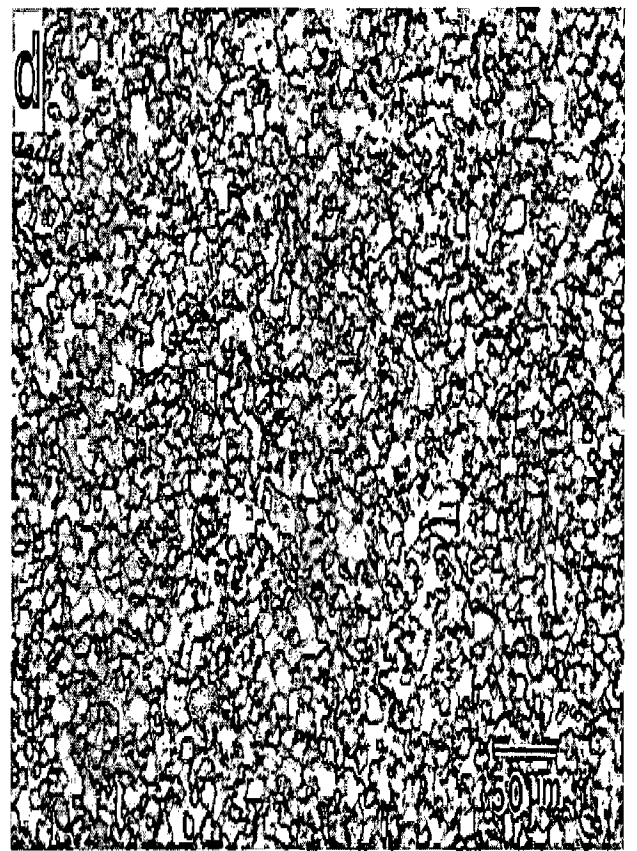
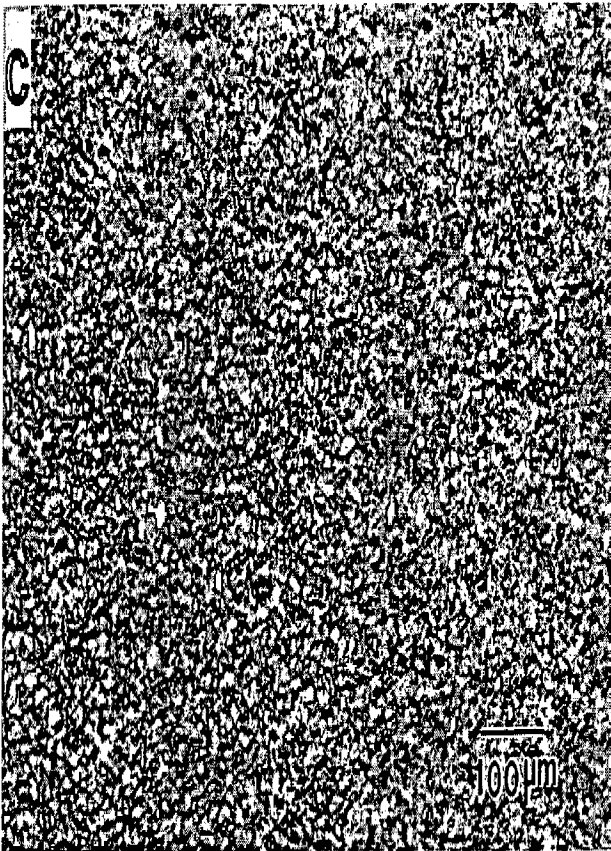
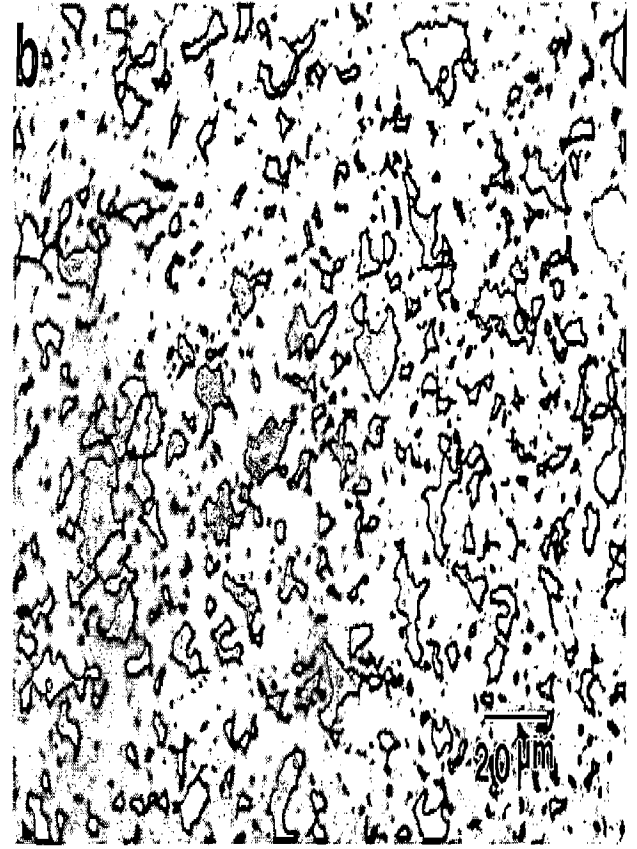
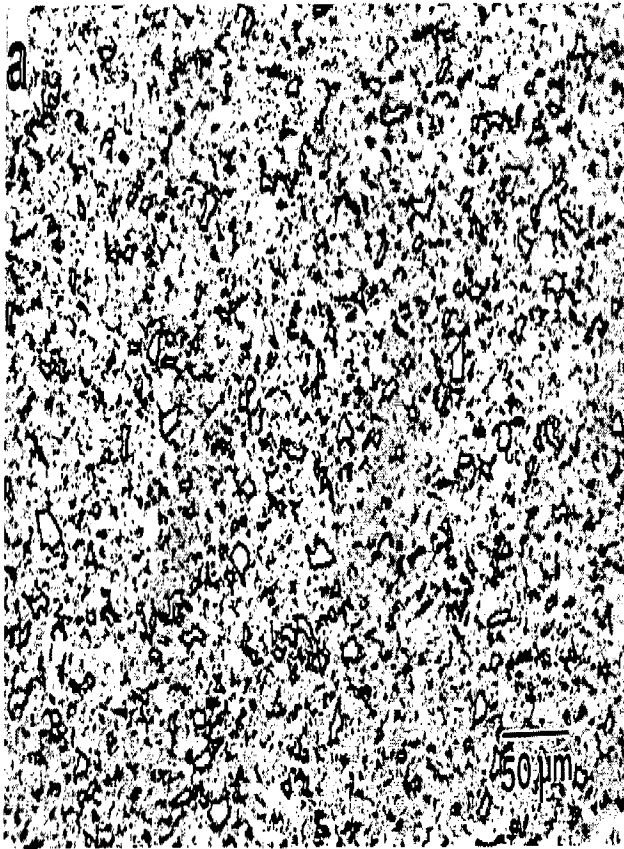


Fig. 5.50 Microstructures of MoSi<sub>2</sub> reinforced with 20 vol% SiC particles (used as MoSi<sub>2</sub> based matrix layer in laminated composites). (a) and (b) are taken under ordinary light while (c) and (d) are taken under polarized light at different magnifications.

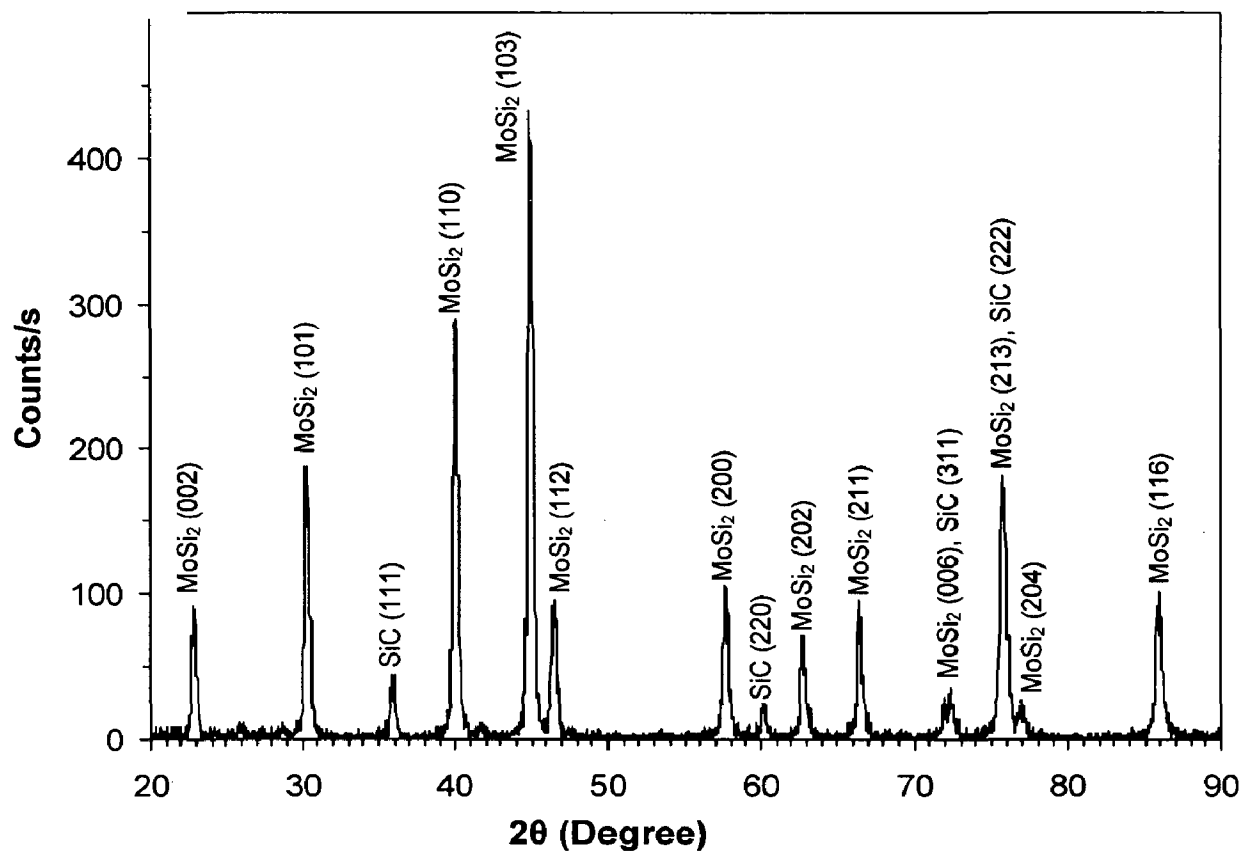


Fig. 5.51 X-ray diffraction pattern of MoSi<sub>2</sub> + 20 vol% SiC<sub>p</sub> composite.

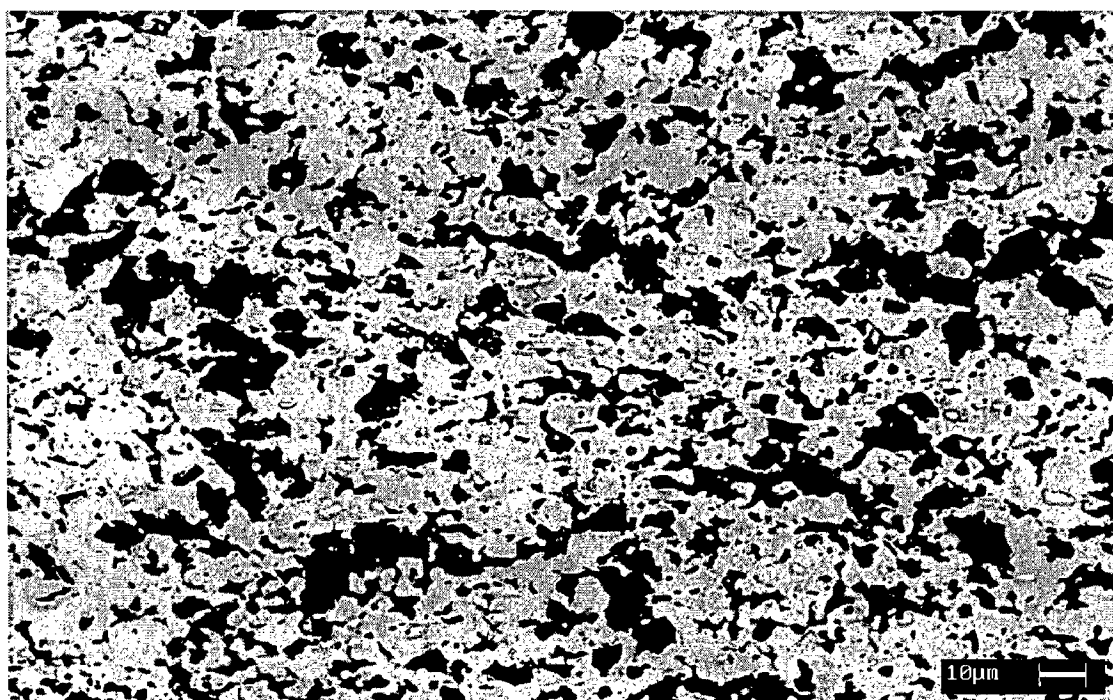


Fig. 5.52 SEM back scattered electron image of MoSi<sub>2</sub> + 20 vol% SiC<sub>p</sub> composite.





Fig. 5.53 Image analysis for calculating volume fraction of SiC particles in SiC<sub>p</sub> reinforced MoSi<sub>2</sub> matrix after processing at high temperature.

Table 5.14 Estimation of volume fraction of phases in MoSi<sub>2</sub> + 20 vol% SiC<sub>p</sub> composite by image analysis software.

S No.	Field Area (mm <sup>2</sup> )	Gray	Bright
1	1.00536	81.95118	18.048812
2	1.00525	77.810686	22.18932
3	1.00519	81.04132	18.95869
4	1.00547	78.34798	21.652011
<b>Average</b>		<b>79.787792</b>	<b>20.212208</b>

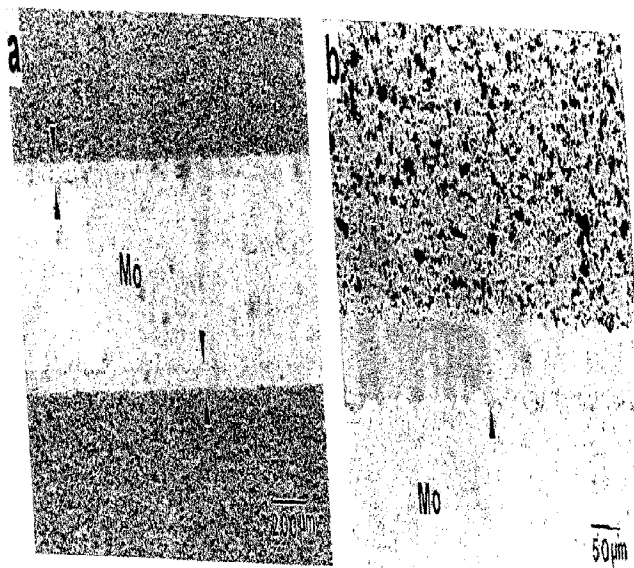


Fig. 5.54 Ordinary light optical microstructures of  $(\text{MoSi}_2 + 20 \text{ vol}\% \text{ SiC}_p)$  + Mo foil laminated composite exhibiting (a) interfacial reaction layers on both sides of Mo foil and (b) interfacial reaction zone at a higher magnification.

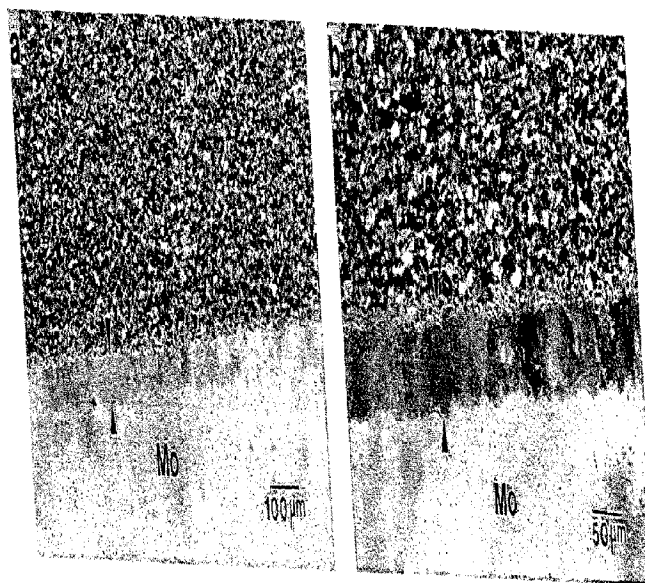


Fig. 5.55 Polarized light optical microstructures of  $(\text{MoSi}_2 + 20 \text{ vol}\% \text{ SiC}_p)$  + Mo foil laminated composite showing interfacial reaction zone at different magnifications.

The SEM back scattered electron images of  $(\text{MoSi}_2 + 20 \text{ vol}\% \text{ SiC}_p) + \text{Mo}$  foil laminated composite are presented in Fig. 5.56. The arrow marks in Fig. 5.56(a) indicate the interfacial reaction layer on both sides of the Mo foil while the same is shown in BSE image taken at a higher magnification in Fig. 5.56(b). The thickness of the interfacial reaction layer was measured to be approximately  $50 \mu\text{m}$  which was smaller than the thickness of the reaction zone developed in Mo foil laminated composite with  $\text{MoSi}_2 + 2 \text{ wt}\% \text{ Al}$  as the matrix. A smaller thickness of the reaction zone in  $(\text{MoSi}_2 + 20 \text{ vol}\% \text{ SiC}_p) + \text{Mo}$  foil composite could be attributed to a lower hot pressing temperature ( $1600 \text{ }^\circ\text{C}$ ) employed as compared to the  $(\text{MoSi}_2 + 2 \text{ wt}\% \text{ Al}) + \text{Mo}$  foil composite which was consolidated at  $1750 \text{ }^\circ\text{C}$ . Diffusion rates of various chemical species increase with increasing temperature. Si is the main diffusing element in the composite systems prepared in the present study and it is expected to penetrate deeper in Mo foil with increased processing temperatures.

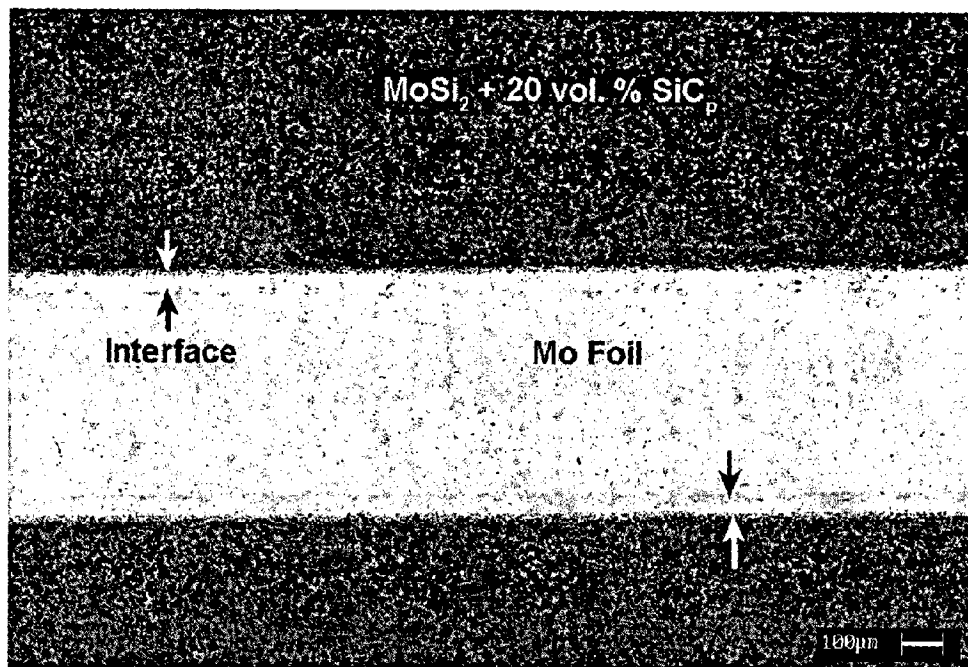
The x-ray diffraction pattern of  $(\text{MoSi}_2 + 20 \text{ vol}\% \text{ SiC}_p) + \text{Mo}$  foil laminated composite as shown in Fig. 5.57, reveals the peaks of  $\text{MoSi}_2$ , SiC and pure Mo. A few peaks of  $\text{Mo}_5\text{Si}_3$  are also detected but most of the  $\text{Mo}_5\text{Si}_3$  peaks were either too small or overlapped with the peaks of other phases. X-ray diffraction data suggests that the interfacial reaction layer consisted of mainly  $\text{Mo}_5\text{Si}_3$  phase. Si diffused from  $\text{MoSi}_2$  and reacted with pure Mo to form  $\text{Mo}_5\text{Si}_3$  at the interface. However, the detailed analysis of the interfacial reaction products was carried out by energy dispersive spectroscopy (EDS) in SEM as well as by EPMA studies.

Figure 5.58 exhibits an SEM secondary electron image of  $(\text{MoSi}_2 + 20 \text{ vol}\% \text{ SiC}_p) + \text{Mo}$  foil laminated composite along with the EDS analysis identifying the presence of  $\text{Mo}_5\text{Si}_3$  and  $\text{Mo}_2\text{C}$  phases in the interfacial reaction layer. The chemical composition obtained by EDS analysis (Table 5.15) has confirmed the  $\text{Mo}_5\text{Si}_3$  phase marked as A and  $\text{Mo}_2\text{C}$  phase marked as B in the SEM micrograph.  $\text{Mo}_2\text{C}$  was found in discrete form within the  $\text{Mo}_5\text{Si}_3$  layer as well as in the form of a thin and continuous layer at pure Mo \  $\text{Mo}_5\text{Si}_3$  interface. The formation of  $\text{Mo}_2\text{C}$  phase in the reaction zone was probably due to the reaction between SiC and pure Mo, which is explained in the subsequent sections. It is believed that  $\text{Mo}_2\text{C}$  did not result from a possible chemical reaction between SiC and  $\text{MoSi}_2$  as this reaction was found to be

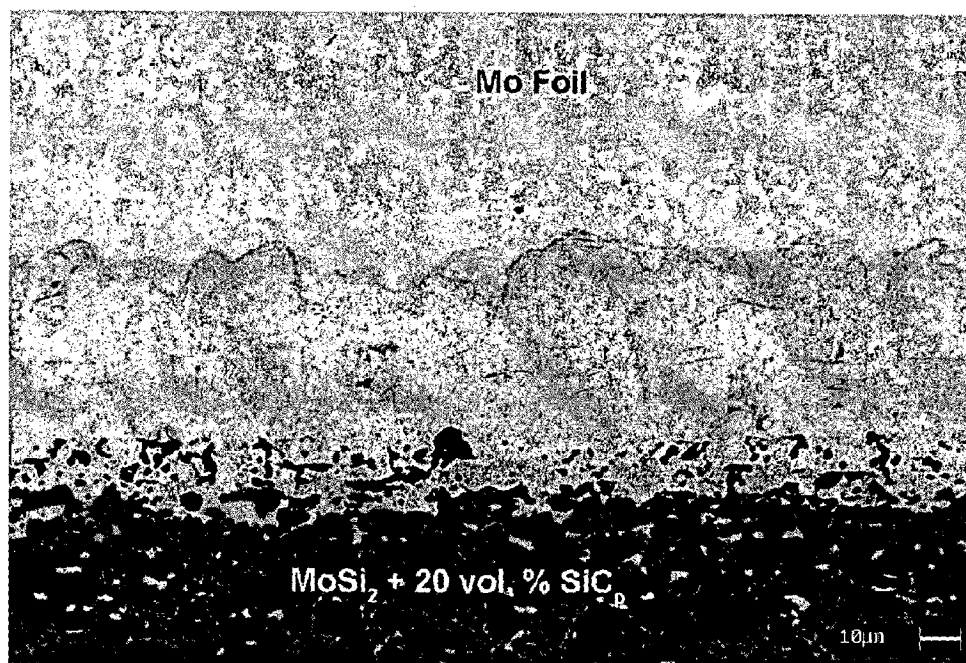
thermodynamically not feasible (Fig. 5.49). In contrast to  $(\text{MoSi}_2 + 2 \text{ wt\% Al}) + \text{Mo}$  foil composite,  $\text{Mo}_3\text{Si}$  phase was not observed in this composite system. Appreciable non-planar morphologies at  $\text{Mo} / \text{Mo}_2\text{C}$  and  $\text{Mo}_2\text{C} / \text{Mo}_5\text{Si}_3$  interfaces are revealed. The non-planar growth fronts of the  $\text{Mo}_5\text{Si}_3$  and  $\text{Mo}_2\text{C}$  layers may reflect anisotropy in diffusion.

Figure 5.59 shows an SEM back scattered electron image of  $(\text{MoSi}_2 + 20 \text{ vol\% SiC}_p) + \text{Mo}$  foil laminated composite along with EDS analysis revealing the  $\text{SiC}$ ,  $\text{SiO}_2$  and  $\text{Mo}_5\text{Si}_3$  phases inside the  $\text{MoSi}_2$  matrix layer. The chemical composition obtained by EDS analysis has confirmed the  $\text{SiC}$ ,  $\text{SiO}_2$  and  $\text{Mo}_5\text{Si}_3$  phases marked as C, D and E, in the SEM micrograph, respectively.  $\text{SiC}$  particles were irregular in shape while most of the  $\text{SiO}_2$  particles were globular. The BSE image along with the EDS analysis reveals that the  $\text{Mo}_5\text{Si}_3$  phase, which forms mainly at the interface in the form of a continuous layer, is also present as discrete particles along with  $\text{SiC}$  particles within the  $\text{MoSi}_2$  matrix. In addition to free  $\text{SiO}_2$ , commercial  $\text{MoSi}_2$  powders are likely to contain some  $\text{Mo}_5\text{Si}_3$  also.  $\text{SiO}_2$  forms due to the oxidation of the surfaces of  $\text{MoSi}_2$  particles during exposure to air or storage. The formation of significant quantity of  $\text{SiO}_2$  leads to depletion of Si in  $\text{MoSi}_2$ , shifting the composition towards the Mo rich side of the Mo - Si binary phase diagram (Fig. 2.3). This possibly leads to the formation of  $\text{Mo}_5\text{Si}_3$ . Table 5.15 presents the composition of the various phases identified in  $(\text{MoSi}_2 + 20 \text{ vol\% SiC}_p) + \text{Mo}$  foil laminated composite as determined by energy dispersive spectroscopy (EDS).

The EPMA images of  $(\text{MoSi}_2 + 20 \text{ vol\% SiC}_p) + \text{Mo}$  foil laminated composite are shown in Fig. 5.60. Figure 5.60(a) is a back scattered electron image while Fig. 5.60(b) exhibits x-ray map of Mo. The x-ray map of Si and the line scan of Si are presented in Figs. 5.60(c) and 5.60(d), respectively. The arrow marks in Fig. 5.60(a) indicate the non-planar growth front of the reaction zone. X-ray map and line scan of Si clearly exhibit the diffusion of Si into Mo forming the interfacial reaction layer. The dark streaks present within the reaction zone are Si free and are indicative of the  $\text{Mo}_2\text{C}$  phase as exhibited earlier in SEM secondary electron image (Fig. 5.58).



(a)



(b)

Fig. 5.56 SEM back scattered electron images of (MoSi<sub>2</sub> + 20 vol% SiC<sub>p</sub>) + Mo foil laminated composite showing (a) interfacial reaction layers on both sides of the Mo foil and (b) interfacial reaction layer at a higher magnification

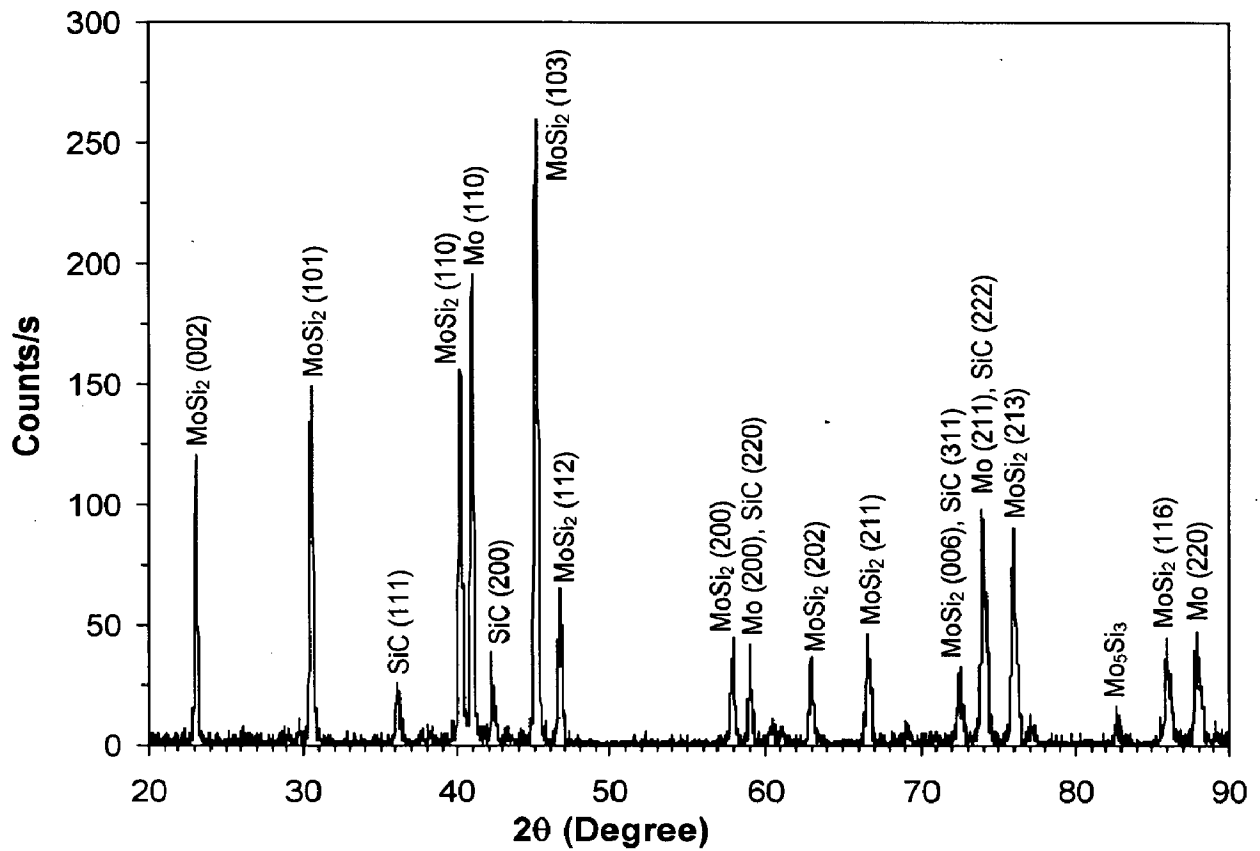


Fig. 5.57 X-ray diffraction pattern of (MoSi<sub>2</sub> + 20 vol% SiC<sub>p</sub>) + Mo foil laminated composite.

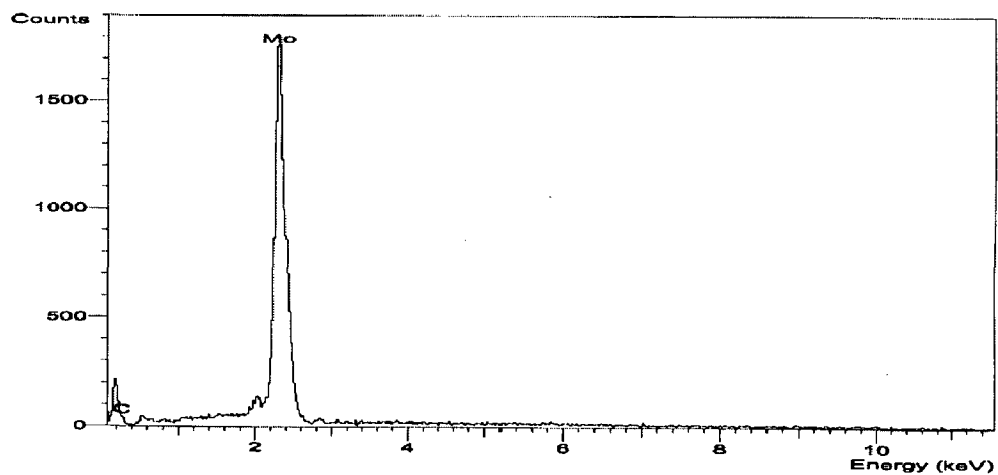
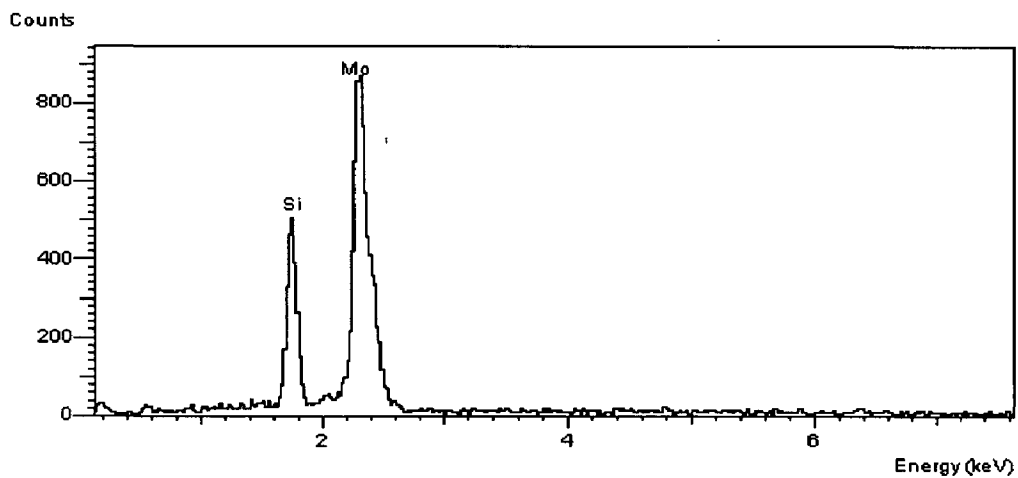
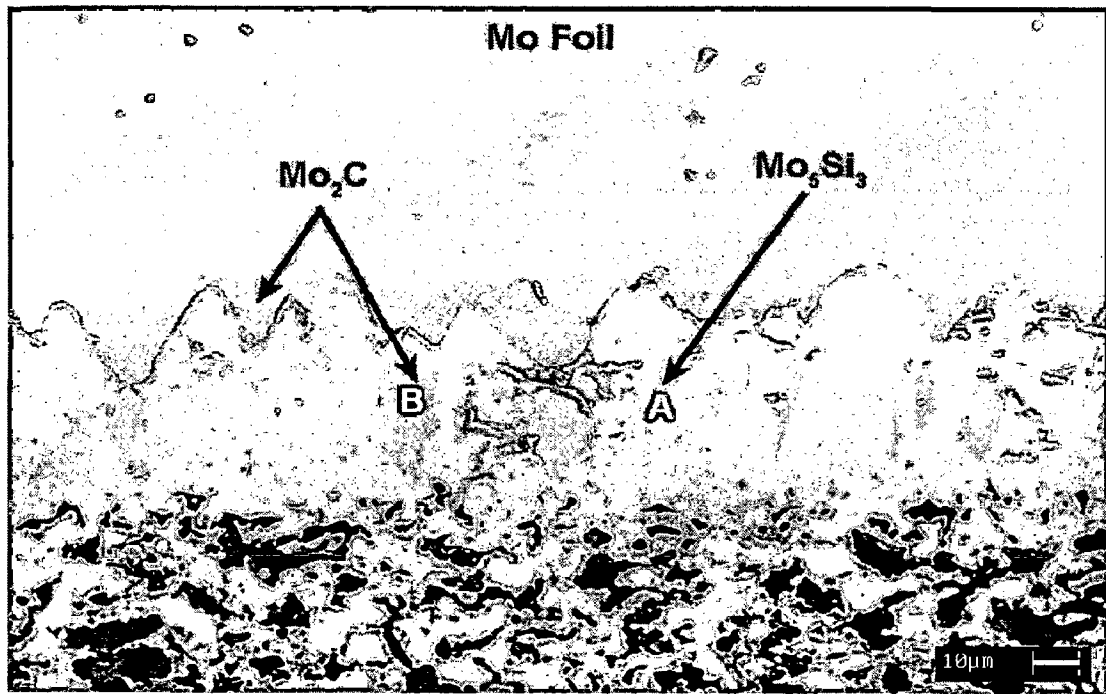


Fig. 5.58 SEM secondary electron image of  $(\text{MoSi}_2 + 20 \text{ vol}\% \text{ SiC}_p) + \text{Mo}$  foil laminated composite and EDS analysis confirming the presence of  $\text{Mo}_5\text{Si}_3$  and  $\text{Mo}_2\text{C}$  phases in the interfacial reaction layer.

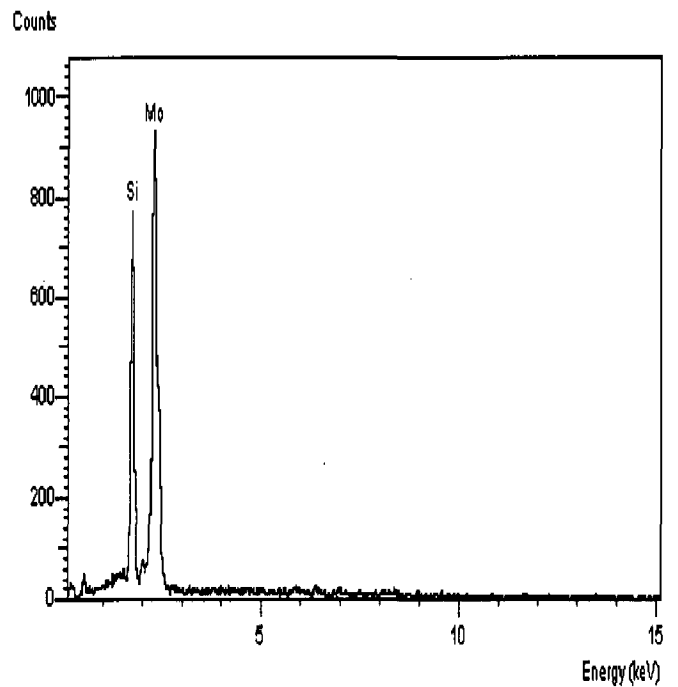
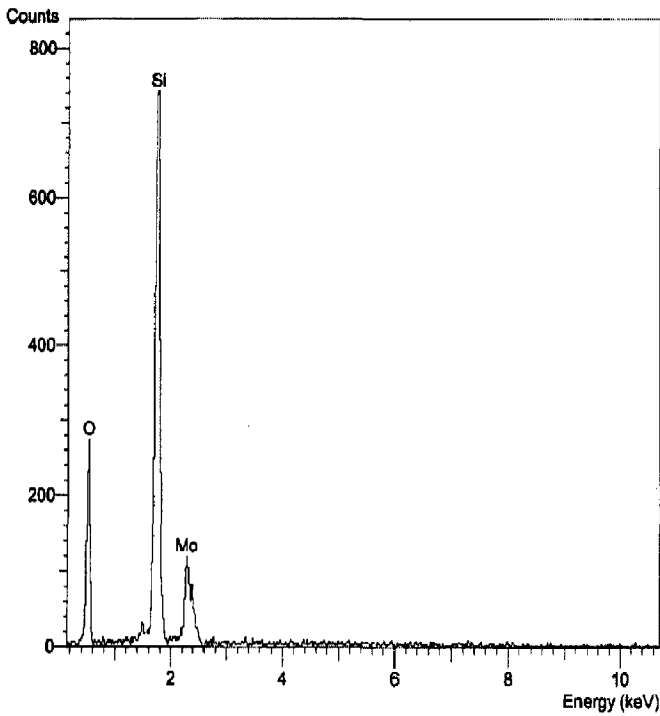
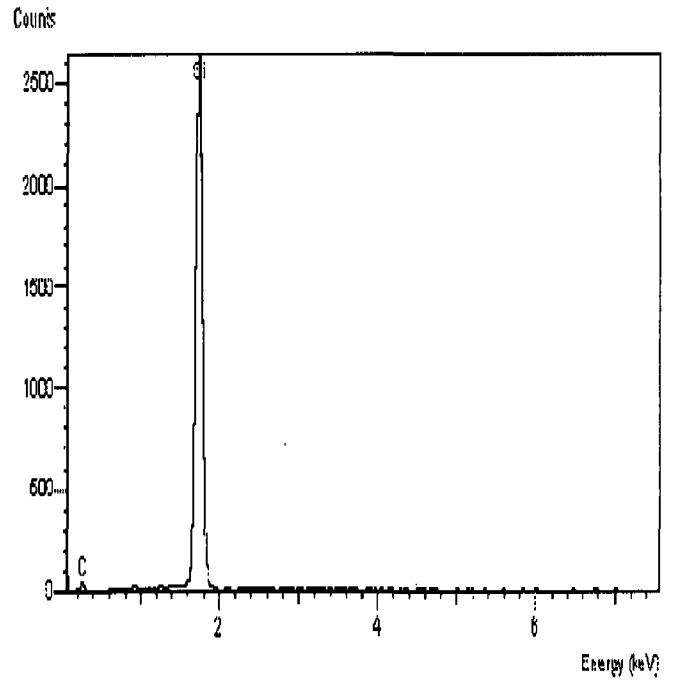
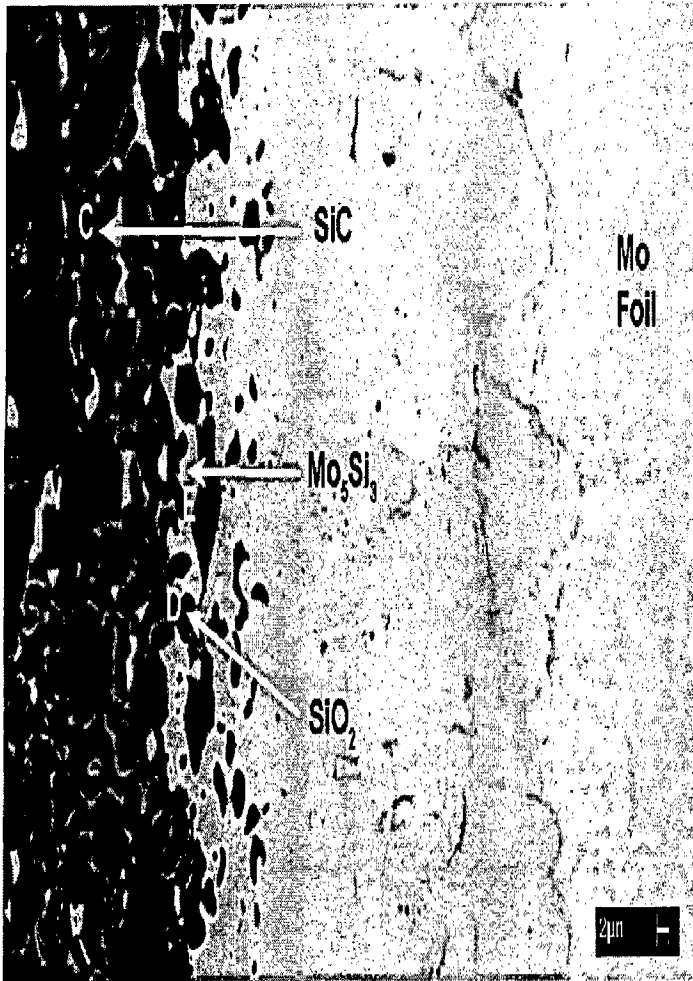


Fig. 5.59 SEM back scattered electron image of  $(\text{MoSi}_2 + 20 \text{ vol}\% \text{ SiC}_p) + \text{Mo}$  foil laminated composite with EDS analysis revealing SiC,  $\text{SiO}_2$  and  $\text{Mo}_5\text{Si}_3$  phases inside the matrix layer.



Table 5.15 Composition of the various phases identified in (MoSi<sub>2</sub> + 20 vol% SiC<sub>p</sub>) + Mo foil laminated composite as determined by energy dispersive spectroscopy (EDS). All compositions are given in atom percent.

Fig. No.	Location	Elements				Phase
		Mo	Si	C	O	
5.58	A	62.11	37.89	-	-	~ Mo <sub>5</sub> Si <sub>3</sub>
	B	68.42	-	31.58	-	~ Mo <sub>2</sub> C
5.59	C	-	49.32	50.68	-	~ SiC
	D	3.54	28.83		67.63	~ SiO <sub>2</sub>
	E	60.80	39.20	-	-	~ Mo <sub>5</sub> Si <sub>3</sub>

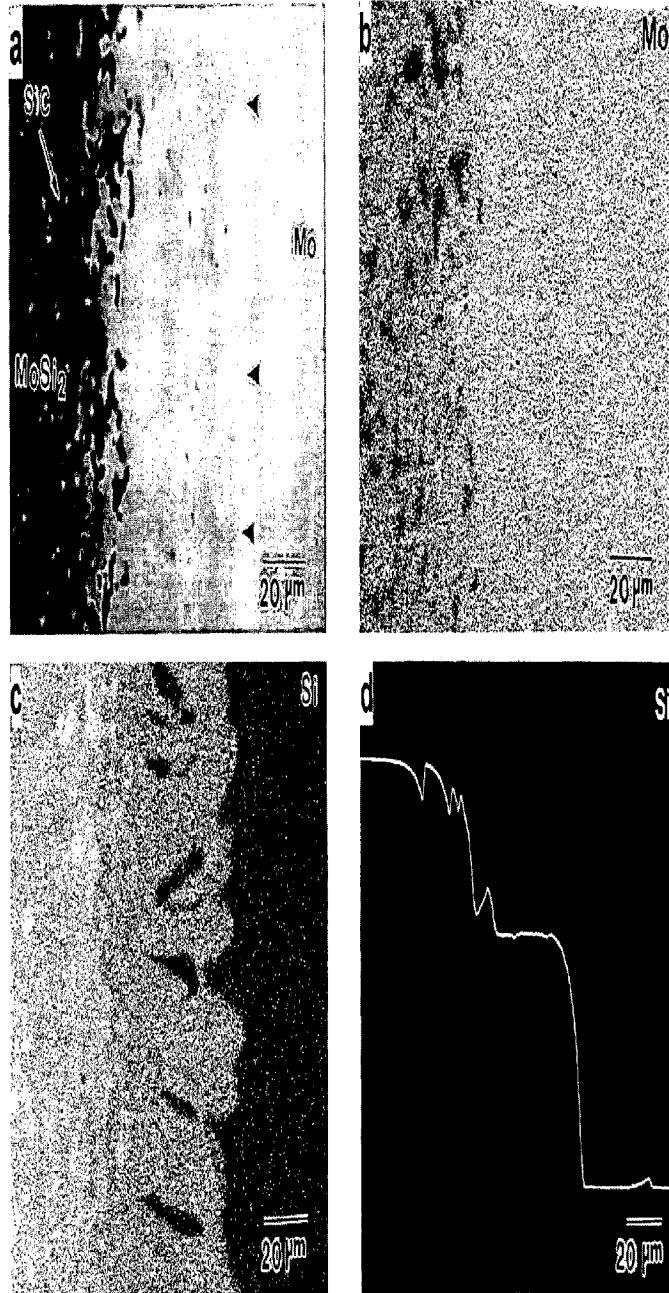


Fig. 5.60 EPMA images of  $(\text{MoSi}_2 + 20 \text{ vol\% SiC}_p) + \text{Mo}$  foil laminated composite (a) back scattered electron image (b) x-ray map of Mo (c) x-ray map of Si and (d) line scan of Si.

Figure 5.61 exhibits an EPMA back scattered electron image of (MoSi<sub>2</sub> + 20 vol% SiC<sub>p</sub>) + Mo foil composite in which the matrix area has been shaded dark to improve the contrast within the interfacial reaction layer revealing the different reaction products. Figure 5.62(a) is a high magnification back scattered electron image of the area enclosed by a rectangle in Fig. 5.61. Figures 5.62(b) and 5.62(c) are the x-ray maps of Si and carbon, respectively. The carbon rich region in Fig. 5.62(c) is completely Si free. This establishes the presence of Mo<sub>2</sub>C phase in between Mo<sub>5</sub>Si<sub>3</sub> and pure Mo phases.

#### 5.4.1.3 (MoSi<sub>2</sub> + 20 vol% SiC<sub>p</sub>) / Ta Foil Laminated Composite

Optical microstructures of (MoSi<sub>2</sub> + 20 vol% SiC<sub>p</sub>) + Ta foil laminated composite are presented in Fig. 5.63. Figure 5.63(a) exhibits the microstructure in as polished condition under ordinary light while the micrograph shown in Fig. 5.63(b) was taken using polarized light (optical etching). The microstructure in as polished condition reveals a uniform distribution of SiC particles and SiO<sub>2</sub> particles distributed as usual. Figure 5.63(b) taken under polarized light reveals the MoSi<sub>2</sub> grain size, which was found to be in the range of 5 – 8 μm. The interfacial reaction layer is indicated by the arrow marks.

The x-ray diffraction pattern of (MoSi<sub>2</sub> + 20 vol% SiC<sub>p</sub>) + Ta foil laminated composite is presented in Fig. 5.64, which exhibits the peaks of MoSi<sub>2</sub>, SiC and pure Ta. A few peaks of Ta<sub>5</sub>Si<sub>3</sub> and Ta<sub>2</sub>Si are also detected but most of the Ta<sub>5</sub>Si<sub>3</sub> and Ta<sub>2</sub>Si peaks were either too small or overlapped with the peaks of the other phases. The x-ray diffraction data suggested that the reaction products formed at the interface are Ta<sub>5</sub>Si<sub>3</sub> and Ta<sub>2</sub>Si due to Si diffusion across the interface.

The thickness of the interfacial reaction layer in (MoSi<sub>2</sub> + 20 vol% SiC<sub>p</sub>) + Ta foil laminated composite was found to be approximately 10 μm which is much smaller than the thickness of the reaction layer in (MoSi<sub>2</sub> + 20 vol% SiC<sub>p</sub>) + Mo foil laminated composite. This suggests that the diffusivity of Si in Ta and Ta<sub>5</sub>Si<sub>3</sub> layers is smaller than the diffusivity of Si in Mo and Mo<sub>5</sub>Si<sub>3</sub> layers.

Figure 5.65 shows the SEM back scattered electron image of (MoSi<sub>2</sub> + 20 vol% SiC<sub>p</sub>) + Ta foil laminated composite. The quantitative chemical analysis as

determined by energy dispersive spectroscopy (EDS) taken at two different locations within the reaction zone is presented in Table 5.16.

EDS analysis revealed the presence of  $Ta_5Si_3$  and  $Ta_2Si$  phases at the locations marked as A and B in Fig. 5.65. The back scattered electron image could not resolve  $Ta_5Si_3$  and  $Ta_2Si$  phases clearly owing to their similar average atomic numbers as described earlier. Apart from Si diffusion from  $MoSi_2$ , some Mo and Ta have also diffused across the interface. Mo dissolved in newly formed  $Ta_5Si_3$  phase forming  $(Ta, Mo)_5Si_3$  while Ta dissolved in  $Mo_5Si_3$  phase formed as a result of Si depletion within  $MoSi_2$  region.

The EPMA images of  $(MoSi_2 + 20 \text{ vol}\% SiC_p) + Ta$  foil laminated composite are shown in Fig. 5.66. Figure 5.66(a) is a back scattered electron image while Figs. 5.66(b) and 5.66(c) exhibit x-ray maps of Mo and Ta respectively. The x-ray map and the line scan of Si are shown in Figs. 5.66(d) and 5.66(e), respectively. The interfacial reaction zone was enriched with Si as well as Mo and Ta as exhibited by x-ray maps of these elements. This further established the interdiffusion of Mo and Ta across the interface. However, the x-ray mapping and the line scan of Si could not clearly resolve  $Ta_5Si_3$  and  $Ta_2Si$  phases separately. The interfacial reaction layer grows on both sides i.e., towards the Ta foil as well as towards  $MoSi_2$  layer. This is evidenced by the presence of  $SiO_2$  particles within the reaction zone adjacent to the  $MoSi_2$  layer as depicted in Fig. 5.67(a). Figure 5.67(a) is a high magnification EPMA back scattered electron image in which the  $MoSi_2$  matrix layer has been shaded dark to have a better contrast within the reaction layer. The x-ray maps of oxygen and Si presented in Figs. 5.67(b) and 5.67(c), respectively indicate that many of the particles present within the reaction zone close to  $MoSi_2$  layer are of  $SiO_2$ .

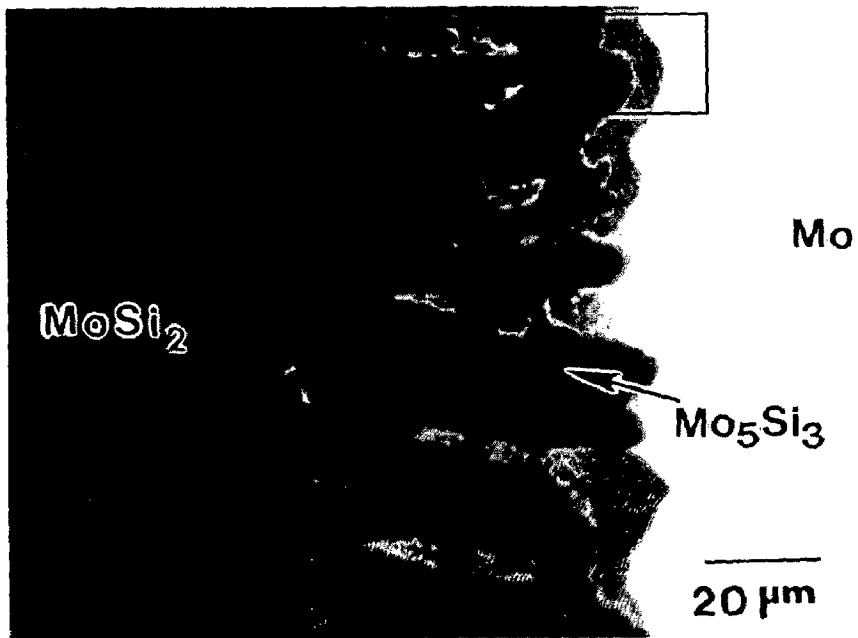


Fig. 5.61 EPMA back scattered electron image of  $(\text{MoSi}_2 + 20\ \text{vol}\% \text{SiC}_p) + \text{Mo}$  foil composite. The matrix area has been shaded dark to improve the contrast within the interfacial reaction layer revealing the different reaction products.

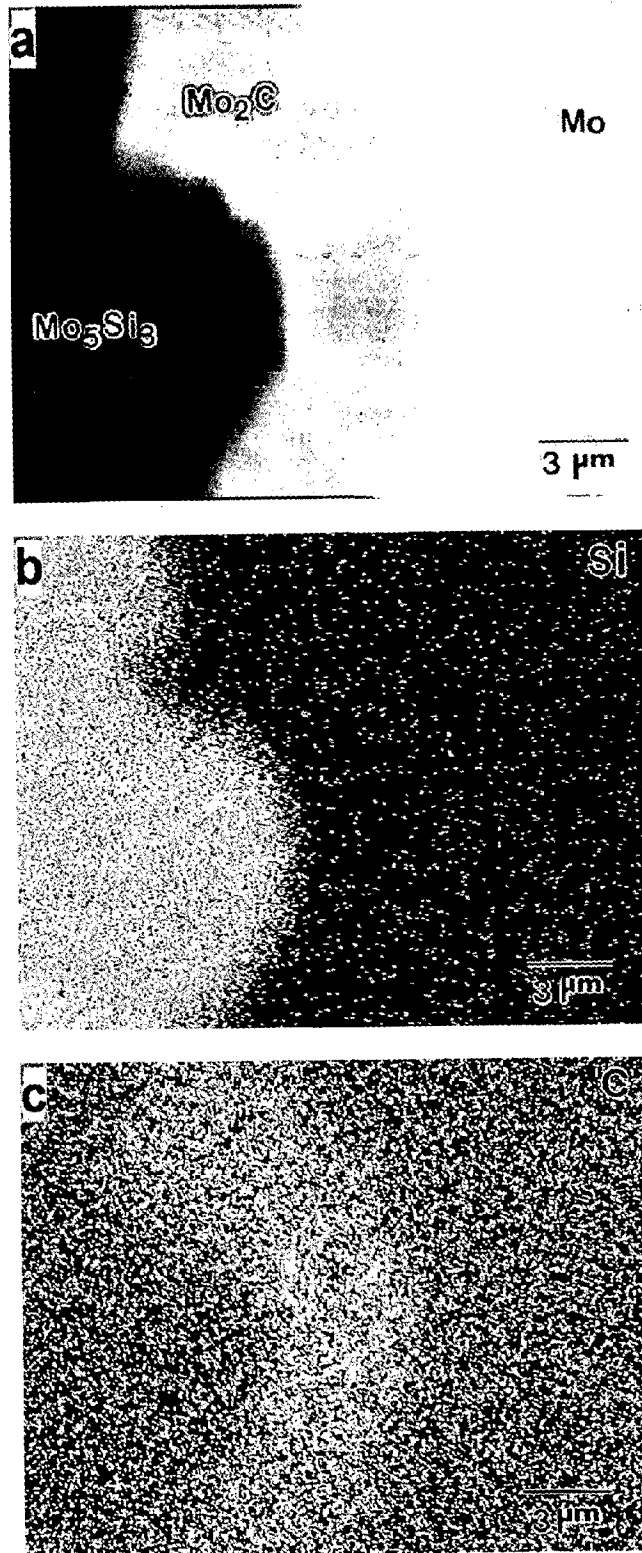
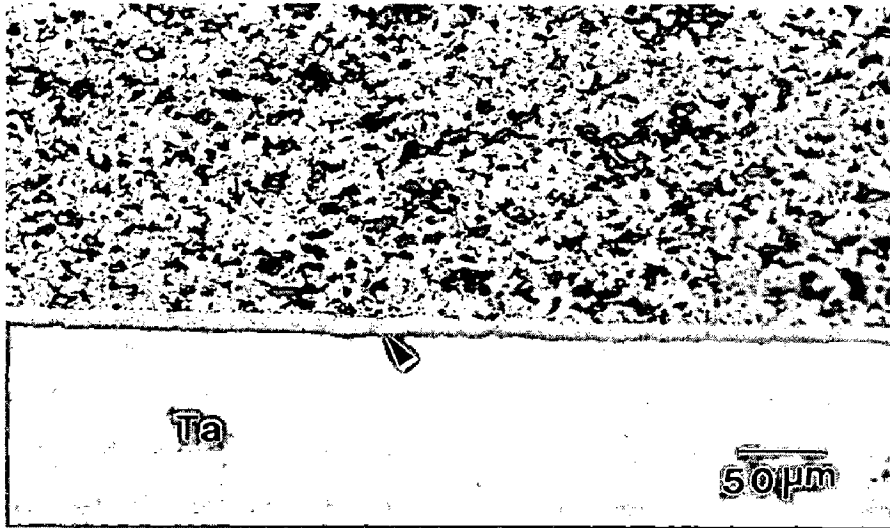
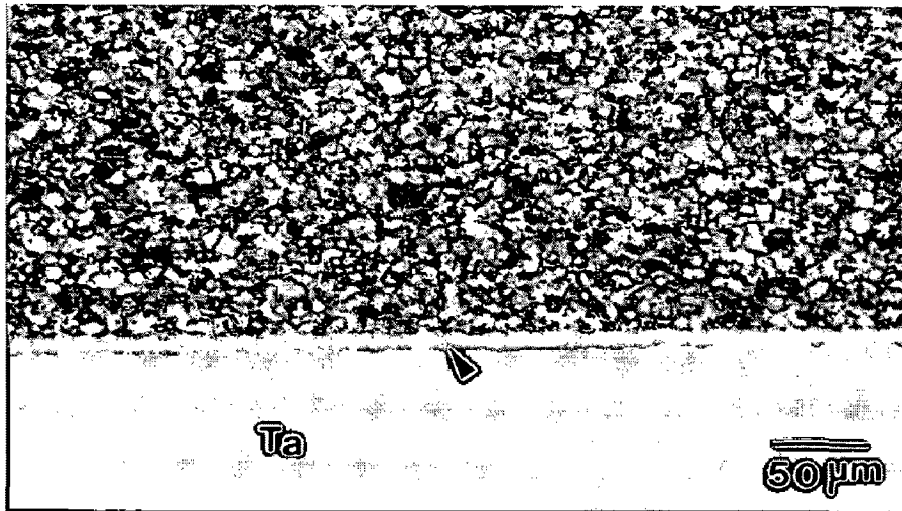


Fig. 5.62 High magnification EPMA images of the area surrounded by a rectangle in Fig. 5.61 (a) back scattered electron image (b) x-ray map of Si and (c) x-ray map of carbon.



(a)



(b)

Fig. 5.63

Optical microstructures of  $(\text{MoSi}_2 + 20 \text{ vol\% SiC}_p) + \text{Ta}$  foil laminated composite (a) micrograph in as polished condition and (b) micrograph after optical etching (using polarized light).

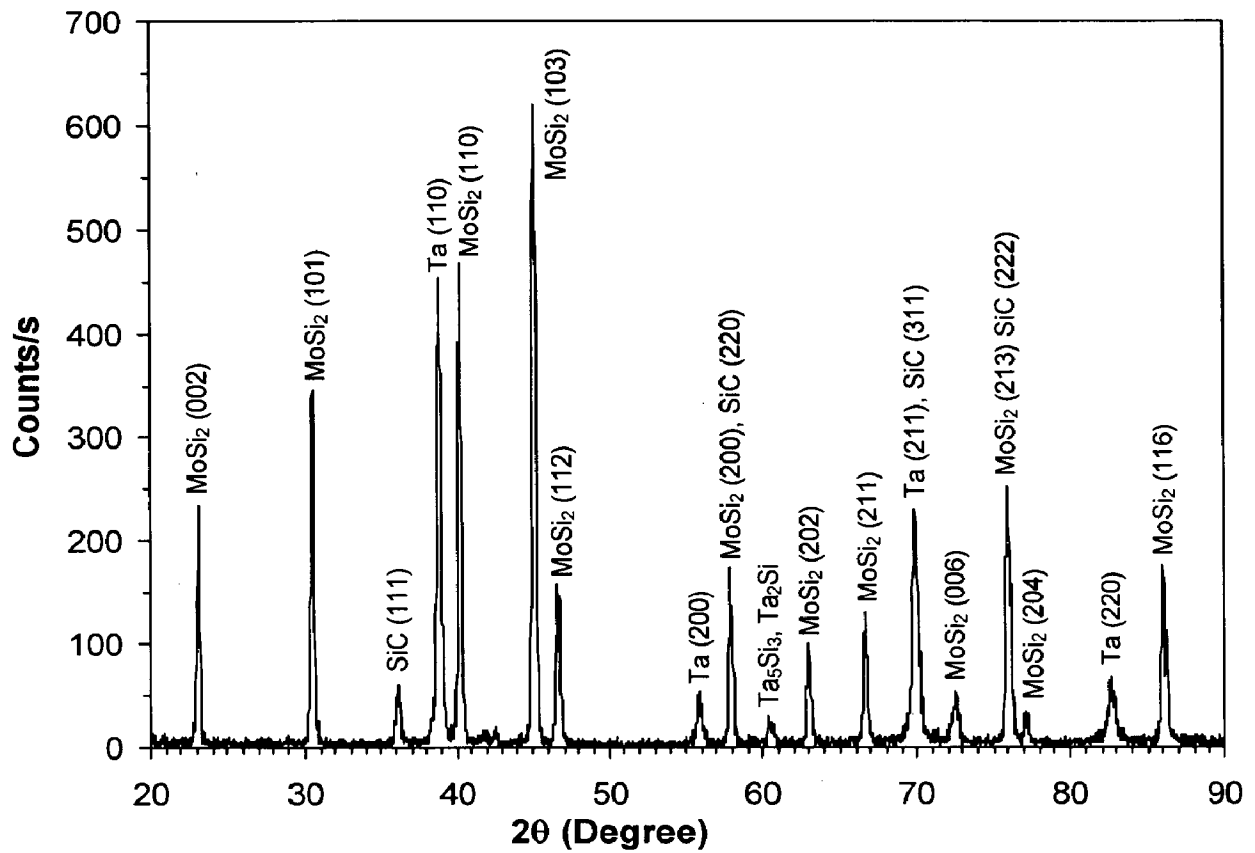


Fig. 5.64 X-ray diffraction pattern of (MoSi<sub>2</sub> + 20 vol% SiC<sub>p</sub>) + Ta foil laminated composite



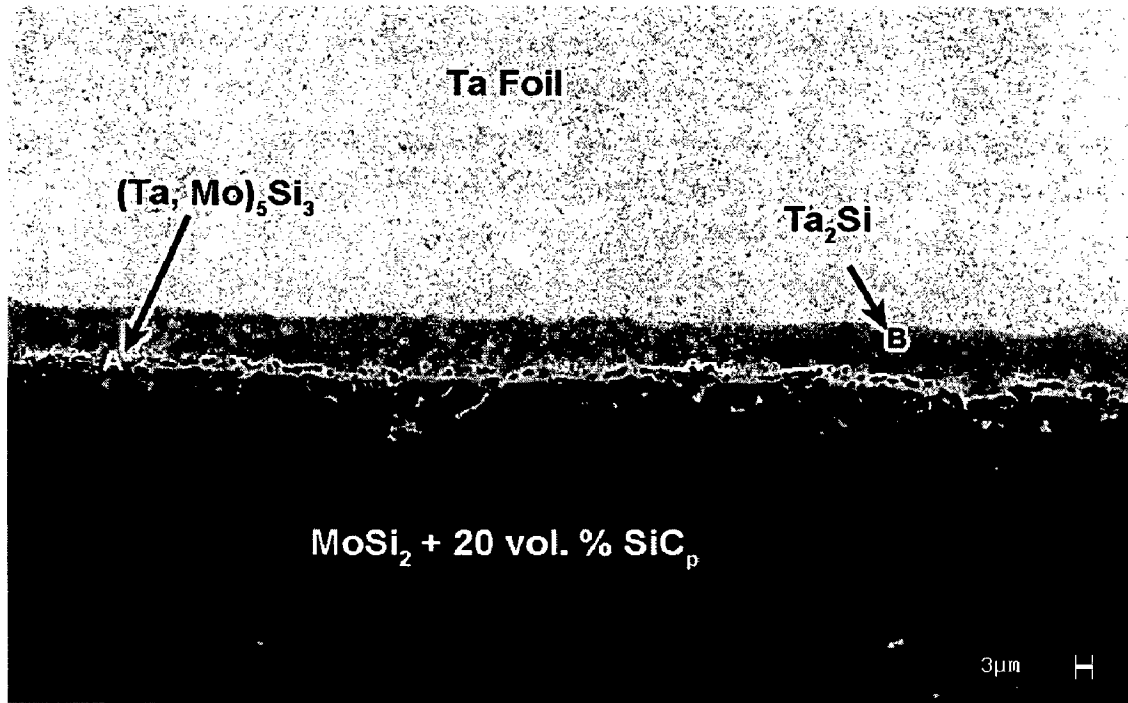


Fig. 5.65 SEM back scattered electron image of  $(\text{MoSi}_2 + 20 \text{ vol}\% \text{ SiC}_p) + \text{Ta}$  foil laminated composite. The locations at which EDS analysis was carried out within the interfacial reaction layer are shown by the arrow marks.

Table 5.16 Composition of the various phases identified in  $(\text{MoSi}_2 + 20 \text{ vol}\% \text{ SiC}_p) + \text{Ta}$  foil laminated composite as determined by energy dispersive spectroscopy (EDS). All compositions are given in atom percent.

Location	Elements			Phase
	Mo	Si	Ta	
A	17.98	38.40	43.62	$\sim (\text{Ta, Mo})_5\text{Si}_3$
B	-	32.26	67.74	$\sim \text{Ta}_2\text{Si}$

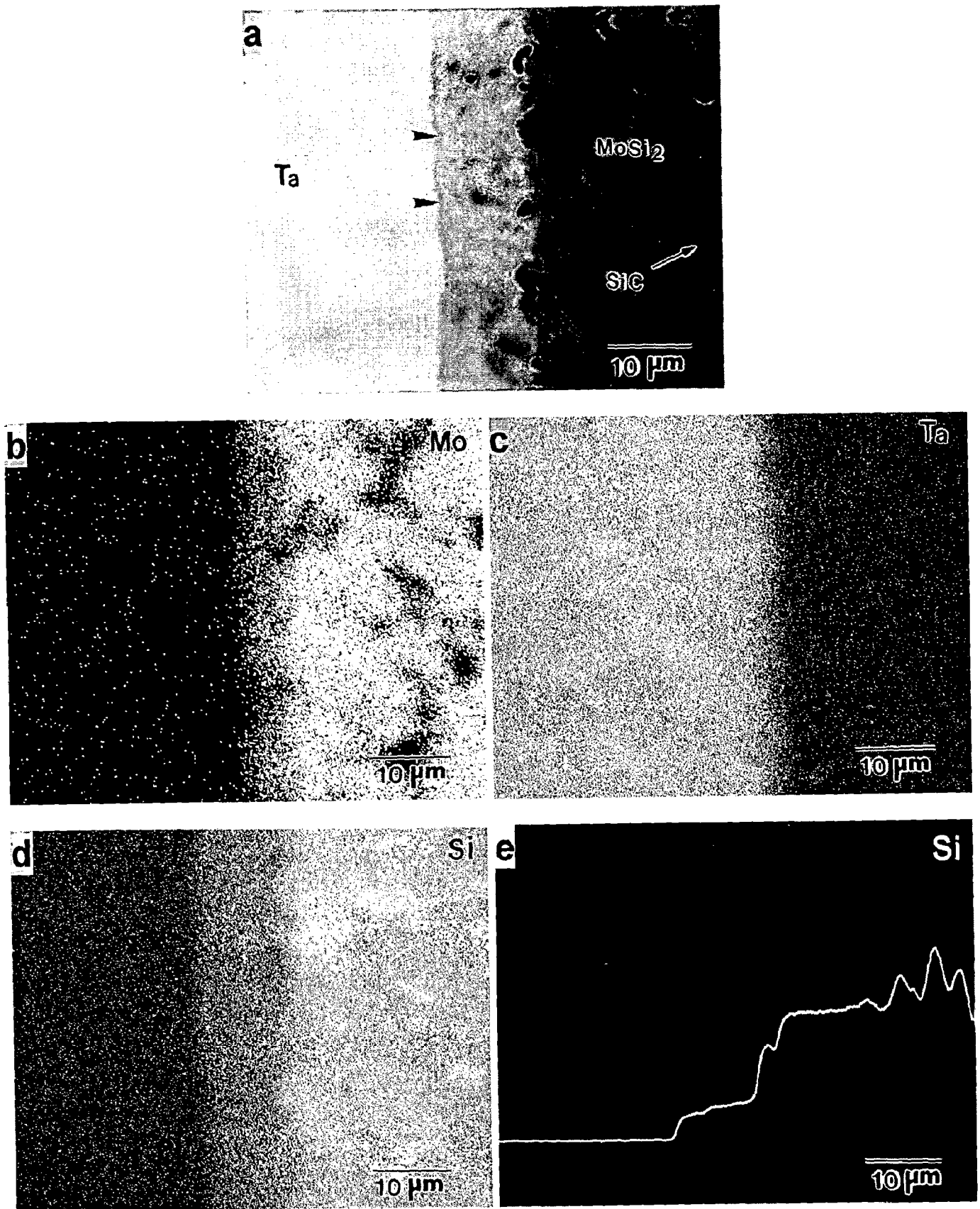


Fig. 5.66 EPMA images of  $(\text{MoSi}_2 + 20 \text{ vol\% SiC}_p) + \text{Ta}$  foil laminated composite (a) back scattered electron image (b) x-ray map of Mo (c) x-ray map of Ta (d) x-ray map of Si and (e) line scan of Si.

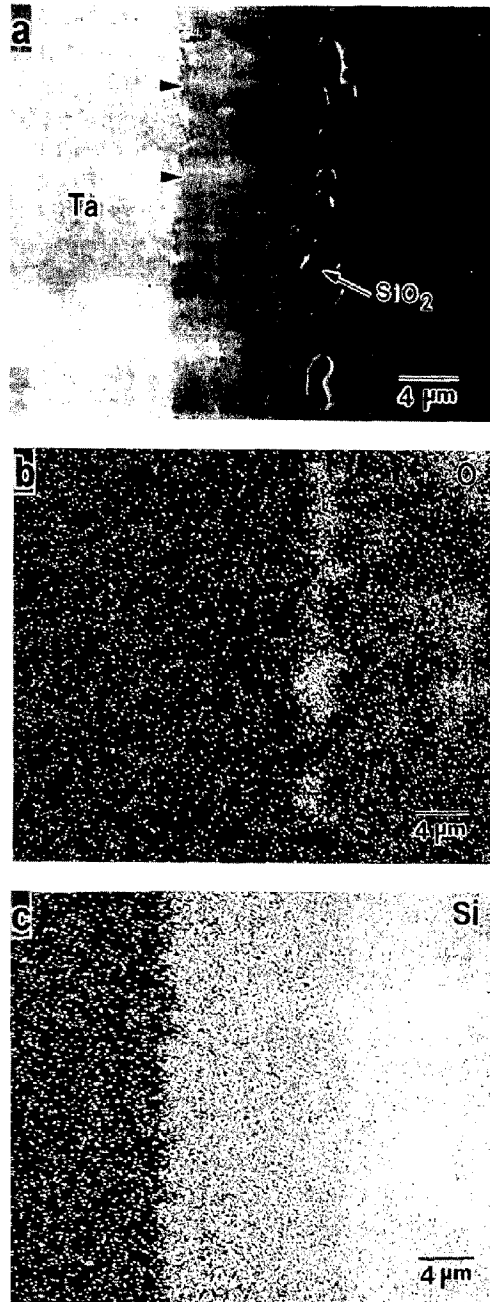


Fig. 5.67 EPMA images of  $(\text{MoSi}_2 + 20 \text{ vol}\% \text{ SiC}_p) + \text{Ta}$  foil composite revealing the presence of  $\text{SiO}_2$  particles (a) BSE image with matrix area shaded dark (b) x-ray map of oxygen and (c) x-ray map of Si.

#### 5.4.1.4 (MoSi<sub>2</sub> + 20 vol% SiC<sub>p</sub>) / Nb Foil Laminated Composite

Figure 5.68 exhibits optical microstructures of (MoSi<sub>2</sub> + 20 vol% SiC<sub>p</sub>) + Nb foil laminated composite in as polished condition using ordinary light as well as using polarized light. The SEM back scattered electron image and the x-ray diffraction pattern of (MoSi<sub>2</sub> + 20 vol% SiC<sub>p</sub>) + Nb foil composite are presented in Figs. 5.69 and 5.70, respectively. The optical as well as SEM microstructures exhibit more or less a uniform distribution of SiC particles. The average grain size of MoSi<sub>2</sub> was measured from the microstructure observed under polarized light and was found to be ~ 6 μm.

The optical microstructures reveal the presence of an interfacial reaction layer between MoSi<sub>2</sub> based matrix and Nb foil reinforcement as indicated by the arrow marks in Figs. 5.68(a) and 5.68(b). The reaction zone is more clearly visible in back scattered electron image (Fig. 5.69), the thickness of which was measured to be approximately 20 μm. The main reaction product between MoSi<sub>2</sub> and Nb is identified as Nb<sub>5</sub>Si<sub>3</sub> by quantitative electron probe micro analysis. The x-ray diffraction data as presented in Fig. 5.70 does not reveal any Nb<sub>5</sub>Si<sub>3</sub> peaks although the peaks of MoSi<sub>2</sub>, SiC and pure Nb are clearly identified. This could be due to only a small amount of Nb<sub>5</sub>Si<sub>3</sub> present in the microstructure, which was not enough to be detected by x-ray diffraction analysis.

Figure 5.71 is a combination of back scattered electron (BSE) image as well as x-ray elemental maps of Si, Mo and Nb for (MoSi<sub>2</sub> + 20 vol% SiC<sub>p</sub>) + Nb foil composite. X-ray images are used to display qualitative x-ray information from a single element as a concentration map. Areas of high concentration appear bright in the map. BSE image (Fig. 5.71(a)) exhibits an approximately 20 μm thick reaction zone between matrix and the Nb foil. Nb and MoSi<sub>2</sub> reacted extensively during the processing, forming a new intermetallic compound at the interface. The quantitative analysis of chemical composition of the reaction products by EPMA is presented in Table 5.17. The typical microprobe data obtained at locations indicated by A, B, C and D in Fig. 5.71(a) correspond to MoSi<sub>2</sub>, Mo<sub>5</sub>Si<sub>3</sub> (with Nb in solid solution), Nb<sub>5</sub>Si<sub>3</sub> (with Mo in solid solution) and pure Nb phases, respectively.

The relatively large and irregular shaped dark particles present in MoSi<sub>2</sub> are of SiC while smaller and rounded dark particles are of free SiO<sub>2</sub>. The SiC and SiO<sub>2</sub>

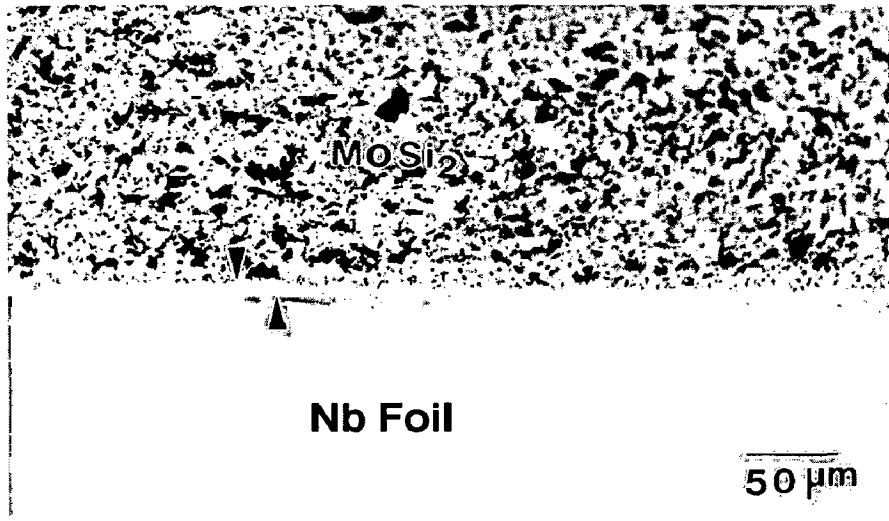
particles are present inside the reaction zone close to the  $\text{MoSi}_2$ . This suggests that the interfacial reaction layer has grown inside both  $\text{MoSi}_2$  based matrix and the Nb foil. The block arrow indicates the probable original interface between  $\text{MoSi}_2$  based matrix and the Nb foil prior to any chemical interaction. The reaction layer towards the Nb foil is much thicker than that towards the matrix.

X-ray maps of Si, Mo and Nb as shown in Figs. 5.71(b), 5.71(c) and 5.71(d) respectively, reveal extensive diffusion of Si into Nb has taken place as compared to the diffusion of Mo and Nb across the interface. Si diffused far deeper into the Nb foil than Mo. Diffusivity of Si is expected to be higher than diffusivity of Nb owing to its lower melting point and a lower atomic size as compared to Nb. Faster Si diffusion than Nb diffusing in the opposite direction may introduce Kirkendall porosity on the  $\text{MoSi}_2$  side as a result of vacant sites left behind by Si. But non-stoichiometry is not possible in  $\text{MoSi}_2$ . The depletion of Si is compensated by some amount of  $\text{MoSi}_2$  converting into  $\text{Mo}_5\text{Si}_3$ . Therefore, Kirkendall porosity is not likely to be present in these composites.

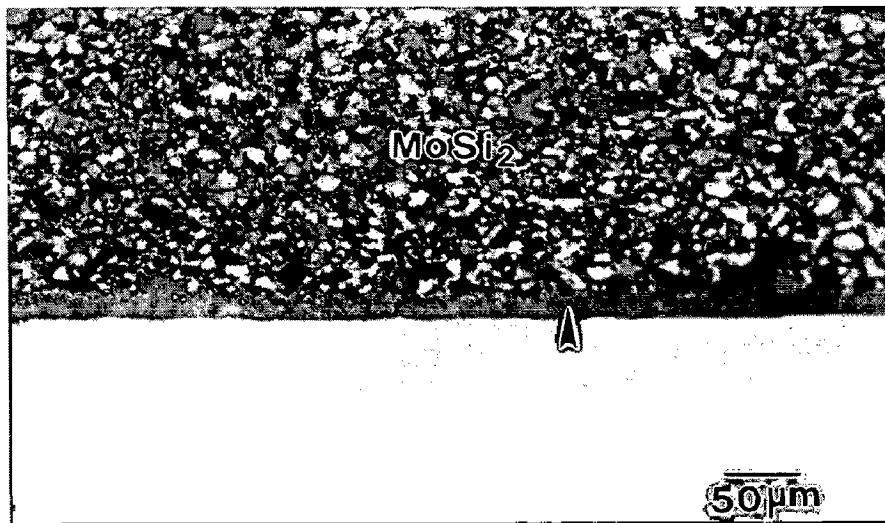
The line scans of Mo and Nb are shown in Figs. 5.72(b) and 5.72(c), respectively in combination with a BSE image taken at a higher magnification and shaded dark to reveal the  $\text{SiO}_2$  particles at the interface (Fig. 5.72(a)). Both the line scans indicated the presence of concentration gradients for Mo and Nb within the reaction zone. The troughs observed in line scan of Mo indicate the scan passing through the SiC particles present inside  $\text{MoSi}_2$ .

Table 5.17 Electron probe micro analysis (EPMA) of the interface between  $\text{MoSi}_2$  + 20 vol%  $\text{SiC}_p$  matrix and Nb foil laminated composite (Fig. 5.71(a)). All compositions are given in atom percent.

Region	Mo	Si	Nb	Phase
A	34.368	65.632	0.000	~ $\text{MoSi}_2$
B	57.401	38.400	4.199	~ $(\text{Mo, Nb})_5\text{Si}_3$
C	1.351	39.137	59.512	~ $(\text{Nb, Mo})_5\text{Si}_3$
D	0.000	0.314	99.686	~ Nb



(a)



(b)

Fig. 5.68

Optical microstructures of (MoSi<sub>2</sub> + 20 vol% SiC<sub>p</sub>) + Nb foil laminated composite (a) micrograph in as polished condition using ordinary light and (b) micrograph using polarized light.

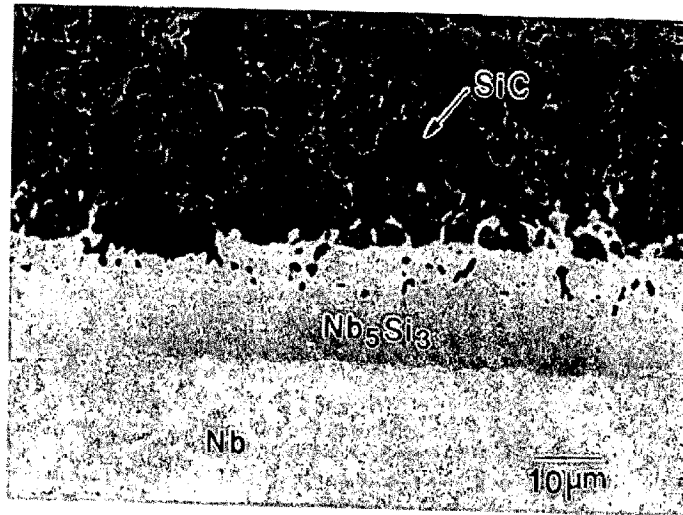


Fig. 5.69 SEM back scattered electron image of  $(\text{MoSi}_2 + 20 \text{ vol\% SiC}_p) + \text{Nb}$  foil laminated composite

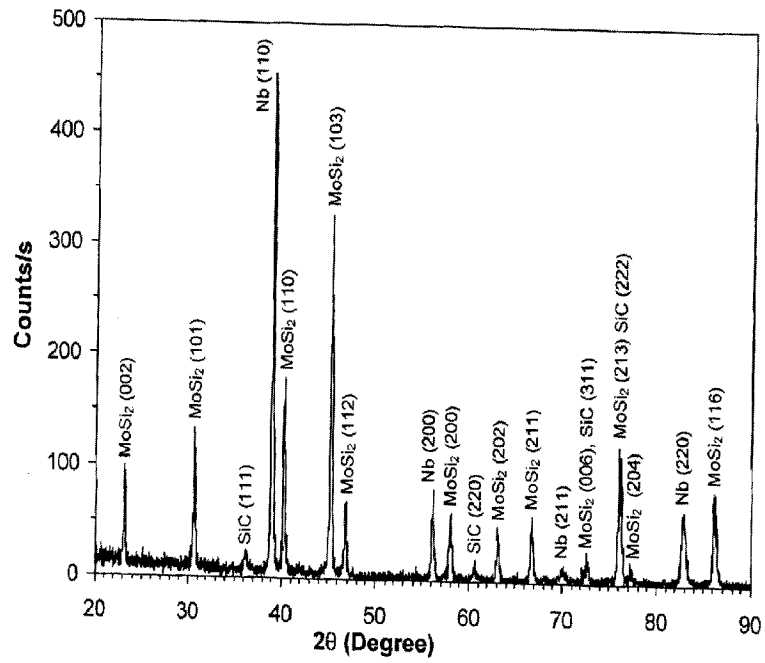


Fig. 5.70 X-ray diffraction pattern of  $(\text{MoSi}_2 + 20 \text{ vol\% SiC}_p) + \text{Nb}$  foil laminated composite.

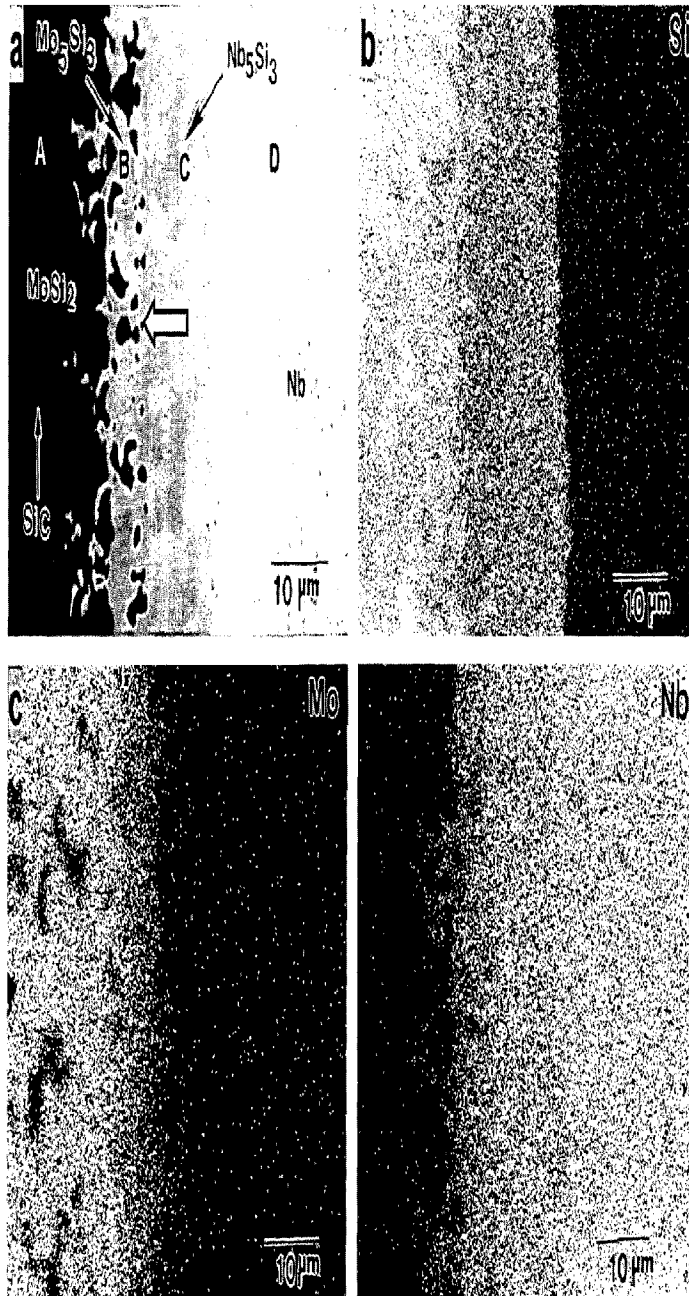


Fig. 5.71 EPMA images of  $(\text{MoSi}_2 + 20 \text{ vol}\% \text{ SiC}_p) + \text{Nb}$  foil laminated composite (a) back scattered electron image (b) x-ray map of Si (c) x-ray map of Mo and (d) x-ray map Nb.



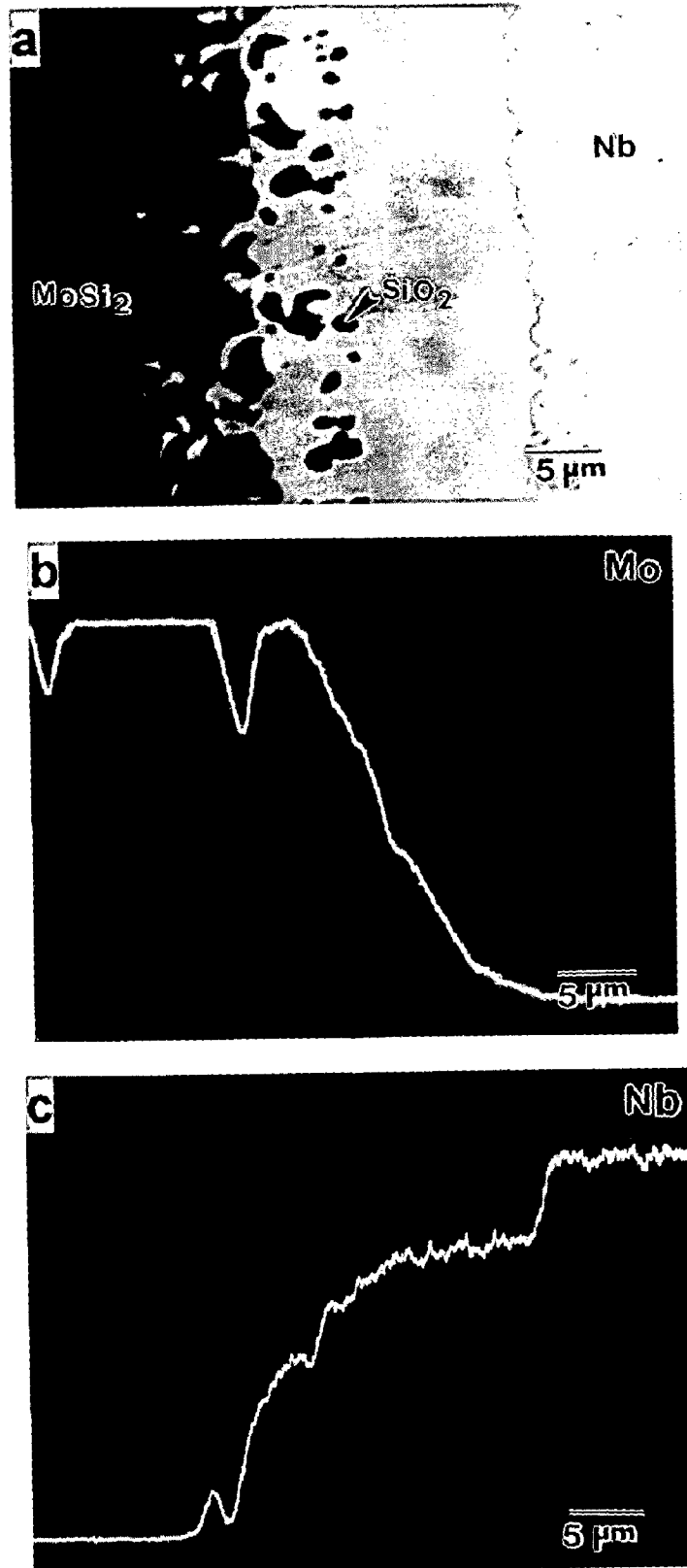


Fig. 5.72 EPMA images of  $(\text{MoSi}_2 + 20 \text{ vol}\% \text{ SiC}_p) + \text{Nb}$  foil composite (a) BSE image with matrix area shaded dark revealing the  $\text{SiO}_2$  particles present at the interface (b) x-ray map of Mo and (c) x-ray map of Nb.

## 5.4.2 Evaluation of Mechanical Properties

The room temperature mechanical properties of  $\text{MoSi}_2 + 20 \text{ vol}\% \text{ SiC}_p$  monolithic,  $(\text{MoSi}_2 + 20 \text{ vol}\% \text{ SiC}_p) + \text{Mo}$  foil,  $(\text{MoSi}_2 + 20 \text{ vol}\% \text{ SiC}_p) + \text{Ta}$  foil and  $(\text{MoSi}_2 + 20 \text{ vol}\% \text{ SiC}_p) + \text{Nb}$  foil laminated composites are presented in Tables 5.18 and 5.19. Each data point in Tables 5.18 and 5.19 is an average of 4 to 5 tests.

### 5.4.2.1 Elastic Modulus

The elastic modulus of  $\text{MoSi}_2 + 20 \text{ vol}\% \text{ SiC}_p$  monolithic material was measured as 438 GPa as against an elastic modulus value of 440 GPa of pure  $\text{MoSi}_2$ . The addition of SiC particles into  $\text{MoSi}_2$  matrix does not alter the modulus of  $\text{MoSi}_2$  as both the materials have almost similar elastic moduli (Table 4.2). The modulus values of the laminated composites with Mo, Ta and Nb foils as measured in a direction perpendicular to the foil plane are found to be lower than the modulus of  $\text{MoSi}_2 + 20 \text{ vol}\% \text{ SiC}_p$  monolithic material used as a matrix layer in the laminated composites. However, in case of Mo and Ta foil laminated composites, the use of  $\text{MoSi}_2 + 20 \text{ vol}\% \text{ SiC}_p$  as the matrix material resulted in higher values of elastic modulus as compared to the  $\text{MoSi}_2 + 2 \text{ wt}\% \text{ Al}$  as the matrix. The modulus value of Nb foil reinforced laminated composite was found to be lower than the modulus of Mo and Ta foil reinforced laminated composites. This could be attributed to a lower elastic modulus of Nb as the elastic properties of a composite material depend on the elastic properties of the constituent materials. Nb possesses an elastic modulus of 103 GPa as compared to the elastic moduli of Mo (324 GPa) and Ta (186 GPa).

### 5.4.2.2 Hardness

The hardness was measured in  $\text{MoSi}_2 + 20 \text{ vol}\% \text{ SiC}_p$  matrix and the ductile metal foils, separately. Figure 5.73 exhibits typical hardness indentation marks in  $\text{MoSi}_2 + 20 \text{ vol}\% \text{ SiC}_p$  monolithic material and in the matrix layer as well as inside the Ta foil in  $(\text{MoSi}_2 + 20 \text{ vol}\% \text{ SiC}_p) + \text{Ta}$  foil laminated composite. The hardness values obtained for monolithic material as well as taken inside the matrix of all the three laminated composites are similar but found to be much higher than the reported value for monolithic  $\text{MoSi}_2$  (9 - 10 GPa) as well as the value calculated from rule of mixture for  $\text{MoSi}_2 + 20 \text{ vol}\% \text{ SiC}_p$  particulate composite (13.2 GPa). The increase in hardness as compared to pure  $\text{MoSi}_2$  is due to the addition of very fine and uniformly distributed

SiC particles in MoSi<sub>2</sub>. SiC is much harder than MoSi<sub>2</sub>. The hardness value of SiC is reported to be ~ 25 GPa (Bhattacharya and Petrovic, 1991). Addition of 20 vol% SiC particles also led to considerable inhibition to grain growth in MoSi<sub>2</sub> matrix during hot pressing, and a much finer grain size was obtained as compared to pure MoSi<sub>2</sub>. Finer grain size and presence of SiC reinforcements led to much higher hardness in the composites.

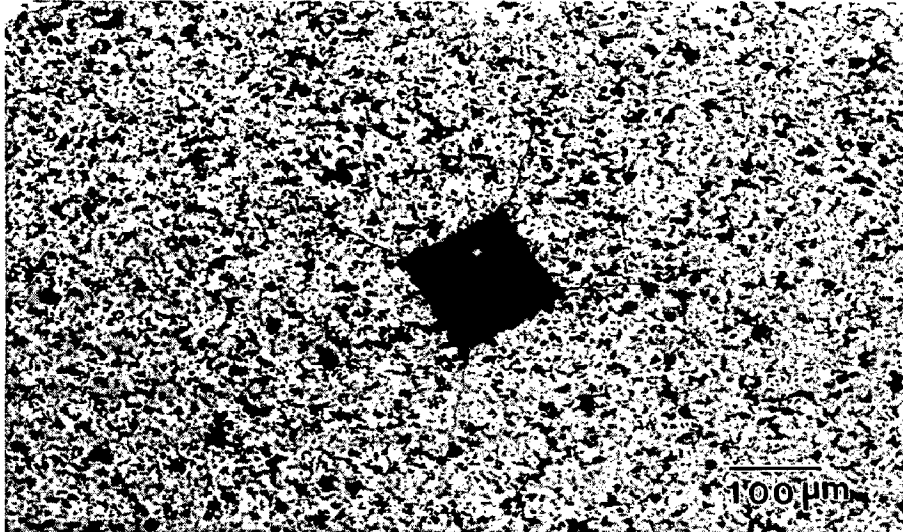
The hardness values of Mo, Ta and Nb foils measured inside the laminated composites are different as compared to the hardness values measured on the as received foils. The hardness of Mo foil has decreased considerably while there was a slight increase in the hardness of Ta and Nb foils after the processing. This probably can be attributed to the two competitive processes that occur during hot pressing, i.e., (i) grain growth and (ii) solid solution strengthening as a result of Si diffusion from MoSi<sub>2</sub> matrix. The change in hardness of the foils after the processing at high temperatures (as compared to the as received condition) is due to the net effect of these two processes. As the Mo foil used was in work-hardened condition, the effect of annealing and grain growth during the high temperature processing was probably more pronounced than solid solution hardening. Apart from Si diffusion from MoSi<sub>2</sub>, oxygen pick-up and contamination from interstitial impurities such as carbon, H<sub>2</sub> and N<sub>2</sub> during processing could well influence the hardness and ductility of the refractory metal foils. The change in hardness of the processed refractory metal foils could also be due to the compressive residual stresses developed in the metal foils after cooling from the high processing temperatures. This shows that the intrinsic mechanical properties of the metal foils in the composites could be different from those of the as received metal foils. Such change imposes difficulty on the prediction and modelling of the composite properties.

Table 5.18 Mechanical properties of  $(\text{MoSi}_2 + 20 \text{ vol\% SiC}_p)$  + Mo, Ta and Nb foil laminated composites.

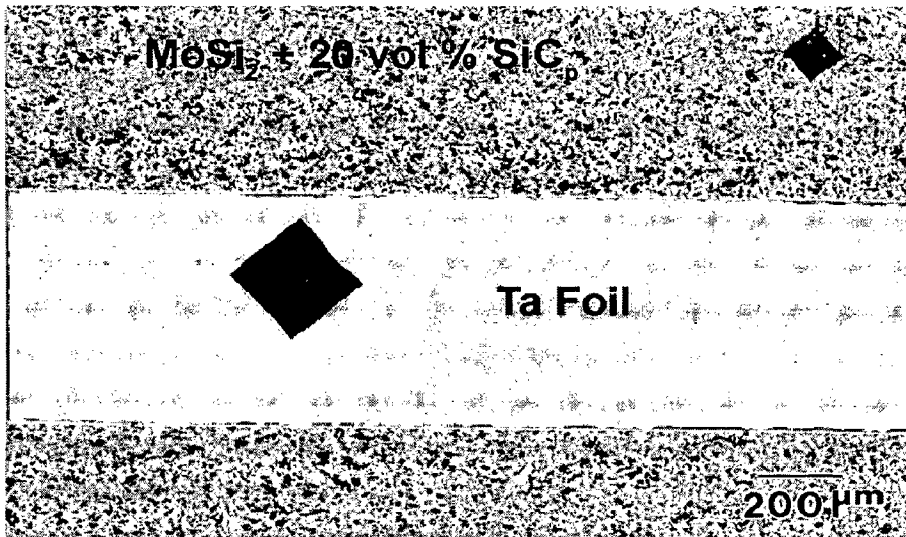
Composite	Elastic Modulus (GPa)	Matrix Hardness (GPa)	Foil Hardness (VHN)	Matrix Indentation Fracture Toughness, $K_{IC}$ ( $\text{MPa}\sqrt{\text{m}}$ )
$(\text{MoSi}_2 + 20 \text{ vol\% SiC}_p)$ Monolithic	438	16.5		5.4
$(\text{MoSi}_2 + 20 \text{ vol\% SiC}_p)$ + Mo Foil	394	15.8	218	5.0
$(\text{MoSi}_2 + 20 \text{ vol\% SiC}_p)$ + Ta Foil	358	16.1	179	5.2
$(\text{MoSi}_2 + 20 \text{ vol\% SiC}_p)$ + Nb Foil	328	16.40	137	5.3

Table 5.19 Mechanical properties of (MoSi<sub>2</sub> + 20 vol% SiC<sub>p</sub>) + Mo Ta and Nb foil laminated composites.

Composite	Flexural Strength (MPa)		Fracture Toughness, K <sub>max</sub> (MPa√m)		Work of Fracture (J/m <sup>2</sup> )	
	Crack Arrestor	Crack Divider	Crack Arrestor	Crack Divider	Crack Arrestor	Crack Divider
	Mode	Mode	Mode	Mode	Mode	Mode
(MoSi <sub>2</sub> + 20 vol% SiC <sub>p</sub> ) Monolithic	290		5.2			
(MoSi <sub>2</sub> + 20 vol% SiC <sub>p</sub> ) + Mo Foil	349	303	15.7	6.2	9,570	1,611
(MoSi <sub>2</sub> + 20 vol% SiC <sub>p</sub> ) + Ta Foil	436	396	20.5	9.9	25,920	7,420
(MoSi <sub>2</sub> + 20 vol% SiC <sub>p</sub> ) + Nb Foil	398	347	17.1	7.8	17,280	4,273



(a)



(b)

Fig. 5.73

Optical micrographs showing typical hardness indentation marks in (a)  $\text{MoSi}_2 + 20 \text{ vol}\% \text{ SiC}_p$  monolithic material and (b)  $(\text{MoSi}_2 + 20 \text{ vol}\% \text{ SiC}_p) + \text{Ta foil}$  laminated composite.

### 5.4.2.3 Indentation Fracture Toughness

The indentation fracture toughness of the  $\text{MoSi}_2 + 20 \text{ vol\% SiC}_p$  particulate composite used as a matrix layer in the laminated composites was measured from the slope of the plot between indentation load ( $P$ ) and crack length ( $c^{3/2}$ ). A typical  $P$  vs.  $c^{3/2}$  graph is presented in Fig. 5.74. The plot obtained was linear and passed through the origin indicating that the hardness of  $\text{MoSi}_2 + 20 \text{ vol\% SiC}_p$  was load independent. Only median cracks were found in monolithic as well in the matrix layer of the laminated composites. Crack lengths were measured using ordinary light optical microscopy. The indentation fracture toughness values measured inside the matrix layers were similar in all the laminated composites having  $\text{MoSi}_2 + 20 \text{ vol\% SiC}_p$  as the matrix. The calculated indentation fracture toughness values were in the range of 5.0 to 5.4  $\text{MPa}\sqrt{\text{m}}$ . Slight variation in laminated composites with Mo, Ta and Nb foils may be attributed to the different levels of residual thermal stresses present in the composites made with different refractory metal foils.

### 5.4.2.4 Crack Interactions with SiC Particles

Localized toughening mechanisms, such as crack deflection, crack microbridging, crack branching and particle fracture can be seen on a large scale, while examining the indentation crack paths in microstructures observed under SEM. Figures 5.75(a) and 5.75(b) are the SEM back scattered electron images of  $\text{MoSi}_2 + 20 \text{ vol\% SiC}_p$  showing the crack interactions with SiC particles. The propagation of the main crack is accompanied by additional cracking in the brittle matrix. The arrowheads (pointing downwards) exhibit the crack deflection by SiC particles. Crack deflection can be observed normally at interfaces between  $\text{MoSi}_2$  and SiC particles. As the main propagating crack encounters a SiC particle, it gets deflected and propagates along the  $\text{MoSi}_2$ - $\text{SiC}_p$  interface and further propagates in  $\text{MoSi}_2$ . Crack deflection results in crack path tortuosity. The large residual thermal stresses present in  $\text{MoSi}_2$ , are likely to produce dislocations and plastic deformation in  $\text{MoSi}_2$  matrix in the vicinity of the SiC particles, at high temperatures when  $\text{MoSi}_2$  can deform plastically (Mitra et al, 1997<sup>a</sup>). This network of dislocations around the particles may be responsible for creating extra resistance to the approaching crack front and deflecting it to paths of lower energy.

Some evidence of SiC particle fracture was also observed as indicated by an inclined arrowhead in Fig. 5.75(b). It is believed that highly irregular shaped SiC

particles having sharp edges located on the way of a propagating crack may undergo fracture. The advancing crack cuts through the elongated and sharp edges of SiC particles.

#### 5.4.2.5 Crack Interactions with Ductile Metal Foils

Figure 5.76(a) is an optical micrograph of  $(\text{MoSi}_2 + 20 \text{ vol}\% \text{ SiC}_p) + \text{Mo}$  foil laminated composite showing a typical hardness indentation mark in  $\text{MoSi}_2$  matrix taken near the interface at 20 kg load. The interfacial reaction layer between  $\text{MoSi}_2$  and Mo foil is depicted by arrow marks. The indentation cracks originating from the corners of the hardness indentation and their interaction with the Mo foil is revealed in Fig. 5.76(b), which was taken at a higher magnification. The indentation crack does not pass through the entire thickness of the reaction layer ending inside the reaction layer itself as shown by an arrowhead in Fig. 5.76(b). The crack propagation probably is arrested at  $\text{Mo}_5\text{Si}_3 / \text{Mo}_2\text{C}$  interface. The reaction zone consists of two different reaction products, which seem to have considerably different mechanical nature. Figure 5.77 exhibits the hardness indentation mark taken close to the interface and the crack paths in  $(\text{MoSi}_2 + 20 \text{ vol}\% \text{ SiC}_p) + \text{Ta}$  foil laminated composite at different magnifications. The indentation crack passes through the interfacial reaction layer but is arrested as soon as it impinges upon the ductile Ta foil. Microstructures showing indentation crack - Nb foil interactions in Nb foil reinforced laminated composite are shown in Fig. 5.78. Figure 5.78(a) is an optical micrograph showing indentation crack paths originating from a hardness indentation taken inside the  $\text{MoSi}_2\text{-SiC}_p$  matrix close to the interface. Vertical arrow marks have been used for easy identification of the interface between matrix and the Nb foil in Fig. 5.78(a). Figure 5.78(b) is a SEM back-scattered electron image of the area enclosed by a rectangle in Fig. 5.78(a) taken at higher magnification. The high magnification SEM image clearly reveals that the indentation cracks pass through the  $\text{Nb}_5\text{Si}_3$  interfacial reaction layer but are stopped at the  $\text{Nb}_5\text{Si}_3 / \text{Nb}$  foil interface as depicted by arrow heads. This suggests that the  $\text{Nb}_5\text{Si}_3$  interface is brittle offering no resistance to crack propagation. No interfacial debonding at the  $\text{Nb}_5\text{Si}_3 / \text{Nb}$  interface is observed. The cracks impinging on Nb foil are arrested at the interface without causing interfacial debonding. These observations of crack interactions with refractory metal foils clearly demonstrate that the ductile metal foils could effectively blunt a propagating crack in laminated composites with a brittle matrix.



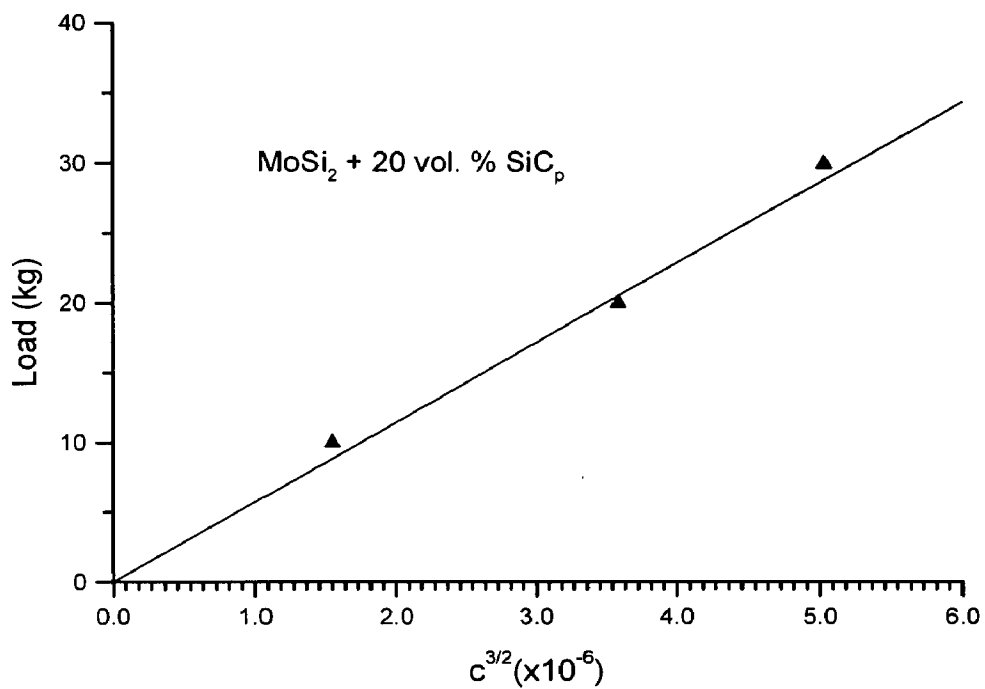


Fig. 5.74 A typical indentation load ( $P$ ) vs. crack length ( $c^{3/2}$ ) graph as obtained in the case of MoSi<sub>2</sub> + 20 vol% SiC<sub>p</sub> matrix. The indentation fracture toughness was estimated from the slope of the linear plot of  $P$  vs.  $c^{3/2}$ .

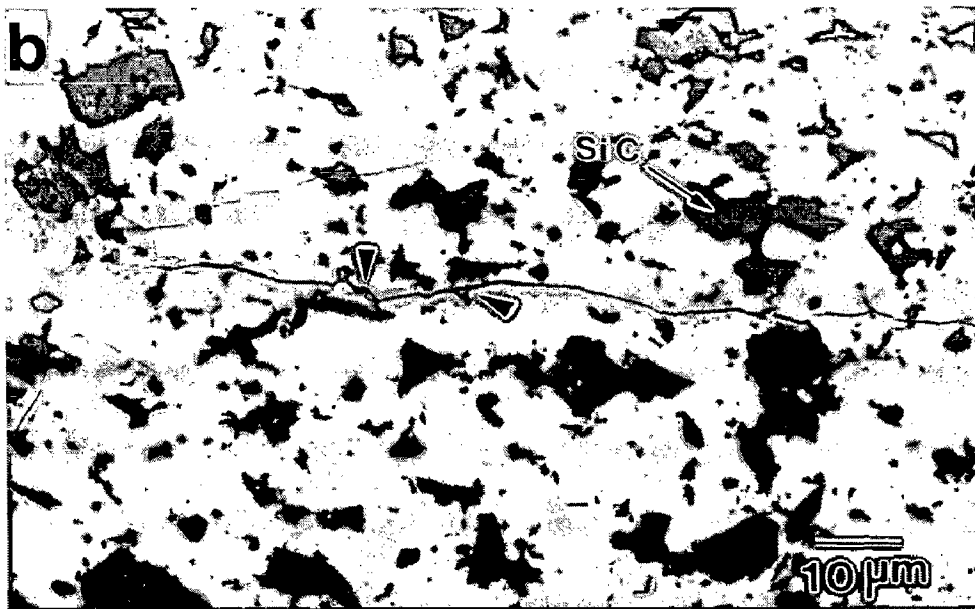
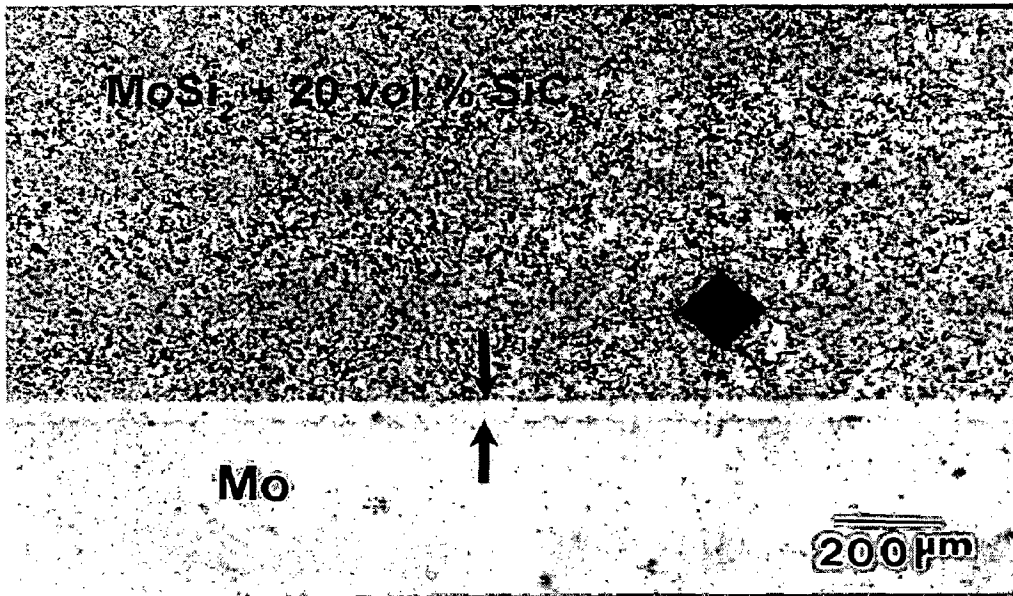
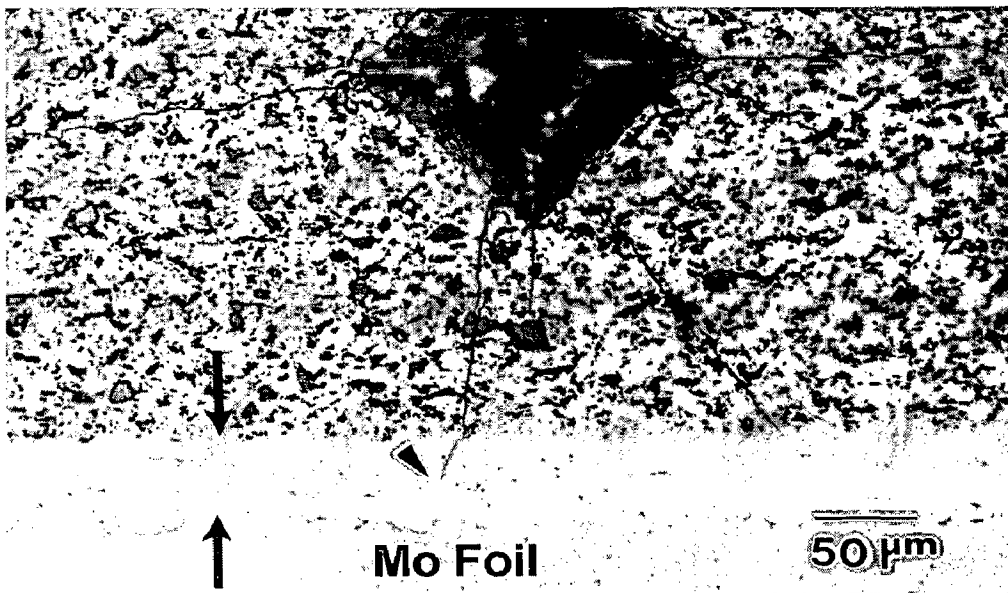


Fig. 5.75

SEM back scattered electron images of  $\text{MoSi}_2 + 20 \text{ vol\% SiC}_p$  monolithic material showing the indentation crack interactions with SiC particles.

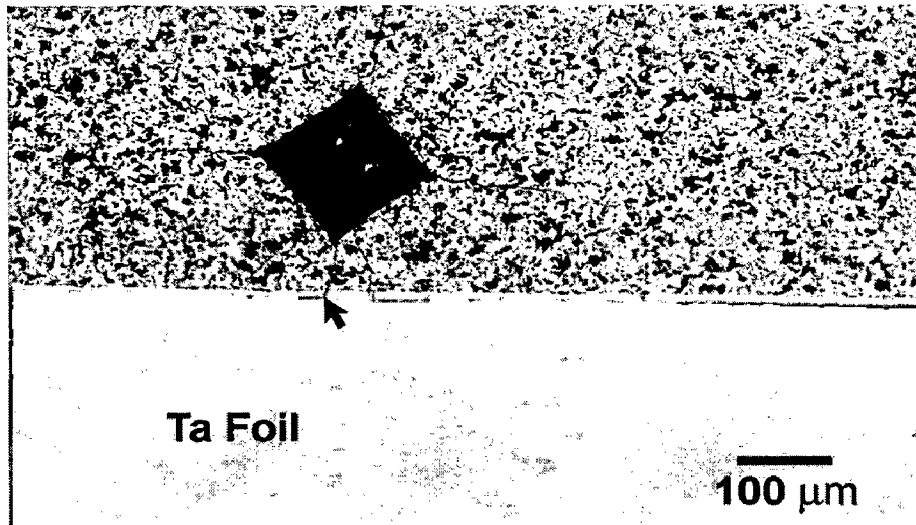


(a)

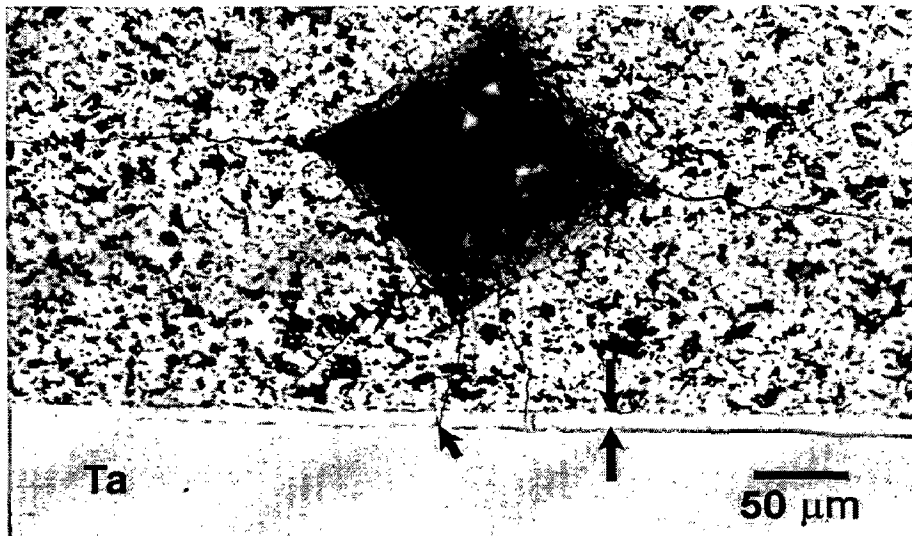


(b)

Fig. 5.76 Optical micrographs of  $(\text{MoSi}_2 + 20 \text{ vol}\% \text{ SiC}_p) + \text{Mo}$  foil laminated composite showing (a) a typical hardness indentation mark in the matrix taken near the interface and (b) the same area as shown in (a) exhibiting crack path interactions with Mo foil, at a higher magnification.

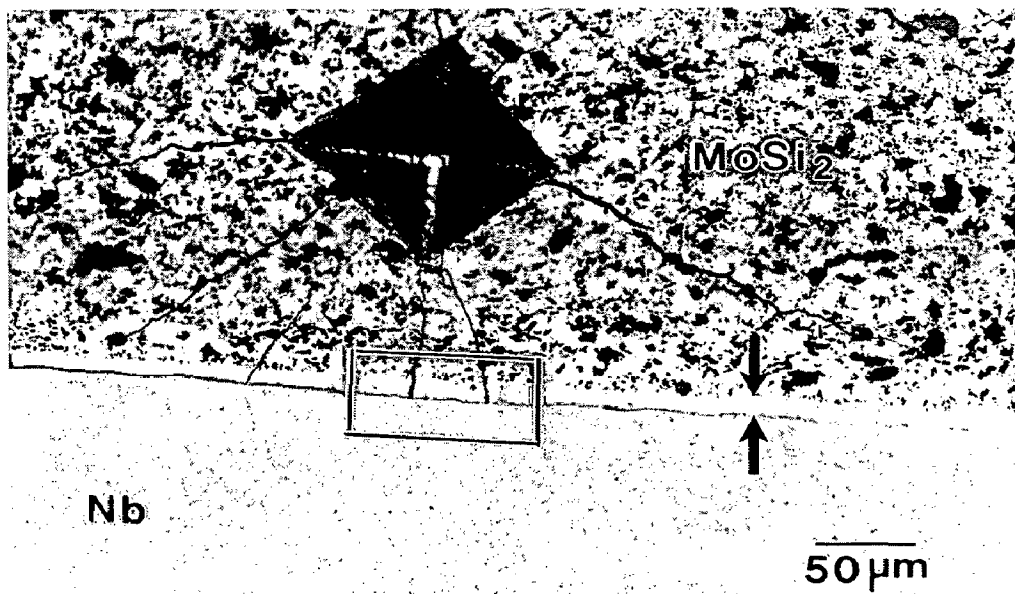


(a)

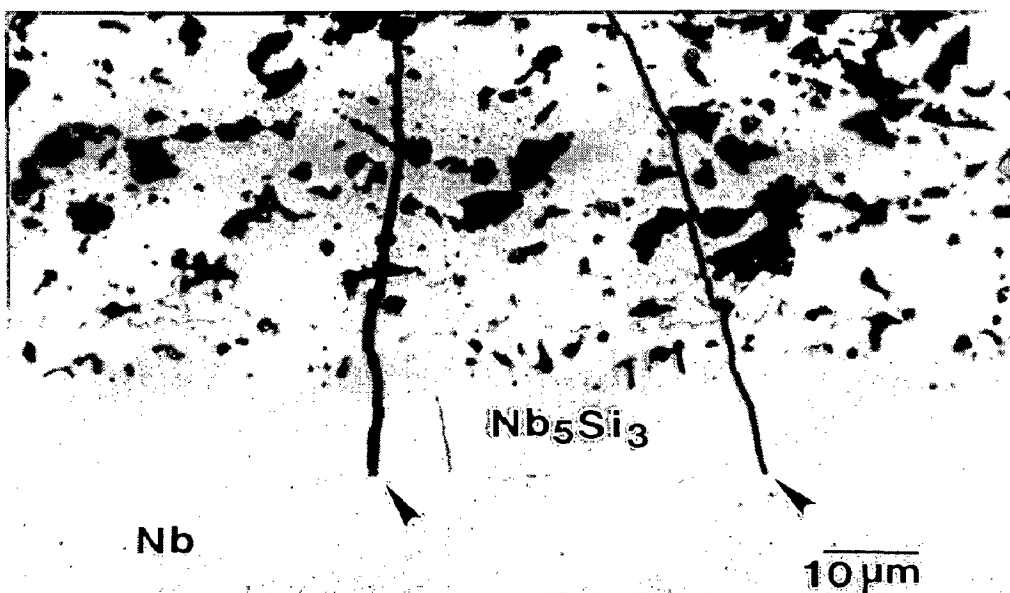


(b)

Fig. 5.77 Optical micrographs showing typical hardness indentation mark and crack paths in  $(\text{MoSi}_2 + 20 \text{ vol}\% \text{ SiC}_p) + \text{Ta}$  foil laminated composite (a) in  $\text{MoSi}_2$  matrix taken close to the interface and (b) same area as in (a) taken at a higher magnification.



(a)



(b)

Fig. 5.78

(a) Optical micrograph showing a typical hardness indentation mark and radial indentation cracks in  $(\text{MoSi}_2 + 20 \text{ vol}\% \text{ SiC}_p) + \text{Nb}$  foil laminated composite (b) SEM back scattered electron image of the area bounded by the rectangle in Fig. 5.78(a) revealing that the cracks have passed through the  $\text{Nb}_5\text{Si}_3$  interfacial reaction layer but were arrested at  $\text{Nb}_5\text{Si}_3$  / pure Nb interface.

A departure from idealized four corner radial cracking was observed in case of all the three laminated composites. Typically, additional cracks were observed to propagate radially from the indentation. The extraneous radial cracks propagating from the sides of an indentation can be termed as secondary radials. A possible explanation for the formation of secondary radials could be the presence of a complex residual stress field in the laminated composites. Because of a non-ideal indentation crack pattern observed in MoSi<sub>2</sub>, absolute indentation fracture toughness values should be regarded as approximate only. The presence of the SiO<sub>2</sub> particles within MoSi<sub>2</sub> grains had no significant effect on radial crack propagation.

#### 5.4.2.6 Room Temperature Fracture Behaviour

The room temperature flexural strength of MoSi<sub>2</sub> + 20 vol% SiC<sub>p</sub> monolithic material was measured as 290 MPa, which was remarkably higher than flexural strength of pure MoSi<sub>2</sub> as reported by Mitra et al (1997<sup>b</sup>). The improvement in flexural strength could be attributed to the strengthening effect of SiC reinforcements, as observed in other MoSi<sub>2</sub> matrix composites reinforced with brittle ceramic particles. In addition, the grain growth in MoSi<sub>2</sub> is also inhibited by fine SiC particles during high temperature processing. The fracture toughness (K<sub>IC</sub>) value of MoSi<sub>2</sub> + 20 vol% SiC<sub>p</sub> monolithic as obtained from notched three point bend test is similar to the fracture toughness calculated by indentation methods. The values obtained from these two tests may not be similar, always. Vasudevan and Petrovic (1992) have argued that indentation fracture toughness methods of obtaining fracture toughness may be more conservative than other tests. However, in the present work, no definite trend could be observed between toughness values obtained by indentation methods and three-point bend test for all the MoSi<sub>2</sub> based particulate composites studied. The moderate increase in fracture toughness by addition of SiC particles in MoSi<sub>2</sub> matrix could be attributed to grain growth inhibition and crack deflection processes by SiC particles as described earlier.

Figure 5.79 shows a typical load-displacement curve obtained from fracture toughness testing of MoSi<sub>2</sub> + 20 vol% SiC<sub>p</sub> particulate composite. The curve resembles that of a brittle solid as no resistance to catastrophic failure is observed. Once a crack becomes unstable it is able to propagate through the specimen without any increase in crack growth resistance. Figure 5.80 is an SEM fractograph of a K<sub>IC</sub>

specimen of  $\text{MoSi}_2 + 20 \text{ vol\% SiC}_p$  monolithic material. It exhibits the brittle transgranular cleavage fracture.

In case of  $(\text{MoSi}_2 + 20 \text{ vol\% SiC}_p) +$  refractory metal foil laminated composites, the strength and toughness values obtained from three-point bend tests as presented in Table 5.19 are for comparative purposes only and should not be treated as absolute values for these properties. The fracture toughness value calculated is called "damage tolerance" and is designated as  $K_{\text{max}}$  rather than  $K_{\text{IC}}$ , since it is calculated from the peak load. Xiao and Abbaschian (1992<sup>a</sup>, 1992<sup>b</sup>) have argued that the value calculated from the peak load of a bending test was actually a reflection of the bridging capability of the ductile phases and could be interpreted as an indicator of the damage tolerance of the composite.

There is a very significant improvement in flexural strength as well as fracture toughness of  $(\text{MoSi}_2 + 20 \text{ vol\% SiC}_p) + \text{Mo}$  foil,  $(\text{MoSi}_2 + 20 \text{ vol\% SiC}_p) + \text{Ta}$  foil and  $(\text{MoSi}_2 + 20 \text{ vol\% SiC}_p) + \text{Nb}$  foil laminated composites. In case of Ta foil laminated composite, the increase in flexural strength is 50 % while the toughness improved by almost a factor of four measured in crack arrester mode as compared to the  $\text{MoSi}_2 + 20 \text{ vol\% SiC}_p$  monolithic material. However, lamination with Mo foil results in relatively lower improvement in flexural strength and fracture toughness of the laminated composite as compared to the lamination with Ta and Nb foils. The flexural strength and fracture toughness values of  $(\text{MoSi}_2 + 20 \text{ vol\% SiC}_p) + \text{Nb}$  foil laminated composite are slightly lower than the values obtained for  $(\text{MoSi}_2 + 20 \text{ vol\% SiC}_p) + \text{Ta}$  foil composite.

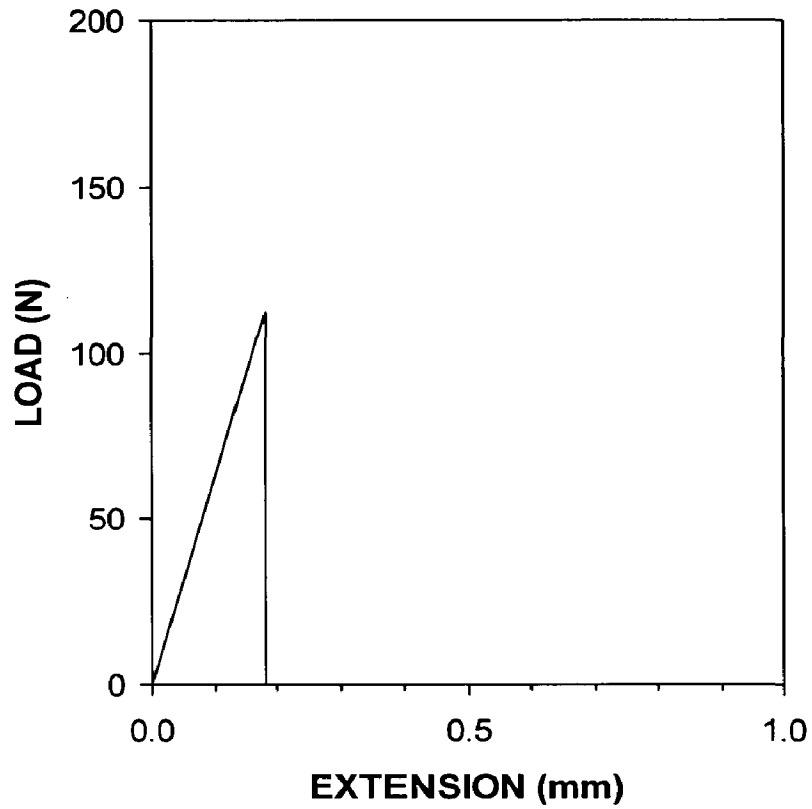


Fig. 5.79 A typical load-displacement curve obtained from fracture toughness testing of  $\text{MoSi}_2 + 20 \text{ vol\% SiC}_p$  matrix (monolithic).

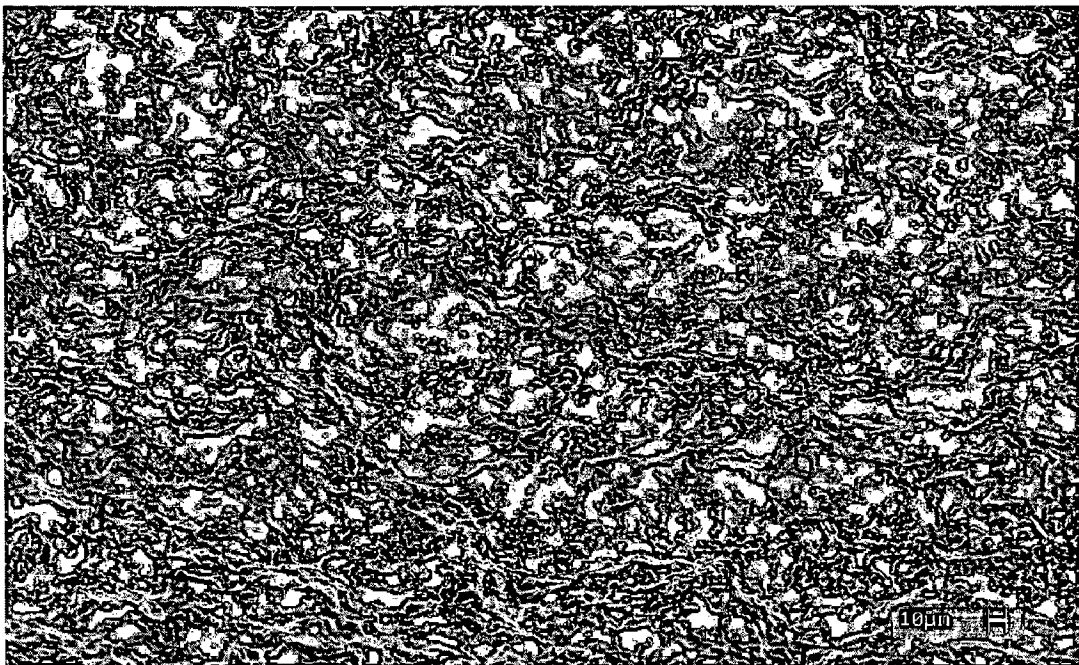


Fig. 5.80 SEM fractograph of fracture toughness (notched three point bend) test specimen of  $\text{MoSi}_2 + 20 \text{ vol\% SiC}_p$  matrix.



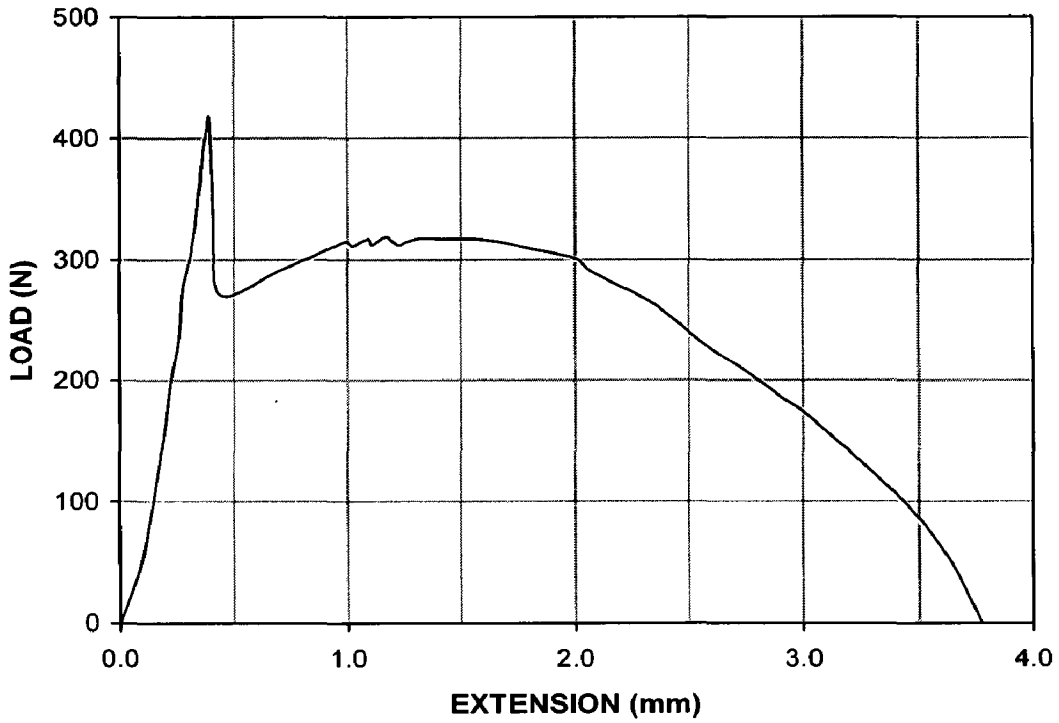
As described earlier, the strength and toughness of the laminated composites have been calculated from the peak load obtained in three point bend tests. The peak load of a bending test carried out on a laminated composite specimen is governed by the yield strength of the refractory metal foil and the degree of constraint on the ductile metal foil applied by the brittle matrix. The degree of constraint on Nb foil is expected to be higher than Ta foil due to a lower thermal expansion mismatch between MoSi<sub>2</sub> based matrix and the Nb foil resulting in lower residual thermal stresses in Nb foil reinforced laminated composite as compared to the Ta foil reinforced laminated composite. The residual thermal stresses in various laminated composites have been calculated in section 4.4.2 and presented in Table 4.5. However, the yield strength of the as received Ta foil was found to be much higher than yield strength of the Nb foil (Table 5.5). The effect of foil yield strength seems to be more pronounced than degree of constraint on peak load achieved in case of Ta and Nb foil reinforced laminated composites. Osman et al (1995) have also observed that as the strength of ductile metal foil increases, fracture toughness of the composite increases. A higher strength ductile layer gives higher fracture toughness than that laminated with a lower strength ductile layer.

However, the strength and toughness of (MoSi<sub>2</sub> + 20 vol% SiC<sub>p</sub>) + Mo foil composite is found to be the minimum among all the three MoSi<sub>2</sub>-SiC<sub>p</sub> matrix laminated composite systems in spite of the fact that the yield strength of the Mo foil was maximum among all the three refractory metal foils used. As noted earlier, the peak load obtained in a bending test conducted on a laminated composite specimen is governed by the strength of the refractory metal foil as well as the interfacial bonding. A strong interfacial bond between MoSi<sub>2</sub> based matrix and the metal foil would result in a higher constraint by the elastic matrix on the metal foil. The load carried by the ductile metal foil is expected to be higher with a high degree of constraint imposed on it. In the case of Mo foil laminated composite, the thermal expansion mismatch between Mo foil and MoSi<sub>2</sub>-SiC<sub>p</sub> matrix is larger than thermal expansion mismatch between Ta / Nb foils and MoSi<sub>2</sub>-SiC<sub>p</sub> matrix. This results in a higher residual tensile hoop stress in the matrix near the Mo foil. The residual tensile stresses have been estimated (section 4.4.2) as 201 MPa, 59 MPa and 14 MPa in Mo, Ta and Nb foil laminated composites, respectively (Table 4.5). The residual stress cannot only result in weak interfacial bonding but also increases the stress

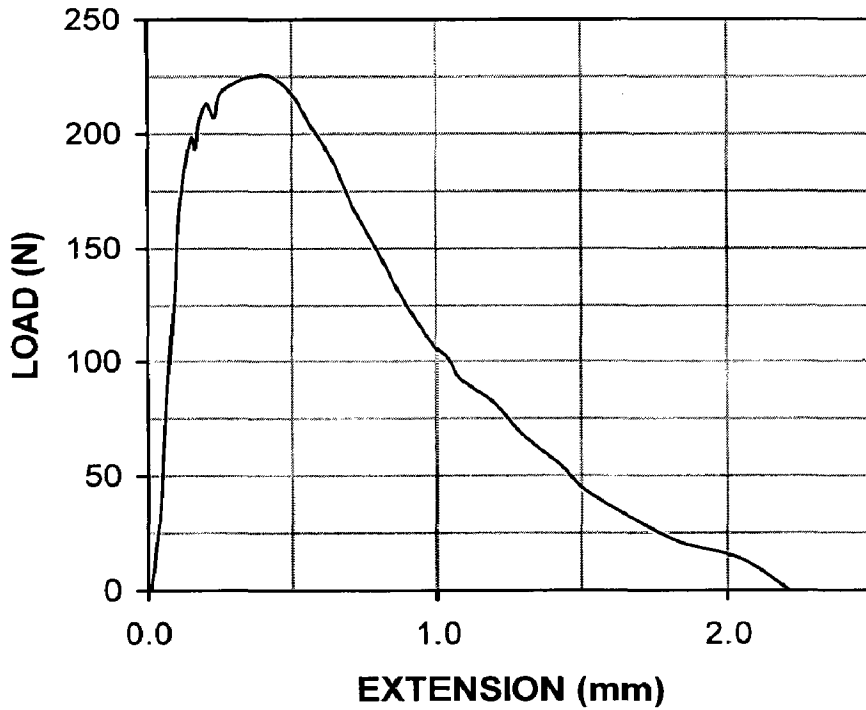
intensity in the composite. Therefore, a reduced peak load ( $P_{max}$ ) in Mo foil laminated composite could be attributed to higher residual stresses in spite of the fact that as received Mo foil has much higher strength than Ta and Nb foils (Table 5.5). Contribution of yield strength to fracture toughness was mainly to increase the maximum stress reached by the constrained ductile reinforcement. However, in the present case of  $(MoSi_2 + 20 \text{ vol\% } SiC_p) + Mo$  foil laminated composite, the poor interfacial bonding seems to have more pronounced effect on the peak load reached than the strength of the foil.

However, the improvements in fracture toughness of the laminated composites tested in crack divider mode were moderate. Only a limited load transfer from matrix to the foil occurs since the primary crack could propagate continuously within the  $MoSi_2-SiC_p$  brittle matrix without encountering any obstacle in the form of a ductile metal foil. Only a small segment of the crack front propagates through the ductile foil and resists the unstable crack propagation through the  $MoSi_2-SiC_p$  layers. The mechanisms of crack propagation in crack arrester and crack divider modes are described in detail in the subsequent sections.

Figure 5.81 depicts typical load-displacement curves of  $(MoSi_2 + 20 \text{ vol\% } SiC_p) + Ta$  foil laminated composite tested in crack arrester mode as well as in crack divider mode. Similar load-displacement curves were obtained in Mo and Nb foil laminated composites. In crack arrester mode, the load drops after reaching to a peak value ( $P_{max}$ ). Beyond this point, the curve depicts only the plastic deformation of the Ta foil. In crack divider mode, the peak load reached was much lower than the peak load in crack arrester mode. The load-displacement curve in crack divider mode also exhibits a lower plastic deformation than obtained in crack arrester mode. In crack divider mode, the Ta foil undergoes a lower plastic stretching before fracture. The load-displacement curves obtained in flexural strength testing were similar to the load-displacement curves obtained in fracture toughness testing in all the laminated composites studied.



(a)



(b)

Fig. 5.81 Typical load-displacement curves obtained from fracture toughness testing of  $(\text{MoSi}_2 + 20 \text{ vol\% SiC}_p) + \text{Ta}$  foil laminated composite (a) crack arrester mode and (b) crack divider mode.

In many of the advanced ceramic matrix composites, linear elastic behavior is violated for common test specimens. Consequently, nonlinear approaches are needed to characterize the material behaviour (Evans, 1990). The concept of work of fracture has been widely applied to characterize the crack growth resistance for extremely complicated non-linear fracture processes (Nakayama, 1965, Tattersall and Tappin, 1966, Sakai and Ichikawa, 1992, Sakai and Bradt, 1993). At elevated temperatures, the fracture of pure  $\text{MoSi}_2$  is also not linear elastic. Therefore, the fracture toughness of  $\text{MoSi}_2$  at elevated temperatures is measured as “work of fracture” and not as  $K_{IC}$ .

The work of fracture was measured from the area under the load – displacement curve as described in section 3.3.2.3(d). A work of fracture value of  $25,920 \text{ J/m}^2$  was obtained in case of laminated composite with Ta foil as compared to a value of  $9,570 \text{ J/m}^2$  in laminated composite with Mo foil. The lower work of fracture obtained in  $(\text{MoSi}_2 + 20 \text{ vol}\% \text{ SiC}_p) + \text{Mo}$  foil laminated composite could be attributed to a much lower ductility of as received Mo foil (Table 5.5) used in synthesizing the laminated composite. In addition to the lower ductility, the stress-strain curve of Mo foil does not show any considerable strain hardening (Fig. 5.9(a)) in contrast to the stress-strain curve of Ta foil (Fig. 5.9(b)). Xiao (1991<sup>b</sup>) has argued that work of fracture increases with increasing work hardening rate. High work hardening rate reinforcements have a relatively longer stage of plastic deformation leading to more energy to be dissipated resulting in higher work of fracture. The work of fracture in crack divider mode for both the laminated composites was lower than work of fracture measured in crack arrester mode.

In case of Ta foil laminated composite, addition of 20 vol% SiC particles in  $\text{MoSi}_2$  matrix resulted in a lower value of work of fracture as compared to the addition of 2 wt% Al in  $\text{MoSi}_2$  matrix (Table 5.14). This could be due to the fact that addition of SiC particles in  $\text{MoSi}_2$  reduces the thermal expansion mismatch between  $\text{MoSi}_2$  matrix and the Ta foil resulting in lower residual thermal stresses in the composite and hence a stronger interfacial bond. A relatively stronger bond would result in high degree of constraint and a lower decohesion length which is expected to reduce the extent of plastic deformation in the Ta foil before a complete fracture.

Similarly, the work of fracture measured in case of Nb foil laminated composite was lower than the work of fracture obtained in case of Ta foil reinforced laminated composite. The work of fracture in a bending test on a laminated composite specimen is a function of strain hardening coefficient and ductility of the metal foil as well as the degree of interfacial debonding. A higher degree of constraint on Nb foil (due to lower residual thermal stresses) is expected to result in a relatively reduced interfacial debonding allowing less Nb to undergo plastic deformation and necking. The Ta foil seems to exhibit a higher strain hardening than Nb foil as observed from the stress – strain curves of as received Ta and Nb foils (Fig. 5.9). However, as received Nb foil was more ductile than the as received Ta foil (Table 5.5). But the same may not be true after the foils are subjected to high processing temperatures during the composite fabrication. Osman et al (1995) have reported that the high level of constraint imposed by the brittle matrix reduces the ductility of lower strength metal foil to a greater extent than that of the high strength metal foil. Since increase in work of fracture is obtained from deforming the constrained metal foils, the toughness of the laminate containing lower strength ductile foil should be lower. Its ductility is reduced more. Work hardening has been reported (Xiao, 1991<sup>a</sup>) as more effective in enhancing the work of fracture because high work hardening rate delays the instability of deformation for constrained ductile reinforcement.

It should be pointed out, however, that the concept of work of fracture has value only as a comparative tool. It is not a design parameter. It can be used as a qualitative measure of toughness, at best. Tattersall and Tappin (1966) analyzed the work of fracture for a wide variety of materials and observed that the work of fracture increased as the fracture toughness increased.

A few fracture toughness test specimens of ( $\text{MoSi}_2 + 20 \text{ vol}\% \text{ SiC}_p$ ) + refractory metal foil laminated composites were unloaded just before the fracture and were observed under optical stereomicroscope as well as under scanning electron microscope. Figures 5.82 and 5.83 depict the SEM secondary electron images of the Ta and Nb foil laminated composite specimens respectively (taken at different magnifications), tested in crack arrester mode. When an advancing crack just impinges the metal foil, no debonding at the  $\text{MoSi}_2$ - $\text{SiC}_p$  layer / metal foil interface

occurs. As external load continues to increase, debonding at the interface and/or multiple fracture of the matrix near the interface occur due to a relatively large lateral deformation of the ductile metal foil as compared to the matrix and load transfer from the matrix to the foil. The debonding relaxes the constraint imposed by the brittle matrix and the ductile metal foil begins to undergo plastic deformation and necking before its fracture into two pieces. The necking in the Ta foil is clearly revealed in Fig. 5.82 as indicated by arrow marks. Necking reduces the x-section at the fracture. The ductile metal foil acts as a barrier to unstable crack growth once initiated in MoSi<sub>2</sub> matrix resulting in ductile phase toughening of MoSi<sub>2</sub>. The most of the specimens tested in crack arrester mode did not separate out into two pieces after the completion of the bend test and were carefully removed and observed under the scanning electron microscope. The specimens were separated into two fractured pieces by applying a little pressure by hands and were further prepared for fractographic examination.

Similarly, Fig. 5.84 shows the SEM secondary electron images of different faces of a fracture toughness test specimen of (MoSi<sub>2</sub> + 20 vol% SiC<sub>p</sub>) + Ta foil laminated composite tested in crack divider mode. The crack initiated and propagated inside the MoSi<sub>2</sub>-SiC<sub>p</sub> layers on both sides of the Ta foil. The small segment of the crack front traveling through the ductile Ta foil lags behind the crack front propagating through the MoSi<sub>2</sub> matrix as Ta foil undergoes plastic stretching, simultaneously with the crack growth. As a result, the specimen did not separate into two pieces even after the test was completed as evidenced by Fig. 5.84(d). Figure 5.84(b) is a high magnification image of the encircled area in Fig. 5.84(a). Towards the end, due to a very small volume of the material left, the sample has gone into mixed mode loading as shear loading comes into the picture.

Figure 5.85 shows the SEM secondary electron images of different faces of a flexural strength specimen (without notch) tested in crack divider mode. Similar to the fracture toughness specimen, the crack initiated and propagated inside the MoSi<sub>2</sub> layers rather rapidly as compared to the crack propagation through the ductile Ta foil resulting in Ta foil holding the broken MoSi<sub>2</sub> layers on both sides as depicted in Fig. 5.85(c). The Ta foil was subjected to tensile loading after getting debonded

completely from the matrix as evidenced by the presence of small cracks perpendicular to the longitudinal direction of the foil (Fig. 5.85(b)).

Figure 5.86 shows SEM fractographs of fracture toughness test specimen of  $(\text{MoSi}_2 + 20 \text{ vol}\% \text{ SiC}_p) + \text{Mo}$  foil laminated composite tested in crack arrester mode. The fractograph in Fig. 5.86(a) was taken at the interfacial area exhibiting fracture surfaces of Mo foil as well as of  $\text{MoSi}_2\text{-SiC}_p$  matrix together. Due to low ductility of the Mo foil, the crack seems to have rapidly propagated through the foil before occurrence of the interfacial debonding or multiple matrix fracture. Low ductility of the Mo foil leads to little lateral deformation of the Mo foil and resultant debonding at the interface. The fractographs shown in Figs. 5.86(b) and 5.86(c) were taken exclusively inside the matrix and the Mo foil regions, respectively. The fracture surface of the  $\text{MoSi}_2\text{-SiC}_p$  matrix layer exhibits the brittle transgranular cleavage fracture with SiC particles revealed. The Mo foil shows a quasi-cleavage fracture. Little or no visible plastic deformation precedes the fracture. The fracture appears granular or crystalline. Because cleavage occurs along well-defined crystallographic planes within each grain, a cleavage fracture changes directions when it crosses grain boundaries. In contrast to the fracture of Mo foil, the fracture surface of Ta foil exhibits micro-tearing with high ductile features as shown in Figs. 5.87(a) and 5.87(b). Figure 5.87(b) taken at a higher magnification shows the tearing ridges.

Figure 5.88(a) is a low magnification SEM fractograph of a fracture toughness test specimen of  $(\text{MoSi}_2 + 20 \text{ vol}\% \text{ SiC}_p) + \text{Nb}$  foil laminated composite tested in crack arrester mode. The arrow shows the direction of crack propagation. The fracture surface reveals debonding at the matrix / foil interface, plastic deformation, necking and fracture of the Nb foil. The region enclosed by the rectangle in Fig. 5.88(a) was viewed at a higher magnification as exhibited in Fig. 5.88(b). The fracture surface of Nb foil appears to be fibrous. A relatively large amount of plastic deformation preceded the fracture. Figures 5.89(a) and 5.89(b) exhibit typical fracture surfaces of the  $\text{MoSi}_2\text{-SiC}_p$  matrix layer and the Nb foil taken separately at higher magnifications. The fracture surface of Nb foil shows ductile features. It exhibits fur tree like features characteristic of pure metals. Some occasional cleavage features are also seen. Such a correlation of macroscopic and microscopic features provides an excellent record of fracture morphology.

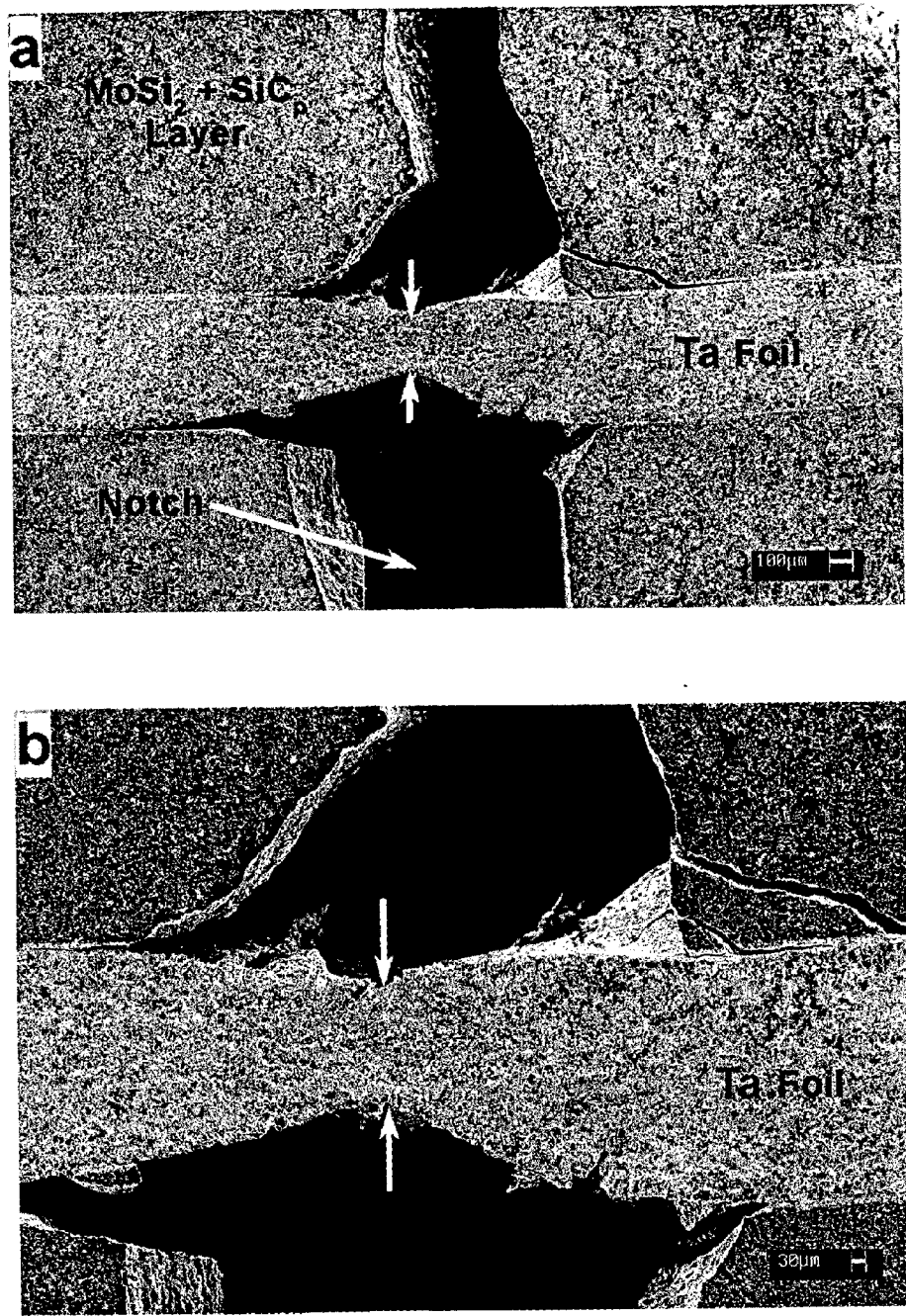


Fig. 5.82 SEM secondary electron images (taken at different magnifications) of a  $K_{IC}$  specimen of  $(\text{MoSi}_2 + 20 \text{ vol}\% \text{ SiC}_p) + \text{Ta}$  foil laminated composite tested in crack arrester mode.



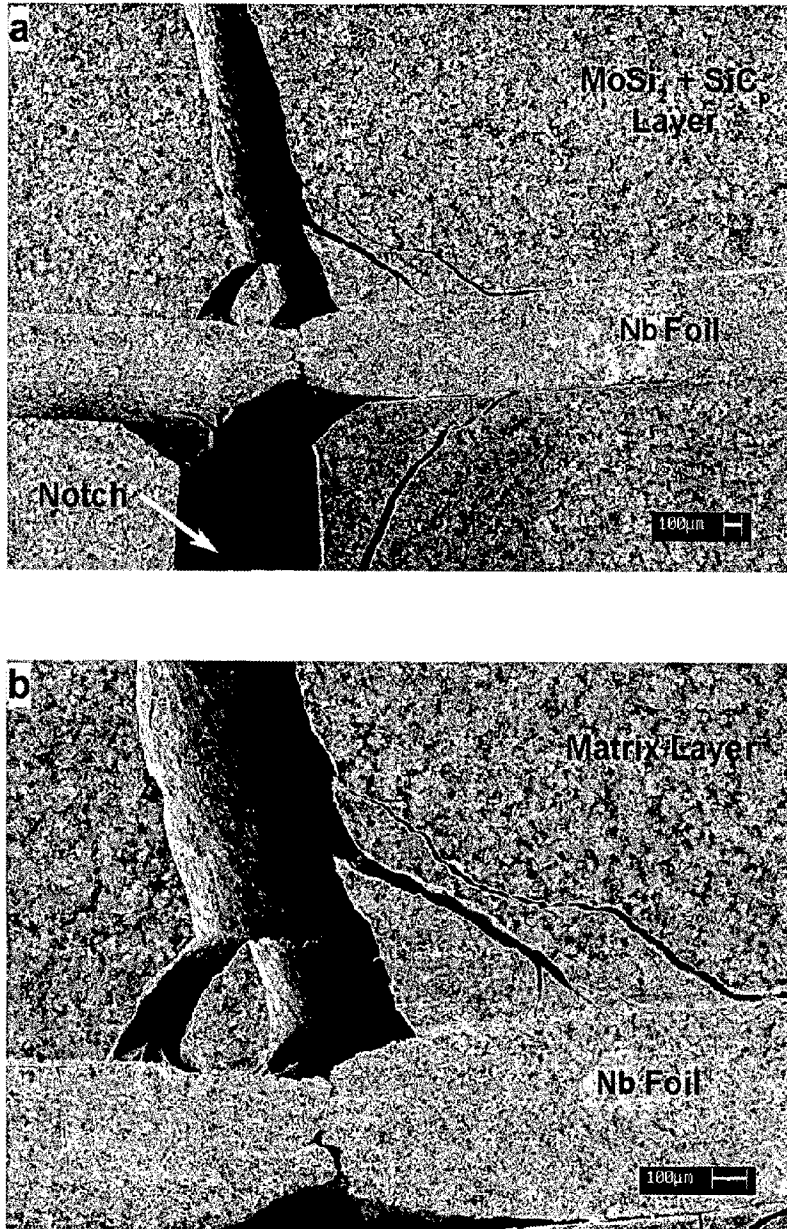


Fig. 5.83 SEM secondary electron images (taken at different magnifications) of a  $K_{IC}$  specimen tested in crack arrester mode showing plastic deformation and necking in Nb metal foil.

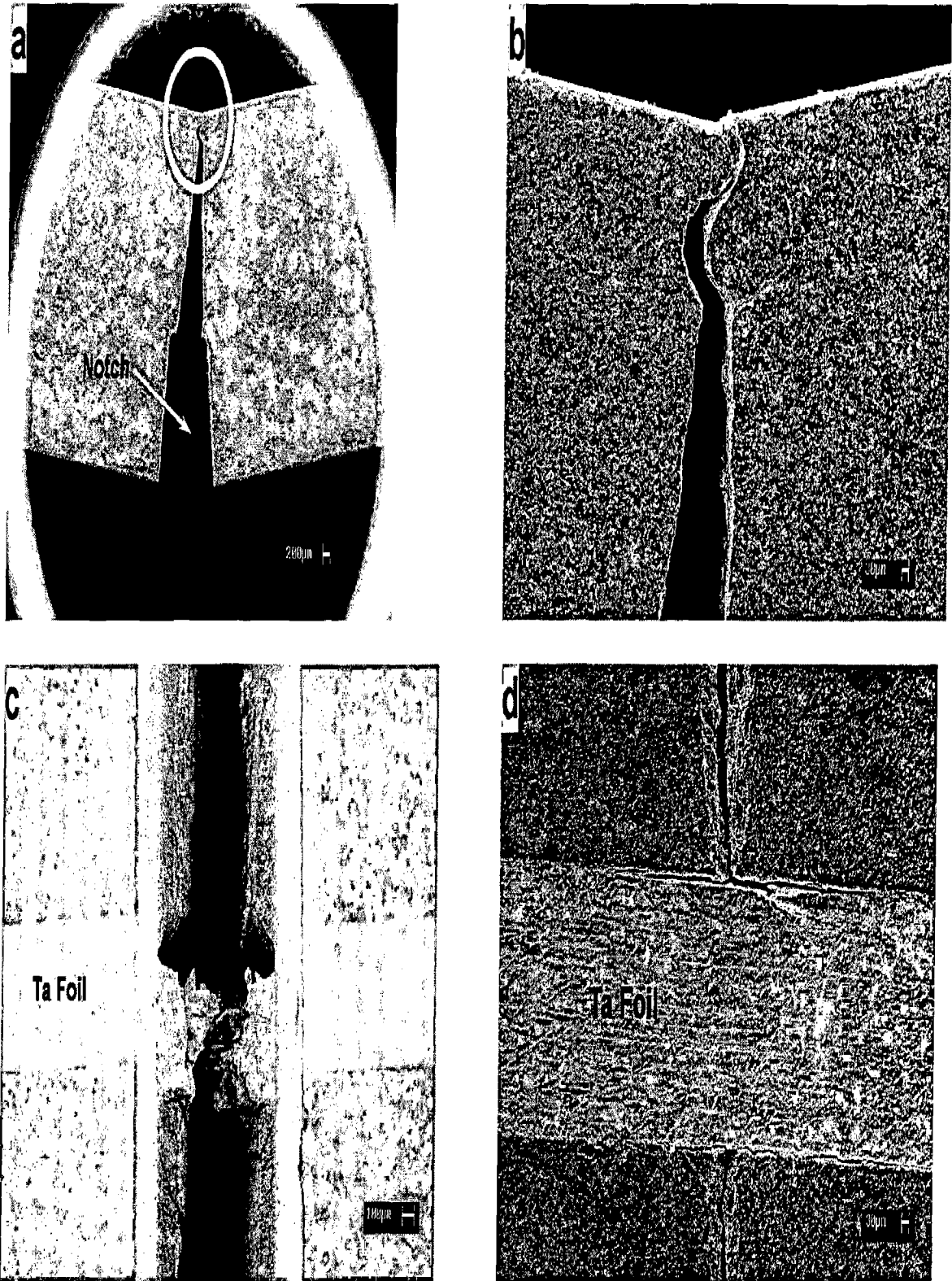


Fig. 5.84 SEM secondary electron images of a fracture toughness ( $K_{Ic}$ ) specimen of  $(\text{MoSi}_2 + 20 \text{ vol}\% \text{ SiC}_p) + \text{Ta foil}$  laminated composite tested in crack divider mode (a) the side along the loading axis (b) the same side at a higher magnification (c) the bottom (notch) side and (d) the top (loading side) view.

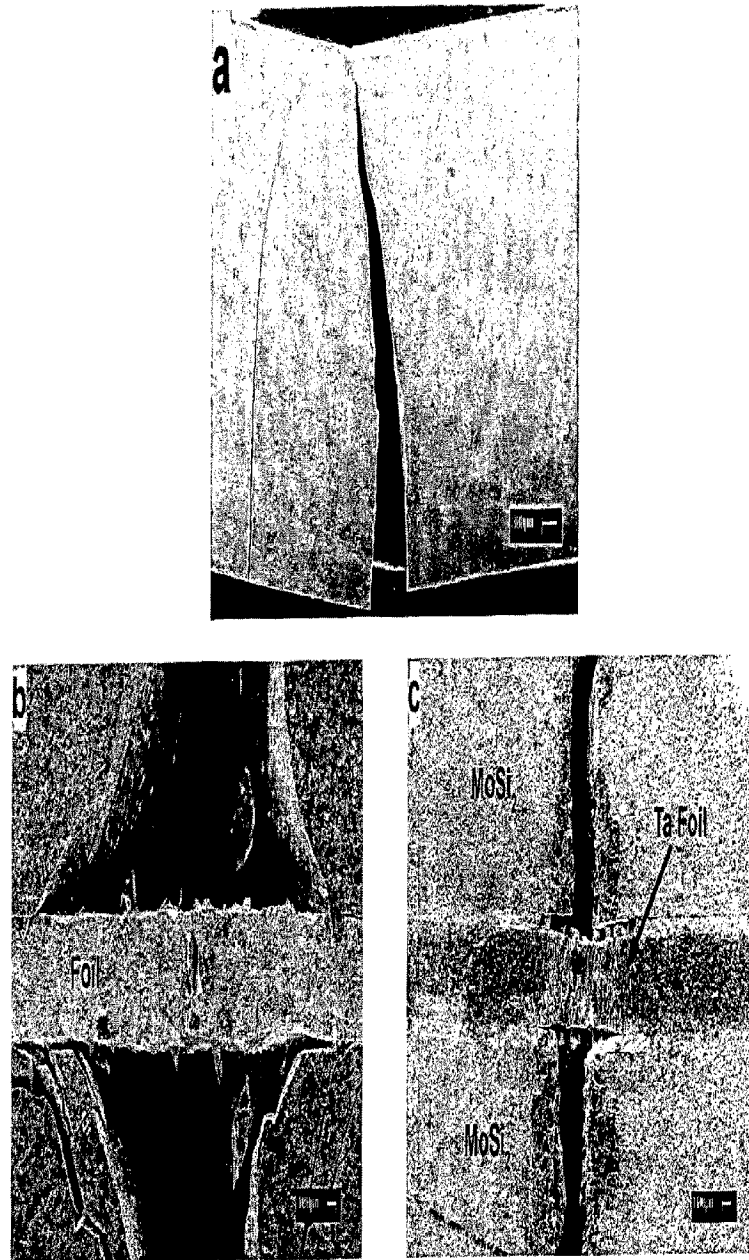
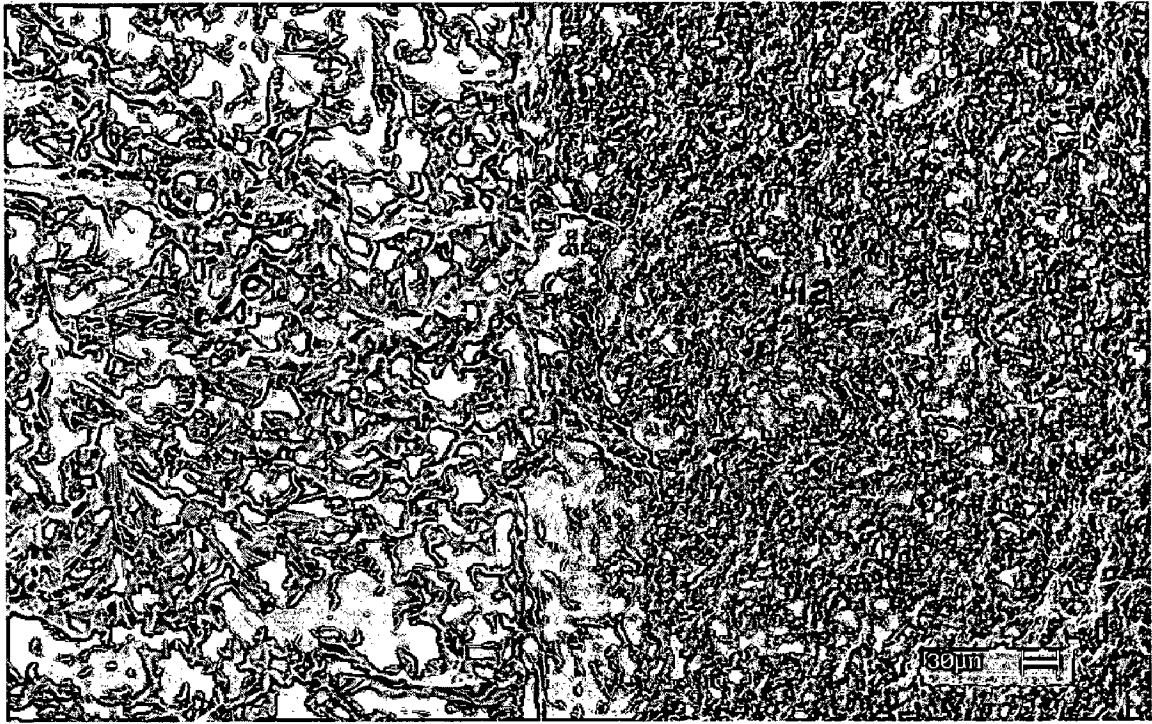
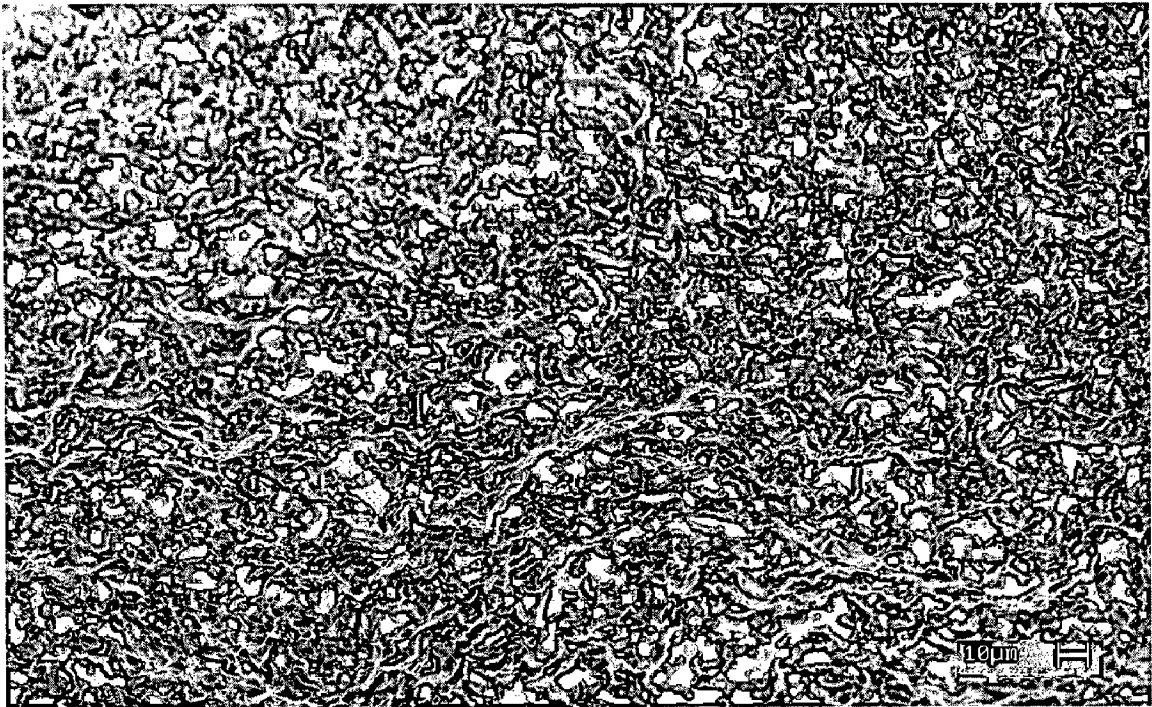


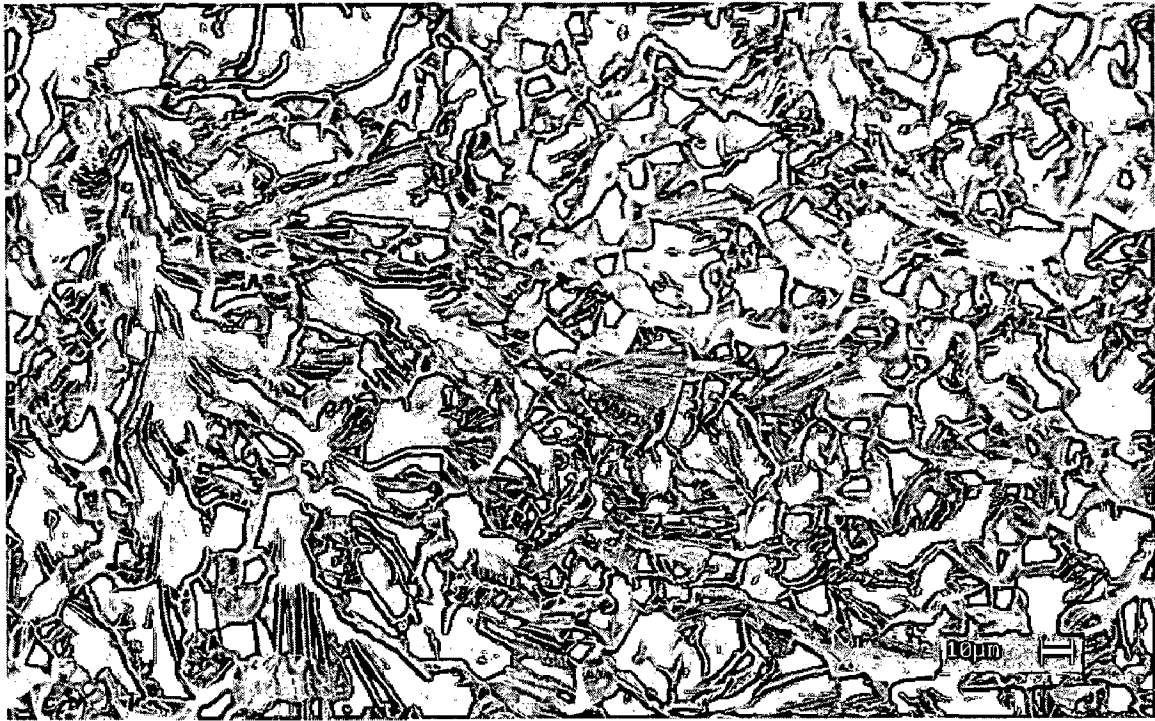
Fig. 5.85 SEM secondary electron images of a flexural strength specimen of  $(\text{MoSi}_2 + 20 \text{ vol\% SiC}_p) + \text{Ta foil}$  laminated composite tested in crack divider mode (a) the side along the loading axis (b) the bottom side and (c) the top view.



(a)

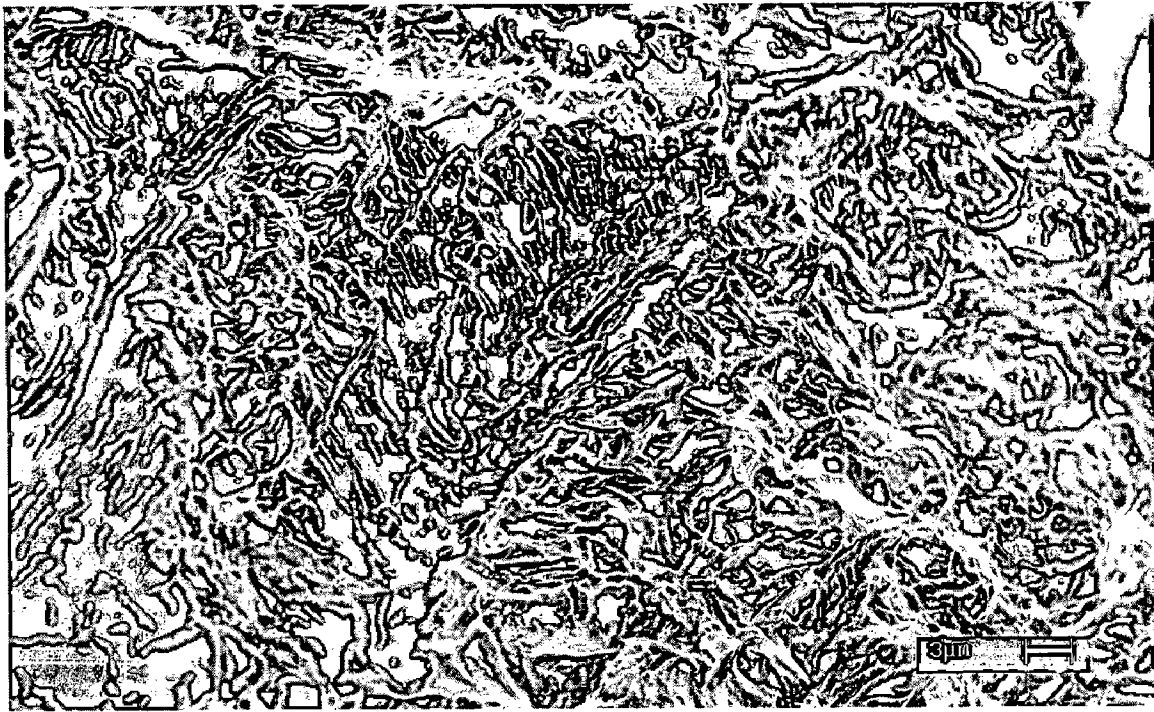


(b)

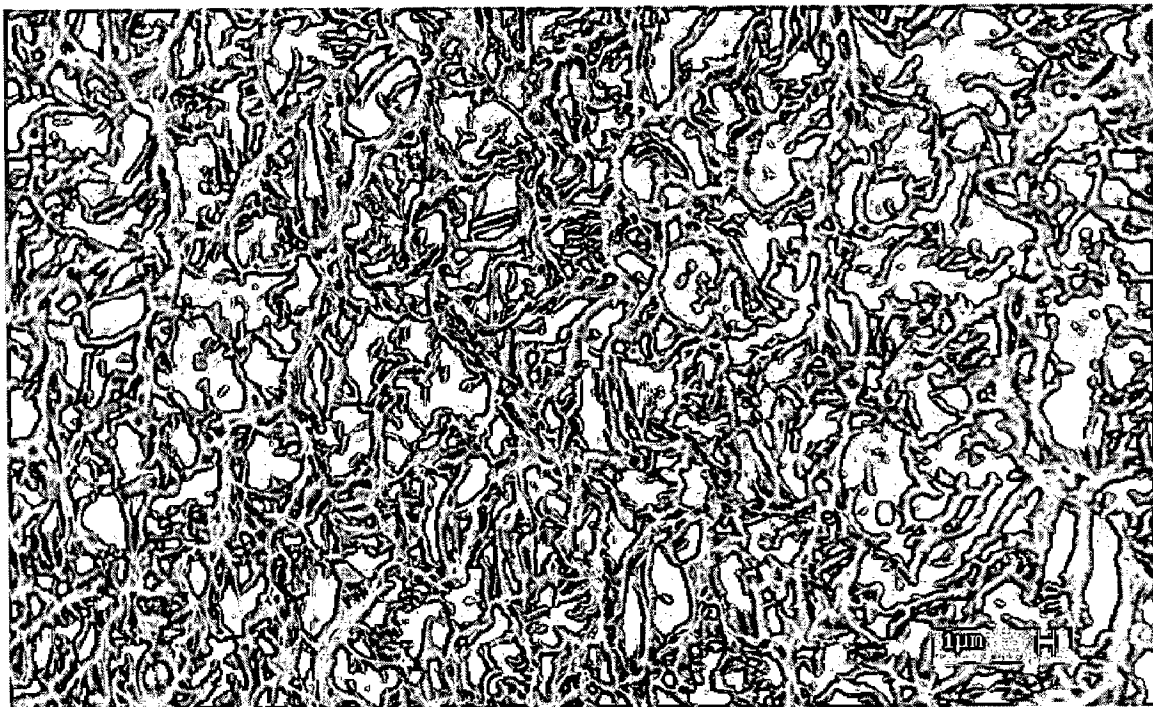


(c)

Fig. 5.86 SEM fractographs of fracture toughness ( $K_{Ic}$ ) test specimen of ( $\text{MoSi}_2 + 20 \text{ vol\% SiC}_p$ ) + Mo foil laminated composite tested in crack arrester mode (a) interfacial area (b) inside matrix layer and (c) Mo foil region.



(a)



(b)

Fig. 5.87 Fracture surfaces of Ta foil taken at different magnifications.

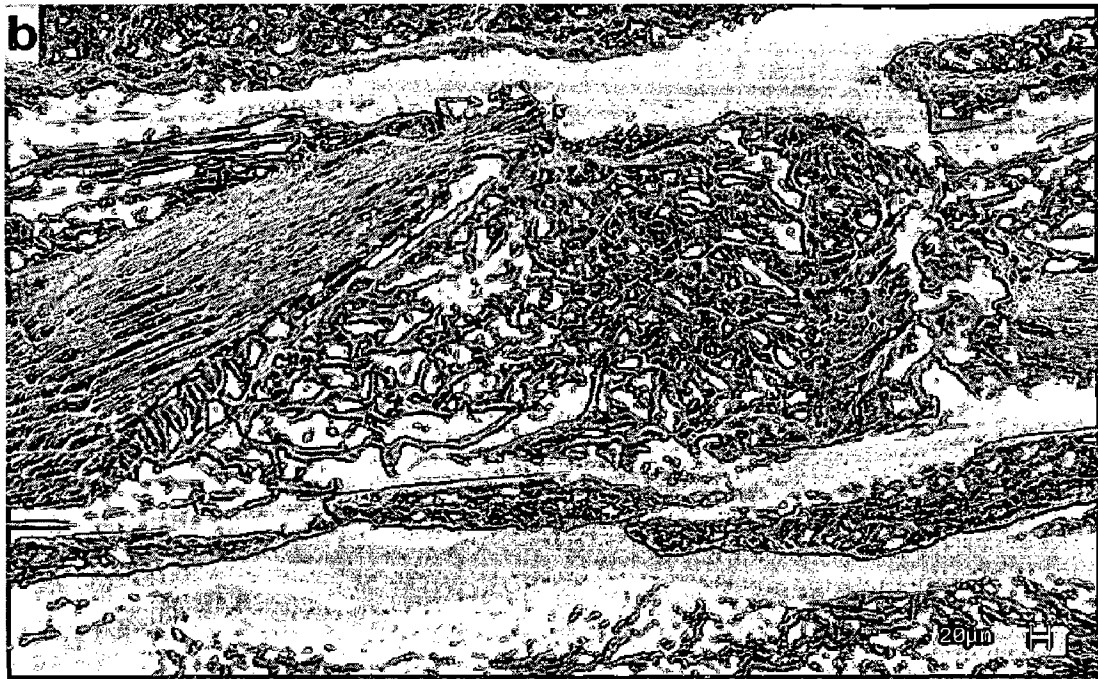
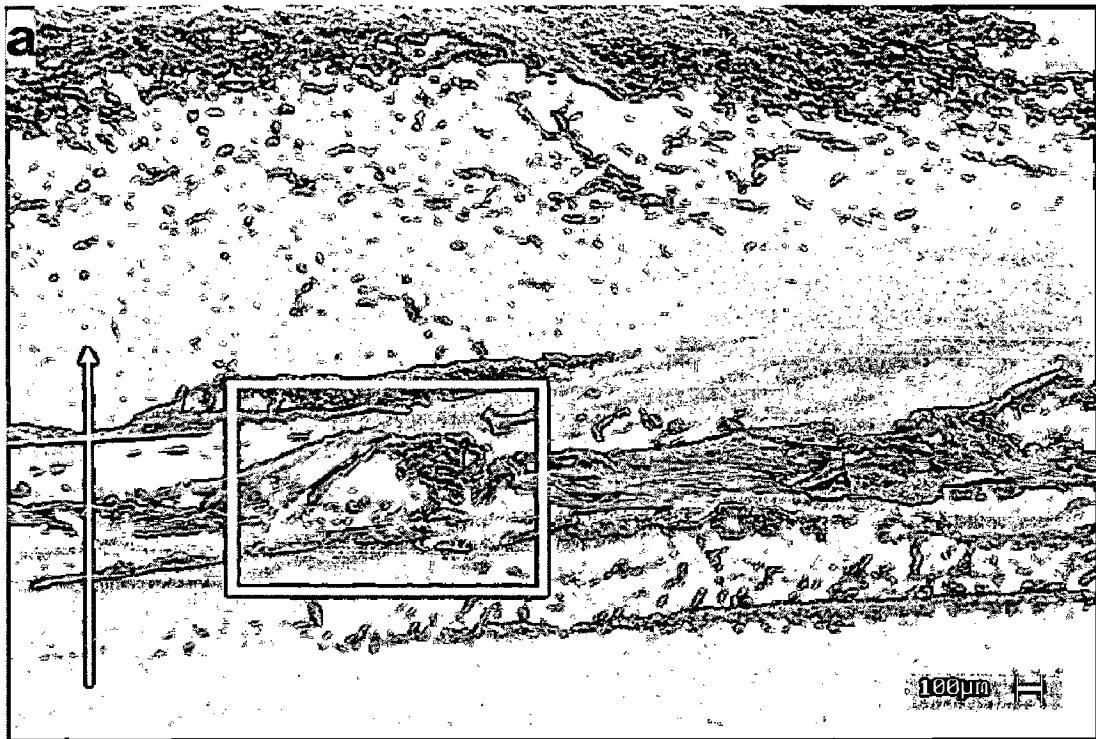
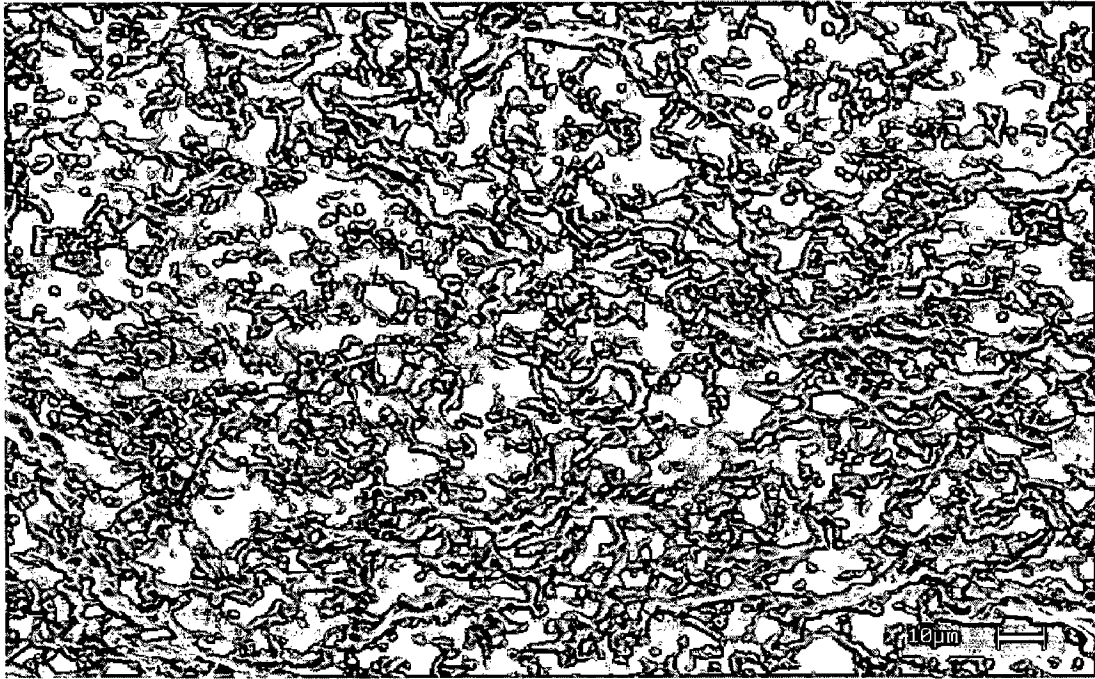
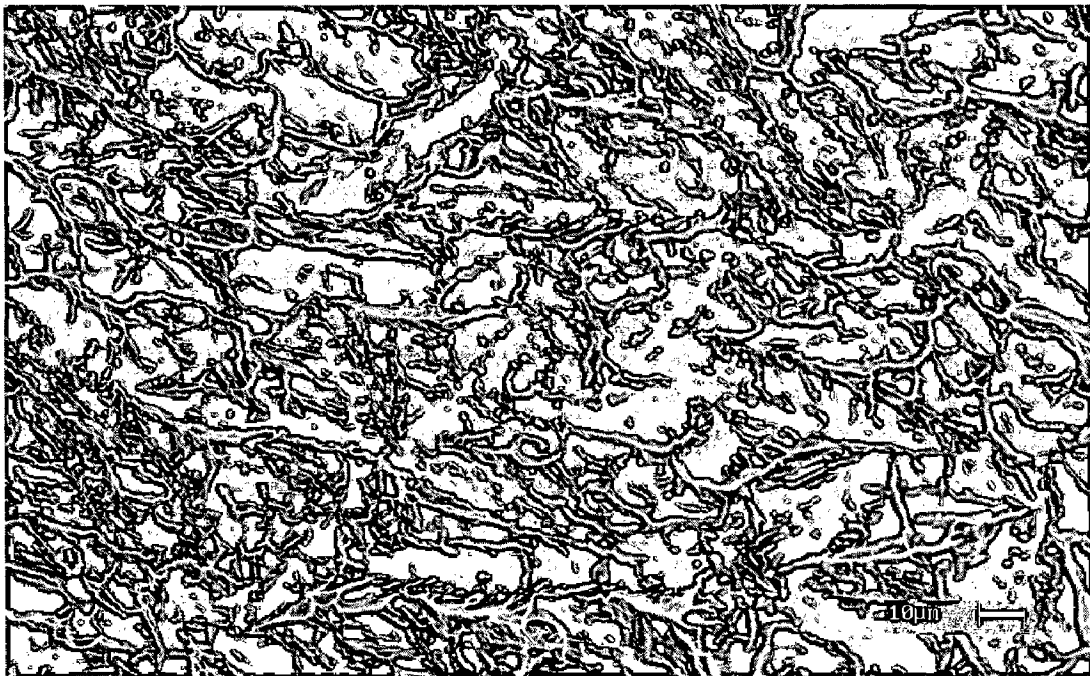


Fig. 5.88 (a) SEM fractograph of fracture toughness ( $K_{IC}$ ) test specimen of  $(\text{MoSi}_2 + 20 \text{ vol}\% \text{ SiC}_p) + \text{Nb}$  foil laminated composite tested in crack arrester mode (b) Enclosed area in Fig. 5.88(a) viewed at a higher magnification.



(a)



(b)

Fig. 5.89 SEM fractographs of fracture toughness ( $K_{Ic}$ ) test specimen of ( $\text{MoSi}_2 + 20 \text{ vol}\% \text{ SiC}_p$ ) + Nb foil laminated composite tested in crack arrester mode (a) fracture surface of the  $\text{MoSi}_2\text{-SiC}_p$  matrix layer and (b) fracture surface of Nb foil.



Figure 5.90 exhibits the SEM fractographs of fracture toughness ( $K_{Ic}$ ) test specimen of  $(\text{MoSi}_2 + 20 \text{ vol\% SiC}_p) + \text{Nb}$  foil laminated composite tested in crack divider mode taken at different locations showing predominantly the Nb foil area. In crack divider mode, the fracture surface of Nb foil revealed alternate regions of having brittle and ductile features. The crack in the foil propagated in tearing mode till some critical load or strain was reached. At this point the crack jumps resulting in cleavage fracture of the foil. The crack growth through the Nb foil was slow. The regions of Nb foil undergoing brittle fracture exhibited transgranular while the ductile regions of Nb foil exhibited microvoid coalescence. As the strain in the foil increases, the microvoids grow, coalesce, and eventually form a continuous fracture surface.

#### 5.4.2.7 Characterization of Interfacial Reaction Layers

Interfaces play an important role in determining the mechanical properties of the composites. In laminated composites synthesized and studied in the present work, interfacial reaction layers of varying thickness were observed. The thickness and micro-hardness values measured for interfacial reaction layers in  $(\text{MoSi}_2 + 20 \text{ vol\% SiC}_p)$  matrix reinforced with Mo, Ta and Nb foils laminated composites are presented in Table 5.20.

The thickness of the reaction zone was  $50 \mu\text{m}$  in case of Mo foil laminated composite while it was  $20 \mu\text{m}$  in Nb foil laminated composite. Ta seems to have better chemical compatibility with  $\text{MoSi}_2$  as it exhibited only a  $10 \mu\text{m}$  thick reaction zone after processing under similar conditions. However, the micro-hardness data presented in Table 5.20 reveals that the silicide phases formed as a result of chemical interactions between  $\text{MoSi}_2$  and Ta foil are harder than the phases formed at the interface in Mo and Nb foil reinforced laminated composites. Micro-hardness measurements were made using indentation loads in the range of 50 g to 300 g for different laminated composites. The variation in applied load was necessitated depending upon the thickness of the interfacial reaction layer. The applied load was selected to ensure that the size of the indentation mark generated falls within the interfacial reaction zone and would not overlap with either  $\text{MoSi}_2$  matrix or the refractory metal foil.

It has to be noted that in all the three laminated composites, the reaction zone consisted of more than one phase. The micro-hardness data presented here is

indicative of the average hardness of the reaction zone in each case. Micro-hardness measurements of individual phases formed within the same interfacial reaction layer of a composite could not be carried out in the present work with the existing micro-hardness testing equipment. To obtain indentation marks well within the individual reaction product phases, indentation loads much smaller in magnitude would be required.

The micro-hardness values were also measured inside the matrix layer and metal foils in all the three laminated composites and are presented in Table 5.20. The micro-hardness values measured inside the  $\text{MoSi}_2 + 20 \text{ vol } \% \text{ SiC}$  matrix were found to be lower than the hardness values measured with indentation loads of 10 – 30 kg. The discrepancy in hardness values measured by different load levels could be due to a much smaller size of indentation mark generated with small loads. The contribution to the hardness by SiC particles is expected to be more with higher loads generating large size indentation marks. SiC is much harder than  $\text{MoSi}_2$ . However, the micro-hardness values of refractory metal foils inside the laminated composites were higher than measured with higher load levels (Table 5.19). For lighter loads (< 300 g), the small amount of elastic recovery becomes appreciable and with very small indentations produced at light loads, the error in locating the actual ends of the indentation becomes greater. Both these factors have the effect of giving a higher hardness reading, so that it is usually observed that the micro-hardness number increases as the load is decreased below about 300 g.

Figures 5.91(a) and 5.91(b) are the optical micrographs showing a typical micro-hardness indentation mark inside the interfacial reaction layer in ( $\text{MoSi}_2 + 20 \text{ vol } \% \text{ SiC}_p$ ) + Mo foil laminated composite taken under ordinary light and polarized light, respectively. The interfacial reaction layer is demarcated by arrow marks. The microstructures also exhibit the indentation marks taken in the matrix layer as well as inside the Mo foil. The indentation mark inside the  $\text{MoSi}_2\text{-SiC}_p$  matrix is encircled to differentiate it from SiC particles present in the matrix. A barreled indentation mark is observed in Mo foil. The barrel shaped indentation is found in cold worked metals. It results from ridging or piling-up of the metal around the faces of the indenter. In this case, the diagonal measurement produces a low value of the contact area so that the hardness numbers obtained are high.

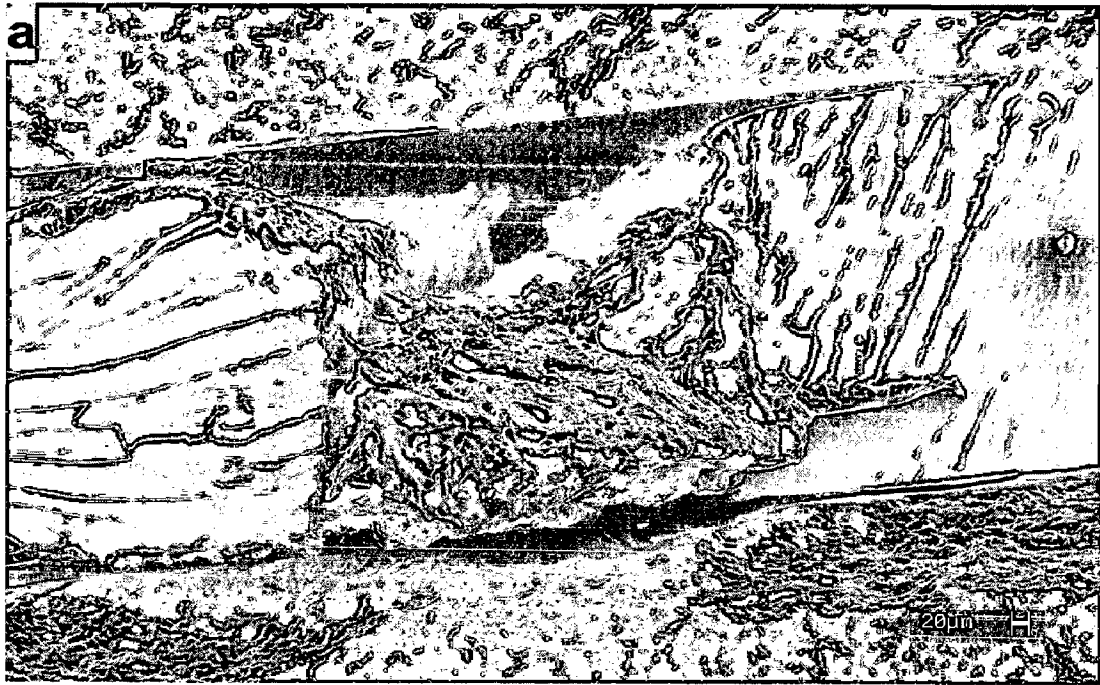
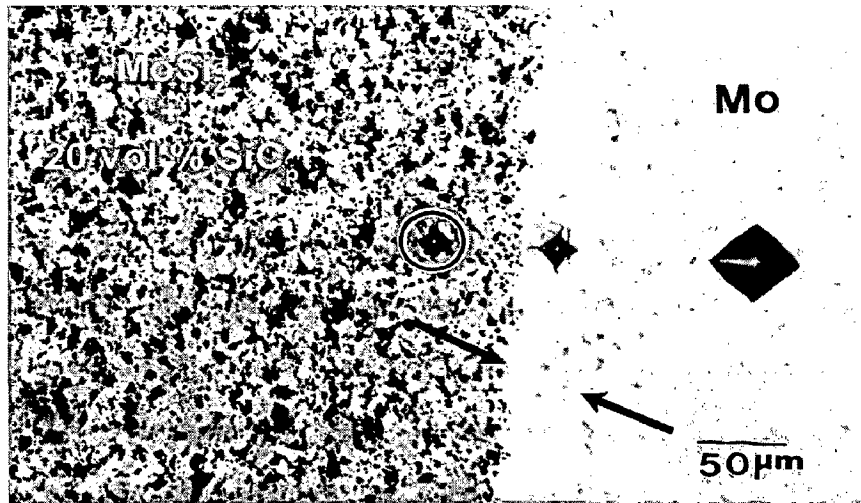


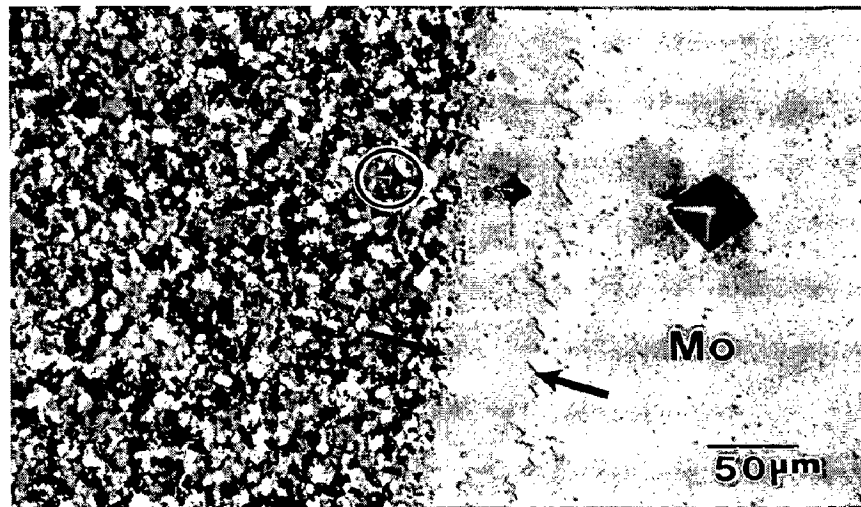
Fig. 5.90 SEM fractographs of fracture toughness ( $K_{Ic}$ ) test specimen of ( $\text{MoSi}_2 + 20 \text{ vol\% SiC}_p$ ) + Nb foil laminated composite tested in crack divider mode taken at different locations showing predominantly the Nb foil area.

Table 5.20 Micro-hardness data for (MoSi<sub>2</sub> + 20 vol% SiC<sub>p</sub>) + Mo, Ta and Nb foils laminated composites.

Laminated Composite	Interfacial Reaction Layer		Microhardness (VHN)	
	Thickness (μm)	Microhardness (VHN)	Foil	Matrix
(MoSi <sub>2</sub> + 20 vol% SiC <sub>p</sub> ) + Mo Foil	50	1298	241	1358
(MoSi <sub>2</sub> + 20 vol% SiC <sub>p</sub> ) + Ta Foil	10	1814	193	1287
(MoSi <sub>2</sub> + 20 vol% SiC <sub>p</sub> ) + Nb Foil	20	1553	145	1333



(a)



(b)

Fig. 5.91 Optical micrographs showing micro-hardness indentation mark inside the interfacial reaction layer in  $(\text{MoSi}_2 + 20 \text{ vol}\% \text{ SiC}_p) + \text{Mo}$  foil laminated composite (a) ordinary light photomicrograph and (b) microstructure using polarized light. The microstructures also show the Indentation marks in the matrix layer (encircled) as well as taken inside the Mo foil.

Figure 5.92(a) exhibits the typical micro-hardness indentation marks inside the interfacial reaction layer, inside  $\text{MoSi}_2$  matrix and inside the pure Ta foil in  $(\text{MoSi}_2 + 20 \text{ vol\% SiC}_p) + \text{Ta}$  foil laminated composite. The interface is depicted by arrow marks. The thickness of the interfacial reaction layer in Ta foil laminated composite was only  $10 \mu\text{m}$  resulting in difficulties in the measurement of its micro-hardness by ensuring that a hardness indentation mark is generated within the thin reaction zone without overlapping with  $\text{MoSi}_2\text{-SiC}_p$  matrix or pure Ta foil. This could be achieved only with a load as low as 50 g. The small indentation marks inside the reaction zone and  $\text{MoSi}_2\text{-SiC}_p$  matrix are enclosed by rectangles in Fig. 5.92(a) for the purpose of easy identification and clarity. The same indentation mark is encircled in Fig. 92(b), which was taken at a higher magnification. In contrast to Mo foil, Ta foil exhibits a pincushion indentation mark due to sinking-in. The pincushion indentation is the result of sinking-in of the metal around the flat faces of the pyramid. This condition is observed with annealed metals and results in an overestimate of the diagonal length. For annealed metals, work hardening of the surface during polishing can also influence the hardness results.

Similarly, Figs. 5.93(a) and 5.93(b) are the optical micrographs showing micro-hardness indentation marks inside the interfacial reaction layer, matrix layer and in pure Nb foil in  $(\text{MoSi}_2 + 20 \text{ vol\% SiC}_p) + \text{Nb}$  foil laminated composite taken at different magnifications. Here again, the Indentation marks inside the interfacial reaction layer and in the near-by matrix are encircled for easy identification.

Looking at Figs. 5.91, 5.92 and 5.93, it is revealed that the sizes of indentation marks are similar in  $\text{MoSi}_2 + 20 \text{ vol\% SiC}_p$  matrix and inside the reaction zones. This suggests that the various interfacial reaction products are also hard and brittle like the matrix. These are formed at the expense of ductile metal foils reducing the effective volume fraction of the ductile phases. Ta not only results in the smallest reaction zone thickness with  $\text{MoSi}_2$  but Ta foil also resulted in the highest improvement in fracture toughness of  $\text{MoSi}_2$  based laminated composites. In fact it is interesting to observe that the improvement in room temperature fracture toughness decreased as the thickness of the reaction zone increased with different refractory metal foils. As interfacial reaction layer thickness increases, more ductile metal is consumed and converted into brittle phases.

However, the role of interfacial reaction products in determining the mechanical properties of the laminated composites is not fully understood at present. Future work is clearly needed in this area. Xiao et al (1992) have observed that the influence of interfaces on fracture toughness of the brittle matrix with ductile reinforcement composites is not as crucial as in brittle matrix with ceramic reinforcement composites due to the local dislocation slip of the ductile phase at the crack tip. The toughness of the MoSi<sub>2</sub> reinforced with ductile refractory metal foils is governed by the combined effects of intrinsic properties of the metal foil (yield strength, strain hardening coefficient and ductility), the foil thickness, thickness and mechanical nature of the interfacial reaction products as well as the residual thermal stresses generated during high temperature processing.

## **5.5 INTERFACE MODIFICATION BY APPLICATION OF INERT COATINGS**

Most of the ductile refractory metals are thermodynamically unstable with MoSi<sub>2</sub>. High processing temperatures are necessary to consolidate the MoSi<sub>2</sub> based materials to obtain a fully dense laminated structure. Mo, Ta and Nb reacted with MoSi<sub>2</sub> at high processing temperatures and formed thick interfacial reaction layers. Extensive diffusion of Si from MoSi<sub>2</sub> occurred towards the refractory metal foils resulting in the formation of M<sub>5</sub>Si<sub>3</sub> (M = Mo, Ta, Nb) type silicide compounds. These newly formed silicide compounds were found to be brittle. These silicides grow at the expense of the ductile phase. Therefore, to obtain the optimum properties in MoSi<sub>2</sub> based laminated composites, it is important to restrict the Si diffusion at the processing as well as service temperatures. One promising approach is the use of an inert diffusion barrier coating on the reinforcements prior to processing of the composites. An inert coating applied on the refractory metal foils may minimize the matrix – reinforcement interactions during processing and service at elevated temperatures. Coatings may also maintain the integrity of the ductile phase at elevated service temperatures.

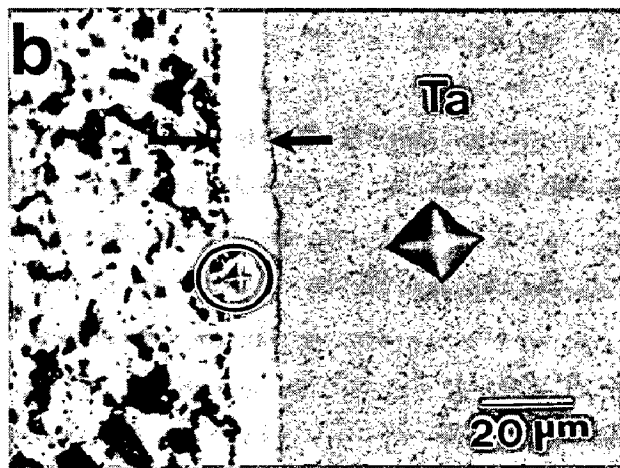
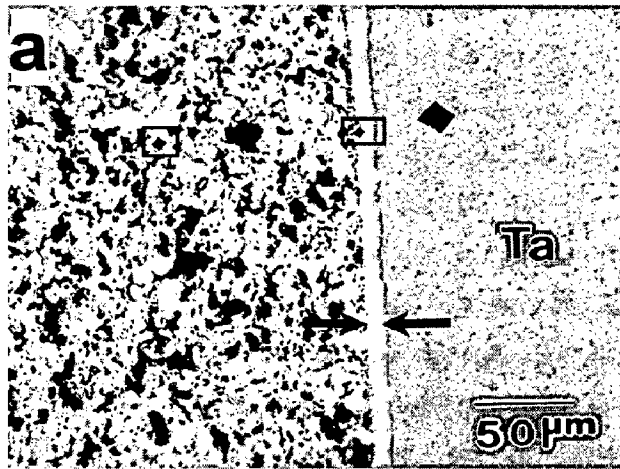


Fig. 5.92 Optical micrographs showing micro-hardness indentation mark inside the interfacial reaction layer in  $(\text{MoSi}_2 + 20 \text{ vol\% SiC}_p) + \text{Ta}$  foil laminated composite taken at different magnifications. The Indentation mark inside the interfacial layer is encircled in Fig. (b) while the same is enclosed by a rectangle in Fig. (a).



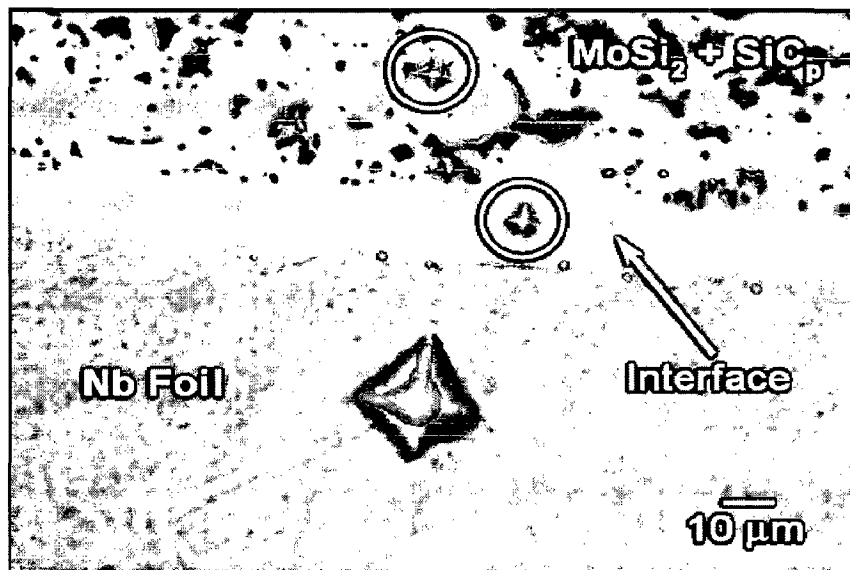
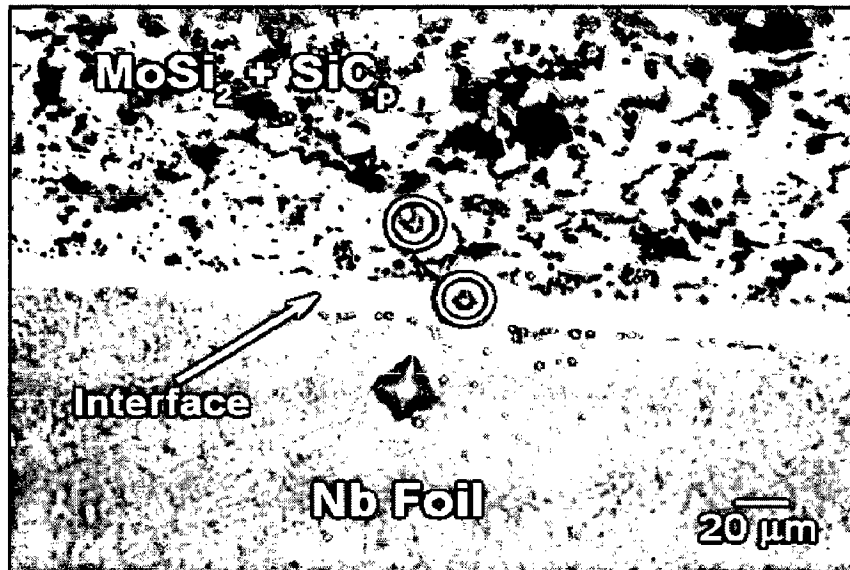
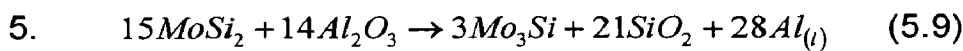
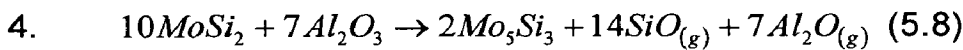
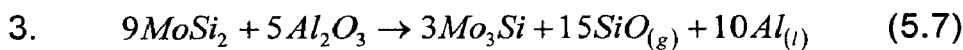
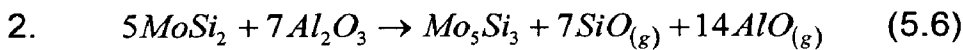
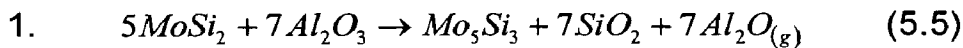


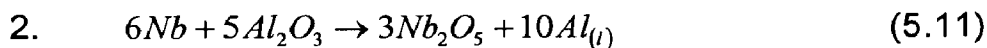
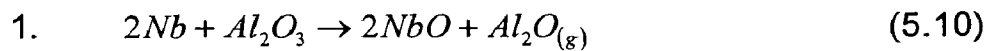
Fig. 5.93 Optical micrographs showing micro-hardness indentation mark inside the interfacial reaction layer in  $(\text{MoSi}_2 + 20 \text{ vol\% SiC}_p) + \text{Nb}$  foil laminated composite taken at different magnifications. The Indentation marks inside the interfacial layer and in the near-by matrix are encircled for the ease of identification.

An inert diffusion barrier coating of  $Al_2O_3$  on Nb foil was applied by plasma spray method prior to consolidation into laminated composite to modify the matrix - reinforcement interface by minimizing the  $MoSi_2$  – Nb foil interactions during high temperature processing. In addition to acting as a diffusion barrier for the elemental constituents of the composite, the coating must be chemically compatible with matrix and the reinforcement. Thermodynamic calculations were performed in order to predict the chemical stability of  $Al_2O_3$  with  $MoSi_2$  and Nb. Using the thermodynamic data available (Barin, 1989), the standard free energy changes for several possible reactions between  $Al_2O_3$  and  $MoSi_2$  and between  $Al_2O_3$  and Nb were calculated. The possible reactions considered between  $Al_2O_3$  and  $MoSi_2$  and between  $Al_2O_3$  and Nb are:

**$Al_2O_3$  vs.  $MoSi_2$ :**



**$Al_2O_3$  vs. Nb:**

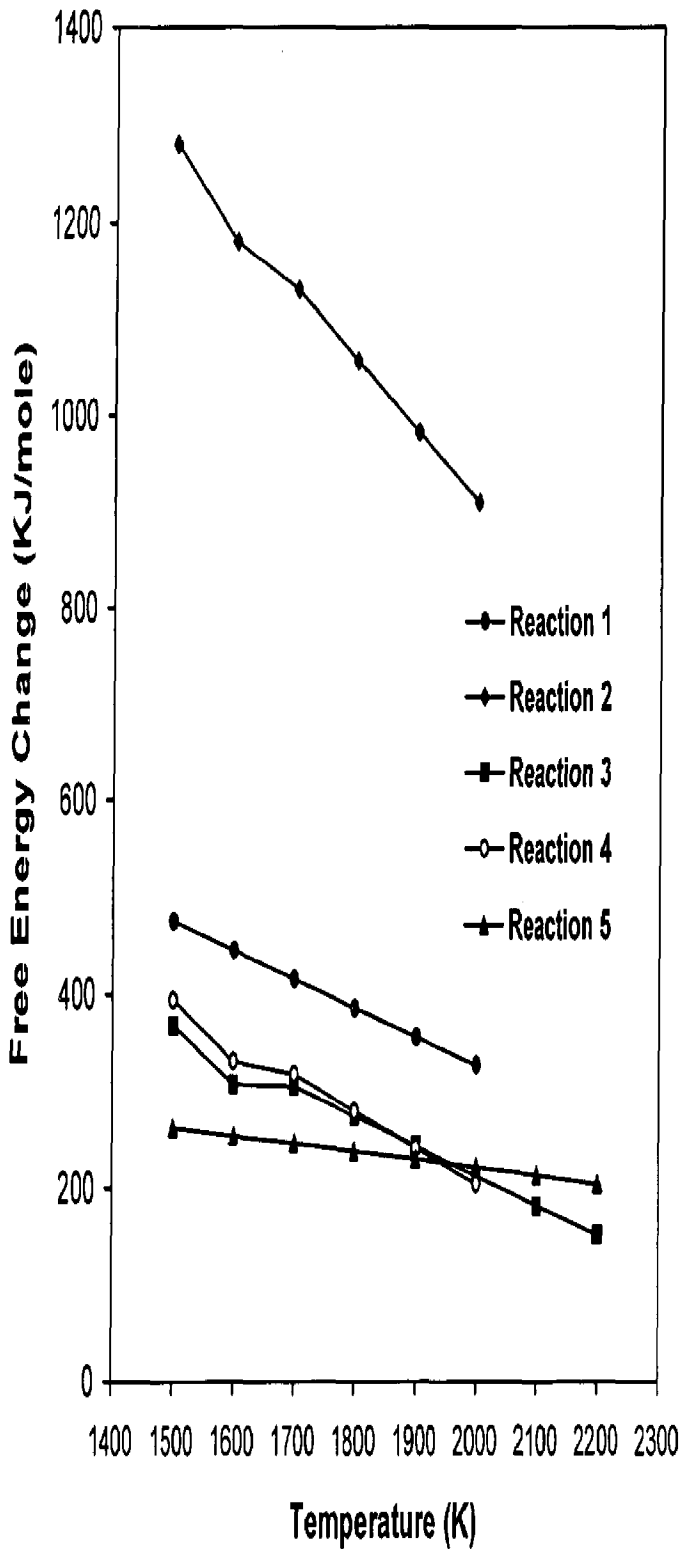


The various reaction components considered in these calculations include  $Al_2O_3$ ,  $Al_{(l)}$ ,  $AlO_{(g)}$ ,  $Al_2O_{(g)}$ ,  $MoSi_2$ ,  $Mo_3Si$ ,  $Mo_5Si_3$ ,  $SiO_{(g)}$ ,  $SiO_2$ , Nb,  $Nb_2O_5$  and NbO. The plots between standard free energy changes with temperature ( $\Delta G$  vs. *Temperature*) for the above chemical reactions are presented in Fig. 5.94. In case of  $Al_2O_3$  vs.  $MoSi_2$ , the equations 5.5 to 5.9 are depicted as reactions 1 to 5 in Fig. 5.94(a), respectively. Equations 5.10 and 5.11 are depicted as reactions 1 and 2 in Fig. 5.94(b). Figure 5.94 clearly exhibits that the  $Al_2O_3$  is chemically stable with  $MoSi_2$  as well as Nb over the entire temperature range.

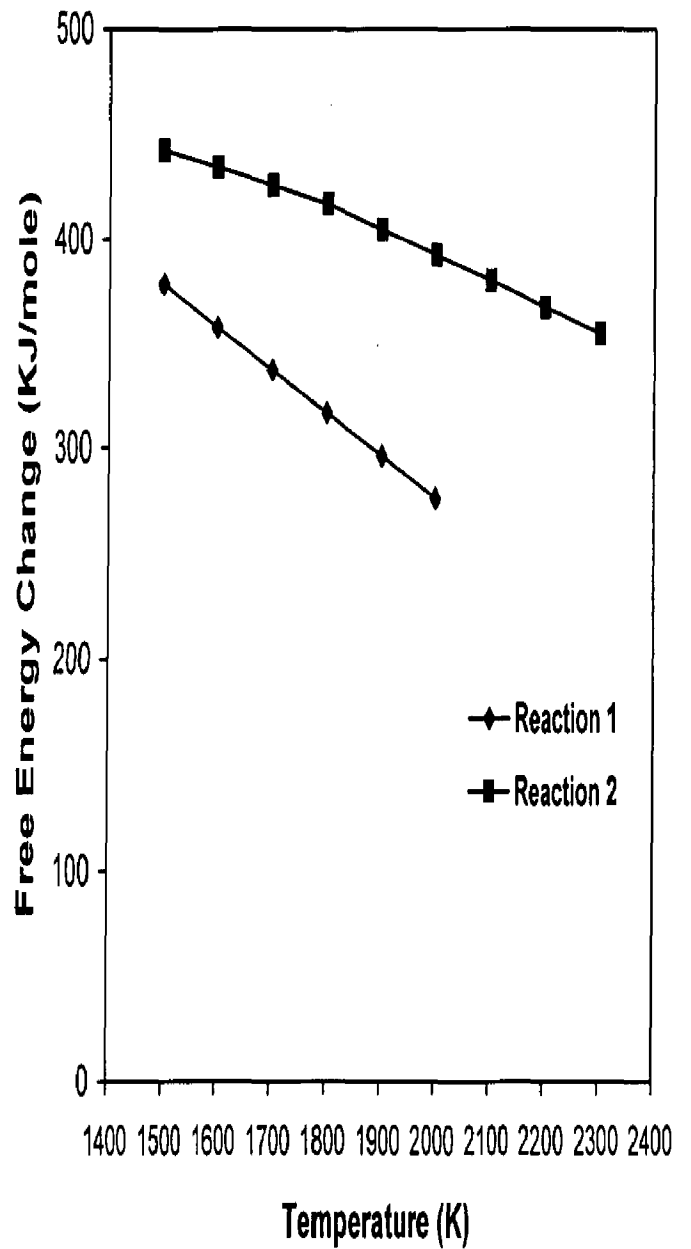
### 5.5.1 Microstructure

The microstructures of  $(\text{MoSi}_2 + 20 \text{ vol\% SiC}_p) + \text{Al}_2\text{O}_3$  coated Nb foil laminated composite are presented in Fig. 5.95. The optical micrographs shown in Figs. 5.95(a) and 5.95(b) were taken under ordinary light and polarized light, respectively. The x-ray diffraction pattern of  $(\text{MoSi}_2 + 20 \text{ vol\% SiC}_p) + \text{Al}_2\text{O}_3$  coated Nb foil composite is presented in Fig. 5.96. The oxide coating appears dark under ordinary light while it appears bright under polarized light. The thickness of the  $\text{Al}_2\text{O}_3$  coating was measured to be  $\sim 50 \mu\text{m}$ . Looking at the optical microstructures, it appears that no interfacial reaction layer has formed between  $\text{MoSi}_2$  based matrix and the Nb reinforcement. This suggests that  $\text{Al}_2\text{O}_3$  coating on Nb foil has completely inhibited the matrix - reinforcement chemical interactions during the high temperature processing. The x-ray diffraction pattern does not reveal the peaks of any new phase formed during the processing other than the peaks of  $\text{MoSi}_2$ ,  $\text{SiC}$  and Nb. However, a few peaks of  $\alpha\text{-Al}_2\text{O}_3$  are observed in x-ray diffraction pattern.  $\text{Al}_2\text{O}_3$  coating acted as an inert diffusion barrier and suppressed the Si diffusion across the interface. The microstructures also reveal that  $\text{Al}_2\text{O}_3$  coating by plasma spray method resulted in rough interfaces between  $\text{Al}_2\text{O}_3$  and Nb and between  $\text{Al}_2\text{O}_3$  and  $\text{MoSi}_2$ . The interfacial roughness is expected to improve the mechanical bonding between  $\text{MoSi}_2 / \text{Al}_2\text{O}_3$  and between  $\text{Al}_2\text{O}_3 / \text{Nb}$  in absence of any chemical interactions between the constituent layers.

The EPMA images (BSE and elemental x-ray maps) of  $\text{MoSi}_2\text{-Al}_2\text{O}_3$  coated Nb foil laminated composite are shown in Fig. 5.97. The back-scattered electron image (Fig. 5.97(a)) does not reveal the presence of any interfacial reaction layer. It appears that Nb and  $\text{MoSi}_2$  did not react during vacuum hot processing, forming new intermetallic compounds at the interface. The  $\text{Al}_2\text{O}_3$  coating separates the  $\text{MoSi}_2$  matrix from Nb foil and acts as a diffusion barrier. The oxide coating also exhibits some porosity, a feature typical of coatings deposited by plasma spray method.

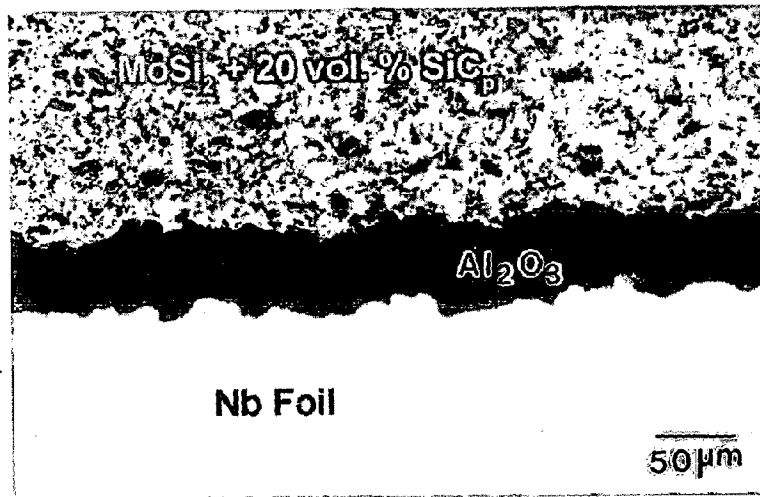


(a)

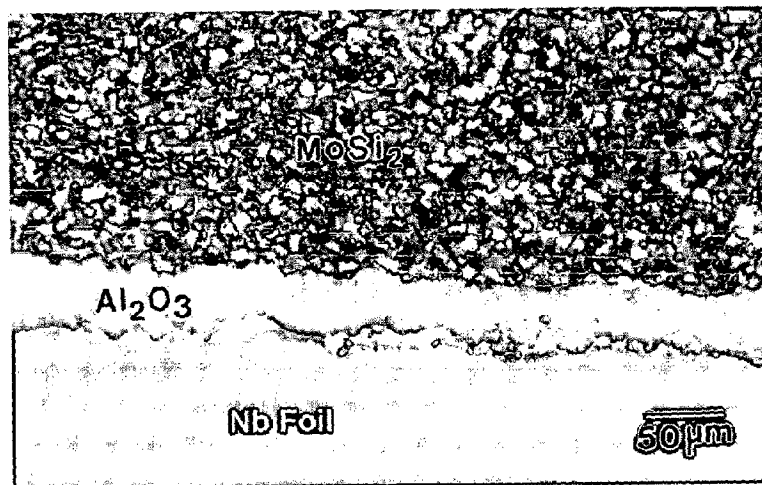


(b)

Fig. 5.94 Standard free energy change (per mole of  $\text{MoSi}_2$ ) for chemical reactions likely to take place between (a)  $\text{Al}_2\text{O}_3$  and  $\text{MoSi}_2$  and (b) between  $\text{Al}_2\text{O}_3$  and  $\text{Nb}$ .



(a)



(b)

Fig. 5.95 Microstructures of  $(\text{MoSi}_2 + 20 \text{ vol}\% \text{ SiC}_p) + \text{Al}_2\text{O}_3$  coated Nb foil laminated composite (a) ordinary light optical micrograph and (b) polarized light optical micrograph.

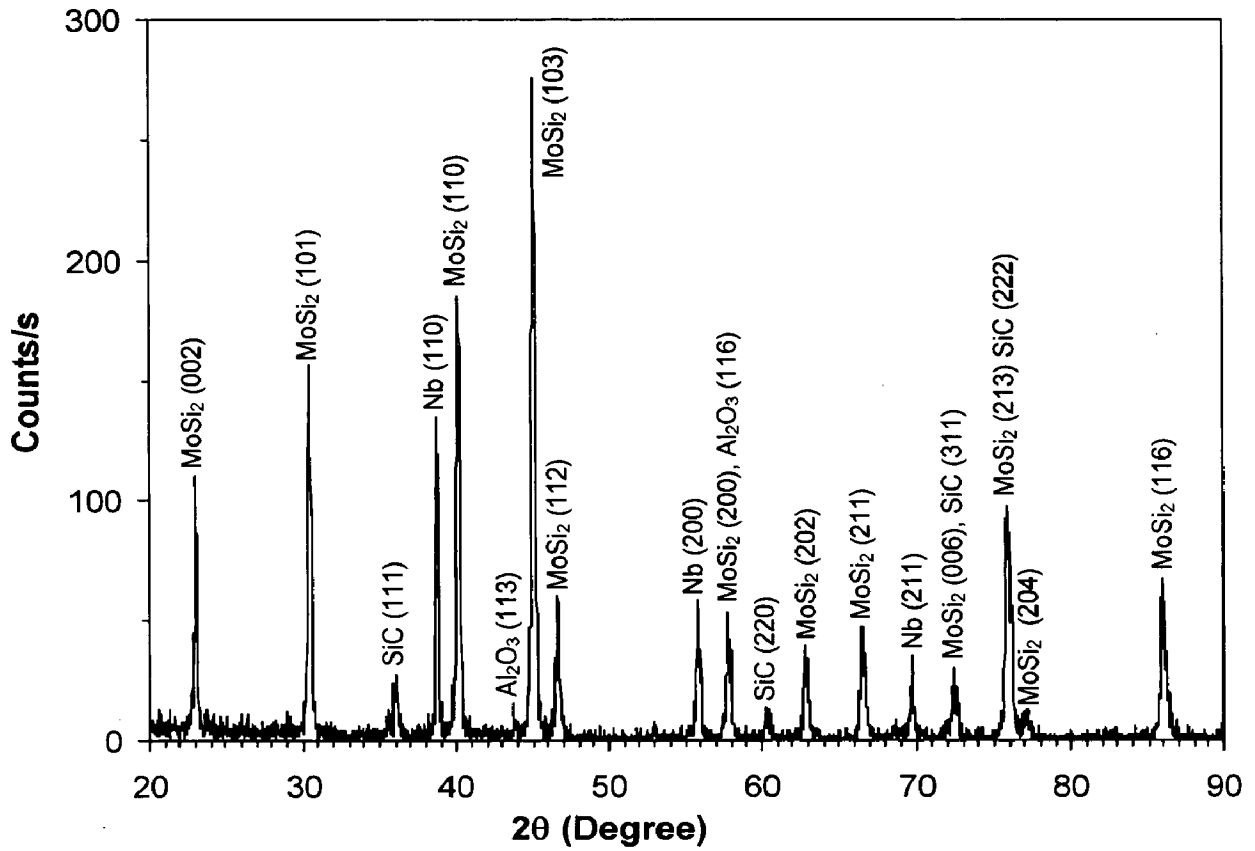


Fig. 5.96 X-ray diffraction pattern of (MoSi<sub>2</sub> + 20 vol% SiC<sub>p</sub>) + Al<sub>2</sub>O<sub>3</sub> coated Nb foil laminated composite.

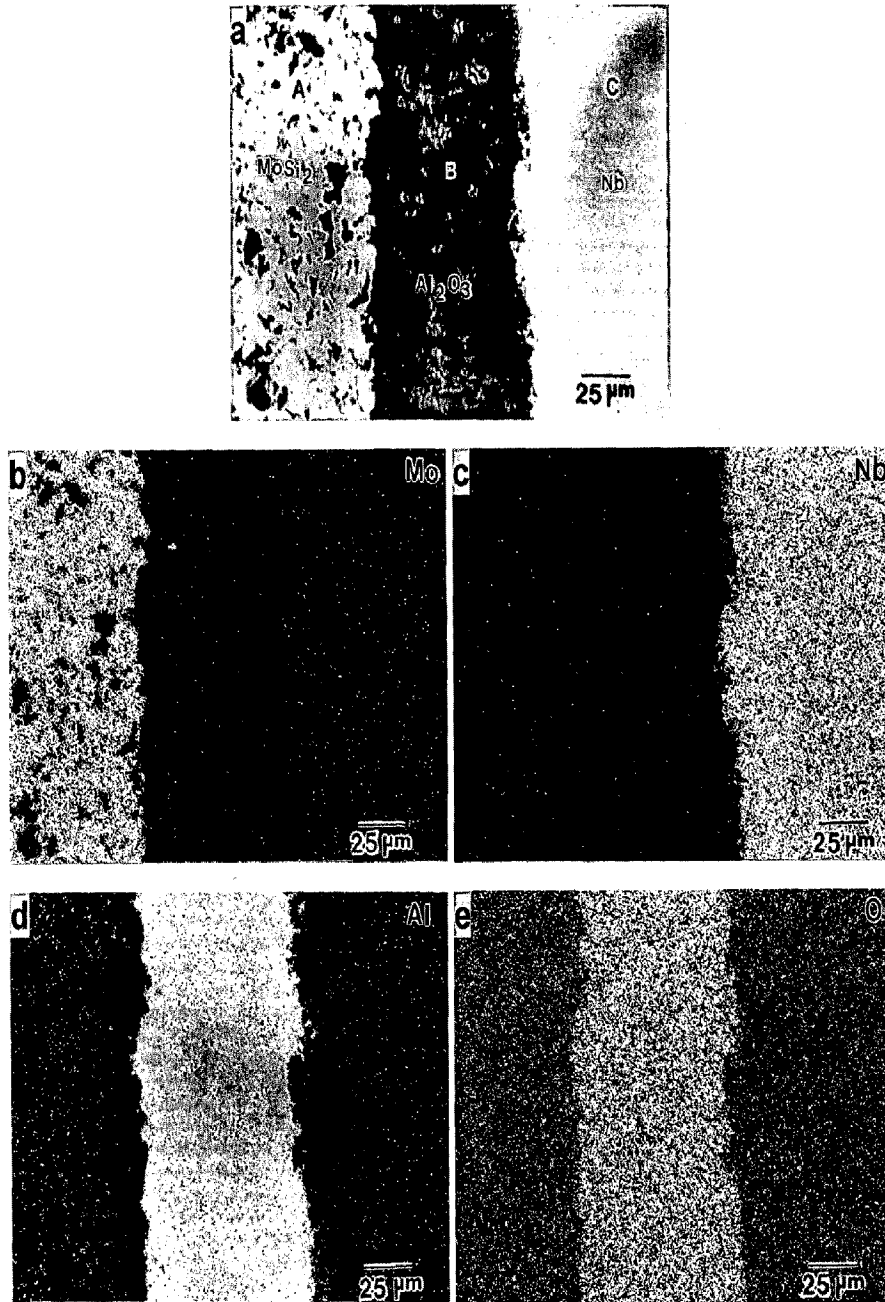


Fig. 5.97 EPMA images of  $(\text{MoSi}_2 + 20 \text{ vol}\% \text{ SiC}_p) + \text{Al}_2\text{O}_3$  coated Nb foil laminated composite (a) back scattered electron image (b) x-ray map of Mo (c) x-ray map of Nb (d) x-ray map Al and (e) x-ray map of oxygen.

The x-ray maps of Mo and Nb as shown in Figs. 5.97(b) and 5.97(c), respectively, also reveal that no diffusion of Mo and Nb has taken place across the interface through the Al<sub>2</sub>O<sub>3</sub> coating. The x-ray maps of Al and oxygen are presented in Figs. 5.97(d) and 5.97(e), respectively. Table 5.21 presents the quantitative micro-probe data taken at different locations marked as A, B, and C in Fig. 5.97(a). The quantitative chemical analysis confirms the phases as MoSi<sub>2</sub>, Al<sub>2</sub>O<sub>3</sub> and Nb in the regions marked as A, B and C, respectively.

Table 5.21 Electron probe micro-analysis (EPMA) of the interface between MoSi<sub>2</sub> + 20 vol% SiC<sub>p</sub> matrix and Al<sub>2</sub>O<sub>3</sub> coated Nb foil laminated composite (Fig. 5.97(a)). All compositions are given in atom percent.

Region	Mo	Si	Nb	Al	O	Phase
A	32.351	67.649	0.000	0.000	0.000	~ MoSi <sub>2</sub>
B	0.000	0.188	0.000	38.446	61.366	~ Al <sub>2</sub> O <sub>3</sub>
C	0.000	0.224	99.776	0.000	0.000	~ Nb

Fig. 5.98(a) shows again, an EPMA back scattered electron image of the Al<sub>2</sub>O<sub>3</sub> coated Nb foil laminated composite. The same image was recorded with higher contrast setting and is shown in Fig. 5.98(b) where the MoSi<sub>2</sub> and Al<sub>2</sub>O<sub>3</sub> phases were shaded completely dark to improve the contrast within the Nb region. This reveals the presence of a very thin Si rich layer at Al<sub>2</sub>O<sub>3</sub> - Nb interface as indicated by the arrow marks. The x-ray map of Si as shown in Fig. 5.98(c), confirms that the thin layer at Al<sub>2</sub>O<sub>3</sub> - Nb foil interface is indeed Si rich. These observations suggest that a small amount of Si has diffused through the Al<sub>2</sub>O<sub>3</sub> coating towards Nb. The thickness of this Si rich reaction layer was found to be ~ 4 to 5 μm. The exact reaction product in this case could not be determined by quantitative analysis because of its very small thickness. However, it is assumed to be Nb<sub>5</sub>Si<sub>3</sub>.

Figure 5.99(a) exhibits the EPMA back scattered electron image of Al<sub>2</sub>O<sub>3</sub> coated Nb foil composite taken at a low magnification showing the Al<sub>2</sub>O<sub>3</sub> coating on both sides of the Nb foil. The x-ray map of Si and the corresponding Si line scan across the interface are shown in Figs. 5.99(b) and 5.99(c), respectively. It is evident from these figures that diffusion of Si has taken place through Al<sub>2</sub>O<sub>3</sub> coating towards the Nb foil. However, the thickness of the interaction zone was reduced to ~ 4 to 5 μm only. Therefore, it was found that even though Al<sub>2</sub>O<sub>3</sub> is chemically compatible with Nb and



MoSi<sub>2</sub>, the coating was not a perfect barrier for Si diffusion. However, the coating was quite effective in suppressing the Nb and Mo diffusion and retarding the Si diffusion substantially, which significantly reduces the growth rate of the reaction layer. Presence of Al<sub>2</sub>O<sub>3</sub> coating in between MoSi<sub>2</sub> matrix and the Nb reinforcement also helps by increasing the diffusion distances for Mo, Nb and Si. The suppression of Nb diffusion across the coating leads to the absence of reaction and formation of new phase at the interface in the MoSi<sub>2</sub> side. Whereas, the suppression of Mo diffusion results in the formation of a thin Si rich layer presumably of Nb<sub>5</sub>Si<sub>3</sub>, instead of the ternary compound (Nb, Mo)<sub>5</sub>Si<sub>3</sub> in the Nb side.

The average thickness of the Al<sub>2</sub>O<sub>3</sub> coating measured was ~ 75 μm on one side of the Nb foil and ~ 50 μm on the other side of the foil. The difference in the coating thickness resulted due to the difficulty in controlling the plasma spray process employed in the present investigation in which the plasma torch was hand-held. Si line scan also indicates a higher concentration of Si at the Nb / Al<sub>2</sub>O<sub>3</sub> interface on the side where the Al<sub>2</sub>O<sub>3</sub> coating was relatively thinner as compared to the Si concentration at the Nb / Al<sub>2</sub>O<sub>3</sub> interface on the thicker Al<sub>2</sub>O<sub>3</sub> coating side. This suggests that the thickness of the Al<sub>2</sub>O<sub>3</sub> coating also plays an important role in controlling the Si diffusion as the diffusion distances vary with thickness of the coating.

### **5.5.2 Mechanical Properties**

The room temperature mechanical properties of (MoSi<sub>2</sub> + 20 vol% SiC<sub>p</sub>) + Al<sub>2</sub>O<sub>3</sub> coated Nb foil laminated composite are presented in Tables 5.22 and 5.23. Each data point in Tables 5.22 and 5.23 is an average of minimum 4 tests.

The elastic modulus of Al<sub>2</sub>O<sub>3</sub> coated Nb foil laminated composite is slightly lower than uncoated Nb foil laminated composite. The higher elastic modulus of the laminated composite with uncoated Nb foil could be due to the presence of Nb<sub>5</sub>Si<sub>3</sub> silicide phase at the expense of some thickness of Nb foil, although the effect of the presence of Nb<sub>5</sub>Si<sub>3</sub> phase on elastic modulus of the composite can not be predicted in absence of the elastic properties of Nb<sub>5</sub>Si<sub>3</sub>.

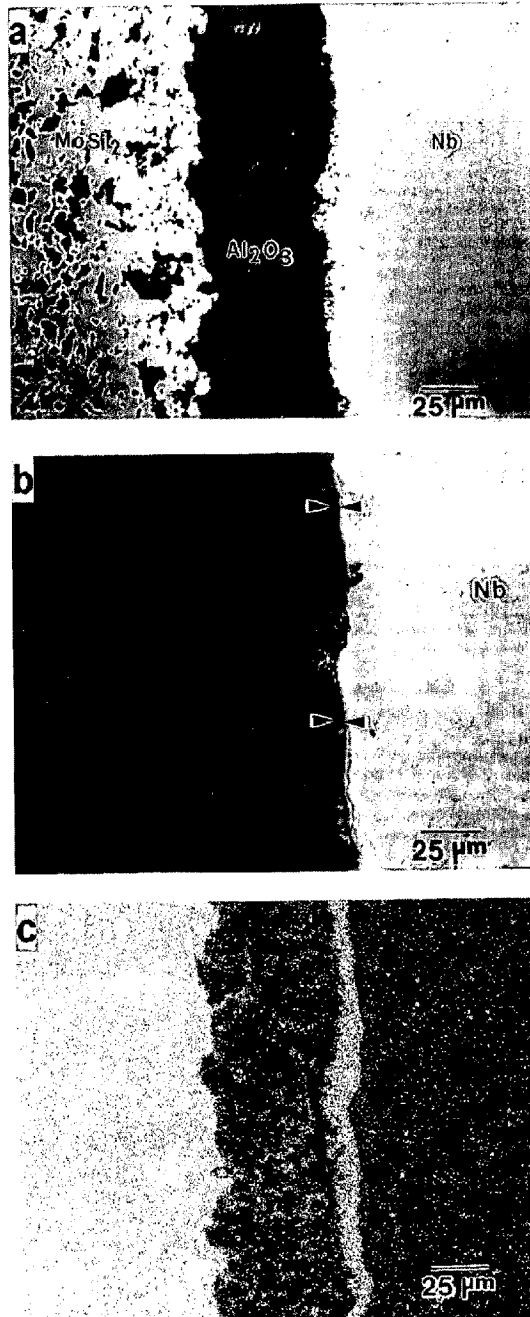


Fig. 5.98 EPMA images of  $(\text{MoSi}_2 + 20 \text{ vol}\% \text{ SiC}_p) + \text{Al}_2\text{O}_3$  coated Nb foil laminated composite (a) back scattered electron image (b) BSE image shaded dark to reveal the Si rich interfacial layer between  $\text{Al}_2\text{O}_3$  coating and Nb foil and (c) x-ray map of Si.

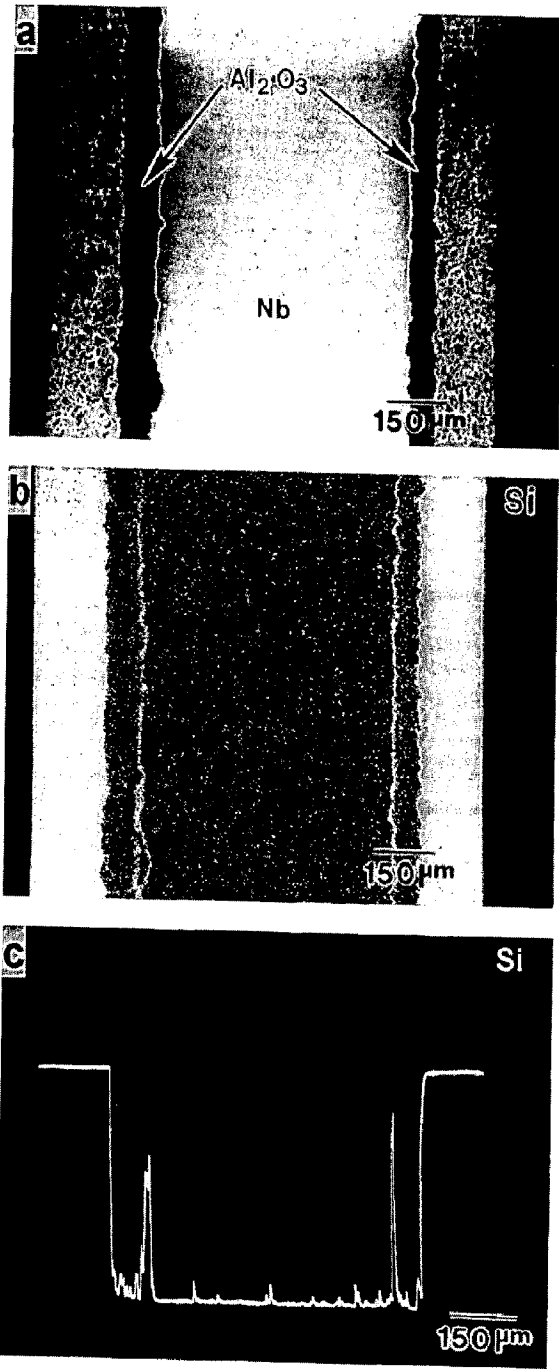


Fig. 5.99 Low magnification EPMA images of (MoSi<sub>2</sub> + 20 vol% SiC<sub>p</sub>) + Al<sub>2</sub>O<sub>3</sub> coated Nb foil composite showing Al<sub>2</sub>O<sub>3</sub> coating on both sides of the Nb foil (a) back scattered electron image (b) x-ray map of Si and (c).line scan of Si.

Table 5.22 Mechanical properties of (MoSi<sub>2</sub> + 20 vol% SiC<sub>p</sub>) + Al<sub>2</sub>O<sub>3</sub> coated Nb foil laminated composite.

Property	Value
Elastic Modulus (GPa)	320
Matrix Hardness (GPa)	16.4
Foil Hardness (VHN)	142
Matrix Indentation Fracture Toughness, K <sub>IC</sub> (MPa√m)	5.3

Table 5.23 Strength and toughness values of (MoSi<sub>2</sub> + 20 vol% SiC<sub>p</sub>) + Al<sub>2</sub>O<sub>3</sub> coated Nb foil laminated composite.

Property	Crack Arrester Mode	Crack Divider Mode
Flexural strength (MPa)	338	311
Fracture Toughness, K <sub>max</sub> (MPa√m)	13.4	6.1
Work of Fracture (J/m <sup>2</sup> )	22,600	3,954

The hardness and the indentation fracture toughness values obtained as measured inside the matrix layer were same as in case of uncoated Nb foil laminated composite. This is understandable as both the laminated composites consist of the same matrix layer ( $\text{MoSi}_2 + 20 \text{ vol } \% \text{ SiC}_p$ ). However, the hardness of the  $\text{Al}_2\text{O}_3$  coated Nb foil is found to be slightly higher than the hardness of the uncoated Nb foil after processing into the laminated structures.

Figure 5.100 shows the behaviour of indentation cracks at the interface in  $\text{Al}_2\text{O}_3$  coated Nb foil reinforced laminated composite. The optical micrograph in Fig. 5.100(a) exhibits that the indentation crack appears to enter inside the Nb foil after passing through the brittle  $\text{Al}_2\text{O}_3$  coating. It does not end at the  $\text{Al}_2\text{O}_3 / \text{Nb}$  interface. The observation of the enclosed area in Fig. 5.100(a) at a much higher magnification under SEM reveals the presence of a thin Si rich layer at the  $\text{Al}_2\text{O}_3 / \text{Nb}$  interface also evident from EPMA studies as described in section 5.5.1. This thin layer of Si rich Nb bearing phase appears to be brittle. The crack propagates through this layer but is stopped as soon as it impinges on Nb as indicated by the arrowhead. As observed in the case of uncoated Nb foil laminated composite, debonding at the interface does not occur here when the crack approaches the interface or just impinges on it.

As presented in Table 5.23, the flexural strength and fracture toughness,  $K_{\text{max}}$  values of  $(\text{MoSi}_2 + 20 \text{ vol } \% \text{ SiC}_p) + \text{Al}_2\text{O}_3$  coated Nb foil laminated composite are lower than the values obtained for  $(\text{MoSi}_2 + 20 \text{ vol } \% \text{ SiC}_p) + \text{uncoated Nb foil laminated composite}$  (Table 5.19) in both crack arrester as well as in crack divider modes. However, the work of fracture for  $\text{Al}_2\text{O}_3$  coated Nb foil reinforced composite is greater than that for the uncoated Nb foil reinforced composite. The observed behaviour could be attributed to a lower constraint due to weaker  $\text{MoSi}_2 / \text{Al}_2\text{O}_3$  interfacial bonding as compared to the bonding between  $\text{MoSi}_2 / \text{Nb}_5\text{Si}_3$  and between  $\text{Nb}_5\text{Si}_3 / \text{Nb}$  in uncoated Nb foil laminated composite. In case of uncoated Nb foil laminated composite, the chemical interactions between  $\text{MoSi}_2\text{-SiC}_p$  matrix and the Nb foil result in the formation of an intermetallic compound  $\text{Nb}_5\text{Si}_3$  which establishes a strong chemical bond between matrix layer and the metal foil. In contrast, the  $\text{MoSi}_2 / \text{Al}_2\text{O}_3$  interfacial bonding in  $\text{Al}_2\text{O}_3$  coated Nb foil laminated composite is essentially of mechanical nature as no chemical interactions take place between  $\text{MoSi}_2\text{-SiC}_p$  matrix layer and the  $\text{Al}_2\text{O}_3$  coating. The mechanical nature of bonding is believed to result in

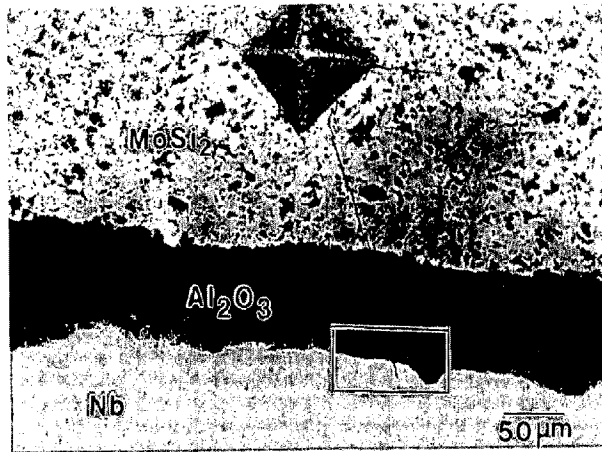
lower interfacial fracture energy as compared to the chemical bonding. Lower the interfacial fracture energy, lower is the constraint imposed by the matrix on the deformation of the Nb foil. A lower matrix constraint results in higher decohesion length at the matrix - reinforcement interface. Due to higher decohesion at the interface, more Nb participates in deformation and deforms under much less constrained conditions. Because of this feature, the total energy consumed to break a specimen (area under the curve) for the  $\text{Al}_2\text{O}_3$  coated Nb foil composite is larger than that to break the uncoated Nb foil composite. A stronger interfacial bond in uncoated Nb foil laminated composite imposes a higher degree of constraint by the brittle matrix on the ductile foil which results in a higher peak load and therefore a higher fracture toughness measured in terms of  $K_{\text{max}}$ .

In addition, the effective thickness of the unreacted Nb foil is higher in case of  $\text{Al}_2\text{O}_3$  coated Nb foil composite as compared to the uncoated Nb foil laminated composite due to limited diffusion of Si through the  $\text{Al}_2\text{O}_3$  coating. Therefore, higher work of fracture is obtained here as more Nb undergoes plastic deformation.

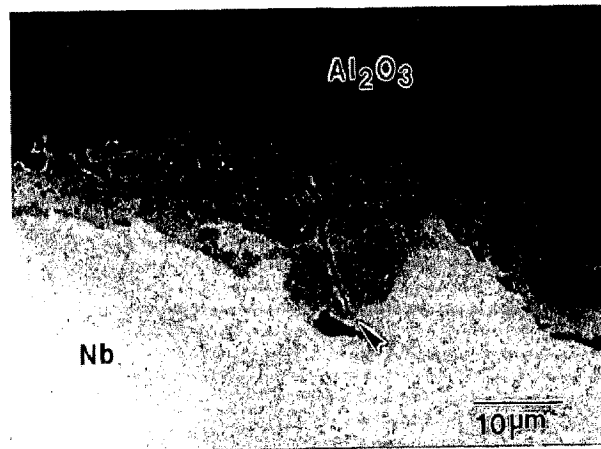
## 5.6 EFFECT OF NB FOIL EMBRITTLEMENT

A laminated composite consisting of alternate layers of  $\text{MoSi}_2 + 20 \text{ vol}\% \text{ SiC}_p$  and Nb foil was prepared by vacuum hot pressing at low vacuum level ( $10^{-2}$  torr) to allow the oxygen pick up by Nb foil during the high temperature processing. All other processing parameters were kept same as described in section 3.2.4.

The room temperature mechanical properties of embrittled Nb foil laminated composite are presented in Table 5.24 and a typical load – displacement curve obtained in crack arrester mode is shown in Fig. 5.101. Nb foil failed in a brittle manner and did not undergo any plastic deformation. The brittle fracture of the Nb was probably due to the diffusion of interstitial oxygen into the foil during high temperature processing under low vacuum conditions. The measurement of Vickers hardness of the Nb foil in the composite exhibited that the hardness increased from 137 to 509 as the Nb foil becomes embrittled indicating an increase in the slip resistance of the Nb. Loss of ductility of the foil leads to little lateral plastic deformation of the Nb and, therefore, is expected to result in negligible decohesion length. The crack propagated straight through the foil resulting in a catastrophic failure.



(a)



(b)

Fig. 5.100 (a) Optical micrograph showing a typical hardness indentation mark and radial indentation cracks in  $(\text{MoSi}_2 + 20\ \text{vol}\% \text{SiC}_p) + \text{Nb}$  foil ( $\text{Al}_2\text{O}_3$  coated) laminated composite (b) SEM back scattered electron image of the area bounded by the rectangle in Fig. 5.100(a).

Table 5.24 Properties of  $(\text{MoSi}_2 + 20 \text{ vol\% SiC}_p) + \text{Nb}$  foil embrittled laminated composite

Property	Crack Arrester Mode	Crack Divider Mode
Hardness of Nb foil (VHN)	509	
Flexural strength (MPa)	301	297
Fracture Toughness, $K_{\max}$ (MPa $\sqrt{\text{m}}$ )	10.1	5.8
Work of Fracture (J/m <sup>2</sup> )	727	375

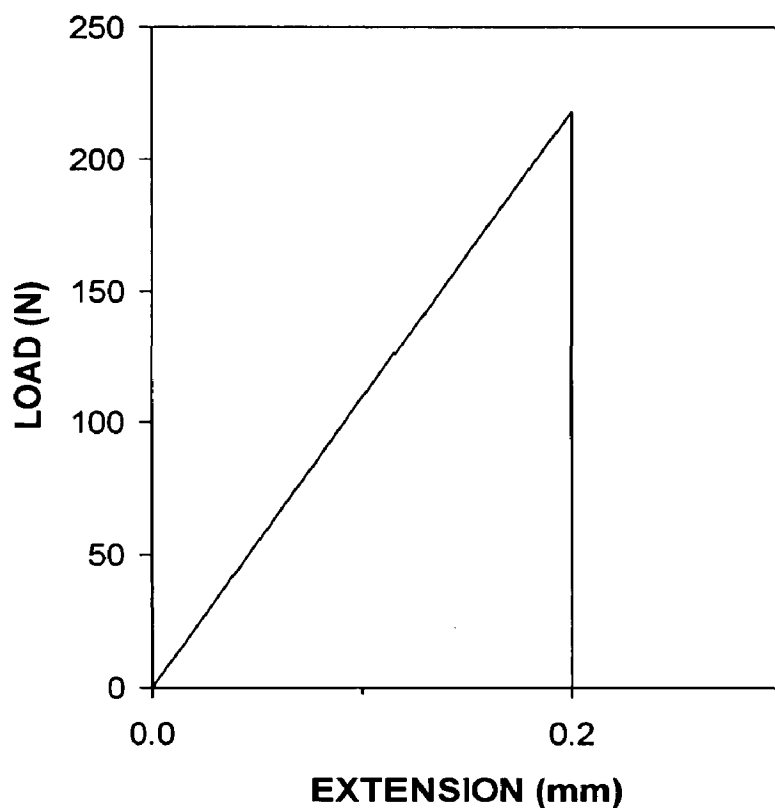


Fig. 5.101 A typical load - displacement curve of  $(\text{MoSi}_2 + 20 \text{ vol\% SiC}_p) + \text{Nb}$  foil embrittled laminated composite tested for fracture toughness in crack arrester mode.



The measured value of the work of fracture in crack arrester mode is  $727 \text{ J/m}^2$ , which is significantly lower as compared to the work of fracture of  $17,280 \text{ J/m}^2$  (Table 5.19) when the Nb foil failed in a ductile manner. There is a significant drop in work of fracture measured in crack divider mode also. However, the decrease in flexural strength and damage tolerance,  $K_{\max}$ , both in crack arrester as well as in crack divider modes is relatively less as compared to the decrease in work of fracture. The flexural strength and the damage tolerance are calculated from the peak load. As described earlier, the peak load in a bending test depends on the degree of constraint imposed by the brittle matrix and the strength of the metal foil, whereas, the work of fracture depends on the extent of interfacial debonding as well as the ability of the metal foil to undergo plastic deformation.

Observation of fracture surface also reveals a change of fracture mode from ductile to cleavage. A typical fracture surface of an embrittled Nb foil in  $(\text{MoSi}_2 + 20 \text{ vol\% SiC}_p) + \text{Nb}$  foil laminated composite tested in crack arrester mode is shown in Fig. 5.102. It exhibits a 100 % brittle cleavage fracture. The fracture surface is marked with cleavage steps and river patterns. Because cleavage occurs along well-defined crystallographic planes within each grain, the cleavage fracture changes directions when it crosses grain or subgrain boundaries. Cleavage fracture initiates on many parallel cleavage planes. As the fracture advances, the number of active planes decreases by a joining process that forms progressively higher cleavage steps. This network of cleavage steps is referred as river pattern. The branches of the river pattern join in the direction of crack propagation. River patterns represent steps between different local cleavage facets at slightly different heights but along the same general cleavage plane. Brittle cleavage fracture can occur in bcc metals such as W, Mo and Nb if embrittled by oxygen, nitrogen or carbon. It has been well established that Nb can be embrittled by oxygen and Si (Hahn et al, 1963, Wilkinson, 1969, Chung and Stoloff, 1978). The hardness of the Nb has been found to increase sharply with increase in oxygen content. The loss of ductility of Nb during processing could result in little improvement in the work of fracture of the composites.

The above results reveal that as a crack approaches the ductile reinforcement in these laminated composite systems, there exists two competitive mechanisms, interfacial debonding and / or multiple matrix fracture with plastic deformation of the

ductile reinforcement or direct crack propagation through the ductile reinforcement. In the case of high ductility of the reinforcement, the crack is blunted by local dislocation slip of the ductile phase. Thus, for the ductile reinforcement to fail, a much higher stress has to be applied which increases shear stresses at the interface due to load transfer and transverse stresses caused by the difference between lateral displacement of the matrix and the reinforcement. Both shear and transverse stresses enhance interfacial debonding and / or multiple matrix fracture. For the case of a low ductility of the reinforcement, the crack can relatively easily propagate through the reinforcement before the occurrence of interfacial debonding or multiple matrix fracture. However, if the thermal expansion mismatch between matrix and the refractory metal foil is large enough to give rise to very high residual stresses in the composite, the crack can propagate along the interface resulting in large scale interfacial debonding and shear failure of the composite specimen as observed in (MoSi<sub>2</sub> + 2 wt% Al) + Mo foil laminated composite, in the present work.

## 5.7 DISCUSSION

In the present investigation, different ductile refractory metals have been used as the reinforcement in MoSi<sub>2</sub> matrix in order to understand the ductile phase toughening of MoSi<sub>2</sub>, which is a brittle material at room temperature. To further investigate the effect of reinforcement morphology, the ductile phases were added in particulate as well continuous (foil) form. Moreover, the MoSi<sub>2</sub> matrix itself was modified by additions of pure Al and SiC particulates to obtain the synergistic effects with ductile reinforcements as well as to improve the thermal compatibility between MoSi<sub>2</sub> and the various ductile phases. Most of these ductile refractory metals react with MoSi<sub>2</sub> matrix at high processing temperatures. An inert diffusion barrier coating of Al<sub>2</sub>O<sub>3</sub> was also tried in case of MoSi<sub>2</sub> with Nb foil laminated composite to restrict the interdiffusion of Si and other elements across the interface between matrix and the reinforcement. Some of the observations and results obtained in the present work as described in earlier sections are further discussed and explained in this section. A variety of reaction products are formed in different MoSi<sub>2</sub> based composites investigated in the present study. The formation of various phases at the interface is also described in the following sections based on the thermodynamic and kinetic principles.

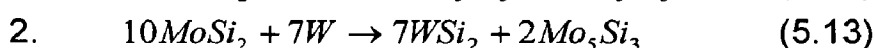
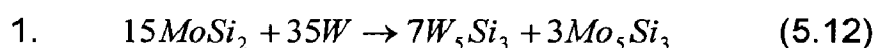


Fig. 5.102 Fracture surface of an embrittled Nb foil in  $(\text{MoSi}_2 + 20 \text{ vol}\% \text{ SiC}_p) + \text{Nb}$  foil laminated composite tested in crack arrester mode.

### 5.7.1 Particulate Composites with Pure MoSi<sub>2</sub> as Matrix

The microstructures of MoSi<sub>2</sub> reinforced with W, Mo and Nb particulate composites reveal the grain size of MoSi<sub>2</sub> is in the range of 10 - 15 μm which is significantly higher than the average particle size of MoSi<sub>2</sub> (6 μm) powder used prior to hot pressing. This is believed to be the effect of grain growth in MoSi<sub>2</sub> at high processing temperatures. Gac and Petrovic (1985) have also reported similar grain growth in the case of pure MoSi<sub>2</sub>. They have observed an average grain size of 30 μm after hot pressing the pure MoSi<sub>2</sub> having an average particle size of 5 μm prior to hot pressing. In their case some grains have been as large as 60 μm in size. However, in the present case, formation of other silicide phases during processing restricts the grain growth of MoSi<sub>2</sub> with W, Mo and Nb particles. Venkateswara Rao et al (1992<sup>a</sup>, 1992<sup>b</sup>) have reported a grain size of 14 μm in case of MoSi<sub>2</sub> + 20 vol% Nb particulate composite hipped at 1700 °C.

Two silicides W<sub>5</sub>Si<sub>3</sub> and WSi<sub>2</sub> are reported in the W-Si binary phase diagram as depicted in Fig. 5.103 (Vahlas et al, 1989). In MoSi<sub>2</sub> + 20 vol% W particulate composite, Si diffuses and reacts with W. The chemical interaction between MoSi<sub>2</sub> and pure W may proceed as per the following reactions:



The standard free energy change ( $\Delta G$ , per mole of MoSi<sub>2</sub>) for the above chemical reactions was calculated and presented in Fig. 5.104. Equations 5.12 and 5.13 are depicted as Reaction 1 and Reaction 2 in Fig. 5.104, respectively. It can be observed from Fig. 5.104 that  $\Delta G$  is more negative for reaction 1 at all temperatures. This suggests that the formation of W<sub>5</sub>Si<sub>3</sub> is more favourable than WSi<sub>2</sub>. The same has been observed in the present study as described in section 5.2.1. Pure W particles are fully converted into W<sub>5</sub>Si<sub>3</sub>. However, the formation of some WSi<sub>2</sub> is also observed due to W diffusion towards MoSi<sub>2</sub>, which is in the form of solid solution with MoSi<sub>2</sub>. The activation energy for WSi<sub>2</sub> growth has been reported as 105 kJ/mole (Gage and Bartlett, 1965), which is lower than the activation energy for Si diffusion in W<sub>5</sub>Si<sub>3</sub> reported as 360 kJ/mole by Tortorici and Dayananda (1999). Growth of WSi<sub>2</sub>

is expected to be much faster than  $W_5Si_3$ . However, the thermodynamic calculations show that  $W_5Si_3$  is more stable than  $WSi_2$  at all temperatures.

The Mo-Si binary system has three stable silicide phases,  $MoSi_2$ ,  $Mo_5Si_3$  and  $Mo_3Si$  as depicted in Mo-Si binary phase diagram in Fig. 1.2 (Gokhale and Abbaschian, 1991). The following possible chemical reactions between  $MoSi_2$  and pure Mo are considered and free energy change vs. temperature for both the reactions is plotted as shown in Fig. 5.105. Equations 5.14 and 5.15 are depicted as Reaction 1 and Reaction 2 in Fig. 5.105, respectively.

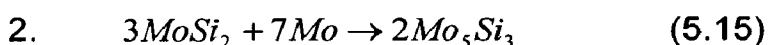
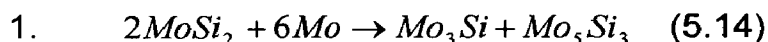
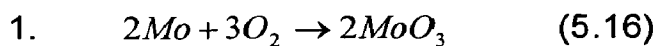


Figure 5.105 exhibits that free energy change per mole of  $MoSi_2$  is slightly more negative at all the temperatures for the formation of  $Mo_5Si_3$  alone as compared to the chemical reaction resulting in the formation of both the silicides,  $Mo_3Si$  and  $Mo_5Si_3$  together.

The x-ray diffraction pattern of  $MoSi_2$  - Mo composite (Fig. 5.17) exhibits the peaks of  $MoO_2$  (melting point 2327 °C) in contrast to the x-ray diffraction pattern of as received Mo powder (Fig. 5.2(b)), which exhibits the peaks of  $MoO_3$ . The  $MoO_3$  is a low melting point (800 °C) oxide and is likely to get vaporized during the processing at high temperatures. However, some oxidation of Mo could have occurred during high temperature processing due to its high affinity with oxygen. This could result in the formation of  $MoO_2$ . The oxidation of pure Mo can proceed according to the following reactions:



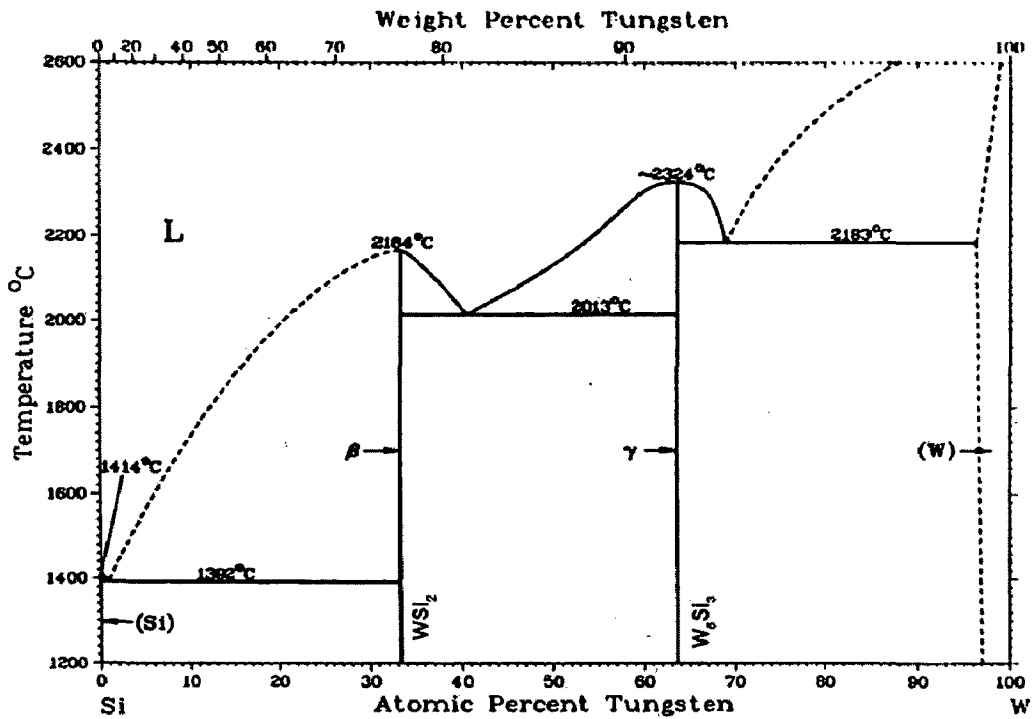


Fig. 5.103 W-Si binary phase diagram

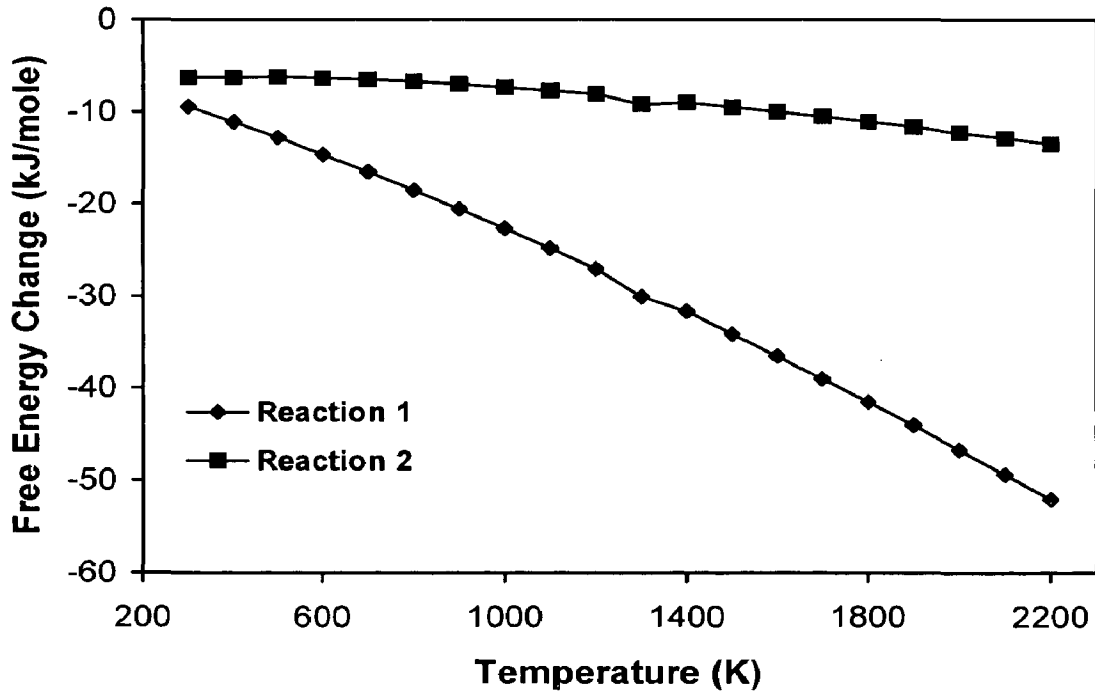


Fig. 5.104 Standard free energy change ( $\Delta G$  vs. *Temperature*) for the possible chemical reactions between  $MoSi_2$  and pure W resulting in the formation of various tungsten silicides.

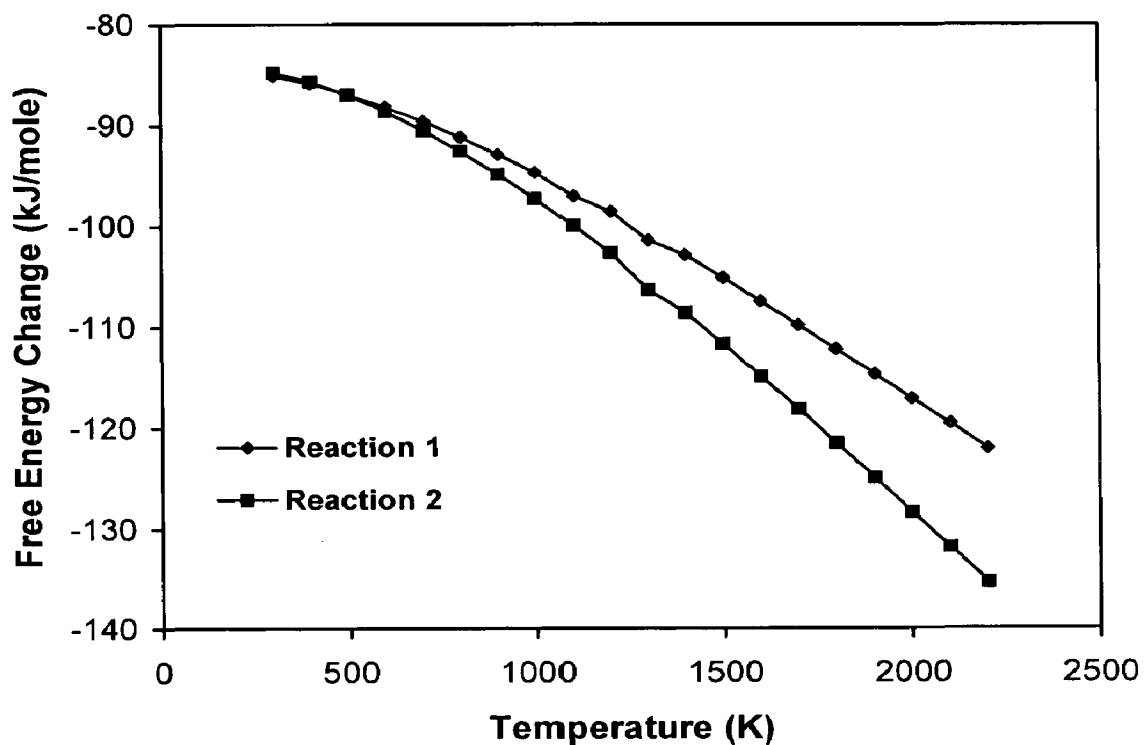
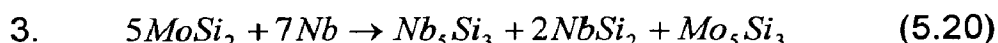
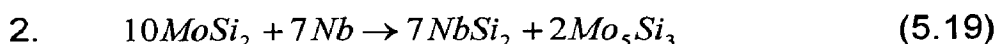


Fig. 5.105 Standard free energy change ( $\Delta G$  vs. *Temperature*) for the possible chemical reactions between  $\text{MoSi}_2$  and pure Mo resulting in the formation of other molybdenum silicides.

The standard free energy change,  $\Delta G$  (per mole of  $O_2$ ) with temperature is plotted for the above reactions in Fig. 5.106 (Equations 5.16 and 5.17 are depicted as Reaction 1 and Reaction 2 in Fig. 5.106, respectively), which shows that  $\Delta G$  is negative for both the oxidation reactions over the entire temperature range. However, the formation of  $MoO_2$  is thermodynamically more favourable ( $\Delta G$  is more negative) as compared to the formation of  $MoO_3$ . If some  $MoO_3$  also forms, it is likely to get vapourized above  $\sim 1200$  °C or is likely to get reduced to  $MoO_2$  as hot pressing is done under carbon atmosphere. Fig. 5.107 shows Mo-O binary phase diagram, which also suggests that under vacuum,  $MoO_2$  is more likely to form due to lower partial pressure of oxygen.

Figure 5.108 shows a Nb-Si binary phase diagram (Schlesinger et al, 1993) exhibiting only two stable silicides,  $NbSi_2$  and  $Nb_5Si_3$  at room temperature. A third phase  $Nb_3Si$  is stable between 1770 to 1980 °C. The possible chemical reactions between  $MoSi_2$  and Nb resulting in the formation of  $Nb_5Si_3$  and  $NbSi_2$  are as follows:



The standard free energy change for the above reactions with respect to temperature is plotted in Fig. 5.109.  $\Delta G$  (per mole of  $MoSi_2$ ) is much more negative for equation 5.18 (depicted in Fig. 5.109 as Reaction 1) leading to the formation of  $Nb_5Si_3$  as compared to reactions 2 and 3 (equations 5.19 and 5.20) which result in the formation of  $NbSi_2$  as one of the reaction products at all temperatures.

As exhibited in Fig. 5.21(c) and 5.21(d), extensive diffusion of Si and Mo has taken place into pure Nb. Si seems to have diffused more rapidly and uniformly than Mo. This is in agreement with the Si and Mo diffusivities in Nb. The diffusivities of Si and Mo in Nb are given by the following equations (Roux & Vignes, 1970, Fitzer & Schmidt, 1971):

$$D_{Si} = 0.51 \times 10^{-2} \exp(-48000/RT) \quad \text{at } T = 700 - 1500 \text{ °C} \quad (5.21)$$

$$D_{Mo} = 92 \exp(-122000/RT) \quad \text{at } T = 1725 - 2182 \text{ °C} \quad (5.22)$$



Although equation (5.21) is valid only between 700 – 1500 °C, the approximate values of diffusivities of Si and Mo in Nb at hot pressing temperature of 1750 °C are calculated as follows:

$$D_{\text{Si in Nb}} = 3.59 \times 10^{-8} \text{ cm}^2/\text{s}$$
$$D_{\text{Mo in Nb}} = 7.38 \times 10^{-12} \text{ cm}^2/\text{s}$$

The diffusivity of Si in Nb at 1750 °C is higher by four orders of magnitude than diffusivity of Mo in Nb. This clearly indicates that Si atoms have diffused much more rapidly than Mo atoms in Nb.

The X-ray diffraction patterns of all the ductile refractory metal particulate reinforced MoSi<sub>2</sub> matrix composites as depicted in Figs. 5.14, 5.17 and 5.20 show one interesting feature, i.e., the peaks of pure W, pure Mo and pure Nb were totally missing. This indicates that most of the refractory metal particles used as reinforcements were completely consumed in the formation of their silicides. Carter & Hurley (1987) have also reported similar observations in case of MoSi<sub>2</sub> reinforced with fine Nb (average size = 5 μm) powder. Coarser Nb particles (average size = 50 μm) were added to minimize the percentage of the reaction products. There was still a substantial reaction layer and cracks occurred in (Nb, Mo)<sub>5</sub>Si<sub>3</sub> layer. They also found that no reaction layer existed in case of a composite consisting of 50 vol% Ta particles and MoSi<sub>2</sub>, suggesting that Ta might be a better ductile metal reinforcement than Nb in MoSi<sub>2</sub>.

It is interesting to note that the flexural strength of all the three composites improved considerably over the monolithic MoSi<sub>2</sub> while retaining the fracture toughness. The most remarkable increase of 117 % was observed in case of MoSi<sub>2</sub>-Mo composite. The increase in flexural strength is due to the formation of R<sub>5</sub>Si<sub>3</sub> type refractory metal silicides as well as grain refinement of MoSi<sub>2</sub> matrix.

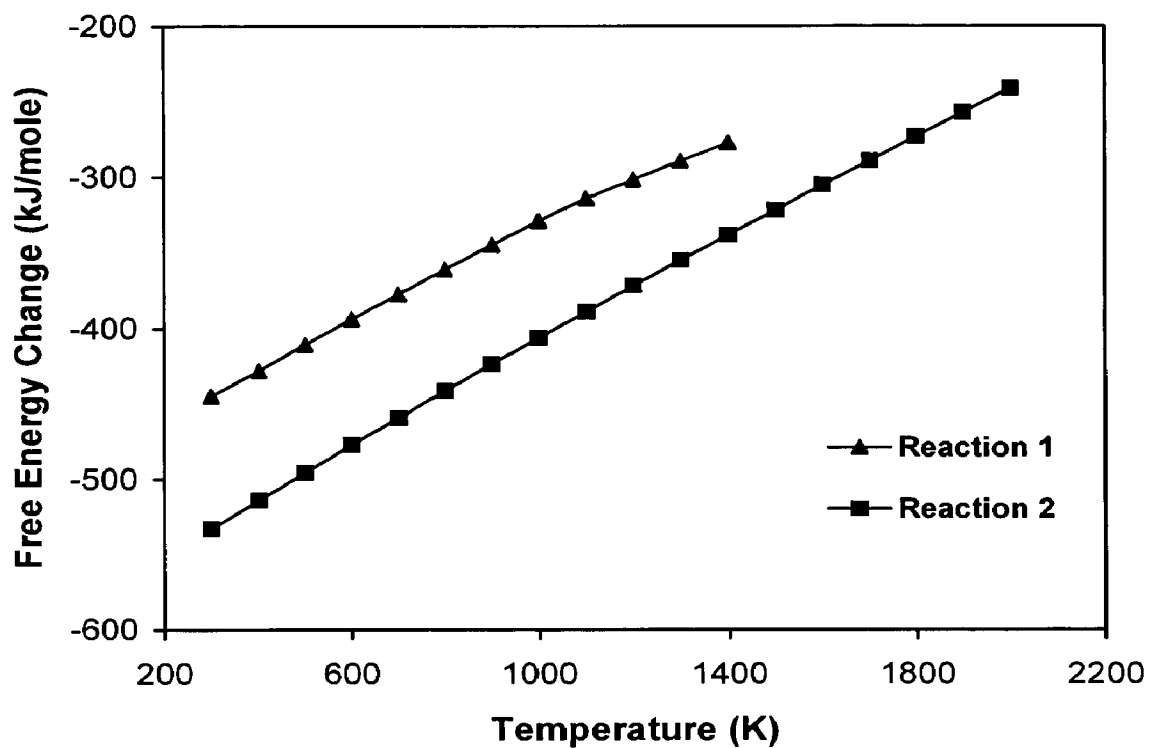


Fig. 5.106 Standard free energy change ( $\Delta G$  vs. temperature) for oxidation of pure Mo.

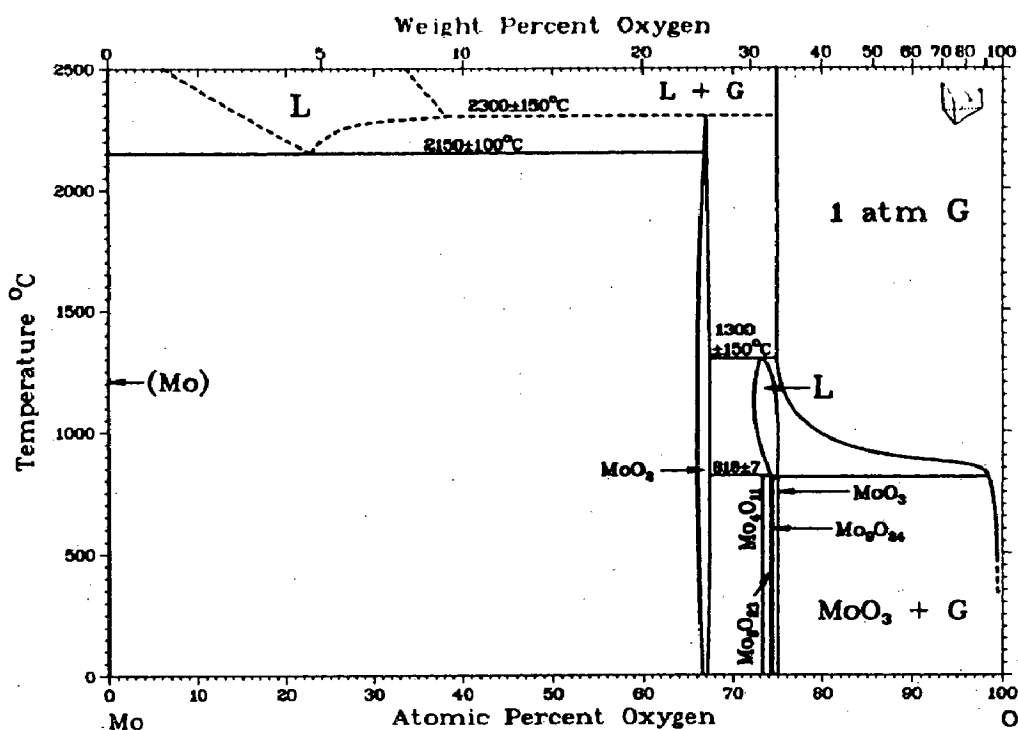


Fig. 5.107 Mo-O binary phase diagram

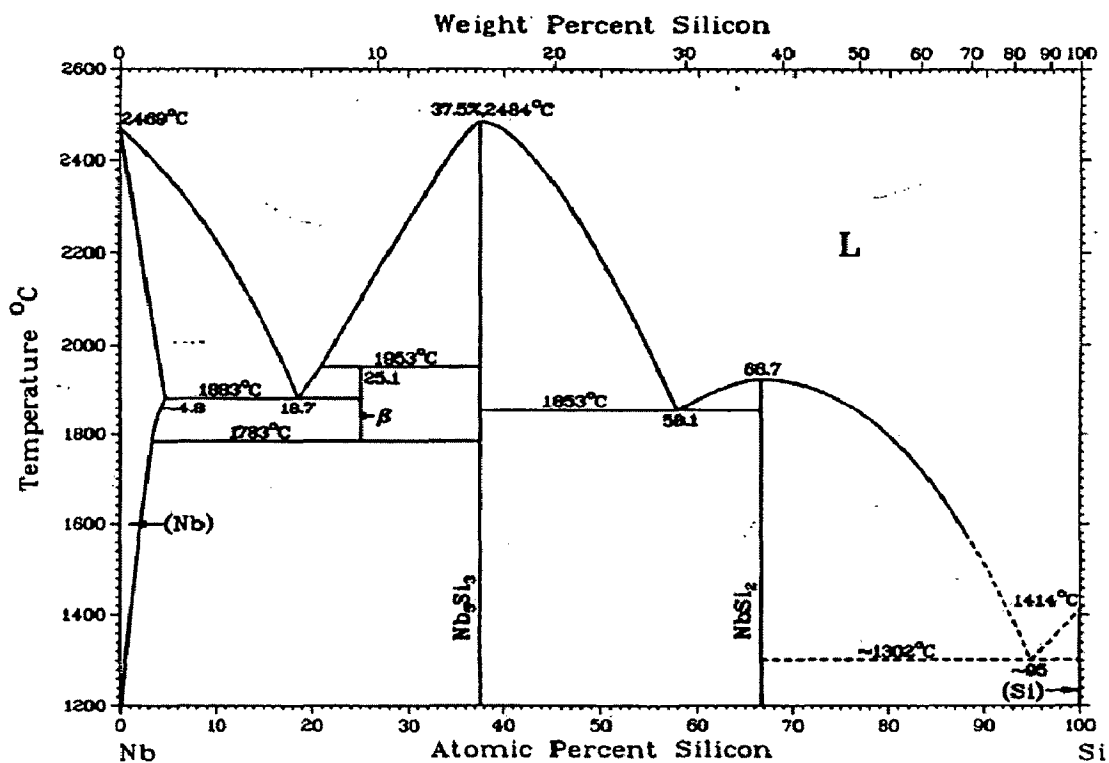


Fig. 5.108 Nb-Si binary phase diagram

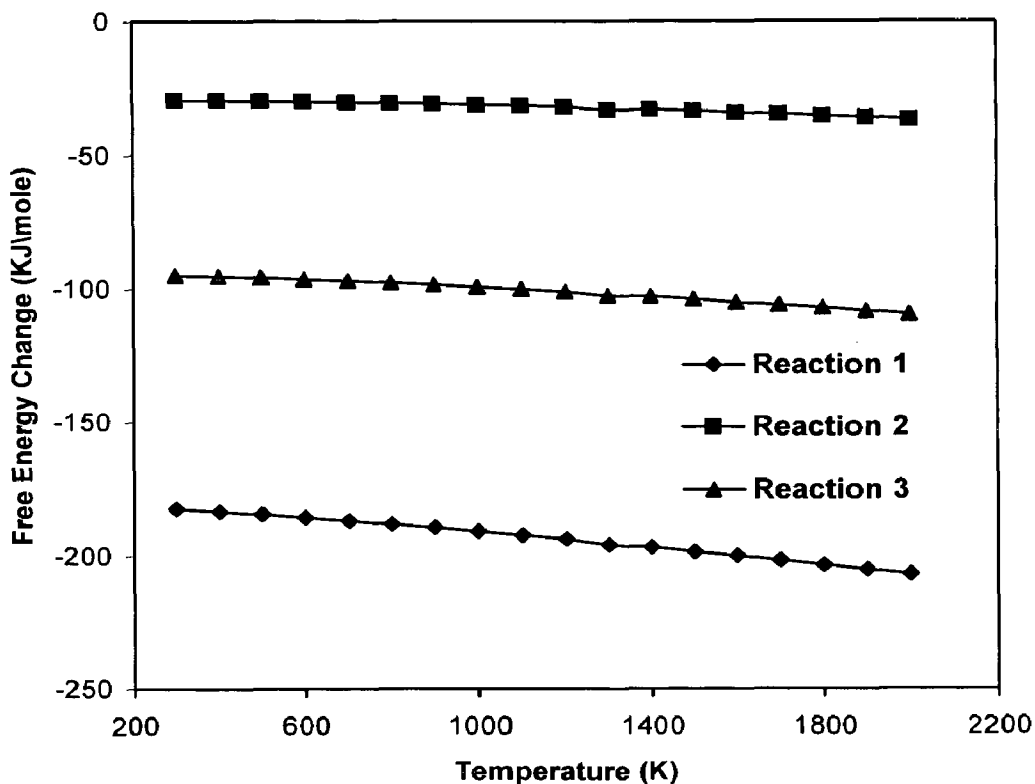


Fig. 5.109 Standard free energy change ( $\Delta G$  vs. *Temperature*) for the possible chemical reactions between MoSi<sub>2</sub> and pure Nb resulting in the formation of niobium silicides.

Kung et al (1992) have shown that the addition of 15 and 30 vol% of  $\text{Mo}_5\text{Si}_3$  in  $\text{MoSi}_2$  increases the hardness at all temperatures between 25 °C to 1000 °C. However, in the present investigation, the increase in hardness of  $\text{MoSi}_2$ -Mo composite was much higher than reported by Kung et al (1992). This may be possibly due to a higher amount of  $\text{Mo}_5\text{Si}_3$  (estimated as 42 %) formed in-situ with addition of 20 vol% pure Mo as compared to the 30 vol%  $\text{Mo}_5\text{Si}_3$  added externally in  $\text{MoSi}_2$  by Kung et al (1992). The hardness of  $\text{MoSi}_2$ -W composite was found to be higher than hardness of  $\text{MoSi}_2$ -Nb and  $\text{MoSi}_2$ -Mo composites. This could be due to the solid solution strengthening of  $\text{MoSi}_2$  matrix as a result of considerable diffusion of elemental W in  $\text{MoSi}_2$ . W more readily dissolves in  $\text{MoSi}_2$  as compared to other refractory metals.

Gibala et al (1992) and Kung et al (1992) have suggested that the strength of  $\text{Mo}_5\text{Si}_3$  is greater than that of  $\text{MoSi}_2$ .  $\text{Mo}_5\text{Si}_3$  has been characterized as one of the several elastically hard and brittle phases, which can potentially strengthen  $\text{MoSi}_2$  at high temperatures. Alman et al (1992) have reported a flexural strength value of  $200 \pm 50$  MPa for  $\text{MoSi}_2 + 20$  vol% Nb particulate composite. Similar value is obtained for  $\text{MoSi}_2 + 20$  vol% Nb composite in the present investigation with a much smaller Nb particle size than used by Alman et al.

The average grain size of  $\text{MoSi}_2$  was measured in the range of 10 - 15  $\mu\text{m}$  in all the three composites as discussed in section 5.2.1 which is significantly lower than the grain size of pure  $\text{MoSi}_2$  reported by Mitra et al (1997<sup>a</sup>). Mitra et al (1997<sup>a</sup>) have found the grain size of hot pressed pure  $\text{MoSi}_2$  was in the range of 20 – 40  $\mu\text{m}$  using the same grade of  $\text{MoSi}_2$  powder. This clearly suggests that addition of 20 vol% of refractory metal particles and their subsequent conversion into other silicide phases could inhibit the grain growth in  $\text{MoSi}_2$  at high processing temperatures. A smaller grain size is expected to further improve the mechanical properties of  $\text{MoSi}_2$  based particulate composites as compared to monolithic  $\text{MoSi}_2$ .

The fracture toughness of  $\text{MoSi}_2 + 20$  vol% Nb particulate composite was measured as 5.0  $\text{MPa}\sqrt{\text{m}}$  in the present work. Venkateswara Rao et al (1992<sup>a</sup>) have reported a similar fracture toughness value of 5.2  $\text{MPa}\sqrt{\text{m}}$  for  $\text{MoSi}_2 + 20$  vol% Nb composite using much coarser Nb particles (particle size = 177  $\mu\text{m}$  to 500 $\mu\text{m}$ ) than those used in the present investigation. The large Nb particles did not convert fully into

Nb<sub>5</sub>Si<sub>3</sub> phase. However, they observed an interfacial reaction layer of approximately 40 μm thickness. They found that cracking was primarily confined to the MoSi<sub>2</sub> matrix and the reaction layer interface separating Nb and MoSi<sub>2</sub>. Cracks essentially avoided the Nb particules and circumvented them by opting for paths around the Nb particles in the reaction product phase (Nb<sub>5</sub>Si<sub>3</sub>) thus, limiting the toughening contribution of the ductile phase.

### **5.7.2 Laminated Composites with (MoSi<sub>2</sub> + 2 wt% Al) as Matrix**

The addition of dispersed ductile phases to brittle MoSi<sub>2</sub> did not result in significant improvement in room temperature fracture toughness of MoSi<sub>2</sub>. Therefore, ductile refractory metals were used in the form of foils having a large aspect ratio (laminated approach). Debonding at the matrix / foil interface promoted crack bridging.

As reported earlier, the powders of MoSi<sub>2</sub> that are commercially available carry with them significant amounts of SiO<sub>2</sub>. The MoSi<sub>2</sub> powder used in the present study was procured from H. C. Stark, Germany and was found to contain about 1.3 wt% oxygen (Table 5.1). Alman et al (1994) have reported the oxygen content of 1.8 wt% in their starting H. C. Stark Grade-C MoSi<sub>2</sub> powder. SiO<sub>2</sub> particles were present at grain boundaries as well as inside the MoSi<sub>2</sub> grains. In the present work, the average particle size of SiO<sub>2</sub> was found to be ~ 2 μm. Wade and Petrovic (1992<sup>a</sup>, 1992<sup>b</sup>) measured the average size of SiO<sub>2</sub> particles inside the MoSi<sub>2</sub> grains as 1 - 3 μm while it was 5 - 8 μm for SiO<sub>2</sub> present at grain boundaries.

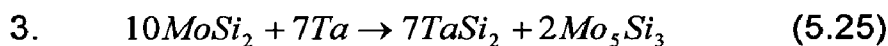
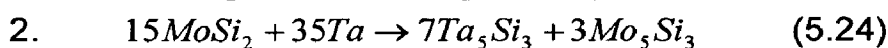
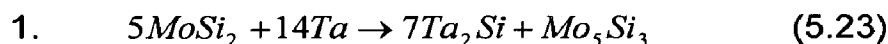
Apart from SiO<sub>2</sub> in starting MoSi<sub>2</sub> powders, the additional oxygen could also be picked up during hot pressing of MoSi<sub>2</sub> powders. Maloy et al (1991) have reported the oxygen content in their hot pressed MoSi<sub>2</sub> as 2.8 wt% (~ 14 vol% SiO<sub>2</sub>), while their starting MoSi<sub>2</sub> powder contained only 0.2 wt% oxygen. MoSi<sub>2</sub> reacts with oxygen during processing, forming vitreous SiO<sub>2</sub> on the surface of MoSi<sub>2</sub> powders. It forms on the surface of almost all powder particles. The SiO<sub>2</sub> on the surface of the powder particles ends up at grain boundaries in the microstructure after consolidation.

The amorphous (glassy phase)  $\text{SiO}_2$  present in  $\text{MoSi}_2$  has been reported to seriously degrade the mechanical properties of  $\text{MoSi}_2$  at room as well as at elevated temperatures. It may lead to intergranular fracture (Maloy et al, 1991). It degrades high temperature strength and creep due to grain boundary sliding of  $\text{MoSi}_2$  (Sadananda et al, 1991, 1993, 1994). The high temperature strength and creep resistance of  $\text{MoSi}_2$  drops sharply beyond 1200 °C due to enhanced plasticity from activation of more slip systems. However, the softening of the material can occur at a lower temperature due to the presence of  $\text{SiO}_2$  (Aikin Jr., 1992<sup>a</sup>, 1992<sup>b</sup>).  $\text{SiO}_2$  is responsible for softening and weakening of  $\text{MoSi}_2$  at elevated temperatures (Aikin Jr., 1992<sup>b</sup>, Gibala et al, 1992). Even the fracture toughness has been found to decrease with increase in temperature above 1000 °C due to the softening of  $\text{SiO}_2$  phase and weakening of grain boundaries (Maloy et al, 1991, 1992).

$\text{SiO}_2$  can be converted into  $\text{Al}_2\text{O}_3$  by adding elemental Al powder in  $\text{MoSi}_2$ . Replacement of  $\text{SiO}_2$  by  $\text{Al}_2\text{O}_3$  in  $\text{MoSi}_2$  leads to a significant improvement in mechanical properties of  $\text{MoSi}_2$ . Al additions in small concentrations have been found to be beneficial for room temperature fracture toughness (Costa e Silva and Kaufman, 1993, 1994, 1995) and high temperature yield and creep strength (Mitra et al, 1997<sup>a</sup>, 1997<sup>b</sup>, 2006). The addition of Al into  $\text{MoSi}_2$  is reported to improve its high temperature bend strength markedly (Niihara and Suzuki, 1999). Addition of Al in  $\text{MoSi}_2$  has also been reported to improve the oxidation resistance of  $\text{MoSi}_2$ . Yanagihara et al (1996) and Stergiou et al (1997) have reported how Al additions help in improving pest and oxidation resistance of  $\text{MoSi}_2$ . Apart from converting  $\text{SiO}_2$  into  $\text{Al}_2\text{O}_3$ , Al also forms solid solution with  $\text{MoSi}_2$ . It occupies Si sites in  $\text{MoSi}_2$  crystal structure. Kisley and Kodash (1989) have observed that the resistance to oxidation of  $\text{Mo}(\text{Si}, \text{Al})_2$  was superior to that of  $\text{MoSi}_2$  because of the formation of a mullite coating. Shah et al (1992) recommended Al additions to  $\text{MoSi}_2$  to increase its metallic character, as Al atoms would substitute Si atoms, and change the nature of bonding. The Mo-Si bond is a mixture of covalent and ionic bonding, with a partial metallic character (Neshpor and Samsonov, 1964). The Al atom substituting the Si atom would be quite effective in increasing the metallic character. Therefore, 2 wt% Al was added to  $\text{MoSi}_2$  powder in the present work prior to hot pressing into laminated structures.

The formation of various silicide phases as a result of chemical interactions between  $\text{MoSi}_2$  and pure Mo have already been explained using thermodynamic calculations in section 5.7.1. In case of  $\text{MoSi}_2 + 20 \text{ vol\% Mo}$  particulate composite, the reaction product consisted of only one silicide phase, i.e.,  $\text{Mo}_5\text{Si}_3$ . However, in case of  $(\text{MoSi}_2 + 2 \text{ wt\% Al}) + \text{Mo}$  foil laminated composite, the reaction zone consisted of two distinct layers of  $\text{Mo}_5\text{Si}_3$  and  $\text{Mo}_3\text{Si}$ . The Mo-Si binary phase diagram suggests that  $\text{Mo}_5\text{Si}_3$  does not co-exist with pure Mo. Therefore, the formation of  $\text{Mo}_3\text{Si}$  was necessitated and it separated  $\text{Mo}_5\text{Si}_3$  from pure Mo. Similar observations have been reported by Tortorici and Dayananda (1999). They found that  $\text{Mo}_3\text{Si}$  and  $\text{Mo}_5\text{Si}_3$  phase layers developed in the diffusion zone in  $\text{MoSi}_2 + \text{pure Mo}$  diffusion couple annealed at  $1500 \text{ }^\circ\text{C}$  for 6 h. The optical microstructure under polarized light reveals the grains of  $\text{Mo}_5\text{Si}_3$ , as  $\text{Mo}_5\text{Si}_3$  has a tetragonal (tI32) crystal structure, which is more anisotropic as compared to the cubic (cP8) structure of  $\text{Mo}_3\text{Si}$ . Tortorici and Dayananda (1999) have also reported  $\text{Mo}_5\text{Si}_3$  layer developing a strong 001 texture.

The Ta-Si binary phase diagram (Schlesinger, 1994) as presented in Fig. 5.110 shows three stable Ta silicide phases,  $\text{TaSi}_2$ ,  $\text{Ta}_5\text{Si}_3$  and  $\text{Ta}_2\text{Si}$ . The possible chemical reactions forming each one of these silicides as a result of  $\text{MoSi}_2$  reacting with Ta are:



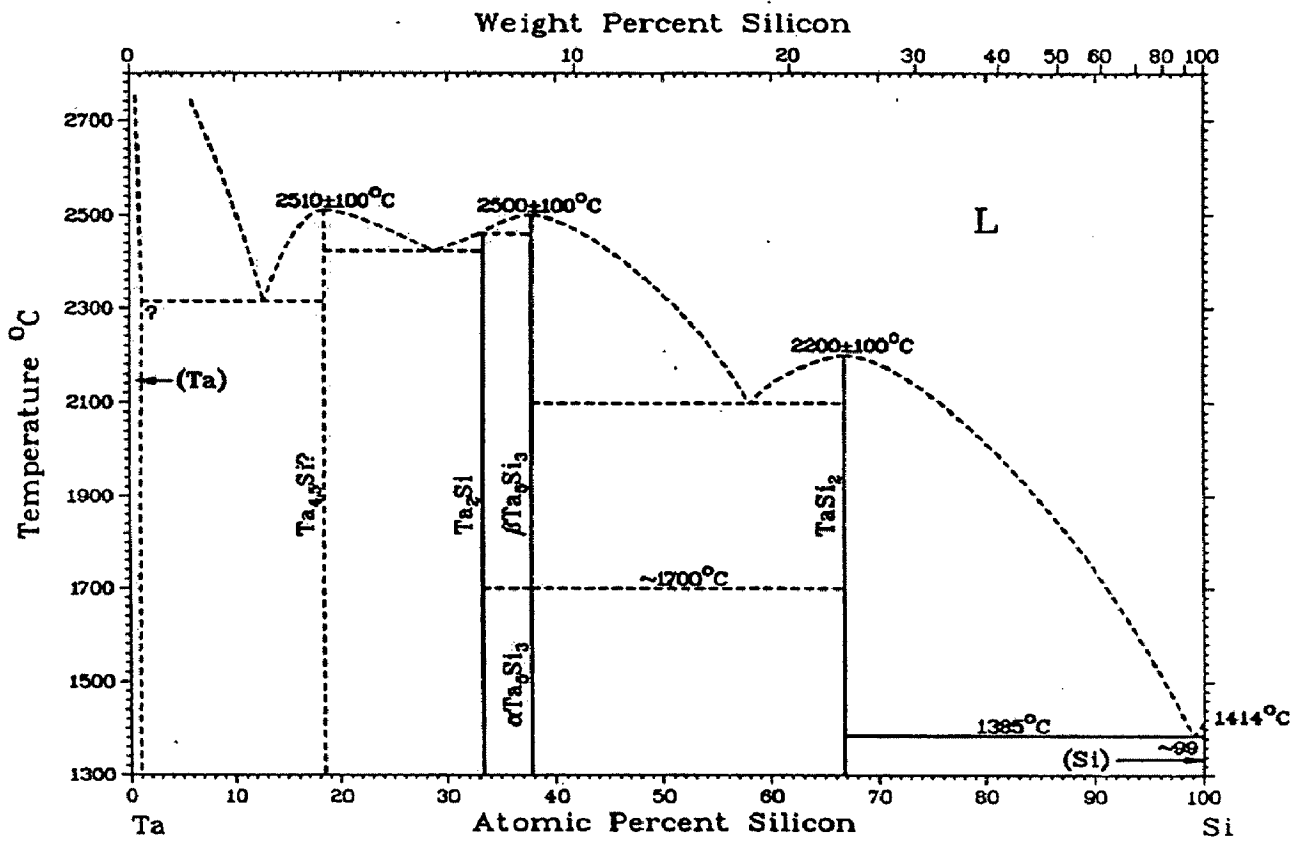


Fig. 5.110 Ta-Si binary phase diagram



The standard free energy change (per mole of  $\text{MoSi}_2$ ) for the above reactions is plotted against the temperature as shown in Fig. 5.111 (Equations 5.23, 5.24 and 5.25 depicted as Reactions 1, 2 and 3, respectively). As seen in this figure,  $\Delta G$  values are negative for all the three reactions considered. However,  $\text{TaSi}_2$  (Reaction 3) seems to be least stable as compared to  $\text{Ta}_5\text{Si}_3$  and  $\text{Ta}_2\text{Si}$ . The free energy change for reaction 3 increases with increasing temperature in contrast to a decreasing  $\Delta G$  with increasing temperature for reactions 1 and 2.  $\Delta G$  values for reactions 1 and 2 exhibit similar trends with only marginal difference. Accordingly,  $\text{Ta}_5\text{Si}_3$  and  $\text{Ta}_2\text{Si}$  phase layers developed in the reaction zone in  $(\text{MoSi}_2 + 2 \text{ wt}\% \text{ Al}) + \text{Ta}$  foil laminated composite (as existing in the Si-rich side of Ta-Si phase diagram). Tortorici and Dayananda (1999) have also reported the development of three phase layers corresponding to  $\text{Ta}_2\text{Si}$ ,  $\text{Ta}_5\text{Si}_3$  and  $(\text{Mo, Ta})_5\text{Si}_3$  in the diffusion zone of  $\text{MoSi}_2 + \text{Ta}$  disk diffusion couple annealed at 1600 °C for 8 h.

In  $\text{MoSi}_2$ -2 wt% Al alloy used as a matrix for the laminated composites in the present investigation, no evidence of the presence of  $\text{Mo}(\text{Si, Al})_2$  phase (hP9) was found in the microstructures as has been confirmed by EPMA and x-ray diffraction data. This is in agreement with the findings of Costa e Silva and Kaufman (1993) who have reported that the microstructures of the  $\text{MoSi}_2$ -2.5 wt% Al and  $\text{MoSi}_2$ -4.1 wt% Al alloys contained  $\text{MoSi}_2$  (C11<sub>b</sub>) and  $\text{Al}_2\text{O}_3$  phases, while that of  $\text{MoSi}_2$ -8.1 wt% Al alloy showed a mixture of  $\text{Mo}(\text{Si, Al})_2$  (C40),  $\text{MoSi}_2$  (C11<sub>b</sub>) and  $\text{Al}_2\text{O}_3$  phases.  $\text{Mo}(\text{Si, Al})_2$  phase was the predominant phase in the  $\text{MoSi}_2$ -8.1 wt% Al alloy. Mitra et al (1999) have also reported the presence of only  $\text{MoSi}_2$  (C11<sub>b</sub>) phase in  $\text{MoSi}_2$ -1.5 wt% Al and  $\text{MoSi}_2$ -3 wt% Al alloys. The presence of  $\text{Mo}(\text{Si, Al})_2$  (C40) phase was confirmed only in  $\text{MoSi}_2$ -5 wt% Al alloy. Al left after complete replacement of  $\text{SiO}_2$  only is absorbed into solid solution in  $\text{MoSi}_2$ .

The hardness of  $\text{MoSi}_2$ -2 wt% Al alloy was found to be slightly higher than that of pure  $\text{MoSi}_2$  (Table 5.12). Increase in hardness may be attributed to the formation of  $\text{Al}_2\text{O}_3$  in-situ. Peralta et al (1997) have reported that 3 at% Al in  $\text{MoSi}_2$  exhibits 25 % lower room temperature hardness than unalloyed  $\text{MoSi}_2$ . They attributed this to *solid solution softening*. Al atoms occupy Si sites replacing some of the Mo-Si covalent bonds into Mo-Al metallic bonds resulting in solid solution softening. However, in the present investigation, no solid solution softening was observed. EPMA results clearly

indicate the absence of Al in solid solution. This could be due to the fact that the entire Al added is consumed in reducing the SiO<sub>2</sub> particles. Al probably reacts with SiO<sub>2</sub> in preference to the formation of solid solution with MoSi<sub>2</sub>.

In the present investigation, the indentation crack lengths in MoSi<sub>2</sub>-2 wt% Al alloy matrix show a large degree of scatter. The MoSi<sub>2</sub>-2 wt% Al alloy possesses a heterogeneous microstructure having a large variation in the grain size (Fig. 5.30), which might as well be responsible for the scatter noticed in the crack lengths. An analysis of the indentation crack paths in these materials however provides an understanding of the fracture micro-mechanism. The indentation crack paths (Fig. 5.42) are mostly transgranular and only partly intergranular. Wade and Petrovic (1992<sup>a</sup>) have explained the transgranular mode of indentation cracking on the basis of presence of crystallographic anisotropy and weak crystal cleavage planes in MoSi<sub>2</sub>. Indentation cracks might have followed paths determined by the local stress distribution, and cleavage planes. The grains with finer size in MoSi<sub>2</sub> seem to be responsible for a tendency towards a more intergranular mode of failure. The coarser grains in MoSi<sub>2</sub> failed by transgranular mode in the present study. Crack paths in unalloyed MoSi<sub>2</sub> have been reported to be straight and long, accounting for lower toughness, as illustrated by Carter and Hurley (1987).

However, in contrast to the observations made in the present work, the indentation crack paths were found to be predominantly intergranular in case of MoSi<sub>2</sub>-5 wt% Al alloy (Mitra et al, 1997<sup>b</sup>). Predominance of intergranular mode of indentation cracking in MoSi<sub>2</sub>-5 wt% Al alloy might be the result of Al in solid solution in MoSi<sub>2</sub>, which might have altered the surface and fracture energy of MoSi<sub>2</sub> along the crystal cleavage planes as discussed by Wade and Petrovic (1992<sup>a</sup>). As Al atoms substitute the Si sites, the metallic component of the bond is believed to be enhanced, and higher energy is required for cleavage. Transgranular cracking was still observed only in a few areas.

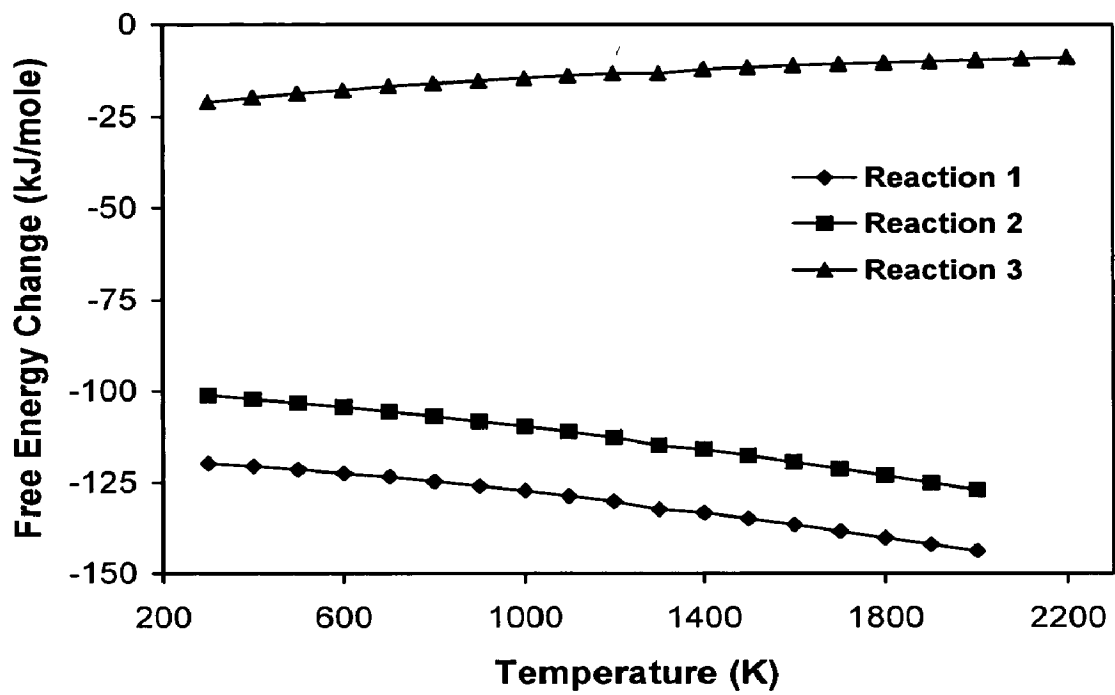


Fig. 5.111 Standard free energy change ( $\Delta G$  vs. *Temperature*) for the possible chemical reactions between  $\text{MoSi}_2$  and pure Ta resulting in the formation of tantalum silicides.

The SEM image in Fig. 5.44(b) reveals that crack branching took place, as the crack approached the metal. Wade and Petrovic (1992<sup>a</sup>) have argued that the advancing indentation cracks in pure MoSi<sub>2</sub> separate into disconnected segments to propagate along the preferential cleavage planes. Mitra et al (1997<sup>a</sup>) have attributed the crack branching in MoSi<sub>2</sub> to microcrack formation ahead of the crack tip. However, in case of MoSi<sub>2</sub> reinforced with Nb fibres, Alman and Stoloff (1995) have attributed the branching of the matrix crack as it approached the fibre to elastic mismatch such as Poisson's ratio and thermal expansion mismatch between MoSi<sub>2</sub> matrix and the Nb fibre. This elastic mismatch results in a positive transverse stress at the interface, which causes the branching of the cracks in MoSi<sub>2</sub> as they approach the Nb reinforcement. Crack branching could also increase the energy requirement at the crack tip for further extension, as more than one crack need to be driven.

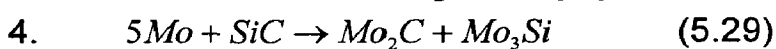
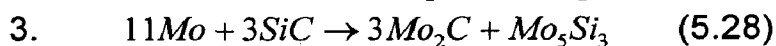
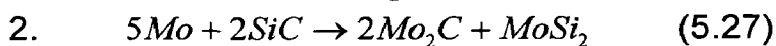
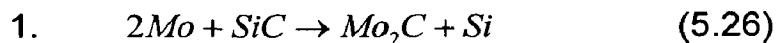
### 5.7.3 Laminated Composites with (MoSi<sub>2</sub> + 20 vol% SiC<sub>p</sub>) as Matrix

Adding SiC particles to MoSi<sub>2</sub> not only serves the purpose of minimizing the thermal expansion mismatch between MoSi<sub>2</sub> and the refractory metal foils but also reinforcement of MoSi<sub>2</sub> with SiC<sub>p</sub> provides improved high temperature mechanical properties in comparison to pure MoSi<sub>2</sub>. No elemental Al was added to MoSi<sub>2</sub> in this case so as to study exclusively the effect of SiC<sub>p</sub> addition to MoSi<sub>2</sub>. SiC reinforcement enhanced the elevated temperature strength significantly by acting as obstacles to dislocation motion (Aikin Jr., 1992<sup>a</sup>, Mitra et al, 1997<sup>b</sup>). SiC strengthens the material at elevated temperatures when the matrix is ductile (Gibbs et al, 1987). The presence of SiC significantly reduced creep rates in MoSi<sub>2</sub> composites (Sadananda et al, 1991, 1993). Creep rates of MoSi<sub>2</sub> reinforced with 20 vol% SiC whiskers have been reported to be ~ 2 orders of magnitude lower than those of polycrystalline MoSi<sub>2</sub> (Sadananda and Feng, 1994). Cook et al (1992) have reported that MoSi<sub>2</sub>-SiC<sub>p</sub> composites possess the best elevated temperature oxidation resistance in comparison to pure MoSi<sub>2</sub> as well as among all ceramic particulate reinforced MoSi<sub>2</sub> composites. The wear resistance of MoSi<sub>2</sub> also increases with increasing amount of SiC. This is due to the fact that SiC is a harder phase than MoSi<sub>2</sub> (Alman et al 1998).

The average grain size of MoSi<sub>2</sub> was measured as 5 – 8 μm in MoSi<sub>2</sub> + 20 vol% SiC<sub>p</sub> monolithic material used as the matrix layer for synthesizing the laminated composites with different refractory metal foils. A much smaller grain size of MoSi<sub>2</sub> in

the present work could be the result of grain growth inhibition by SiC particles during hot pressing. The average grain size is almost same as the average particle size of MoSi<sub>2</sub>. The concept of adding SiC particles to MoSi<sub>2</sub> to limit the grain growth was reported by Fitzer and Remmele (1985). As SiC content increases, grain size of MoSi<sub>2</sub> decreases. Grain growth inhibition and grain refinement in MoSi<sub>2</sub>-SiC<sub>p</sub> composite has also been reported by Bhattacharya and Petrovic (1991). They have reported an average grain size of 5 μm in case of MoSi<sub>2</sub>-40 vol% SiC<sub>p</sub> composite. They observed that the grain refinement reached more or less at a saturation level for MoSi<sub>2</sub> containing more than 20 vol% SiC<sub>p</sub>.

In case of (MoSi<sub>2</sub> + 20 vol% SiC<sub>p</sub>) + Mo foil laminated composite, the interfacial reaction products formed are Mo<sub>5</sub>Si<sub>3</sub> and Mo<sub>2</sub>C. Mo<sub>2</sub>C layer separated the Mo<sub>5</sub>Si<sub>3</sub> layer from pure Mo foil. Formation of Mo<sub>2</sub>C is not expected as a result of reaction between MoSi<sub>2</sub> and SiC as both are highly stable with each other thermodynamically throughout the entire temperature range as depicted in Fig. 5.49. However, the thermodynamic calculations revealed that SiC is not stable in the presence of pure Mo. The following possible reactions between Mo and SiC are considered and the calculated free energy change data is plotted against the temperature and exhibited in Fig. 5.112 (Equations 5.26, 5.27, 5.28 and 5.29 depicted as Reactions 1, 2, 3 and 4, respectively).



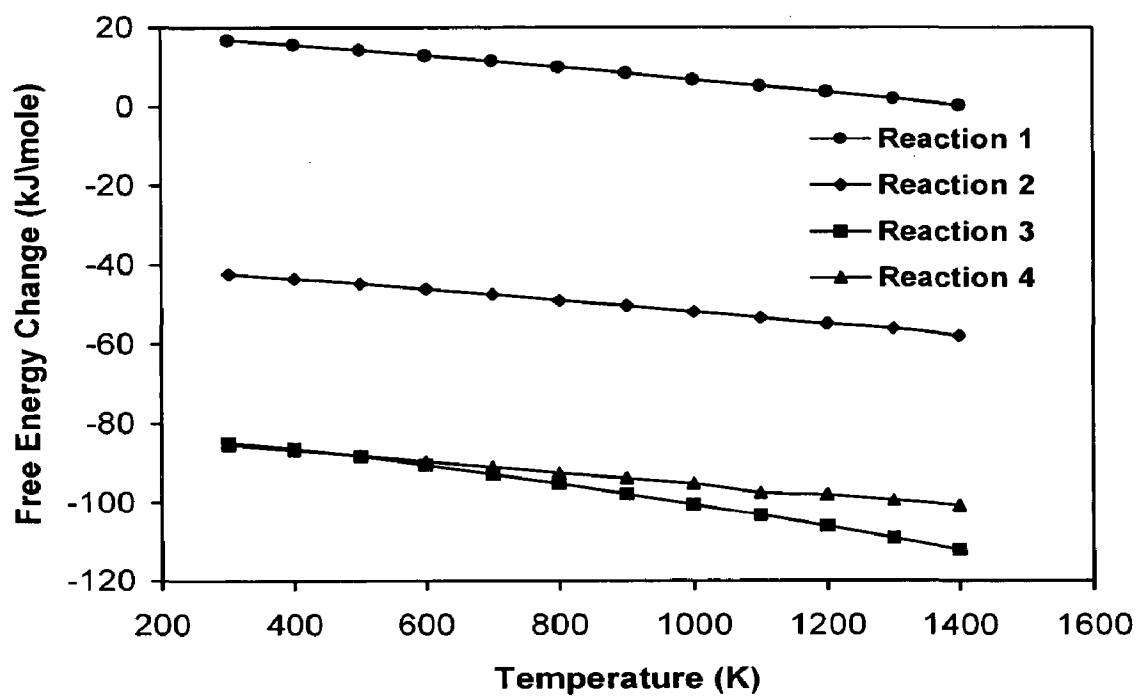


Fig. 5.112 Standard free energy change ( $\Delta G$  vs. *Temperature*) for the possible chemical reactions between SiC and pure Mo resulting in the formation of Mo<sub>2</sub>C.

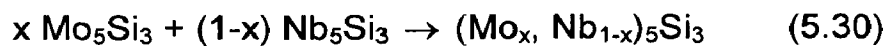
It is evident from Fig. 5.112 that  $\Delta G$  (per mole of SiC) is negative for all the reactions except the reaction 1 for the entire temperature range.  $\Delta G$  for reaction 1 also shows a decreasing trend with increase in temperature. This clearly establishes that SiC is not stable with pure Mo and results in the formation of  $\text{Mo}_2\text{C}$ . The data also indicates that the reaction 3 resulting in the formation of  $\text{Mo}_2\text{C}$  with  $\text{Mo}_5\text{Si}_3$  is most feasible at temperatures above 700 °C. This explains the resulting microstructure in the reaction zone as a result of chemical interactions between  $\text{MoSi}_2$  matrix and Mo foil in the presence of SiC. Reid (1965) has reported the precipitation of  $\text{Mo}_2\text{C}$  on the surface of pure Mo containing carbon as impurity after annealing at 2000 °C for 1 h in vacuum. However, the Mo foils used in the present work did not contain any carbon (Table 5.3).

Figure 5.113 is an isothermal section of Mo-Si-C ternary phase diagram at 1600 °C (Nowotny et al, 1954). The phase designated as  $\text{Mo}_3\text{Si}_2$  is now referred to as  $\text{Mo}_5\text{Si}_3$ . SiC additions are known to be thermodynamically stable in  $\text{MoSi}_2$ . A narrow two-phase field indicated by the single tie-line exists between  $\text{MoSi}_2$  and SiC and thus a two-phase mixture is stable at 1600 °C. However, according to Fig. 5.113, a composite of  $\text{MoSi}_2$ ,  $\text{Mo}_5\text{Si}_3$  and SiC would not be thermodynamically stable at 1600 °C. No three-phase triangle exists at this temperature for these three phases. The ternary phase  $\text{Mo}_5\text{Si}_3\text{C}$  ( $\text{Mo}_{\leq 5}\text{Si}_3\text{C}_{\leq 1}$ ) also known as the Nowotny phase and indicated as Mo-Si-C in the ternary diagram would form in these composites at 1600 °C (Parthe et al, 1965). However, the existence of  $\text{MoSi}_2$ , SiC and  $\text{Mo}_5\text{Si}_3$  together has been observed in laminated composites prepared with ( $\text{MoSi}_2 + 20$  vol%  $\text{SiC}_p$ ) as the matrix in the present study as shown in Fig. 5.58. This is consistent with the observations of van Loo et al (1982). They have shown that a three-phase field does exist between  $\text{MoSi}_2$ ,  $\text{Mo}_5\text{Si}_3$  and SiC at lower temperatures. At lower temperatures, the triple phase composite would be stable.

Meschter (1991, 1992) has reported the presence of  $\text{Mo}_5\text{Si}_3$  in Starck  $\text{MoSi}_2$  powder in small quantity. Some  $\text{Mo}_5\text{Si}_3$  can also form during high temperature processing. The formation of carbon stabilized  $\text{Mo}_5\text{Si}_3$  was justified by Cotton et al (1991) from carbon intake during hot pressing using the graphite dies.

The formation of various silicide phases as a result of chemical interactions between MoSi<sub>2</sub> and pure Ta have already been explained using thermodynamic calculations in section 5.7.2. The reaction zone between MoSi<sub>2</sub>-SiC<sub>p</sub> and pure Ta consisted of (Ta, Mo)<sub>5</sub>Si<sub>3</sub> and Ta<sub>2</sub>Si phases. This is in agreement with earlier studies by Tortorici and Dayananda (1999). Tortorici and Dayananda observed the development of three phase layers, corresponding to (Mo, Ta)<sub>5</sub>Si<sub>3</sub>, Ta<sub>5</sub>Si<sub>3</sub> and Ta<sub>2</sub>Si in the diffusion zone formed in MoSi<sub>2</sub> + Ta diffusion couple annealed at 1600 °C for 8 h. The melting point of Mo is lower than Ta and therefore, Mo is expected to diffuse faster than Ta. However, Tortorici and Dayananda (1999) experimentally found that the diffusivity of Ta in (Mo,Ta)<sub>5</sub>Si<sub>3</sub> layer was larger in magnitude than diffusivity of Mo.

In case of (MoSi<sub>2</sub> + 20 vol% SiC<sub>p</sub>) + Nb foil laminated composite, the microstructure in the reaction zone exhibits the presence of Nb<sub>5</sub>Si<sub>3</sub> along with Mo<sub>5</sub>Si<sub>3</sub> with no evidence of NbSi<sub>2</sub> phase. The thermodynamic calculations exploring the formation of various silicide phases in the reaction zone between MoSi<sub>2</sub>-SiC<sub>p</sub> and pure Nb have already been described in section 5.7.1. The formation of solid solution (Mo<sub>x</sub>, Nb<sub>1-x</sub>)<sub>5</sub>Si<sub>3</sub> from mixing of the pure components can be described by the following reaction:



However, no data on the free energy of mixing for the above reaction is available.



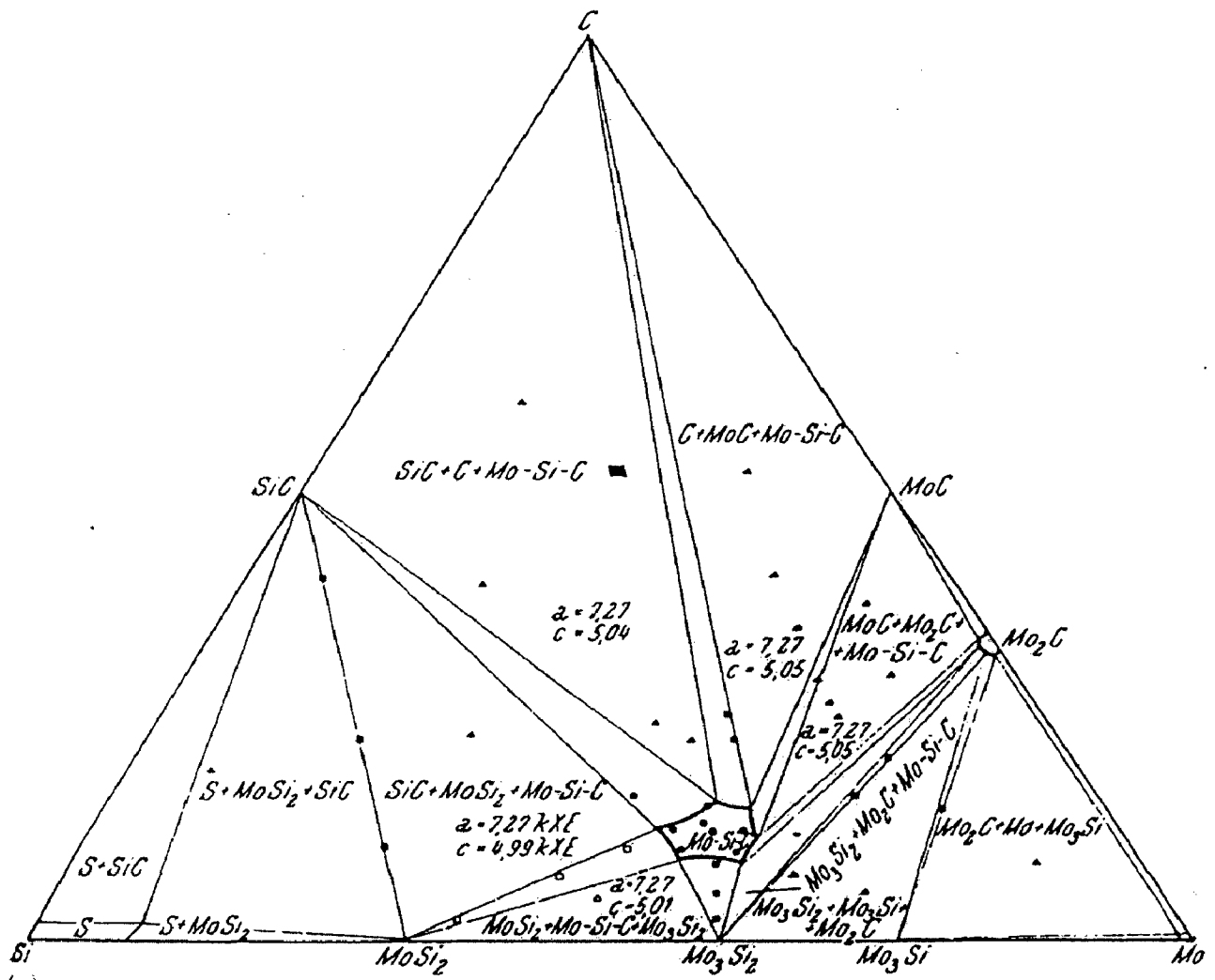


Fig. 5.113 An isothermal section of Mo-Si-C ternary phase diagram at 1600 °C.

Figure 5.114 exhibits an isothermal section of Mo-Si-Nb ternary phase diagram at 800 °C (Savitskiy et al, 1965). Isothermal sections of ternary phase diagrams contain three different kinds of regions, namely, single-phase, two-phase and three-phase regions. In Fig. 5.114, there are four distinct single-phase regions, which are depicted as black areas. These are (i) Nb and Mo dissolving completely in each other as a body centered cubic (bcc) solid solution (ii)  $\text{Mo}_3\text{Si}$  phase region (iii) a continuous solid solution from  $\text{Nb}_5\text{Si}_3$  to  $\text{Mo}_5\text{Si}_3$  and (iv)  $\text{NbSi}_2$  phase (hP9) having a crystal structure different from  $\text{MoSi}_2$  (tI6). Between single-phase regions are the two-phase regions, which contain tie lines whose ends are the compositions of the saturated phases in an equilibrium co-existing mixture. A narrow two-phase region lies between the disilicides. The three-phase regions are the triangular regions in which three phases are in equilibrium with compositions given by the corners. Each side of the triangle is a limiting tie line of the adjacent two-phase field.

The analysis of interfacial reaction layers in composites requires the use of these diagrams. Savitsky et al (1963) have reported that the isopleth through  $\text{MoSi}_2$  / Nb shows two four-phase equilibriums at 1740 °C and 1730 °C associated with  $\text{MoSi}_2$  / Nb vertical section. They also found that the relevant phase fields remain essentially unchanged below 1730 °C. Therefore, an attempt has been made to analyze the composition path in the present study on the basis of the isothermal section at 800 °C which is the only one available ternary phase diagram of this system in the literature (Savitsky et al, 1965).

In  $(\text{MoSi}_2 + 20 \text{ vol\% SiC}_p) / \text{Nb}$  foil laminated composite, it was found that the interface consists of a Nb rich  $(\text{Nb, Mo})_5\text{Si}_3$  layer and a Mo rich  $(\text{Mo, Nb})_5\text{Si}_3$  layer as shown in Fig. 5.71(a). Based on the microprobe data taken across the reaction layers and plotted on the ternary triangle, a possible graph of the diffusion path is obtained as shown in Fig. 5.115. It runs from the pure Nb corner into the single-phase bcc region (dissolving a very small amount of Si) and then jumps across the two-phase field to  $\text{Nb}_5\text{Si}_3$ . Sharp interface between pure Nb and  $\text{Nb}_5\text{Si}_3$  layer (Fig. 5.71(a)) indicates that the composition path runs along the tie line in the corresponding two-phase region. The jump occurs at positions in the sample corresponding to the location of the boundary between the phases. The path then

runs across the  $\text{Nb}_5\text{Si}_3$  -  $\text{Mo}_5\text{Si}_3$  single-phase region. The non-planar interface between  $\text{MoSi}_2$  and  $\text{Mo}_5\text{Si}_3$  phases as revealed in Fig. 5.71(a) suggests that the composition path crosses the corresponding two-phase region by cutting across the tie lines and therefore, the diffusion path is further plotted passing through the  $\text{Mo}_5\text{Si}_3$  -  $\text{MoSi}_2$  two-phase region before reaching  $\text{MoSi}_2$ .

It is revealed from Fig. 5.115 that the diffusion path zigzags across the line connecting the two compositions of the two reacting materials satisfying the condition that the path must lie on both sides of the connecting line, which contains the average composition, to conserve the mass within the reaction zone. The route that the path takes across the ternary triangle is related to the identity of the fast diffusing species. The ends of the diffusion path, near the  $\text{MoSi}_2$  end and the Nb end, both point either toward or away from the Si corner. This fact indicates that the Si is the fastest diffusing species in  $\text{MoSi}_2$ - $\text{SiC}_p$  / Nb composite system.

As seen in Fig. 5.71(a), the interface between Nb and  $\text{Nb}_5\text{Si}_3$  is relatively planar while the interface between  $\text{Mo}_5\text{Si}_3$  and  $\text{MoSi}_2$  is non-planar. Tortorici and Dayananda (1999) have also reported the development of  $\text{Nb}_5\text{Si}_3$  and  $(\text{Mo}, \text{Nb})_5\text{Si}_3$  layers in the diffusion zone in  $\text{MoSi}_2$  + Nb diffusion couple annealed at 1600 °C for 16 h with a planar interface between Nb and  $\text{Nb}_5\text{Si}_3$ . They also reported that the diffusivity of Nb in  $(\text{Mo}, \text{Nb})_5\text{Si}_3$  layer was larger in magnitude than the diffusivity of Mo. The melting point of Nb is lower than Mo and therefore, Nb is expected to diffuse faster than Mo.

The melting points and atomic sizes of various elements present in the composite systems studied in the present work are given in Table 5.25.

Table 5.25 Melting points and atomic sizes of elements forming various phases present in the laminated composites.

Property	Si	W	Mo	Ta	Nb
Melting Point (°C)	1414	3407	2623	3020	2469
Atom Size (Å)	1.17	1.37	1.36	1.43	1.43

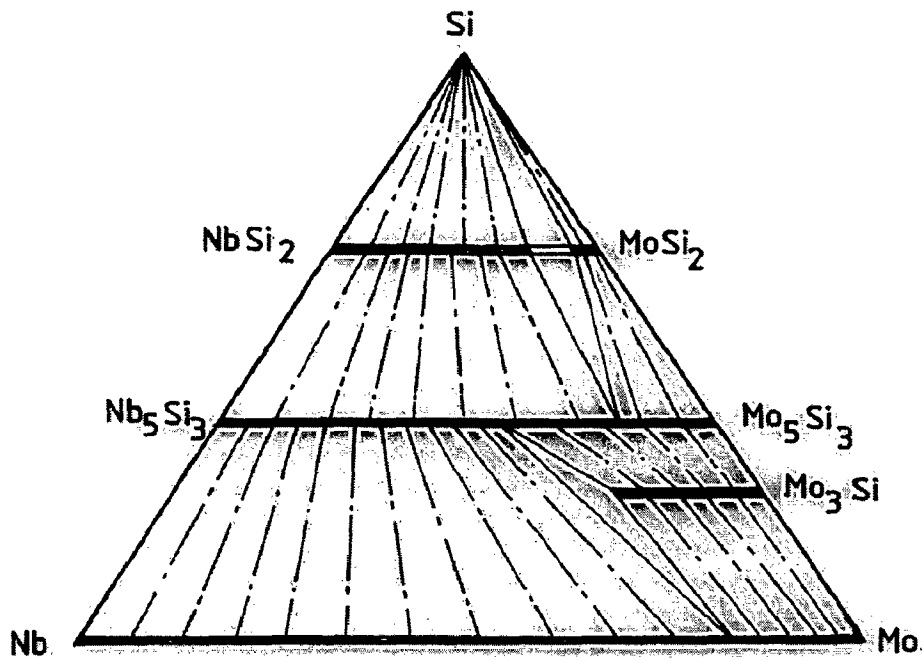


Fig. 5.114 Mo-Si-Nb isothermal section at 800 °C (Savitskiy et al, 1965). The composition widths of the compounds are schematic.

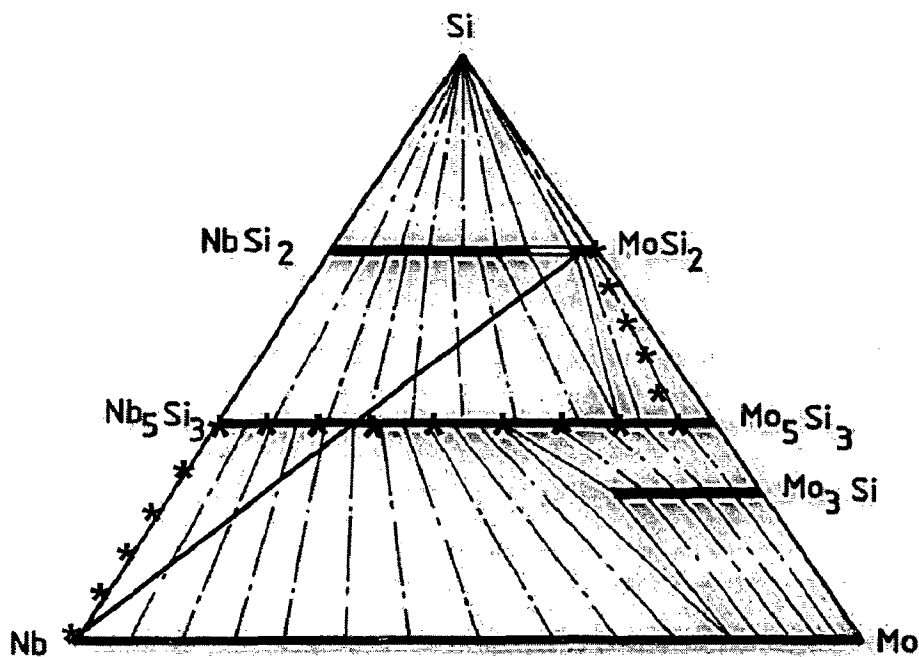


Fig. 5.115 Schematic diffusion path observed for the reaction between Nb and  $\text{MoSi}_2$  at 1600 °C superimposed on the ternary triangle of Fig. 5.114 at 800 °C.

Si has the lowest melting point and the smallest atom size among all the diffusing species and therefore, is likely to have the highest diffusivity among all the elements present in these composites. At the processing temperature, Si is diffusing at a temperature greater than its melting point. Si diffusion is believed to occur by several mechanisms including lattice diffusion, grain boundary diffusion, dislocation diffusion and surface diffusion. The diffusivity is generally higher along the grain boundaries, dislocations and the free surfaces like pores and microcracks. The grain boundary regions are not as closely packed as the crystal. The activation energy for grain boundary diffusion is appreciably less than that for lattice diffusion. However, the grain boundary diffusion is more important at lower temperatures. The dislocation density in ceramics and intermetallics is appreciably lower than metals. The diffusion of Si through such regions in these composites is not likely to be controlled by dislocation diffusion mechanism. In the initial stages of consolidation, Si can diffuse through free surfaces. However, in the fully consolidated composite, Si diffusion is most likely to occur by vacancy mechanism through its own sub-lattice. At a processing temperature of about 1600 °C, high concentration of vacancies is expected. The energy of a Si atom on a Mo site is expected to be higher than on a Si site. However, if this energy difference is small enough, some Si atoms may reside in Mo sites. As MoSi<sub>2</sub> is a stoichiometric compound, if Si atom diffuses by moving into adjacent vacant Mo site, there will be a high probability of the Si atom returning to its own vacant Si site on its next jump. Therefore, it may be preferable that Si atom diffuses only through its own sub-lattice.

In laminated composites consisting of alternate layers of (MoSi<sub>2</sub> + 20 vol% SiC<sub>p</sub>) and Mo, Ta and Nb foils, the total thickness of the interfacial reaction zone was found to be as 50 μm, 10 μm and 20 μm, respectively. This is consistent with the reported values of Si diffusivity and activation energies as reported by Tortorici and Dayananda (1998, 1999) for the development of reaction zones having different phases in these laminated composites. The main reaction product was identified to be M<sub>5</sub>Si<sub>3</sub> type of silicide (M = Mo, Ta, Nb) in all the laminated composites studied in the present work. The diffusivity of Si (D<sub>si</sub>) in Ta<sub>5</sub>Si<sub>3</sub> at 1600 °C was reported as 7.1x10<sup>-17</sup> m<sup>2</sup>/s, which was one order of magnitude lower than the diffusivity of Si in Nb<sub>5</sub>Si<sub>3</sub> (D<sub>si</sub> = 5.4x10<sup>-16</sup> m<sup>2</sup>/s). They reported activation energy of 210 kJ/mole for the

growth of  $\text{Mo}_5\text{Si}_3$  layer as compared to the activation energy of 265 kJ/mole for  $\text{Nb}_5\text{Si}_3$  phase. Lower the activation energy for diffusion, higher is the diffusivity. Tortorici and Dayananda (1998, 1999) have also found smaller thickness of the diffusion layers in ternary couples ( $\text{MoSi}_2\text{-Nb}$ ,  $\text{MoSi}_2\text{-Ta}$ ) than those for  $\text{MoSi}_2\text{-Mo}$  binary couples.

Nb is the most widely used ductile metal added in  $\text{MoSi}_2$  as the reinforcement for toughening. Different workers have used Nb in the form of particulates, short fibers, continuous wires, chopped wire mesh and foils. The composites were prepared by vacuum hot pressing as well as by hot isostatic pressing at different processing temperatures and pressures applied for different lengths of time. Most of the workers (Xiao et al 1990, Alman et al 1992, Venkateswara Rao et al 1992<sup>b</sup>, Chen et al 1994<sup>a</sup>, 1994<sup>b</sup> and Soboyejo et al 1996) have reported  $(\text{Mo, Nb})_5\text{Si}_3$  and  $\text{Nb}_5\text{Si}_3$  as the main reaction products formed during the processing at high temperatures. Only in a few cases (Xiao and Abbaschian 1992<sup>a</sup>, 1992<sup>b</sup> and Alman et al 1994), the presence of  $\text{NbSi}_2$  was also reported along with  $(\text{Mo, Nb})_5\text{Si}_3$  in the reaction zone. However, in the present work, no evidence of the formation of  $\text{NbSi}_2$  as an interfacial reaction product was found. A large variation in the thickness of the reaction zone ranging from 10  $\mu\text{m}$  to 75  $\mu\text{m}$  has been reported by different workers. It is obvious that the differences in the reaction zone thickness resulted from the different processing parameters used by different workers. Processing at lower temperatures results in a smaller thickness of the interfacial reaction zone but higher processing temperatures are needed to obtain a fully dense composite. Therefore, for the development of ductile phase reinforced  $\text{MoSi}_2$  based composites, the process parameters need to be optimized to minimize the chemical interactions between the constituents as well as to obtain a fully dense composite material.

The hardness value obtained for the  $\text{MoSi}_2 + 20 \text{ vol}\% \text{ SiC}_p$  monolithic material was found to be much higher than the reported value for pure  $\text{MoSi}_2$  (9 - 10 GPa) as well as the value calculated by rule of mixture for  $\text{MoSi}_2 + 20 \text{ vol}\% \text{ SiC}_p$  particulate composite (13.2 GPa). The increase in hardness as compared to pure  $\text{MoSi}_2$  is due to the addition of much harder SiC particles in  $\text{MoSi}_2$ . A fine and uniformly distributed network of SiC particles in  $\text{MoSi}_2$  also led to a considerable grain refinement in  $\text{MoSi}_2$  matrix. Bhattacharya and Petrovic (1991) have observed that hardness increases with

increasing SiC content. They also found that all their experimental hardness values were higher than as predicted by rule of mixture. They reported a hardness value of 14 GPa for MoSi<sub>2</sub> + 20 vol% SiC<sub>p</sub>. The higher hardness obtained in the present work for the same composite could be due to a smaller SiC particle size used.

The fracture toughness of MoSi<sub>2</sub> + 20 vol% SiC<sub>p</sub> monolithic material was measured as 5.2 MPa√m. Bhattacharya and Petrovic (1991) have observed that similar to the hardness values, the indentation fracture toughness of MoSi<sub>2</sub> also increased with increasing SiC content. They also reported that there was a levelling off of the toughness values at about 20 vol% SiC<sub>p</sub> content, beyond which addition of more SiC did not seem to improve the toughness of MoSi<sub>2</sub>. However, literature data reveals a large scatter in fracture toughness of SiC reinforced MoSi<sub>2</sub> matrix composites as compiled and presented in Table 1.8. The variation in fracture toughness values reported in literature is possibly due to the differences in average particle sizes of SiC and MoSi<sub>2</sub>, SiO<sub>2</sub> content, grain sizes, densities of MoSi<sub>2</sub> and processing parameters used in different investigations.

Crack deflection has been identified as a major toughening mechanism in ceramic particles reinforced MoSi<sub>2</sub> based composites (Carter and Hurley, 1987). Faber and Evans (1983) have discussed in detail the mechanism of fracture toughness enhancement in ceramics due to crack deflection around second phase particles as described in section 1.7.1.3. As the crack approaches a second phase particle, it 'tilts' out of the original plane of propagation and as it approaches the next particle, it tilts in the reverse direction, undergoing 'twist'. The stress intensity ahead of the tilted crack has mode I (opening) and mode II (sliding) components, whereas the twisted crack stress intensity possesses mode I and mode III (tearing) components. The local stress intensity factors are a function of deflection angle and contribute to toughening, as stress intensity factor corresponding to mode I is lowered significantly. In the present work, localized toughening mechanisms, such as crack deflection, crack microbridging, crack branching and particle fracture as seen in Figs. 5.75(a) and 5.75(b) explain the improvement in fracture toughness of MoSi<sub>2</sub> + 20 vol% SiC<sub>p</sub> composite as compared to that of pure MoSi<sub>2</sub>.

Faber and Evans (1983) proposed that the toughening increment due to spherical reinforcements from pure tilt induced deflection could be given as:

$$G_c = (1 + 0.87V_p)G_m \quad (5.31)$$

Where,  $G_c$  = fracture energy of the composite  
 $G_m$  = fracture energy of the matrix  
 $V_p$  = volume fraction of the particles

$$\frac{G_c}{G_m} = 1 + 0.87V_p \quad (5.32)$$

By addition of 20 vol% spheres,  $\frac{G_c}{G_m} = 1.17$

Twist will further enhance this toughening ratio. Crack twist contributions from uniformly distributed spheres elevate,  $\frac{G_c}{G_m} \sim 1.3$

The near-tip stress intensity is reduced by 30% by crack deflection. Assuming linear elastic fracture behaviour of the composite:

The toughening ratio (Soboyejo et al, 1996)  $\lambda_d = \frac{G_c}{G_m} = \frac{K_c}{K_m}$  (5.33)

The fracture toughness of MoSi<sub>2</sub> + 20 vol% SiC<sub>p</sub> in the present investigation was measured as 5.2 MPa√m which yields a toughening ratio of 1.28, thus validating the model proposed by Faber and Evans (1983).

The tri-layer MoSi<sub>2</sub>-SiC<sub>p</sub> matrix laminated composites prepared and studied in the present work contain only 10 vol% of the ductile phase in the form of a foil. The fracture toughness of (MoSi<sub>2</sub> + 20 vol% SiC<sub>p</sub>) + 10 vol% Nb was measured as 17.1 MPa√m (Table 5.19B) in crack arrester mode exhibiting a significant increase of more than 3 times over the MoSi<sub>2</sub> + 20 vol% SiC<sub>p</sub> matrix. Similar values of fracture toughness of pure MoSi<sub>2</sub> + Nb foil laminates have been reported by other workers in limited number of studies carried out on MoSi<sub>2</sub> / Nb laminated composite system. Xiao et al (1991) have reported a fracture toughness value of 15.2 MPa√m for MoSi<sub>2</sub> + 20 vol% Nb foil laminated composite. Chen et al (1994<sup>a</sup>, 1994<sup>b</sup>) found a K<sub>IC</sub> value of 18.0 ± 2.0 MPa√m for MoSi<sub>2</sub> + 20 vol% Nb foil composite. They also reported a flexural strength value of 386 MPa for MoSi<sub>2</sub> + 20 vol% Nb foil laminated composite. In the present



work, a marginally higher flexural strength value of 398 MPa was obtained for (MoSi<sub>2</sub> + 20 vol% SiC<sub>p</sub>) + Nb foil laminated composite. The improvement in flexural strength of laminated composites is essentially due to the contribution of the load necessary to debond the refractory metal foil from the matrix. Shaw and Abbaschian (1994) studied the effect of Nb foil thickness on the fracture toughness of MoSi<sub>2</sub> + 20 vol% Nb laminated composites. They measured fracture toughness values as 12.2 MPa√m, 15.2 MPa√m, 15.4 MPa√m and 17.6 MPa√m with Nb foils having thickness of 0.127 mm, 0.25 mm, 0.50 mm and 1.0 mm, respectively. As thickness of the Nb foil increases, fracture toughness also increases. They observed that K<sub>max</sub>, the damage tolerance was actually an indicator of the bridging capability of the ductile phase and should be related to the combined effects of size and intrinsic properties of the ductile laminas. Xiao (1991<sup>b</sup>) has observed that in case of MoSi<sub>2</sub> + Nb foil laminated composite, when the yield strength of the Nb foil was high, fracture toughness was also high.

However, caution must be exercised in making a comparison of the mechanical properties of brittle materials, because of the general lack of detailed fabrication and testing information in the literature. Different methods for measuring fracture toughness often gave different results. The direct comparison of the fracture toughness data must be done very carefully since the material processing conditions are not the same. Therefore, comparisons of literature data should be considered only qualitative. It should be noted that in all these studies, pure MoSi<sub>2</sub> was used as the matrix layer. SiC particulates were not added in MoSi<sub>2</sub> matrix in contrast to the present work. Addition of SiC particulates in MoSi<sub>2</sub> not only improves the thermal compatibility between matrix and the refractory metal foils but also is expected to result in improved elevated temperature properties of MoSi<sub>2</sub>. However, at room temperature, apart from crack bridging by ductile metal foils, additional toughening results from crack deflection and branching that occurs as a consequence of crack – SiC particles interactions. Therefore, the present results indicate that a hybrid approach of using a combination of brittle and ductile reinforcements in different morphologies in MoSi<sub>2</sub> matrix is the key for the development of MoSi<sub>2</sub> as a high temperature structural material.

The results of residual thermal stress analysis as obtained in Chapter 4 clearly reveal that the various composites processed in the present study contain large magnitudes of residual stresses. In case of ceramic matrix composites, cracking may occur in the matrix to relieve the high level of thermal stresses while, in metal matrix composites, matrix is likely to deform plastically instead of cracking.

However, no cracking was observed in MoSi<sub>2</sub> reinforced with 20 vol% SiC particulates in as processed condition at room temperature as observed in the microstructures presented in Figs 5.50 and 5.52. This is in agreement with the criterion for matrix cracking as proposed by Lu et al (1991<sup>a</sup> and 1991<sup>b</sup>). They have described a non-dimensional quantity,  $R$ , which relates the thermal expansion mismatch stress,  $\sigma$  to the fracture toughness of the matrix,  $K_{IC}$  and the size of the reinforcement phase,  $r$  as follows:

$$R = r \left( \frac{\sigma}{K_{IC}} \right)^2 \quad (5.34)$$

where,  $r$  is the particle radius for particle reinforced composites or fiber radius for fiber-reinforced composites. When  $R \leq 1$ , the matrix cracking will not occur. When  $R > 10$  all forms of matrix cracking will occur profusely. A large particle size, higher residual thermal stresses and a low fracture toughness of the matrix material will promote matrix cracking.

In the present case of MoSi<sub>2</sub> + 20 vol% SiC<sub>p</sub> composite, the residual thermal tensile stress in the matrix,  $\sigma_{\theta} = 1372$  MPa; fracture toughness of pure MoSi<sub>2</sub> matrix,  $K_{IC} = 3.0$  MPa√m; average radius of SiC particles,  $r = 1 \mu\text{m} = 1 \times 10^{-6}$  m. Substituting these values in the above equation,  $R = 0.21$  which is  $< 1$ . Therefore, no cracking in MoSi<sub>2</sub> matrix would occur.

No cracking in the matrix of the various laminated composites prepared in the present study is observed. Extending the above criterion for matrix cracking for laminated composites and using a fracture toughness,  $K_{IC}$  value of the matrix material as 4.0 MPa√m and  $r = 0.25$  mm =  $0.25 \times 10^{-3}$  m (assuming  $r$  = half the foil

thickness), the calculated values of  $R$  for different laminated composites investigated in the present study are presented in Table 5.26

Table 5.26 Residual thermal stresses and  $R$  values for different laminated composites.

Composite	Residual Tensile Stress in the Matrix, $\sigma_\theta$ (MPa)	$R$
(MoSi <sub>2</sub> + 20 vol% SiC <sub>p</sub> ) + Mo Foil	201	0.63
(MoSi <sub>2</sub> + 20 vol% SiC <sub>p</sub> ) + Ta Foil	59	0.05
(MoSi <sub>2</sub> + 20 vol% SiC <sub>p</sub> ) + Nb Foil	14	0.003

Since  $R < 1$  in all the cases, no matrix cracking is expected.

It can be shown that for spherical particles, the total area of particle / matrix interface per unit volume of the composite is given by (Chawla, 1993):

$$I_A = \frac{6V_r}{d} \quad (5.35)$$

where,  $V_r$  = volume fraction of the reinforcement  
 $d$  = average particle size (diameter).

Using the above equation, the interfacial area between MoSi<sub>2</sub> and SiC particles, which are assumed to be spherical, is estimated to be  $6 \times 10^3 \text{ cm}^2$  per  $\text{cm}^3$  of volume in MoSi<sub>2</sub> + 20 vol% SiC<sub>p</sub> matrix. This large interfacial area between MoSi<sub>2</sub> and SiC<sub>p</sub> may influence the mechanical behaviour of the composite (the actual interfacial area would be much larger as the SiC particles used in the present study are quite irregular in shape as revealed in Fig. 5.75).

MoSi<sub>2</sub> and SiC are thermodynamically stable with each other at all temperatures as shown in Fig. 5.49 and no atomic diffusion is expected to take place across the MoSi<sub>2</sub> / SiC interface. MoSi<sub>2</sub> matrix is expected to shrink more than the SiC particle on cooling from the processing temperature due to a higher coefficient of

thermal expansion of MoSi<sub>2</sub> than SiC. This would lead to gripping of the SiC particle by the matrix even in the absence of any chemical bonding. As MoSi<sub>2</sub> behaves like metals at high temperatures, it can also penetrate the crevices on the SiC particle surface by viscous flow or high temperature diffusion leading to some mechanical bonding (keying effect). In case of a pure mechanical bond, the interfacial shear strength,  $\tau_i$  is given by (Chawla, 1993):

$$\tau_i = \mu\sigma_r$$

where,  $\sigma_r$  is the radial compressive stress in the particle and  $\mu$  is the coefficient of friction.

In the present study,  $\sigma_r$  has been estimated as 1568 MPa (as described in section 4.3.1) while,  $\mu$  varies from 0.1 to 0.6 for most of the ceramic matrix composite systems. This suggests that the interfacial bond between MoSi<sub>2</sub> and SiC particles is quite strong even in the absence of any chemical interactions between the two. The interface is also expected to be incoherent i.e., no matching of lattice planes across the boundary as in case of most of the particle reinforced ceramic matrix composites. High-resolution TEM investigations by Mitra et al (1995, 1997<sup>b</sup>) revealed the interface between MoSi<sub>2</sub> and SiC to be atomically abrupt.

However, in the present investigation it was found that the indentation cracks get deflected by SiC particles and propagate along the SiC / MoSi<sub>2</sub> interface (as exhibited by arrow marks in Figs. 5.75(a) and 5.75(b)). The crack propagation along the SiC / MoSi<sub>2</sub> interface is believed to be due to the presence of an amorphous SiO<sub>2</sub> layer at the SiC / MoSi<sub>2</sub> interface. The commercially available powders of both MoSi<sub>2</sub> and SiC used in the present study were found to contain significant amounts of oxygen (Table 5.3). The oxygen is reported to be present mostly in the form of a thin SiO<sub>2</sub> layer on the powder particle surfaces and as fine SiO<sub>2</sub> particles inside the MoSi<sub>2</sub> grains or at the grain boundaries. High-resolution TEM studies (Mitra et al, 1997<sup>a</sup>) have shown that the MoSi<sub>2</sub> / SiC interfaces have an amorphous glassy region of 5-8 nm thickness. They verified the existence of the amorphous region from the diffuse selected area diffraction pattern. This has been previously observed by Lim et al (1989) at RB-SiC / MoSi<sub>2</sub> interfaces and by Suzuki et al (1993) at XD<sup>TM</sup> MoSi<sub>2</sub> /

SiC interfaces. The low fracture energy of amorphous SiO<sub>2</sub> film may provide a relatively easy path for crack propagation.

A few of the SiC particles having elongated and sharp edges are cut through by the advancing crack as revealed in Fig. 5.75(b). This may be attributed to the fact that the sharp edges in a particle are generally the areas of high stress concentration.

A crack in the matrix layer can lead to debonding at the interface of laminated composite, followed by crack deflection, crack bridging etc. All these additional energy-absorbing phenomena lead to enhanced fracture toughness and a non-catastrophic failure mode. Cook and Gordon (1964) were the first to analyze the interfacial debonding ahead of a propagating crack at a weak interface resulting in crack deflection.

At the tip of any crack, a tri-axial state of stress is present. The stress distribution at the crack tip is shown schematically in Fig. 5.116 (Cook and Gordon, 1964). The main applied stress component,  $\sigma_y$ , has a very high value at the crack tip, and decreases sharply with distance from the crack tip. The stress component acting normal to the interface,  $\sigma_x$ , is zero at the crack tip. It rises to a maximum value at a small distance from the crack tip and then falls off in a manner similar to  $\sigma_y$ . Now, it is easy to visualize that if the interface tensile strength is less than the maximum value of  $\sigma_x$ , then the interface will fail in front of the crack tip. According to the estimates of Cook and Gordon, if interfacial tensile strength  $\leq 1/5 \sigma_y$  i.e., the main stress component, will cause the opening of interface in front of the crack tip.

Cook and Gordon analyzed the crack deflection at an interface between materials of identical elastic constants, i.e., the same material joined at an interface. However, two materials that meet at an interface are likely to have different elastic constants as in the case of laminated composites prepared in the present investigation. The elastic moduli of MoSi<sub>2</sub> based matrix and the ductile metal foils are vastly different. The modulus mismatch causes shearing of the crack surfaces (He and Hutchinson, 1989<sup>a</sup>, 1989<sup>b</sup>) resulting in a mixed mode stress state in the vicinity of an interface crack tip involving both the tensile and shear components. This, in

turn, results in a mixed-mode fracture at the crack tip or in the wake of the crack. This means that instead of a simple, one parameter description by the critical stress intensity factor  $K_{IC}$ , a more complex formalism of fracture mechanics is needed to describe the situation. The parameter  $K$  under such a situation becomes scale sensitive, but the critical strain energy release rate,  $G_{IC}$ , is not a scale sensitive parameter.

The “elastic mismatch” or the measure of elastic anisotropy,  $\alpha$ , is given by:

$$\alpha = \frac{\bar{E}_1 - \bar{E}_2}{\bar{E}_1 + \bar{E}_2} \quad (5.36)$$

where,  $\bar{E} = \frac{E}{1-\nu^2}$  and  $\alpha$  can also be written as

$$\alpha = \frac{G_1(1-\nu_2) - G_2(1-\nu_1)}{G_1(1-\nu_2) + G_2(1-\nu_1)} \quad (5.37)$$

$$\beta = \frac{1}{2} \left[ \frac{G_1(1-2\nu_2) - G_2(1-2\nu_1)}{G_1(1-\nu_2) + G_2(1-\nu_1)} \right] \quad (5.38)$$

$\alpha$  and  $\beta$  are called Dundurs parameters.

These expressions have been used by He and Hutchinson (1989<sup>a</sup>, 1989<sup>b</sup>), Evans and Marshall (1989), Ruhle and Evans (1988) and Gupta et al (1993) to analyze the conditions for fiber / matrix debonding in terms of the energy requirements. The results are shown in Fig. 5.117 (Evans and Marshall, 1989) in terms of a chart of  $G_i/G_f$  versus  $\alpha$ , where  $G_i$  is the mixed-mode interfacial fracture energy of the interface,  $G_f$  is the mode I fracture energy of the fiber, and  $\alpha$  is the measure of elastic anisotropy as defined above.

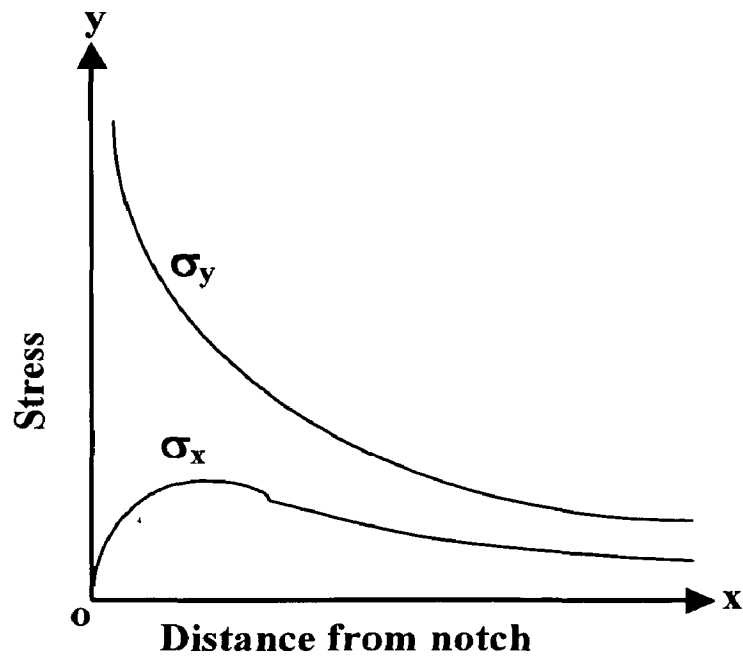
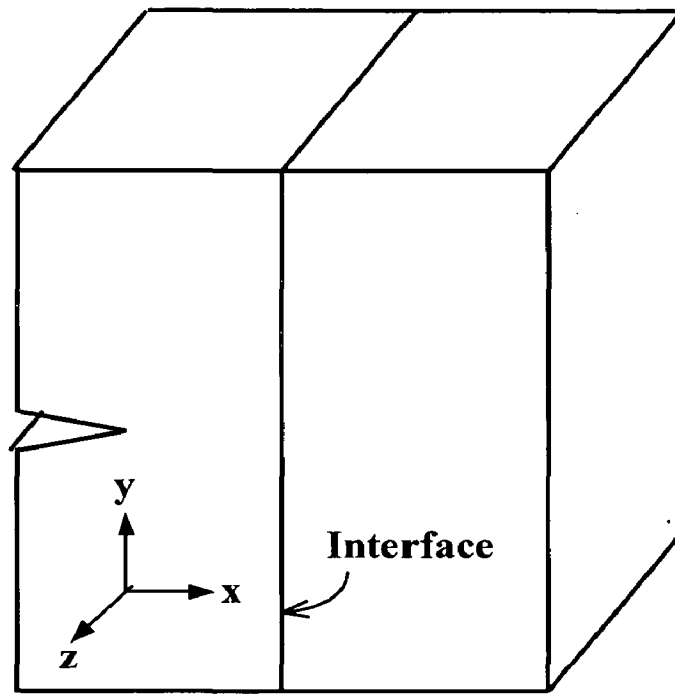


Fig. 5.116 Schematic of stress distribution at a crack tip.

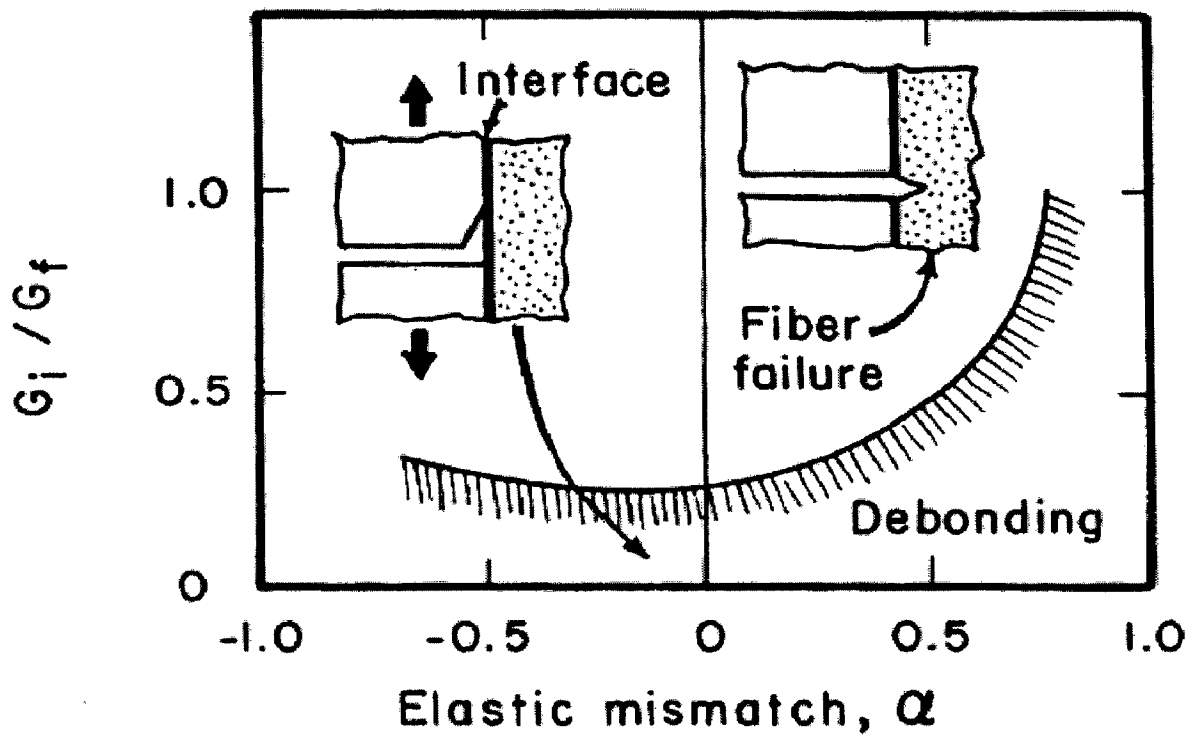


Fig. 5.117 A chart of  $G_i/G_f$  vs.  $\alpha$



Venkateshwar Rao et al (1992<sup>a</sup>, 1992<sup>b</sup>) have used the debonding criterion for MoSi<sub>2</sub> / Nb particulate composites as given by Tirosh and Tetelman (1976). Tirosh and Tetelman (1976) have argued that debonding will occur along the interface if  $G_i/G_p < 0.4$ , where  $G_p$  is the fracture energy of the particle. Venkateshwar Rao et al (1992<sup>a</sup>, 1992<sup>b</sup>) have calculated the elastic mismatch parameter,  $\alpha$  for MoSi<sub>2</sub> / Nb system as 0.57,  $G_i = 50 - 60 \text{ J/m}^2$  (assumed same as fracture energy of MoSi<sub>2</sub>) and  $G_p = G_{Nb} = 200 - 500 \text{ J/m}^2$  (Lu et al, 1991<sup>b</sup>). Using these values,  $G_i/G_p < 0.4$  is readily satisfied for MoSi<sub>2</sub> / Nb particulate system.

In another study, Xiao et al (1990, 1991) have shown that in MoSi<sub>2</sub> / Nb foil laminated composites, debonding at the interface does not occur in advance of the crack, when a crack approaches the interface or just impinges on it for both uncoated and coated Nb foil. They measured the interfacial fracture energies,  $G_i$  as  $> 33.7 \text{ J/m}^2$ ,  $16 \text{ J/m}^2$  and  $13 \text{ J/m}^2$  for uncoated, Al<sub>2</sub>O<sub>3</sub> coated and ZrO<sub>2</sub> coated Nb foil composites, respectively. They explained their observations based on Cook and Gordon (1964) theory. According to Xiao et al (1991), Cook and Gordon found that for an elliptical crack, interfacial fracture energy of 1/5 (or less) of the matrix fracture energy would cause interfacial debonding in advance of the crack. Xiao et al (1991) measured the fracture energy of the matrix (pure MoSi<sub>2</sub> in this case) as  $33.7 \text{ J/m}^2$ . Since the fracture energies of all the interfaces measured by them were higher than 1/5 of the matrix fracture energy, debonding did not occur in advance of the crack.

However, it has to be noted that Cook and Gordon theory is applicable for materials having the same elastic moduli (elastic mismatch  $\alpha = 0$ ). Secondly, Cook and Gordon used the term interfacial tensile strength in their debonding criterion and not the interfacial fracture energy as interpreted by Xiao et al (1991).

Table 5.27 Elastic constants of different ductile refractory metals and the MoSi<sub>2</sub> based matrix layer.

Parameters	(MoSi <sub>2</sub> + 20 Vol% SiC <sub>p</sub> )	Mo	Ta	Nb
$E$	436	324	186	103
$\nu$	0.15	0.32	0.35	0.38
$\bar{E}$	446	361	212	120

Table 5.28 Elastic mismatch parameter,  $\alpha$  for various laminated composites consisting of different refractory metal foils sandwiched between two layers of MoSi<sub>2</sub> + 20 vol% SiC<sub>p</sub> matrix.

Composite	Elastic Mismatch Parameter, $\alpha$
(MoSi <sub>2</sub> + 20 Vol% SiC <sub>p</sub> ) + Mo foil	-0.10
(MoSi <sub>2</sub> + 20 Vol% SiC <sub>p</sub> ) + Ta foil	-0.36
(MoSi <sub>2</sub> + 20 Vol% SiC <sub>p</sub> ) + Nb foil	-0.61

Using the limited data available, an attempt has been made to predict the interfacial debonding in (MoSi<sub>2</sub> + 20 vol% SiC<sub>p</sub>) + Nb foil (uncoated and Al<sub>2</sub>O<sub>3</sub> coated) laminated composites prepared in the present study. Taking  $\alpha = -0.61$  (as calculated in Table 5.27), the interfacial fracture energies,  $G_i = 33.7 \text{ J/m}^2$  and  $16 \text{ J/m}^2$  for uncoated and Al<sub>2</sub>O<sub>3</sub> coated Nb foils, respectively (as measured by Xiao et al, 1991) and  $G_f = G_{Nb} = 200 - 500 \text{ J/m}^2$  (Lu et al, 1991<sup>b</sup>), the criterion for debonding,  $G_i/G_f < 0.4$  is readily satisfied.

However, in the present study, no debonding at the interface was observed for both uncoated and Al<sub>2</sub>O<sub>3</sub> coated Nb foil / MoSi<sub>2</sub> laminated composites upon impingement of the crack on the interface as shown in Figs. 5.78 and 5.100. The possible explanation for the contradiction between the observed behaviour in the present work and the prediction from the theoretical model could be due to the fact that He and Hutchinson (1989<sup>b</sup>) developed the debonding criterion for ceramic matrix composites reinforced with ceramic fibers. Ceramic fibers are brittle and do not have slip capability. In the present case, the reinforcement is a ductile phase. It is believed that the impingement of the crack on the interface causes local dislocation slip in the reinforcement instead of interfacial failure, leading to the release of the stress concentration. The present results suggest that interfacial failure was not the only mechanism of blunting cracks in case of ductile reinforcements. The slip capability of ductile reinforcement can play an important role.

It should be noted that the above analysis has been over simplified to get an idea of interfacial debonding in laminated composites. A more precise treatment of this problem should consider the properties of a Nb / Nb<sub>5</sub>Si<sub>3</sub> / (Mo, Nb)<sub>5</sub>Si<sub>3</sub> / MoSi<sub>2</sub> layered structure. The varying composition of the interfacial reaction layer and the absence of the elastic properties of other silicide phases of Mo and Nb precluded solution to this problem.

In notched three-point bend tests ( $K_{IC}$  measurement in crack arrester mode), the crack initiated at the notch tip and propagated in MoSi<sub>2</sub> matrix until it impinged upon the Nb foil. Further propagation of the crack was arrested due to local dislocation slip in the ductile Nb foil. However, with increasing applied load (and therefore, with increasing stress intensity at the crack tip), multiple cracking in the

matrix in the vicinity of the main propagating crack resulted in limited debonding at the interface. This limited debonding at the interface decreased the constraint imposed by the brittle matrix on the ductile Nb foil and allowed the Nb foil to undergo plastic deformation resulting in necking as depicted in SEM images of the tested  $K_{IC}$  specimens (Figs. 5.82 and 5.83). The multiple cracks at the interface added to the relaxation of the crack tip stress intensity and effectively enlarged the initial plastic zone in the ductile phase. Once the foil begins to neck, the load carrying capacity of the foil decreases, and thus the processes that cause foil / matrix debonding, cease.

In notched three-point bend test of (MoSi<sub>2</sub> + 2 wt% Al) + Mo foil laminated composite, extensive debonding occurred at the interface (Fig. 5.47) resulting in the shear failure of the test specimens. However, in case of (MoSi<sub>2</sub> + 20 vol% SiC<sub>p</sub>) + Mo foil laminated composite, the test specimens failed in pure flexure (no shear failure was observed). This can probably be attributed to a lower value of  $G_i/G_{Mo}$  in Mo foil / MoSi<sub>2</sub> laminated composite with Al in MoSi<sub>2</sub> matrix as compared to the Mo foil / MoSi<sub>2</sub> laminated composite with SiC<sub>p</sub> in MoSi<sub>2</sub> matrix. The SiC<sub>p</sub> addition in MoSi<sub>2</sub> matrix reduces the thermal expansion mismatch between the layers of MoSi<sub>2</sub> based matrix and the Mo foil resulting in relatively lower residual tensile stresses in the composite and hence a relatively stronger interface. A low value of  $G_i/G_{Mo}$  will lead to more chances of interfacial debonding as depicted in Fig. 5.117. In addition to a lower value of  $G_i/G_{Mo}$ , a higher thickness of the interfacial reaction zone in (MoSi<sub>2</sub> + 2 wt% Al) + Mo foil laminated composite as compared to the reaction zone thickness in (MoSi<sub>2</sub> + 20 vol% SiC<sub>p</sub>) + Mo foil composite may also play an important role in enhancing the interfacial debonding and shear failure.

In case of ductile refractory metal (Me) particles reinforced MoSi<sub>2</sub> matrix composites, the metal particles were completely converted into Me<sub>5</sub>Si<sub>3</sub> type brittle silicides due to extensive diffusion of Si. In this case, it is assumed that the value of  $G_i/G_f$  will be close to 1. It is clear from Fig. 5.117 that the crack will propagate through the reinforcing phase without any interfacial debonding. The results obtained in the present investigation validated the above argument as presented in Fig. 5.28(b) which is a SEM back scattered electron image exhibiting the indentation crack passing through the W<sub>5</sub>Si<sub>3</sub> phase without any interfacial debonding in MoSi<sub>2</sub> +

20 vol% W composite. The incident of crack bridging as shown in Fig. 5.28(a) was observed very rarely and the same may be attributed to some left over unreacted metal particles.

Figure 5.118 exhibits a typical load - displacement curve obtained in fracture toughness ( $K_{IC}$ ) testing of a laminated composite consisting of alternate layers of ( $MoSi_2 + 20 \text{ vol\% } SiC_p$ ) and ductile refractory metal foil in crack arrester mode. The load - displacement curve is distinguishingly different than a typical load - displacement curve of a brittle ceramic material. The curve exhibits an initial linear increase in the load similar to a brittle material. It shows a significant instantaneous drop in the load after reaching to a peak value,  $P_{max}$ . Beyond this point, the load - displacement curve exhibits plastic deformation, a characteristic feature of a ductile metal. It more or less resembles with a typical load - displacement curve of a metal.

At the early stages of loading, the crack initiates at the notch tip and propagates in  $MoSi_2$  matrix until it impinges upon the ductile metal foil. The advancing crack gets arrested at the matrix \ foil interface and the subsequent crack growth would require re-nucleation. This is in contrast with the particle, short fibre or continuous fibre reinforced composites, where the crack can propagate continuously throughout the matrix without the need for re-nucleation. The arresting of the propagating crack could be due to the local dislocation slip in the ductile metal foil. With further increase in applied load, the crack re-nucleates on the other side of the metal foil and propagates throughout the entire thickness of the matrix layer at a load level much lower than the peak load,  $P_{max}$ . Because of a statistical distribution of crack nucleation sites on the other side of the foil, it is not necessary that the re-nucleation be coplanar with the original crack. Once the primary crack has propagated throughout the  $MoSi_2$  matrix, the load is transferred and mainly carried by the metal foil alone till debonding at the matrix / reinforcement interface takes place. The peak load for the laminated composite specimens was found to be 3 - 4 times higher than the peak load value obtained for the  $MoSi_2 + 20 \text{ vol\% } SiC_p$  monolithic specimen. Xiao et al (1991) have also reported a similar observation and found that a primary crack had already propagated throughout the entire thickness of the  $MoSi_2$  matrix when the load was about 23 % of the peak load. A typical stereo photomicrograph of the  $K_{IC}$  specimen tested in crack arrester mode is shown in Fig. 5.119. The specimen was unloaded

just before the separation into two pieces to study the macroscopic crack growth behaviour.

The crack propagation throughout the entire thickness of the matrix at a load level considerably below the peak load of the composite may be explained using the principle of strain compatibility in composite materials. During the initial loading and prior to cracking of the matrix, the matrix carries most of the applied load because the elastic modulus of the  $\text{MoSi}_2$  based matrix is much higher than that of the refractory metal foils. For the metal foils to carry the same stress as the matrix, they need to be elongated much more than the matrix (assuming no constrained deformation). However, the metal foils are bonded to the brittle matrix, which results in a constraint from the matrix on the deformation of the foils. Constraint is referred to a phenomenon that when a ductile phase is embedded in a brittle matrix, it can no longer deform freely, and instead it will deform under the restriction of the matrix. Therefore, the reinforcement with a lower elastic modulus will carry a minor part of the load until a matrix crack has opened appreciably to allow the reinforcement to strain. This is clearly impossible unless the matrix fractures. Beyond this level, the load is carried by the metal foil alone.

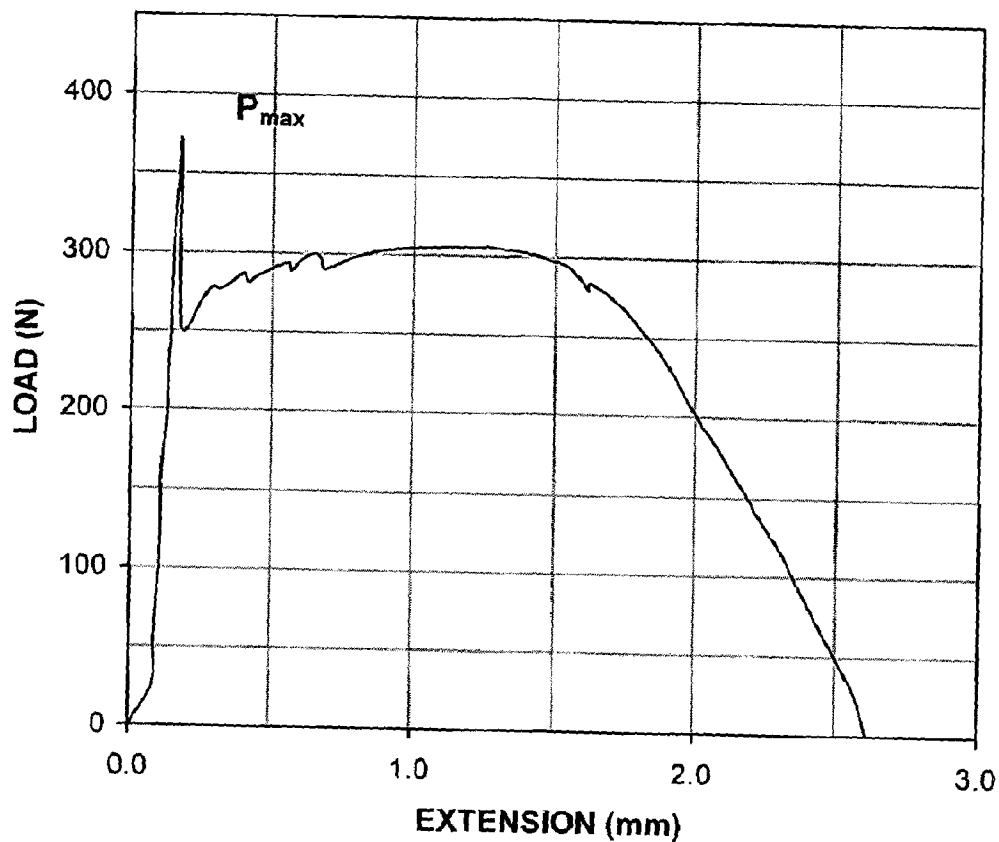


Fig. 5.118 A typical load-displacement curve obtained in fracture toughness ( $K_{IC}$ ) testing of ( $\text{MoSi}_2 + 20 \text{ vol\% SiC}_p$ ) + Nb foil laminated composite in crack arrester mode.

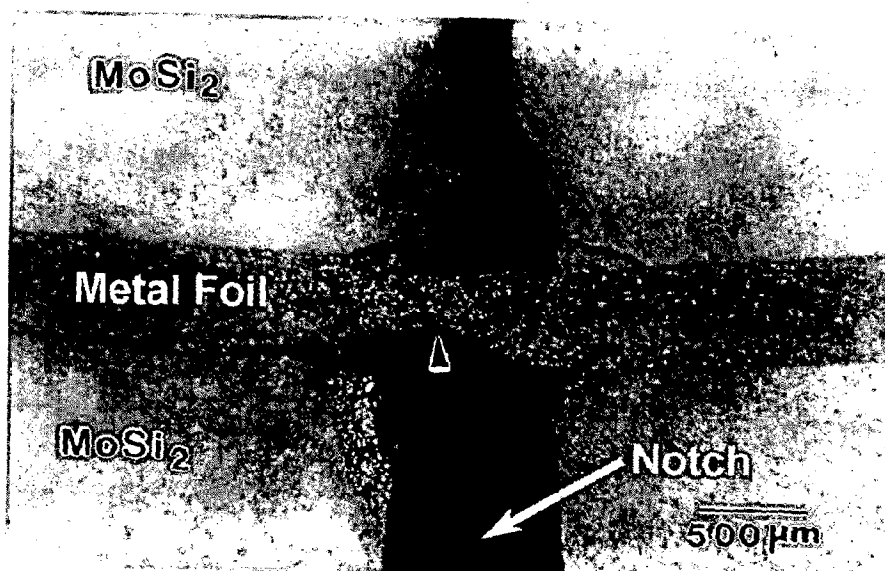


Fig. 5.119 A typical stereo photomicrograph of a  $K_{IC}$  specimen of  $\text{MoSi}_2$  / ductile refractory metal foil laminated composite tested in crack arrester mode. The specimen was unloaded just before the separation into two pieces.

The stress required to deform the constrained ductile foil would be greater than the normal stress required to deform the same foil in an unconstrained state. This can be explained on the basis of a thin foil of soft material bonded between two hard materials subjected to a uniaxial tensile stress, say  $\sigma_1$ . If the softer material is to elongate under the tensile stress, it must also contract laterally. However, the adjoining material to which it is bonded resists the lateral contraction resulting in the development of tensile stresses acting on the thin foil in the transverse directions, say  $\sigma_2$  and  $\sigma_3$  (Hayden et al, 1986). Due to these transverse stresses, the maximum shear stress  $\tau_{\max} = (\sigma_1 - \sigma_3)/2$ , which is responsible for yielding to occur (Dieter, 1987) reduces. Therefore, the applied tensile stress has to be much higher for yielding to occur when the foil is constrained. Finite element methods by Evans and Mcmeeking (1986), slip line field analysis by Sigl et al (1988) and direct experimental analysis of the deformation of a ductile inclusion in a brittle matrix by Ashby et al (1989) have revealed that a stress to yield a constrained ductile inclusion can be as great as six times that for the ductile inclusion in an unconstrained state. The maximum load,  $P_{\max}$ , increases with increasing degree of constraint. Owing to the cracking of the matrix at a load level considerably below the peak load of the composite, the  $K_{\max}$  value calculated from the peak load of the bend test is actually a reflection of the bridging capability of the ductile phase and may be interpreted as an indicator of the damage tolerance of the composite.

As the load level is increased to the peak load,  $P_{\max}$ , a momentary drop in the load is observed with a discernable "popping" noise detected from the specimen. The opening of the primary crack as well as formation and propagation of the secondary cracks in the vicinity of the main propagating crack in the matrix result in stretching of the metal foil and in a relatively large lateral deformation of the ductile metal reinforcement compared to the matrix. Large lateral displacement of the metal foil gives rise to transverse stresses, which can be large enough to cause limited interfacial debonding. Both interfacial failure and matrix fracture create a "gauge length" at the matrix / reinforcement interface, which is virtually a region, free from constraints of the matrix and can be called as decohesion length as shown schematically in Fig. 5.120. In this region, the matrix-imposed constraints are relaxed and the foil can deform freely in a unidirectional tensile stress state until it fails in a ductile manner. Once the foil begins



to neck, the load carrying capacity of the foil decreases, and thus the processes that cause foil / matrix debonding, cease. In the load-displacement curve, the displacement comes from the deformation of the metal foil inside the region of decohesion because the foil outside this region is bonded to the matrix and undergoes only elastic deformation. The deformation of the constrained ductile refractory metal foils can be divided into elastic deformation, plastic deformation within the decohesion region and the localized plastic deformation within the necking region.

The fracture toughness,  $K_{max}$ , is calculated from the peak load ( $P_{max}$ ) measured from the load - displacement curve of the notched three-point bend test.  $P_{max}$  does not exactly correspond to the stress intensity factor at failure but is a good approximation to it (Barker & Baratta 1980, Munz 1981, Newman, Jr., 1984).  $K_{max}$  is an indicator of the damage tolerance of the composite and thus, the value calculated is called "damage tolerance" and is designated as  $K_{max}$  rather than  $K_{IC}$ .

The mechanism of crack propagation in crack divider mode is quite different than in crack arrester mode. A typical load - displacement curve obtained in fracture toughness ( $K_{IC}$ ) testing of laminated composites in crack divider mode is shown in Fig. 5.121. After an initial linear increase in the load, the curve exhibits plastic stretching before a significant momentary drop in the load is observed as represented by the region P-Q in Fig. 5.121.

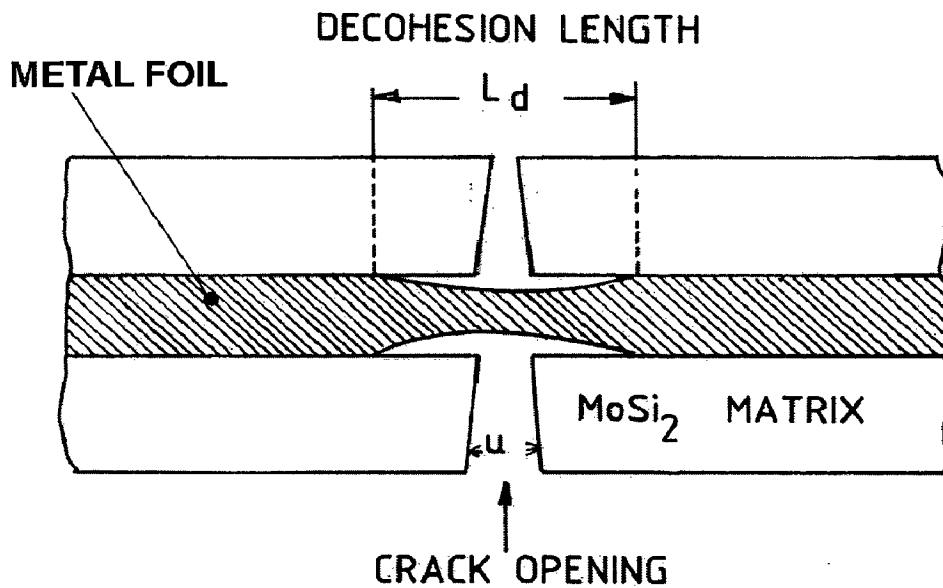


Fig. 5.120 Schematic representation of a  $K_{IC}$  specimen of a tri-layer laminated composite tested in crack arrester mode showing necking and plastic deformation in ductile metal foil and crack advancement in the brittle matrix.

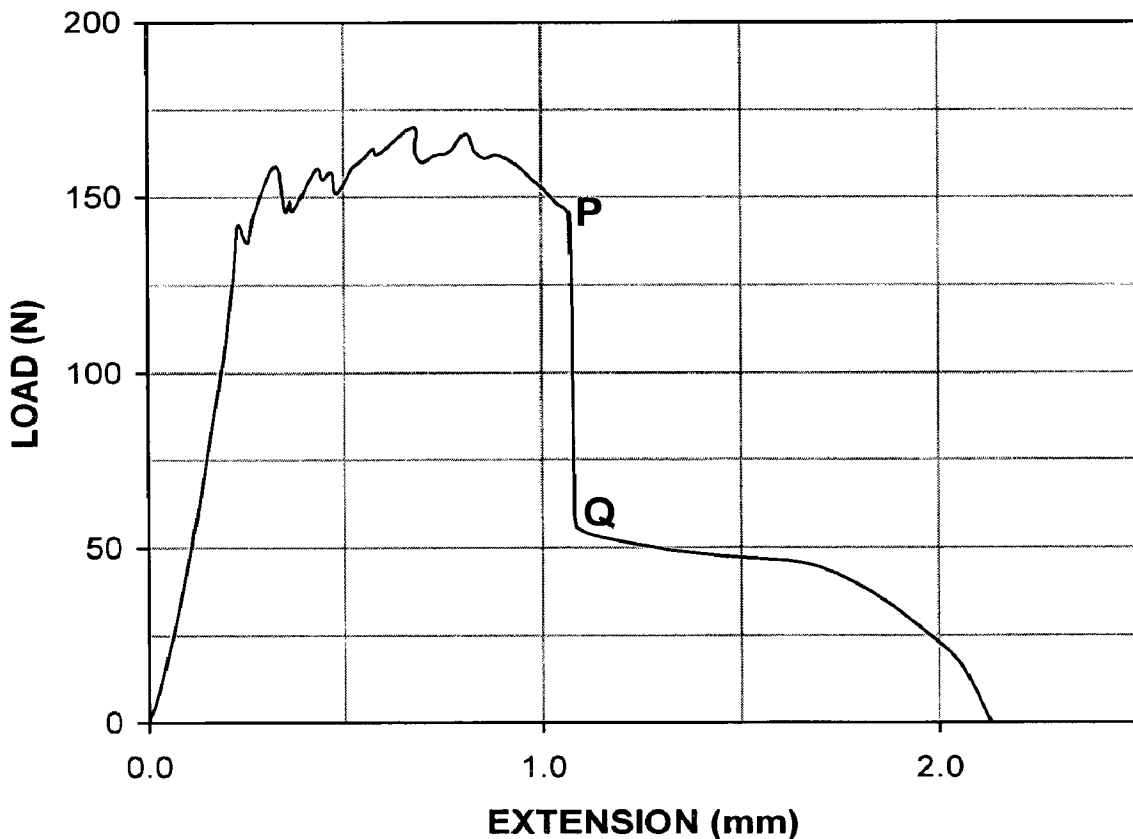


Fig. 5.121 A typical load-displacement curve obtained in fracture toughness ( $K_{IC}$ ) testing of  $(\text{MoSi}_2 + 20 \text{ vol}\% \text{ SiC}_p) + \text{Nb}$  foil laminated composite in crack divider mode.

Figure 5.122(a) is a schematic representation of a  $K_{IC}$  test specimen of a laminated tri-layer composite used for testing in crack divider mode. The arrow marks show the leading edge of the notch as well as the direction of the crack propagation. As depicted in the schematic diagram, the crack front is divided into two parts. The one, which propagates through the brittle  $MoSi_2$  matrix layers on both sides of the metal foil, and a small segment propagating through the metal foil. Figures 5.122(b), (c) and (d) are the stereo photomicrographs of the three sides of the fracture toughness specimen as designated by ABCD, BQRC and PQRS in Fig. 5.122(a), respectively as viewed after completion of the test. These stereo photomicrographs clearly reveal that the crack has propagated through the entire thickness of both the  $MoSi_2$  matrix layers. However, the segment moving through the ductile metal foil has not yet propagated through the entire thickness of the foil as observed in Fig. 5.122(d), which is the rear view of the specimen. A small volume of the ductile metal still holds the specimen and prevents its separation into two pieces. The specimen did not separate out completely in two pieces even after completion of the test.

It is apparent that crack growth through the laminate in the crack divider orientation occurs in a discontinuous manner with rapid catastrophic crack growth in  $MoSi_2$  and slow ductile tearing in the metal foil. The crack is expected to propagate continuously in the matrix once initiated. However, the segment, which moves through the ductile foil, lags behind the main propagating crack due to plastic stretching of the foil. This essentially resists the unstable crack propagation through the matrix. This mechanism of crack propagation can be referred to as 'crack front convolution' and is schematically presented in Fig. 5.123.

In crack divider mode, the crack can propagate continuously within the  $MoSi_2$  matrix without the need for re-nucleation in contrast to the crack arrester mode. In crack arrester mode, once the primary crack has propagated throughout the  $MoSi_2$  matrix, the load is transferred and carried mainly by the metal foil alone till debonding at the matrix - reinforcement interface takes place. While in crack divider mode, the primary crack propagation inside both the matrix layers can result in simultaneous debonding at the interface. This reduces the constraint on the metal foil resulting in its simultaneous plastic stretching. Therefore, it is assumed that the full load transfer from matrix to the

metal foil does not take place except during the last stage of the loading when the matrix is fully broken with a small part of the metal foil still remaining intact. This possibly explains a lower peak load reached (and hence a lower  $K_{max}$ ) in crack divider mode as compared to the fracture toughness testing in crack arrester mode.

It is believed that the crack propagates through the foil in a jerky manner. It jumps into steps. The serrations in the load – displacement curve are probably the manifestations of this jerky movement. At point Q, the main crack has already propagated throughout the matrix. Beyond this point, the curve represents only the plastic stretching of the remaining metal foil. The typical features observed on the fracture surfaces in crack divider mode support the jerky movement of the crack through the ductile metal foil.

Figure 5.124(a) exhibits a SEM fractograph of  $(MoSi_2 + 20 \text{ vol\% } SiC_p) + Nb$  foil laminated composite  $K_{IC}$  specimen, tested in crack divider mode. The fractograph has been taken at a relatively low magnification showing the notched as well as the fractured area covering both  $MoSi_2$  matrix and the Nb foil. The arrow mark shows the direction of the crack propagation. Very interesting features on the fracture surface of the foil are observed. It exhibits exclusive regions containing features of brittle as well as ductile fracture, alternately. The areas marked as A and B in Fig. 5.124(a) are shown in Figs. 5.124(b) and 5.124(c), respectively taken at higher magnifications. Figure 5.124(b) reveals a brittle cleavage fracture with river patterns while Fig. 5.124(c) reveals microvoids formation typical of a ductile fracture surface. Fracture surface appearance changes from cleavage to ductile dimple fracture. This indicates that the crack propagates slowly with appreciable plastic deformation of the ductile foil before jumping inside the foil resulting in brittle cleavage fracture of the foil. The crack moves in plane strain condition in the matrix region while, it moves in plane stress conditions in the foil region.

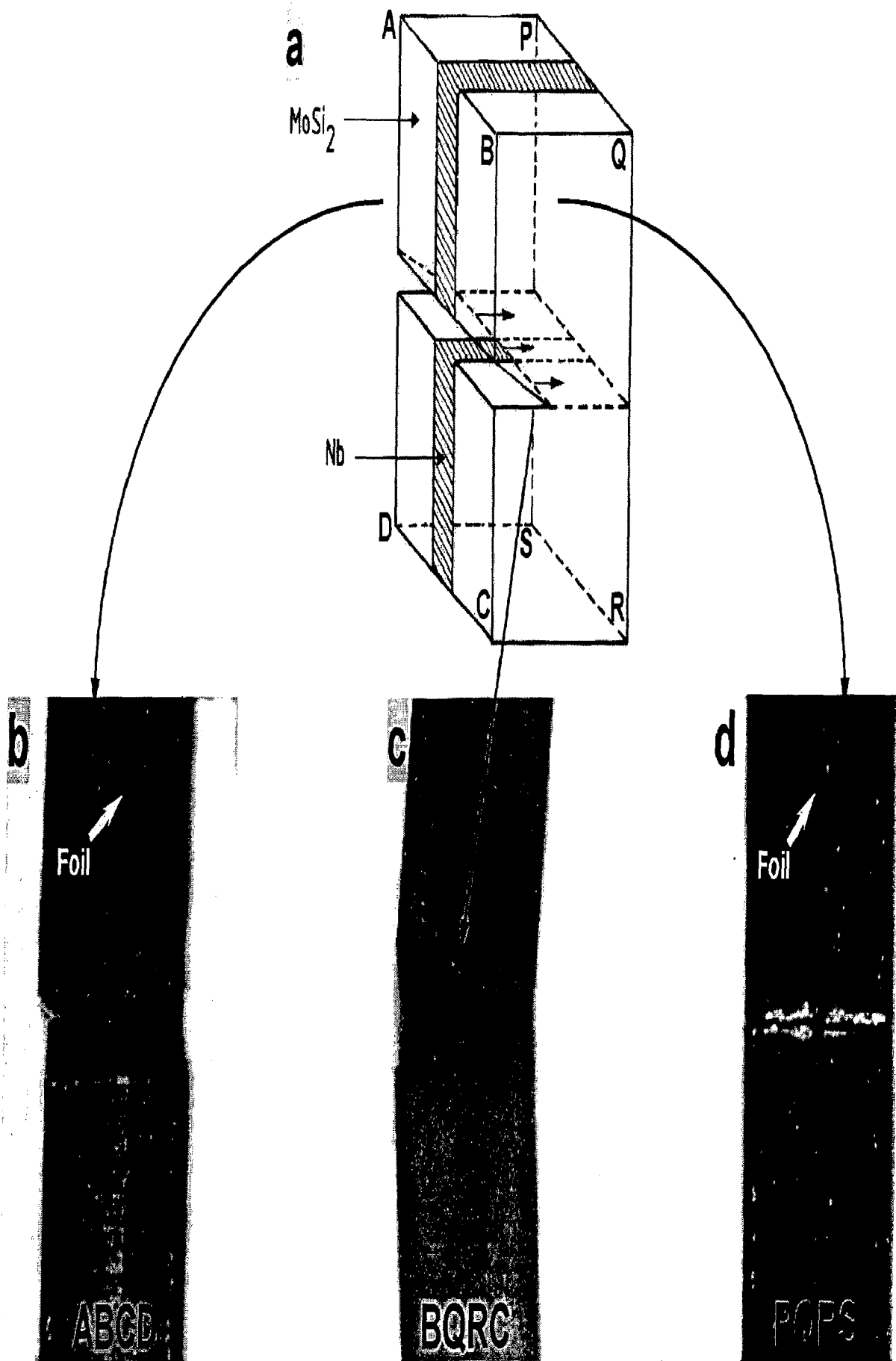


Fig. 5.122 (a) Schematic representation of a  $K_{IC}$  test specimen of a tri-layer laminated composite used for testing in crack divider mode. (b), (c) and (d) are the stereo photomicrographs of the three sides of the specimen as designated by ABCD, BQRC and PQRS in Fig. a, respectively after the completion of the test. The specimen did not separate out completely in two pieces.

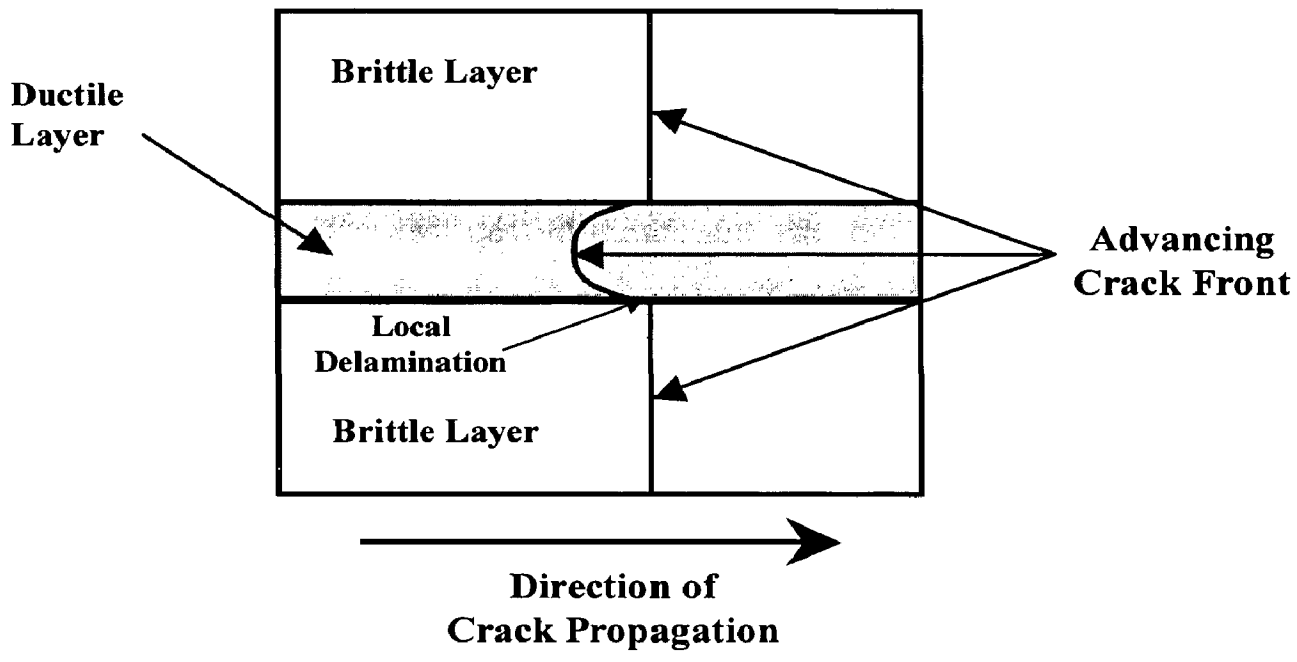


Fig. 5.123 Schematic representation of mechanism of crack propagation (crack front convolution) in alternate  $\text{MoSi}_2$  / ductile metal foil tri-layer laminated composites.

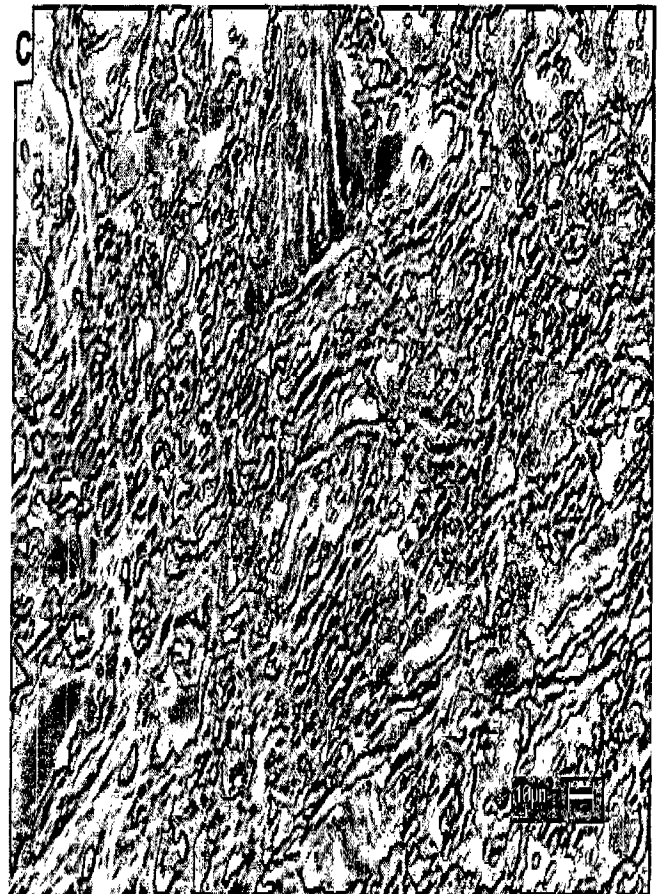
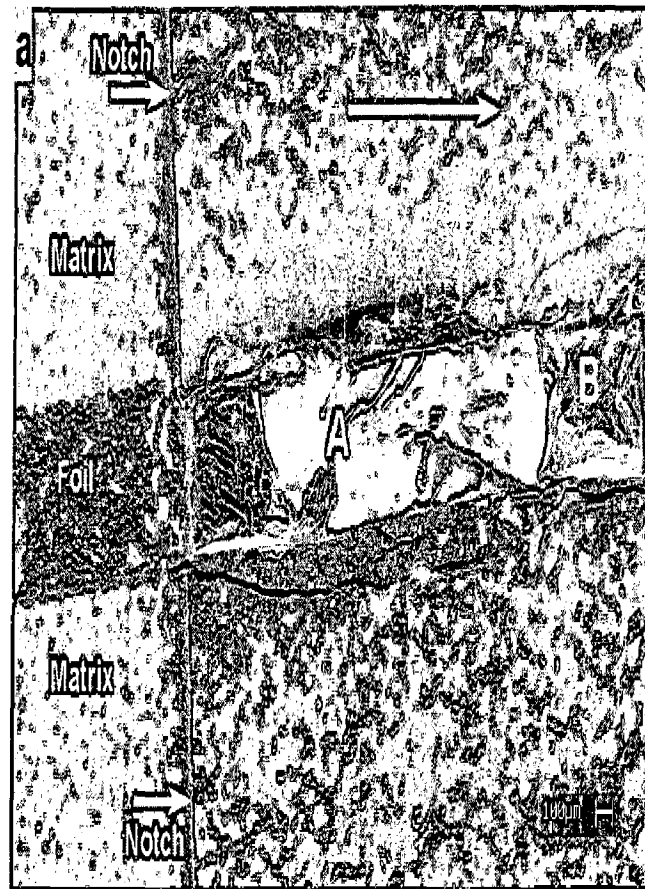


Fig. 5.124 SEM fractographs of  $K_{IC}$  test specimen (crack divider mode) of Nb foil laminated composite (a) at low magnification showing notched as well as fractured area covering both matrix and the foil, while (b) and (c) are the foil areas designated as A and B in Fig. (a) taken at higher magnifications.

#### 5.7.4 (MoSi<sub>2</sub> + 20 vol% SiC<sub>p</sub>) + Al<sub>2</sub>O<sub>3</sub> Coated Nb Foil Laminated Composite

The EPMA studies as shown in Figs. 5.98 and 5.9 clearly reveal that a small amount of Si has diffused through the Al<sub>2</sub>O<sub>3</sub> coating towards Nb forming a thin Si rich reaction layer towards the Nb side. It is assumed that the Si diffusion occurs through the porosity present in Al<sub>2</sub>O<sub>3</sub> coating deposited by plasma spray method. Such plasma sprayed coatings are reported to have typically 5 to 10 % porosity. However, Si diffusion may also occur through vacant sites present in Al<sub>2</sub>O<sub>3</sub> lattice.  $\alpha$ -Al<sub>2</sub>O<sub>3</sub> has a hexagonal crystal structure with Al ions at the octahedral interstitial sites. Each Al ion is surrounded by six equidistant oxygen ions. Figure 5.125 shows the hexagonal close-packed structure of  $\alpha$ -Al<sub>2</sub>O<sub>3</sub> (Chawla, 1993). A and B layers contain oxygen ions while C layers contain Al ions and vacant sites. The C layers are only two-thirds full for charge neutrality. The Si atom is smaller in size than Al atom. The ionic radius of Si is 0.39 Å (atom radius = 1.17 Å) while ionic radius of Al is 0.57 Å (atom radius = 1.43 Å) (Ohring, 1995). Therefore, it is assumed that Si could also diffuse through Al<sub>2</sub>O<sub>3</sub> by occupying the vacant Al sites.

The diffusion of Si through Al<sub>2</sub>O<sub>3</sub> coating observed in this study is consistent with those of earlier studies. Coatings such as Y<sub>2</sub>O<sub>3</sub> (Lu et al, 1991<sup>a</sup>, 1991<sup>b</sup>) and ZrO<sub>2</sub> (Xiao et al, 1990) have also been reported thermodynamically stable with both MoSi<sub>2</sub> and Nb. These were also found to inhibit interdiffusion between MoSi<sub>2</sub> and Nb. Xiao et al (1990) have measured the thickness of the reaction layer in MoSi<sub>2</sub> reinforced with Nb wires as 30  $\mu$ m after vacuum hot pressing at 1700 °C. They found that the thickness of the reaction layer was reduced to 4 – 6  $\mu$ m after applying ZrO<sub>2</sub> coating on Nb wires. They identified the reaction product to be Nb<sub>5</sub>Si<sub>3</sub> on the Nb side of the coating (at ZrO<sub>2</sub>-Nb interface). Xiao et al (1990) have also studied the growth rate of the interaction layer of Nb<sub>5</sub>Si<sub>3</sub> in ZrO<sub>2</sub> coated Nb filament reinforced MoSi<sub>2</sub> composite by annealing the samples for 100 h at 1300°C. The thickness of Nb<sub>5</sub>Si<sub>3</sub> increased from 4  $\mu$ m to 6  $\mu$ m only after 100 h. The reaction layer thickness followed a parabolic function of the annealing time. They reported that the growth rate of Nb<sub>5</sub>Si<sub>3</sub> at the ZrO<sub>2</sub>-Nb interface was controlled by the diffusion of Si through Nb<sub>5</sub>Si<sub>3</sub> rather than through the ZrO<sub>2</sub> coating. Diffusion of Si was relatively faster in ZrO<sub>2</sub>.



Xiao and Abbaschian (1992<sup>b</sup>) have reported similar observations for Al<sub>2</sub>O<sub>3</sub> coated Nb filament reinforced MoSi<sub>2</sub> matrix composite also. Based on the thickness of the reaction layer, they have estimated apparent diffusivity of Si through the Al<sub>2</sub>O<sub>3</sub> coating as  $> 2.0 \times 10^{-8}$  cm<sup>2</sup>/sec at 1400 °C. This was considerably higher than the bulk diffusion of Si in the ceramic materials, suggesting that Si diffusion might have occurred via different diffusion paths rather than bulk diffusion. The potential fast diffusion paths may be through the grain boundaries and the free surfaces generated by the porosity in the coating.

Xiao et al (1990) have applied Al<sub>2</sub>O<sub>3</sub> coating on Nb by different methods including sol-gel process and physical vapour deposition (PVD). Al<sub>2</sub>O<sub>3</sub> coating by PVD provided relatively dense coating while sol-gel process resulted in thicker coatings. However, the sol-gel process resulted in extensive cracking in the coating due to the inherent large volume shrinkage associated with the process. The thickness of the Al<sub>2</sub>O<sub>3</sub> coatings varied between 3 to 20 μm by different coating methods employed by Xiao et al (1990). Such Al<sub>2</sub>O<sub>3</sub> coatings became discontinuous as the hot pressing temperature was increased to 1700 °C and resulted in extensive reaction between MoSi<sub>2</sub> and Nb due to breakdown of the coating. However, the plasma spray technique employed in the present work resulted in much thicker Al<sub>2</sub>O<sub>3</sub> coating, 50 - 75 μm as depicted in Fig. 5.95. No breakdown of Al<sub>2</sub>O<sub>3</sub> coating was observed and integrity of the coating remained intact up to the hot pressing temperature of 1600 °C employed in the present work.

It is believed that the effectiveness of the coating as a diffusion barrier is affected by the quality and integrity of the coating itself. In order to reduce the Si diffusion further, grain boundary area and processing defects must be minimized in the coating. If the coating is thick as well as dense enough, the diffusion of Si can be effectively limited, and therefore the interaction between refractory metal foils and MoSi<sub>2</sub> can be prevented. The plasma spray method employed in the present work resulted in sufficiently thick and stable coatings. However, the problem of porosity in plasma spray coatings needs to be addressed further.

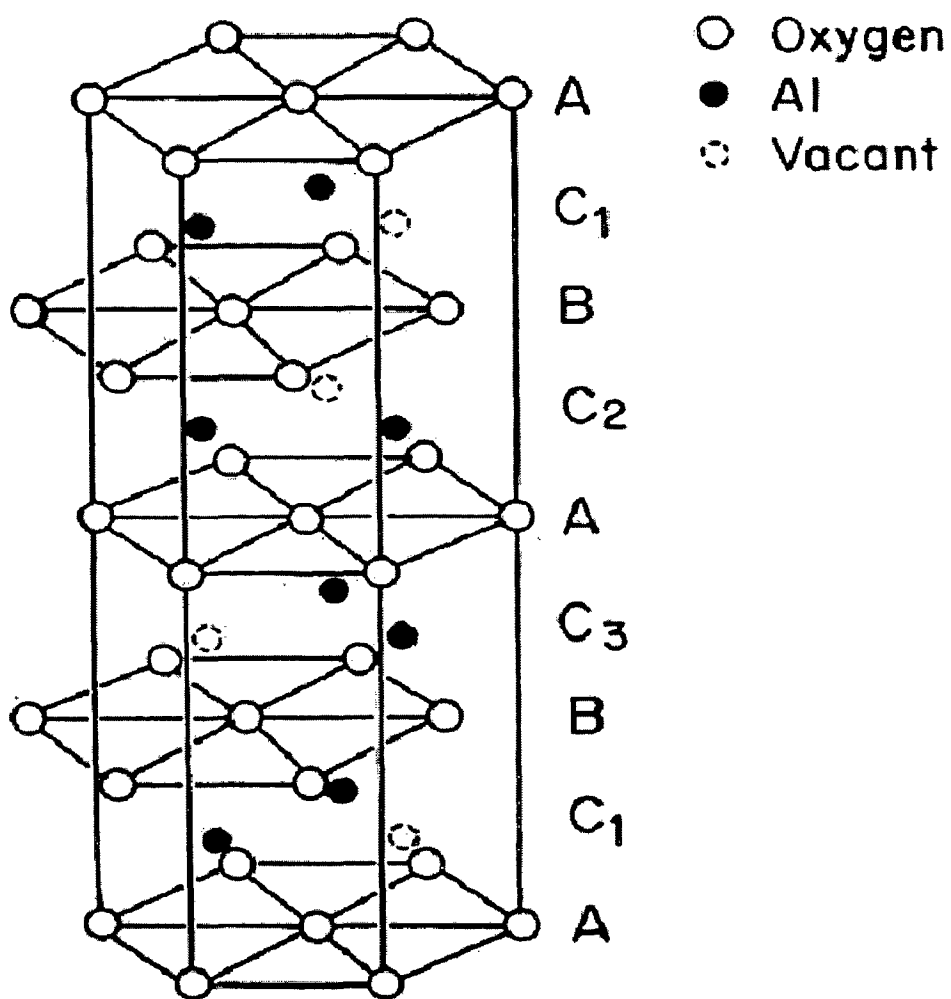


Fig. 5.125 Crystal structure of  $\alpha$ - $\text{Al}_2\text{O}_3$

The lower values of flexural strength and fracture toughness,  $K_{\max}$  of  $(\text{MoSi}_2 + 20 \text{ vol}\% \text{ SiC}_p) + \text{Al}_2\text{O}_3$  coated Nb foil laminated composite as compared to the values obtained for uncoated Nb foil laminated composite could be attributed to a relatively weak interfacial bonding in  $\text{Al}_2\text{O}_3$  coated Nb foil laminated composite. The bonding between  $\text{MoSi}_2 / \text{Al}_2\text{O}_3$  is supposed to be primarily of mechanical nature in contrast to the chemical bonding between  $\text{MoSi}_2 / (\text{Mo, Nb})_5\text{Si}_3 / (\text{Nb, Mo})_5\text{Si}_3 / \text{Nb}$ .

In a related study, Xiao and Abbaschian (1992<sup>b</sup>) have shown that uncoated interface has higher interfacial fracture energy than the fracture energy of the  $\text{MoSi}_2$  matrix, while the oxide-coated interfaces have lower interfacial fracture energy than fracture energy of the  $\text{MoSi}_2$  matrix. Fracture energy of the oxide bond was lower than the bonds between two intermetallics or between a metal and an intermetallic. It was at a level of  $16 \text{ J/m}^2$ , which was even lower than the fracture energy of the  $\text{Al}_2\text{O}_3$  itself ( $23.1 \text{ J/m}^2$ ) as reported by Shaw et al (1995). The low fracture energy of the oxide bond is attributed to the low bond strength between  $\text{Al}_2\text{O}_3$  and the silicides involved. As concluded by Sutton and Feingold (1966), the bond strength between oxide and other materials is directly related to the amount of interaction between the two materials, and the free energy of formation of the oxides of other materials is an important criterion in determining the interaction. Weak bonding will result when the conditions are unfavourable for the formation of other oxides. In the present case, elemental Mo, Nb and Si have a higher free energy of formation of their oxides in comparison with  $\text{Al}_2\text{O}_3$  (Lynch and Burte, 1968). The thermodynamic calculations carried out in the present investigation also reveal the same. As a result, the formation of silica, Nb and Mo oxides, is unfavourable in terms of the free energy change. Therefore, it is expected that the reactivity of the silicides and pure Nb with  $\text{Al}_2\text{O}_3$  would be very low, resulting in low bond strength. On the other hand, if the free energy of formation is lower for forming other oxides instead of  $\text{Al}_2\text{O}_3$ , strong bond may form.

Based on their experiments on measurement of the interfacial fracture energies in pure  $\text{MoSi}_2 / \text{Nb}$  foil system, Xiao and Abbaschian (1992<sup>a</sup>) divided the interfaces at the interfacial region into 3 categories:

- (i) an interface (bonding) between the oxide coating and intermetallics, e.g.,  $\text{Al}_2\text{O}_3 / \text{MoSi}_2$  and  $\text{Al}_2\text{O}_3 / \text{Nb}_5\text{Si}_3$  interfaces.
- (ii) a bond between two intermetallics, e.g.,  $\text{MoSi}_2 / \text{Nb}_5\text{Si}_3$  interface.
- (iii) a bond between a metal and an intermetallic, e.g.,  $\text{Nb} / \text{Nb}_5\text{Si}_3$ .

No direct bonding between oxide and metal was observed. A thin Si rich reaction layer which has been reported by Xiao and Abbaschian as of  $\text{Nb}_5\text{Si}_3$  separates  $\text{Al}_2\text{O}_3$  from the Nb.

However, the weak interfacial bonding in  $\text{Al}_2\text{O}_3$  coated Nb foil reinforced laminated composite results in greater work of fracture as compared to the uncoated Nb foil reinforced laminated composite. Lower interfacial fracture energy results in lower constraint imposed by the matrix on the Nb foil. Therefore, more Nb participates in deformation resulting in higher work of fracture. In fact, there seems to be confusion in the existing literature as how best the fracture toughness of the ductile phase reinforced brittle matrix composites can be described. If fracture toughness is calculated in terms of  $K_{\text{max}}$ , strong interfacial bonding would be desirable. If fracture toughness is measured as work of fracture, a relatively weak interfacial bonding is preferable.

## 5.8 SUMMARY OF RESULTS

Improvement in room temperature fracture toughness in terms of damage tolerance and work of fracture of various laminated composite systems investigated in the present work is depicted in the form of bar charts in Fig. 5.126 and Fig. 5.127, respectively.

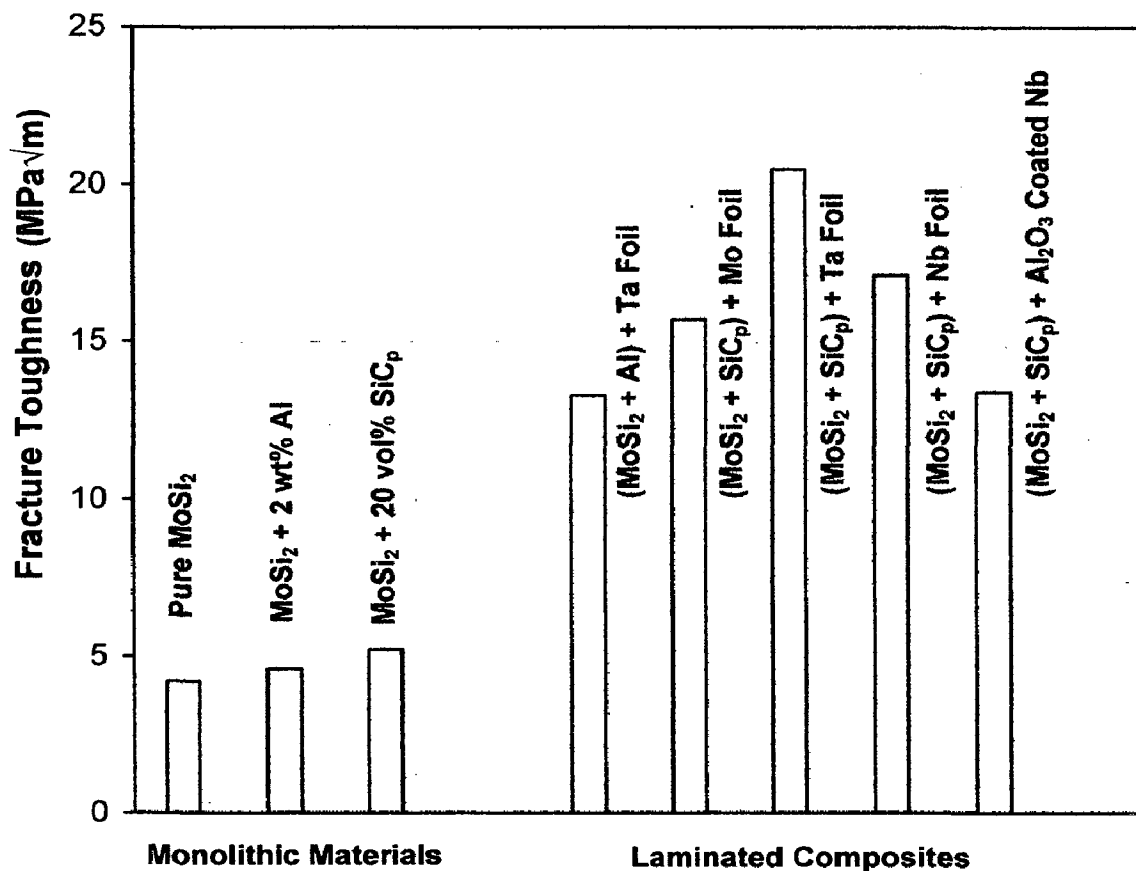


Fig. 5.126 Improvement in room temperature fracture toughness (damage tolerance,  $K_{max}$ ) of various laminated composites investigated in the present study.

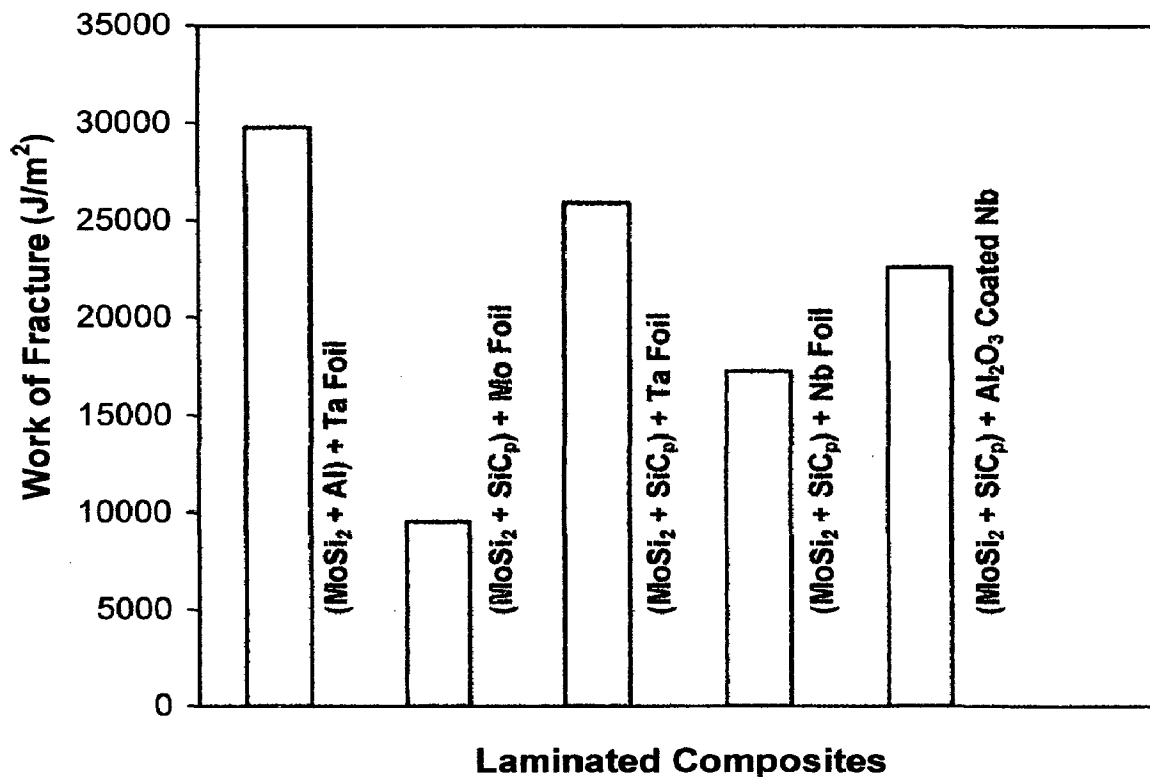


Fig. 5.127 Improvement in room temperature fracture toughness (work of fracture) of various laminated composites investigated in the present study.

Gac and Petrovic (1985) have observed that a flexural strength value of 310 MPa was within an acceptable use regime for structural applications of MoSi<sub>2</sub> based materials. Petrovic and Vasudevan (1999) have proposed that industrial applications of MoSi<sub>2</sub> would typically require a K<sub>IC</sub> value of 10 MPa√m while a K<sub>IC</sub> value of 15 MPa√m at room temperature would be acceptable for aerospace applications of MoSi<sub>2</sub>. These proposed target properties have been met or exceeded in the present work by ductile phase toughening of MoSi<sub>2</sub> and designing the MoSi<sub>2</sub> based composites in the laminated form consisting of alternate layers of MoSi<sub>2</sub> based matrix and the ductile refractory metal foils. Addition of SiC particles in MoSi<sub>2</sub> matrix not only results in improved thermal compatibility between MoSi<sub>2</sub> and refractory metal foils but also is expected to impart improved high temperature strength and creep resistance to MoSi<sub>2</sub>.

While the understanding of the sources of fracture toughness in laminated systems is at a relatively early stage, there are some areas that are emerging as important:

- (i) Delamination appears to play an important role in activating key extrinsic toughening mechanisms.
- (ii) Different mechanisms are dominant depending upon the orientation of the crack relative to the layer architecture.
- (iii) In the crack divider orientation, improvement in fracture toughness relative to un-laminated systems are modest. Further improvements in the toughness in the crack divider orientation are desirable as this is often the key orientation for many structural applications. It is envisaged that a multi-layer laminated composite consisting of several alternate layers of MoSi<sub>2</sub> based matrix and the ductile refractory metal foils would result in acceptable levels of fracture toughness in crack divider mode.

In the present investigation, a novel hybrid approach incorporating brittle as well ductile reinforcements in MoSi<sub>2</sub> has been adopted. Most of the work reported in the literature is on pure MoSi<sub>2</sub> matrix reinforced with Nb foil laminated composites. However, in the present study, MoSi<sub>2</sub> matrix was modified by additions of SiC particles to obtain the synergistic effects with ductile reinforcements as well as to improve the thermal compatibility between MoSi<sub>2</sub> and the various ductile phases. A critical review

of literature reveals that most of the workers have used only Nb as a ductile refractory metal reinforcement in the development of MoSi<sub>2</sub> based laminated composites. The present study has attempted to explore the feasibility of using other refractory metals as well, like Mo and Ta. Reinforcement of MoSi<sub>2</sub>-SiC<sub>p</sub> matrix with Ta foil resulted in a higher value of fracture toughness than obtained for MoSi<sub>2</sub> / Nb system as reported in the literature. Ta was also found to be thermodynamically more stable with MoSi<sub>2</sub> than Nb resulting in a lower thickness of the interfacial reaction zone. Moreover, in the present work, the fracture behaviour of various laminated composites has been studied in both crack arrester as well as in crack divider orientations. Only very limited data has been reported in the literature on the toughness measurements of MoSi<sub>2</sub> based laminated composites in crack divider mode. The analysis of residual thermal stresses in composite systems has often been neglected. An attempt has been made in the present work to carry out a comprehensive analysis of residual thermal stresses in MoSi<sub>2</sub> based laminated composites.

MoSi<sub>2</sub> based composites are at present in their infancy. They are currently at the same level of development as were the structural ceramics in the early 1970s. Optimization of MoSi<sub>2</sub> matrix composites will require the combined skills of both metallurgists and ceramists. It is anticipated that optimized composite microstructures may require a variety of reinforcements and architectures. A hybrid approach with both brittle and ductile reinforcements to composite design seems to be a promising path to improved properties. Nevertheless, the experiments and models in the present work establish the necessary basis for understanding and designing MoSi<sub>2</sub> matrix composites with toughness larger than that of simple MoSi<sub>2</sub>. The observations and results obtained in the present work have not only validated the existing information base but also have added to the existing knowledge and suggests ways of further improving upon the properties of MoSi<sub>2</sub>.



---

## CONCLUSIONS

---

In the present work, various aspects of ductile phase toughening of  $\text{MoSi}_2$  have been explored, an area which has received a relatively limited attention. Substantial amount of work was carried out by incorporating a variety of ductile refractory metals like W, Mo, Ta and Nb as reinforcements in  $\text{MoSi}_2$  based matrix. The composites were prepared by two different approaches, ductile refractory metals in particulate form (discontinuously reinforced) and in foil form (laminated approach).  $\text{MoSi}_2$  matrix was also modified by adding 2 wt% Al and 20 vol%  $\text{SiC}_p$  (hybrid composites) to obtain tailored microstructures and optimized mechanical properties. Interfacial modification was carried out by applying a diffusion barrier coating on a metal foil to study its effect on microstructure and fracture toughness. An attempt has also been made to understand the nature and magnitude of residual thermal stresses in  $\text{MoSi}_2$  based particulate and laminated composite systems by analytical methods as well as by FEM analysis. The following conclusions have emerged from the present investigation:

1. Extensive diffusion of Si into ductile reinforcements during high temperature processing has led to complete conversion of W, Mo and Nb particles into their silicides, identified as  $\text{R}_5\text{Si}_3$  (R = W, Mo or Nb ).
2. The room temperature hardness and flexural strength of W, Mo and Nb particle reinforced  $\text{MoSi}_2$  matrix composites have improved, while retaining the fracture toughness of the monolithic  $\text{MoSi}_2$ . Improved Hardness and strength may be

attributed to grain refinement and the formation of hard and brittle silicide phases. However, the silicides formed are unable to offer significant improvement in toughness by way of crack deflection or bridging mechanisms.

3. Addition of Al into  $\text{MoSi}_2$  matrix led to substantial decrease in the amount of free  $\text{SiO}_2$  in the composite as Al reacted with  $\text{SiO}_2$  to form  $\text{Al}_2\text{O}_3$  in-situ. However, removal or replacement of  $\text{SiO}_2$  by  $\text{Al}_2\text{O}_3$  seemed to have only a moderate effect on room temperature fracture toughness.
4. Interfacial reaction layers are observed to form between  $\text{MoSi}_2$ -2 wt% Al matrix and Mo and Ta foil reinforcements, which are identified to be brittle silicide phases consuming a part of thickness of ductile metal foils.
5. The fracture toughness of  $\text{MoSi}_2$ -2 wt% Al + Ta foil laminated composite improves moderately over that of matrix, while  $\text{MoSi}_2$ -2 wt% Al + Mo foil laminated composite failed in shear presumably due to a relatively large thermal expansion mismatch between  $\text{MoSi}_2$  and pure Mo.
6. In  $\text{MoSi}_2$ -20 vol% SiC particulate composite, SiC particle is under compressive stress while  $\text{MoSi}_2$  matrix is under radial compressive stress and tangential tensile stress, which are found to be maximum at particle / matrix interface and decrease with increasing distance from the interface as revealed by theoretical analysis of residual thermal stresses.
7. In  $\text{MoSi}_2$ -SiC<sub>p</sub> + refractory metal foil laminated composites, the refractory metal foils are under compressive stresses, while the  $\text{MoSi}_2$ -SiC<sub>p</sub> matrix layer is under tensile stresses. The Nb foil reinforced laminated composite was found to possess the lowest residual stresses owing to a lower thermal expansion mismatch between  $\text{MoSi}_2$ -SiC<sub>p</sub> matrix and the Nb foil as compared to the Mo and Ta foils.
8. The residual thermal stresses estimated by finite element methods (FEM) are similar to those given by analytical approach, thus validating the analytical expressions used in the present study.

9. At high processing temperatures, chemical interactions between MoSi<sub>2</sub>-SiC<sub>p</sub> layer and refractory metal foils result in Interfacial reaction layers of varying thickness. The Ta foil laminated composite exhibited a minimum reaction zone thickness of only 10 μm suggesting that the Ta has better chemical compatibility with MoSi<sub>2</sub> as compared to Mo and Nb.
10. No shear failure occurred in MoSi<sub>2</sub>-20 vol% SiC<sub>p</sub> + Mo foil laminated composite since the addition of SiC particles in MoSi<sub>2</sub> matrix improves the thermal compatibility between MoSi<sub>2</sub> and the refractory metal foils by lowering the thermal expansion mismatch between the two. At the same time, presence of SiC<sub>p</sub> reinforcements in MoSi<sub>2</sub> led to fine grain size and consequently, moderate increase in room temperature hardness, flexural strength and fracture toughness of pure MoSi<sub>2</sub>.
11. In Mo, Ta and Nb foil reinforced ((MoSi<sub>2</sub> + 20 vol% SiC<sub>p</sub>) matrix laminated composites tested in crack arrester mode, there is significant improvement in room temperature fracture toughness over that in monolithic MoSi<sub>2</sub>, which could be attributed to the combined effects of crack bridging by ductile metal foils and a high degree of constraint imposed by the brittle MoSi<sub>2</sub>-SiC matrix on the ductile foils. The highest improvement in room temperature fracture toughness is observed in case of Ta foil laminated composite.
12. The fracture toughness of laminated composites measured in crack divider mode, improves moderately since in crack divider orientation, crack could propagate through the entire thickness of the MoSi<sub>2</sub>-SiC<sub>p</sub> matrix without getting arrested by the ductile foil and the need for renucleation.
13. Application of Al<sub>2</sub>O<sub>3</sub> coating on Nb foil inhibited the matrix - reinforcement chemical interactions to a large extent during processing at high temperatures by suppressing diffusion of Mo and Nb but a very thin Si rich layer could form at the Al<sub>2</sub>O<sub>3</sub> / Nb interface due to a limited diffusion of Si through the Al<sub>2</sub>O<sub>3</sub> coating.
14. In the Al<sub>2</sub>O<sub>3</sub> coated Nb foil laminated composite, the fracture toughness is lower as compared to that in uncoated Nb foil reinforced laminated composite, which may be attributed to a lower peak load achieved in bending test due to a

relatively weak  $\text{MoSi}_2\text{-Al}_2\text{O}_3$  bond. However, the fracture toughness measured as the 'work of fracture' for  $\text{Al}_2\text{O}_3$  coated Nb foil composite is higher than that for the laminated composite with uncoated Nb foil.

15. The fracture toughness measured in terms of work of fracture for the laminated composite systems exhibited a trend opposite to the damage tolerance calculated from the peak load. A lower degree of constraint presumably gives rise to a higher decohesion length resulting in a lower peak load while it allows more plastic stretching of ductile phase leading to a higher work of fracture.
16. The embrittlement of Nb foil due to oxygen pick up during high temperature processing under relatively poor vacuum conditions may allow little improvement in the work of fracture of the laminated composite as compared to the monolithic  $\text{MoSi}_2$ , due to the loss of ductility of Nb foil and its brittle failure.

In summary, it has been successfully demonstrated that ductile phase toughening of  $\text{MoSi}_2$  is a viable approach to improve room temperature fracture toughness of  $\text{MoSi}_2$  based materials. The experiments and models establish the necessary basis for understanding and designing the  $\text{MoSi}_2$  matrix composites with toughness levels much larger than that of monolithic  $\text{MoSi}_2$ . The principles and the methods of residual thermal stress analysis employed in the present work may hold equally good and useful for other ceramic matrix composite systems under development.

---

## REFERENCES

---

1. Adler T.A. and Houska C.R. (1978), "Integrated Intensities and Lattice Parameters of MoSi<sub>2</sub>", Journal of American Ceramic Society, Vol. 61, pp. 182-183.
2. Aikin R.M., Jr. (1992<sup>a</sup>), "Strengthening of Discontinuously Reinforced MoSi<sub>2</sub> Composites at High Temperatures", Materials Science and Engineering A, Vol. A155, pp. 121-133.
3. Aikin R.M., Jr. (1992<sup>b</sup>), "On the Ductile to Brittle Transition Temperature in MoSi<sub>2</sub>", Scripta Metallurgica, Vol. 26, p.1025.
4. Alman D.E. and Stoloff N.S. (1992), "Effect of Ductile Phase Reinforcement Morphology on Toughening of MoSi<sub>2</sub>", Intermetallic Matrix Composites II, Proceedings Materials Research Society Symposium, Vol. 273, pp. 247-252.
5. Alman D.E. and Stoloff N.S. (1994), "The Effect of Nb Morphology on the Cyclic Oxidation Resistance of MoSi<sub>2</sub>/20 vol% Nb Composites", Metallurgical and Materials Transactions A, Vol. 25A, pp. 1033-1040.
6. Alman D.E. and Stoloff N.S. (1995), "The Effect of Nb Morphology on the Fracture Behaviour of MoSi<sub>2</sub>/Nb Composites", Metallurgical and Materials Transactions A, Vol. 26A, pp. 289-303.
7. Alman D.E., Hawk J.A., Petrovic J.J., Henager C.H., Singh M. (1998), Wear of Engineering Materials, Eds. Hawk J., ASM International, Materials Park, Ohio, p. 51.
8. Alman D.E., Hawk J.A., Petty A.V. (Jr.) (1994), Proceedings Materials Research Society Symposium, Vol. 350, p.195.

9. Alman D.E., Shaw K.G., Stoloff N.S. and Rajan K. (1992), "Fabrication, Structure and Properties of MoSi<sub>2</sub> Base Composites", *Materials Science and Engineering*, Vol. A155, pp. 8593.
10. Alouani M., Albers R.C. and Methfessel M. (1991), "Calculated Elastic Constants and Structural Properties of Mo and MoSi<sub>2</sub>", *Phys. Rev. B*, Vol. 43, pp. 6500-6509.
11. Aronsson A., Lundstrom T. and Rundqist S. (1965), *Borides, Silicides and Phosphides*, Methuen, London, p. 17.
12. Ashby M.F., Blunt F.J. and Bannister M. (1989), "Flow Characteristics of Highly Constrained Metal Wires", *Acta Metallurgica et Materialia*, Vol. 37, pp. 1847-1857.
13. ASTM Standard C1161-94 (Re-approved 1996), "Standard Test Method for Flexural Strength of Advanced Ceramics at Ambient Temperature", Vol. 15.01, American Society for Testing and Materials, Philadelphia, USA, pp. 309-315.
14. ASTM Standard C1341-97, "Standard Test Method for Flexural Properties of Continuous Fiber Reinforced Advanced Ceramic Composites", Vol. 15.01, American Society for Testing and Materials, Philadelphia, USA, pp. 586-603.
15. Badrinarayanan K., Mckelvey A.L., Venkateswara Rao K.T. and Ritchie R.O. (1996), "Fracture and Fatigue Crack Growth Behaviour in Ductile Phase Toughened MoSi<sub>2</sub>: Effects of Nb Wire vs. Particulate Reinforcements", *Metallurgical and Materials Transactions A*, Vol. 27A, pp. 3781-3792.
16. Barin I. (1989), *Thermochemical Data of Pure substances*, Vol. 1 & Vol. 2, VCH Verlagsgesellschaft, mbH, D-6940, Weinheim, Germany.
17. Barker L.M. and Baratta F.I. (1980), "Comparisons of Fracture Toughness Measurements by the Short Rod and ASTM Standard Method of Test of Metallic Materials (E 399-78)", *Journal of Testing and Evaluation*, Vol. 8, pp. 97-102.
18. Bartlett A.H., Castro R.G., Butt D.P., Kung H. and Petrovic J. J. (1996), "Plasma Sprayed MoSi<sub>2</sub>/Al<sub>2</sub>O<sub>3</sub> Laminate Composite Tubes as Lances in Pyrometallurgical Operations", *Industrial Heating*, January 1996 Issue.
19. Berkowitz-Mattuc J.B. (1966), *Final Report, Contract NASW-1167*, Cambridge, MA, NASA.
20. Berkowitz-Mattuck J. B., Rossetti M. and Lee D. W. (1970), "Enhanced Oxidation of MoSi<sub>2</sub> Under Tensile Stress: Relation to Pest Mechanism", *Metallurgical Transaction*, Vol. 1, pp. 479-483.
21. Bhattacharya A.K. and Petrovic J.J. (1991), "Hardness and Fracture Toughness of SiC Particle Reinforced MoSi<sub>2</sub> Composites", *Journal of American Ceramic Society*, Vol. 74, pp. 2700-2703.

22. Boettinger W.J., Perepezko J.H. and Frankwicz P.S. (1992), "Application of Ternary Phase Diagrams to the Development of MoSi<sub>2</sub> Based Materials", *Materials Science and Engineering*, Vol. A155, pp. 33-44.
  23. Brooks D., Lederich R.J. and Soboyejo W.O. (1994), "An Investigation of the Effects of Brittle and Ductile Reinforcement on the Fatigue and Fracture Behaviour of MoSi<sub>2</sub> Composites", *Proceedings Symposium on the Fatigue and Fracture of Ordered Intermetallic Materials*, Eds. Soboyejo W.O., Srivatsan T.S. and Davidson D.L., *The Minerals, Metals and Materials Society*, pp. 55-74.
  24. Budiansky B., Amazigo J.C. and Evans A.G. (1988), "Small Scale Crack Bridging and the Fracture Toughness of Particulate Reinforced Ceramics", *Journal of Mech. Phys. Solids*, Vol. 36, pp. 167-187.
  25. Carter D.H. and Hurley G.F. (1987), "Crack Deflection as a Toughening Mechanism in SiC Whisker Reinforced MoSi<sub>2</sub>", *Journal of American Ceramic Society*, Vol. 70, pp. C79-C81..
  26. Castro R.G., Hellmann J.R., Segall A.E. and Shelleman D.L. (1994), "Fabrication and Testing of Plasma Spray Formed MoSi<sub>2</sub> and MoSi<sub>2</sub> Composite Tubes", *Proceedings Materials Research Society Symposium*, Vol. 322, pp. 81-86.
  27. Castro R.G., Smith R.W., Rollett A.D. and Stanek P.W. (1992), "Ductile Phase Toughening of MoSi<sub>2</sub> by Low Pressure Plasma Spraying", *Materials Science and Engineering*, Vol. A155, p. 101.
  28. Chawla K.K. (1987), *Composite Materials: Science and Engineering*, Springer-Verlag, New York, p. 193.
  29. Chawla K.K. (1993), *Ceramic Matrix Composites*, Chapman and Hall, London.
  30. Chen L.C., Bahtishi N., Lederich R. and Soboyejo W. (1994<sup>a</sup>), "Ductile Phase Toughening of MoSi<sub>2</sub>: Effect of Reinforcement Morphology", *Proceedings Materials Research Society Symposium*, Vol. 350, pp. 183-188.
  31. Chen L.C., Brooks D., Lederich R.J. and Soboyejo W.O. (1994<sup>b</sup>), "Ductile Phase Toughening of MoSi<sub>2</sub>: Effects of Reinforcement Morphology", *Proceedings Symposium on Intermetallic Composites III*, Eds. Graves J.A., Miracle D.B. and Bowman R.R., MRS, Pittsburgh, PA, Vol. 350, pp. 183-188.
  32. Chung D.W. and Stoloff N.S. (1978), "Fatigue Behavior of Niobium-Hydrogen Alloys", *Metallurgical Transactions A*, Vol. 9A, pp. 1387-1399.
  33. Claussen N. (1975), "Fracture Toughness of Al<sub>2</sub>O<sub>3</sub> with a Unstabilized ZrO<sub>2</sub> Dispersed Phase", *American Ceramic Society Bulletin*, Vol. 54, p. 403.
- Clegg W.J. and Seddon L.R. (1992), 2<sup>nd</sup> European Conference on Advanced Materials, Euromat '91, Cambridge, Institute of Materials, p. 226.

35. Clegg W.J., Kendall K. and Alford N.M. (1990), "A Simple Way to Make Tough Ceramics", *Nature*, Vol. 347, pp. 455-457.
36. Cook J. and Gordon J.E. (1964), *Proceedings Royal Society of London A*, Vol. 282, p. 508.
37. Cook J., Khan A., Lee E. and Mahapatra R. (1992), *High Temperature Structural Silicides*, Eds. Vasudevan A.K. and Petrovic J.J., Elsevier Science Publishers, Amsterdam.
38. Corten J.T. (1967), "Micromechanics and Fracture Behaviour of Composites" *Modern Composite Materials*, Eds. Broutman L.J. and Krock R.H., Addison-Wesley, Massachusetts, pp. 20-30.
39. Costa e Silva A. and Kaufman M.J. (1993), "Microstructural Modifications of MoSi<sub>2</sub> Through Al Additions", *Scripta Metallurgica*, Vol. 29, pp. 1141-1145.
40. Costa e Silva A. and Kaufman M.J. (1994), *Processing and Fabrication of Advanced Materials III*, Eds. Ravi V.A., Srivatsan T.S. and Moore J.J., TMS, Warrendale, PA, USA, p. 585.
41. Costa e Silva A. and Kaufman M.J. (1995), "Applications of In situ Reactions to MoSi<sub>2</sub>-Based Materials", *Materials Science and Engineering*, Vol. A195, pp. 75-88.
42. Cotterell B. and Rice J.R. (1980), *International Journal of Fracture*, Vol. 16, p. 155.
43. Cotton J.D., Kim Y.S. and Kaufman M.J. (1991), "Intrinsic Second Phase Particles in Powder processed MoSi<sub>2</sub>", *Materials Science and Engineering*, Vol. A144, pp. 281-287.
44. Denso Company (1992), *Nikkei New Materials*, August 3, 1992, p. 34.
45. Deve H.E., Evans A.G., Odette G.R., Mehrabian R., Emiliani M.L. And Hecht R.J. (1990), "Ductile Reinforcement Toughening of  $\gamma$ -TiAl: Effects of Debonding and Ductility", *Acta Metallurgica et Materialia*, Vol. 37, pp. 1491-1502.
46. Deve H.E., Weber C.H. and Maloney M. (1992), "On the Toughness and Creep behaviour of Fiber Reinforced MoSi<sub>2</sub> Intermetallics", *Materials Science and Engineering*, Vol. A153, pp. 668-675.
47. Dieter G.E. (1987), *Mechanical Metallurgy*, McGraw Hill Book Company, Singapore.
48. Dusza J. and Sajgalik P. (1995), "Fracture Toughness and Strength Testing of Ceramic Composites", *Handbook of Advanced Materials Testing*, Eds Nicholas P C and Paul N C, Marcel Dekker, Inc., New York, pp. 399-435.
49. Elliot C.K., Odette G.R., Lucas G.E. and Shekherd J.W. (1988), "Toughness Mechanisms in Intermetallic  $\gamma$ -TiAl Alloys Containing Ductile



Proceedings Materials Research Society Symposium, Eds. Lemkey F.D., Fishman S.G. and Evans A.G., Materials Research Society, Pittsburg, PA.

50. Evans A.G. (1990), "Perspective on the Development of High Toughness Ceramics", *Journal of American Ceramic Society*, Vol. 73, p. 187.
51. Evans A.G. and Charles E.A. (1976), "Fracture Toughness Determination by Indentation", *Journal of American Ceramic Society*, Vol. 59, p. 371.
52. Evans A.G. and Faber K.T. (1984), "Crack Growth Resistance of Microcracking Brittle Materials", *Journal of American Ceramic Society*, Vol. 67, pp. 255-260.
53. Evans A.G. and Hutchinson J.W. (1989), "Effects of Non-planarity on the Mixed Mode Fracture Resistance of Bimaterial Interfaces", *Acta Metallurgica et Materialia*, Vol. 37, p. 909-916.
54. Evans A.G. and Marshall D.B. (1989), "The Mechanical Behaviour of Ceramics Matrix Composites", *Acta Metallurgica et Materialia*, Vol. 37, pp. 2567-2583.
55. Evans A.G. and McMeeking R.M. (1986), "On the Toughening of Ceramics by Strong Reinforcements", *Acta Metallurgica et Materialia*, Vol. 34, pp. 2435-2441.
56. Faber K.T. and Evans A.G. (1983), "Crack Deflection Process – I Theory", *Acta Metallurgica et Materialia*, Vol. 31, p. 565.
57. Fitzer E. (1988), in *Whisker and Fiber Toughened Ceramics*, Eds. Bradley R.A., Clark D.E., Larsen D.C. and Stiegler J.O., ASM International TM, p. 165.
58. Fitzer E. and Remmele W. (1985), "Possibilities and Limits of Metal Reinforced Refractory Silicides Especially  $\text{MoSi}_2$ ", *Proceedings, 5<sup>th</sup> International Conference on Composite Materials (ICCM-V)*, Eds. Harrigan W.C. Jr., Strife J. and Dhingra A.K., AIME, Warrendale, PA, pp. 515-530..
59. Fitzer E. and Schmidt F.K. (1971), "Si Diffusion in  $\text{Me}_5\text{Si}_3$  Phases of the Metals Nb, Ta, Mo and W to 1700 °C", *High Temperature High Pressure*, Vol. 3, pp. 445-460.
60. Fitzer E., Rubishch O., Schlichting J. and Sewdas I. (1973), *Special Ceramics*, Vol. 6.
61. Flinn B.D., Ruhle M. and Evans A.G. (1989), "Toughening in Composites of  $\text{Al}_2\text{O}_3$  Reinforced Al", *Acta Metallurgica et Materialia*, Vol. 37, pp. 3001-3002.
62. Frankwicz P.S., Perepezko J.H. and Anton D.L. (1993), *Proceedings Materials Research Society Symposium*, Vol. 288, p. 159.

63. Gac F.D. and Petrovic J. J. (1985), "Feasibility of a Composite of SiC Whiskers in an MoSi<sub>2</sub> Matrix", *Journal of American Ceramic Society*, Vol. 68, pp. C200-C201.
64. Gage P.R. and Bartlett R.W. (1965), "Diffusion Kinetics Affecting Formation of Silicide Coatings on Mo and W", *Transactions of The Metallurgical Society of AIME*. Vol. 233, pp. 832-834.
65. Gibala R., Ghosh A.K., Van Aken D.G., Srolovitz D.J., Basu A., Chang H., Mason D.P. and Yang W. (1992), "Mechanical Behaviour and Interface Design of MoSi<sub>2</sub> Based Alloys and Composites", *Materials Science and Engineering*, Vol. A155, pp. 147-158.
66. Gibbs W.S., Petrovic J.J. and Honnell R.E. (1987), "SiC Whisker-MoSi<sub>2</sub> Matrix Composites", *Ceramic Engineering and Science Proceedings*, Vol. 8, pp. 645-648.
67. Gokhale A.B. and Abbaschian G.J. (1986), "Molybdenum-Silicon", in *Binary Alloy Phase Diagrams*, Vol. 2, Ed. Massalski T.B., American Society for Metals, Metals Park, OH, pp. 1631-1632.
68. Gupta V., Yuan J. and Martinez D. (1993), "Calculation, Measurement, and Control of Interface Strength in Composites", *Journal of American Ceramic Society*, Vol. 76, pp. 305-315.
69. Hahn G.T., Gilbert A. and Jaffee R.I. (1963), *Refractory Metals and Alloys III*, Eds. Semchyshen M. and Perlmutter I., Interscience Publishers, New York, NY, p. 23.
70. Hardwick D.A., Martin P.L. and Moores R.J. (1992), "Reaction Synthesis of MoSi<sub>2</sub> from High Purity Elemental Powders", *Scripta Metallurgica*, Vol. 27, pp. 391-394.
71. Hashin Z. and Shtrikman S.A. (1963), *Journal of Mechanics and Physics of Solids*, Vol. 11, p. 127.
72. Hayden H.W., Moffatt W.G. and Wulff J. (1986), *The structure and Properties of Materials*, Vol. III, Mechanical Behaviour, Wiley Eastern Limited, New Delhi, p. 137.
73. He M.Y. and Hutchinson J.W. (1989<sup>a</sup>), *International Journal of Solid Structures*, Vol. 25, p. 1053.
74. He M.Y. and Hutchinson J.W. (1989<sup>b</sup>), "Kinking of a Crackout of an Interface", *Journal of Applied Mechanics*, Vol. 56, pp. 270-278.
75. Hebsur M.G. (1994), "Pest Resistant and Low CTE MoSi<sub>2</sub> Matrix for High Temperature Structural Applications", *Proceedings Materials Research Society Symposium*, Vol. 350, pp. 177-182.

76. Hebsur M.G. and Nathal M.V. (1997), *Structural Intermetallics*, Eds. Nathal M.V., Darolia R., Liu C.T., Martin P.L., Miracle D.B., Wagner R., Yamaguchi M., The Minerals, Metals and Materials Society, p. 949.
77. Heikinheimo E., Kodentsov A., Van Beek J.A., Klomp J.T. and Van Loo F.J.J. (1992), "Reactions in the Systems Mo-Si<sub>3</sub>N<sub>4</sub> and Ni-Si<sub>3</sub>N<sub>4</sub>", *Acta Metallurgica et Materialia* , Vol. 40, pp. S111-S119.
78. Henager C.H., Jr., Brimhall J.L. and Hirth J.P. (1992), "Synthesis of Composites in-situ Using Displacement reactions", *Ceramic Engineering and Science Proceedings*, Vol. 13, pp. 596-604.
79. Hertzberg R.W. (1983), *Deformation and Fracture Mechanics of Engineering Materials*, Wiley, New York, p. 328.
80. Hoenigschmid O. (1907), *Monatsh. Chem.*, Vol. 28, p. 1017.
81. Hutchinson J.W. (1987), "Crack Tip Shielding by Microcracking in Brittle Solids", *Acta Metallurgica et Materialia*, Vol. 35, pp. 1605-1619.
82. Ito K., Inui H., Shirai Y. and Yamaguchi M. (1995), "Plastic Deformation of MoSi<sub>2</sub> Single Crystals", *Philosophical Magazine*, Vol. A72, pp. 1075-1097.
83. Jackson M.R., Rairden J.R., Smith J.S. and Smith R.W. (1981), *Journal of Metals*, p. 33.
84. Jeng Y.L., Wolfenstine J., Lavernia E.J., Bailey D.E. and Sickinger A. (1993), *Scripta Metallurgica Materiala*, Vol. 28, p. 453.
85. Kanthal (1956), Swed. Patent 155,836.
86. Kanthal Corporation (1995), *Furnace Products*.
87. Kieffer R., Konopicky K. and Benesovsky F. (1951), Austrian Patent 179,100.
88. Kisley P.S. and Kodash V.U. (1989), "The mullite coatings on heaters made of molybdenum disilicide" *Ceramics International*, Vol.15, p. 189-191.
89. Krstic V.D. (1983), *Philosophical Magazine*, Vol. 48, p. 695.
90. Krstic V.D., Nicholson P.S. and Hoagland R.G. (1981), "Toughening of Glasses by Metal Particles", *Journal of American Ceramic Society*, Vol. 64, pp. 499-504.
91. Kung H., Chang H. and Gibala R. (1992), "Interfacial Structures of MoSi<sub>2</sub>-Mo<sub>5</sub>Si<sub>3</sub> Eutectic Alloys", *Proceedings of Materials Research Society Symposium*, Vol. 238, pp. 599-604.
92. Kung H., Mason D.P., Basu A., Chang H., Van Aken D.C, Ghosh A.K. and Gibala R. (1992), "The Structure and Properties of MoSi<sub>2</sub>-Mo<sub>5</sub>Si<sub>3</sub> Composites", *Proceedings of Materials Research Society Symposium*, Vol. 273, pp. 241-246.

93. Lange F. F., (1970), "The Interaction of a Crack Front with a Second-Phase Dispersion", *Philosophical Magazine*, Vol. 22, pp. 983-992.
94. Larsen D.C. and Stuchly S.L. (1990), "The Mechanical Evaluation of Ceramic Fiber Composites", *Fiber Reinforced Ceramic Composites: Materials, Processing and Technology*, Eds. Mazdiasni K.S., Noyes Publications, New Jersey, pp. 182-217.
95. Lawn B.R. (1983), "Physics of Fracture", *Journal of American Ceramic Society*, Vol. 66, pp. 83-91.
96. Lim C.B., Yano T. and Iseki T. (1989), "Microstructure and Mechanical Properties of RB-SiC/ MoSi<sub>2</sub> Composites", *Journal of Materials Science*, Vol. 24, pp. 4144-4151.
97. Lu T.C., Evans A.G., Hecht R.J. and Mehrabian R. (1991<sup>a</sup>), "Toughening of MoSi<sub>2</sub> with a Ductile (Niobium) Reinforcement", *Acta Metallurgica et Materialia*, Vol. 39, pp. 1853-1862.
98. Lu T.C., Yang J., Evans A.G., Hecht R.J. and Mehrabian R. (1991<sup>b</sup>), "Matrix Cracking in Intermetallic Composites Caused by Thermal Expansion Mismatch", *Acta Metallurgica Materiala*, Vol. 39, pp.1883-1890.
99. Lynch C.T. and Burte H.M. (1968), *Metal Matrix Composites*, ASTM STP 438, ASTM, Philadelphia, PA, p. 3.
100. Lynch J.F., Ruderer C.G. and Duckworth W.H. (Eds.) (1966), "Engineering Properties of Selected Ceramic Materials", *American Ceramic Society*, Columbus, OH.
101. Maloy S.A., Heuer A.H., Lewandowski J.J. and Petrovic J.J. (1991), "Carbon Additions to MoSi<sub>2</sub>: Improved High Temperature Mechanical Properties", *Journal of American Ceramic Society*, Vol. 74, pp. 2704-2706.
102. Maloy S.A., Lewandowski J.J., Heuer A.H. and Petrovic J.J. (1992), "Effects of Carbon Additions on High Temperature Mechanical Properties of MoSi<sub>2</sub>", *Materials Science and Engineering*, Vol. A155, p. 159.
103. Maloy S.A., Mitchell T.E., Petrovic J.J., Heuer A.H. and Lewandowski J.J. (1994), "The Temperature and Strain Rate Dependence of the Flow Stress in MoSi<sub>2</sub> Single Crystals" *Proceedings of Materials Research Society Symposium*, Vol. 322, p. 21.
104. Marshall D.B. and Evans A.G. (1981), "Comment on Elastic/Plastic Indentation Damage in Ceramics: The Median / Radial Crack System", *Journal of American Ceramic Society*, Vol. 64, pp. c-182 – c-183.
105. Massalski T.B. (1986), *Binary Alloy Phase Diagrams*, ASM, Metals Park, OH, 2, p. 1631.

106. Mataga P.A. (1989), "Deformation of Crack-Bridging Ductile Reinforcements in Toughened Brittle Materials", *Acta Metallurgica et Materialia*, Vol. 37, pp. 3349-3359.
107. Maxwell W.A. (1951), "Study of MoSi<sub>2</sub> for Elevated Temperature Applications", *Proceedings Metallurgy and Materials Information Meet*, Oak Ridge, TN, April 16-18, Rep. TID-5061 (DEL), NSA-12.
108. Meschter P.J. (1991), "Oxidation of Nb Particulate-Reinforced MoSi<sub>2</sub>", *Scripta Metallurgica*, Vol. 25, pp. 521-524.
109. Meschter P.J. (1992), "Low Temperature Oxidation of MoSi<sub>2</sub>", *Metallurgical Transactions*, Vol. 23A, pp. 1763-1772.
110. Meschter P.J. and Schwartz D. (1989), "Silicide Matrix Materials for High Temperature Applications", *Journal of Metals*, Vol. 41, pp.52-55.
111. Mitra R. (2006), "Mechanical Behaviour and Oxidation Resistance of Structural Silicides", *International Materials Reviews*, Vol. 51, pp. 13-64.
112. Mitra R. and Rama Rao V.V. (1999), "Effect of Minor Alloying with Al on Oxidation Behaviour of MoSi<sub>2</sub> at 1200 °C", *Materials Science and Engineering*, Vol. A260, pp. 146-160.
113. Mitra R., Mahajan Y.R., Prasad N.E. and Chiou W.A. (1997<sup>a</sup>), "Processing-Microstructure-Property Relationships in Reaction Hot Pressed MoSi<sub>2</sub> and MoSi<sub>2</sub>-SiC Composites", *Materials Science and Engineering*, Vol. A225, pp. 105-117.
114. Mitra R., Mahajan Y.R., Prasad N.E., Chiou W.A. and Ganguly C. (1995), "Reaction Hot Pressing and Characterization of MoSi<sub>2</sub>/SiC<sub>p</sub> Composites", *Key Engineering Materials*, Vol. 11, pp. 108-110.
115. Mitra R., Prasad N.E., Rao A. Venugopal and Mahajan Y.R. (1997<sup>b</sup>), "Mo and Ti Silicide Based Composites and Alloys", *Structural Intermetallics 1997*, Eds. Nathal M.V., Darolia R., Liu C.T., Martin P.L., Miracle D.B., Wagner R. and Yamaguchi M., The Minerals, Metals and Materials Society, pp. 959-968.
116. Mitra R., Rama Rao V.V. and Venugopal Rao A. (1999), "Effect of Small Al Additions on Microstructure and Mechanical Properties of MoSi<sub>2</sub>", *Intermetallics*, Vol. 7, pp. 213-232.
117. Moussa R., Coppolani I. and Osterstook F. (1982), *British Ceramic Society*, Vol. 32, p. 237.
118. Munz D. (1981), "Determination of fracture toughness of high strength aluminum alloys with chevron notched short rod and short bar specimens", *Engineering Fracture Mechanics*, Vol. 15, pp. 231-236.
119. Murakami Y (1987), *Stress Intensity Factors Handbook*, Vol. 1 and 2, Oxford, Pergamon.

120. Nakamura M., Matsumoto S. and Hirano T. (1990), "Elastic Constants of  $\text{MoSi}_2$  and  $\text{WSi}_2$  Single Crystals", *Journal of Materials Science*, Vol. 25, p. 3309.
121. Nakayama J. (1965), "Direct Measurement of Fracture Energies of Brittle Heterogeneous Materials", *Journal of American Ceramic Society*, Vol. 48, pp. 583-587.
122. Nekkanti R.M. and Dimiduk D.M. (1990), *Proceedings Materials Research Society Symposium*, Vol. 194, p. 175.
123. Neshpor V.S. and Samsonov G.V. (1964), *Phy. Met. & Metall.*, Vol. 18(2), p. 31.
124. Newman J.C., Jr., (1984), *Chevron-Notched Specimens: Testing and Stress Analysis*, ASTM STP 855, Eds. Underwood J.H., Freiman S.W. and Baratta F.I., ASTM, Philadelphia, PA, p. 5.
125. Niihara K. and Suzuki Y. (1999), "Strong Monolithic and Composite  $\text{MoSi}_2$  Materials by Nanostructure Design", *Materials Science and Engineering*, Vol. A261, pp. 6-15.
126. Niihara K., Morena R. and Hasselman D.P.H. (1983), "Indentation Fracture Toughness of Brittle Materials for Palmqvist Cracks", *Fracture Mechanics of Ceramics 5*, Eds. Bradt R.C., Hasselman D.P.H. and Lange F.F., Plenum Press, New York, pp. 97-105.
127. Nowotny H., Parthe E., Kieffer R. and Benesovsky F. (1954), *Monatsh. Chem.*, Vol. 85, p. 255.
128. Oeschner M., Hillman C. and Lange F.F. (1996), "Crack Bifurcation in Laminar Ceramic Composites", *Journal of American Ceramic Society*, Vol. 79, pp. 1834-1838.
129. Ohring M. (1995), *Engineering Materials Science*, Academic Press, Inc., 525 B Street, Suite 1900, San Diego, CA 92101-4495, p. 789.
130. Ortiz M. (1988), *International Journal of Solid Structures*, Vol. 24, p. 231.
131. Osman T.M., Lewandowski J.J., Hunt W.H., Jr., Lesuer D.R. and Riddle R.A. (1995), *Intrinsic and Extrinsic Fracture Mechanics in Inorganic Composite Systems*, Eds. Lewandowski J.J. and Hunt W.H., Jr., TMS, Warrendale, PA, p. 103.
132. Palmqvist S. (1962), *Arch. Eisenhüttenwes.*, Vol. 33, p. 629.
133. Papadakis E.P. (1967), *Journal of Acoustic Society of America*, Vol. 42, p. 1045.
134. Parthe E., Jeitschko W. and Sadagopan V. (1965), *Acta Crystallogr.*, Vol. 19, p. 1031.

135. Peralta P., Maloy S.A., Chu F., Petrovic J.J. and Mitchell T.E. (1997), "Mechanical Properties of Monocrystalline C11<sub>b</sub> MoSi<sub>2</sub> with Small Aluminum Additions", *Scripta Materialia*, Vol. 37, pp. 1599-1604.
136. Petrovic J.J. (1995), "Mechanical Behaviour of MoSi<sub>2</sub> and MoSi<sub>2</sub> Composites", *Materials Science and Engineering*, Vol. A192/193, pp. 31-37.
137. Petrovic J.J. (1997), "High Temperature Structural Silicides", *Ceramic Engineering and Science Proceedings*, Vol. 18, pp. 3-17.
138. Petrovic J.J. and Honnell R.E. (1990<sup>a</sup>), "SiC Reinforced MoSi<sub>2</sub> / WSi<sub>2</sub> Alloy Matrix Composites", *Ceramic Engineering and Science Proceedings*, Vol. 11, p. 734.
139. Petrovic J.J. and Honnell R.E. (1990<sup>b</sup>), "Partially Stabilized ZrO<sub>2</sub> Particle – MoSi<sub>2</sub> Matrix Composites", *Journal of Materials Science*, Vol. 25, pp. 4453-4456.
140. Petrovic J.J. and Honnell R.E. (1991), "SiC Reinforced MoSi<sub>2</sub> Based Matrix Composites", in *Ceramic Transactions*, Vol. 19, *Advanced Composite Materials*, Ed. Sacks M.D., American Ceramic Society, Westerville, OH, pp. 817-830.
141. Petrovic J.J. and Vasudevan A.K. (1999), "Key Developments in High Temperature Structural Silicides", *Materials Science and Engineering*, Vol. A261, pp. 1-5.
142. Petrovic J.J., Bhattacharya A.K., Honnell R.E., Mitchell T.E., Wade R.K. and McClellan K.J. (1992), "ZrO<sub>2</sub> and SiC Particle Reinforced MoSi<sub>2</sub> Matrix Composites", *Materials Science and Engineering*, Vol. A155, p. 259.
143. Petrovic J.J., Honnell R.E., Mitchell T.E., Wade R.K. and McClellan K.J. (1991), "ZrO<sub>2</sub> Reinforced MoSi<sub>2</sub> Matrix Composites", *Ceramic Engineering and Science Proceedings*, Vol. 12, p. 1633.
144. Phillips A.J., Clegg W.J. and Clyne T.W. (1992<sup>a</sup>), "Fracture Behaviour of Ceramic Laminates in Bending—I. Modelling of Crack Propagation", *Acta Metallurgica et Materialia et Materialia*, Vol. 41, pp. 805-817.
145. Phillips A.J., Clegg W.J. and Clyne T.W. (1992<sup>b</sup>), *Acta Metallurgica et Materialia* , Vol. 41, p. 819.
146. Reid C.N. (1965), "Precipitation of Mo<sub>2</sub>C on a Free Surface", *Transactions of The Metallurgical Society of AIME*, Vol. 233, pp. 834-836.
147. Rice J.R. (1968), *Fracture*, Ed. Liebowitz H., Vol. 2, p. 191.
148. Ritchie R.O. (1988), "Mechanisms of Fatigue Crack Propagation in Metals, Ceramics and Composites: Role of Crack Tip Shielding", *Materials Science and Engineering*, Vol. A103, pp. 15-28.
149. Roux F. and Vignes A. (1970), *Rev. Phys. Appl.*, Vol. 5, p. 393.

150. Ruhle M. and Evans A.G. (1988), "Structure and Chemistry of Metal/Ceramic Interfaces", *Material Science and Engineering*, Vol. A107, pp. 187-197.
151. Sadananda K. and Feng C.R. (1994), "A Review of Creep of Silicides and Composites", *Materials Research Society Symposium Proceedings*, Vol. 322, p. 157.
152. Sadananda K., Feng C.R., Jones H.N. and Petrovic J.J. (1993), "Creep of Intermetallic Composites", in *Proceedings International Symposium on Structural Intermetallics*, Seven Springs, 26-30 September.
153. Sadananda K., Jones H., Feng J., Petrovic J.J. and Vasudevan A.K. (1991), "Creep of Monolithic and SiC Whisker Reinforced MoSi<sub>2</sub>", *Ceramic Engineering and Science Proceedings*, Vol. 12, pp. 1671-1678.
154. Sakai M. and Bradt R.C. (1993), "Fracture Toughness Testing of Brittle Materials", *International Materials Review*, Vol. 38, pp. 53-78.
155. Sakai M. and Ichikawa H. (1992), "Work-of-Fracture of Brittle Materials with Microcracking and Crack Bridging", *International Journal of Fracture*, Vol. 55, pp. 65-79.
156. Savitskiy E.M., Baron V.V. and Bychkova M.I. (1963), *Trudy Inst. Met. Baikova, Acad. Naut SSSR*, Vol. 12, p. 179.
157. Savitskiy E.M., Baron V.V., Bychkova M.I., Bakuta S.A. and Gladyshevskiy E.I. (1965), *Russian Metall.*, Vol. 2, p. 91.
158. Schlesinger M.E. (1994), "The Si-Ta (Silicon-Tantalum) System", *Journal of Phase Equilibrium*, Vol. 15, p. 90.
159. Schlesinger M.E., Okamoto H., Gokhale A.B. and Abbaschian R. (1993), *Journal of Phase Equilibria*, Vol. 14, p. 502.
160. Schlichting J. (1978), "MoSi<sub>2</sub> as Component of Modern High Temperature Composites", *High Temperature-High Pressures*, Vol. 10, pp. 241-269.
161. Schwartz D.S. (1992), Report No. MDC 92-Q0409, McDonnell Douglas Aerospace, St. Louis.
162. Selsing J. (1961), "Internal Stresses in Ceramics", *Journal of American Ceramic Society*, Vol. 44, p. 419.
163. Shah D.M., Berczick D. and Anton D.L. (1992), "Appraisal of Other Silicides as Structural Materials", *Materials Science and Engineering*, Vol. A155, pp. 45-57.
164. Shaw L. and Abbaschian R. (1993), "Control of the Interfacial Reactions in Nb Toughened MoSi<sub>2</sub>", *Journal of American Ceramic Society*, Vol. 76, pp. 2305-2311.



165. Shaw L. and Abbaschian R. (1994), "Toughening MoSi<sub>2</sub> with Nb Metal – Effects of Size and Orientation of Ductile Laminae", *Acta Metallurgica et Materialia*, Vol. 42, pp. 213-223.
166. Shaw L. and Abbaschian R. (1995), "Al<sub>2</sub>O<sub>3</sub> Coatings as Diffusion Barriers Deposited from Particulate-Containing Sol-Gel Solutions", *Journal of American Ceramic Society*, Vol. 78, pp. 3376-3382.
167. Shaw L., Miracle D. and Abbaschian R. (1995), "Microstructure and Mechanical Properties of Metal/Oxide and Metal/Silicide Interfaces", *Acta Metallurgica et Materialia*, Vol. 43, pp. 4267-4279.
168. Shetty D.K., Wright I.G., Mincer P.N. and Clauer A.H. (1985), "Indentation Fracture of WC-Co Cermets", *Journal of Material Science*, Vol. 20, p. 1873-1882.
169. Sigl L.S. and Exner H.E. (1987), "Experimental Study of the Mechanics of Fracture in WC-Co Alloys", *Metallurgical Transactions A*, Vol. 18A, pp. 1299-1308.
170. Sigl L.S., Mataga P.A., Dalgleish B.J., McMeeking R.M. and Evans A.G. (1988), "On the Toughness of Brittle Materials reinforced with a Ductile Phase", *Acta Metallurgica et Materialia*, Vol. 36, pp. 945-953.
171. Singh M. and Bose A. (1992), "MoSi<sub>2</sub> Matrix Composites", *Processing and Fabrication of Advanced Materials for High Temperature Applications*, Eds. Ravi V.A. and Srivatsan T.S., The Minerals, Metals and Materials Society, pp. 95-109.
172. Smith S.S. and Pletka B.J. (1983), *Fracture Mechanics of Ceramics 6*, Eds. Bradt R. C., Hasselman D.P.H. and Lange F.F., Plenum Press, New York, p. 189.
173. Soboyejo W.O., Ye F., Chen L.C., Bahtishi N., Schwartz D.S. and Lederich R.J. (1996), "Effects of Reinforcement Morphology on the Fatigue Fracture Behaviour of MoSi<sub>2</sub>/Nb Composites", *Acta Metallurgica et Materialia*, Vol. 44, pp. 2027-2041.
174. Stergiou A., Tsakirooulos P. and Brown A. (1997), "The Intermediate and High Temperature Oxidation Behaviour of Mo(Si<sub>1-x</sub>Al<sub>x</sub>)<sub>2</sub> Intermetallic Alloys", *Intermetallics*, Vol. 5, pp. 69-81.
175. Stoloff N.S. (1999), "An Overview of Powder Processing of Silicides and Their Composites", *Materials Science and Engineering*, Vol. A261, pp. 169-180.
176. Suresh S. (1983), *Metallurgical Transactions*, Vol. 14A, p. 2375.
177. Sutton W.H. and Feingold E. (1966), *Materials Science Research*, Vol. 3, p. 577.
178. Suzuki M., Nutt S.R. and Aikin R.M., Jr., (1993), "Creep Behavior of an SiC-Reinforced XD<sup>TM</sup> MoSi<sub>2</sub> Composite", *Materials Science and Engineering*, Vol. A162, pp. 73-82.

179. Svechnikov V.N., Kocherzhinskii Y.A. and Yupko L.M. (1971), *Diagrammy Sostoyaniya Metal Sist.* Nauka, Ed. Ageev N.V., Moscow, p.116.
180. Tanaka K. (1987), "Elastic / Plastic Indentation Hardness and Indentation Fracture Toughness: The Inclusion Core Model", *Journal of Materials Science*, Vol. 22, pp. 1501-1508.
181. Tattersall H.G. and Tappin G. (1966), *Journal of Material Science*, Vol. 1, p. 296.
182. Timoshenko S. and Goodier J.N. (1951), *Theory of Elasticity*, McGraw-Hill, New York, p. 416.
183. Tirosh J. and Tetelman A.S. (1976), "Fracture Conditions of a Crack Approaching a Disturbance", *International Journal of Fracture*, Vo. 12, pp. 187-199.
184. Tiwari R., Herman H. and Sampath S. (1992), "Vacuum Plasma Spraying of MoSi<sub>2</sub> and Its Composites", *Materials Science and Engineering*, Vol. A155, pp. 95-100.
185. Tortorici P.C. and Dayananda M.A. (1998), "Diffusion Structures in Mo vs. Si Solid-Solid Diffusion Couples", *Scripta Materialia*, Vol. 38, pp. 1863-1869.
186. Tortorici P.C. and Dayananda M.A. (1999), "Interdiffusion and Diffusion Structure Development in Selected Refractory Metal Silicides", *Materials Science and Engineering*, Vol. A261, pp. 64-77.
187. Tuffe S.C., Plucknett K.P. and Wilkinson D.S. (1993), "Processing and Mechanical Properties of Alumina Platelet Reinforced Molybdenum Disilicide Laminates", *Ceramic Engineering and Science Proceedings*, Vol. 14, pp. 1199-1208.
188. Turner P S, 1946, *J. Res. Nat. Bur. Standards*, 37, 239.
189. Umakoshi Y., Sakagami T., Hirano T. and Yamane T. (1990), "High Temperature Deformation of MoSi<sub>2</sub> Single Crystals with the C11<sub>b</sub> Structure", *Acta Metallurgica et Materialia* ,, Vol. 38, p. 909.
190. Unal O., Petrovic J.J., Carter D.H and Mitchell T.E. (1990), "Dislocations and Plastic Deformation in MoSi<sub>2</sub>", *Journal of American Ceramic Society*, Vol. 73, pp. 1752-1757.
191. Vahlas C., Chevalier P.Y. and Blanquet E. (1989), *CALPHAD*, Vol. 13, p. 273.
192. Van Loo F.J.J., Smet F.S., Rieck G.D. and Verspui G. (1982), *High Temperature – High Pressures*, Vol. 14, p. 25.
193. Vandeervoort G.F. (1984), *Metallography Principles and Practice*, *Materials Science and Engineering Series*, McGraw Hill, p. 410.

206. Xiao L., Kim Y.S. and Abbaschian R. (1990), "Ductile Phase Toughening of  $\text{MoSi}_2$  – Chemical Compatibility and Fracture toughness", *Intermetallic Matrix Composites, Proceedings Materials Research Society Symposium*, Vol. 194, pp. 399-404.
207. Xiao L., Kim Y.S., Abbaschian R. and Hecht R.J. (1991), "Processing and Mechanical Properties of Nb Reinforced  $\text{MoSi}_2$  Composites", *Materials Science and Engineering*, Vol. A144, pp. 277-285.
208. Yanagihara K., Maruyama T. and Nagata K. (1996), "Effect of Third Elements on the Pesting Suppression of Mo-Si-X Intermetallics (X = Al, Ta, Ti, Zr and Y)", *Intermetallics*, Vol. 4, pp. S133-S139.
209. Yang J.M. and Jeng S.M. (1990), *Intermetallic Matrix Composites, Proceedings Materials Research Society Symposium*, Vol. 194, p. 138.
210. Yang J.M. and Jeng S.M. (1991), "Interface and Mechanical Behavior of  $\text{MoSi}_2$ -Based Composites", *Journal of Materials Research*, Vol. 6, pp. 505-513.
211. Yang J.M., Kai W. and Jeng S.M. (1989), *Scripta Metallurgica*, Vol. 23, p. 1953.

194. Vasudevan A.K. and Petrovic J.J. (1992), "A Comparative Overview of MoSi<sub>2</sub> Composites", *Materials Science and Engineering*, Vol. A155, pp. 1-17.
195. Vasudevan A.K., Petrovic J.J. and Sadananda K. (1991), "High Temperature Structural Silicide Composites", in *Proceedings of the 12<sup>th</sup> RISO International Symposium on Metallurgy and Materials Science, Metal Matrix Composites*, Eds. Hanson N., Jensen D.J., Leffers P., Lihlt H., Loren T., Peterson A.S., Peterson O.B. and Ralph B., RISO National Laboratory, Roskilde, Denmark, pp. 707-12.
196. Venkateswara Rao K.T. and Ritchie R.O. (1994), "Fracture and Fatigue Considerations in the Development of Ductile Phase Reinforced Intermetallic Matrix Composites", *Fatigue and Fracture of Ordered Intermetallic Materials I*, Eds. Soboyejo W.O., Srivatsan T.S. and Davidson D.L., The Minerals, Metals and Materials Society.
197. Venkateswara Rao K.T., Odette G.R. and Ritchie R.O. (1992<sup>a</sup>), "On the Contrasting Role of Ductile Phase reinforcements in the Fracture Toughness and Fatigue Crack Propagation Behaviour of TiNb/ $\gamma$ -TiAl Intermetallic Matrix Composites", *Acta Metallurgica et Materialia*, Vol. 40, pp. 353-361.
198. Venkateswara Rao K.T., Soboyejo W.O. and Ritchie R.O. (1992<sup>b</sup>), "Ductile Phase Toughening and Fatigue Crack Growth in Nb Reinforced MoSi<sub>2</sub> Intermetallic Composites", *Metallurgical Transaction A*, Vol. 23A, pp. 2249-2257.
199. Wade R.K. and Petrovic J.J. (1992<sup>a</sup>), "Fracture Modes in MoSi<sub>2</sub>", *Journal of American Ceramic Society*, Vol. 75, pp. 1682-1684.
200. Wade R.K. and Petrovic J.J. (1992<sup>b</sup>), "Processing Temperature Effects on MoSi<sub>2</sub>", *Journal of American Ceramic Society*, Vol. 75, pp. 3160-3162.
201. Wilkinson W.D. (1969), *Properties of Refractory Metals*, Gordon and Breach, New York, NY, p. 53.
202. Xiao L. (1991<sup>a</sup>), "Study of the Flow Behaviour of Constrained Ductile Phases – I. Experiment", *Developments in Ceramic and Metal Matrix Composites*, Ed. Upadhyaya K., The Minerals, Metals and Materials Society, pp. 115-124.
203. Xiao L. (1991<sup>a</sup>), "Study of the Flow Behaviour of Constrained Ductile Phases – II. Modeling", *Developments in Ceramic and Metal Matrix Composites*, Ed. Upadhyaya K., The Minerals, Metals and Materials Society, pp. 359-369.
204. Xiao L. and Abbaschian R. (1992<sup>a</sup>), "Interfacial Modification in Nb / MoSi<sub>2</sub> Composites and its Effects on Fracture Toughness", *Materials Science and Engineering*, Vol. A155, pp. 135-145.
205. Xiao L. and Abbaschian R. (1992<sup>b</sup>), "Role of Matrix / Reinforcement Interfaces in the Fracture Toughness of Brittle Materials Toughened by Ductile Reinforcements", *Metallurgical Transactions A*, Vol. 23A, pp. 2863-2872.